

30 NOVEMBER 1966

FINAL REPORT

ADVANCE STUDY OF AN APPLICATIONS  
TECHNOLOGY SATELLITE (ATS-4) MISSION

National Aeronautics and Space Administration  
Goddard Space Flight Center  
Greenbelt, Md.

FACILITY FORM 602  
N 67-24611  
(ACCESSION NUMBER)  
325  
(PAGES)  
CR-81765  
(NASA CR OR TMX OR AD NUMBER)

(THRU)  
1  
(CODE)  
31  
(CATEGORY)

## FOREWORD

This Final Report describes the results of the various technical studies performed by Lockheed Missiles & Space Company and its subcontractor, Electro-Optical Systems, Inc., on the Advance Study of the Applications Technology Satellite (ATS-4). The study was performed for the National Aeronautics and Space Administration, Goddard Space Flight Center, Greenbelt, Maryland, under contract NASW-1412.



PRECEDING PAGE BLANK NOT FILMED.

## CONTENTS

Section		Page
1	SUMMARY	1-1
	1.1 Introduction	1-1
	1.2 Project Objectives	1-1
	1.3 Project Feasibility	1-3
2	EXPERIMENT DESCRIPTION AND JUSTIFICATION	2-1
	2.1 Large-Aperture Antenna Experiment	2-1
	2.2 Orientation Control Experiment	2-3
	2.3 Phased-Array Experiment	2-6
	2.4 Interferometer Experiment	2-8
3	SPACECRAFT DESCRIPTION	3-1
	3.1 Configuration	3-1
	3.2 Propulsion	3-5
	3.3 Attitude Control	3-6
	3.4 Electrical	3-10
	3.5 Telemetry Tracking and Command Subsystems	3-12
	3.6 Spacecraft Tradeoff and Analysis	3-14
	3.7 Launch-Phase Sequence	3-14
	3.8 Experiment Operational Phase Sequence	3-17
	3.9 Ground Equipment	3-19
4	ASCENT PERFORMANCE AND STATIONKEEPING DEFINITION	4-1
	4.1 Launch-Vehicle Selection	4-1
	4.2 Launch-Vehicle Performance	4-6
	4.3 Injection Errors	4-10
	4.3.1 Atlas/Agena Injection Errors	4-11

Section	Page
4.3.2 Methods of Reducing Corrective Velocity Requirements	4-12
4.3.3 Atlas/Centaur/Kick-Stage Injection Error	4-13
4.3.4 Titan IIC Injection Errors	4-15
4.3.5 Spin-Stabilized Spacecraft	4-18
4.4 Spacecraft Sequence of Events	4-26
4.4.1 Ascent Sequence of Events	4-27
4.4.2 Postinjection Sequence of Events	4-29
4.4.3 Injection Error Correction	4-34
4.5 Ephemeris Determination and Tracking	4-37
4.6 Spacecraft Stationkeeping	4-40
4.6.1 Solar Wind	4-43
4.6.2 Solar Pressure	4-44
4.6.3 Sun's Magnetic Field	4-44
4.6.4 Sun-Moon Perturbations	4-44
4.6.5 Earth Triaxiality	4-45
4.6.6 Micrometeoroids	4-45
4.6.7 Stationkeeping Velocity Requirements	4-46
5 SPACECRAFT DEFINITION	5-1
5.1 Selected Configuration	5-1
5.1.1 General Description	5-1
5.1.2 Equipment Racks and Fabricated Structures	5-4
5.1.3 Equipment Location and Layout	5-6
5.1.4 Thermal Control	5-9
5.2 Alternative Configurations	5-13
5.3 Structural	5-15
5.3.1 Dynamics Analysis	5-16
5.3.2 Equipment List and Weights	5-21
5.3.3 Launch-Vehicle Interface	5-21
5.4 Electrical	5-28
5.4.1 Selected System	5-28
5.4.2 Alternatives Considered	5-28

## Section

## Page

5.4.3	Power Profile	5-31
5.4.4	Solar Array Sizing	5-33
5.4.5	Solar Array Design	5-36
5.4.6	Power Conditioning	5-45
5.4.7	Battery	5-55
5.4.8	Redundancy Considerations	5-70
5.5	Propulsion	5-72
5.5.1	Selected System	5-72
5.5.2	Table of Alternatives	5-77
5.5.3	Injection Motor	5-81
5.5.4	Hydrazine System	5-82
5.5.5	Ion-Engine System	5-85
5.5.6	Resistance Jet System	5-104
5.6	Tracking, Telemetry, and Command	5-113
5.6.1	Command Summary	5-113
5.6.2	Instrumentation Summary	5-117
5.6.3	System Diagram	5-120
5.6.4	Link Calculation	5-128
5.6.5	TT&C Antennas	5-135
5.6.6	Weight and Power Summary	5-135
5.7	Experiment Integration	5-137
5.7.1	Integration Approach	5-137
5.7.2	Orientation Control Experiment	5-138
5.7.3	Parabolic Antenna	5-140
5.7.4	Phased-Array Antenna	5-142
5.7.5	Interferometer	5-143
6	EXPERIMENT DEFINITION	6-1
6.1	Orientation Control	6-1
6.1.1	Selected System	6-1
6.1.2	Alternative Attitude Control Techniques	6-3
6.1.3	Coarse Attitude Control Equipment	6-5

Section		Page
6.1.4	Functional Analytic Description	6-12
6.1.5	Functional Analytic Description – Fine Attitude Control System	6-47
6.1.6	Experiment Operations	6-83
6.1.7	Attitude Control Impulse Calculations	6-89
6.1.8	Attitude Verification	6-95
6.2	Evaluation of Petaline and Flexrib Antenna Concepts	6-99
6.2.1	Flexrib Antenna	6-102
6.2.2	Petaline Antenna	6-116
6.2.3	Instrumentation	6-151
6.2.4	Antenna Feed Description	6-167
6.2.5	Link Calculations, Equipment Descriptions, and Antenna and Feed Weights	6-169
6.3	Phased Array	6-181
6.3.1	Requirements and Objectives	6-181
6.3.2	Study Objectives	6-181
6.3.3	System Comparisons and Tradeoffs	6-182
6.3.4	The LMSC Switched Multiple-Feed System	6-186
6.3.5	The Switching and Electronic System	6-194
6.3.6	Power Link Calculations, Weight Considerations	6-200
6.3.7	Conclusion	6-202
6.4	Interferometer Experiment	6-203
6.4.1	Recommended Interferometer Configuration	6-203
6.4.2	Interferometer Experiment Interfaces	6-206
6.5	Experiment Plan	6-208
6.5.1	Operating Modes	6-208
6.5.2	Orbit Injection	6-209
6.5.3	Deployment	6-209
6.5.4	Operating Checks	6-209
6.5.5	Parabola Contour Measurements	6-211
6.5.6	Interferometer Tests	6-211
6.5.7	Orientation-Control-System Tests	6-211

Section		Page
	6.5.8 Parabolic Antenna Tests	6-212
	6.5.9 Phased-Array Antenna Tests	6-212
	6.5.10 Secondary Experiments	6-213
	6.5.11 Operating Demonstrations	6-213
	6.5.12 Preliminary Test Schedule	6-214
7	GROUND SYSTEM DEFINITION	7-1
	7.1 Hardware Requirements	7-1
	7.2 Software Requirements	7-3
	7.3 System Operation	7-9
	7.4 Existing Stations/Equipments Employed	7-10
	7.5 New Stations/Equipments Required	7-11
8	DEVELOPMENT APPROACH	8-1
	8.1 Development Tasks	8-1
	8.1.1 System Requirements Definition	8-2
	8.1.2 Interface Definition and Control	8-8
	8.1.3 Design Documentation and Change Control	8-10
	8.1.4 Design Reviews	8-14
	8.1.5 ATS-4 Test Program	8-16
	8.1.6 Operations Planning	8-22
	8.2 Critical Developments	8-24
	8.2.1 Criteria for Criticality	8-25
	8.2.2 Spacecraft System Developments	8-25
	8.2.3 Spacecraft Structure	8-27
	8.2.4 Propulsion Subsystem	8-35
	8.2.5 Electrical Subsystem	8-36
	8.2.6 TT&C Subsystem	8-37
	8.2.7 Orientation Control Experiment	8-37
	8.2.8 Parabolic Antenna Experiment	8-38
	8.2.9 Phased-Array Experiment	8-39
	8.2.10 Interferometer Experiment	8-40

Section	Page
8.3 Reliability Plan	8-41
8.3.1 Objective	8-41
8.3.2 Reliability Program Requirements	8-42
8.3.3 Conformance to Proven Practices	8-47
8.3.4 Reliability Engineering	8-47
9 SCHEDULES AND COSTS	9-1
9.1 Program Schedule	9-1
9.1.1 Phase B/C – Project Definition and Design	9-2
9.1.2 Phase D – Development and Operation	9-5
9.1.3 Major Test Hardware	9-6
9.1.4 Major Facilities Requirements	9-8
9.2 Program Cost	9-8

## ILLUSTRATIONS

Figure		Page
2-1	30-ft-Diam. Flexrib Antenna	2-2
3-1	ATS-4 Spacecraft Ascent Configuration	3-2
3-2	ATS-4 Spacecraft Orbit Configuration	3-3
3-3	Block Diagram of ATS-4 Attitude-Control System	3-7
3-4	Block Diagram of ATS-4 TT&C System	3-13
4-1	Launch-Vehicle Selection Parameters	4-2
4-2	Plot of Effectiveness Factor vs. Program Cost	4-3
4-3	Launch-Vehicle Cost Percentage vs. Program Cost	4-4
4-4	Centaur Performance With Existing Kick Motors	4-9
4-5	Effects of Thrust Misalignment on Injection Velocity of a Spin-Stabilized Spacecraft	4-19
4-6	Effects of Thrust Misalignment on Injection-Vector Direction of a Spin-Stabilized Spacecraft	4-21
4-7	Locus of Roll Axis During Burn (Initial Cone Angle = 0 deg)	4-24
4-8	Locus of Roll Axis During Burn (No Thrust Misalignment)	4-25
4-9	Injection-Error Correction	4-36
4-10	Spacecraft Positional Error Geometry	4-39
4-11	Effects of Pointing Accuracy of Satellite Position Errors	4-41
4-12	Allowable Position Error Envelope	4-42
5-1	ATS-4 Spacecraft Orbit Configuration	5-2
5-2	ATS-4 Spacecraft Ascent Configuration	5-3
5-3	Equipment Rack Structure	5-5
5-4	Equipment Rack Installation	5-7
5-5	Sensor Section Equipment Installation	5-8
5-6	Sensor Section Structure	5-10
5-7	Typical Configurations of Selection Matrix	5-14

Figure		Page
5-8	Dynamic Model of ATS-4 Spacecraft	5-17
5-9	Dynamic Modal Analysis	5-18
5-10	Dynamics Analysis Results	5-19
5-11	Solar-Array Structural Deflections vs. Damping Ratio	5-20
5-12	Centaur Weight Performance Using Delta Injection Motor	5-24
5-13	Spacecraft Structural Adapter	5-26
5-14	Alternate Solar-Panel Configurations	5-30
5-15	ATS-4 Power Profile	5-32
5-16	Electrical Layout of One Panel	5-37
5-17	Mechanical Configuration of Folded Array	5-38
5-18	Solar-Array Drive	5-41
5-19	Cylindrical Boom Structural Resonance	5-44
5-20	Power Regulation Alternatives	5-47
5-21	Voltage-Current Characteristics of Regulation System	5-49
5-22	Battery Charger Functional Block Diagram	5-53
5-23	Shadow Time, 24-hr Equatorial Orbit	5-56
5-24	End-of-Charge Voltage as a Function of Charge Current	5-61
5-25	Overcharge Capability of Hermetically Sealed Ni-Cd Cell	5-63
5-26	Ni-Cd Cell Charge Acceptance vs. Charge Rate	5-64
5-27	End-of-Charge Voltage vs. Temperature	5-66
5-28	Memory Effects in Ni-Cd Battery	5-68
5-29	Estimated Cycle Life of Ni-Cd Battery	5-69
5-30	Secondary-Propulsion Functions	5-76
5-31	Delta-Injection Motor, TE-364-3	5-83
5-32	Attitude Control Limit Cycle Behavior	5-89
5-33	ATS-4 Ion-Thruster Location	5-92
5-34	Cesium-Bombardment Ion Engine (Cutaway View)	5-94
5-35	Ion-Engine Cluster Concept	5-96
5-36	Performance of Bombardment Ion Engines	5-98
5-37	Weight of Cesium Reservoir and Neutralizer	5-99



Figure		Page
5-38	Ion-Thruster Weight	5-100
5-39	Power Required for Ion Engine	5-101
5-40	Power Conditioner	5-102
5-41	Ammonia Resistojet	5-107
5-42	Resistojet System Weight vs. Required Impulse	5-108
5-43	Power vs. Thrust Level for Resistojets of $I_{sp} = 200$ sec (First Estimates)	5-110
5-44	Power vs. Thrust Level for Resistojets of $I_{sp} = 200$ sec (Second Estimates)	5-111
5-45	Block Diagram of ATS-4 TT&C Subsystem	5-121
5-46	Primary PCM Multiplexer Block Diagram	5-124
6-1	Block Diagram of Thermopile Edge Tracker	6-9
6-2	Cutaway View of Autonetics G10B Gyro	6-11
6-3	Coarse-Mode Control Loop	6-15
6-4	Coarse-Mode Thruster Locations	6-17
6-5	Gyrocompassing Loop	6-18
6-6	Roll-Axis Response to Pointing Command	6-21
6-7	Pitch-Axis Response to Pointing Command	6-22
6-8	Yaw-Axis Response to Pointing Command	6-23
6-9	Coarse-Mode Limit Cycle Operation	6-26
6-10	Coarse-Mode Operation With Disturbing Torques	6-27
6-11	Coarse-Mode Operation With Horizon-Sensor Noise	6-29
6-12	Coarse-Mode Control System	6-31
6-13	Hybrid Integrator	6-32
6-14	Pulse-Width Modulator Characteristics	6-33
6-15	Inverse Modulation Block Diagram	6-35
6-16	Bode Plot With Real and Complex Second-Order Roots	6-39
6-17	Control System Block Diagram With Single Bending Mode	6-46
6-18	Block Diagram of Fine Attitude-Control System	6-48
6-19	Interferometer Geometry	6-50
6-20	Interferometer Attitude Measurement	6-51

Figure		Page
6-21	Interferometer Direction Cosine Geometry	6-62
6-22	Deadband Operation Under Constant Torque	6-64
6-23	Attitude-Error Probability Distribution	6-65
6-24	Block Diagram of Deadband Selection Logic	6-66
6-25	Attitude vs. Time Plot	6-67
6-26	Deadband Noise Suppression	6-69
6-27	Impulse Bit Control Relation	6-71
6-28	Impulse Bit Controller Block Diagram	6-72
6-29	Digital Approximation to Control Equation	6-75
6-30	Transient-State Bit Control	6-77
6-31	Digital Pseudo-Rate Circuit Block Diagram	6-80
6-32	V-Register Counting Control	6-81
6-33	Adaptive Autopilot Block Diagram	6-84
6-34	Solar-Torque Profiles	6-90
6-35	Star-Field Reader Block Diagram	6-98
6-36	30-ft-Diam. Flexrib Antenna	6-103
6-37	Beginning of Antenna Deployment Cycle	6-109
6-38	Closeup of Guide Shoe and Support	6-110
6-39	Fully Deployed Antenna (20-ft-Diam. Model)	6-111
6-40	Conceptual Design of Cassegrainian Antenna System With $F/D = 0.5$	6-117
6-41	Conceptual Design of Non-Cassegrainian Antenna System With $F/D = 0.5$	6-118
6-42	Furled Antenna Packaged in Launch Shroud	6-119
6-43	Typical Electroformed Structure	6-120
6-44	Flat Layout - Electroforming Mandrel	6-121
6-45	Formed-Petal Electroforming Mandrel	6-122
6-46	Realizable Gain	6-126
6-47	Gain Degradation	6-129
6-48	Gain Degradation With Random Phase Errors	6-130
6-49	Hole Pattern	6-132

Figure		Page
6-50	Petal Specific Weight vs. Thickness	6-134
6-51	Petal Cross Section	6-135
6-52	Area Moment of Inertia	6-136
6-53	Coordinates of ATS-4 Antenna Petals	6-140
6-54	Unfurling Mechanism	6-143
6-55	Lazy-Tong Linkage	6-145
6-56	Petal Latching Mechanism	6-146
6-57	Feed Support Configurations	6-148
6-58	Strain-Gage Instrumentation	6-160
6-59	Strain-Gage Circuit Diagram	6-161
6-60	Schematic of Optical System	6-163
6-61	Detector Output Characteristics	6-164
6-62	30-ft Parabola Spiral Feed Antennas	6-168
6-63	100-MHz Transmitter	6-173
6-64	800-MHz Transmitter	6-174
6-65	2,300-MHz Transmitter	6-175
6-66	7,300-MHz Transmitter	6-176
6-67	1.7- and 2.1- GHz Receivers	6-177
6-68	8-GHz Receiver	6-178
6-69	Diplexing System	6-180
6-70	Normal and Constrained Lenses	6-188
6-71	16 of 256 Positions (Circles Represent 3-db Contours)	6-190
6-72	Lens Bandwidth	6-192
6-73	45-db Lens Array	6-193
6-74	Single-Channel (Two-Beam) Configuration	6-195
6-75	Block Diagram of Switch Multiple-Beam System	6-196
6-76	Preliminary Test Schedule	6-215
7-1	Ground Vehicle Interface	7-2
7-2	Ground Transmitter Configuration	7-7
7-3	Backup-Ascent Telemetry Configuration	7-12

Figure		Page
8-1	ATS-4 Design Change Approval Flow	8-12
8-2	ATS-4 Design Change Incorporation	8-13
8-3	ATS-4 Design Review Phasing	8-15
8-5	Reliability Flow Diagram, Phase I	8-43
8-6	Reliability Flow Diagram, Phase II	8-45
8-7	Reliability Allocation Block Diagram	8-52
8-8	Complexity vs. Failure Rate for Several Values of ATS-4 Reliability for 2 yr	8-55
9-1	Expected ATS-4 Program Schedule	9-3

## TABLES

Table		Page
2-1	Orientation Control Equipment Usage by Flight Mode	2-5
3-1	ATS-4 Weight Performance	3-16
3-2	Major Facility Requirements	3-20
4-1	Spacecraft and Launch-Vehicle Peculiarities	4-5
4-2	Approximate Penalties of Peculiarities	4-5
4-3	SLV-3A/Agena and Titan IIC Performance	4-7
4-4	Weight Performance With Existing Kick Motors	4-8
4-5	Corrective Velocity Requirement, SLV-3A/Agena	4-14
4-6	Centaur Guidance Compensated Parameters	4-15
4-7	Centaur State-Vector Injection Errors	4-16
4-8	Centaur Orbital Element Errors	4-17
4-9	Spacecraft Moments of Inertia	4-22
4-10	Injection Error Comparison, Centaur-Launched ATS-4 Spacecraft	4-26
4-11	ATS-4 Ascent Sequence of Events	4-28
4-12	Longitude Conditions for Synchronous-Orbit Injection	4-30
4-13	Direct Injection Sequences	4-31
4-14	Approximate Orbital-Element Errors vs. Time	4-37
4-15	Perturbations of Synchronous Satellite	4-46
5-1	ATS-4 Weights	5-22
5-2	ATS-4 Weight Reduction From Liftoff to Orbit Injection	5-23
5-3	Peak Power Requirements	5-35
5-4	Solar-Array Weight Breakdown	5-43
5-5	Comparison of Regulation Methods	5-48
5-6	Wet Life of Sealed Secondary Batteries	5-57
5-7	Thruster Alternative Configurations	5-78

Table		Page
5-8	Comparison of Thruster Alternatives for ATS-4	5-80
5-9	Candidate Motors	5-82
5-10	Hydrazine System Weight	5-84
5-11	Disturbing Torques	5-86
5-12	Maximum Total Torques	5-87
5-13	North-South Thrusting Requirements for the 1,800-lb ATS-4	5-91
5-14	Performance and Weight of Separate Ion Thrusters	5-103
5-15	Performance and Weight of Ion Thruster System	5-104
5-16	Propellant Storage and Feed System Weight Breakdown	5-109
5-17	Resistojet Weight and Performance	5-112
5-18	Subsystem Instrumentation Summary	5-117
5-19	ATS-4 Instrumentation Requirements	5-118
5-20	Primary PCM Telemeter Requirements	5-123
5-21	Primary PCM Telemeter Capabilities	5-125
5-22	Instrumentation Allocation	5-127
5-23	4-GHz Down Link	5-129
5-24	6-GHz Up Link	5-132
5-25	136.47-MHz Down Link	5-133
5-26	148.26-MHz Up Link	5-134
5-27	TT&C Size, Weight, and Power	5-136
6-1	Attitude Control System Gyro Candidates	6-5
6-2	Attitude Control System Horizon Sensor Candidates	6-6
6-3	Sources of Error	6-8
6-4	G10B Gyro Error Sources	6-13
6-5	G10B Gyro Performance Errors, g-Sensitive	6-14
6-6	Attitude-Error Sources	6-37
6-7	Ascent Coast and On-Orbit Attitude Errors, Coarse System	6-38
6-8	Orientation for Apogee Motor-Burn Attitude Errors	6-41
6-9	Injection Attitude Errors	6-43
6-10	Impulse-Bit Controller Sequence of Events	6-74

Table		Page
6-11	Impulse-Bit Magnitude and Expected Scallop Period	6-78
6-12	Logic Equations for Deadband Gates	6-82
6-13	Control-System Variable Parameters	6-87
6-14	Orientation-Control Experiment Sequence	6-88
6-15	Attitude-Control System Gas Consumption	6-93
6-16	Attitude Verification Candidates	6-96
6-17	Weight Summary	6-123
6-18	Antenna System Characteristics	6-123
6-19	Open Area	6-131
6-20	Change in Stress for Two Hole Diameters	6-138
6-21	Characteristics, Constraints, and Loading for Petal Structural Analysis	6-141
6-22	Order of Magnitude of Deflection	6-144
6-23	Magnification vs. Feed Height	6-147
6-24	Summary of Computer Run Results	6-150
6-25	Summary of Strain-Gage Specifications	6-161
6-26	Optical System Specifications	6-166
6-27	Parabola Experiments Link Calculations	6-170
6-28	Available Bandwidths	6-171
6-29	30-ft Parabola RF-System Characteristics	6-179
6-30	System Building Blocks	6-198
6-31	Link Gain	6-201
6-32	Weight Estimates	6-202
6-33	Interferometer Error Sources for a 16-Wavelength Baseline and 20-deg Off-Axis Source	6-204
6-34	ATS-4 Interferometer Critical Design Parameters	6-206
6-35	Effects of Equipment Failure on Major Experiments	6-210
6-36	Results of Test Methods	6-214
7-1	Interferometer Link Calculation	7-4
7-2	Phased-Array Up Link	7-5
7-3	Phased-Array Down Link	7-6

Table		Page
8-1	ATS-4 System Requirements Analysis	8-4
8-2	Typical Interface Specification Items	8-9
8-3	Launch-Base Sequence of Operations for ATS-4 Spacecraft	8-23
8-4	Criteria for Identifying Critical ATS-4 Developments	8-25
8-5	ATS-4 Equipment Development Subsystem/Experiment Spacecraft Structure	8-28
8-6	ATS-4 Equipment Development Subsystem/Experiment Propulsion	8-29
8-7	ATS-4 Equipment Development Subsystem/Experiment Electrical	8-30
8-8	ATS-4 Equipment Development Subsystem/Experiment TT&C	8-31
8-9	ATS-4 Equipment Development Subsystem/Experiment Orientation Control	8-32
8-10	ATS-4 Equipment Development Subsystem/Experiment Parabolic Antenna	8-33
8-11	ATS-4 Equipment Development Subsystem/Experiment Interferometer/Phased Array	8-34
9-1	ATS-4 Spacecraft Test Articles	9-7
9-2	Major Development Test Facilities	9-9
9-3	Cost Summary	9-10



## Section 1

### SUMMARY

#### 1.1 INTRODUCTION

The primary purpose of the ATS-4 Program is to demonstrate the employment of large-aperture antennas in conjunction with precision spacecraft stabilization techniques.

In this study, a number of alternatives were studied in the areas of launch vehicles, spacecraft configurations, subsystems, and experiments. Trade studies were performed where the choices were not immediately evident, and a single preferred system was evolved. More detailed studies were performed in some areas to confirm feasibility. A program plan was developed that identified critical elements, and planning cost figures were developed for the total program.

Lockheed Missiles & Space Company was assisted by Electro-Optical Systems in the areas of electric power, electric propulsion, and petaline-type antennas.

The study concluded that the spacecraft and the experiments are feasible, that meaningful experiments and demonstrations can be conducted with a spacecraft placed in synchronous orbit by existing launch vehicles, and that the spacecraft development will advance the state-of-the-art without requiring major inventions for success.

#### 1.2 PROJECT OBJECTIVES

The ATS-4 program will provide a significant step toward the NASA goals of manned and unmanned exploration of space and of the application of earth satellites to promote human welfare.

Specifically, the employment of large parabolic antennas on an accurately stabilized platform will shift the complexity of present-day ground stations to the spacecraft,

permitting communication and navigation services to be offered to a variety of users (ships, aircraft, small ground terminals) who are not able to provide large ground installations.

The large-aperture phased array will increase the flexibility of space operations by permitting rapid switching of communication links among various users. This capability will permit establishment of relay satellites to provide continuous communication with astronauts during critical rendezvous and EVA operations.

A precision, three-axis stabilized platform is a requirement for almost all advanced earth-orbiting missions and will provide the base from which communications relays to deep space will be established. Platform accuracy that will be achieved on ATS-4 will be adequate for many of these missions and will form a development step toward the higher accuracy required for astronomy and laser communication links.

All of NASA's long-range objectives depend on the attainment of long life in satellites and spacecraft. Simple satellites have already demonstrated useful active lifetimes, but ATS-4 will be the first program in which a large actively stabilized vehicle will be operated continuously for 2 or more years.

An additional benefit to accrue from the development and flight of the ATS-4 spacecraft will be the flight qualification of the spacecraft subsystems and equipment. Past experience has shown that the agencies responsible for the development and flight of spacecraft with specific mission objectives are prone to select techniques and equipment which have a demonstrated history of successful flight performance. The urge to advance technology on the flight of a scientific satellite has been made, justifiably, secondary to the desire to successfully complete the scientific mission.

Because such satellites do not breed technological advance, programs such as ATS-4 are necessary to insure that the technological pre-eminence of the national space effort is maintained. Furthermore, it is of importance that the ATS-4 program and other similar efforts achieve the maximum advancement of technology consistent with economic considerations.

In recognition of this need, the area of attitude control of the ATS-4 spacecraft was identified as presenting conflicting requirements. On one hand, the attitude control function is critical to successful performance of the parabolic antenna, phased-array, and interferometer experiments. Because of this dependency, the techniques and equipment used for attitude control should be flight-proven and representative of the best of current technology. On the other hand, the mission of the ATS-4 program is to advance technology which would dictate a control system design which would provide a significant technological advance.

In view of this conflict, it would appear desirable to provide two independent, but complementary, attitude control systems; one system representing a flight-proven configuration, the other composed of experimental hardware. This approach has a further benefit in that it provides redundancy in the attitude control function which helps in assuring that the 2-yr lifetime requirement is met.

The ATS-4 program will also contribute to technology by providing instrumented orbital tests of a variety of advanced components, such as ion engines, adaptive autopilots, and interferometers.

### 1.3 PROJECT FEASIBILITY

The results of the ATS-4 study program conducted by LMSC and Electro-Optical Systems indicate that the requirements for the ATS-4 mission can be met with a high degree of certainty, although several general areas have been identified that will require intensive effort to provide maximum confidence in meeting all mission objectives.

The first area of concern is the requirement for 2-yr lifetime of the spacecraft. To evaluate the configuration selection, a reliability analysis was performed. As a postulated reliability requirement, a goal of 0.91 probability of at least one of two spacecraft surviving for 2 yr was selected. This goal requires a 2-yr reliability of 0.70 for an individual spacecraft. In reviewing the reliability of the selected configuration, it is evident that the use of redundancy and backup equipment is necessary in the attitude-

control, telemetry and command, and electrical power subsystems to achieve space-craft reliability goals. In certain areas, even the use of multiple-redundant equipment is not sufficient to meet the reliability goal if currently available equipment using state-of-the art components is used. For this reason, it is recommended that the component parts assembled into ATS-4 equipment be subjected to a rigorous reliability testing program. The use of parameter-drift screening techniques now in use on the Minute-man programs is strongly recommended for ATS-4 parts.

The requirement for  $\pm 0.1$ -deg pointing accuracy made necessary by the narrow beam-width of the 30-ft reflector when operated at X-band provides a second area requiring intensive investigation. The recommended spacecraft configuration incorporates a unique adaptive autopilot concept which, when used with the radio-interferometer, will provide the required control accuracy. Other factors affecting the necessary precision of antenna pointing are equipment mechanical alignment, structural deflections caused by thermal effects and the application of control forces, and the coupling of structural resonances into the control-system dynamics. The foregoing items, while requiring attention, appear amenable to solution by straightforward techniques. The recommended configuration contains provisions for aligning the various attitude sensors relative to the spacecraft axes and to each other by means of accurately referenced mounting surfaces. Application of analytic and design effort in the area of structural deformations under thermal and dynamic loading can assure that alignment errors resulting from those sources are held to acceptable values. LMSC is studying the structural resonance problem by evaluating various techniques of supplying structural damping (nonhomogeneous boom materials and energy-absorbing joints and fittings) and by limiting the upper cyclic frequencies of control-force application by means of the adaptive autopilot control logic.

In summary, it can be stated that the control-system development is critical to the success of the ATS-4 spacecraft. While this is true, the results of LMSC's study indicate that the problems existing in this area can be solved with careful attention to detail.

Certain of the ATS-4 experiments will be delivered to the spacecraft contractor as Government-furnished equipment. For this reason, extensive system engineering effort will be required on the part of the spacecraft contractor and NASA/GSFC to assure spacecraft/experiment interface compatibility. LMSC recommends that extensive testing be performed to provide experimental demonstration that such interface compatibility has been achieved. In particular, because of the quantity of radio-frequency equipment required for this mission, as well as the number of potentially interference-sensitive attitude sensors, rigid procedures for control electromagnetic interference must be established and electromagnetic compatibility demonstrated by test are recommended.

In the area of equipment developments, LMSC has identified specific items as critical equipment. Four criteria were used in identifying these items:

- Developments that require a state-of-the-art advance beyond currently developed flight hardware
- Equipment that requires more than 18 mo for development of flight-qualified hardware
- Equipment requirements for which alternate solutions are possible requiring further evaluation and selection
- Equipment for which demonstration of qualification to the flight environment is difficult

Examples of equipment meeting one or more of these criteria are: ammonia-resistance jet and ion-engine thrusters, solar-array drive mechanisms, electronic assemblies for orientation control, and the 30-ft parabola and antenna feed assembly. Techniques recommended for assuring successful development of such items include extensive analysis and simulation, breadboard evaluation and testing, extended life testing, and overstress testing.

A detailed discussion of the critical areas of the ATS-4 system development and recommended development approaches is contained in Section 8.

## Section 2

### EXPERIMENT DESCRIPTION AND JUSTIFICATION

#### 2.1 LARGE-APERTURE ANTENNA EXPERIMENT

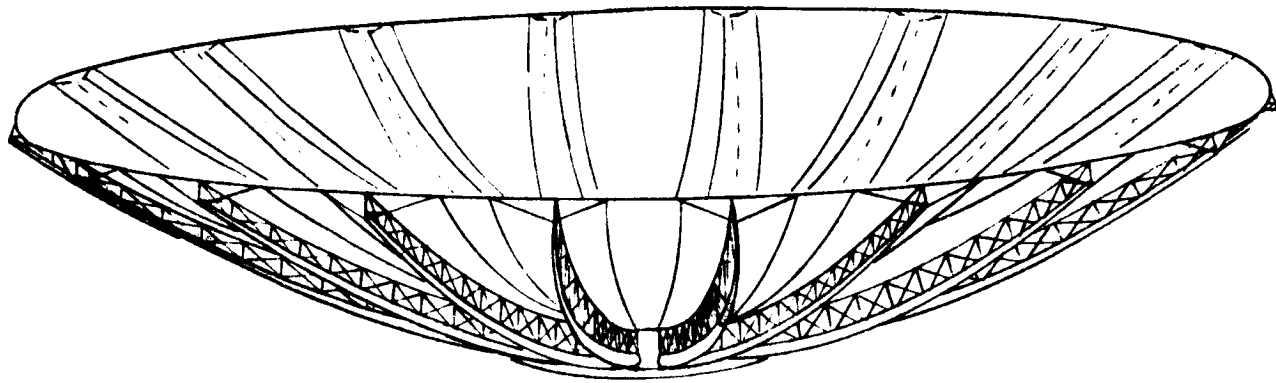
Present communication satellites use simple, low-gain antennas on the spacecraft and require sophisticated ground systems for their operation. Many communication services are limited to simple ground stations and must shift the complexity to the relay satellite. Aircraft, ships, satellites, meteorological sensors, and home receivers are examples of these services.

Many large parabolic ground antennas have been built, and the techniques for achieving the required tolerances are well known. Large space parabolas, however, impose two new problems: the necessity for erection in space, and the achievement of close tolerances on extremely lightweight structures.

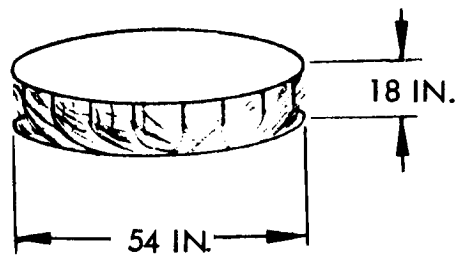
This experiment will develop the best way to solve these problems for an antenna of a size and frequency coverage suitable for many specialized communications applications. Techniques for packaging to fit within allowable shrouds and to survive the ascent environment will be demonstrated. Instrumentation will be developed to measure the contour of the parabola on orbit (along with temperature and strain measurements) to permit comparisons among ground tests, analysis, and on-orbit performance.

The 30-ft flexrib parabola (Fig. 2-1) chosen for the ATS-4 consists of 20 ribs of open-truss construction torsionally stiffened by elliptical sections. To the interior of the rib surface is attached a reflecting skin. The ribs are stiffened thin section which, when furled, are tightly wrapped about a center hub or drum.

When furled, the antenna is wrapped into a package 4.5 ft in diameter and 1.5 ft deep. There is a 1-ft-diam. open cylindrical section in the center of the drum. Power to



OPEN



FURLED

Fig. 2-1 30-ft-Diam. Flexrib Antenna

deploy the antenna is provided by a 0.25-hp electrical motor that drives a ring gear to turn the drum and force the ribs outward.

The flexrib design combines excellent furled-to-unfurled dimensional ratio, can be relatively light in weight, and has few dynamic or environmental problems when in the stowed position during ascent, since the wrapped ribs and skin are very densely packed. Details are reported in subsection 6.2.

Optical measurements of the parabola and feed system would be conducted as follows:

- Measure contour at approximately 3-hr intervals for 24 hr to evaluate thermal effects.
- Measure critical points while attitude thrusters are operating.
- Measure critical points while stationkeeping thrusters are operating.

The following electrical tests should be accomplished:

- Evaluate the electrical performance of the antenna system and verify by RF power measurements the ability of the orientation-control system to direct the antenna beam.
- Measure antenna gain, boresight direction, and beamwidth for each specified frequency by angular displacement of satellite platform.
- At the highest frequency, determine stability of gain and pointing direction with respect to thermal effects, attitude-thruster torques, and stationkeeping forces.
- Verify ability of the system to point at fixed targets and to "command-track" moving targets by direct measurement of signal strength in the communication links.

## 2.2 ORIENTATION CONTROL EXPERIMENT

At the initiation of the ATS-4 study, LMSC determined that the performance of the attitude control system of the spacecraft was critical to the performance of the parabolic reflector, phased-array, and interferometer experiments. For this reason, it



was decided to provide a control system whose components and techniques would be demonstrated in flight before the first launch of ATS-4. The system configuration selected provides an integrated approach to attitude control by using the same equipment for the transfer orbit coast, orbit injection, and on-orbit operation.

This basic system will provide a high assurance of meeting the performance requirements imposed by the ATS-4 mission; however, it does not provide an extensive advance in technology. For this reason, LMSC recommends that an experimental control system be developed for flight on the ATS-4 mission.

A concept was developed of a system configuration which would extend the technology of mass-expulsion control systems into the area of high-accuracy, long-life satellites, and which would also provide an operational evaluation of the radio interferometer in a control loop. This system concept utilizes the interferometer as the attitude reference (an adaptive autopilot which optimizes the frequency of attitude control impulse firing in relation to the allowable attitude error) and cesium bombardment ion thrusters to provide control torques.

Both systems are discussed further in Section 3 and are covered in detail in subsection 6.1. The equipment used in the various flight modes is given in Table 2-1.

The following procedures should be followed in testing the orientation-control system:

- Use the primary attitude sensor (star-field sensor) as a reference to calibrate the horizon sensor and interferometer.
- Measure thruster fuel/power consumption, duty cycle, and attitude error as a function of deadband settings.
- For optimum deadband setting, monitor thruster performance and attitude error over a 24-hr period.
- Determine effect of stationkeeping propulsion on attitude error.
- Determine time to reduce errors to tolerance after change in attitude of up to 17 deg.

Table 2-1

## ORIENTATION CONTROL EQUIPMENT USAGE BY FLIGHT MODE

Flight Mode	Attitude Reference	Signal Processing	Actuation System
Transfer Orbit Coast	Horizon Sensor, Gyros	Hybrid Integrator, Pulse-Width Modulator	Ammonia Resistance Jets
Reorientation for Injection Burn	Gyros	Hybrid Integrator, Pulse-Width Modulator	Ammonia Resistance Jets
Injection Burn	Gyros	Hybrid Integrator, Pulse-Width Modulator	Hydrazine Thrusters
Injection Error Correction/Station Acquisition	Gyros	Hybrid Integrator, Inverse Modulator	Hydrazine Thrusters
Orbit (Coarse Mode)	Horizon Sensor, Gyros	Hybrid Integrator, Pulse-Width Modulator	Ammonia Resistance Jets
Orbit (Fine Mode)	Interferometer, Yaw Gyro or Attitude Computer	Adaptive Autopilot	Cesium Bombardment Ion Engines

- Measure attitude error when responding to a commanded rate of up to  $10^{-2}$  radians/min.
- Repeat for the experimental attitude-control system.
- Analyze attitude and stationkeeping thruster operation to validate assumptions regarding perturbing forces.
- Interchange sensors and thrusters between control systems.

### 2.3 PHASED-ARRAY EXPERIMENT

Electronically steered or phased arrays offer the possibility of high gain and narrow beamwidth without the necessity for mechanical motions or reorientation of the spacecraft. If pilot-tone schemes are used to direct the beams, tolerances may be relaxed on the orientation of the space platform and gravity gradient stabilization methods become applicable at synchronous altitudes.

Although phased arrays have been used in ground applications, particularly for radar, they must be considerably simplified and reduced in weight and power to make them suitable for multibeam space communications. This experiment will evolve the best way to adapt phased-array techniques to spacecraft and will demonstrate their utility for satellite relay communications.

The purpose of the ATS-4 phased-array experiment is to demonstrate the feasibility of a synchronous satellite communications system using a high-gain, electronically steerable array with multibeam capability. To achieve this purpose the experiment must demonstrate the following:

- Deployment of the phased-array system
- Alignment of the array to the reference axes
- Steering of the array beams to within 0.1 deg of the direction of desired fixed or mobile ground stations by purely electrical means (without physical motion)
- Tracking of the ground stations (either by self-tracking or by command) at rates and accuracies compatible with the satellite stabilization system
- Acquisition of the desired signals
- Multibeam capability

Two approaches to the experiment were studied. The first is the Hughes system under development for NASA/GSFC. The second approach is a concept developed at LMSC.

The Lockheed phased array is an outgrowth of earlier LMSC studies of scanning and beamwidth control in array systems. It takes advantage of the fact that only limited scan ability is needed to provide full earth coverage from synchronous altitude. A metallic lens is used to constrain the beamwidth and to establish the system gain. Scanning is accomplished by electronic switching of the feed assembly. Details are reported in Section 6.

The LMSC array can operate in either a command or a pilot-tone mode. For the command mode, the following tests should be performed:

- Measure gain, boresight direction, and beamwidth of each transmit and receive beam by angular displacement of the satellite platform.
- Measure interaction and cross-talk among beams.
- Demonstrate simultaneous capability of four beams when commanded to four ground stations.
- Show ability to maintain required gain when "command-tracking" a moving target.
- Demonstrate ability to maintain operation by means of a ground-command loop during attitude oscillations such as might occur with a gravity-gradient system.
- Determine limitation on a fast-scan operational mode for possible application to readout of ground or airborne sensors.

For the pilot-tone mode, the following tests apply:

- Verify antenna gain, boresight direction, and beamwidth of each transmit and receive beam by off-setting the pilot-tone direction, using a number of separated ground transmitters, or using a pilot-tone transmitter in an aircraft.

- Demonstrate simultaneous transmission and reception on four beams under control of pilot tones.
- Evaluate susceptibility of pilot tones to capture by unintentional interfering sources.
- Demonstrate ability to maintain communications during angular oscillations of satellite platform.

## 2.4 INTERFEROMETER EXPERIMENT

Sensors for spacecraft attitude determination have generally measured the earth's horizon or the direction to the sun or to a star. There are several applications where it would be useful to reference the spacecraft attitude to a radio emitter to provide precise pointing to the object of the communication. This technique could be useful, for example, in tracking another satellite or a space probe.

Several techniques exist for determining the direction to a radiating source; of these, the interferometer is the most accurate. Interferometers are commonly used in ground based instrumentation to determine the direction to space objects, their use as an onboard attitude reference is new.

The experiment will develop an optimum design for the interferometer, will evaluate its accuracy in orbit by comparison with a star-field scanner, and will compare several modes of operation.

The initial consideration in determining the recommended experiment configuration was that of accuracy and ambiguity resolution. The measurement accuracy of the interferometer is a function of the antenna spacing in wavelengths. A spacing of two wavelengths will provide nonambiguous readout of attitude angle for a range of approximately 15.5 deg. This is of the order of magnitude of the angle subtended by the earth when viewed from synchronous altitude.

To provide 0.1-deg (attitude) accuracy with a phase measurement accuracy of  $\pm 1.0$  deg (electrical), a baseline of 1.6 wavelengths is required. Since the phase-resolution error is only one component of the total error, a 16-wavelength baseline should be incorporated in addition to the two-wavelength baseline to limit the total output error to approximately 0.02 deg (three sigma). The results of a detailed error analysis are given in Table 6-33.

Interferometer reference signals are generated by a beacon transmitter provided for this purpose at each ATS-4 ground station. The selected frequency of operation is 5 GHz, which is separated in frequency from other vehicle radiations. A 1-kw transmitter and a 10-ft-diam parabolic antenna provide the required beacon signal. This radiated power provides a 6.5-db carrier-to-noise ratio with a 1-MHz IF bandwidth and 8-db noise figure. Details of the ground equipment and link-gain calculations are given in Section 7. The ground system uses a fixed antenna that must be positioned in angle to within  $\pm 0.4$  deg. Vehicle antenna operation is possible with an orientation between the antenna boresight and incoming ray vector of  $\pm 17$  deg. The following procedure should be followed in testing the interferometer system:

- Calibrate the interferometer, using a star-field reader with ground reduction of star data.
- Repeat calibration over a 24-hr period to evaluate thermal distortions.
- Measure transfer characteristic and determine angular limits of operation.
- Verify ability to command biases in sensor error signal.
- Demonstrate ability of interferometer to provide position fixes on selected ground transmitters.

## Section 3 SPACECRAFT DESCRIPTION

### 3.1 CONFIGURATION

The ATS-4 vehicle (Figs. 3-1 and 3-2) consists of a group of structural forms comprising an equipment section, a sensor section, a parabolic antenna drum, and boom-mounted equipments including the solar arrays, antenna feed, and phased array.

The vehicle is mounted on an adapter section which is 5 ft in diameter at the Centaur mounting ring and 41 in. diameter where it mates to the equipment section. The adapter contains the explosive bolts and springs for separation of the vehicle. The largest structural member is the equipment section rack that is 84 in. in diameter, and has a 57-in. diameter interior cylinder in which the injection motor is housed. The rack is constructed of magnesium alloy rings, stiffeners, and panels.

To the forward face of this rack is mounted the hub, or drum, of the 30-ft flexrib antenna. The two solar-array extension booms are attached to spring-hinge fittings which mount to the forward exterior ring of the rack. For ascent, the booms attached to these fittings, and the folded solar-array panels and rotation motors at the ends of the booms, are folded forward within the 15-deg shroud cone.

Immediately forward of the flexrib antenna drum is the sensor section rack. This rack is extended axially after orbit injection by the tri-beam device, and stiffened by two folding tubular struts.

In the ascent mode, the solar-array panels are stowed in fittings on the forward face of the sensor section. The phased-array experiment is mounted on the exterior of the vehicle along the X-X axis, and is extended by a tri-beam device mounted within an interior compartment.

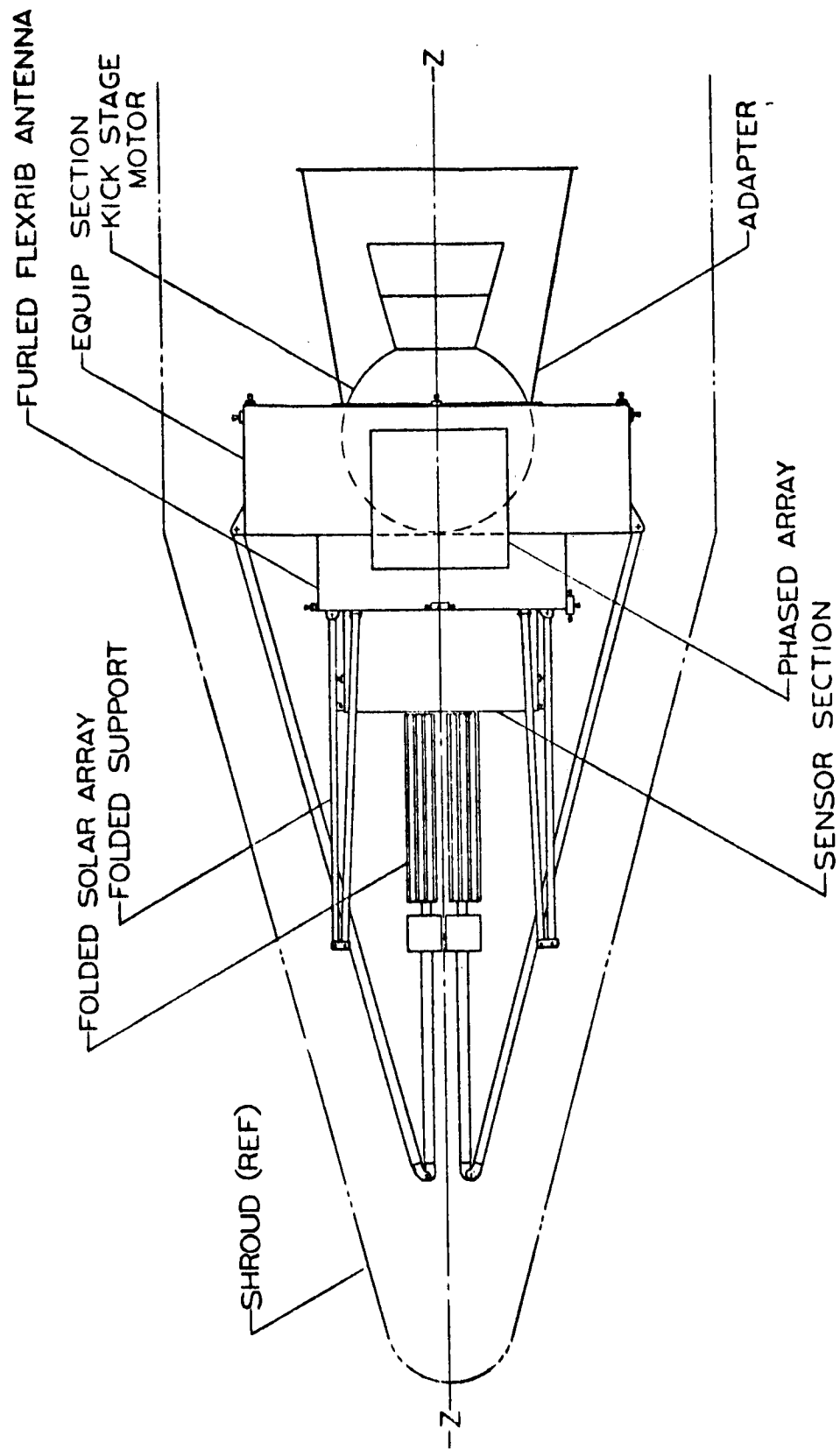
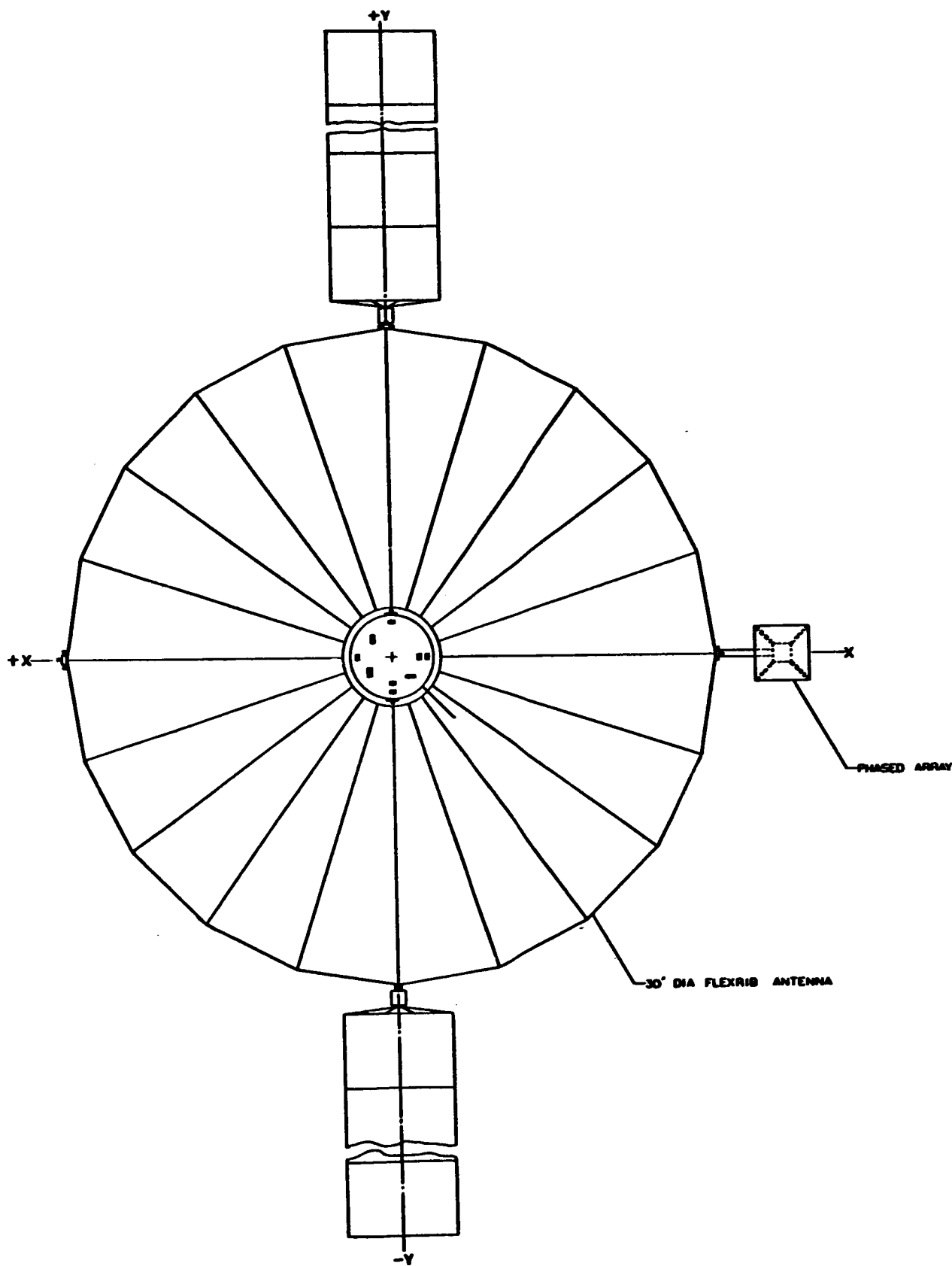


Fig. 3-1 ATS-4 Spacecraft Ascent Configuration





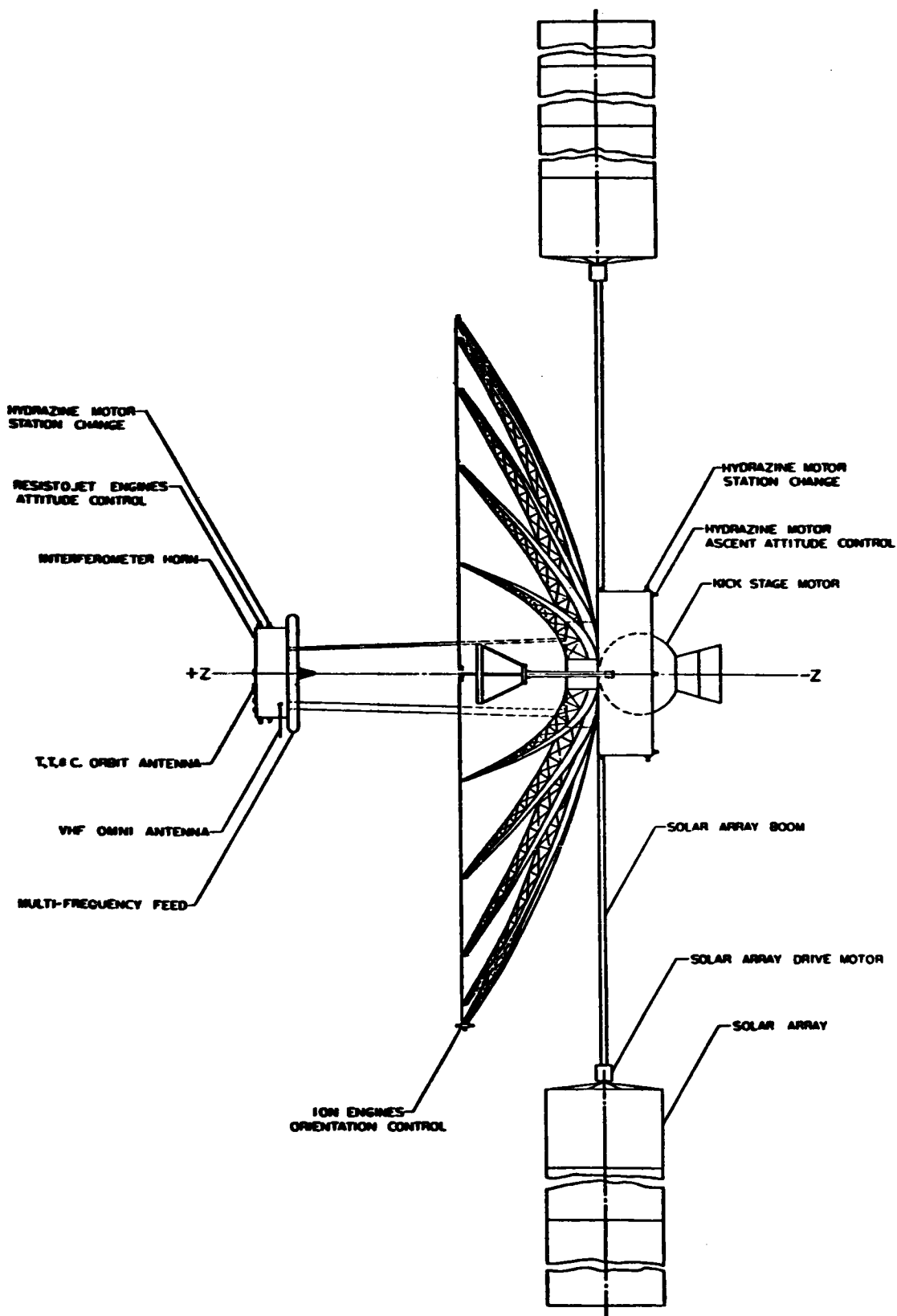


Fig. 3-2 ATS 4 Spacecraft Orbit Configuration

The equipment section contains two hydrazine monopropellant tanks with associated plumbing and regulators, secondary batteries, power-regulation equipment, main wiring harnesses, TT&C equipment including the low-frequency transponders for the parabola experiment, special instrumentation for antenna evaluation, and tri-beam extension device for the phased-array experiment. The sensor section, which is extended by the tri-beam device, houses the ammonia storage tank for the resistance-jet attitude control system, hydrazine tank for the orbit translation motors, two transponders and receivers for the parabolic antenna experiment, complete interferometer unit, attitude control sensors including gyro package, horizon sensor, flight control electronics, and tri-beam machine for extension of the unit. The sensor section also have provisions for mounting the feed for the parabolic antenna.

### 3.2 PROPULSION

The propulsion system consists of the TE-364-3 improved Delta-rocket motor assembly for orbit injection, a monopropellant hydrazine system for attitude control during injection motor burn and for station acquisition and injection-error corrections, a set of cesium ion engines for attitude control and stationkeeping, and a backup attitude control system using ammonia resistance jets. The resistance-jet system is also used for three-axes control during the ascent-coast period.

Hydrazine System. The ATS-4 vehicle designed by LMSC contains all the sensor subsystems necessary for three-axes control on orbit. These units (horizon sensor, inertial reference gyro package, etc.) can be used for three-axes stabilization during the ascent coast period and the kick-stage burn, thus negating the requirement for spin stabilization with its concurrent problems of precise mass moment management, spin and de-spin systems, active nutation control, heavy spin-table adapters, and restrictive control on secondary payloads. The equipment section contains the hydrazine tankage and thrusters to provide attitude control during kick-stage burn. There are four 60-lb thrust motors for pitch and yaw control, and four 1-lb motors for roll control. The equipment section also mounts two additional 1-lb-thrust motors which, in combination with two additional 1-lb thrusters in the lower sensor section, provide the capacity for injection error correction, station acquisition, and station change. This system was selected from a matrix analysis because it provided the most efficient means of attitude control during kick-stage burn, and the quickest possible means of acquiring the synchronous station.

Cesium Ion-Engine System. The requirement for 0.1-deg attitude control in a static as well as maneuvering mode, the 2-yr orbit lifetime, and the desirability of extending the technology of mass expulsion systems led to the choice of cesium ion engines for orbit attitude control and for stationkeeping. The engines are located on the periphery of the deployed 30-ft antenna, thrusting through the deployed vehicle c. g. There are four clusters of three motors each, with each cluster containing two 250- $\mu$ lb thrusters and one 500- $\mu$ lb thruster. These thrusters provide pitch, roll, and yaw attitude control, and NS-EW stationkeeping. Two of the 12 thrusters are redundant and are normally held in a reserve mode.

Ammonia Resistance-Jet System. The ammonia resistance-jet system is completely separate from and redundant to the ion-engine system and is used for attitude control backup. It has the primary attitude control function during the ascent coast phase. The entire ammonia resistance-jet system is located in the sensor section of the vehicle. It consists of a low-pressure ammonia tank and six thrusters of 2 mlb each mounted in two clusters. There is sufficient ammonia capacity to provide complete backup attitude control including maneuvers for the 2-yr projected orbit life.

### 3.3 ATTITUDE CONTROL

Lockheed has recommended a unique approach to solving the attitude control requirements for the ATS-4 mission. The approach taken was to use common equipment in each of the various modes (i. e., transfer orbit coast, injection motor burn, and synchronous orbit operation) wherever possible. In addition, an alternate control system channel has been recommended to provide for a technological advance and to provide the system redundancy necessary for 2-yr orbit life. A block diagram of the system is shown in Fig. 3-3.

The control system recommended for the multimode operation is referred to as the "coarse mode" system. It consists of a wide-altitude range horizon sensor and an inertial reference assembly consisting of three two-degree-of-freedom gas-bearing gyros (miniaturized versions of the Minuteman gyros) as attitude references. The

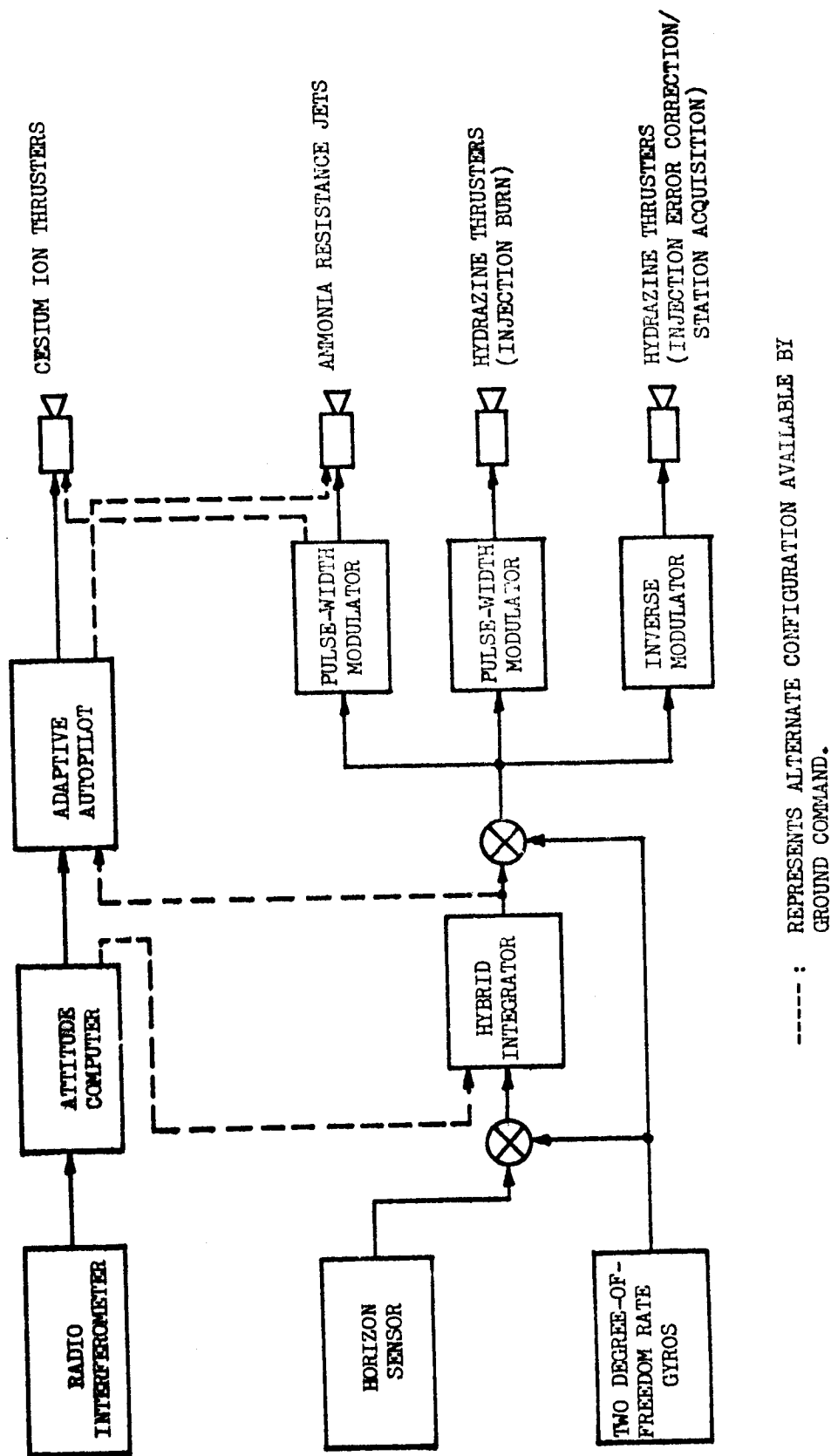


Fig. 3-3 Block Diagram of ATS-4 Attitude-Control System

horizon sensor provides pitch and roll error signals during coast and orbital operation. A yaw reference is maintained by injecting the sensor roll error signal into the yaw channel in a fast-response form of gyrocompassing. The gyro outputs which are proportional to the spacecraft inertial rates are summed with the horizon sensor outputs and integrated by a hybrid (analog-digital) integrator to provide a position error signal. The position error signal for each channel is summed with the appropriate gyro rate signal and is used as an input to a modulator/driver threshold circuit which commands control torques generated by 2-mlb ammonia resistance jets. The coarse control system is used in its entirety during the transfer orbit coast and for synchronous orbit operation. For operation during the injection phase, the horizon sensor outputs are removed from the control loop, which changes the control system coordinates from orbit-fixed to inertially-fixed. In the inertial mode, the spacecraft attitude is maneuvered to the proper injection burn orientation, before the injection burn phase, by using the resistance-jet thrusters to provide the necessary torques. While the injection motor is thrusting, the spacecraft is also inertially stabilized using hydrazine monopropellant thrusters to provide control torques. The control system is operated in the inertial mode also during the firing of pairs of small hydrazine thrusters used to provide the injection error correction and station acquisition velocity increments. These thrusters, which are located symmetrically above and below the spacecraft c.g., are operated in a self-compensating mode (inverse modulation) to correct attitude errors caused by differential thrust levels, thrust misalignment, and lever-arm uncertainty. In the inverse modulation mode, both thrusters are on until a significant attitude error develops; at that time, the appropriate thruster is turned off to counteract the attitude error.

The coarse system is thus capable of providing ascent, injection, and orbital control with a high degree of equipment commonality. As the term "coarse mode" implies, it is less accurate (pitch, roll:  $\pm 0.2$  deg; yaw:  $\pm 0.9$  deg) than is required for X-band operation of the parabola experiment. To provide the necessary accuracy ( $\pm 0.1$  deg), a "fine mode" control system using the interferometer (as an attitude reference), an adaptive signal processor, and cesium bombardment ion thrusters have been recommended.

Operation of the interferometer with either a single ground station or with two stations has been considered. The use of two ground stations permits the derivation of yaw attitude errors in addition to pitch and roll if a simple, onboard digital computer is used. The recommended adaptive signal processing technique uses digital techniques to solve a unique control equation which optimizes the size of the control impulse bits so as to minimize the number of thruster cycles consistent with the allowable attitude error.

Cesium bombardment ion engines were selected to provide control torques. Use of ion thrusters would provide technological growth in an area that will permit the extension of existing control system technology into the field of long-life synchronous satellites. Current experience with low-altitude satellites indicates that attitude control propellant usage rates of 0.25 lb/day of nitrogen are obtainable. The reduced torque levels and increased lever-arm lengths to be experienced with the ATS-4 spacecraft, in combination with the two-order-of-magnitude improvement in specific impulse provided by ion engines, permit the extension to long-life satellites of control system techniques developed for low-altitude, limited-life vehicles.

It should be noted that the fine-control system contains no mechanical moving parts. In particular, the ion thrusters are essentially valveless, relying upon evaporation of liquid cesium to control propellant flow.

The technology advances presented by the recommended experimental configuration are as follows. First, the fine mode system provides the capability of evaluating the use of a radio-interferometer as an attitude sensor in a control loop, of determining the performance of a unique form of adaptive controller, and of demonstrating the feasibility of using ion thrusters as control actuators on a long-life satellite. Second, the coarse mode control system development would provide NASA with a standardized attitude control subsystem package with flexibility to permit its use on later spacecraft. In addition, the coarse-mode system represents a minimum risk approach to meeting the bulk of the ATS-4 mission requirements. This approach provides maximum assurance that the other ATS-4 experimental goals will be fulfilled.

An experimental program has been recommended by LMSC for the control system experiment. There are four basic phases to the experimental plan:

- The horizon sensor and interferometer accuracies will be calibrated against a star-field reader which will be the primary attitude reference.
- The performance of both the coarse and fine mode control systems will be evaluated for control accuracy and impulse expenditure. In this phase, various control system parameters (e.g., gains, deadband limits, time constants, etc.) would be varied and the effects of the variations analyzed.
- Several alternate control system configurations are possible by interchanging attitude sensors and torque actuators between the two control systems. These alternate configurations will be evaluated to determine their comparative performance.
- Variations in the spacecraft parameters will be made. Such variations would include varying the spacecraft solar-torque profile by deploying a solar sail, varying the moments of inertia by extending booms, and applying constant disturbing torques. The results of analytical studies would be verified by these operations.

### 3.4 ELECTRICAL

Selected System. The selected power system consists of a pair of conventional symmetrically deployed solar array panels mounted on booms, a set of array tracking motors, nickel-cadmium secondary batteries, and power conditioning equipment. Initial sizing is based on a 900-w peak power requirement to the end of the first year of operation. The solar cells selected are N/P, 2 cm by 2 cm, 12 mils thick, with a 6-mil  $\text{SiO}_2$  coverglass.

Solar Arrays. The solar array will be  $135 \text{ ft}^2$  in area and will weigh approximately 162 lb. The array will consist of two panels, each 5 ft by 13.5 ft, consisting of four subpanels, each 5 ft by 3.375 ft. The panels will be folded into an 8-in. width. The subpanels will be fabricated from 0.5-in. aluminum honeycomb with a 0.005-in. aluminum facing and a 1.25-in. aluminum structural support member.



The array will be driven continuously by a DC motor operating an enclosed harmonic drive. An intermediate rotating sleeve will provide a bearing rotational speed and a slip-ring surface speed high enough to prevent cold welding and low enough to prevent excessive wear.

The arrays and motor drives will be extended on prefabricated triangular booms. These booms are similar to the boom extended by the tri-beam device. The booms are spring loaded for extension and damped during extension by hydraulic dampers which have been successfully used by LMSC on previous programs.

Batteries and Power Conditioning. Nickel-cadmium batteries will provide power during solar occultation and during ascent and solar acquisition. The array is sized to meet peak-power demands and the batteries will not be used for power smoothing during normal sunlight operations.

The recommended charging technique for the Ni-Cd battery is a constant current charge with a float charge at a very low constant-current rate. Full charge can be determined by measuring both battery temperature and voltage. The solar array voltage will always be higher than the battery voltage, therefore a step-down type of charger can be used. For maximum efficiency, a series-switching charger was selected. Three command inputs have been included in each charger to add a capability for ground control. Although normally not needed, these commands allow a high degree of control flexibility in the event of a charger or battery failure. Two other control circuits are included to inhibit charging during conditions of high temperature and low array voltage.

Three types of batteries were considered for the ATS-4 mission; silver-zinc, silver-cadmium, and nickel-cadmium. Of the three, the Ni-Cd battery has found the greatest application for space missions. The cycle life (in many thousands of cycles) has been achieved on short-cycle applications. The wet stand of these batteries at 75° F far surpasses the mission lifetime requirement. Ni-Cd batteries were therefore chosen as the only type readily meeting mission requirements.

Two basic methods of power regulation are adaptable to the mission: active shunt regulation and series regulation. Passive shunt regulation (with zener diodes) was not considered because of associated high thermal loads. A shunt regulator can operate on either the entire array or only on a portion. Shunt regulation of the battery causes excessive drain, so a separate series regulation is required for battery operation. A series regulator can operate in a continuous DC mode or in a switching mode. The efficiency for the switching mode is approximately 90 percent, while in the DC mode efficiencies can be as low as 50 percent, for a two-to-one input voltage variation.

The series-switching regulator operates more efficiently over a wide range of power levels. At low power levels, excessive power and heat must be dissipated through the shunt-regulator dissipating resistors. Because of these factors, a series-switching regulation method was selected for the ATS-4 power system.

### 3.5 TELEMETRY TRACKING AND COMMAND SUBSYSTEMS

The vehicle TT&C subsystem consists of primary and backup equipment. The primary TT&C transponder configuration consists of a 6-GHz receiver and a 4-w, 4-GHz transmitter of the type used on earlier ATS experiments. Command decoding is performed by 216 redundant command AVCO multitone decoders of the type developed for the ISIS program. Command requirements are for 188 discrete commands, and an additional spare capability of 28 commands is provided. Primary telemetry is of PCM format and provides analog and digital inputs. Instrumentation requirements are for 615 analog points and the allocation provides for 175 spares. Digital readout of 566 bits is required and an additional 74-bit spare capability is provided. These instrumentation inputs are accommodated on a 256-channel main multiplexer and three 256-channel submultiplexers. Supercommutation provides sample rates from 1024 sps down to 0.25 sps. The resulting composite main frame rate is 131 kbps/sec. Backup TT&C equipments include ground-station-compatible VHF units consisting of a 2-w, 136-MHz transmitter and a 148-MHz AVCO tone receiver. Range and range rate tracking is provided by both the primary and backup transponders. The backup telemeter capability is limited to ascent performance and failure diagnostic instrumentation. The VHF down

link is limited to a bit rate of 192-bps and radiates via an omnidirectional antenna. In the event of primary transmitter failure, the primary telemetry clock rate is reduced to 192 bps and transmitted via the VHF link. This limits primary experiment data to low-response or static data when operated in this failure mode. The backup command receiver addresses the same redundant command decoders. An additional capability for magnitude or digital word commands is provided. These commands are loaded by the normal discrete commands into serial registers in the primary telemetry unit. All TT&C equipment is compatible with ground station capability except the high-data-rate PCM telemetry required for experiment instrumentation. These equipments are all existing qualified units with the exception of the mission-peculiar primary telemetry. A block diagram of the TT&C system is shown in Fig. 3-4.

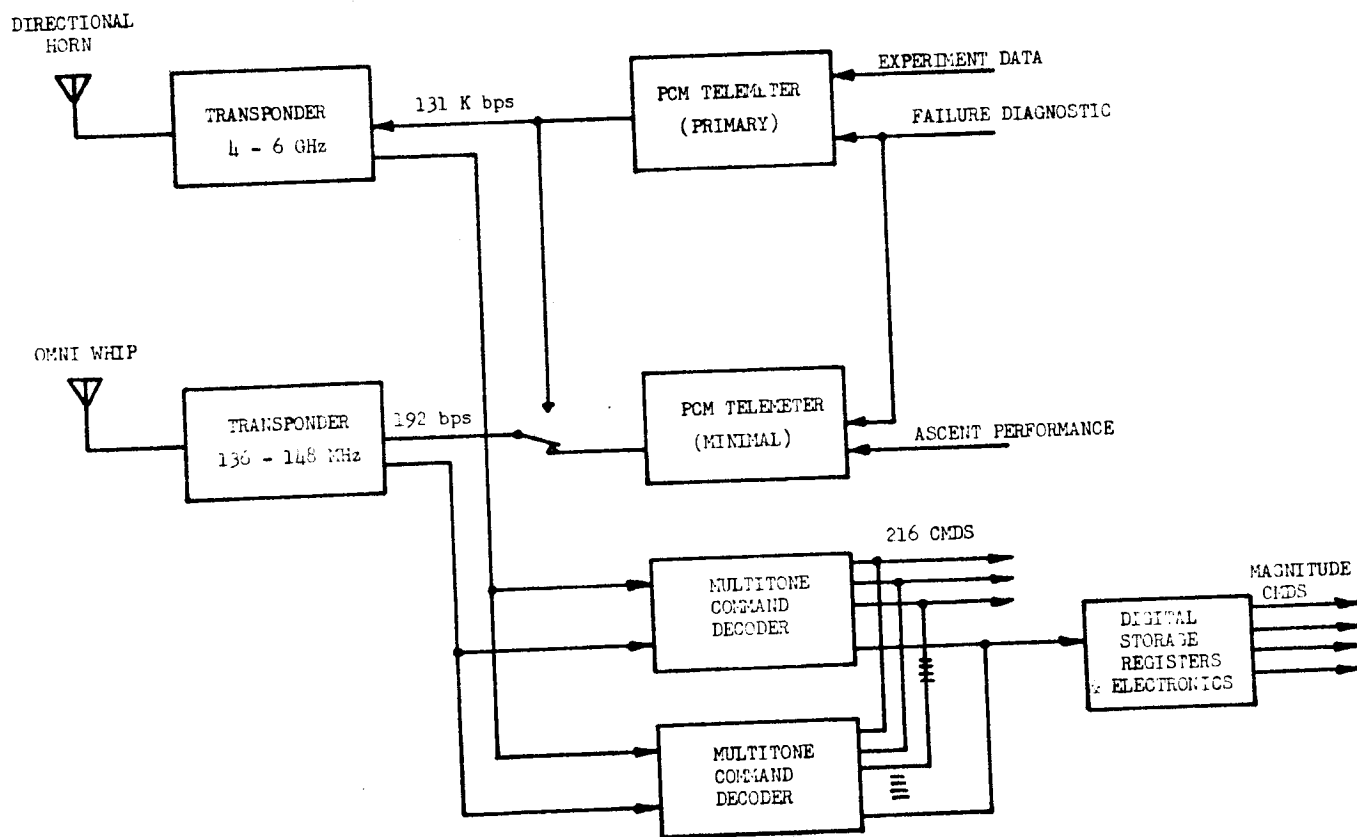


Fig. 3-4 Block of ATS-4 TT&C System

### 3.6 SPACECRAFT TRADEOFF AND ANALYSIS

These studies are covered in Sections 4, 5, and 6.

### 3.7 LAUNCH-PHASE SEQUENCE

The launch sequence of events recommended by LMSC is based upon an actively stabilized transfer orbit/coast/injection motor-burn phase. Initial injection would occur at the first transfer orbit apogee at approximately  $100^{\circ}$  E longitude (above Singapore) into a subsynchronous orbit which would result in an eastward drift. The drift would be used to move the satellite to a station at  $147^{\circ}$  W longitude, at which point the elevation angles to the spacecraft from Rosman, N. C., and the Australia transportable ground stations are approximately equal. Upon reaching  $147^{\circ}$  W longitude, the orbit would be synchronized by firing two 1-lb hydrazine thrusters.

Note that this sequence does not require ground tracking during coast and injection for any purpose other than to obtain status information. No ground commanding of injection motor ignition or of control thrusters is required for the spacecraft to achieve orbit. For status monitoring and obtaining tracking data for early ephemeris convergence, coverage of the transfer ellipse and injection phase is possible from the Tananarive STADAN ground station as well as from the transportable station in Australia.

The sequence is initiated by separation of the spacecraft from the Centaur after a  $90^{\circ}$ -deg pitchdown maneuver. At this time, active attitude control of the spacecraft is assumed by a system (known as the "coarse mode" system) consisting of a horizon sensor, three-axes gyro inertial reference, signal processor, and ammonia resistance jets. This "coarse" system uses the identical sensing and signal processing equipment used during the injection burn phase and during a large percentage of the synchronous orbit operation. During the transfer orbit coast, the spacecraft is oriented toward the earth by using the horizon sensor to provide pitch and roll reference. A form of gyrocompassing is used to maintain the yaw reference.

Before reaching the first apogee of the transfer orbit, the horizon sensors are removed from the control loop and the vehicle is stabilized inertially using the gyros as the attitude reference. A pitch maneuver and a yaw maneuver are then performed in sequence to orient the spacecraft correctly for injection-motor burn.

During the burn phase, the attitude-reference function continues to be performed by the gyros. Hydrazine monopropellant thrusters are commanded to fire by the processed gyro output signals in order to provide the required control torques during motor burn.

An analysis of the expected injection errors indicates that the equivalent three-sigma velocity error from all sources is 130 fps. This analysis assumed three-sigma velocity vector pointing errors of  $\pm 1.0$  deg in each axis. The actual three-sigma errors are  $\pm 0.25$  deg in pitch and roll and  $\pm 0.9$  deg in yaw; however, a conservative allowance of impulse propellant for injection error correction equivalent to 130 fps has been provided in the recommended configuration.

After injection, it is recommended that the solar panels be deployed immediately in order to recharge the secondary batteries. Because the initial orientation of the arrays after deployment may not face the sun when the spacecraft is oriented to the nadir, it may be desirable to orient the vehicle inertially with the solar panels facing the sun. The ability of the control system to orient the vehicle in this manner reduces launch-window restrictions and eliminates the requirement for a high-speed slew capability for the solar array drive.

As mentioned earlier, the nominal orbit expected after injection is biased so as to provide an eastward drift. The recommended velocity bias is 100 fps less than synchronous velocity; the expected injection errors are divided between a 107-fps in-plane error and a 75-fps error normal to the orbit plane. Based upon two-station tracking (Tananarive and Australia), 5 hr of tracking will be required to establish the ephemeris with sufficient accuracy to permit correction of injection accuracies. At the next equatorial crossing, a pair of 1-lb hydrazine thrusters would be fired to remove all of the out-of-plane error and a portion of the in-plane error in order to

Table 3-1  
ATS-4 WEIGHT PERFORMANCE

Item	Weight (lb)
Weight at Liftoff	4,000
Shroud Drop Weight	<u>-18</u>
	3,982
Adapter Weight	<u>-168</u>
	3,814
Performance Loss (7.7-deg Inclination Reduction)	<u>-607</u>
Maximum Spacecraft Weight Injected Into Transfer Ellipse	3,207
Secondary Experiments, Contingency	<u>-201</u>
Current Spacecraft Weight	3,006
Transfer Ellipse Expendible Usage	<u>-0-</u>
Weight at Apogee Firing	3,006
Kick-Motor and Attitude Control Propellant	<u>-1,440</u>
Weight After Apogee Firing	1,566
Injection-Error/Station-Acquisition Propellant	<u>-51</u>
Weight on Station	1,515

place the spacecraft in a transfer ellipse to the desired drift orbit. It should be noted that during this period of thrusting the spacecraft is inertially stabilized at a biased yaw attitude. This attitude places the thrust axes of the two hydrazine motors in the proper vertical plane so that the resulting velocity increment corresponds to the vector sum of the two error components. After this initial firing, the hydrazine motors are fired again at the time of tangency between this transfer orbit and the desired drift orbit. This second firing will inject the spacecraft into the nominal drift orbit.

The parabolic reflector and phased array would be deployed, and the feed support section would be extended after injection-motor burnout and before the first error-correction burn.

A performance analysis of the orbital weight capability of the SLV-3C/Centaur/kick-stage combination was made with results as shown in Table 3-1. The results of trade studies which led to this recommended sequence are contained in Section 4.

### 3.8 EXPERIMENT OPERATIONAL PHASE SEQUENCE

A preliminary orbital test plan was developed to provide ground rules for the spacecraft studies and for the ground facility plan. The order of the test sequence is significant but the details within each experiment and the duration of the experiments are subject to change.

The orbital test plan divides into four sections:

- Operating Checks

Immediately after the deployment sequence is completed, a series of functional operating checks should be made on the spacecraft subsystems, experiments, and instrumentation. These tests will identify possible problem areas that may require replanning. This sequence may require 1-2 days.

- Engineering Tests

- (1) Parabola Contour. Optical and strain gage measurements of reflector surface, temperature measurements, and verification of feed position. These measurements require three days with brief rechecks during the life of the spacecraft.
- (2) Interferometer. Calibration and detailed performance tests. The interferometer will then serve as attitude reference for other experiments. These tests require five days with later rechecks to evaluate drift or environmental effects.
- (3) Orientation. Complete measurement of sensor, thruster, and control-system performance. Operation of this system is basic to conduct of the parabola experiment (and possible secondary experiments). These measurements require 15 days with rechecks over the life of the vehicle.
- (4) Parabola. Measurement of radiation pattern and electrical performance in transmission and reception. These measurements require 15 days with later rechecks to measure possible environmental degradation.
- (5) Phased Array. Pattern measurement and complete performance tests. Requires 15 days with later rechecks.
- (6) Secondary Experiments. These tests are listed last on the basis of assumed priority. It is possible that they could be conducted earlier on a noninterference basis.

- Operating Demonstration

A series of tests should be conducted to demonstrate the variety of possible applications and to evaluate the system performance under quasi-operational conditions. These tests could include communication with small ground terminals, ships, aircraft, and satellites. Readout of space probes could also be shown while operating in an inertially stabilized mode. These demonstrations could occupy 3-6 mo.

- Life Tests

One of the purposes of the mission is to demonstrate a 2-yr operating life. This could best be done by making the vehicle available to a government



or commercial agency for operational use with arrangements for periodic engineering tests to detect any changes in performance.

More details are reported in subsection 6.5 and Section 7.

### 3.9 GROUND EQUIPMENT

On the basis of the preliminary assessment completed during this phase of the ATS-4 program, it is estimated that facilities now available will be adequate (with minor modification) to serve the program requirements for design and manufacture. The major facility requirements anticipated for the program are listed in Table 3-2.

Ground station requirements for operational phase of the ATS-4 program can be satisfied by existing STADAN stations. These ground stations utilized Tananarive for initial tracking support, Rosman for primary support, and secondary support from Mojave and a mobile station at Toowoomba, Australia. Some ground augmentation is required to support the various RF experiments; however, all augmentation can be effected by use of existing equipment designs with the exception of VHF and low UHF antenna feed design. Primary TT&C is via existing 4- and 6-GHz equipment and backup TT&C provided by 136- and 148-MHz links. Tracking is provided by existing range and range rate equipment; command encoding is performed by existing tone command units. Backup telemetry is processed by existing PCM data handling equipment, and primary high-data-rate telemetry will require the addition of a standard IRIG PCM ground station. Three new ground transmitter systems are required for up-links associated with the vehicle experiments. These include a 1-kw S-band transmitter and 6-ft antenna for transmission at 1,700 MHz and 2,100 MHz, and an 8-GHz transmitter and 4-ft antenna which will also have capability for phased array up-links at 7,625 MHz and 7,875 MHz. A third 1-kw beacon transmitter is provided but is a fixed 5-GHz CW signal for use by the vehicle interferometer. The down-links associated with the vehicle 30-ft parabola experiment, require the addition of parametric-amplifier and frequency-down converters at different frequencies in order to be compatible with the existing bank of 135-MHz receivers.

Table 3-2  
MAJOR FACILITY REQUIREMENTS

Requirement	Selected Facility or Candidate(s)	Capabilities	Problem Areas
RF Anechoic Chamber	NASA MSC, Houston, Texas	Quiet zone 20-ft diam. by 57-ft long; larger vehicles accepted with low loss	ATS-4 fit not established; possible schedule conflicts
Launch Phase Simulator	NASA Goddard, Launch Phase Simulator Facility, Greenbelt, Md.  OR  LMSC Santa Cruz Flight Simulator	Acceleration, depressurization, vibration, and acoustic environment - 10-ft diam. by 15-ft long  Depressurization, vibration, and ascent-heating simulation - 14 by 18 ft	Possible extension of chamber needed to accept ATS-4 in launch configuration; no ascent thermal simulation capability  No acceleration-profile simulation capability
Space Flight Environment Simulator	USAF AEDC, Mk I Aerospace Systems Environmental Chamber, Tullahoma, Tenn.  NASA Manned Spacecraft Center Environmental Chamber A	Interior space 35 by 65 ft; operating pressure 10 <sup>-7</sup> Torr; liquid nitrogen cold wall; carbon-arc and quartz-lamp heating  Interior space 54 by 90 ft; operating pressure 10 <sup>-5</sup> Torr; nitrogen cold wall; carbon-arc heating	Possible scheduling conflict with USAF programs  Possible schedule conflict with manned programs
Spacecraft/ Launch-Vehicle Combined Systems Test Facility	NASA Combined Systems Test Stand, General Dynamics/Convair, San Diego	Interface validation; integrated systems checkout for Atlas/Centaur/payload	Possible minor modifications to stand to accept ATS-4 spacecraft
Launch Facility	Launch Complex 36, ETR, Cape Kennedy, Fla.	Two launch pads (A, B), with central blockhouse	Possible minor modifications to service towers

## Section 4

### ASCENT PERFORMANCE AND STATIONKEEPING DEFINITION

This section discusses selection of the launch vehicle and justification for the choice. This is followed by an analysis of the selected launch-vehicle kick-stage performance, results of the injection-error analysis performed on the candidate launch vehicles, recommendations for a sequence of events for separation of the spacecraft from the launch vehicle through correction of injection errors, information on perturbations experienced by a synchronous satellite, and the resulting sequence of station-keeping thrusting. A discussion of the station selection and acquisition problem and a review of the requirements for ephemeris accuracy also are included.

#### 4.1 LAUNCH-VEHICLE SELECTION

Several parameters of the three candidate launch vehicles were analyzed to determine the one most adaptable to the ATS-4 mission. These parameters were weight deliverable on orbit, cost effectiveness (weight on orbit per dollar of launch vehicle cost), an effectiveness factor equal to the product of weight in orbit and the difference between total cost of the program and cost of two launch vehicles and, finally, percentage of total program cost required to procure two launch vehicles. Weight-capabilities data and launch-vehicle costs used in the analysis were modified to reflect estimated weights and costs for equipment necessary to modify the launch vehicle to meet ATS-4 mission requirements.

Because the analysis indicates that the SLV-3C/Centaur has sufficient weight capability to perform the ATS-4 mission, and its other ratings are superior to the other two candidates, it is recommended for the ATS-4 mission. Results of the analysis are given in Figs. 4-1 through 4-3. The mission-peculiar equipment weight and cost values used in the analysis are tabulated in Tables 4-1 and 4-2. Two separate configurations of Centaur-launched spacecraft were analyzed. The first, identified as

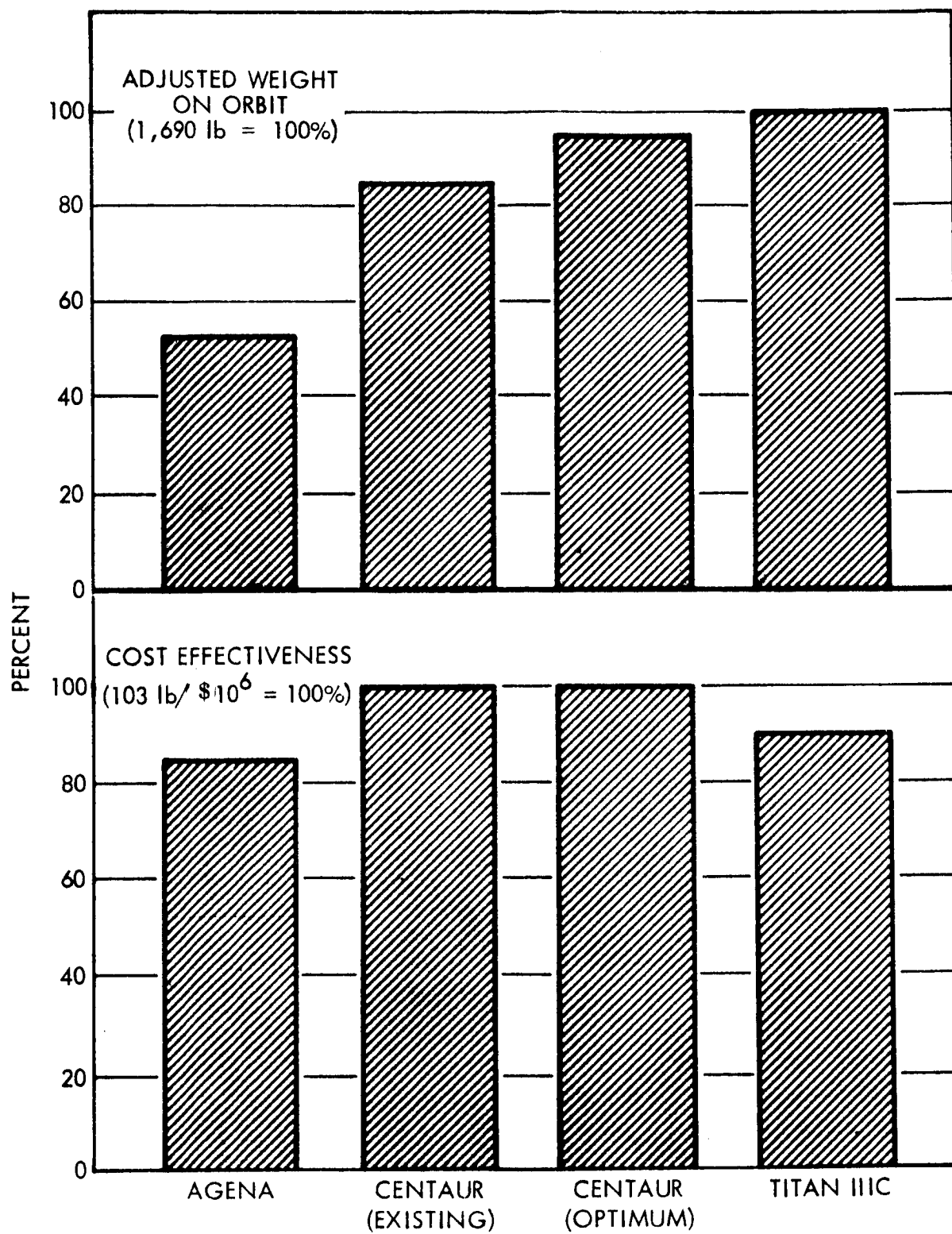


Fig. 4-1 Launch-Vehicle Selection Parameters

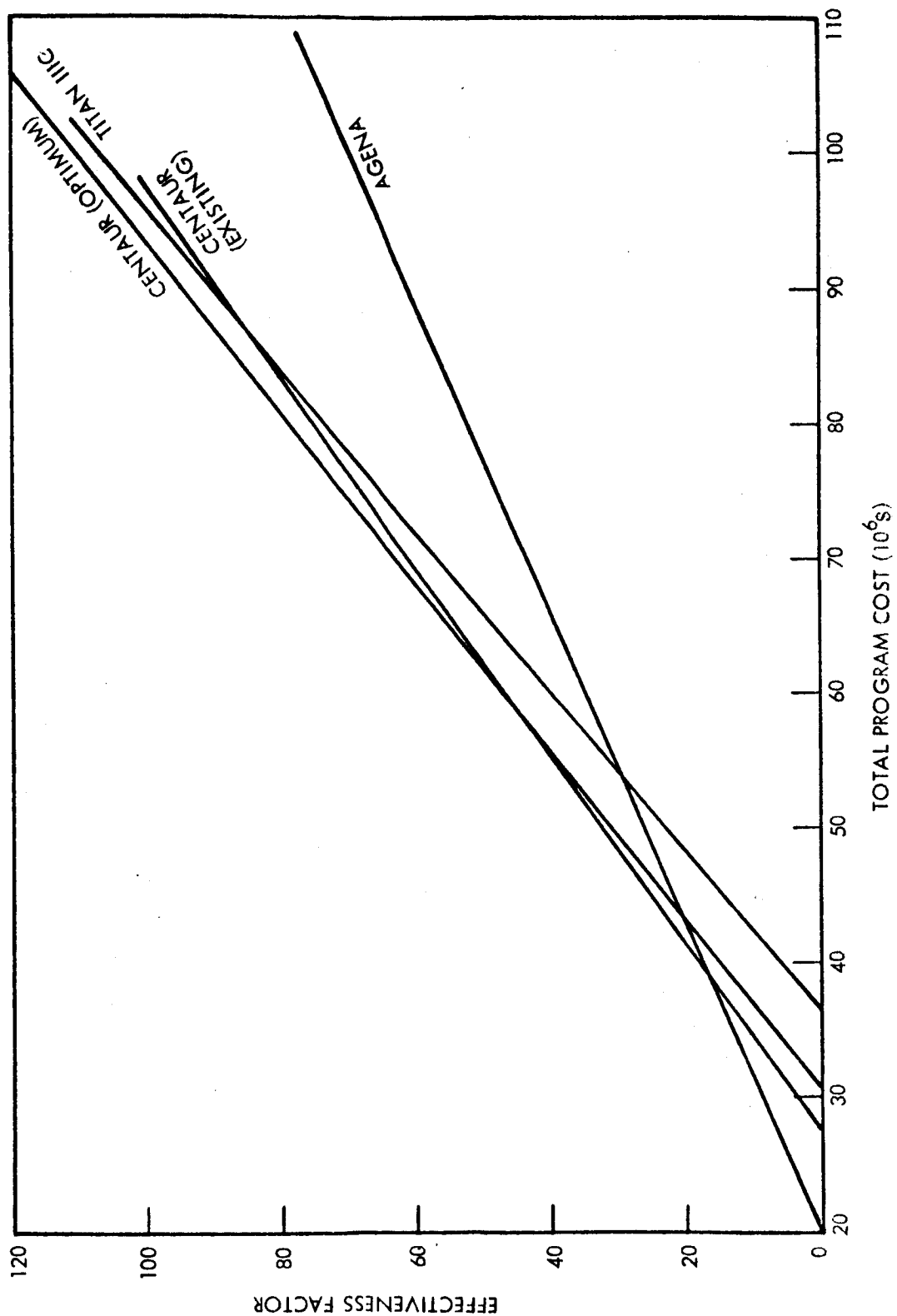


Fig. 4-2 Plot of Effectiveness Factor vs. Program Cost

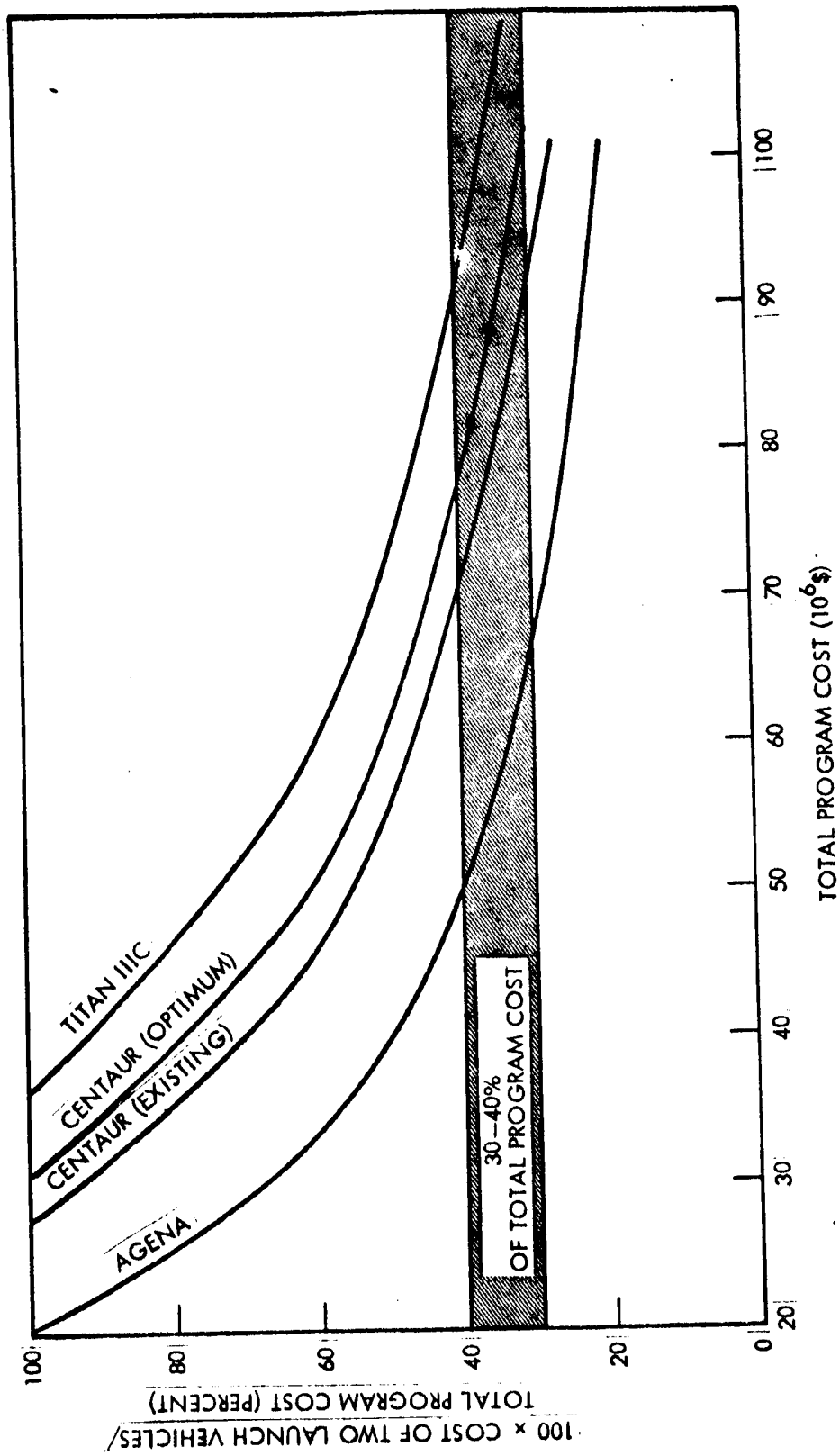


Fig. 4-3 Launch-Vehicle Cost Percentage vs. Program Cost

Table 4-1  
SPACECRAFT AND LAUNCH-VEHICLE PECULIARS

Vehicle	Spacecraft Peculiars	Launch-Vehicle Modifications
Agena	Kick-stage propulsion Injection-error propulsion Injection-attitude control	Qualify Advent shroud
Centaur <sub>3</sub>	Injection-error propulsion	None <sup>(a)</sup>
Centaur <sub>4</sub>	Kick-stage propulsion Injection-error propulsion Injection-attitude control	Added structure <sup>(a)</sup>
Titan	Injection-error propulsion	Spacecraft umbilical provisions <sup>(a)</sup>

(a) Additional shroud modifications for petaline antenna.

Table 4-2  
APPROXIMATE PENALTIES OF PECULIARS

Spacecraft Peculiars	Weight (lb)	Cost (10 <sup>6</sup> \$)
Agena Kick-Stage Propulsion	—	1.5
Centaur Kick-Stage Propulsion (Optimum)	—	1.5
Agena Injection-Error Propulsion	38	—
Centaur Injection-Error Propulsion	29	—
Titan Injection-Error Propulsion	17	—
Centaur Structural Modification	90	0.35
Qualification of Advent Shroud	22	0.5
Titan Umbilical Modification	—	0.25
Titan Shroud Extension	60	0.35
Centaur Injection-Attitude Control	61	0.2
Agena Injection-Attitude Control	57	0.2

Centaur (existing), utilizes the spherical solid-propellant kick motor that is in qualification as an upper stage for Thor-Delta. The second configuration is based upon use of a solid-propellant kick motor optimized for the 4,000-lb limitation imposed upon Centaur.

Results of the cost-effectiveness analysis (Fig. 4-1) indicate that both Centaur configurations are equal at 103 lb per million dollars and are superior from this point of view to Agena and Titan. The plot of the effectiveness factor in Fig. 4-2 shows that for total program costs between 20 and \$39 million the Agena is the optimum launch vehicle, from 39 to \$59 million the Centaur with an existing kick motor is optimum, and from 59 to \$110 million the Centaur with an optimum kick motor is the preferred configuration.

#### 4.2 LAUNCH-VEHICLE PERFORMANCE

During the study, several estimates of performance of the three launch vehicles were made. In particular, the SLV-3C/Centaur combination was analyzed on the basis of several ground rules. These included optimum performance based upon data from the "Centaur Payload Users' Manual," a simplified model as provided by NASA/Lewis Research Center, a maximum spacecraft plus adapter structure weight of 3,000 lb, and a maximum spacecraft plus adapter structure weight of 4,000 lb using both an optimized design for the kick motor and spherical solid-propellant motors that are currently qualified. The use of beryllium additive solid-propellant motors was considered briefly but was discarded because of the required development costs.

The performance capabilities for the SLV-3A/Agena and Titan IIC launch vehicles are given in Table 4-3.



Table 4-3

## SLV-3A/AGENA AND TITAN IIIC PERFORMANCE

Item	Weight (lb)
SLV-3A/Agena <sup>(a)</sup>	
Spacecraft loaded weight (less adapter)	2,145
Less propellant weight	<u>-1,020</u>
	1,125
Less motor inerts	<u>- 88</u>
	1,037
Titan IIIC <sup>(b)</sup>	
Loaded weight on Titan	1,950
Less adapter structure	<u>-200</u>
Spacecraft loaded weight	1,750

- (a) Assumes kick-motor  $I_{sp} = 290$  sec, mass fraction = 0.92, and shroud weight = 200 lb.  
 (b) Assumes standard Titan shroud.

As previously indicated, initial performance calculations for the ATS-4 mission using the SLV-3C/Centaur launch vehicle were based upon a 4,000-lb weight for the loaded spacecraft plus structural adapter. This configuration would require development and qualification of an optimized spherical solid-propellant motor for the kick stage.

There are three existing spherical solid-propellant motors (two have been qualified and the third is presently in qualification) that could be used for the ATS-4 application but with some degradation in performance. Because all three of these motors have a total impulse capability that is less than that required for the optimized stage, the loaded-spacecraft-plus-adapter weight is less than 4,000 lb. The excess performance of the Centaur with nonoptimum motors can be used to reduce the 28.5-deg inclination of the transfer ellipse at the time of injection into that orbit. The new transfer

orbit with less than 28.5 deg inclination will permit circularization at synchronous altitude with the smaller motors.

An analysis has been performed with the three motors under consideration to determine the total spacecraft weight (less total kick-motor weight) that could be placed on synchronous orbit by this technique. This analysis was performed by determining the allowable spacecraft weight on the Centaur as a function of the additional velocity increment required to reduce inclination over the range from 7.0 to 15.0 deg. A value of  $\Delta V/\Delta W$  of -1.5 fps/lb was used to determine Centaur weight performance loss. A spacecraft ignition weight was determined for each of the three motors as a function of the reduction in inclination at the synchronous injection. The resulting spacecraft weight and reduction of inclination angle were used to plot the Centaur performance curve and the kick-stage performance curves for the three motors on a common graph of loaded spacecraft weight versus reduction of inclination angle at transfer injection (Fig. 4-4). The intersections of the curves represent the resulting performance capabilities and inclination change for the three motors. The loaded spacecraft weight was then reduced by the total weight of each of the three motors. The results are given in Table 4-4. The loaded spacecraft weight for the optimized motor configuration less the weight of the kick motor ( $I_{sp} = 290$  sec and mass fraction = 0.92) is also given.

Table 4-4  
WEIGHT PERFORMANCE WITH EXISTING KICK MOTORS

Motor	Spacecraft Weight Less Motor Weight (lb)	Inclination Angle Reduction (deg)
Surveyor	1,425	9.49
Burner II	1,575	7.57
Delta	1,623	7.03
Delta (Revised Analysis)	1,636	7.70

Results of the analysis are conservative for the following reasons. The weight of the spacecraft adapter used in this analysis was estimated to be 300 lb for an adapter

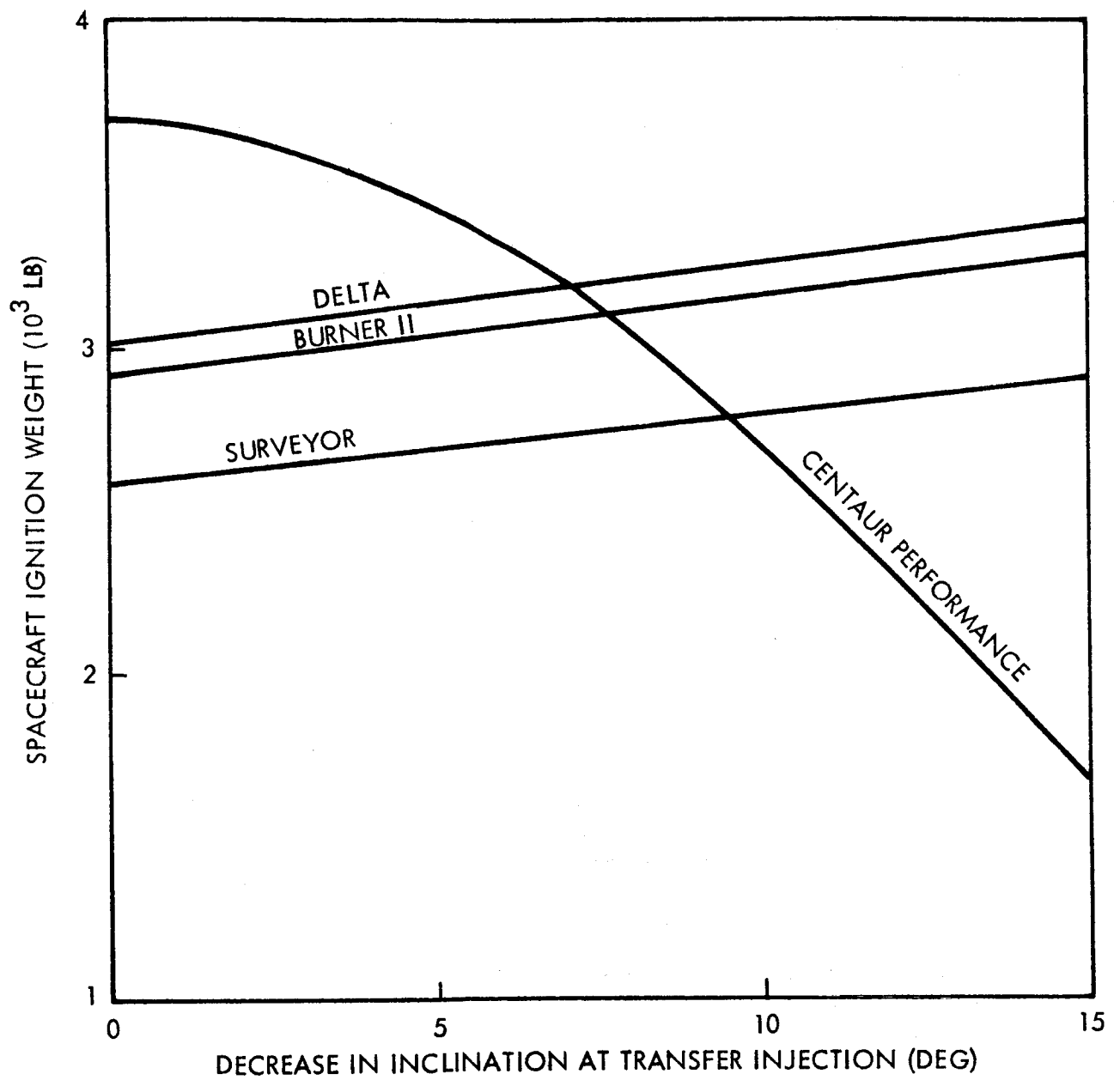


Fig. 4-4 Centaur Performance With Existing Kick Motors

mating with the Centaur at Station 219. Subsequently, NASA advised that the 5-ft diameter mounting circle used for Surveyor launchings should be used. The smaller adapter weight has been estimated to be 137 lb. A revised analysis using this weight was performed and is tabulated in Table 3-1. The corresponding weight value is also given as the last entry in Table 4-4. In addition, the  $\Delta V/\Delta W$  value of -1.5 fps/lb is based upon a Centaur payload weight of 4,000 lb. If Eq. (4.1) is differentiated to obtain Eq. (4.2), the magnitude of  $\partial V/\partial W_f$  can be seen to increase with decreasing  $W_f$ :

$$V = gI_{sp} \ln \left( 1 + \frac{W_{prop}}{W_f} \right) \quad (4.1)$$

differentiating gives

$$\frac{\partial V}{\partial W} = -g I_{sp} \left( \frac{W_{prop}}{W_f^2 + W_f W_{prop}} \right) \quad (4.2)$$

where

$W_{prop}$  = Centaur second-burn propellant weight

$W_f$  = Centaur plus spacecraft weight at second-burn cutoff

The resulting spacecraft weight degradation is, therefore, less than that derived in the analysis for a constant value of  $W_{prop}$ .

#### 4.3 INJECTION ERRORS

An analysis of the injection errors has been performed for each of the three candidate launch vehicles. Error sources have been combined to determine the equivalent velocity increment required to correct the error. In addition, analyses have been made of the injection errors experienced with a spin-stabilized spacecraft because of thrust misalignment torques and initial tipoff body rates. These analyses considered

configurations for which the axis of the maximum moment of inertia was parallel or perpendicular to the spin axis. The results of these analyses are discussed in the following paragraphs.

#### 4.3.1 Atlas/Agena Injection Errors

A detailed error analysis of injection of the Atlas/Agena kick stage into a synchronous-equatorial orbit has been performed.\* This error analysis considered 57 relevant error sources of the booster system. The errors were considered one at a time as they might perturb the reference trajectory, and then they were combined by a random statistical (Monte Carlo) technique to produce orbit element and state vector errors of the final orbit. The error analysis was conducted under the following ground rules:

- Nominal spacecraft motor burn
- No adjustment of spacecraft attitude after Agena/spacecraft separation
- Spacecraft motor ignition controlled to occur at a fixed time from liftoff
- Effects of Agena residual rates at time of separation not included

The errors from this analysis can be converted to velocity correction requirements on basis of the following assumptions:

- The spacecraft contributes 44.2 fps error because of 1 percent variation in total impulse.
- Correlation between velocity and radius errors is one-to-one. The velocity and radius (in-plane) correction can be made in two burns 180 deg apart; this is a Hohmann transfer.
- The error orbit is near circular.
- The correction can be applied at zero time error.
- The inclination error can be removed with the same propulsion system that removes the period and eccentricity errors.

---

\*Lockheed Missiles & Space Company, Application Technology Satellites Trajectories and Performance Capabilities Study, Task 30-7, Vol. I, LMSC-A811729, Contract NASA 3-3805, 13 Apr 1966

Results of the detailed error analysis and subsequent  $\Delta V$  conversion show that the correction requires a velocity capability of 441 fps. This velocity requirement can be reduced in the following various ways.

#### 4.3.2 Methods of Reducing Corrective Velocity Requirements

Examination of the effect of error sources on the orbital elements reveals several large errors that, if eliminated or reduced, could decrease the corrective velocity requirement significantly. A large error is introduced when the Agena is reoriented after second burn to point the spacecraft properly for its circularization and inclination reduction burn. The 5 percent gyro torquer error enters this timed maneuver and causes an angular error between the thrust vector of the vehicle and the desired velocity vector that is added. This error can be kept to a minimum by yawing the vehicle 180 deg, gyrocompassing for 360 sec, and then yawing 53 deg. The alternative is a yaw maneuver of 127 deg, which introduces a 127/53 larger error. The pointing error can be reduced by two methods. The first is use of a more accurate torquer, and the second is use of external reference sensors on the spacecraft to correct trajectory errors.

Another large error results from the prelaunch set kick-stage ignition time. The dispersed trajectory that results from an actual flight can be corrected partially by initiating the kick-stage burn at the equatorial crossing rather than at a preselected time based on a nominal mission trajectory. This requires an inertial guidance system or ground tracking to provide a corrective ignition signal.

The first means for reducing errors is ground control of kick-stage ignition. Ground control, to cause the kick-stage burn to occur at the node, can correct perturbing errors and reduce the total total velocity requirement to 333 fps. This results from a decrease in inclination angle error from 1.86 to 1.52 deg.

While the foregoing reduction is significant, a greater reduction in error can be obtained by yawing the spacecraft more accurately to the 53-deg offset required to eliminate the orbit inclination at apogee. The baseline case uses a 5 percent gyro

torquing error. If this error were eliminated completely, and assuming a prelaunched fixed-time firing spacecraft motor, the velocity requirement would be reduced to 238 fps. The torquing error contributes to both in-plane velocity and inclination error. By eliminating the torquing error, the velocity error is reduced approximately to half and the inclination error to 1.22 deg.

The torquing error cannot be eliminated completely; however, it may be feasible to use 1 percent accurate torquers either on the Agena or on the spacecraft. (In the latter case, the spacecraft would torque the vehicle 53 deg after the Agena yaws 180 deg and then gyrocompasses.) The velocity requirement is 245 fps for a 1 percent torque accuracy with a 53-deg maneuver.

Correction of the pointing error with external sensors (sun and horizon) on the spacecraft could limit the pointing error to 1 deg for any torquing accuracy. With no corrective ignition signal and a 1-deg pointing error, the velocity requirement would be reduced to 302 fps. This requirement is for a fixed time of ignition for the kick stage.

Reduction of both ignition-command and pointing errors brings velocity requirement down to 152 fps. This corrective velocity can be attained, coincidentally, either by reducing the torquing error to 1 percent or by employing external sensors to limit the pointing error to 1 deg during the kick-motor burn. A summary of the corrective velocity requirements is presented in Table 4-5.

#### 4.3.3 Atlas/Centaur/Kick-Stage Injection Error

This error analysis was accomplished with a digital computer program that applied the acceleration profile of the Atlas/Centaur during the mission to acceleration-sensitive components in the inertial guidance system. These were combined with time-dependent errors that were accumulated to the end of the Centaur second burn. Error in the final state vectors and orbital elements were calculated for each error source. The individual state vector and orbital element errors were then combined statistically, by assuming independence of errors, to form the error in each element resulting from all the error sources acting simultaneously.

Table 4-5

**CORRECTIVE VELOCITY REQUIREMENT,  
SLV-3A/AGENA**

Item	Corrective Velocity (fps)
Baseline	441
Ignition by Ground Command	333
1 Percent Torquer Accuracy(a)	245
External Sensors to Limit Point to 1 Deg(a)	302
Ignition by Ground Command and 1 Percent Torquer Accuracy	152
Ignition by Ground Command and 1-Deg Pointing by External Sensors	152

(a) No ground command

It was assumed in the analysis that the Centaur second-burn time is adjusted in flight to correct for a non-nominal flight; i.e., burn occurs at the equatorial crossing. Lack of such correction would introduce an additional inclination error. Another important assumption was that, after Centaur burn, separation on the spacecraft is completed without introduction of an additional pointing error. In addition, it was assumed that the vernier propulsion system of the Centaur eliminates the tailoff error.

The list of error sources used in the analysis is presented in Table 4-6; it was obtained from NASA/Lewis Research Center. The resulting injection-state vector errors are listed in Table 4-7 and the orbital element errors in Table 4-8. These errors are for the inertial guidance system only.

To correct orbit errors resulting from inertial guidance errors (Tables 4-7 and 4-8), the velocity requirement is 41 fps. This requirement is based upon perfect guidance after separation and nominal spacecraft propulsion. If spacecraft errors of 1-deg pointing and



Table 4-6

## CENTAUR GUIDANCE COMPENSATED PARAMETERS

Parameters	Three-Sigma Uncertainty
Accelerometer Scale Factor, ppm	210
Accelerometer Alignment, $\mu$ radians	200
Accelerometer Bias, $\mu$ radians	200
Gyro Mass Unbalance Drift, deg/hr/g	0.25
Gyro Random Drift, deg/hr	0.25
Gyro Anisoelastic Drift, deg/hr/g <sup>2</sup>	0.60
Initial Alignment: Pitch, $\mu$ radians	200
Yaw	200
Azimuth	250

1 percent total impulse uncertainly boost are introduced, the velocity requirement to 118 fps. Without the assumption that time of spacecraft ignition is adjusted, the velocity requirement increases, but only to 120 fps when statistically combined by the square root of the sum of the squares of all errors.

A reduction could be made in the velocity required to correct the orbit by using the Centaur guidance system reference to apogee of the transfer orbit. This would reduce the attitude error, and thereby the total velocity requirements to 66.6 fps. The price of this reduction in velocity requirement is additional batteries and hydrogen peroxide to provide Centaur power and control during the approximate 5.25-hr transfer orbit.

#### 4.3.4 Titan IIC Injection Errors

Error analysis for Titan IIC was accomplished in the same manner on the same computer program as the Centaur error analysis except that inertial guidance was used all the way with the Titan. As a result of smaller error sources and inertial guidance to final injection, the spacecraft corrective orbital velocity required is only 69.55 fps.

Table 4-7

## CENTAUR STATE-VECTOR INJECTION ERROR

ERROR SOURCE	VALUE	UNITS	POSITION (FT)		VELOCITY (FT/SEC)	
			TAN. (X)	NORMAL (Y)	TAN. (X)	NORMAL (Y)
ACCEL. BIAS	4.0000E 01	G*1.E-6	4.0753E 04	2.2333E 04	2.8659E 00	1.5453E 00
ACCEL. SCALE FACTOR	4.0000E 01	1.E-6	5.6260E 04	3.0547E 04	3.6209E 00	1.9660E 00
LEVEL ALIGNMENT	4.0000E 01	ARC SEC	1.4861E 04	1.0949E 04	3.8540E 00	2.0997E 00
AZIMUTH ALIGNMENT	4.5000E 01	ARC SEC	-1.4615E 04	-2.7115E 04	1.4667E-01	2.5660E-01
GYRO MASS UNBAL.	2.5000E-01	DEG/HR/G	1.0537E 05	6.7231E 04	1.1195E 01	6.0955E 00
GYRO RANDOM DRIFT	2.5000E-01	DEG/HR	2.2048E 05	1.2435E 05	1.8645E 01	1.0139E 01
GYR+ ANISO. DRIFT	6.0000E-01	DEG/HR-G*2.	0.	0.	-0.	0.
ACCEL. ALIGNMENT	4.0000E 01	ARC SEC	1.1851E 05	6.8740E 04	9.8314E 00	5.3453E 00
ACCEL. NONLINEARITY	0.	G/G*2.	0.	0.	-0.	0.
1ST TAILOFF	0.	FPS	0.	0.	-0.	0.
2ND TAILOFF	0.	FPS	0.	0.	-0.	0.
3RD TAILOFF	0.	FPS	0.	0.	-0.	0.
LAST TAILOFF	7.0000E 00	FPS	-0.	-0.	-5.1342E 00	2.7876E 00
RSS (W/O TAIL OFF)			2.8110E 05	1.6430E 05	2.4611E 01	1.3388E 01
RSS TOTAL			2.8110E 05	1.6430E 05	2.5141E 01	1.3676E 01

Table 4-8

## CENTAUR ORBITAL ELEMENT ERRORS

ERROR SOURCE	VALUE	UNITS	PERIOD (SEC)	ECCENTRICITY	INCLINATION (DEG)	RANGE (DEG)
ACCEL. BIAS	4.0000E-01	G*1.E-6	7.8565E 01	4.9017E-04	1.2748E-02	1.6859E-02
ACCEL. SCALE FACTOR	4.0000E-01	1.E-6	8.8803E 01	8.1034E-04	1.6869E-02	2.3274E-02
LEVEL ALIGNMENT	4.0000E-01	ARC SEC	1.8648E 02	8.0814E-04	1.2765E-02	6.1479E-03
AZIMUTH ALIGNMENT	4.5000E-01	ARC SEC	3.7642E 00	1.7647E-05	1.1312E-02	6.0460E-03
GYRO MASS UMBAL.	2.5000E-01	DEG/HR/G	4.1649E 02	2.8144E-03	4.4430E-02	4.3591E-02
GYRO RANDOM DRIFT	2.5000E-01	DEG/HR	5.5740E 02	4.9885E-03	7.7251E-02	9.1268E-02
GYR+ ANISO. DRIFT	6.0000E-01	DEG/HR-G*2.	0.	0.	0.	0.
ACCEL. ALIGNMENT	4.0000E-01	ARC SEC	3.1991E 02	2.4079E-03	4.1615E-02	4.9028E-02
ACCEL. NONLINEARITY	0.	G/G*2.	0.	0.	0.	0.
1ST TAILOFF	0.	FPS	0.	0.	0.	0.
2ND TAILOFF	0.	FPS	0.	0.	0.	0.
3RD TAILOFF	0.	FPS	0.	0.	0.	0.
LAST TAILOFF	7.0000E-00	FPS	1.3177E 02	7.5980E-04	1.5845E-02	0.
RSS (W/O TAIL OFF)			8.2555E 02	6.3367E-03	1.0204E-01	1.1629E-01
RSS TOTAL			8.3600E 02	6.3821E-03	1.0326E-01	1.1629E-01

Again, corrective time of burn capability was assumed to be within the capability of the system and was not introduced as an error. Also, the yaw maneuver was assumed to be without error. The actual accuracy in these two areas should be investigated further as the final errors could be increased if the assumptions are not valid.

#### 4.3.5 Spin-Stabilized Spacecraft

A spacecraft can be spin stabilized with no resulting pointing error other than that given as initial conditions if the moment of inertia of the spin axis is greater than that for the pitch and yaw axes. The pitch and yaw moments of inertia must also be equal within 1 percent. Although there is a tipoff error, the spacecraft structure and parts are flexible and will provide hysteresis damping during the 5.3-hr coast. This damping will eliminate the wobble created by the tipoff. Upon arrival at the apogee of the transfer orbit, the spacecraft will have two errors that may be corrected by external reference. These errors are, as indicated previously, the timing of the kick motor and the pointing error both inherited from the booster. The pointing error can be corrected by a sun reference system that is assumed to be accurate to 1 deg. The timing error can be corrected by the ground control of the ignition time on the basis of adequate tracking information.

The kick motor contributes an error to the final orbit by the misalignment of the thrust with the c.g. of the spacecraft. The net result of the misalignment is a torque about the pitch and yaw axis, which causes the vehicle to precess during burn. Since the mass is changing significantly, the precession is a nonlinear problem that was solved by integrating the equation over the burn time. The computer program results were provided parametrically. Equations were also developed to scale these data to any parametric combination. Figure 4-5 shows the error in added velocity,  $\delta V$ , for pitch moments that are 0.5 of the pitch moment of inertia,  $I_y$ . The  $\delta V$  for any pitch moment can be found from the following:

$$\delta V = \delta V \text{ graph } \frac{(\text{pitch moment})^2}{\text{pitch moment graph}} \quad (4.3)$$

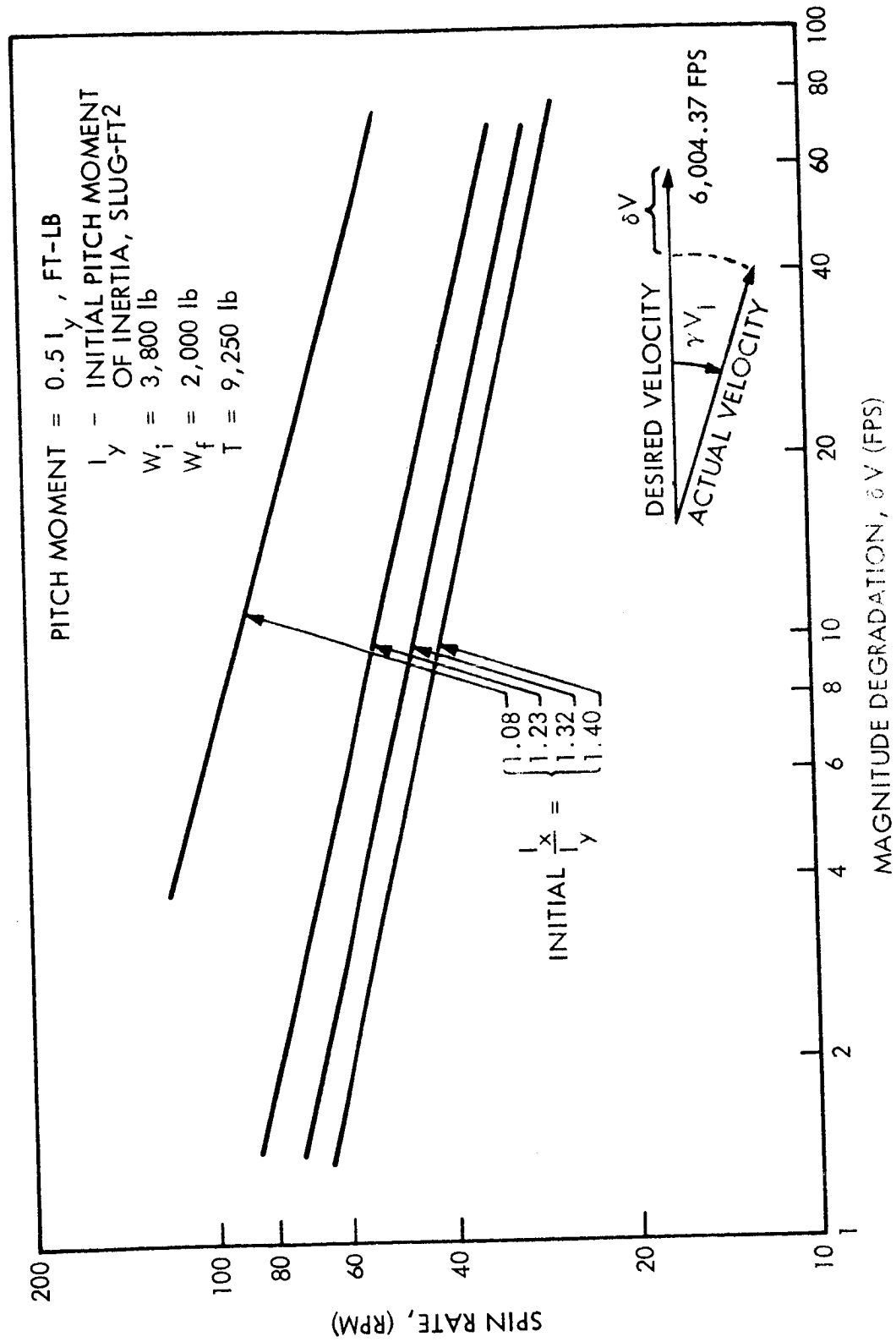


Fig. 4-5 Effects of Thrust Misalignment on Injection Velocity of a Spin-Stabilized Spacecraft

The angle error of the added velocity can be scaled from the graph value obtained with a pitch moment that is also  $0.5 I_y$  (Fig. 4-6). The equation for this scaling is

$$\gamma_{VI} = \gamma_{VI \text{ graph}} \frac{\text{pitch moment graph}}{\text{pitch moment}} \quad (4.4)$$

This value of  $\gamma_{VI}$  can then be used to determine the velocity error perpendicular to  $\delta V$  by the relationship

$$\delta V_p = 6,028 \sin \gamma_{VI}$$

The preceding analysis is not applicable to the ATS-4 spacecraft using the petaline antenna because the moment-of-inertia ratios are different for the petaline antenna.

The following analysis differs from the foregoing in that the moment-of-inertia ratio of the spin axis to its orthogonal axes is less than one, which conforms to the petaline configuration. The significance of the moment-of-inertia ratio is that an elastic body is only stable when spinning about its maximum moment axis. (A completely rigid body is stable spinning about either its minimum or maximum moment-of-inertia axis.)

The results of this analysis show that the corrective velocity capability required to make up for the spinning spacecraft errors is 279 fps. This is for an assumed initial-condition pointing error of 2.5 deg and a thrust misalignment moment of 100 ft-lb. (In addition, there is an impulse uncertainty that adds 44 fps, 3 sigma, velocity error.) The initial-condition error assumption is based on the spacecraft being able to correct attitude during the 5.3-hr coast since the spacecraft, as configured, is unstable while spinning about its minimum moment-of-inertia axis.

Because of the long furled parabolic antenna, the spacecraft design results in a longitudinal (roll) moment of inertia much less than the pitch or yaw moments as shown in Table 4-9.

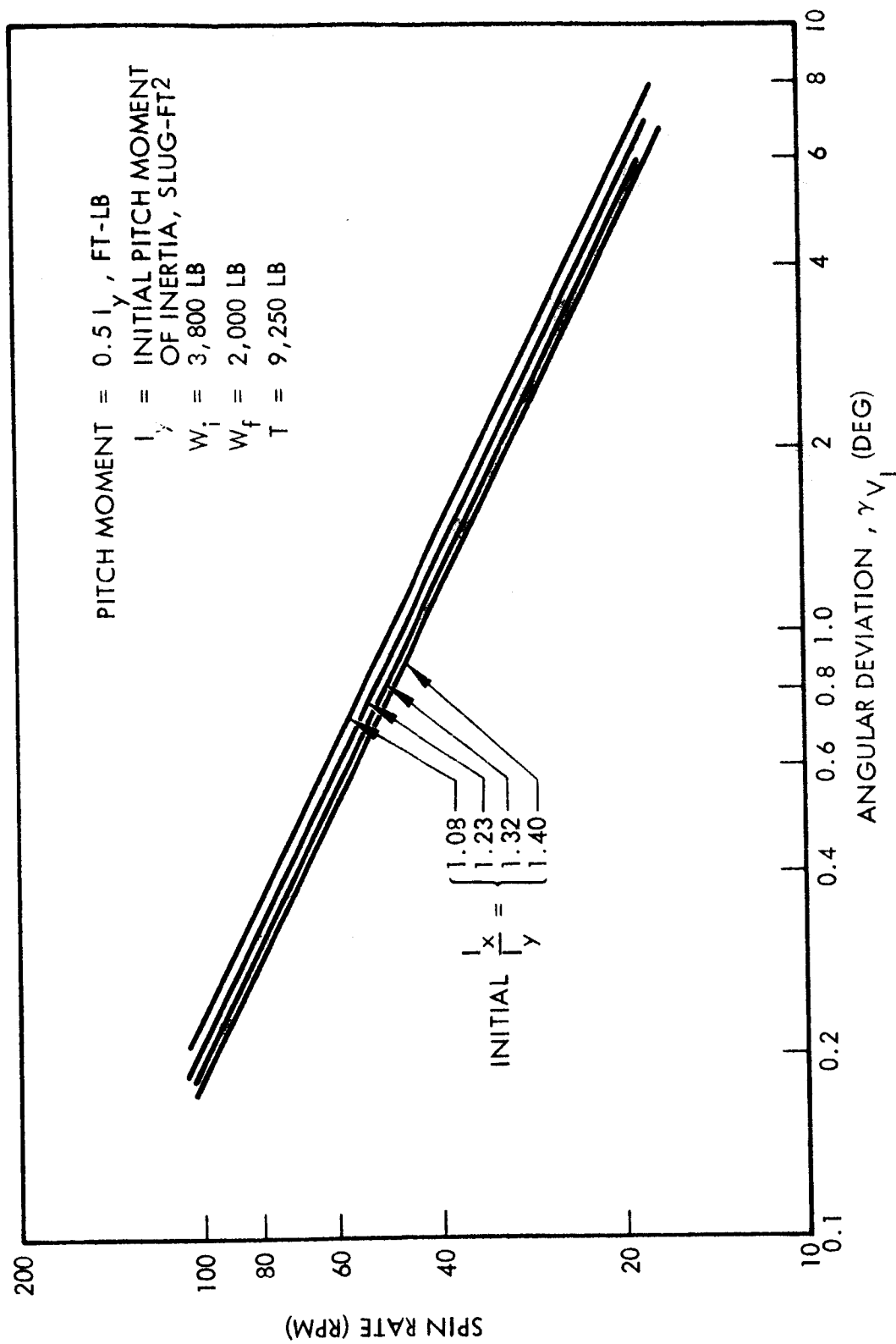


Fig. 4-6 Effects of Thrust Misalignment on Injection-Vector Direction of a Spin-Stabilized Spacecraft

Table 4-9

## SPACECRAFT MOMENTS OF INERTIA

Axis	Used in Simulation		Actual	
	Initial (slug ft <sup>2</sup> )	Burnout (slug ft <sup>2</sup> )	Initial (slug ft <sup>2</sup> )	Burnout (slug ft <sup>2</sup> )
Pitch	2,673	2,096	2,768	2,332
Roll	496	441	496	441
Yaw	2,673	2,096	2,578	2,162

To determine the velocity error induced when the spacecraft is spin stabilized, a computer simulation of dynamic motion was conducted; equations describing the dynamics have been developed. The computer simulation integrates the equations numerically since a closed-form solution is impossible because of the varying mass. The numerically integrated results were verified by comparison with closed-form solutions that use average mass.

The problem of determining total velocity error can be divided into three parts. The first part considers attitude drift during the 5.3-hr coast, which is primarily a function of the initial wobble, spin rate, and physical characteristics of the spacecraft. It can be shown that tumbling will occur for an elastic spacecraft that is spinning about the minimum moment of inertia axis.

An actual example of this phenomenon was observed in the tumbling of Explorer I after 90 min in orbit. This was attributed to the flexible antennas, which provided hysteresis damping. The actual motion of any particular spinning spacecraft must be determined with equations developed to describe that particular configuration. A key in determining the dynamic motion is to build an accurate model of all the sources of hysteresis damping in the spacecraft. Because of the difficulties involved, the coast part of the mission was not simulated as it is assumed that corrective measures must be applied during the coast period; i.e., active control must be used.



The velocity error contribution during the 64-sec circularization burn forms the other two parts of total velocity error – attitude error caused by the initial wobble angle and error resulting from thrust misalignment. During the short burn, the spacecraft can be assumed to be a rigid body. The rigid body is acted upon by the thrust misalignment, which produces a moment perpendicular to the rotating axis. Motion of the roll axis during the burn is shown in Fig. 4-7 for 30 rpm at a 100-ft-lb thrust misalignment torque. It can be seen in the figure that the resulting angular deviation in the flight-path angle is 2.4 deg, which produces a velocity error of 252 fps.

The initial wobble angle is, of course, dependent on the control system chosen for the 5.3-hr coast and the attitude error prior to the coast. The locus of the roll axis is shown in Fig. 4-8 for an initial condition of 5 deg full cone angle prior to burning and a maximum roll rate of 30 rpm. It can be seen that the initial wobble angle grows only a small amount during this burn. A good approximation for this configuration and mission, then, is that the final angular error resulting from an initial wobble angle is equal to the initial angle.

The injection errors for the ATS-4 spacecraft are compared in Table 4-10 for the actively stabilized and spin stabilized cases. The values given are equivalent velocity errors for a Centaur-launched spacecraft. Actively stabilized error represents the errors to be expected for an attitude error of 1 deg in each axis and kick-stage ignition being commanded by a clock started at liftoff. Actual error estimates are 0.25 deg for pitch and roll and 0.90 deg for yaw, which gives a tabulated error somewhat larger than should be experienced.

The spin-stabilized error does not include the contributions resulting from kick-motor impulse uncertainties and from ignition timing errors, and is, therefore, an optimistic estimate. Spin-stabilized ascent requires 159 fps additional velocity in order to remove injection errors. To attain this velocity, 34.4 lb of additional propellant is required ( $I_{sp} = 230$  sec) for a 1,600-lb spacecraft. In addition, because of the unfavorable moment-of-inertia ratio of the spacecraft, an active stabilization system

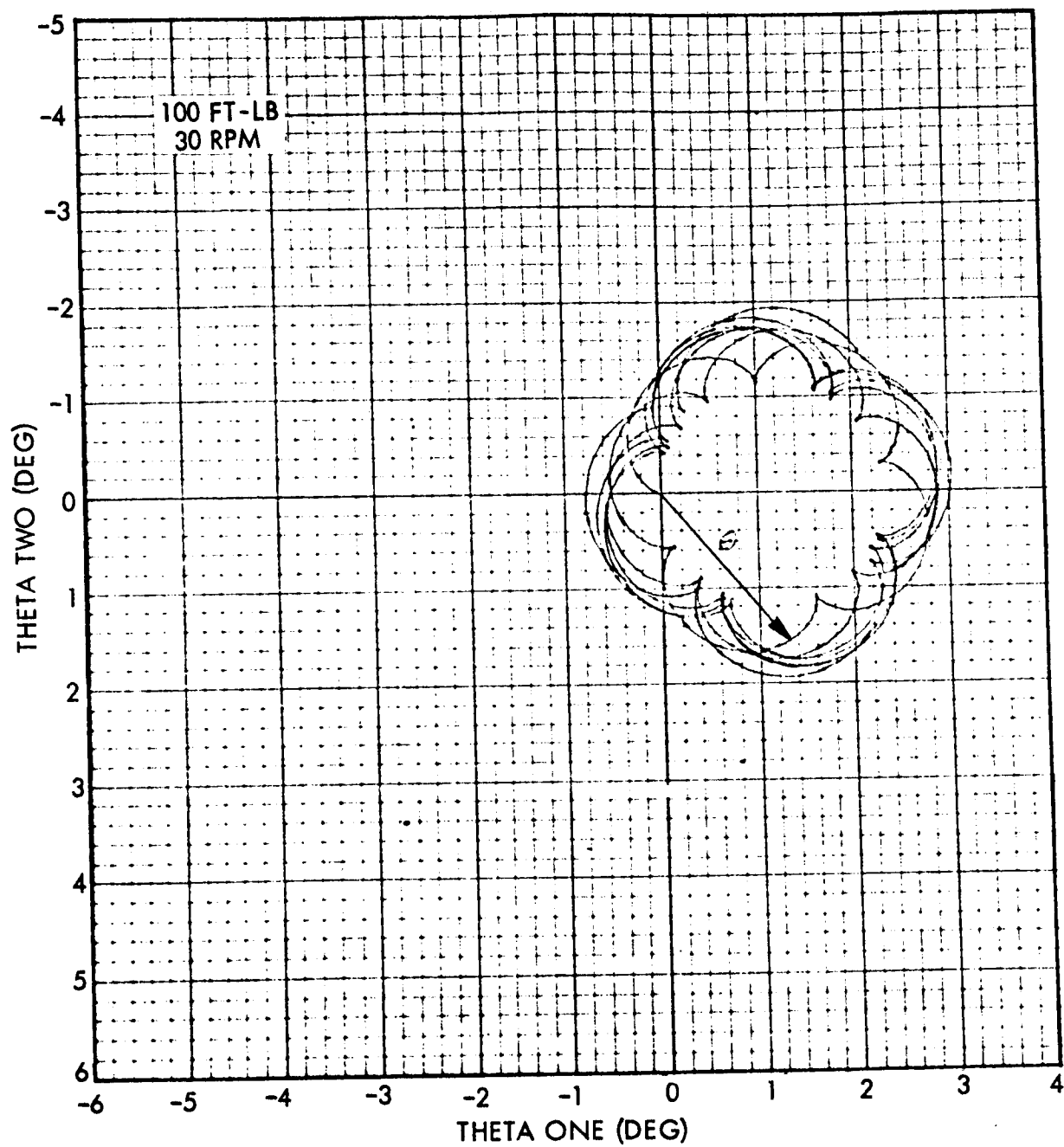


Fig. 4-7 Locus of Roll Axis During Burn (Initial Cone Angle = 0 deg)

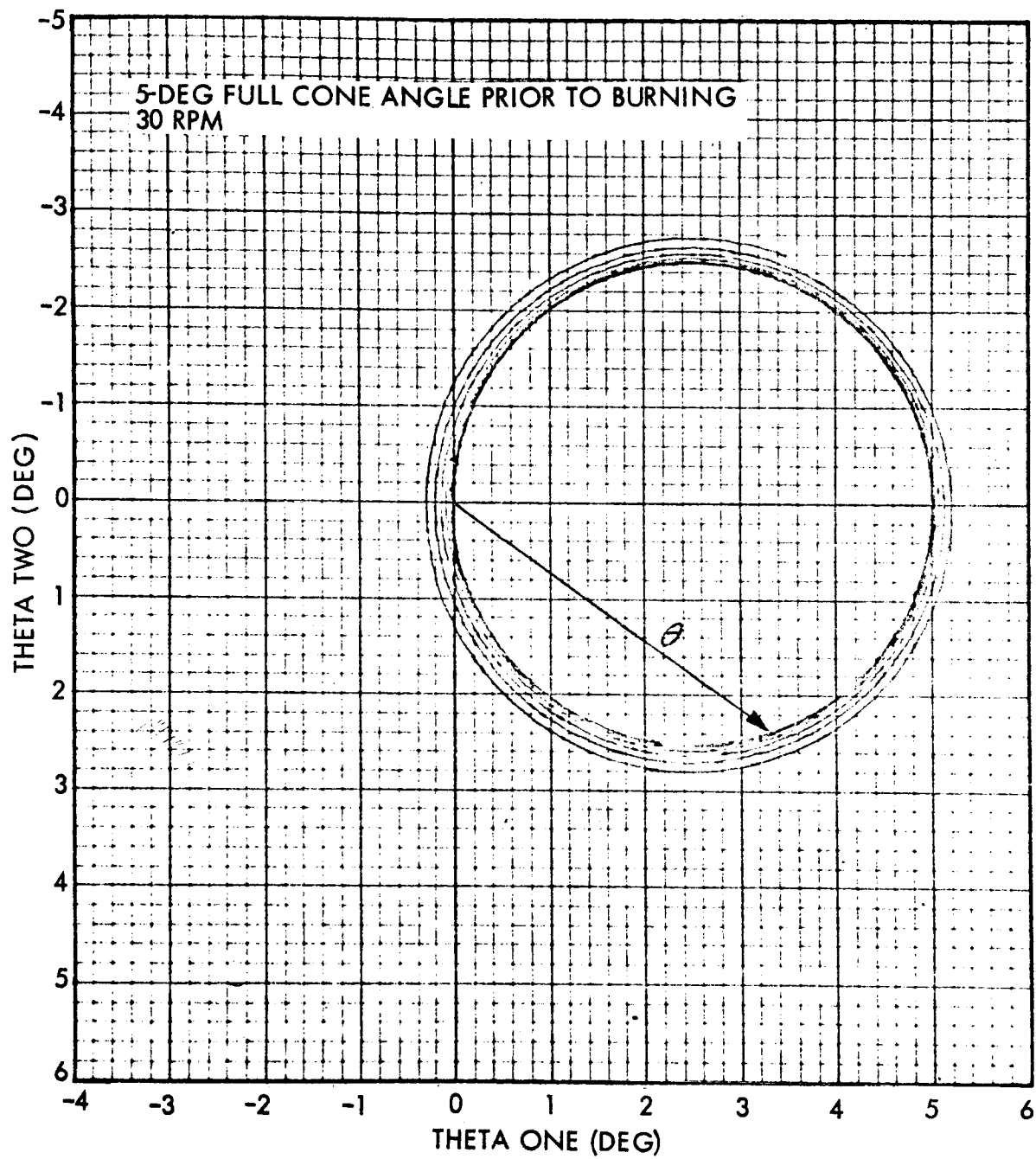


Fig. 4-8 Locus of Roll Axis During Burn (No Thrust Misalignment)

and a spin-despin mechanism would be required for the ascent phase. The total weight of required equipment and propellant to perform a spin-stabilized injection is estimated to exceed the 60-lb increment needed for the actively stabilized spacecraft. For this reason, an active control system appears to be a more desirable approach and is, therefore, recommended.

Table 4-10

INJECTION ERROR COMPARISON, CENTAUR-LAUNCHED  
ATS-4 SPACECRAFT

Stabilization Technique	Injection Error (fps)	Weight <sup>(a)</sup> (lb)
Active	120	62.0
Spin	279	79.4

	Active (lb)	Spin (lb)
(a) 1. Propellant Weight	12.0	34.4
2. Equivalent Propellant Weight	1.0	34.4
3. Additional Thrusters	60.0	0.0
4. Spin/Despin Mechanism	0.0	25.0
5. Ascent Control Weight	<u>1.0</u>	<u>20.0</u>
Total (Items 2 through 5)	62.0	79.4

#### 4.4 SPACECRAFT SEQUENCE OF EVENTS

This subsection covers the event sequences for two phases of the ATS-4 mission. The phases are: (1) from spacecraft separation from the Centaur upper stage through the kick-motor burn phase to reorientation of the spacecraft attitude for deployment, and (2) from the initiation of solar-array deployment through the arrival of the spacecraft at the desired station.

The sequence of the first phase reflects the recommended mode of operation during the ascent phase, using an active control system during the transfer ellipse and the

injection-motor burn. Sequences of events for injection at 100° E longitude and 55° W longitude, followed by drift to the appropriate synchronous stations, have been developed.

#### 4.4.1 Ascent Sequence of Events

As previously mentioned, the event sequence for the initial phase of spacecraft operation begins with the Centaur/spacecraft separation event. It is assumed that the Centaur can perform a 90-deg pitchdown maneuver after injection into the transfer ellipse so as to place the kick-motor thrust axis (orbital yaw axis) parallel to the local vertical.

After separation, the spacecraft attitude will be controlled during the transfer-ellipse coast by the coarse orbital attitude-control system until just before transfer orbit apogee. This coarse system uses a wide-range horizon sensor and a three-axis gyro package as an attitude reference. The yaw reference is maintained by a gyrocompassing technique in which the roll horizon sensor output is fed into the yaw channel to improve dynamic response in yaw (see subsection 6.1).

Before reaching the transfer-orbit apogee, the spacecraft must be reoriented to align the kick-motor thrust axis so as to provide the proper injection velocity vector. This maneuver is performed by disabling the horizon-sensor outputs (including the gyrocompassing loop), which leaves the spacecraft inertially stabilized, and then performing an open-loop pitch-up maneuver of approximately 90 deg, followed by a yaw-right maneuver of 53 deg. Details of this maneuver sequence, followed by the kick-motor burn and attitude-reorientation phase, are given in Table 4-11. The magnitudes of two pitch maneuvers are not precisely 90 deg; the 1.1-deg difference is caused by the apparent pitch rate experienced by an inertially fixed body in a rotating (orbit-fixed) coordinate set.

It may be necessary to orient the vehicle with respect to the sun rather than the earth immediately after burnout of the kick motor. This will be required if the solar arrays when first deployed are not oriented normal to the sun-spacecraft line. If it is required that the vehicle be earth-oriented immediately after injection, a constraint is

Table 4-11

## ATS-4 ASCENT SEQUENCE OF EVENTS

Event Number	Time from Launch	Event
1	4 hr, 51 min, 15 sec = $X_1$	Stop gyrocompassing, disable horizon sensor, start +88.9-deg pitch maneuver
2	$X_1$ + 15 min, 20 sec	Terminate pitch maneuver, initiate +53-deg yaw maneuver
3	$X_1$ + 23 min, 40 sec	Terminate yaw maneuver
4	$X_1$ + 23 min, 44 sec	Ignite four 60-lb $N_2H_4$ thrusters
5	$X_1$ + 23 min, 45 sec	Kick-motor ignition, $N_2H_4$ thrusters to control mode
6	$X_1$ + 24 min, 27 sec	Kick-motor burnout, disable hydrazine thrusters
7	$X_1$ + 24 min, 32 sec	Initiate -53-deg yaw maneuver
8	$X_1$ + 32 min, 52 sec	Terminate yaw maneuver, initiate -91.1-deg pitch maneuver
9	$X_1$ + 48 min, 16 sec (5 hr, 39 min, 36 sec)	Terminate pitch maneuver, enable horizon sensor, start gyro-compassing

placed on the allowable launch window, initial position of the deployed solar arrays, and/or design of the solar-array drive. Because the recommended control system permits the spacecraft to be stabilized inertially, the panels could be oriented normal to the sun upon deployment. The array drive would be off and the vehicle stabilized with respect to the sun until the angle between the spacecraft yaw axis and the local vertical is at a minimum. At that time, the horizon sensors would be enabled, the spacecraft would revert to an earth-fixed orientation, and the solar-array drive would start. The capability to perform this sequence eliminates possible restrictions upon the launch window and upon the solar-array drive mechanism in that the array is not required to slew rapidly.

#### 4.4.2 Postinjection Sequence of Events

The postinjection phase of operation is dependent on whether synchronous injection is made at the first or second transfer-ellipse apogee following injection into the transfer orbit at the first descending node of the parking orbit. If synchronous injection is made at the first apogee, the injection point will be at approximately 100° E longitude. If injection is delayed until the second apogee, the initial station will be at approximately 55° W longitude. As will be shown, injection at the first transfer ellipse apogee is recommended.

An analysis has been performed to determine the optimum permanent station for the ATS-4 satellite. This analysis and its results are included in the following paragraphs.

The initial station for the ATS-4 satellite should be located at a longitude where at least two of the three ground stations (Rosman, N. C. ; Mojave, Calif. ; and Canberra, Australia) can view the spacecraft at elevation angles in excess of 5 deg. Such a constraint will reduce the possibility of multipath effects and minimize possible path disturbances in the atmosphere. The spacecraft should be within view of at least one ground station while in the process of initially acquiring a station.

The time and location of the injection from the parking orbit into the transfer ellipse will determine the approximate longitude of transfer ellipse apogee. Injection into a synchronous (or near-synchronous) circular orbit will occur at an apogee of the transfer ellipse. A launch from AFETR on an azimuth of approximately 90 deg will result in the longitude conditions given in Table 4-12.

Discussions with NASA/GSFC indicate that the Rosman and Mojave sites should be considered as primary stations and the Canberra station as secondary for use by ATS-4. The geodetic coordinates of the stations are as follows:

<u>Station</u>	<u>Longitude</u>	<u>Latitude</u>
Rosman	277° 07' 41" E	35° 12' 00" N
Mojave	243° 06' 03" E	35° 19' 50" N
Canberra	148° 57' 00" E	35° 38' 00" S

Table 4-12

## LONGITUDE CONDITIONS FOR SYNCHRONOUS-ORBIT INJECTION

Location of Injection Into Transfer Ellipse	Location of First Descending Perigee	Location of First Ascending Perigee
Longitude of Transfer Ellipse Injection	0° W	169° E
Longitude of First Apogee	98° E	93° W
Longitude of Second Apogee	55° W	110° E

Notes: Additional west longitude per additional revolution in the parking orbit: 22.5°

Additional west longitude per additional revolution in the transfer orbit: 157°

For maximum (and equal) elevation angles from both Mojave and Rosman, the initial synchronous station for ATS 4 should be 109° 53' W (250° 07' E) longitude. For approximately equal elevation angles from Rosman and Canberra, the synchronous station for ATS-4 should be 146° 58' W (213° 02' E) longitude.

Direct (nondrifting) injection at these two stations can be achieved by the sequences shown in Table 4-13. The sequences are those that permit injection within  $\pm 12$  deg of the desired station with the exception of the descending-injection second-transfer apogee case. The approximate times from launch to injection into a synchronous (or near-synchronous) orbit are indicated in the table. For the synchronous station to service Rosman/Mojave (109° 53' W), the most desirable method for reaching station by means of direct injection would be injecting into the transfer ellipse at the second ascending equatorial crossing; however, because of 25-min restriction in coast time for the Centaur, injection at 55° W at the second transfer-ellipse apogee is necessary.

The most rapid sequence for reaching synchronous orbit (if the resulting longitude station is not critical) includes injection into the transfer ellipse at the first descending equatorial crossing. The time required from launch to synchronous (or near-synchronous) orbit injection by this sequence is approximately 5.5 hr. If injection into the transfer ellipse is delayed until the first ascending crossing, the time will be extended to 6.25 hr, a half period of the parking orbit (44 min).



Table 4-13

## DIRECT INJECTION SEQUENCES

Item	Station Location			
	109° 53' W		146° 58' W	
	Ascending	Descending	Ascending	Descending
Number of Transfer Orbits	7	2/14	5	13
Longitude, °W	112	55/97	158	141
Time from Launch to Injection, hr	79.6	16/152.2	58.7	141.7
Number of Parking Orbits	1	9	2	11
Longitude, °W	115.5	104.5	138	149.5
Time from Launch to Injection, hr	7.8	19.0	9.3	22.0

Because these are the two shortest time periods for arrival at synchronous altitude, they provide maximum weight performance and minimum injection errors. The initial longitude stations for these two sequences are approximately 98°E for descending transfer injection and 93°W for ascending transfer injection. In addition, injection into the synchronous orbit at the second apogee of the transfer ellipse results in an initial station of 55°W.

Injection into a synchronous orbit at 55°W would place the spacecraft in view of both the Rosman and Mojave stations; however, it would lie east of the two "ideal" stations at 109° 53' W and 146° 58' W. If the 55°W station is satisfactory for all experiments, no station acquisition drifts are necessary. If, however, it is desired to reach one of the "ideal" stations, the spacecraft must be placed in an orbit with energy higher than that of a synchronous orbit; this would result in a westward drift of the spacecraft toward the desired station. Alternatively, the spacecraft could be placed in a lower-energy eastward-drifting orbit to reach the desired station. This approach is undesirable because it places the spacecraft out of view of any of the tracking stations for a portion of the drift orbit.

The foregoing alternatives require that the launch vehicle be capable of delaying the injection into the transfer ellipse until the first ascending equatorial crossing.

On an eastward-drift orbit, there is a performance gain if the specific-impulse to mass ratio of the station-acquisition thrusters exceeds that of the apogee motor for the drift velocity increment.

If the drift orbit is established with a period equivalent to that of an orbit whose apogee occurs at synchronous altitude but with apogee velocity  $\Delta V$  fps less than synchronous-orbit circular velocity, the longitude drift rate will be  $0.107 \Delta V$  deg/day. An orbit with this drift rate can be established in three ways. The first method is to perform the injection into a circular orbit with period equivalent to the period of a subsynchronous elliptical orbit. The remaining two methods are injection into the elliptical orbit at apogee or at perigee. The circular orbit is preferred when station acquisition thrusting will be performed in a low-level continuous mode by means such as ion engines or resistojets. The thrust level for such thrusters can be sized neglecting perturbation effects by the use of the following equations:

$$\Delta V = \frac{gFt}{W} \quad (4.5)$$

$$\Delta \lambda = \frac{KgFt^2}{2W} \quad (4.6)$$

$$t = \frac{W \Delta V}{gF} \quad (4.7)$$

$$F = \frac{(\Delta V)^2 W k}{2g \Delta \lambda} \quad (4.8)$$

where

- F = thrust level, lb
- $\Delta V$  = velocity increment less than synchronous circular-orbit velocity, fps
- W = spacecraft weight, lb
- $\Delta \lambda$  = longitude change from initiation of thrust to orbit station, deg
- t = time from initiation of thrust to orbit station acquisition, sec
- g = 32.2 ft/sec<sup>2</sup>
- k = 0.107/86,400 deg/sec/fps

A  $\Delta V$  of 100 fps for a 1,200-lb spacecraft requires thrust levels of 1.55 and 2.05 mlb for the 109° 53' W and 146° 58' W stations, respectively. The time required would be approximately 27.8 days to reach 109° 53' W.

To synchronize and circularize the spacecraft orbit at the desired station when it is in the elliptic drift orbit, a velocity increment  $\Delta V$  is added as impulsive at the apogee nearest the desired station. To minimize subsequent corrective thrust, the period of the drift orbit should be such that the time of crossing the station longitude is coincident with the time of an apogee. The equations for this determination are as follows:

$$\Delta V = \frac{\Delta \lambda}{K n} \quad (4.9)$$

for apogee injection into drift orbit or

$$\Delta V = \frac{\Delta \lambda}{K(n + 1/2)} \quad (4.10)$$

for perigee injection into drift orbit, where  $n$  = number of days (an integer).

For the 147° W station, the  $\Delta V$  required for a 10-day drift to station (apogee-to-apogee) is 107.5 fps.

From the foregoing discussion it can be seen that there are several possible orbital stations for the ATS-4 spacecraft. The recommended station location for the mission is  $147^{\circ}\text{W}$  longitude, which would be reached from an injection at  $100^{\circ}\text{E}$  longitude. (Injection-error correction and station-acquisition impulse would be provided by 1-lb hydrazine thrusters.) This recommendation is based upon the following reasoning:

- Time from launch to spacecraft deployment is minimized. This results in minimum requirements for expendables (attitude control impulse and electric power) during ascent as well as maximum ascent reliability.
- Injection at  $100^{\circ}\text{E}$  permits biased injection conditions to provide a nominal eastward drift. As mentioned earlier, an eastward-drift orbit can give a performance gain. Also, tracking of the spacecraft by two stations (the Tananarive and Canberra stations) is possible, which would permit rapid convergence of the ephemeris after injection.
- Positioning of the spacecraft at  $147^{\circ}\text{W}$  provides the optimum geometry for two-station (Rosman and Canberra) operation of the interferometer in the attitude control mode.
- The  $147^{\circ}\text{W}$  orbital station permits operation with all three ATS-4 tracking stations — Rosman, Mojave, and Canberra stations.
- Use of 1-lb thrusters permits rapid correction of injection errors which prevents the possibility of drifting in the wrong direction.

It should be noted that, if use of the  $55^{\circ}\text{W}$  longitude injection point becomes necessary because of other considerations, the recommended spacecraft design is capable of performing such an injection sequence. A pitch-spin (or tumble) stabilization during the first complete transfer orbit would probably be used to limit the required electrical power. Near perigee, at completion of the first revolution, the pitch tumble would be stopped. The spacecraft would then be stabilized actively for the final half-transfer orbit in a manner identical to the  $100^{\circ}\text{E}$  injection sequence.

#### 4.4.3 Injection Error Correction

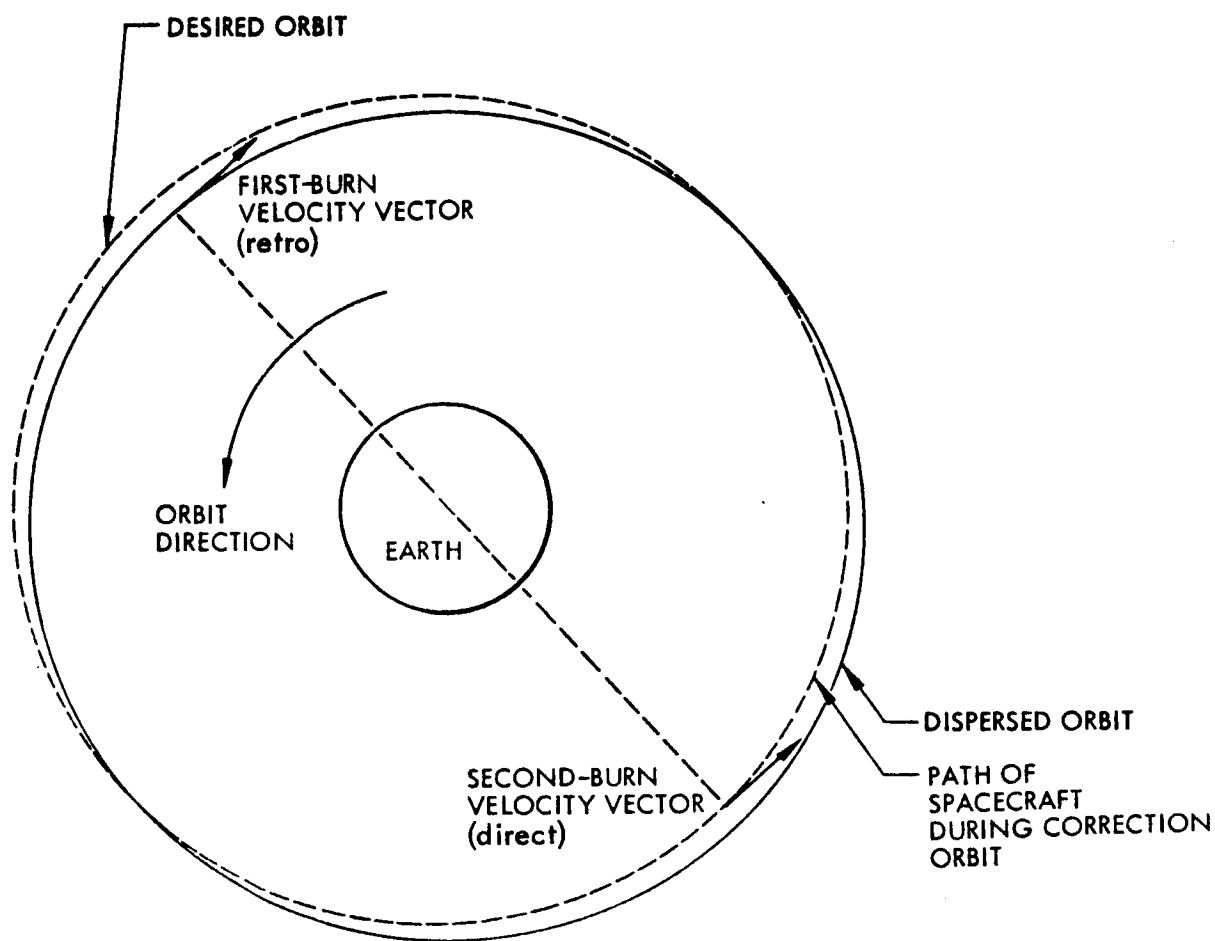
It is assumed that the orbit into which the spacecraft will be injected initially will be biased so as to provide a drift in the desired direction. For example, if injection

is made at  $100^{\circ}$  E longitude, the nominal injection orbit would be biased for a period less than 24 hr so as to provide an eastward drift. Similarly, the nominal orbit for  $55^{\circ}$  W injection would be supersynchronous to attain a westward drift.

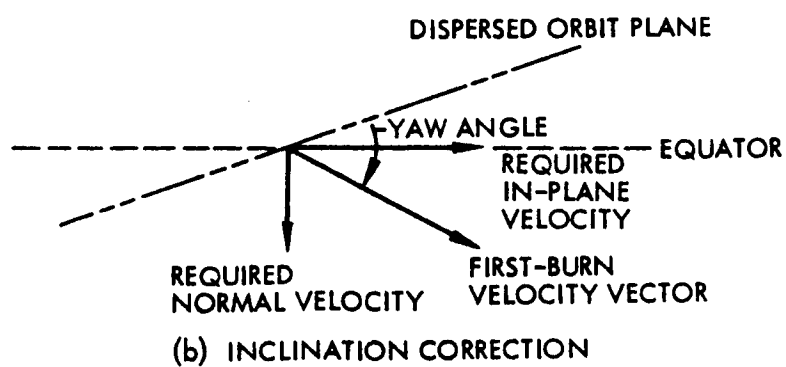
A biased orbit provides the most efficient injection sequence from the point of view of weight performance for either choice of injection point. For an eastward-drift orbit, biasing to a subsynchronous orbit eliminates the requirement for the spacecraft to thrust in order to initiate the desired drift. In addition, biasing minimizes the possibility that injection errors will cause an orbital drift in the wrong direction. In the case of a westward drift, the kick motor can provide the excess energy needed to place the spacecraft in the supersynchronous orbit more efficiently than the hydrazine thrusters used for station change.

To determine the parameters of the biased injection orbit, consideration must be given to the impulse propellant available to correct injection errors. In the work statement for the ATS-4 study, the requirement was included for 100 fps of station-change velocity and velocity allowance for correction of injection errors. For the Centaur launch vehicle, the injection errors have been estimated to be 120 fps; however, a propellant loading equivalent to 130-fps injection error has been incorporated in the spacecraft design. If the 100-fps allowance for station change is used to synchronize the spacecraft orbit after drifting to station, it is evident that the maximum bias that can be used is for an orbit of velocity 100 fps less than synchronous orbit velocity.

As indicated in subsection 4.3, the injection errors can be resolved into three orthogonal velocity components — normal or inclination, tangential or period, and radial or eccentricity. In removing the injection errors (Fig. 4-9), error correction velocity requirements can be reduced if the radial and tangential errors are removed by a two-burn approximate Hohman transfer between the dispersed orbit and the nominal orbit (fig. 4-9a) in which both the first in-track and the total inclination velocity increments are applied as shown in Fig. 4-9b. As shown in that figure, the vehicle must be yawed to permit addition of the required velocity by a single thruster (or pair of thrusters whose thrust axes are coplanar).



(a) IN-PLANE CORRECTION



(b) INCLINATION CORRECTION

Fig. 4-9 Injection-Error Correction

In the case of injection at 100° E, the spacecraft would be injected into an orbit at a velocity 100 fps below that for a synchronous orbit. The three-sigma error components for the Centaur combination are approximately 72 fps normal (inclination) error and 104 fps in-track (combined radial and tangential) velocity error. If three-sigma errors were experienced, the normal error and 69 fps of the in-track error would be removed at an equatorial crossing of the dispersed orbit, which would place the spacecraft on a transfer ellipse to the desired orbit. After 12-hr, the remaining 35 fps of the in-track error would be corrected, and the spacecraft would be placed on the nominal orbit.

#### 4.5 EPHEMERIS DETERMINATION AND TRACKING

The ascent sequence of events for the spacecraft does not require tracking or commanding of the vehicle in order to inject the vehicle into the nearly synchronous drift orbit with the injection errors (120 fps) given in subsection 4.3.1. Tracking would be desirable for determination of the vehicle trajectory and status during this phase, however.

Tracking of the spacecraft during the injection and postinjection phases at 100° E by the Tananarive and Canberra stations. The expected errors as a function of time of tracking have been analyzed and the results tabulated in Table 4-14.

Table 4-14  
APPROXIMATE ORBITAL-ELEMENT ERRORS VS. TIME<sup>(a)</sup>

Days of Tracking	Eccentricity ( $\times 10^{-7}$ )	Inclination ( $10^{-7}$ radians)	Period ( $10^{-1}$ sec)	Radial Velocity ( $10^{-2}$ ft/sec)	Intrack Velocity ( $10^{-3}$ ft/sec)	Crosstrack Velocity ( $10^{-3}$ ft/sec)
1	2.0	7.0	1.0	6.2	4.2	7.0
2	0.75	3.3	0.35	3.1	1.5	3.3
3	0.41	2.3	0.17	3.1	0.72	2.3

(a) Errors represent one-sigma values.

It should be noted that the analysis from which the values in Table 4-14 were obtained was not done for the two stations mentioned. The values were derived for two stations, each located 2,700 nm from the subsatellite point and spaced 90 deg in azimuth with respect to the subsatellite point. The data should be considered as approximate and as being representative of expected values of the actual errors.

To evaluate the requirements for ephemeris accuracy, analysis was performed to determine the effect in satellite position uncertainties upon the accuracy of antenna pointing. The following paragraphs cover the analysis and its results.

The required accuracy for knowledge of position of the ATS-4 synchronous satellite can be related directly to the requirement for pointing accuracy as stated in the Orientation Control Equipment portion of the work statement. If the main beam of the parabolic antenna must be pointed by means of open-loop commands to any point on the visible surface of the earth at an accuracy of  $\pm 0.1$  deg, satellite position must be known adequately so that spacecraft pitch, roll, and yaw angles can be computed to this accuracy.

The required accuracy in radial and horizontal positions is derived as follows. From Fig. 4-10a, it can be seen that:

$$\tan \phi = \frac{R \sin \zeta}{(R + h) - R \cos \zeta} \quad (4.11)$$

and, for angles  $\phi < 10$  deg

$$\phi \approx \tan \phi \quad (4.12)$$

Therefore,

$$\frac{\partial \phi}{\partial h} = - \frac{R \sin \zeta}{[(R + h) - R \cos \zeta]^2} \quad (4.13)$$



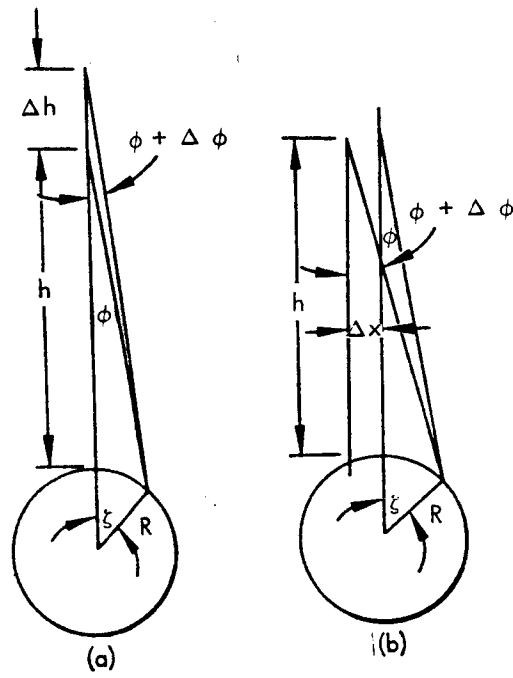


Fig. 4-10 Spacecraft Positional Error Geometry

The function  $\partial\phi/\partial h$  and the resulting values of  $\Delta h$  corresponding to  $\Delta\phi = 0.1$  deg are plotted as a function of  $\phi$  in Fig. 4-11. From the plot, it can be seen that  $\Delta h$  approaches 250 nm as  $\phi$  approaches the limb.

From Fig. 4-10b it can be seen that Equation (4.11) holds and that:

$$\tan(\phi + \Delta\phi) = \frac{R \sin \zeta + \Delta x}{(R + h) - R \cos \zeta} \quad (4.14)$$

If  $\tan(\phi + \Delta\phi) \approx (\phi + \Delta\phi)$ , then

$$\frac{\partial\phi}{\partial x} = \frac{1}{(R + h) - R \cos \zeta} \quad (4.15)$$

Values of  $\Delta x$  corresponding to  $\Delta\phi = 0.1$  deg are plotted in Fig. 4-10; it can be seen that  $\Delta x = 34$  nm near the nadir.

The allowable error in position can now be evaluated. If the contribution of position uncertainty to pointing error is arbitrarily restricted to a value of 10 percent, the allowable error in position corresponds to 0.0436-deg pointing error. When the altitude and horizontal error components are combined on a root-sum-square basis, the curve of Fig. 4-12 results. These errors are assumed to have been determined on the basis of 95 percent probability.

From the foregoing analysis, it can be seen that the expected ephemeris errors will not cause significant antenna-pointing errors.

#### 4.6 SPACECRAFT STATIONKEEPING

An analysis has been performed to determine the magnitude of the various perturbations that would act upon the ATS-4 spacecraft and to estimate the resulting stationkeeping velocity requirements. The result of that analysis follows.

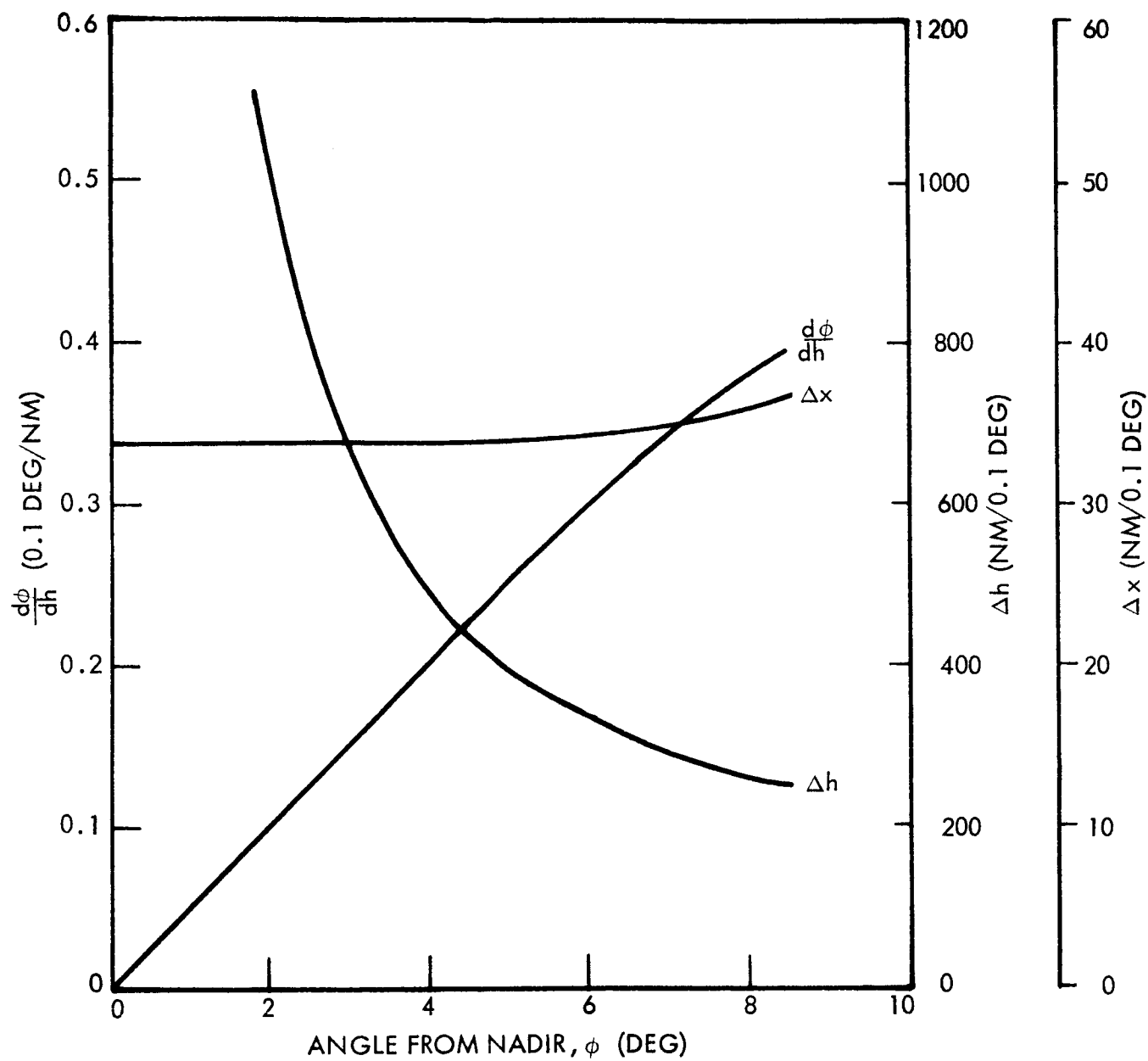


Fig. 4-11 Effects on Pointing Accuracy of Satellite Position Errors

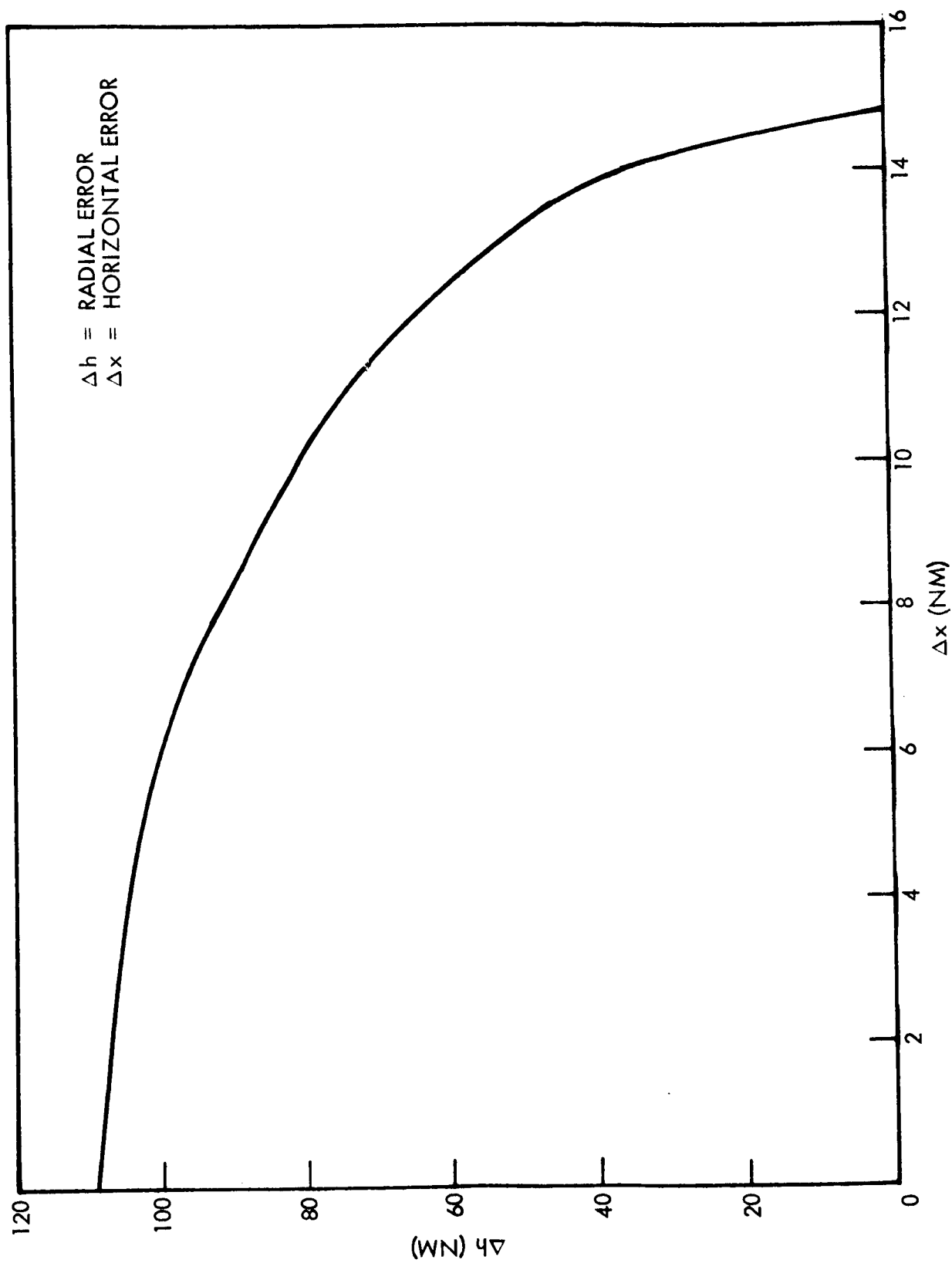


Fig. 4-12 Allowable Position Error Envelope

#### 4.6.1 Solar Wind

Of the known causes of perturbations of an earth satellite, the solar wind\* is the only one that is believed to be intermittent. The intensity of proton radiation is highly dependent on solar-surface conditions, and is greatest during an active sun (high sunspot activity) and lowest during a quiet sun (low sunspot activity.) According to Lockheed handbook data,\*\*proton flux at a distance of the earth from the sun and during a quiet period is approximately  $9.0 \times 10^8$  protons/cm<sup>2</sup> sec (with proton velocity of  $3.0 \times 10^7$  cm/sec relative to the earth) and during an active sun flux may increase to  $1.5 \times 10^2$  protons/cm<sup>2</sup> sec (with the proton velocity of  $1.5 \times 10^8$  cm/sec).

The force acting on the satellite antenna ("dish") because of incident protons can be computed. The pressure exerted on a surface facing the particle stream (assuming elastic collision) is,  $P = 2 Nmv$ , where  $N$  = particle flux,  $m$  = mass of particle,  $v$  = velocity of particle. Since the mass of proton is  $1.66 \times 10^{-24}$  gm, the pressures corresponding to a quiet and an active sun are, respectively,  $8.96 \times 10^{-8}$  and  $7.46 \times 10^{-4}$  dynes/cm<sup>2</sup>, ( $18.8 \times 10^{-11}$  and  $15.6 \times 10^{-7}$  lb/ft<sup>2</sup>). The area of the dish is 706 ft<sup>2</sup>, but only 0.285 of this area is opaque (from a front view). In addition, the solar array presents an area of 135 ft<sup>2</sup>. Hence, the forces acting on the satellite will be  $6.3 \times 10^{-8}$  and  $5.2 \times 10^{-4}$  lb, for a quiet and an active sun, respectively. Assuming the satellite to have a mass of 1,800 lb, the satellite will acquire accelerations of  $1.12 \times 10^{-9}$  and  $0.93 \times 10^{-5}$  ft/sec<sup>2</sup>, relative to the earth.

Since an active sun is associated with high sunspot activity, the high proton flux ( $10^{12}$  protons/cm<sup>2</sup> sec) can be expected to persist as long as the sunspots are visible from the earth. Since the life of a sunspot may be several weeks, the sunspot will be visible to the earth for a period of 10 or 12 days (the sun's rotation period is 25 days). An effect of proton flux on the satellite will be to give the originally circular orbit a small ellipticity. It can be shown that the proton flux will produce orbit eccentricities, for a single revolution about the earth (1 day), of  $3.4 \times 10^{-8}$  and  $2.8 \times 10^{-4}$  for a quiet and an active sun, respectively.

---

\*By solar wind, we mean particle radiation from the sun; specifically, protons.

\*\* Lockheed Missiles & Space Company, Satellite Environment Handbook, Dec 1960.

#### 4.6.2 Solar Pressure

The electromagnetic radiation of the sun exerts a pressure of  $1.945 \times 10^{-7}$  lb/ft<sup>2</sup> on a perfectly reflecting surface at a distance of the earth from the sun. Taking reflectivity of the antenna and its particular geometry into account, it can be shown that the force acting on the antenna, when it is facing the sun, is  $61.0 \times 10^{-6}$  lb, and, when sideways,  $46.0 \times 10^{-6}$  lb. The pressure on a 135-ft solar array will add  $23 \times 10^{-6}$  lb. For an 1,800-lb satellite, the maximum acceleration resulting from electromagnetic radiation of the sun will be  $1.34 \times 10^{-6}$  ft/sec<sup>2</sup>, or 43.5 fps. The eccentricity acquired by an originally circular orbit after one revolution of the satellite about the earth (1 day) will be  $1.25 \times 10^{-5}$  and this eccentricity will reach a maximum of  $1.46 \times 10^{-3}$  in 6 mo and return to zero in 1 yr.

#### 4.6.3 Sun's Magnetic Field

Since the satellite will be constructed of partially magnetic materials, eddy currents should be induced in the satellite as it moves through the earth magnetic field, which would result in a magnetic field in the satellite that will interact with the earth's field. However, since the satellite is in a synchronous orbit, it will be stationary relative to the earth's magnetic field and, hence, no voltages will be induced in the satellite by this field. The sun's magnetic field, however, would be expected to perturb the satellite, since the satellite does experience motion relative to its field. According to Dr. Leverett Davis at the California Institute of Technology, the earth magnetic field completely shields the effect of the sun's magnetic field out to distance of 10 earth radii. Since the synchronous orbit has a radius of 6.62 earth radii, it must be concluded that the sun's field exerts no effect on the satellite.

#### 4.6.4 Sun-Moon Perturbations

The gravitational attractions of the sun and moon will cause the orbital plane of the satellite to increase its inclination to the equatorial plane at an initial (for the first

10 yr) rate of 0.8525 deg/yr. Of this, 0.2691 deg/yr is due to the sun and 0.5834 deg/yr is due to the moon. The velocity impulse (applied at the node of the satellite orbit) required to negate this rate of orbit inclination is 150 fps/yr.

#### 4.6.5 Earth Triaxiality

The motion of near-earth satellites indicates that the earth's equatorial section is actually elliptical instead of circular. Since the earth's polar section is known to be elliptical (oblate earth), the earth has only three principal axes of inertia; therefore, it is called a triaxial ellipsoid. The circumferential acceleration (i.e., acceleration in the direction of the flight path) experienced by a satellite in the earth's equatorial plane because of earth's elliptical equatorial section is  $6\mu J_2^2 (R^2/r^4) \sin 2\gamma$ , where,  $\mu$  = earth's gravitational constant,  $J_2^2$  = measure of ellipticity of earth's equator,  $R$  = earth's equatorial radius,  $r$  = radius of satellite orbit, and  $\gamma$  = angle measured in equatorial plane between minor axis of earth's elliptical equator and position of satellite. A recent value of  $J_2^2$  is  $1.70 \times 10^{-6}$  with the earth's equatorial minor axis at  $72^\circ$  E. For a satellite at the synchronous orbit altitude, the resulting maximum circumferential acceleration is  $1.71 \times 10^{-7}$  ft/sec<sup>2</sup>, or 5.4 fps/yr.

Kaula\* reported that the  $J_{31}$ ,  $J_{33}$ ,  $J_{42}$ , and  $J_{44}$  terms increase this to 6.2 fps/yr at  $117^\circ$  E. Guier\*\* of JHU/APL found this maximum acceleration in close agreement with observed behavior of Syncom II.

#### 4.6.6 Micrometeoroids

Micrometeoroids are small (between  $10^{-6}$  and  $10^{-2}$  m in diameter) bodies orbiting the sun in highly elliptical orbits. They vary in mass between  $10^{-13}$  and  $10^{-1}$  kg. In its orbit around the sun, the earth encounters several streams of these particles; the most

---

\*Athens, 1965.

\*\*Recent Progress in Satellite Geodesy, Jan 1965.

prominent occur during the months of June, July, August, and December. The average pressure exerted by micrometeoroids in the vicinity of the earth is  $0.92 \times 10^{-13}$  lb/ft<sup>2</sup>. Since the area of the antenna is 706 ft<sup>2</sup>, the maximum force acting on the satellite will be  $6.5 \times 10^{-11}$  lb, and for an 1,800 lb satellite, the corresponding acceleration will be  $2.6 \times 10^{-12}$  ft/sec<sup>2</sup>, or  $8.2 \times 10^{-5}$  fps/yr.

Table 4-15 summarizes the accelerations (on an 1,800-lb satellite) caused by the above six causes of perturbations.

Table 4-15  
PERTURBATIONS OF SYNCHRONOUS SATELLITE<sup>(a)</sup>

Source of Perturbation	Magnitude of Perturbation
Solar Wind	$2.9 \times 10^{-7}$ g (intermittent)
Solar Pressure	$4.3 \times 10^{-8}$ g = 43.5 fps/yr
Sun's Magnetic Field	—
Sun-Moon Gravitation	$1.48 \times 10^{-7}$ g = 150 fps/yr
Earth's Triaxiality	$6.17 \times 10^{-9}$ g = 6.24 fps/yr
Micrometeoroids	$8.09 \times 10^{-14}$ g = $8.2 \times 10^{-5}$ fps/yr

(a) Mass of satellite = 1,800 lb.

#### 4.6.7 Stationkeeping Velocity Requirements

On the basis of the foregoing results, an allowance for stationkeeping impulse equivalent to 279 fps of velocity change has been made for the ATS-4 spacecraft. This quantity provides for 2 yr of triaxiality and solar pressure perturbations in the east-west direction as well as 1 yr's cancellation of the effects of sun-moon gravitation. The latter component has been increased in the impulse allowance to 180 fps to account for the nonimpulsive application of north-south stationkeeping velocity.



The desirability of maintaining a satellite in a constant position relative to the earth has long been recognized, but the precision with which this should be done is dependent on satellite utilization.

For the primary experiments defined for ATS-4, there is no requirement for station-keeping *per se* if the initial station is located at about  $105^{\circ}$  W, as previously stated. The drift, eccentricity, and inclination after 2 yr in orbit would not reach values large enough to affect the conduct of the experiments, other than to meet the stipulation that orientation must be controlled while maintaining station. The operational requirement to perform north-south stationkeeping for 1 yr and east-west for 2 yr has not led to any definition of precision. However, the possibility of evaluating schemes for precise stationkeeping aboard an ATS is attractive because it can lead to the following:

- Onboard closed-loop orientation control, related to horizon scanners or stellar-inertial references, that would not need an onboard guidance computer to calculate orientation angles modified by actual ephemerides
- Large nonsteerable antennas at the ground terminals
- Active navigation beacons, whose position can be assumed constant by a receiving terminal
- Improved observations of tidal effects on geodetic parameters
- Use of laser relay links without the need for complex mechanization of a dual precise-pointing requirement

For design purposes it can be presumed that, since the satellite position can be measured to within about 100 to 120 m with a repeatability of about 25 m, it will be desirable to attempt to maintain the station to within this accuracy, at least for a period long enough to evaluate the capability of the system. This will require the propulsion system to negate the solar pressure effects in the east-west direction, in addition to the triaxiality and sun-moon gravitational perturbations.

To accommodate the first two goals indicated above, stationkeeping to 0.01 deg, or about 6 km, will be sufficient, and the present design includes sufficient propellant

and a low enough thrust level to perform north-south stationkeeping for 1 yr and east-west for 2 yr. To reach the latter three goals will require precise phasing of the north-south corrections with regard to the lunar and solar ascensions because the amplitude of the small oscillations superimposed on the inclination drift are of the order of 100 to 200 m and should be corrected. This latter requirement could use propellant at about twice the rate needed to counter the secular drift and will, therefore, only be attempted for a short experimental period

The stationkeeping provisions are somewhat arbitrary, and will not be allowed to affect the primary experiments unduly. The provision for negating the solar pressure could be dropped readily, so it need not be supported by redundancy. The stipulated north-south stationkeeping requirement for 1 yr will be met from an operational and functional point of view provided at least one thruster remains operating, since functionally it is the perturbation from translational thrust that defines the operating requirement.

## Section 5

### SPACECRAFT DEFINITION

#### 5.1 SELECTED CONFIGURATION

As a result of conceptual design studies and configuration analyses performed during the ATS-4 Phase A program, LMSC proposes a spacecraft vehicle that includes all proposed experiments and meets all performance requirements. The general arrangement of this vehicle in its deployed, or orbit, mode is shown in Fig. 5-1.

The vehicle design is largely influenced by the 30-ft diameter antenna and its feed. The LMSC concept employs the flexrib antenna, a design with a high furred-to-unfurled ratio (7:1). It also uses the LMSC-developed tri-beam extendible boom device to extend the antenna feed and the sensor section. In its ascent or stowed configuration, the spacecraft can use the existing Surveyor shroud, with a 4-ft extension on the barrel section. The vehicle in its ascent configuration is shown in Fig. 5-2.

##### 5.1.1 General Description

The ATS-4 vehicle consists of a group of structural forms - a sensor section and an equipment rack, parabolic antenna drum, and various boom-mounted equipments including solar arrays, experiments, and an antenna feed separation system. The largest structural member is the equipment rack that mates to the booster adapter. This rack, 84 in. in diameter, has a 57-in. diameter interior cylinder which houses the injection motor. The rack is constructed of magnesium rings, stiffeners, and panels. The hub drum of the 30-ft flexrib antenna is attached to the forward face of the rack. The two solar array extension booms are attached to the forward exterior ring of the rack and are stowed for ascent in a folded deck lying along the vehicle Y-Y axis. Immediately forward of the flexrib antenna drum is the lower sensor section,

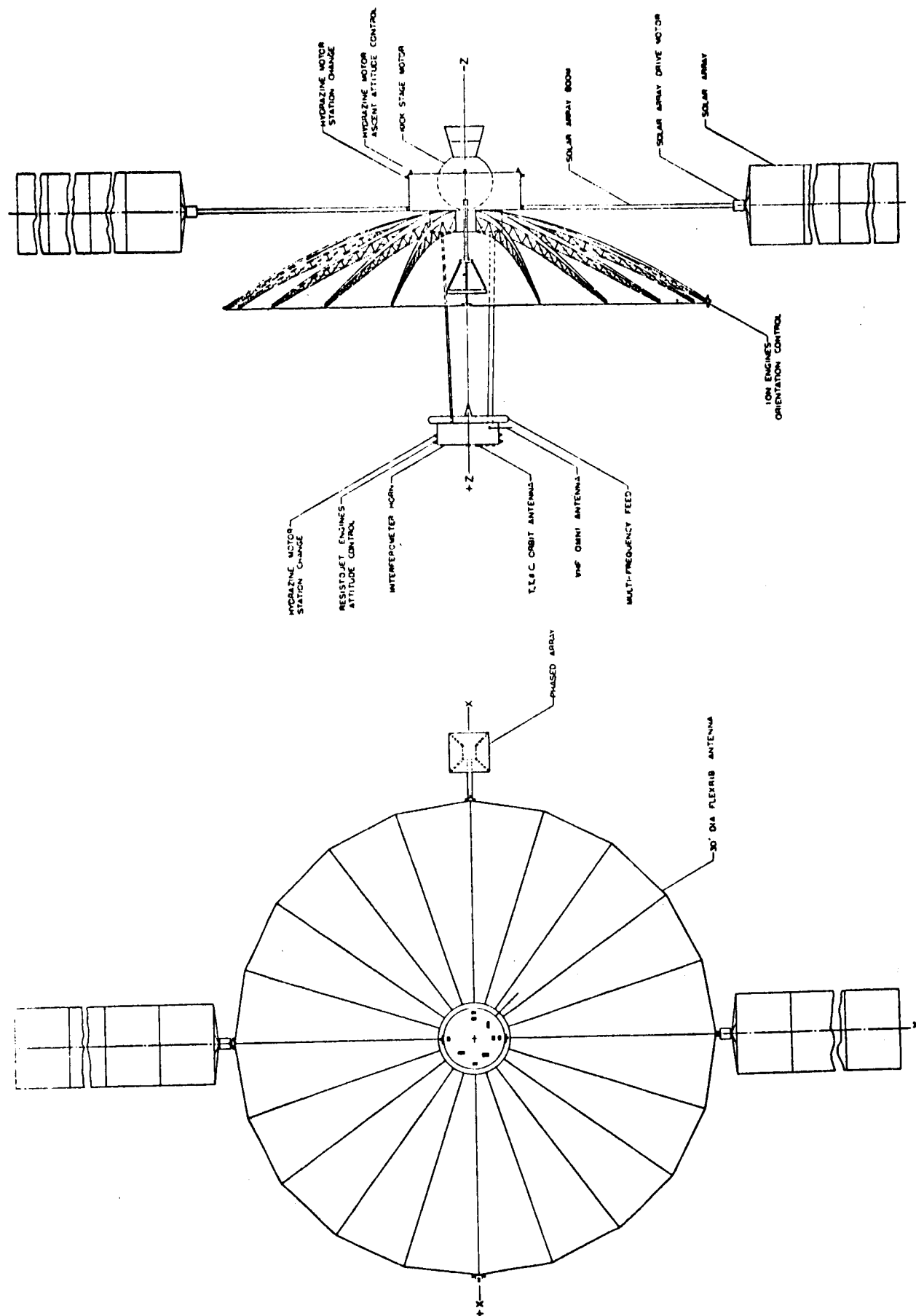


Fig. 5-1 ATS-4 Spacecraft Orbit Configuration

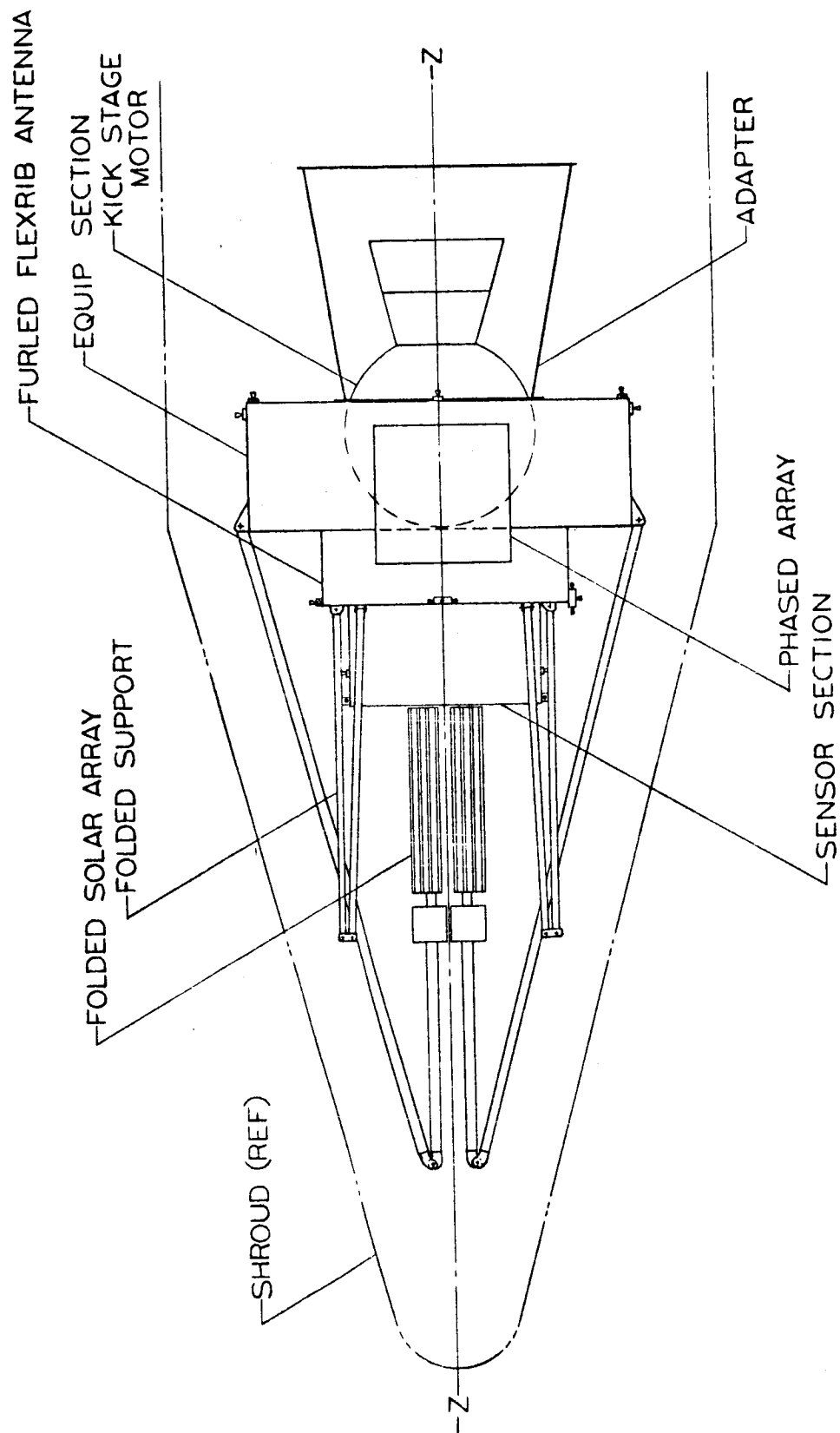


Fig. 5-2 ATS-4 Spacecraft Ascent Configuration

which also serves as the mount for the parabola feed. This rack is extended after orbit injection by the tri-beam device and two folding tubular struts. The use of the extendible feed design is made possible by the flat, unfurled package of the flexrib reflector. The design requires a shroud extension of less than 2 ft. For comparison, if petal-type antennas are used, the Surveyor shroud must be increased at least 10 ft in the barrel section, with concurrent performance penalty and additional program costs for testing and qualification.

The phased-array experiment is stowed in the upper equipment rack. It is extended along the vehicle X-X axis for a distance of 18 ft, placing it beyond the rim of the deployed antenna. The unit, which weighs approximately 100 lb, uses a small tri-beam extension device, which is 4-in. across the flat section. Use of the tri-beam for deployment of the phased array permits the most compact possible stowage of the boom since the beam-forming machine permits extension of wiring and cabling as the beam itself is extended.

#### 5.1.2 Equipment Racks and Fabricated Structures

The equipment section, shown in Fig. 5-3, is a doughnut-shaped structure having an 84-in. outside diameter and a 28-in. depth. It is constructed of formed extruded aluminum rings with magnesium alloy shear webs between the upper and lower surfaces. These shear webs divide the section into eight bays in which the various system equipments are grouped. The upper and lower skins, as well as the removable external panels, serve as thermal control surfaces during orbit. Equipment is accessible through the removable panels, and attachments are included for the equipment trays. At the shear web location, beams are provided for attaching the kick-stage motor and the spacecraft adapter. These beams transmit ascent and motor firing loads to the basic structure.

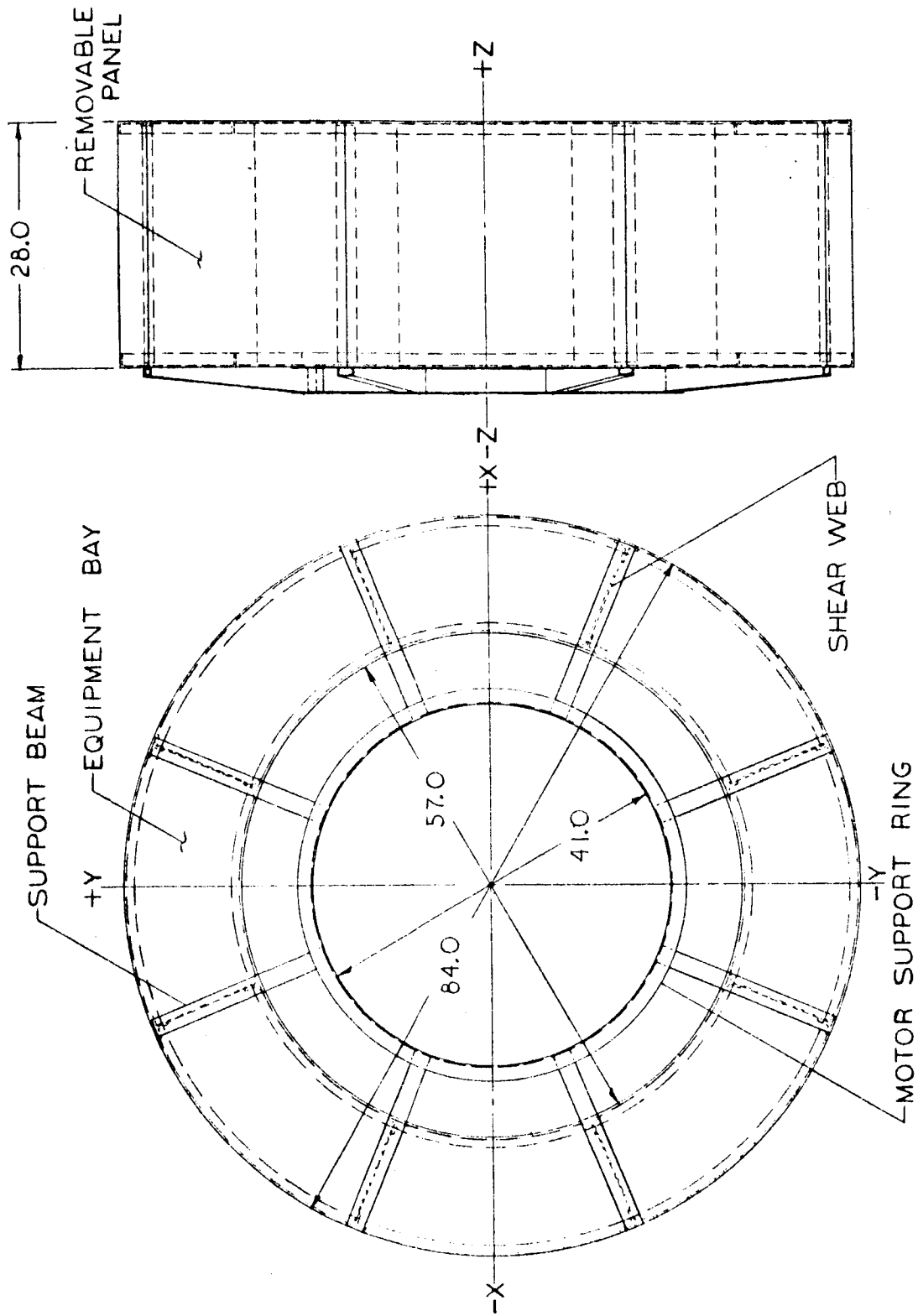


Fig. 5-3 Equipment Rack Structure

### 5.1.3 Equipment Location and Layout

In Figs. 5-4 and 5-5, the vehicle subsystem equipments in the equipment section and the sensor section are located and identified. With the exception of pressure vessels and plumbing, all equipments are mounted on detachable trays. These trays are similar in concept to the modularized-assembly method used on the Agena and other space vehicles in that each section, or module, can be independently given a preassembly checkout, and then mounted in the vehicle for subsystem and system checkout.

The exact location of all equipments cannot be determined in the conceptual design stage since this will require thermal-control analyses of each item including calculations of its surface emissivity and absorptivity. A description of the thermal-control system characteristics planned for the ATS-4 vehicle is given in subsection 5.1.4.

The equipment section will contain the following:

- The two hydrazine tanks, with associated plumbing and regulation equipment
- The Ni-Cd batteries, power regulation equipment, vehicle main bus, and central power distribution system
- Portions of the guidance and controls system (thruster junction boxes)
- Vehicle tracking, telemetry and control equipments, including all but two transponders and receivers for the 30-ft parabola experiment
- Vehicle special instrumentation for parabolic antenna evaluation
- Tri-beam extension device for the phased array experiment
- Vehicle-mounted electronics associated with the phased array experiment

The twin criteria of mass properties and thermal constraints dictate the actual location of these subsystem components. It may be required, for example, to relocate the batteries or to divide and mount them with components that provide a more benign thermal environment. Maintaining the batteries within the prescribed temperature limits is the most difficult problem in controlling the thermal environment.



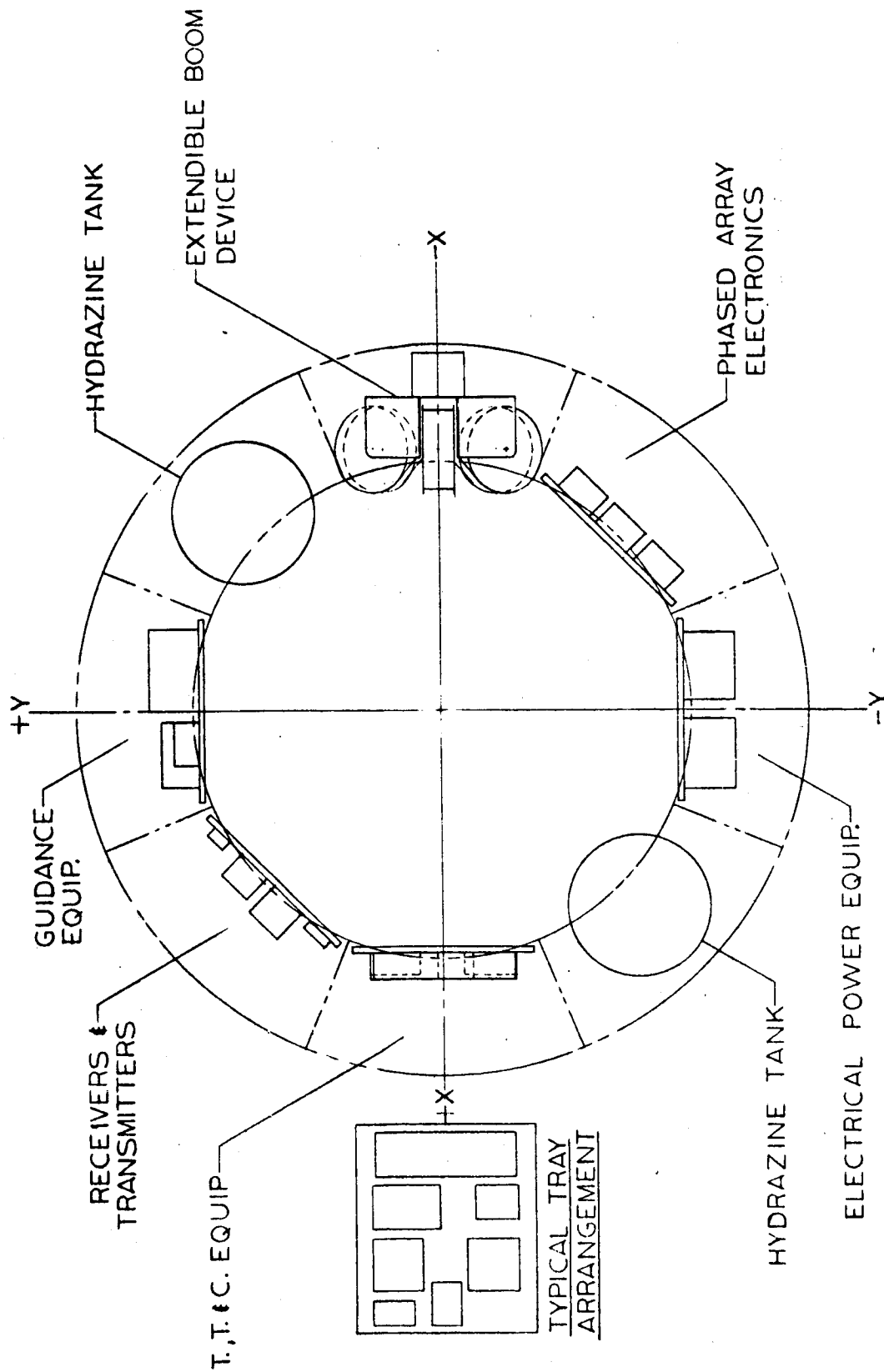


Fig. 5-4 Equipment Rack Installation

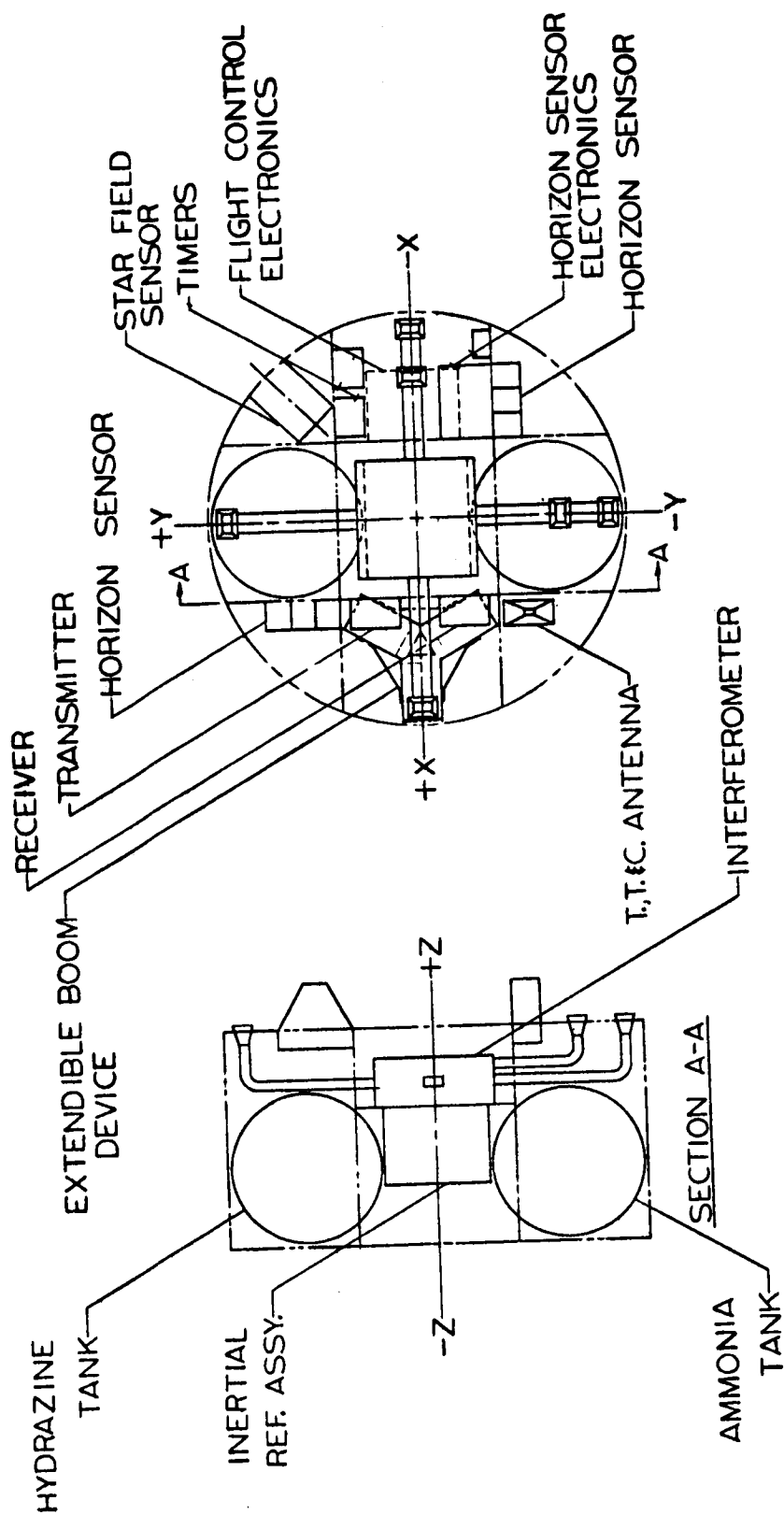


Fig. 5-5 Sensor Section Equipment Installation

Also, battery location complicates the mass properties and wiring harness problem. The exact location of the subsystem components in the equipment section is one of the first tasks to be undertaken in the next phase of the ATS-4 program.

The smaller equipment rack, called the sensor section, is extended on-orbit by the tri-beam system. This structure is shown in Fig. 5-6. This equipment rack houses:

- An ammonia storage tank for the resistance-jet attitude control system
- A hydrazine tank for the orbit translation nozzles
- Two transponders and receivers for the parabolic antenna experiment
- The complete interferometer unit, including antenna horns
- Guidance and control system sensors, including the strapped-down gyro package, horizon sensor, and flight controls electronics package containing the adaptive autopilot, standard autopilot, and attitude computer
- The tri-beam machine for extending the sensor section from the main equipment section. The sensor section also has provision for mounting the feed for the parabolic antenna experiment.

#### 5.1.4 Thermal Control

Constraints and Requirements. The spacecraft thermal design is largely dictated by absolute temperature requirements and/or the most rigid constraints for orbital temperature fluctuations and temperature gradients. These are:

- Batteries: 40° to 100° F
- Hydrazine tanks and engines: 40° to 100° F

Temperature limits of other equipment are;

- Solar cells: Upper limit of 130° F
- Electronic components: -30° to 165° F

Temperature Control of the ATS-4 Vehicle and Equipments. The vehicle temperatures will be passively controlled. The energy exchange with the space environment will be controlled by applying appropriate surface finishes to the vehicle exterior in a pattern that will result in an adequate ratio of solar absorptivity to infrared emissivity to maintain all equipments within their required limits.

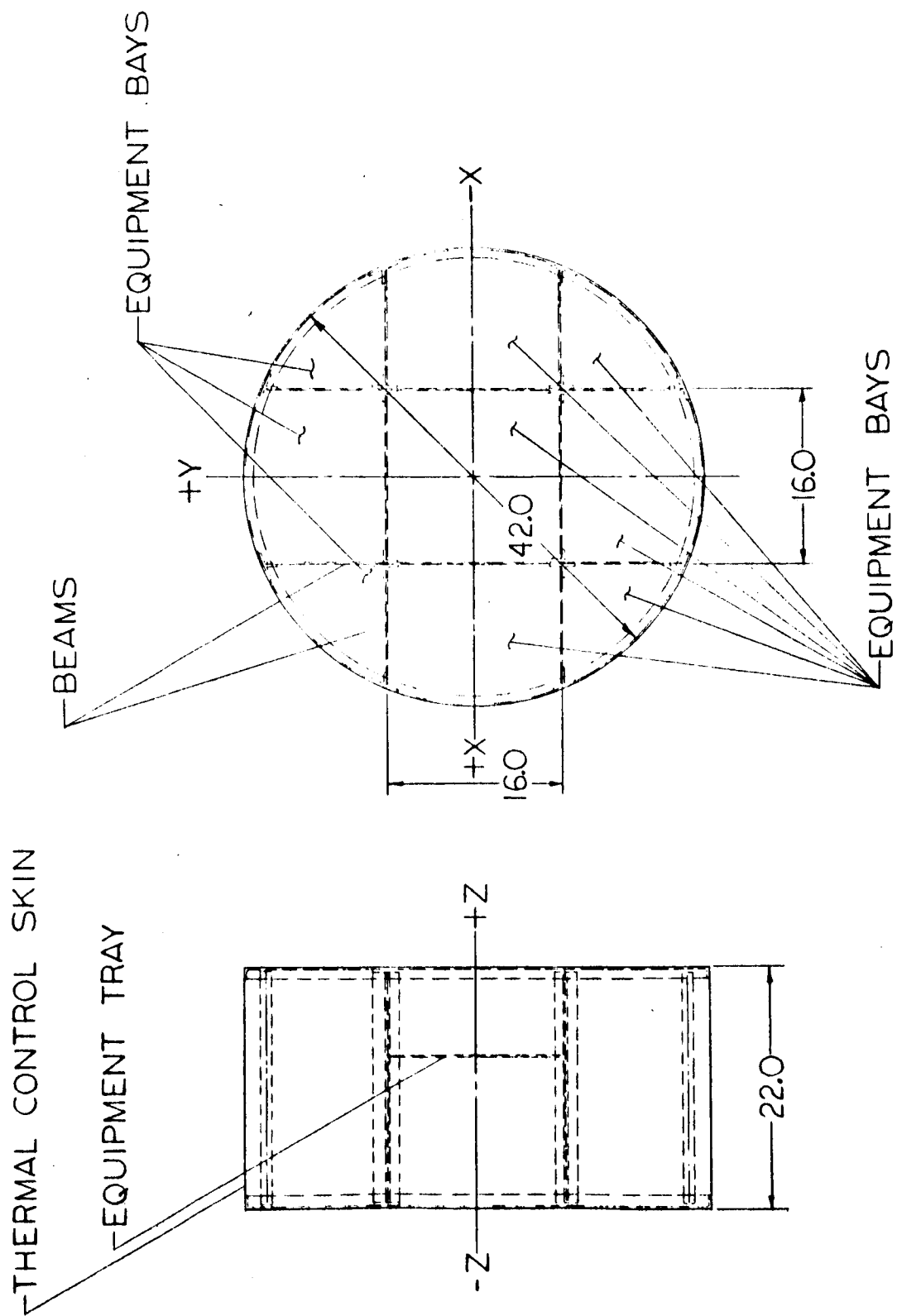


Fig. 5-6 Sensor Section Structure

Certain areas of the vehicle exterior will be exposed to maximum solar heating in an equatorial synchronous orbit; these areas may require thermal shields in the form of double skin sections or multilayer insulated blankets. The thermal design goal will be to minimize the effects of this maximum solar heating and the 1.2-hr shading total and to maintain the total energy input through any one orbit to as constant a value as possible. Thermal isolation may be required between the double skin sections to achieve a substantial temperature gradient and to be able to maintain an acceptable temperature level within the vehicle.

For the same reasons, the top and bottom sections of the equipment racks may require a double skin section or application of insulation material. Detailed computer studies will have to be performed to determine this requirement.

Equipment with wide temperature limits and no appreciable heat dissipation should be mounted in the leading and trailing sections of the vehicle, where the maximum and minimum temperature levels are expected. Equipment with high internal power dissipation will probably have to be mounted in the side sections of the vehicle (sections seeing minimum sun) so that the heat may be dissipated through the exterior skins in that area.

Mounting equipment directly to the web structures of the vehicle is generally desirable. Good heat conduction paths can be provided by flush mounting. This method of installation will be required for equipment with high power dissipations (batteries, transmitters, etc.). In some cases the thermal resistance between the mating surfaces of the equipment and web structures are appreciable and application of thermal conduction grease will be required. Dow-Corning #340 thermal conduction grease has been used frequently on the various LMSC programs and has proven effective.

Mounting equipment on top of angles, channels, and brackets will restrict the heat flow capability from equipment to the main vehicle structure. This method of mounting will therefore be avoided unless the particular equipment has no appreciable heat dissipation or requires thermal isolation.

The temperature increases of high-power transmitters during operation will be large and additional heat sink capabilities may have to be provided. Mounting the transmitter units flush to thin web structures will probably not conduct the generated heat adequately. The additional heat sink requirements may be provided by mounting the transmitters on aluminum plates that can be mounted to the vehicle web structures. The thickness of the heat sinks will depend on the heat flow characteristics of the various transmitters during the extreme operation cycles.

The operation cycles of all the equipment affect the temperature rises of the critical units and a complete evaluation of the effect of the duty cycle on vehicle equipment will be made once such a duty cycle is established.

The narrow operating temperature limits associated with batteries generally present thermal problems. In order to minimize the extreme temperature effects of the space environment, the batteries should be located close to the center of the vehicle. Mounting the batteries flush to the interior web structure is required to provide good heat conduction. Battery heat dissipations during charge and discharge cycles will be defined for use in thermal analysis.

Extendible Boom. It is necessary to keep the temperature gradient between the three faces of the extendible boom to a minimum. A temperature differential of 10° F between the face illuminated by the sun and the shaded face will cause a differential expansion in the length of 12.5 ft between the two faces, resulting in a shift in location of the antenna feed (due to bending in the boom) of about 1 in. Calculations have been made that show that the temperature difference between the two faces can be held to less than 10° F if the following requirements are met:

- Apply a surface finish with low absorptivity to the exterior face of the boom ( $\alpha = 0.18$  or less).
- Apply black kemacryl paint to the interior surfaces of the boom ( $\alpha/\epsilon = \frac{0.93}{0.88}$ )

- Inclose the beam in a double-walled aluminized Mylar sleeve.
- Locate lightening holes (to account for at least 25 percent of the surface area) in the several boom sections such that they are staggered with respect to each other along the boom length. When the entire boom is shaded by the earth, the vehicle itself, the solar arrays, or the antenna, considerable cooldown will result. During a 3-hr shade period (when the solar array shades the boom), a cooldown on the order of 300° F can be expected. If such a decrease in temperature is incompatible with any equipment contained in the boom (such as power cables, gas lines, etc), special protection for these items or a radiation shield around the entire boom may be necessary.

## 5.2 ALTERNATIVE CONFIGURATIONS

A complete series of design analyses was completed prior to selection of the vehicle configuration shown in subsection 5.1. Several of these design studies are illustrated in Fig. 5-7. Although only four basic types are shown, the study included six different configurations, four types of solar array or power systems, etc. For each of these configurations, estimates were made of vehicle inert weight, and evaluations conducted on suitability for the selected boosters, shroud applicability, operational characteristics, and suitability to the ATS-4 mission.

With the dismissal of the types of configurations described above, a decision was made to develop a configuration suitable for any of the proposed booster vehicles, i.e., Atlas/Agena, Atlas/Centaur, and Titan III-C/Transtage. In addition, it was determined that the configuration should have the flexibility to accept either petaline or flexrib antennas, operate either with or without injection motors depending upon the type of booster used, and accept additional experiments without needless or expensive redesign. A basic vehicle was designed with these attributes and subjected to the following evaluation criteria:

- The design must provide sufficient performance margin to accomplish the mission on a  $-3\sigma$  basis.

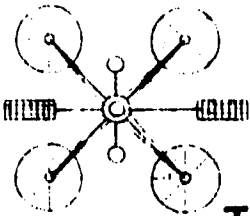
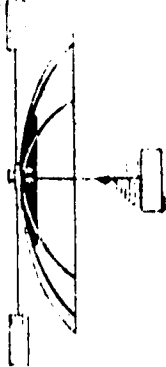
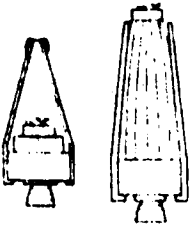

VEHICLE TYPE	EXTENT OF ANALYSIS	FAVORABLE	UNFAVORABLE
 <b>4-DISH</b>	DESIGN - WEIGHTS-CG'S- EQUIPMENT LIST- ELECTRONICS - RELIABILITY DYNAMICS -	HIGH GAIN WITH WIDE BEAM WIDTH- NO EXTENSIVE ANTENNA DEVELOPMENT - GOOD CONTROL MOMENTS -	STRUCTURAL WEIGHT - ALIGNMENT PROBLEM - NOT MULTI-PURPOSE - DEPLOYMENT RELIABILITY- TITAN ONLY -
 <b>MULTI-NESTED DISHES</b>	DESIGN - WEIGHTS - EQUIPMENT LIST- DEPLOYMENT - ELECTRONICS -	MAXIMUM GAIN AT ALL SPECIFIED FREQUENCIES -	TITAN ONLY - FURLED VOLUME - WEIGHT -
 <b>SPIN STABILIZED SERIES</b>	LAYOUTS CG'S-MOMENTS- GUIDANCE AND CONTROLS - INJ. ERROR ANAL-	SIMPLIFIED ASCENT SEQUENCE- CAN UTILIZE ATLAS/AGENA BOOSTER -	NO SOLID ANTENNAS - DIFFICULT TO VARY EXPERIMENTS- NOT MULTI-PURPOSE - INJECTION DYNAMICS PROBLEMS- ASCENT GUIDANCE ERRORS -
 <b>SEPARATE TITAN AND CENTAUR DESIGNS</b>	DETAILED LAYOUTS EQUIPMENT LISTS SHROUD ANALYSIS PERF. ANAL. WEIGHT-TRADEOFFS	OPTIMUM DESIGN, CENTAUR - OPTIMUM DESIGN, TITAN III-C - MINIMUM SHROUD LENGTHS - WIDEST PERF. MARGIN -	NOT MULTI-PURPOSE

Fig. 5-7 Typical Configurations of Selection Matrix



- The design must be compatible with both Centaur and Titan boosters.
- The design must be adaptable to additional technology experiments.
- The design must require minimum shroud, booster, and AGE modifications.

Rating factors were applied to each criterion. The result of these studies is the configuration described in subsection 5.1, which utilizes the flexrib antenna and is injected by the Centaur booster. Continued performance analysis studies, as well as cost effectiveness studies, showed that this combination provided the best means of achieving mission success at the lowest total system cost.

All of these design and performance analyses were conducted with the single purpose of determining the most efficient system. Selection of the flexrib antenna, for example, was based on an evaluation of 14 significant factors, the impact of each factor having a first-order effect on the antenna and second-order effects on the vehicle design.

It is significant to note, however, that the LMSC design can be adapted to petal-type antennas, or to any other type of antenna that falls within the weight allocation for this class of booster.

### 5.3 STRUCTURAL

Based on the conceptual design outlined in subsection 5.1, LMSC has investigated several potential problem areas involving the vehicle structure and its dynamic response to both ascent and orbit control force functions. The results of this preliminary evaluation are described in this subsection.

The equipment list and weight statement included in subsection 5.3.2 includes the latest estimate of vehicle weights based on calculations and actual weight data taken from similar flight hardware. Much attention has been devoted to design analysis of the vehicle adapter. The analysis considered lightweight shell structures, corrugated sandwich structures, panel and corrugation structures, etc. A simple adapter section of monocoque design was chosen on the basis of data supplied by LMSC structures engineering. Section 5.3.3 describes this structure and its components.

### 5.3.1 Dynamics Analysis

A preliminary dynamics response analysis was made of the ATS-4 to determine the magnitude of elastic deflections when the vehicle is subjected to control forces. This analysis concentrated on the deployed solar arrays and booms - that portion of the deployed vehicle which, in LMSC's opinion, presented the most significant problem.

The general configuration analyzed is shown in Fig. 5-8. The mass and inertia data used in the analysis are presented in Table 5-10. The modal data computed for translation, pitch, and torsion modes of vibration are outlined in Fig. 5-9, and elastic deflections of the solar arrays with respect to the main body structure are shown in Fig. 5-10. Cases I and II in Fig. 5-10 show the worst cases for the orbit adjust control forces. The input forces were assumed to be step forces. Cases III, IV, and V show the worst cases of the orientation control forces in which these forces were assumed single square-wave impulses tuned to the first structural mode.

Fig. 5-11 presents the maximum elastic deflection of the solar arrays versus structural damping for a steady-state sinusoidally varying control force of  $0.250 \times 10^{-3}$  lb tuned to the first pitch mode.

In these analyses it was assumed that the booms were aluminum tubes. Since the analysis was made, the design has been changed to prefabricated tri-beam sections with Velcro tape for fastening and permanent spot fasteners for torsional stiffness. These beams exhibit great natural damping, however the data necessary for revision of the dynamics analyses were not available in time for this report. LMSC will continue to evaluate the use of damped extension booms, including several sections of the tri-beam as well as foam-filled thin-walled aluminum tubing.

The preliminary result of this analysis indicates that although the structural frequency of the configuration is low enough that the orientation control forces could be tuned to it, the use of damped structural booms will limit the deflections to acceptable values.

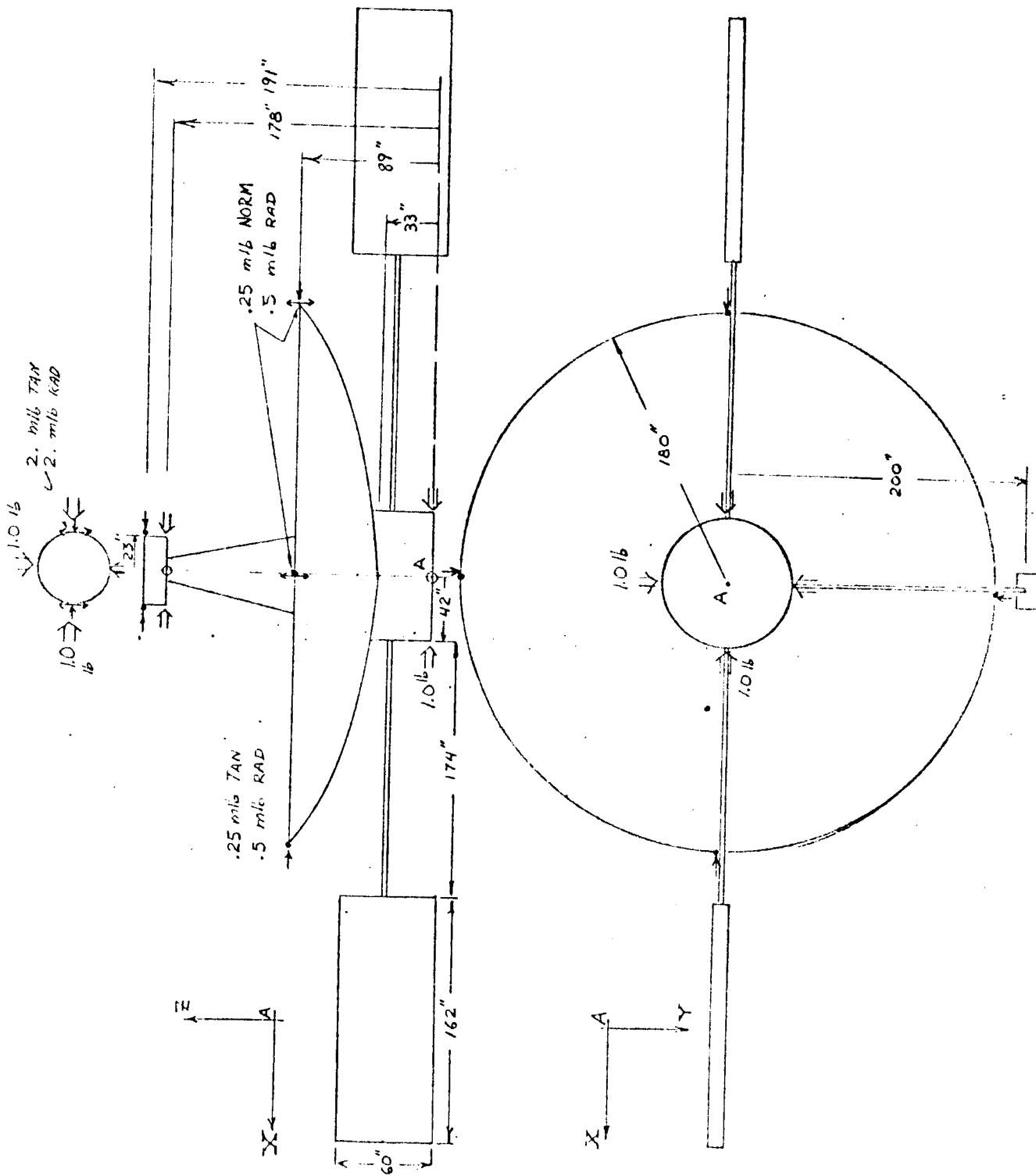
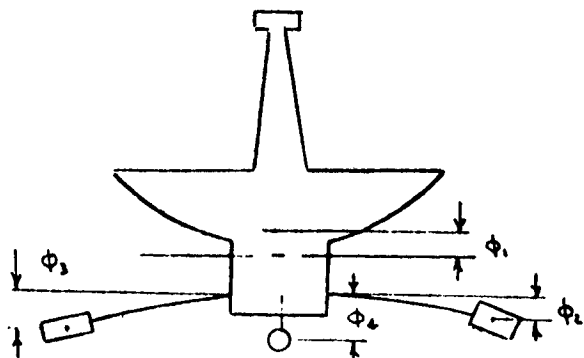


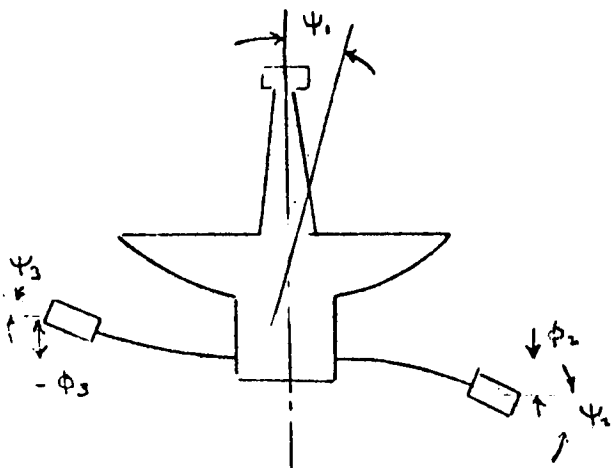
Fig. 5-8 Dynamic Model of A TS-4 Spacecraft

# TRANSLATION



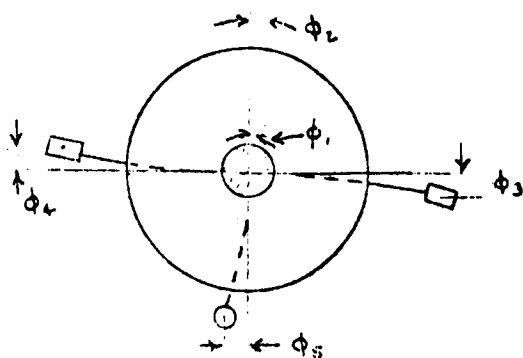
FREQ. (CPS)	GEN. MASS LB-SEC <sup>2</sup> -IN <sup>-1</sup>	$\phi_1$	$\phi_2$	$\phi_3$	$\phi_4$
.20	1.04	.251	-1.0	-1.0	-1.0

# PITCH



FREQ (CPS)	GEN. MASS (LB-SEC <sup>2</sup> -IN <sup>-1</sup> )	$\phi_1$ $\psi_1$	$\phi_2$ $\psi_2$	$\phi_3$ $\psi_3$
.19	.577	-.138 -.00003	1.0 .0060	.89 .0054
.28	1.33	-.017 -.0052	-.77 -.017	1.0 .0082
1.93	4.30	-.086 -.00014	.19 -.015	1.0 -.077

# TORSION

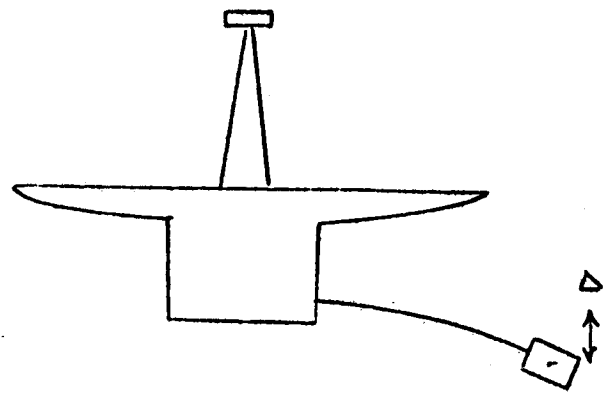


FREQ. (CPS)	* GEN. MASS	$\phi_1$ (RAD)	$\phi_2$ (RAD)	$\phi_3$ (IN)	$\phi_4$ (IN)	$\phi_5$ (IN)
.20	$.39 \times 10^5$	$-.60 \times 10^{-15}$	$-.60 \times 10^{-15}$	300	-300	$-.91 \times 10^{-5}$
.30	$.13 \times 10^5$	.38	.38	-86.5	-86.5	200
.84	$.43 \times 10^5$	1.0	.94	-16.5	-16.5	.42

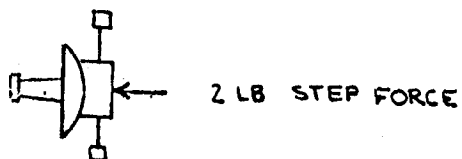
\* LB-SEC<sup>2</sup>-IN

Fig. 5-9 Dynamic Modal Analysis

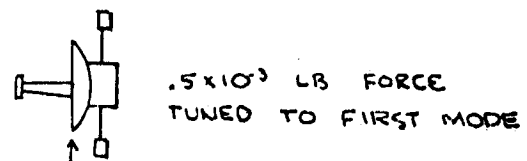
CASE	$\Delta$ - RELATIVE DEFLECTION
I	0.41 IN
II	0.47 IN
III	$3.3 \times 10^{-4}$ IN.
IV	$1.5 \times 10^{-4}$ IN.
V	$4.8 \times 10^{-4}$ IN.



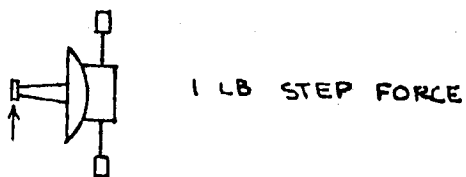
#### I TRANSLATION



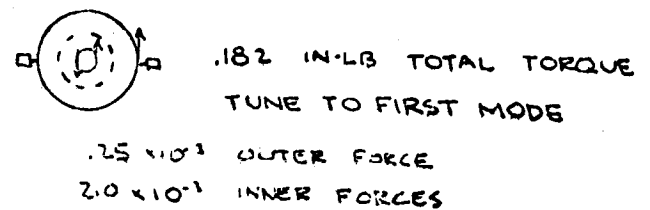
#### IV PITCH



#### II PITCH



#### V TORSION



#### III PITCH

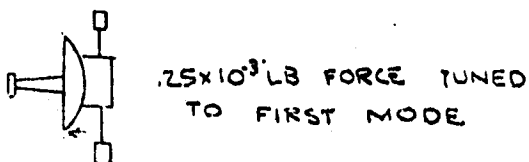


Fig. 5-10 Dynamics Analysis Results

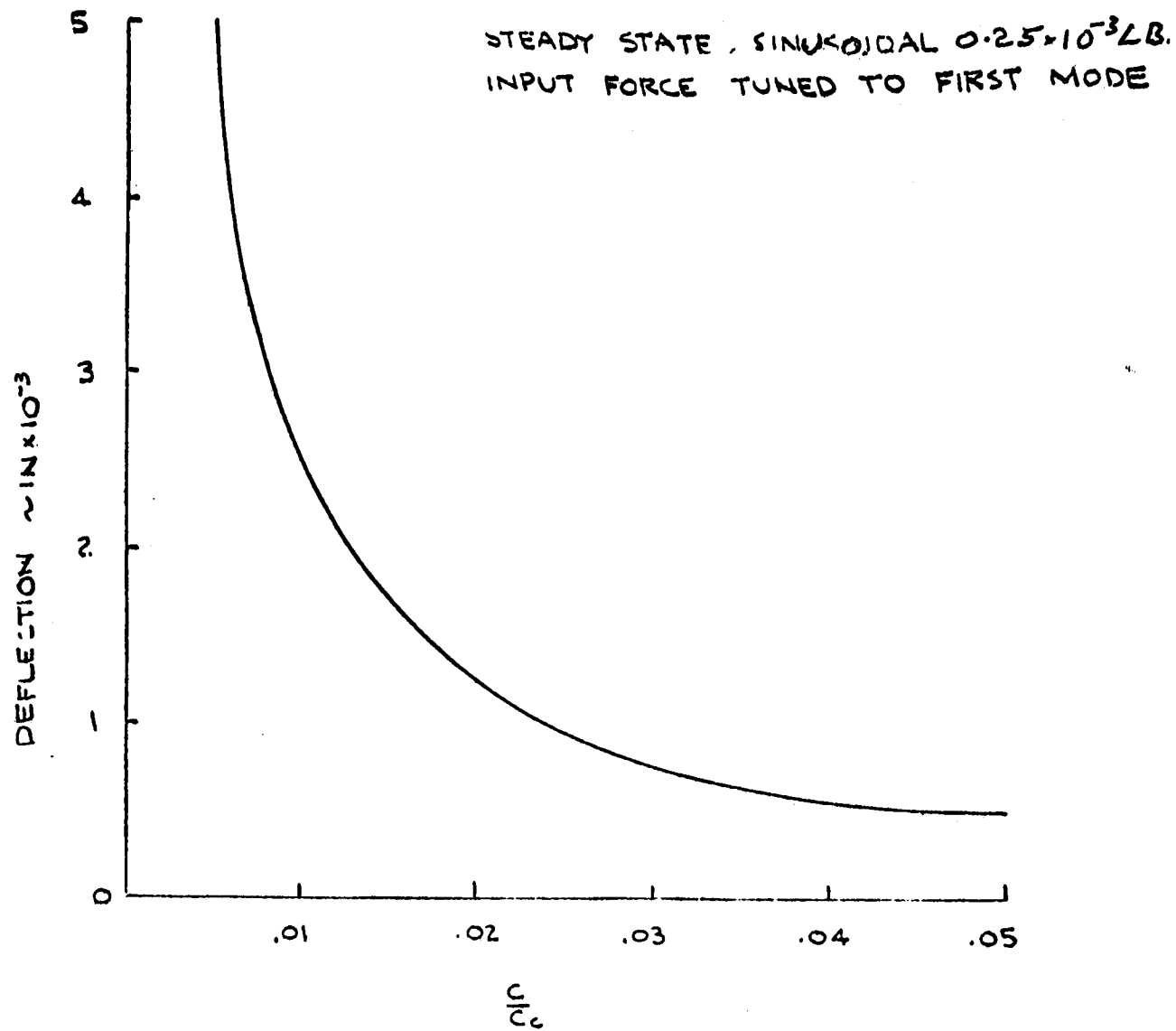


Fig. 5-11 Solar-Array Structural Deflections vs. Damping Ratio

### 5.3.2 Equipment List and Weights

A list of ATS-4 vehicle equipments, with assigned weights, is shown in Table 5-1. Each of the major vehicle subsystems is summarized, with the weights of the more significant components listed.

In Table 5-2, and in Fig. 5-12, are shown the weight versus performance values for the spacecraft described in the equipment list. Note that the vehicle has a 201-lb contingency that can be used to cover design weight changes, or can be effectively utilized for additional payloads or experiments.

This final weight statement reflects the combined results of both LMSC and EOS engineering and analysis for this phase of the ATS-4 program. Weights for structures, wiring, propellants, phased array, and interferometer were calculated. The weight of the flexrib antenna was extrapolated from hub and rib structures already fabricated by LMSC; solar array and power system weights were extrapolated from current EOS hardware. Extendible boom weights, particularly tri-beam weights were taken from existing LMSC hardware. Weights and volumes for electronics components were taken directly from catalogue specifications.

### 5.3.3 Launch-Vehicle Interface

Payload Adapter. The adapter section forms the structural connection between the ATS-4 spacecraft and the Centaur forward bulkhead to provide an acceptable load distribution at the Centaur payload adapter ring. The payload adapter includes attachments for payload separation mechanisms, an inflight electrical disconnect mechanism, and a range-safety destruct unit.

Table 5-1

## ATS-4 WEIGHTS

Subsystem	Weight (lb)	Subsystem	Weight (lb)
Attitude Control	93.0	Solar Array Drive (2)	14.0
Horizon Sensor	20.0	Batteries (1080 w-hr Ni-Cd)	108.0
Inertial Reference	19.0	Series Regulators (Pri., Redundant)	25.0
Flight Control Electronics	10.0	Interferometer	36.0
Adaptive Autopilot/Attitude Comp.	15.0	Phased Array	131.0
Star Field Sensor (2)	20.0	Hughes 30-db Array	112.0
Electronic Timer (2)	9.0	Phased Array Support Boom and Mechanism	19.0
Initial Acquisition/Transfer Orbit Control	1,616.8	Transponders (Experiments)	46.0
Injection Attitude Control Prop.	9.8	100-MHz Transmitter	8.0
60-lb N <sub>2</sub> H <sub>4</sub> Thruster (4)	24.0	800-MHz Transmitter	7.0
1-lb N <sub>2</sub> H <sub>4</sub> Thruster (4)	6.0	1,700-MHz Receiver	5.0
Plumbing, Valves	7.0	2,100-MHz Receiver	5.0
Injection Motor	1,570.0	2,300-MHz Transmitter	7.0
Transfer Ellipse Control Prop.	Negligible	7,300-MHz Transmitter	7.0
Vernier Propulsion	87.5	8,000-MHz Receiver	5.0
Impulse Propulsion (230 ft/sec)	51.3	Diplexers, TR Switches	2.0
N <sub>2</sub> H <sub>4</sub> Tankage	14.0	Antenna Reflector	222.0
Plumbing, Transducers, Valves	15.2	Reflector (30-ft Flexrib)	200.0
N <sub>2</sub> Pressurization Gas	1.0	Contour Instrumentation	22.0
1-lb N <sub>2</sub> H <sub>4</sub> Thruster (4)	6.0	Antenna Feed	7.0
Stationkeeping/Attitude Control Propulsion	86.7	Wiring Harnesses	65.0
NH <sub>3</sub> Control Impulse (3,500 lb-sec)	17.5	Thermal Control	10.0
Resistojet Cluster (3 thrusters ea.) (2)	6.0	Structure	229.0
NH <sub>3</sub> Tankage/Regulator	19.0	Feed Support	30.0
Plumbing, Transducers	5.0	Extendible Boom	19.0
Ion Clusters (3 thrusters ea.) (4)	39.2	Strut (2)	11.0
TT&C	50.8	Lower Module	72.0
Transponder, 4-6 GHz	10.2	Upper Module	127.0
Transponder, VHF	3.8	Adapter	167.5
PCM Telemeter, Primary	17.0	5-ft Adapter Section	137.0
PCM Telemeter, Minimal	9.0	Separation Mechanism	13.0
Command Decoders (2 ea.)	9.5	Destruct Charge	1.5
Orbit Antenna, 4-6 GHz	0.8	Lateral Stabilizer (4)	16.0
Ascent/Orbit Antenna, VHF	0.5		
Electric Power	325.0		
Solar Array Panel (2)	162.0		
Solar Array Boom (2)	16.0		



Table 5-2

ATS-4 WEIGHT REDUCTION FROM LIFTOFF TO  
ORBIT INJECTION

Item	Weight (lb)
Weight at Liftoff	4,000
Shroud Drop Weight	<u>18</u>
	3,982
Adapter Weight	<u>168</u>
	3,814
Performance Loss (7.7-deg Incl Removed)*	<u>607</u>
Maximum Spacecraft Weight Into Transfer Ellipse	3,207
Secondary Experiments, Contingency	<u>201</u>
Current Spacecraft Weight	3,006
Transfer Ellipse Expendible Usage	<u>0</u>
Weight at Apogee Firing	3,006
Kick Motor and Attitude Control Propellant	<u>1,440</u>
Weight After Apogee Firing	1,566
Injection Error/Station Acquisition Propellant	<u>51</u>
Weight on Station	1,515

\*See Fig. 5-12.

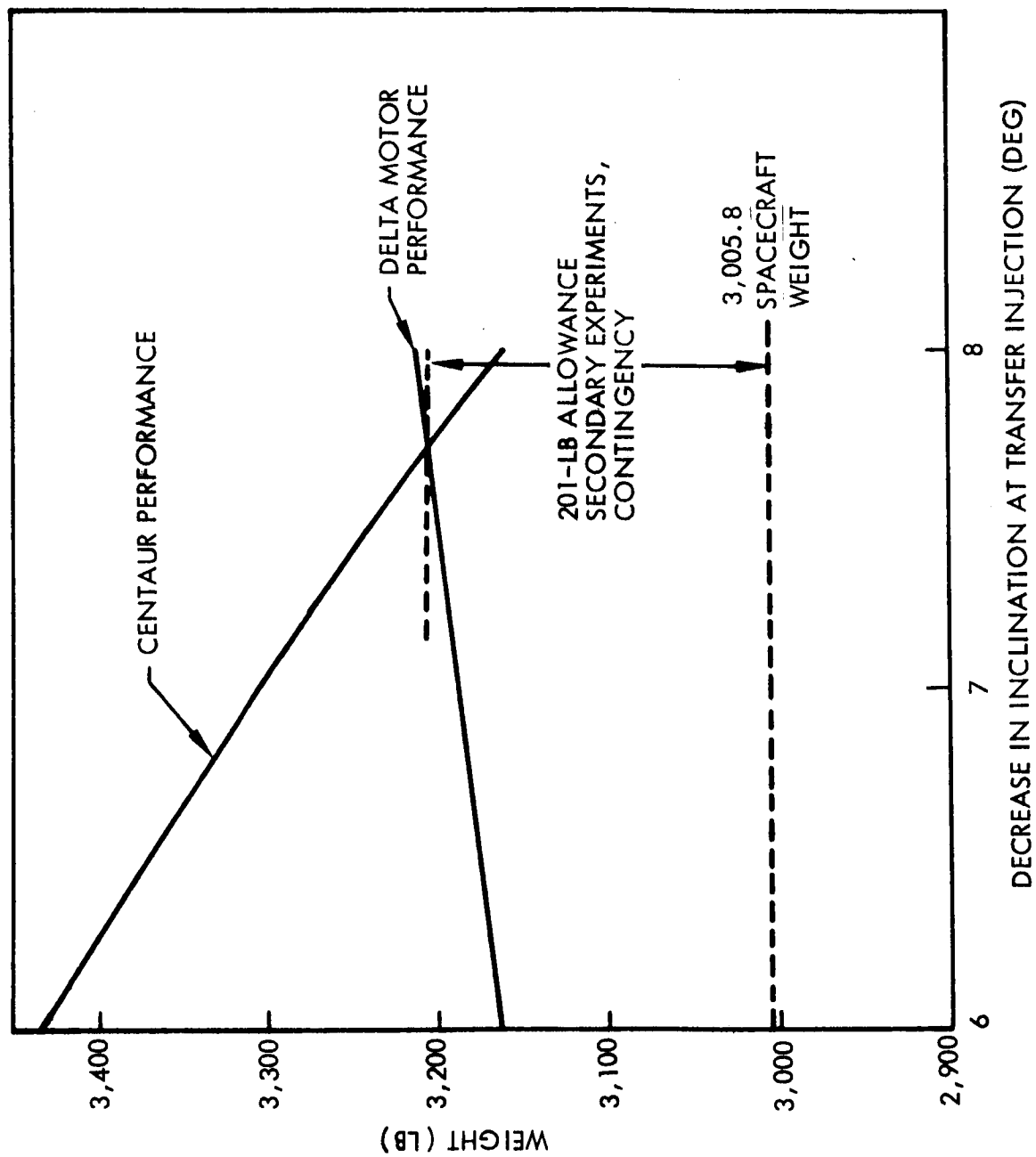


Fig. 5-12 Centaur Weight Performance Using Delta Injection Motor

As shown in Fig. 5-13, the adapter is a truncated aluminum skin and ring conical structure. It is mounted on a 5-ft diameter ring on the Centaur forward bulkhead. The separation system for the ATS-4 vehicle will utilize the Surveyor-type system consisting of a pyrotechnic-actuated separation latch and a set of compressed helical springs located at each 120-deg interval. Upon separation, the spring sets located close to the latches impart a longitudinal motion of approximately 1 ft/sec and a maximum angular rotation rate of less than 3 deg/sec to the satellite. The shock imparted by latch actuation at the separation plane is less than 5 g.

Electrical Interface. The ATS-4 vehicle will use the Surveyor-type electrical interface which is a 52-pin connector located between the adapter and the satellite vehicle. A wiring harness is provided leading from the electrical connector to terminal points on the Centaur. The terminal points include the electrical ground-connect umbilical, the telemetering system, and the flight control system. The electrical interface permits transmittal of payload environmental data and engineering data through Centaur telemetry to the ground and allows transmission of flight control commands from the Centaur autopilot to the payload. A separation command from the Centaur flight control system disconnects the electrical connector, and 5 sec later the satellite vehicle separation squibs ignite, separating the payload from the Centaur.

Prelaunch checkout of the spacecraft is by means of the electrical umbilical leads running to the Centaur/payload connector. The spacecraft checkout is integrated into the Centaur launch countdown procedure.

Environmental Control. Support facilities are available at the launch site to supply a conditioned atmosphere to the payload. The system has two air conditioning units, one of which serves as a backup. Conditioned air is provided during standby and until the Centaur vehicle starts tanking liquid hydrogen; gaseous nitrogen is then provided as the cooling medium. The inert nitrogen is also used to prevent an explosion hazard in the payload shroud.

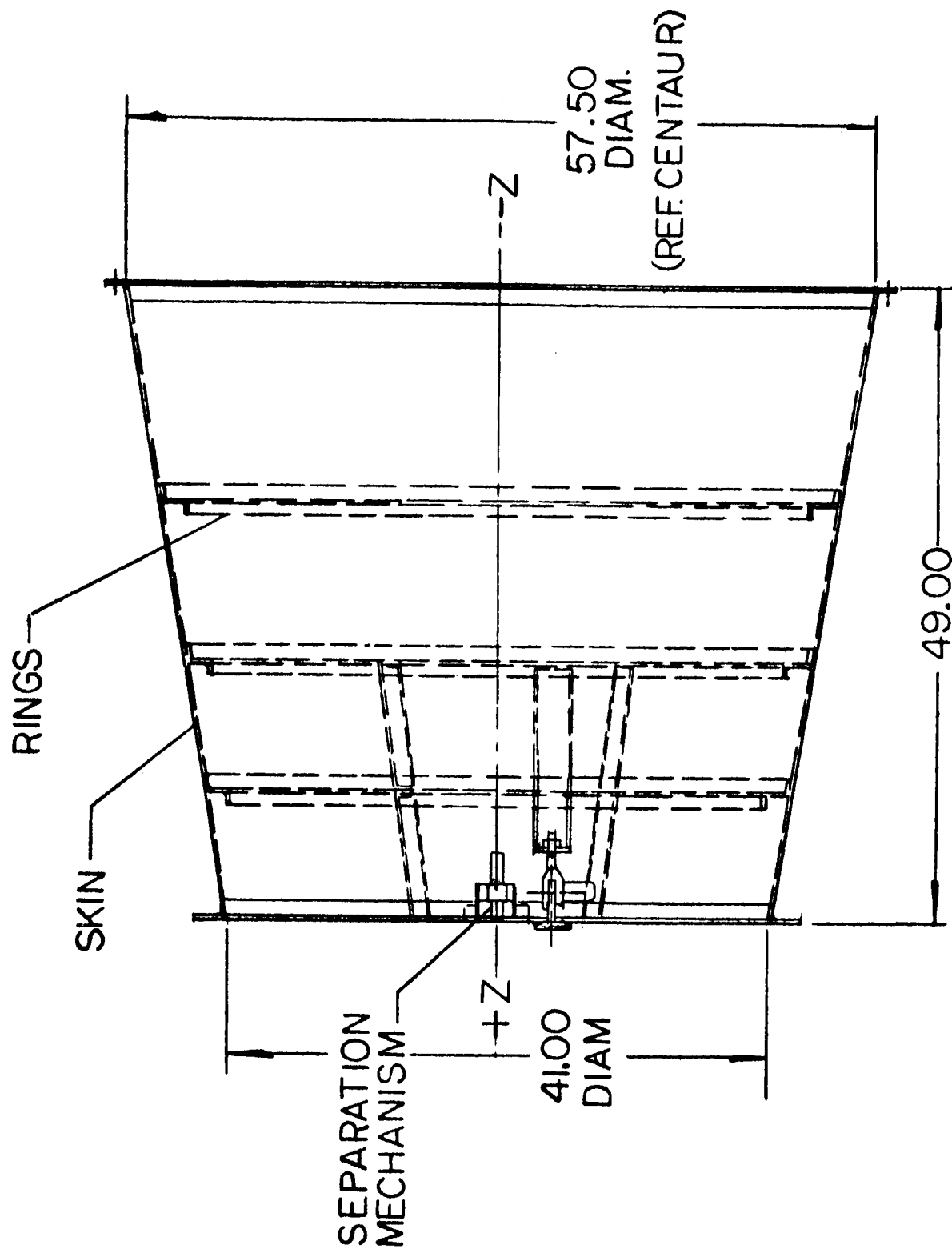


Fig. 5-13 Spacecraft Structural Adapter

Payload Fairing. The ATS-4 vehicle will use a modified Surveyor shroud with a lengthened cylindrical section. The basic shape is a 30-deg conical section with a spherical nose cap mated to a 10-ft diameter barrel section. The cylindrical section contains access doors to the payload adapter and Centaur forward equipment.

The nose fairing is fabricated of laminated fiberglass cloth faces and a fiberglass honeycomb core. It has a split line along the vehicle X-axis to allow fairing jettisoning during flight. Sealing provisions are included as dictated by payload air conditioning requirements and, in conjunction with the fairing vent system, by the structural requirement to maintain a positive external pressure over the surface of the fairing during flight.

When the Centaur vehicle clears the limits of the atmosphere, the nose fairing (including the cylindrical section) is jettisoned. Explosive latches installed along the split line between the two halves and a linear-shaped charge located circumferentially just forward of the bolted connection to the Centaur tank are ignited on command from the Centaur flight control system and all connections are severed. Nitrogen gas stored in two bottles near the forward end of the conical section provides the jettison force. The nitrogen gas is released from the bottles by ignition of an explosive pin-puller mechanism; the resultant reactive force in conjunction with the acceleration of the vehicle rotates the fairing halves clear of the vehicle. The maximum shock imparted to the payload during this separation sequence is less than 5 g.

## 5.4 ELECTRICAL

### 5.4.1 Selected System

A conventional photovoltaic solar power system designed on the basis of present technology has been selected. It consists of two symmetrically deployed panels mounted on booms that extend beyond the shadow line of the antenna. These panels will face the sun continuously, since the booms will be parallel to the earth's axis and will be rotated once per day by the mechanism described in subsection 5.4.5. Initial sizing is based on a 900-w peak power requirement to the end of the first year of operation. The solar cells selected are N/P, 2 by 2 cm, 12 mils thick, with a 6-mil  $\text{SiO}_2$  coverglass.

The solar array will be  $135 \text{ ft}^2$  in area and will weigh approximately 162 lb. The array will consist of two panels, each 5 by 13.5 ft consisting of four subpanels, each 5 by 3.375 ft. The panels will be mounted on each side of the spacecraft and will be folded into an 8-in. width. The subpanel will be fabricated from 0.5-in. aluminum honeycomb with a 0.005-in. aluminum facing and a 1.25-in. thick aluminum structural support member.

The array will be driven continuously by a DC motor operating an enclosed harmonic drive. An intermediate rotating sleeve will provide a bearing rotational speed and a slip-ring surface speed high enough to prevent cold welding and low enough to prevent excessive wear.

Nickel-cadmium batteries will be used to provide power during solar occultation, and during ascent and solar acquisition. The array is sized to meet peak-power demands and the batteries will not be used for power smoothing during normal sunlit operations.

### 5.4.2 Alternatives Considered

The need for an operational power system using space-proven technology dictated the use of solar-photovoltaic systems. Solar thermionic systems are potentially attractive

but need further development. Reactor and isotope systems would be far heavier and would present system integration and operation problems.

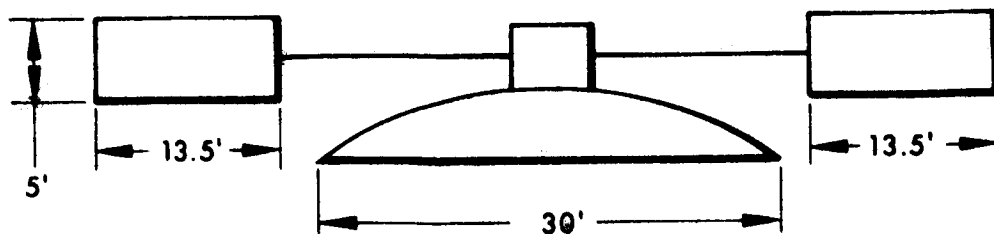
Various nonoriented arrays were considered early in the study. These included body-mounted, cylindrical, cruciform, and triform (three-panel) configurations. However, all of these would be heavier than the chosen semioriented array by a factor of more than three in every case, and this would add at least 300 lb to the spacecraft weight.

A fully oriented array was given brief consideration. This system uses articulation of the panels through  $\pm 23\text{-}1/2$  deg to keep the array normal to the sunline. The saving in array weight (8.3 percent) would have been almost offset by the added mechanization, and the complexity, reliability, and packaging and design problems indicated that the extra articulation was not worthwhile.

The possibility of using a single boom-mounted array instead of a dual symmetrical configuration was considered briefly. The reduction in complexity was offset by some increase in solar pressure torques and unbalance in the launch configuration. It was concluded that this alternative was acceptable but not particularly desirable, since symmetry is always simpler to handle in the design phase.

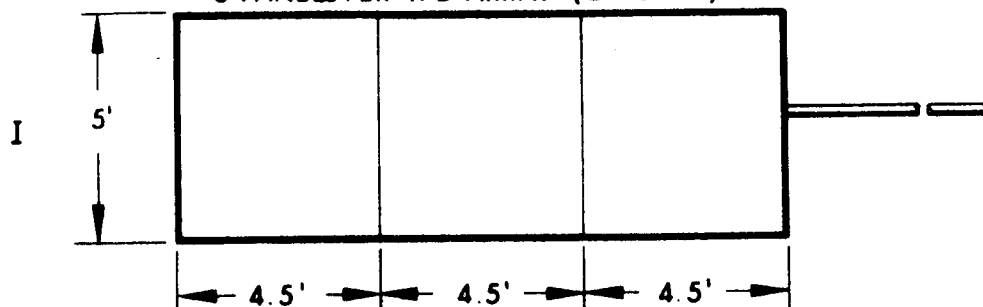
A size of 13.5 by 5 ft was selected for each half-array, and consideration given to dividing each into three, four, or five panels as shown in Fig. 5-14. Of the arrangements shown, Configuration II was found most readily compatible with the spacecraft launch configuration.

The use of aluminum honeycomb and facing material for the substrate was based on space-proven practice. Much lighter substrates are under development, including fiberglass tape stretched on beryllium frames, and electroformed hollow-core integral structures in nickel and aluminum/magnesium alloys. These substrates would reduce the basic panel weights to below  $0.5 \text{ lb/ft}^2$  and  $0.3 \text{ lb/ft}^2$ , respectively, thus saving 60 or 90 lb of total weight. However, these lighter substrates have not yet been tested in space, and they, therefore, were not selected for the present operational requirement.

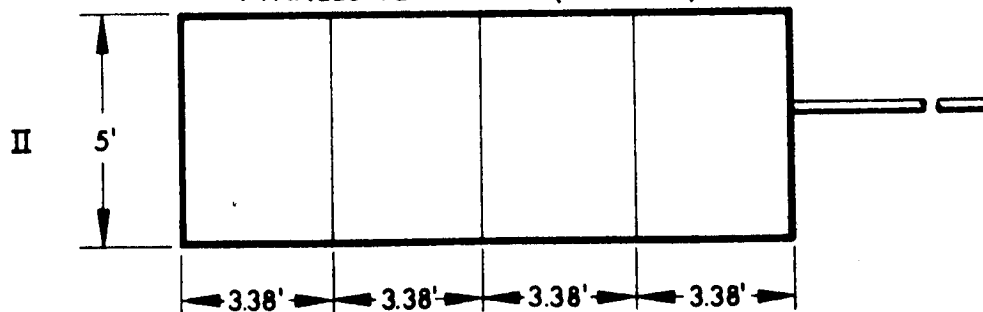


### POSSIBLE ARRAY CONFIGURATIONS

#### 3 PANELS PER 1/2 ARRAY (2 FOLDS)



#### 4 PANELS PER ARRAY (3 FOLDS)



#### 5 PANELS PER 1/2 ARRAY (4 FOLDS)

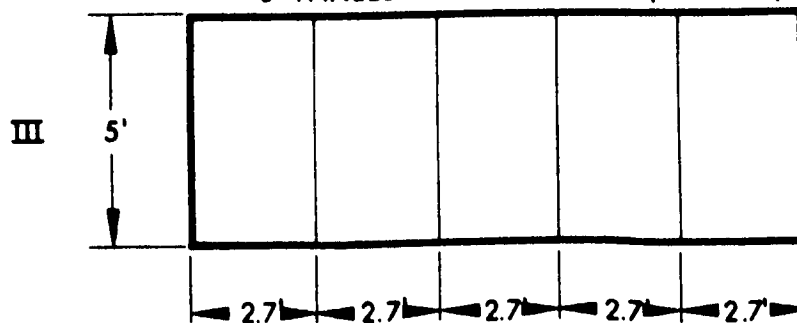


Fig. 5-14 Alternate Solar-Panel Configurations



Use of a nonfolding array in which two large panels would be mounted alongside a furled petaline antenna was considered; however, this concept was discarded for two primary reasons. First, the dynamic envelope between the antenna and shroud would be restricted severely and, second, the malfunction of either one of the panel deployment mechanisms could interfere with deployment of the antenna.

Two stepping rotation array-drive approaches were considered. One would avoid slip rings by using flexible wiring that would be allowed to twist for one or more days, followed by unwinding by rapid reversal of the panel rotation. This maneuver would put a transient into the spacecraft attitude control system that would limit the duration and timing of orientation testing. The other stepping approach uses a ratchet-solenoid drive instead of a continuously running motor. It appears to have no direct advantages over the harmonic drive, but has the disadvantage of permitting sliding and rolling surfaces to remain in stationary contact for discrete periods. An alternative to the motor-driven harmonic drive is now undergoing extensive testing. It uses a stator wound in such a way that wave generation can be accomplished magnetically without the need for a physical rotor. Such a magnetic drive would not need to be sealed for lubrication of bearings or slip rings. It was not selected for the present design because it has not yet been operated in space, but it is an attractive alternative.

The use of batteries to smooth the power profile during each day's operation was rejected because of the prohibitively large number of cycles involved and because such batteries would outweigh the solar array saving by 7 to 1.

#### 5.4.3 Power Profile

The power profile (Fig. 5-15) shows typical utilization of power over a 12-hr period, being the sum of the requirements for the following:

- Ion engines (113 w) for north translation (8 hr on, 4 hr off) occurring 4 min later each day. The south thruster will be used similarly during the next half day.



Fig. 5-15 ATS-4 Power Profile

- Ion engines (113 w) for east translation (4 hr on, 8 hr off) starting at 4 AM each day. The west thruster would be switched on at 4 PM each day.
- Bias disturbing torques, due to solar pressure or translational thrust, which are anticipated to occur for periods of several hours each half day. One thruster of each attitude pair would draw 65 w for up to 3 min each half hour and 5 w for 27 min. Its partner would draw 65 w for up to 1 min and 5 w for 29 min. When the translation thruster in the appropriate cluster is in operation at the time an on command is received, 5 w would be needed to keep it on standby. If the attitude sensors and logic are capable of tighter operation than  $\pm 0.1$  deg, the attitude cycles could be considerably shorter (down to a few minutes), but provision must be made for early operation in the long-period mode.
- Other continuous power demands (see Fig. 5-15), including operation of attitude and orientation control sensors and logic, phased-array and parabolic antennas, tracking, and telemetry and command systems, as well as fixed losses.

The total power shown in Fig. 5-15 will not be provided simultaneously. The hydrazine control system will be operated only during ascent and acquisition. The phased-array experiment will be conducted while a single ion engine is used for stationkeeping (to demonstrate capability) and resistance jets are used for attitude control. Table 5-3 summarizes the peak power demands. The design figure of 900 w at the end of the first year carries a 10 percent contingency on operation of the phased-array antenna while stationkeeping.

#### 5.4.4 Solar Array Sizing

Design Factors. The design factor are as follows:

<u>Parameter</u>	<u>First Year</u>	<u>Second Year</u>
$K_1$ Radiation Degradation (6 mils $\text{SiO}_2$ )	0.869	0.839
$K_2$ Coverglass Transmission Loss	0.920	0.910
$K_3$ Adhesive and Ultraviolet Darkening	0.990	0.980

<u>Parameter</u>	<u>First Year</u>	<u>Second Year</u>
K <sub>4</sub> Minimum Seasonal Insolation	0.965	0.965
K <sub>5</sub> Packing Factor	0.90	0.90
K <sub>6</sub> Ratio of Active to Inactive Area	0.95	0.95
K <sub>7</sub> Operation Off Maximum Power Point	0.95	0.95
K <sub>8</sub> Fabrication and Mismatch Losses	0.95	0.95
K <sub>9</sub> Off Ecliptic Factor	0.917	0.917
K <sub>10</sub> Temperature Coefficient of Power	0.4%/°C	0.4%/°C
K <sub>T</sub> Total	0.4929	0.4659

Design Data. Design data are as follows:

- Solar cell efficiency = 10.5%
- Specific power,  $P/A = \eta K_T L = 130 \times 0.105 \times 0.4929 = 6.727 \text{ w/ft}^2$   
First Year  
 $= 130 \times 0.105 \times 0.4659 = 6.358 \text{ w/ft}^2$  Second Year

Optimization of Coverglass Thickness. If array weight is  $1.03 \text{ lb/ft}^2$  + coverglass, and if specific power at end of 2 yr is  $6.36 \text{ w/ft}^2$  (6 mils), then optimization values are as follows:

<u>Coverglass Thickness</u> <u>(mils)</u>	<u>Specific Power</u> <u>(w/ft<sup>2</sup>)</u>	<u>Array Specific Weight</u> <u>(lb/ft<sup>2</sup>)</u>	<u>Specific Power</u> <u>(w/lb)</u>
3	6.06	1.065	5.69
6	6.36	1.10	5.78
12	6.61	1.17	5.65
20	6.67	1.27	5.25
30	6.69	1.38	4.85
45	6.71	1.56	4.30
60	6.71	1.73	3.88

It can be seen from the above that a standard 6-mil coverglass is the best choice for the present design.

Table 5-3

## PEAK POWER REQUIREMENTS

Load	Total Power (w)	Mode 1 (a) (w)	Mode 2 (b) (w)
Ion Thrusters for Stationkeeping and Orientation Control	380 (four operating)	256 (two on, four standby)	150 (one on, five standby) +45 (resistojets)
Hydrazine Control Equipment	25	—	—
Orientation Control Equipment	40	40	—
Attitude Control Equipment	60	60	60
Phased-Array Antenna	408	—	408
Interferometer	12	12	—
Parabolic Antenna Electronics	161	161	—
TT&C	50	40	40
Power System Loss	40	40	40
Power Limiter Loss	120	59	84
Totals	1,396	678	837

(a) Mode 1 is regular operation with the parabolic antenna.

(b) Mode 2 is occasional operation with the phased-array antenna.

#### 5.4.5 Solar Array Design

Power Characteristics and Array Geometry. Details of the array characteristics are as follows:

- Power/unit area (first year) =  $6.73 \text{ w/ft}^2$
- $A = \frac{900}{6.73} = 133.7 \text{ ft}^2$
- Array is split into two sections of  $66.85 \text{ ft}^2$
- Number of solar cells at 0.90 PF = 27,944 (1/2 array has 13,972 cells)
- Voltage requirement = 29 v at  $50^\circ\text{C}$
- $v_{\text{mp}} = 0.450 \text{ v}$  at  $28^\circ\text{C}$  (10 ohm-cm N/P silicon)
- Voltage coefficient of temperature =  $-2.1 \text{ mv}/^\circ\text{C}^*$
- $v_{\text{mp}}$  at  $50^\circ\text{C} = 0.450 - 0.0021(22) = 0.404 \text{ v}$
- Cells in series to give 29 v =  $\frac{29}{0.404} = 72$
- cells in parallel =  $\frac{13,972}{72} = 194$  per 1/2 array
- Length of 72 cells =  $\frac{72 \times 0.788}{0.95} = 59.7 \text{ in.} \approx 60 \text{ in. (5 ft)}$
- Length of 194 cells =  $\frac{194 \times 0.788}{0.95} = 160.9 \text{ in.} \approx 162 \text{ in. (13.5 ft)}$

The layout of an individual panel is shown in Fig. 5-16, and the mechanical configuration of the four panels that form one half of the array is shown folded in Fig. 5-17.

Deployment Mechanization. The deployment design concept uses a spring and dashpot assembly. The solar array is maintained in its packed configuration by a series of pretensioned cables. These cables compress the panels so that the shear blocks remain engaged. The shear blocks prevent the panels from sliding relative to each other during launch. In effect, the tension cables and shear blocks provide a load transfer system that makes the solar array structure a rigid package.

---

\*Heliotek Data Book.

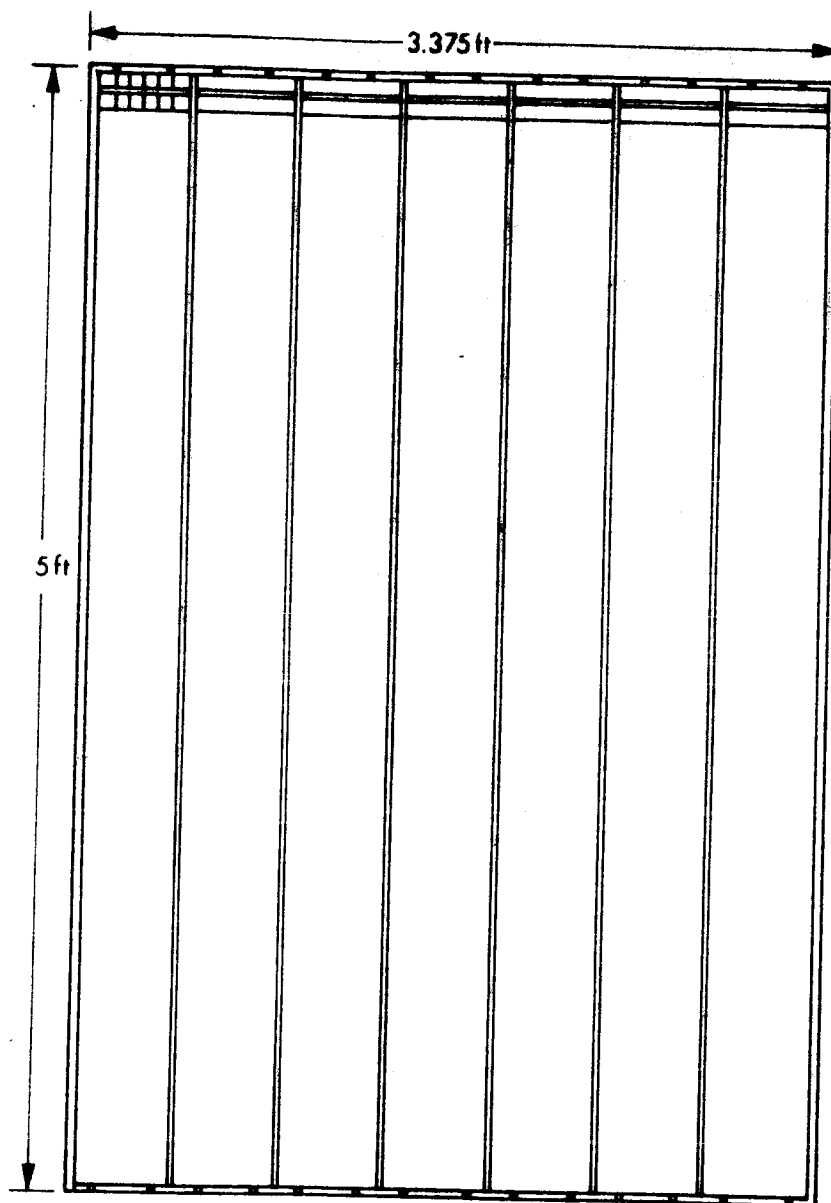


Fig. 5-16 Electrical Layout of One Panel

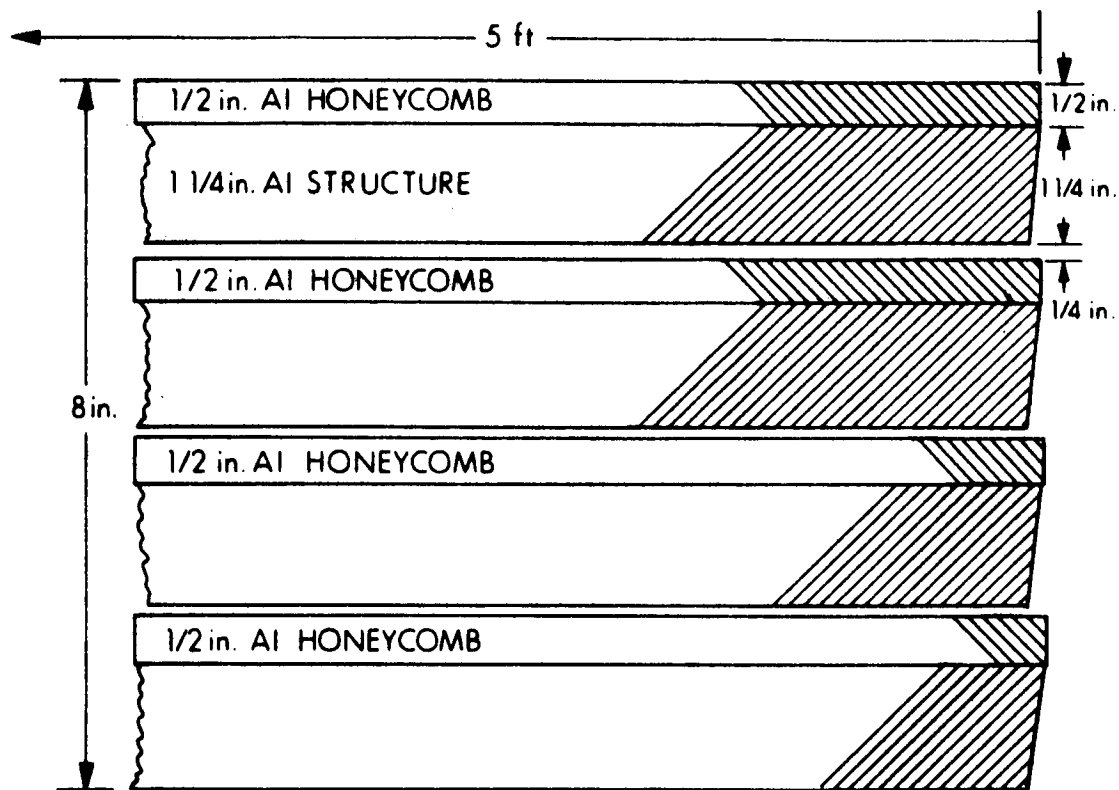


Fig. 5-17 Mechanical Configuration of Folded Array



The deployment sequence starts as the satellite support truss is removed. An electrical impulse to the cable cutters severs the pretensioned cables. A retractor reels in the cables, with guides preventing the cables from contacting and damaging the active surfaces of the array. The retracting action occurs with sufficient speed to prevent interference with the deployment of the panels. The panels are then free to be deployed by a mechanical spring.

The spring provides positive force at the end of travel to ensure continuous pressure upon the deployed panels. This bias ensures that the latches will engage.

Viscous dampers engage the panels as they approach the full-open position. These dampers are provided to reduce the opening shocks. A second engagement occurs at the end of panel travel to lock them in the deployed position. The latch is provided to prevent the panel hinges from opening during a violent attitude maneuver. In normal attitude control, the hinges are forced together by the positive pressure of the deployment springs.

The restraint device consists of the four principal elements. These elements are the cable, a cutter, a preloader, and a retractor.

The cable retractor is powered by a special motor produced by Hunter Spring Company. The reel contains sufficient cable for many actuations so the unit need not be disassembled to replace the cable. The cable is 60-mil-diameter wire rope made from corrosion-resistant steel. It is preloaded to a tension of 100 lb. The cable cutter is a Space Ordnance Systems unit that is modified by the addition of a threaded sleeve to accept the cable preloader. The unit contains a guillotine-type cutter that severs the cable upon command. The cable cutter is actuated by a single pyrotechnic cartridge containing a dual bridge wire for redundant electrical ignition.

The cable preloader consists of two elements, one at each end of the cable. At the retractor end is a unidirectional clutch that allows the cable to pass freely through in one direction, but that must be disengaged to allow the cable to pass through the

other way. The cable is strung through the guide and cutter, and a shank ball is placed on the end. The one-way chuck is engaged, and the preload stud is unscrewed; the cable is thereby tensioned.

The deployment driver mechanism consists of a coil spring located at the interpanel hinges. The spring is made of beryllium copper sized to provide a positive torque when the array is deployed fully. Springs are located at the panel hinges, each spring providing a 10 in.-lb torque to deploy the panel. This results in a deployment time of 5 sec for the end panel and 15 sec for a set of two outboard panels.

The deceleration damper mechanism is a unidirectional viscous decelerator. The damper is sized to absorb most of the panel rotational kinetic energy. The panel contacts the damper during the last 10 deg of travel. The counter force of the damper produces a negative torque that decelerates the panel.

The damper design includes a bellows seal, in addition to O-ring seals, to prevent leakage of the damper fluid onto other surfaces of the array or satellite.

The proposed latch is a grooved tongue that fits between two splined cylinders. Each cylinder contains a unidirectional clutch. As the tongue is inserted, the cylinders rotate. Reversal of this motion causes the clutch to engage, which prevents the cylinders from rotating. This type of mechanism loads down tighter after every load reversal. This tightening is caused by the geometry and location of the pivot arms, and it, in turn, causes the cylinders to be forced more tightly against the tongue. The latch can only be released by loading the panel in the direction of unfurling and depressing a release arm.

Rotation Mechanism. A two-stage harmonic drive mechanism provides the once-per-day shaft rotation; an intermediate rotating sleeve provides moderate bearing and surface speeds to the slip-ring contacts for power transmission.

Figure 5-18 shows the selected scheme. A standard gearhead motor and harmonic drive assembly (United Shoe Machinery Corp., Harmonic Drive Division, Beverly,

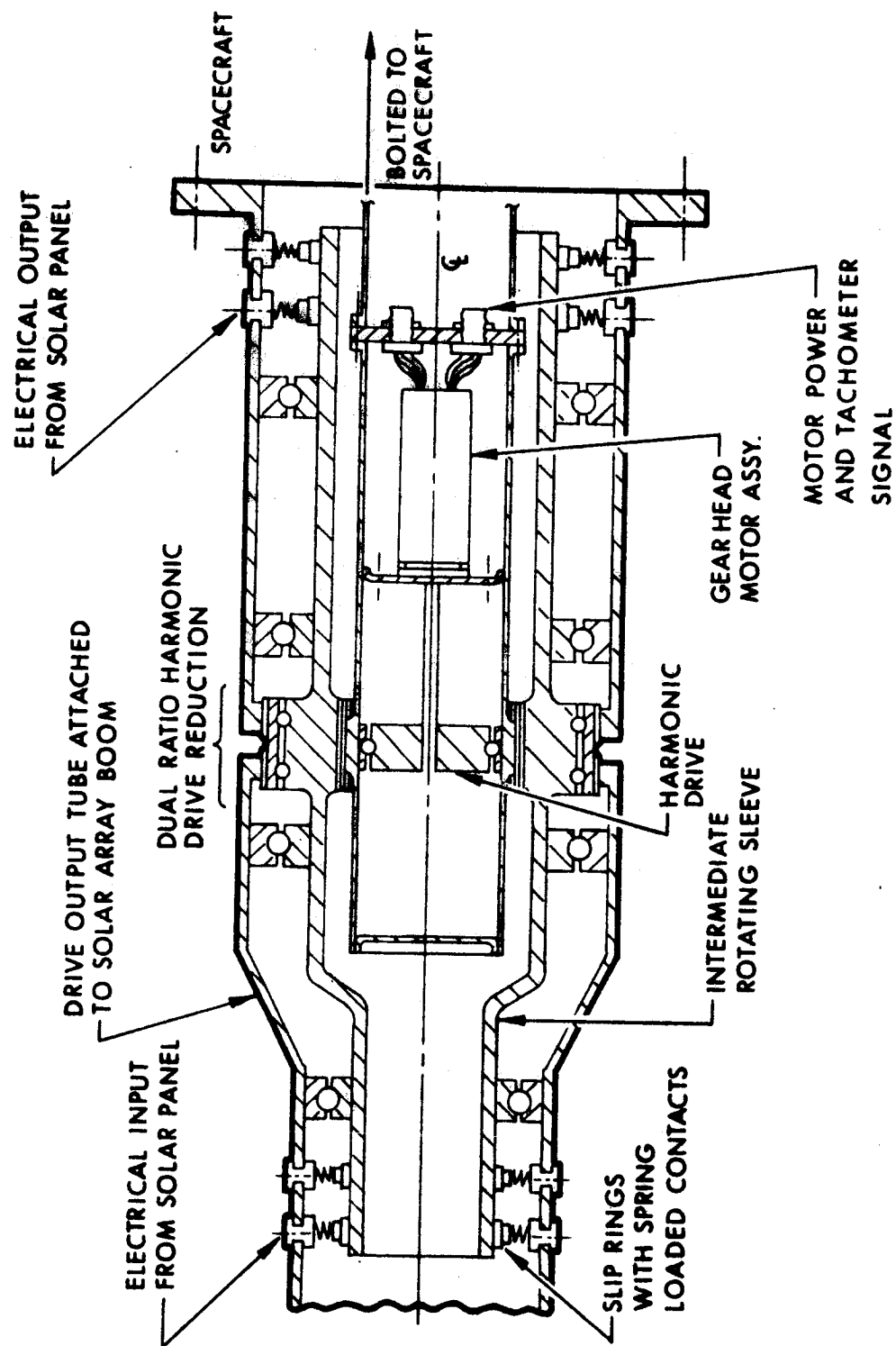


Fig. 5-18 Solar-Array Drive

Mass.) is mounted on a central shaft attached to the spacecraft. The bearings are lubricated and the entire envelope is filled with dry inert gas and sealed. The inner rotor of the harmonic drive is a wave generator that flexes the thin-walled envelope and causes the engagement of external teeth (splines) to change in relation to the internal teeth of the intermediate sleeve.

The intermediate sleeve is a rigid tubular member mounted inside a short sleeve attached to the spacecraft as shown. Ball bearings are shown for simplicity, but tapered or barrel rollers would be used. The intermediate sleeve is thus cantilevered from the spacecraft and carries the solar array boom at its outer end, which is also cantilevered on similar bearings. The speed of rotation of this sleeve can be selected readily from standard drive units at 1 to 20 rpm, which appears (without in-depth analysis) to offer suitable bearing and slip-ring speeds. At mid-length, the sleeve carries an external wave generator that drives a floating flexible splined idler ring whose external teeth engage with internal teeth on (1) the fixed sleeve and (2) the drive output tube. By selecting different numbers of teeth between each part of the idler and the members they drive, a slow differential driving of the output shaft is produced. Standard designs can readily give gear ratios of 1,500/1 to 30,000/1, which provides the necessary 24-hr rotation.

Drive speed control for the DC motor is achieved through a tachometer readout and control logic that will vary the speed on command from a comparator in the on-board programmer timer, or from ground command.

The slip-ring assemblies use multiple contacts, and the slip rings are interconnected by insulated wiring running in grooves in the rotating sleeve.

Dry lubrication of the bearings, spline teeth, and sliprings will be by molybdenum disulphide or by one of the newer refractory metal selenides or telurides (e.g.,  $\text{NbSe}_2$ ) being developed by Bemol, Inc., Newton, Mass., for Ilikon Corp., Natick Mass.

Preliminary Mechanical Analysis. A preliminary mechanical analysis of the ATS-4 solar array has been performed. A weight breakdown, natural frequencies, and moments of inertia are given in Table 5-4. Boom frequency versus weight is given in Fig. 5-19 for cylindrical aluminum booms. It should be noted that the recommended boom construction uses the LMSC tri-beam, and the following data are given for information only.

Table 5-4  
SOLAR-ARRAY WEIGHT BREAKDOWN

Item	Weight (lb)(a)
Nonstructural Weight	6.75
0.005 in. Aluminum Face Sheet Weight	2.43
Core and Adhesive Weight	2.11
I-Beam Weight	0.24
Reinforcements and Boom Mounts	1.00
Hinges and Latches	0.68
	<hr/> 13.21 per panel

Four Panels, lb	52.84
Deployment Mechanism, lb	4.00
	<hr/> 56.84 per array
Natural Frequency of Subpanel, cps	22.15
Natural Frequency of I-Beam, cps	12.0
Moment of Inertia of Both Arrays Fully Extended, Around Center of Spacecraft, lb-ft-sec <sup>2</sup>	2,542.7

(a) For each of four panels (60 in. wide by 40.5 in. long) supported by two parallel lengthwise aluminum I-beams spaced 17 in. from the panel center line.

Figure 5-19 is only approximate at higher boom weights since the boom-array mass is a distributed system if boom weight is appreciable compared to panel weight. Telescoping hollow aluminum booms are assumed (five sections at 3.33 ft each\* for a

\*With outside diameters of approximately 1.3, 1.6, 1.9, 2.2 and 2.5 in.

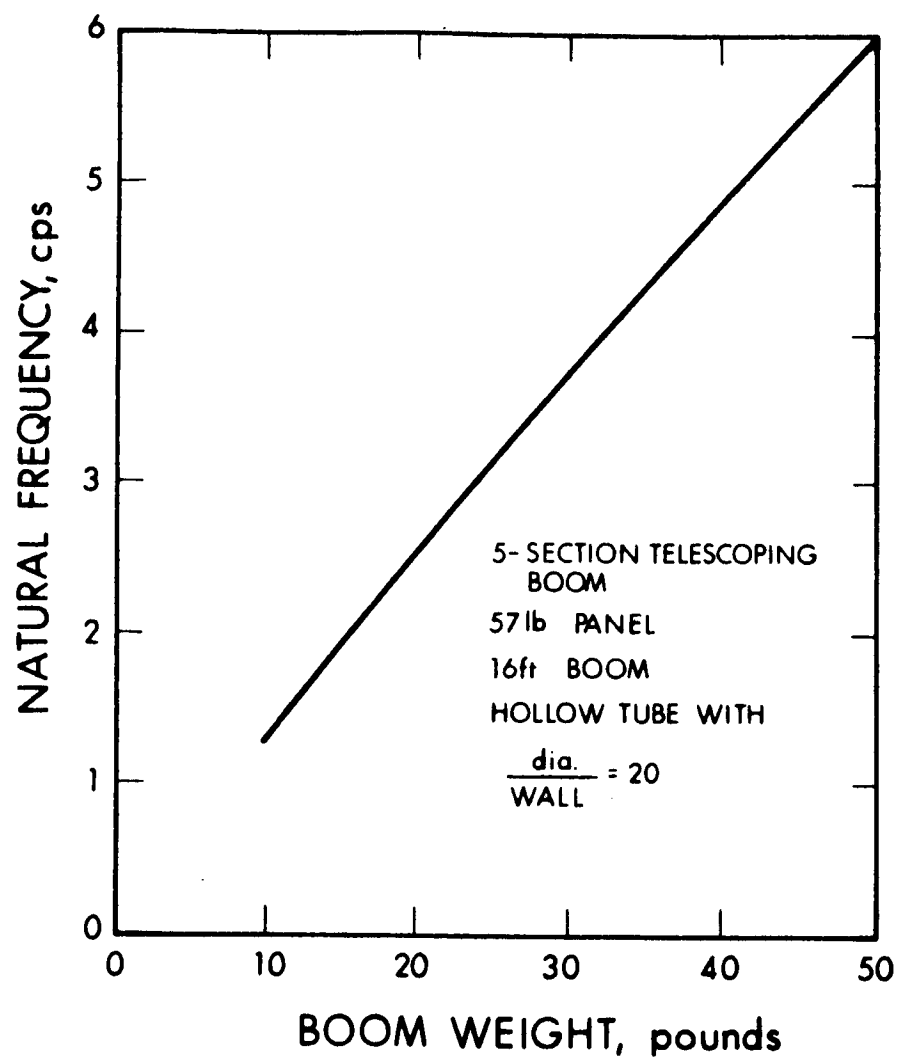


Fig. 5-19 Cylindrical Boom Structural Resonance

16-ft extended boom) so that the boom collapses into the length of the panel array. Each section is a hollow tube with a boom diameter that is 20 times wall thickness. This is close enough to optimum design for present purposes. Other configurations were checked and they fell under the curve of Fig. 5-19.

Since the only severe dynamic loads on the array occur when it is folded during launch, the substrate was designed to conform to a stiffness criterion rather than an allowable strength criterion. The loaded substrate honeycomb was designed for a natural frequency of 20 cps or greater, and the beams, assuming the solar panel as a dead weight were designed for a natural frequency of 10 cps or greater.

#### 5.4.6 Power Conditioning

There are several constraints and operating parameters that set boundary conditions on the power conditioning subsystem and determine, to a great extent, the basic configuration of the system. These are as follows:

- Number of solar panel electrical sections
- Number of separate secondary batteries
- Solar panel voltage variations
- Battery voltages
- Required output voltage

The first two items are fixed independently of the power conditioning subsystem and cannot be altered to meet its requirements. The solar panel voltages and battery voltages can be selected to suit the design of the power conditioning subsystem. The satellite bus or regulated output voltage has been fixed by power-system user requirements; the solar panel and battery voltages (charge and discharge conditions) are then determined by the type of regulation method used.

Regulation Method. Two basic regulation methods are adaptable to this mission. These methods are active shunt regulation and series regulation. Passive shunt regulation (with zener diodes) was not considered because of the associated high thermal loads. At the  $-130^{\circ}\text{F}$  panel temperature, the thermal loads dissipated by

the diodes cause them to operate at 250° F. This requires large heat sinks on the array to prevent damage to the substrate or solar cells.

Feasible regulation methods are shown in Fig. 5-20. All of these methods operate on the main satellite bus. Several variations exist for each regulation method.

A shunt regulator can operate on either the entire array or only on a portion of the array. Shunt regulation of the battery causes excessive drain, so a separate series regulation is required for battery operation.

A series regulator can operate in a continuous DC mode or a switching mode. The efficiency for the switching mode is approximately 90 percent while, in the DC mode, efficiencies can be as low as 50 percent for a two-to-one input voltage variation.

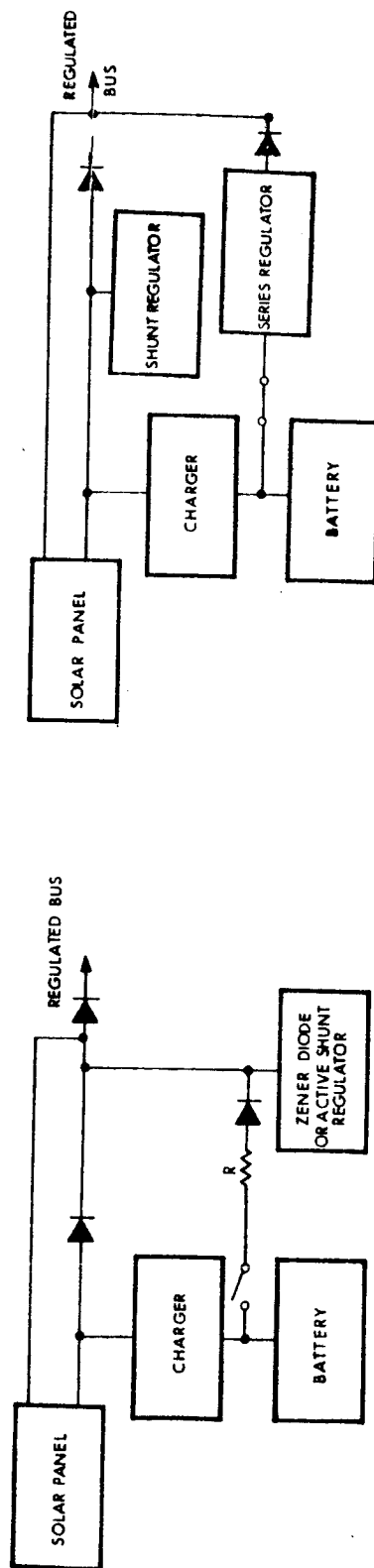
Table 5-5 presents the relative power dissipation levels for the various regulation methods. The two methods that are prime considerations are the partial shunt (with separate battery regulator) mode and the series-switching mode.

The partial shunt mode requires a lead to each array section, which results in an increase of 50 percent in the number of slip rings for the rotating array. The alternative is to place the entire power conditioning assembly on the solar array. This is neither considered desirable from the standpoint of array mass nor because of the required additional thermal control.

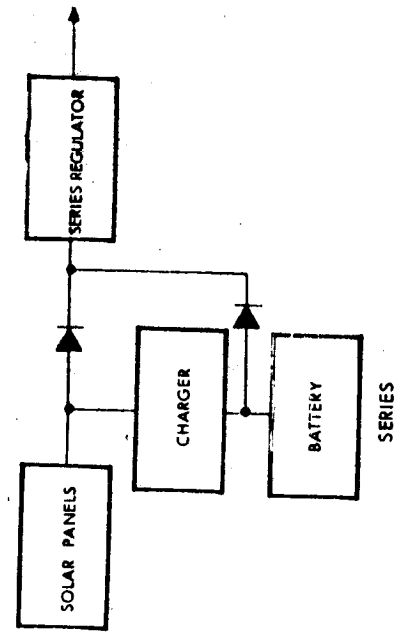
The series-switching regulator, furthermore, operates more efficiently over a wide range of power levels. At low power levels, excessive power and heat must be dissipated through the shunt regulator dissipating resistors.

Because of these factors, a series-switching regulation method was selected for this mission.

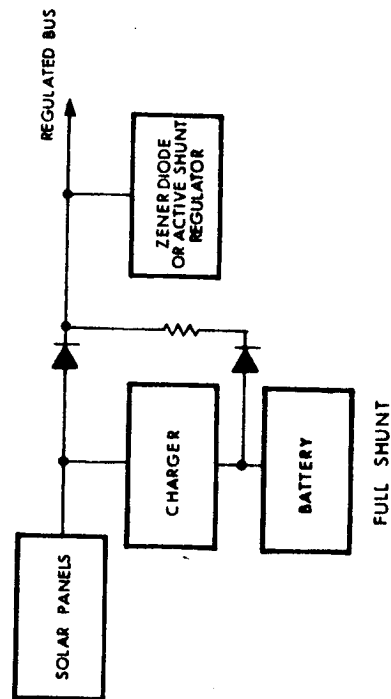




PARTIAL SHUNT



PARTIAL SHUNT



FULL SHUNT

Fig. 5-20 Power Regulation Alternatives

**Table 5-5**  
**COMPARISON OF REGULATION METHODS**

Regulation Method	Power Dissipated (w)		Remarks
	Battery Mode	Solar Panel Mode	
Shunt (partial array)	175	154	Requires active switching of battery
Shunt (partial array)	19	154	Separate regulators for each mode
Shunt (full array)	175	512	Requires solar panel current at MPP <sup>(a)</sup> in excess of 32 amp
Series (DC mode)	52	390	Requires solar panel current at MPP <sup>(a)</sup> in excess of 32 amp
Series (switching mode)	19	125	Single regulator for both sources; requires filters for ripple and voltage spikes

(a) Maximum power point (solar array).

**Series-Switching Regulation.** Operation of the regulation method is related intimately to the solar-panel characteristic, its variations, and the input properties of the main bus regulator.

The regulator input volt-ampere characteristic, when regulating, follows the constant power curve shown in Fig. 5-21. This curve can be superimposed on the solar-panel output volt-ampere characteristic, and subsystem operation occurs where the two curves intersect.

Since the regulator has a finite regulation range, its path of operation follows the straight load line indicated until the input voltage reaches a level allowing regulation to take place. Operation then follows the constant power curve as determined by the load at the regulated bus voltage.

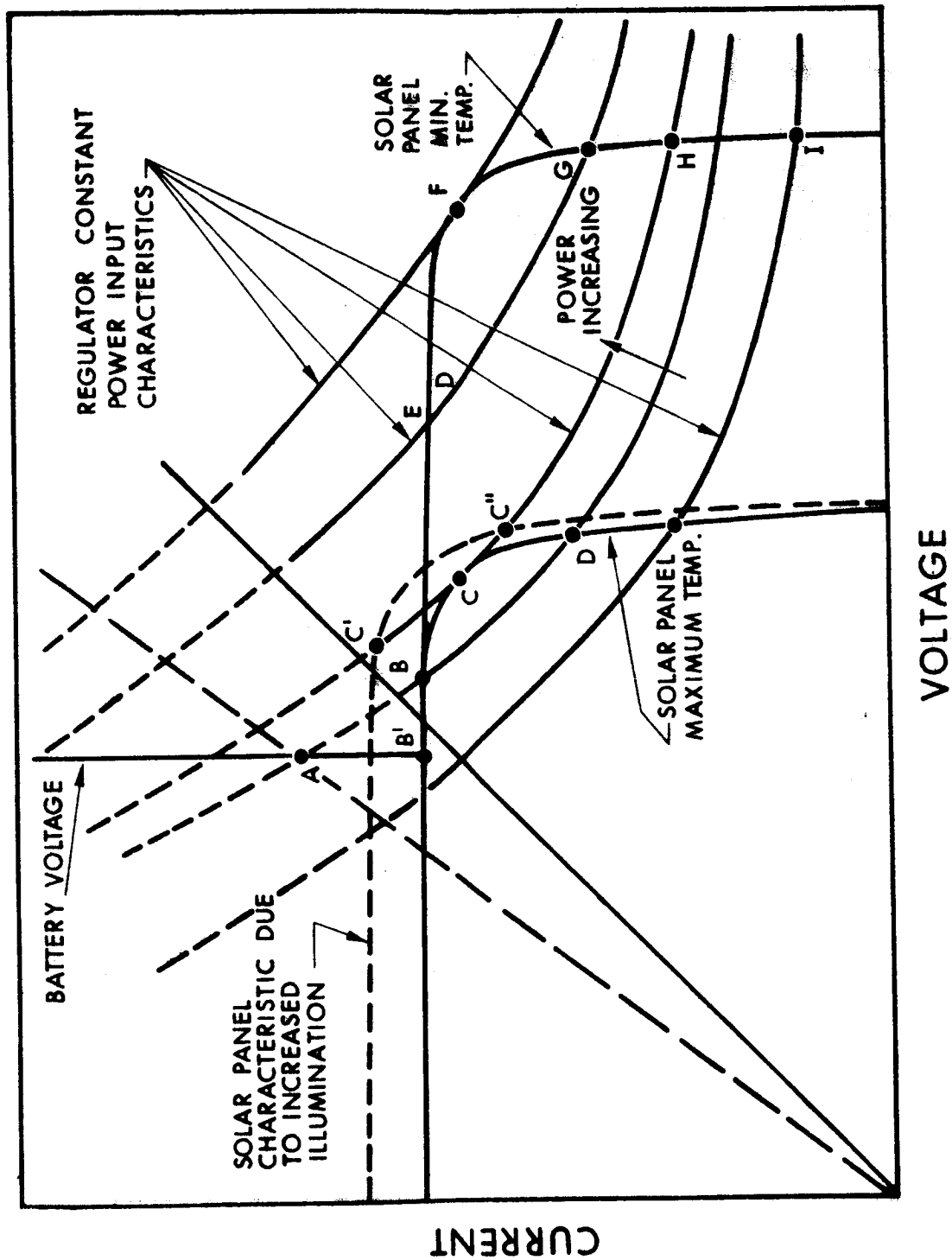


Fig. 5-21 Voltage-Current Characteristics of Regulation System

The battery voltage is significant in that operation cannot exist below this voltage. For a regulator operating on the dotted load line, operation can occur where the composite regulator input characteristic intersects the solar-panel characteristic. On the second power-level curve, operation could occur at points A, B, or D of the maximum temperature solar-panel characteristic.

Stable operation occurs only at D or A. Point A is a condition wherein the batteries are in a sharing mode with the solar panels. In this case, the current supplied by the panel is that from the voltage axis to point B'. That supplied by the battery is from point B' to point A.

Since battery sharing (point A) is an undesirable condition, it is necessary to operate at point D. If the load presented by the regulator appears capacitive, any disturbance when operating at point D will cause operation to return to point D. An inductive load will cause stable operation at point B.

A battery sharing mode, if not self-correcting because of the nature of the load seen by the solar panels (i. e. , capacitive), can be corrected easily once it occurs. This is accomplished by superimposing a sufficiently large and short voltage pulse onto the raw DC bus. This forces operation out of the sharing mode and back to point D. This may be done by detecting the condition and applying the corrective pulse or by periodically providing the corrective pulse regardless of the state of operation of the solar panels and batteries.

Battery sharing can also be prevented by designing the regulator to operate along a load line such as the solid line shown in Fig. 5-21. In this case, the regulator input never intersects the battery voltage line. Operation will always occur at point D.

The maximum power available from the solar panel does not occur at point D. It occurs at point C or F. Operation at other than these points of maximum power means that the solar panels are oversized for the power levels used.

When the solar panels are at their minimum temperature operation takes place at point H. The duration of operation at point H occurs only at the end of occultation, and as the array temperature increases, operation returns to point C.

Although it is desirable to size the solar panels to operate at their maximum power capacity, this point will vary with degradation of the solar panel (due to radiation, etc.) and with the time of year, since the distance from the sun is changing. With increased illumination intensity, as indicated by the dotted solar panel characteristic, operation will occur at C'' or C'. Operation at C', which is a battery-sharing mode, can be prevented with the use of voltage pulses, as described previously.

The series-switching regulator will be designed to operate with a circuit to provide a voltage pulse on the raw DC bus. This will prevent battery sharing from occurring.

With operation occurring at D for the normal load, the battery chargers are designed to draw sufficient current to cause the point of operation to move towards point C. They have the further characteristic that they will never draw enough solar panel current to decrease the solar panel or raw DC bus voltage below approximately 24 v. Although the regulator will regulate with an input voltage as low as 18 v, the raw DC bus voltage must be greater than the battery charging voltage in the solar panel mode of operation. This is necessary to keep the battery and charger isolated from the raw DC bus by keeping the isolating diode back-biased.

In the battery-operated mode, the battery discharge voltage (or the raw DC bus voltage) is never less than the regulation threshold voltage of the main satellite bus regulator.

The solar panel and battery operating voltages selected for the series-switching regulator are as follows:

- Battery voltage at 50 percent discharge: 20.0 v
- Battery voltage at full charge: 22.5 v (open circuit)
- Battery voltage, beginning of charge: 21.5 v

- Battery voltage, end of charge: 25.0 v
- Maximum power point, solar panel voltage, beginning of life: 29 v
- Maximum power point, solar panel voltage, end of life: 28 v

When emerging from occultation, the solar panel temperature will be near  $-130^{\circ}\text{C}$ . The panel voltage under these conditions will be:

- Voltage at maximum power point: 49 v
- Open-circuit voltage: 58 v

Under these boundary conditions, the diode logic matrix will provide the selection of the source power.

Battery Charging. The desired battery charging technique determined the type of charge control circuitry required. The recommended charging technique for the nickel-cadmium battery is a constant-current charge with a float charge at a very low constant-current rate. Full charge will be determined by measuring both battery temperature and voltage. Therefore, control parameters for charging must include battery current, temperature, and voltage.

The solar array voltage was selected to be always higher than the battery voltage. A stepdown type of charger can then be used. For maximum efficiency, a series-switching charger was selected, which is very similar in operation to a series-switching voltage regulator. However, as mentioned in the previous paragraph, the control parameters must include battery current, temperature, and voltage sensing. In addition, solar array voltage must also be a control parameter to prevent the possibility of the battery chargers loading the array to the point of load-sharing with the battery.

The block diagram of the battery charger is shown in Fig. 5-22. Three command inputs have been included in each charger to add a capability for control from the ground. Although normally not needed, these commands allow a high degree of control and flexibility in the event of a charger or battery failure.

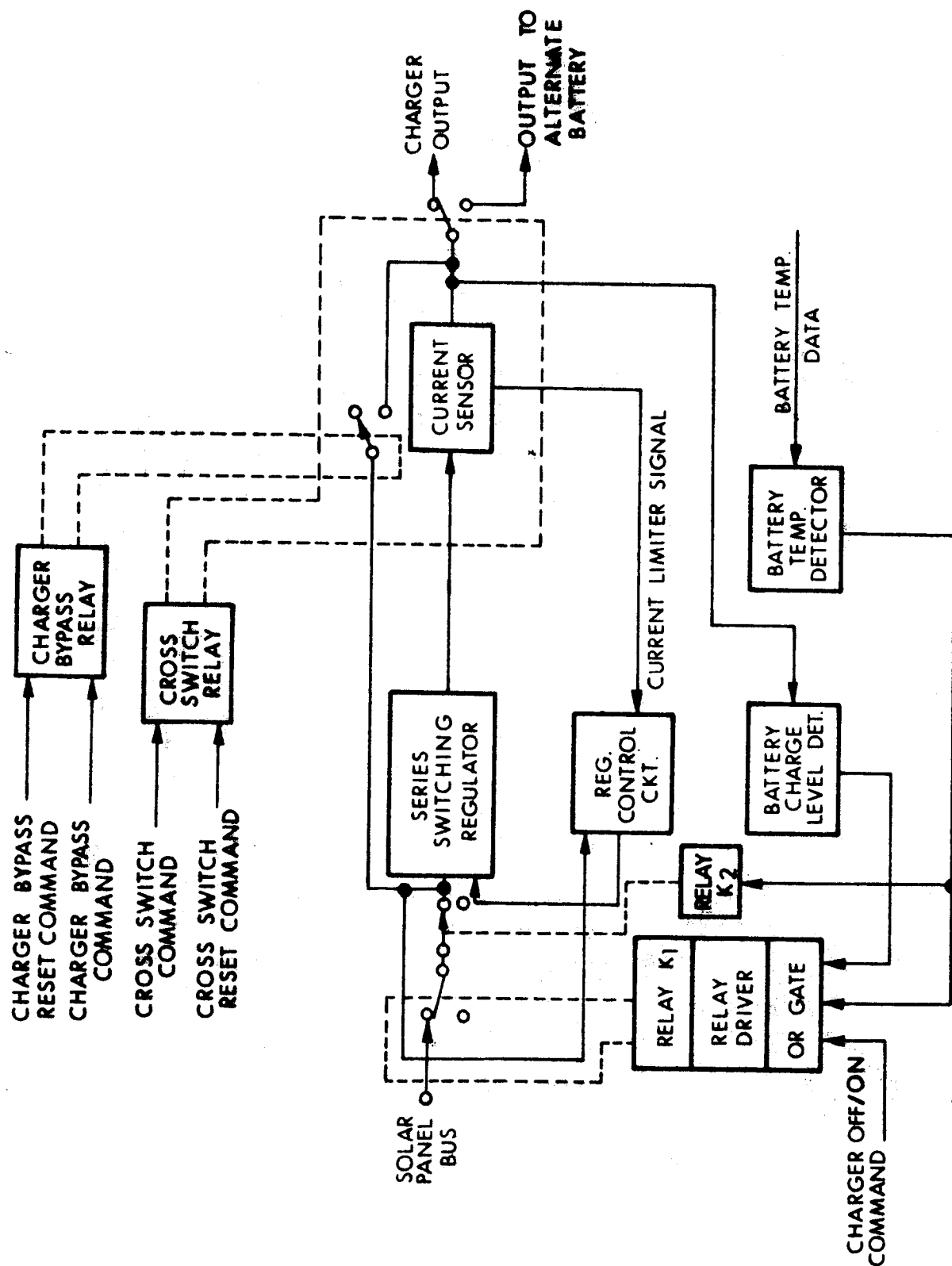


Fig. 5-22 Battery Charger Functional Block Diagram

The commands are: battery charger off command, which opens a relay in the input to the charger; cross switch command, which switches the charger to the opposite battery; battery charger bypass command, which closes a relay bypassing the charger. The last command (bypass) allows charging of the battery directly from four sections of the solar array. This function permits a quick emergency battery charge in the event both chargers fail.

Power for the charger is obtained from two solar array sections. This power is applied to the series switch formed by the high-power switching transistor. The output from the series switch is fed through an LC filter and current sensor to the battery.

The current sensor output signal is fed to a two-position charge current control circuit which is set for a 0.9-amp charge current and a 0.2-amp float current. The output of the current control circuit is fed to the pulse-width modulator circuit which generates the drive pulses for the series switch. The width of the pulses is varied to control the output current at the desired value.

The full-charge detector monitors battery temperature and voltage. When a condition of full charge is sensed, the detector triggers the current control to the 0.2-amp position. The full-charge detector and current control are reset to the 0.9-amp position by the battery-use signal from the power switch and logic circuits.

Two other control circuits are included to inhibit charging during conditions of high temperature and low array voltage. A battery temperature control circuit terminates charging if the battery temperature exceeds 100° F. When the temperature drops below 95° F, charging automatically resumes. This is accomplished by a low-hysteresis Schmitt trigger circuit driven by the output of a thermistor temperature-sensing circuit. A second circuit monitors the solar array voltage and decreases or terminates the charging if the input voltage to the charger falls near the battery-sharing level.



#### 5.4.7 Battery

The time spent in the earth shadow by the satellite is a varying function with time-of-year, as shown in Fig. 5-23. The satellite is in the shadow for a total of 84 hr annually during the two equinoxes. As the satellite approaches the equinox, the time in the shadow, which occurs once per day, increases gradually for approximately 22 days, to a maximum of 70 min. The shadow time then cycles back to zero in another 22 days. The batteries, therefore, would be required to perform through approximately 88 charge/discharge cycles per year for a total of 176 cycles over a 2-yr period.

Selection. The battery types that can be considered for this mission are sealed silver-zinc, silver-cadmium, and nickel-cadmium. The majority of data available on the cyclic life of silver depolarized rechargeable batteries indicates that silver-zinc batteries will not meet the mission requirements. The data available are quite scattered and conducted on different cycles and under different test conditions; therefore, it is extremely difficult to obtain reliable values for cycle life capability.

The ATS-4 mission, furthermore, requires a total wet life of 2 yr from launch date. This wet-life requirement presents serious problems for the silver-zinc battery. The battery deteriorates whether in use or not; the deterioration accelerates at elevated temperatures. This is caused by the separator materials which are subject to deterioration by the electrolyte over long periods of time. At 75° F, sealed silver-zinc cells have marginal wet stand-capability beyond 1 yr in charged condition and beyond 1 to 3 yr in the discharged condition.

Silver-cadmium batteries have been successfully tested at a 50-percent depth of discharge on a 24-hr charge/discharge cycle and have shown capability in excess of the required 176 cycles. The wet stand-life of silver-cadmium batteries is greater than for silver-zinc batteries; nevertheless, they have not shown reliable life at 75° F beyond 2 yr. Battery manufacturers, furthermore, will not guarantee the life of these batteries beyond 2 yr.

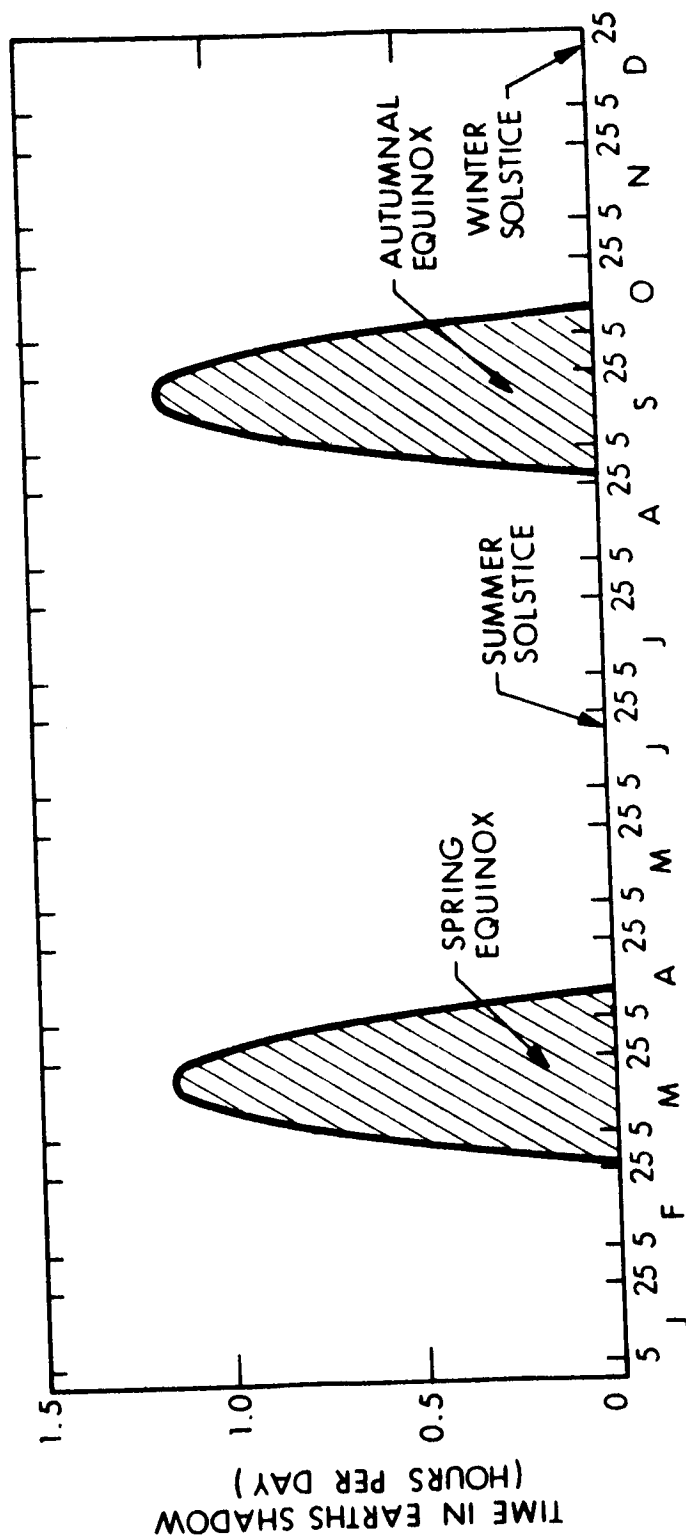


Fig. 5-23 Shadow Time, 24-hr Equatorial Orbit

The nickel-cadmium battery has found the greatest application for space missions. The cycle life in the many thousands of cycles has been achieved on short-cycle (100 min) applications. The wet stand of these batteries at 75° F far surpasses the 2-yr requirement, and is a guarantee that the battery manufacturer will accept.

A summary of the wet stand-capability for sealed secondary batteries is shown in Table 5-6. These data were compiled from test data as well as the characteristics which battery manufacturers are willing to guarantee. Based upon these factors the nickel-cadmium battery is the only type which readily will meet the mission design requirement of 2 yr.

Table 5-6  
WET LIFE OF SEALED SECONDARY BATTERIES (YR)

Temperature (° F)	Condition	Ag-Zn	Ag-Cd	Ni-Cd
32	Discharged	2-3	3-4	8
	Charged	1-2	2-3	8
75	Discharged	1-2	2-3	8
	Charged	0.5-1.0	1-2	8
120	Discharged	0.4-0.5	1-2	4
	Charged	0.2-0.3	0.5-1	4

Depth of Discharge. Having selected the battery type, the next consideration was depth of discharge and redundancy. Considerable data exist on life testing of nickel cadmium batteries at different depths of discharge and conditions on short cycles (100 min). This cycle consists of 35-min discharge and 65-min charge. The cycle of concern here consists of 20 hr of charge and 1.2 hr of discharge. It is misleading and incorrect to use the 100-min cycle data as a basis for predicting the performance capability of nickel-cadmium batteries for the 24-hr cycle. Unfortunately, few life-cycle data exist for the 24-hr-cycle condition. However testing conducted at NAD, Crane, Indiana, on the 24-hr cycle has shown that greater than 288 cycles at 50-percent depth are attainable with standard cells.

Considering the above, the long wet life of the mission, the manufacturer's recommendations, and the limited test data available, a conservative 50-percent depth was selected for this application. This results in the use of a standard 20 amp-hr cell as the building block for the battery. This cell type (Gulton VO-20HSB) has been subjected to a range of test conditions and considerable operating life has been demonstrated. Consideration was given to the use of the standard 12 amp-hr cell (Gulton VO-12HSB), but this would require a deeper depth of discharge (marginal for the life required).

Redundancy. Secondary batteries exhibit two predominant modes of failure. The first mode of failure occurs early in life and is due to manufacturing discrepancies which can be eliminated by proper screening and acceptance testing. The second mode of failure occurs at the end of life due to wearout, which is beyond the mission requirement for a properly sized battery. Some random, unpredictable failure may occur during the normal mission life that results from process variations that are not picked up by initial screening; however, the rate of this kind of failure is low.

To guard against this type of failure, a redundant battery was considered. Also to be considered in this application is mass distribution and the difficulties resulting from one heavy battery located in the satellite. Therefore, a redundant battery approach was selected for this mission. Three batteries, each independently capable of meeting the cycling requirements, when operated two at a time, will be utilized.

Using two batteries at a time results in a total available energy of 864 w-hr at a value of 12 w-hr/lb for Ni-Cd batteries. For the maximum duration of shadow (1.2 hr), energy required for spacecraft operation is 577 w-hr, assuming that the 4.6-GHz TT&C link, primary PCM telemeter, interferometer, inertial reference gyro package, conventional autopilot electronics, ion thrusters, and all parabola electronics except the 100-MHz transmitter are on for the total 1.2-hr period. This operation requires 67 percent of total available capacity of the two batteries. This deep-discharge operation has been demonstrated to be compatible with long-duration space operation of Ni-Cd batteries.

During the ascent phase, the total battery complement will be used to supply the vehicle bus. The available energy in this mode is 1,296 w-hr. Assuming a 6-hr operational requirement including the countdown, the launch vehicle phase, the transfer ellipse coast, injection, and the predeployment phase, the required energy is 750 w-hr. This value is based on the assumption that the horizon sensor, gyros, conventional autopilot electronics, and resistance jets are on for the full period, and that the VHF TT&C system including the minimal PCM telemeter are exercised with a 20 percent duty cycle. The 750 w-hr represents a requirement for 58 percent of the available energy, which provides a safe margin.

Screening. The method to overcome initial failure rate will be to screen each cell prior to assembling it into a battery. This screening will be done by subjecting each cell to a leakage test, overcharge test, capacity test, short-circuit test, and cycling test. Cells for assembly in a battery will be matched within 5 percent of capacity. This tolerance has proved successful for the batteries used in many satellite programs. Typically, 2- to 4-percent rejections are encountered due to shorts and leaks, and another 5 percent are rejected due to out-of-capacity tolerance. Cells passing these tests will then be assembled into a battery. The wet life for the battery is established from the date of manufacture of the oldest cell within the battery.

The following paragraphs summarize the procedures and tests to which each cell will be subjected prior to assembly into the battery.

The completely fabricated cells (with electrolyte added and pressure gages attached) are put on a continuous constant-current charge at the C/10 rate for a minimum of 24 hr in an environmental temperature of  $78 \pm 3^\circ \text{F}$ . At the end of this 24-hr period, the pressures and voltages are recorded. If any cell has a pressure greater than 50 psig or a voltage greater than 1.5 v, the cell is rejected. The cover assembly and the terminals are then sprayed with phenolphthalein solution to detect any possible gas leaks. Cells which have passed this phase of the test are then subjected to cycling tests.

The cells are placed on a continuous cycling routine for a minimum of 10 days consisting of 1.2 hr of discharge at the C/5 rate and 20 hr of charge at the C/20 rate. The cells are then placed on a constant-current charge at the C/10 rate for a minimum of 24 hr.

If, at the end of this period, any cell has a pressure greater than 50 psig or a terminal voltage greater than 1.5 v, the cell is rejected. The cover assembly and the terminals of the accepted cells are sprayed with phenolphthalein solution to detect any possible gas leaks. Cells which have passed this phase of testing are then subjected to capacity tests.

The cells are discharged at the C/2 rate to 1.0 v per cell. The cell pressure at the end of the capacity check must be below zero psig. If the cell fails to meet this, it is rejected. Cells which have passed the capacity test are evacuated, filled with a mixture of 5-percent helium and 95-percent oxygen (to atmospheric pressure), pressure gages are removed, and the pinch tube is crimped and welded. The cells are then subjected to the short-circuit test. Each cell is shorted for a minimum of 16 hr, after which it is charged at the C/10 rate for 5 min. All leads are then removed and the cells left on open-circuit stand for a minimum of 24 hr. If at the end of this period any open-circuit cell voltage is less than 1.15 v, the cell is rejected. Cells which have passed this test are then cleaned, stamped, and subjected to the leak detection test.

The cells are placed on a constant-current charge at the C/10 rate for 24 hr. The cell is tested for leaks on a helium leak detector which is evacuated to  $10^{-6}$  Torr. If a leak rate of less than  $10^{-7}$  std cc/sec of helium is indicated, the cell is accepted. Cells which have passed this test are placed on a constant-current charge at the C/10 rate for 24 hr followed by a C/2 discharge to 1.0 v per cell. The cell is rejected if the rated capacity is not achieved, but accepted if it is achieved. The cells are then cleaned and prepared for the mechanical examination or inspection phase of the program.

Charging Technique. A number of approaches are available to recharge the batteries during the daylight portion of the orbit. Conventional charging techniques consist of constant-potential charging and constant-current charging, as well as modifications of these two methods. The major disadvantage of constant-voltage charging is high sensitivity to small shifts of the battery voltage due to temperature. If the charging voltage is set slightly lower than the battery, it will not fully charge. If the charging voltage is set too high, excessive overcharge can occur. Figure 5-24 shows typical end-of-charge voltage as a function of charge current.

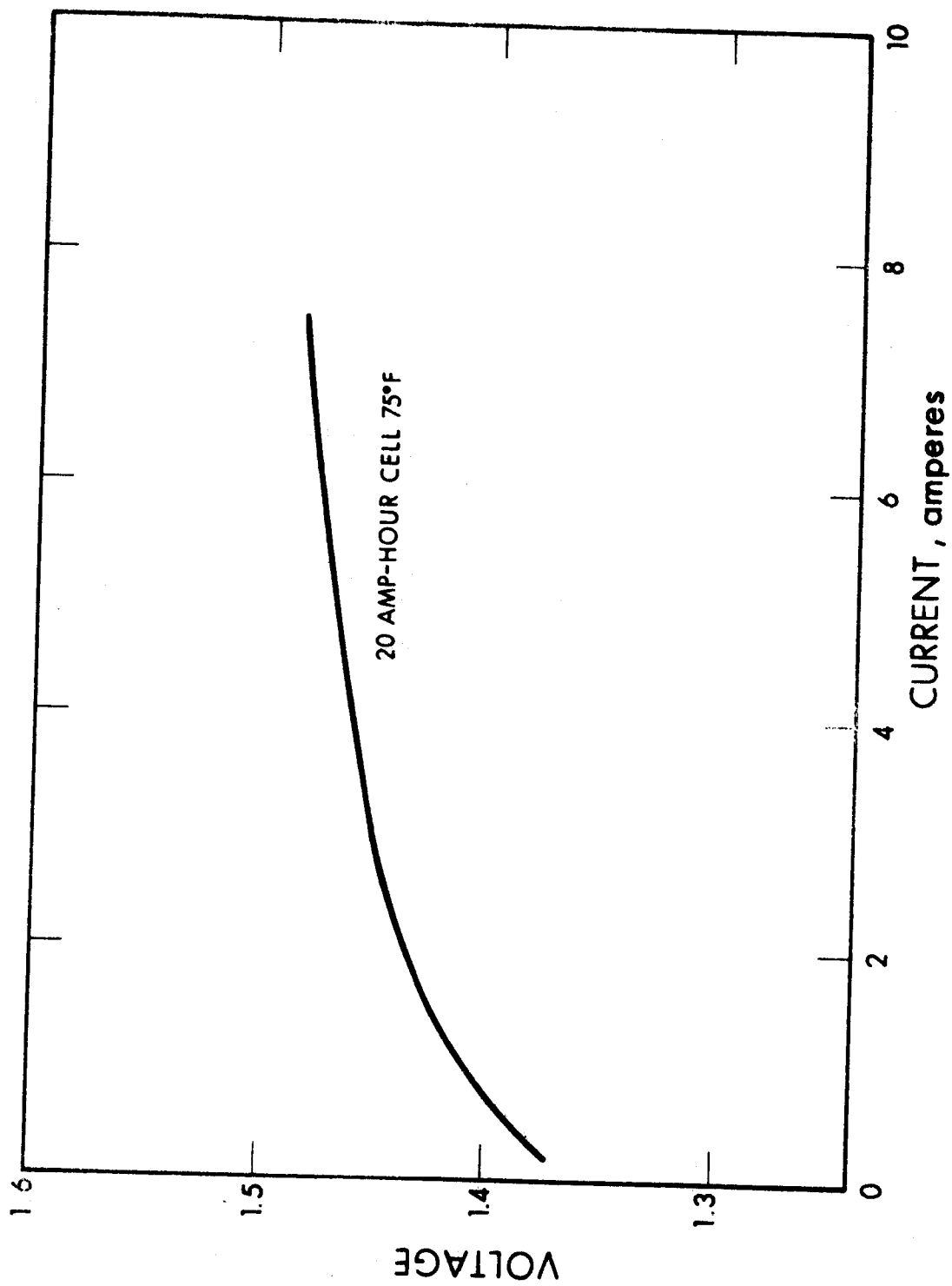


Fig. 5-24 End-of-Charge Voltage as a Function of Charge Current

Because of these difficulties, a modified constant-current method is selected for this application. Since the mission time for recharge is relatively long, a low-rate constant-current technique can be utilized. This will recharge the battery, but the current will be below the overcharge capability of the cells.

Near the fully charged condition, the electrochemical reaction slowly changes from a regeneration of the active electrode material to an electrolysis of the water in the electrolyte. This causes the evolution of oxygen, the rate of which is a function of the charge current. If the rate of overcharge is kept below some limiting value, the sealed cell has a mechanism whereby the evolved oxygen reacts with the negative electrode causing a reversal of the charge reaction.

By a suitable combination of the electrode area, the amount of electrolyte, the separator material, the internal cell geometry, and the charge current, an equilibrium condition is obtained. The cell will then be kept at a full state of charge while avoiding a pressure buildup in the cell. Therefore, the cells will have the capability of internally recombining gas generated due to overcharge at the established constant-charge current without excessive pressure buildup.

If one cell in a series string comes up to full charge before the others, it will be capable of accepting the overcharge without damage. Standard nickel-cadmium cells generally have overcharge capability at the 10-hr charge rate. Figure 5-25 shows overcharge capabilities of the cells selected for this mission.

For the nickel-cadmium battery, charge acceptance efficiency is a function of charge rate. If the battery is recharged at a 10-hr rate, a 30-percent overcharge is required. If recharged at the 20-hr rate, approximately 100 percent overcharge is required. Figure 5-26 shows typical charge-acceptance versus charge-rate data for the battery cells; therefore, a range of charge currents can be selected if proper consideration is given to charge time and efficiency.

To minimize the power load on the solar array from a total system standpoint, a charging rate of 0.9 amp is selected. When the battery is operating at 25-percent depth-of-discharge, it will be fully recharged in 10 hr. If it is running at 50-percent depth-of-



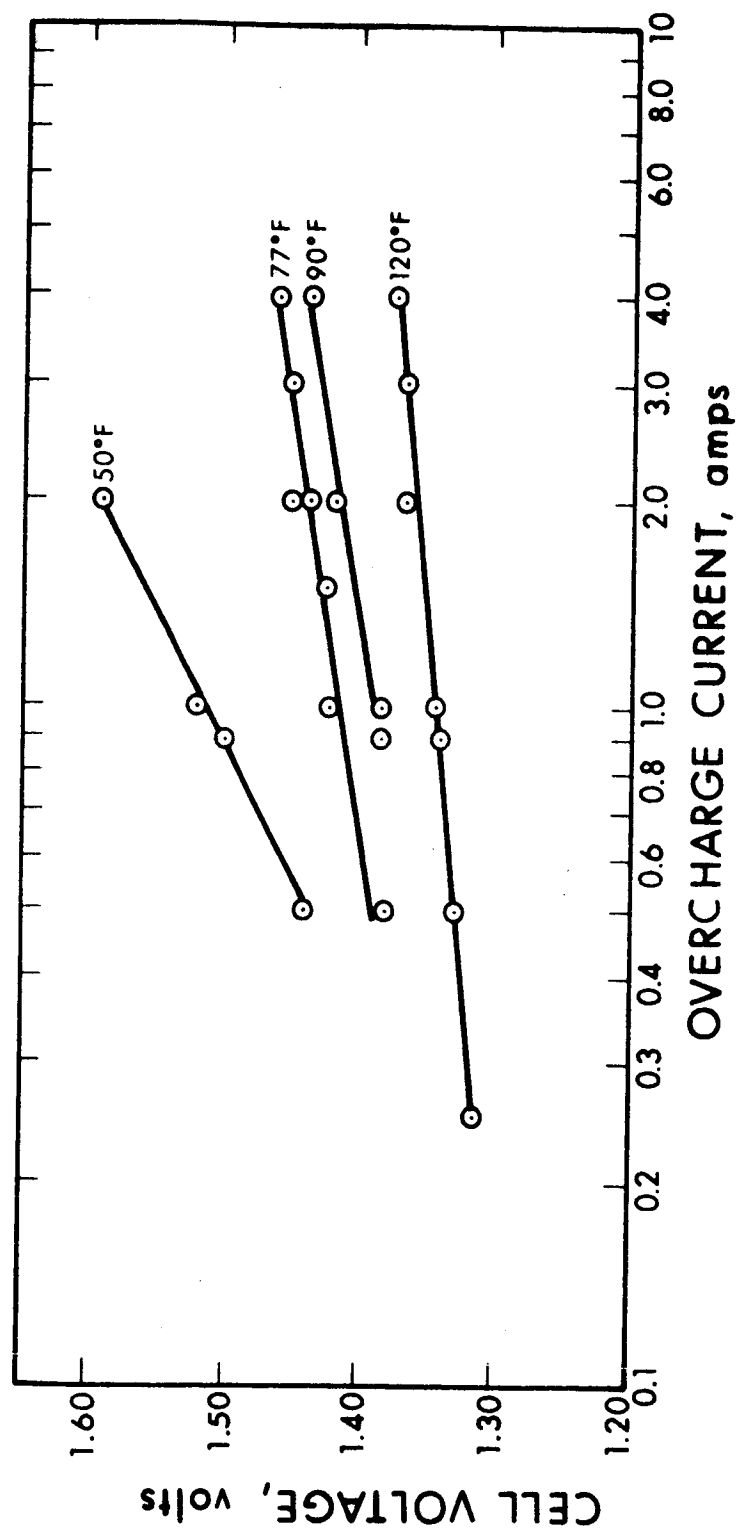


Fig. 5-25 Overcharge Capability of Hermetically Sealed Ni-Cd Cell

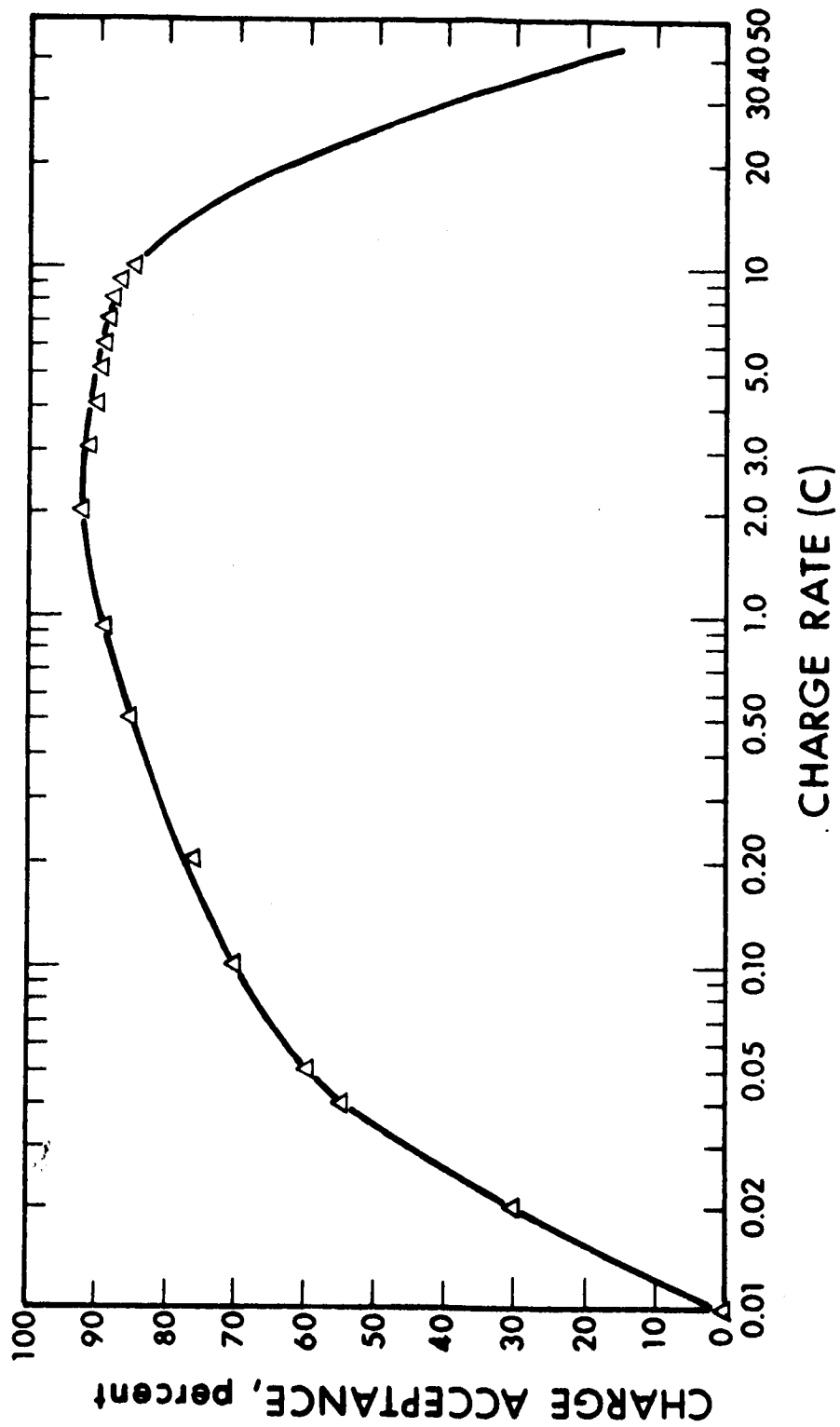


Fig. 5-26 Ni-Cd Cell Charge Acceptance vs. Charge Rate

discharge, 20 hr will be needed to recharge. This is based on a 50-percent (of total amp-hr) charge efficiency.

A straight constant-current charge is acceptable during the normal charging period. Provision, however, should be made to reduce the charging current when the battery reaches full charge, even though the charge current is well below the overcharge capability of the cells. This is recommended since there is substantial evidence that the cycle life of a sealed nickel-cadmium cell is directly related to the rate and amount of overcharge per cycle. Cells that are overcharged at high rates tend to have short cycle life, even if the rate used is a safe rate with respect to pressure rise. Cells overcharged at the same rate tend to have cycle lives inversely proportional to the length of time the cell is overcharged per cycle.

During overcharge, oxygen is continuously generated in the nickel electrode which can gradually react with the cell separator materials and reduce its structural integrity. Likewise, the continual negative potential on the cadmium electrode could cause the deposition of metallic cadmium on the electrode that could cause internal shorts. Since life is adversely affected by overcharging, the charge control design will minimize the rate and duration of overcharge to the fullest extent possible. Therefore, when the battery comes up to full charge, the charge current will be reduced to a lower float level to maintain capacity.

The nickel-cadmium battery does not exhibit a sharp change in terminal voltage when it reaches full charge, but the voltage does gradually increase as charge proceeds. An end-of-charge voltage point will provide the signal to switch the charge to the lower levels. This value will be set slightly high to assure full charge.

This end-of-charge voltage varies as a function of temperature, as shown in Fig. 5-27. Also shown is the end-point level to be used for the control circuit. After full charge is reached, the current will be reduced to a 100-hr-rate float level (0.2 amp) to maintain capacity.

An alternate approach in the described charge method may be considered, since at the low charge rate an end-point may not be readily detectable. A Henderson coulometer

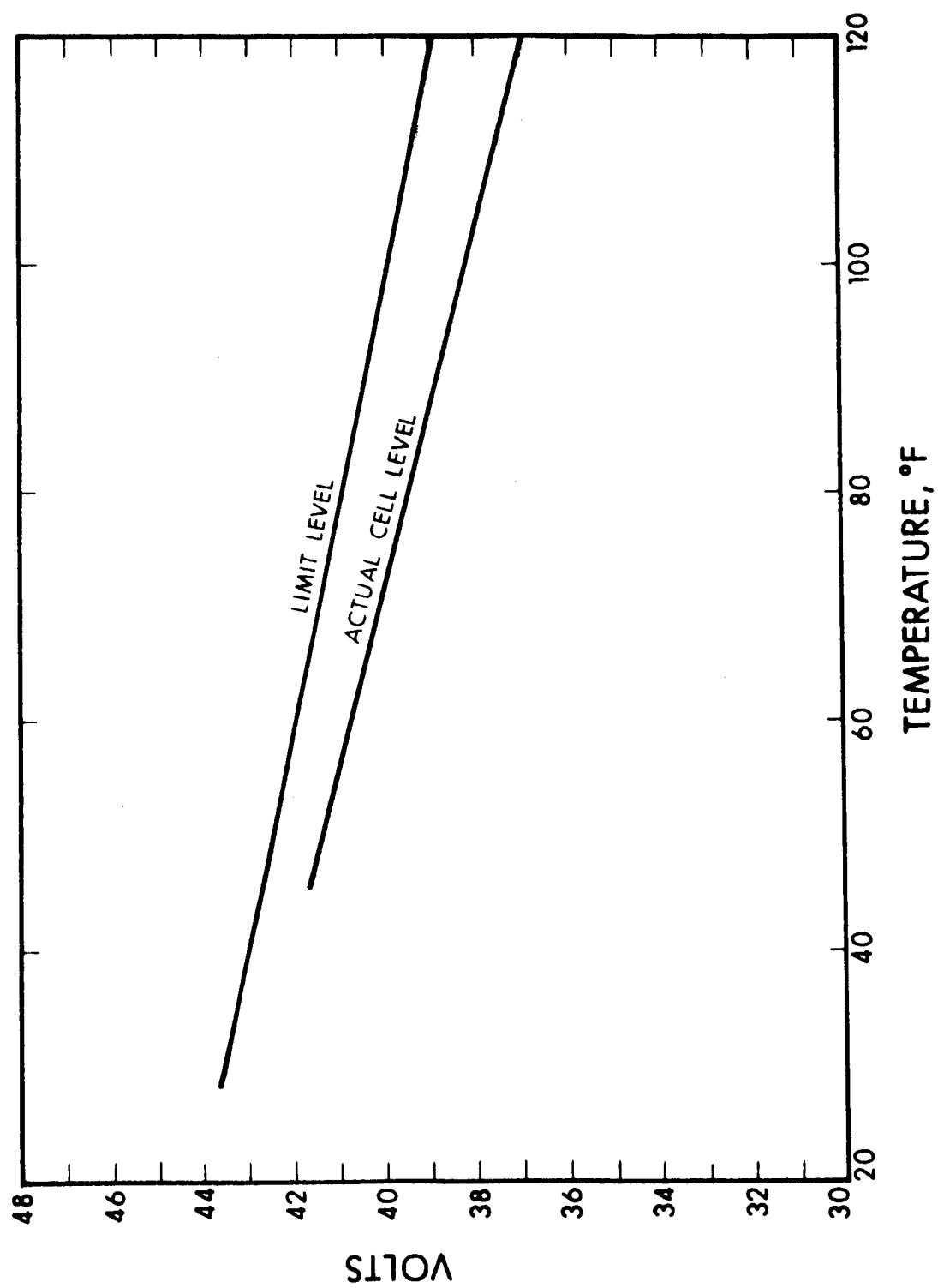


Fig. 5-27 End-of-Charge Voltage vs. Temperature

(a single cell in series with the battery that contains positive and negative electrodes of cadmium) could be used to signal 200-percent replacement of capacity and then switch to the float level. However, this technique has not been flight-tested, and can only be considered as a potential backup.

Memory Effect. Under certain operation conditions, a so-called memory effect has been observed in nickel-cadmium batteries. This effect results in the lowering of operating voltage and temporary loss of usable capacity when a battery is cycled continuously at a shallow depth-of-discharge. Figure 5-28 shows the gradual decay of discharge voltage with cycling of a Ni-Cd cell run at 20-percent depth. As the battery is continuously cycled at 20-percent depth-of-discharge for a long period, some capacity is lost; if a full-depth discharge is attempted, the initial capacity is not available. The capacity can be recovered by a slow discharge and recharge.

This effect would only be of concern when one unit fails and the remaining units are switched from 33 1/3- to 50-percent depth. For this mission, however, the discharge period varied during the cycle from zero to 1.2 hr. The limited number of cycles and the variation in discharge time and depth should eliminate the onset of any memory effect.

Temperature Environment. Nickel-cadmium batteries are sensitive to both operating and storage temperatures. Operation and storage above 100° F affects life and causes degradation in the cells. At temperatures below 40° F, a reduced output in voltage and capacity occurs. Low-temperature storage in theory has no adverse effects on the performance or life. The unit could reach the freezing point of the electrolyte (-25 to -40° F) before damage occurs. To prevent damage from thermal expansion and contractions, it is desirable to avoid these low temperatures.

Figure 5-29 shows the effect of temperature upon cycle life for 100-min cycles. Precautions are necessary to maintain the battery temperature within the +40 to +100° F range to retain sufficient life margins. The eclipse operation helps this temperature control since the low-temperature environment occurs during the night when the batteries are discharging and generating the greatest amount of heat.

Dynamic Environment. The Gulton VO-20HSB battery cells have been subjected to a wide range of shock, vibration, and acceleration levels. The cells have withstood 40-g perpendicular shock and 22-g transverse shock with no deterioration in performance.

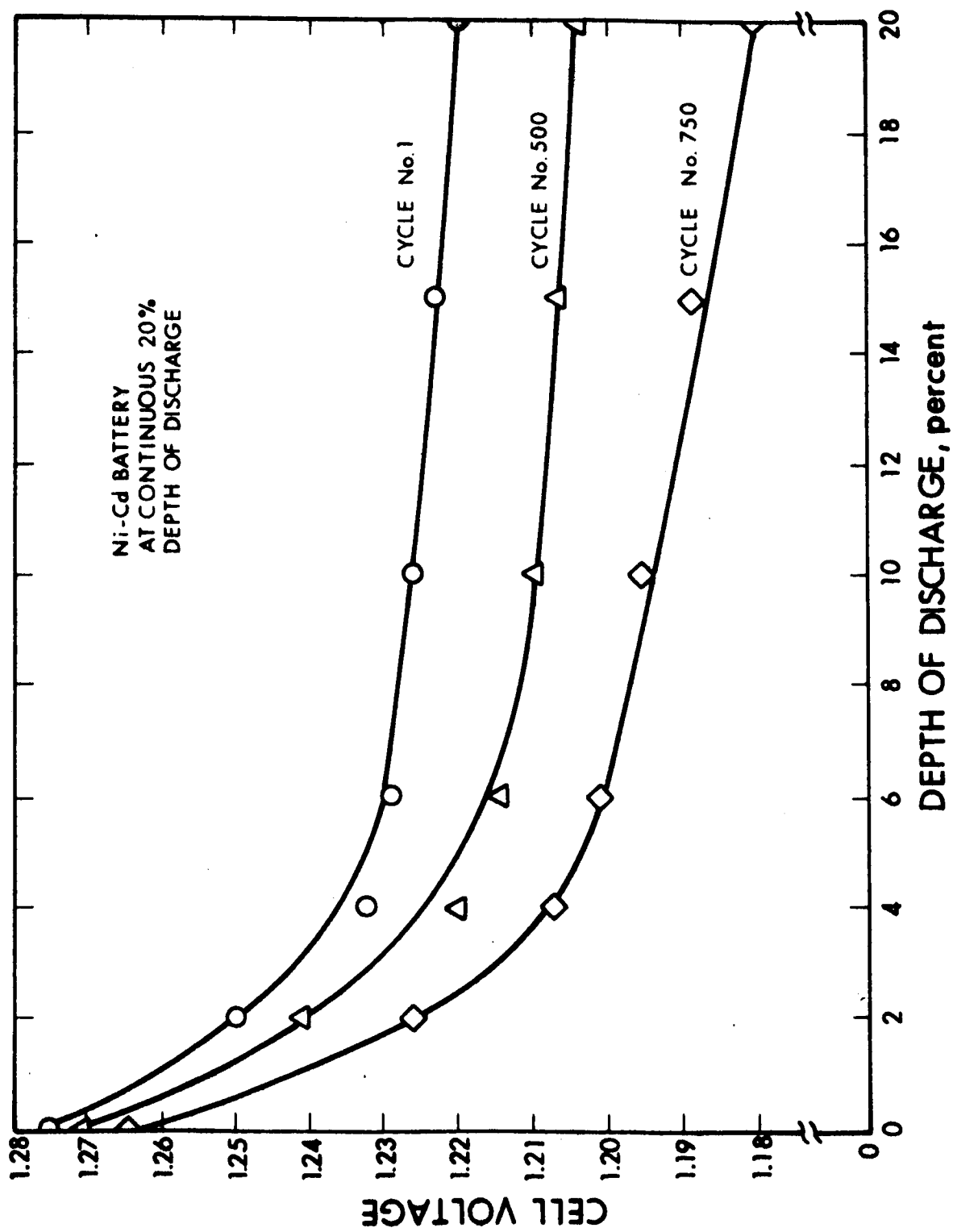


Fig. 5-28 Memory Effects in Ni-Cd Battery

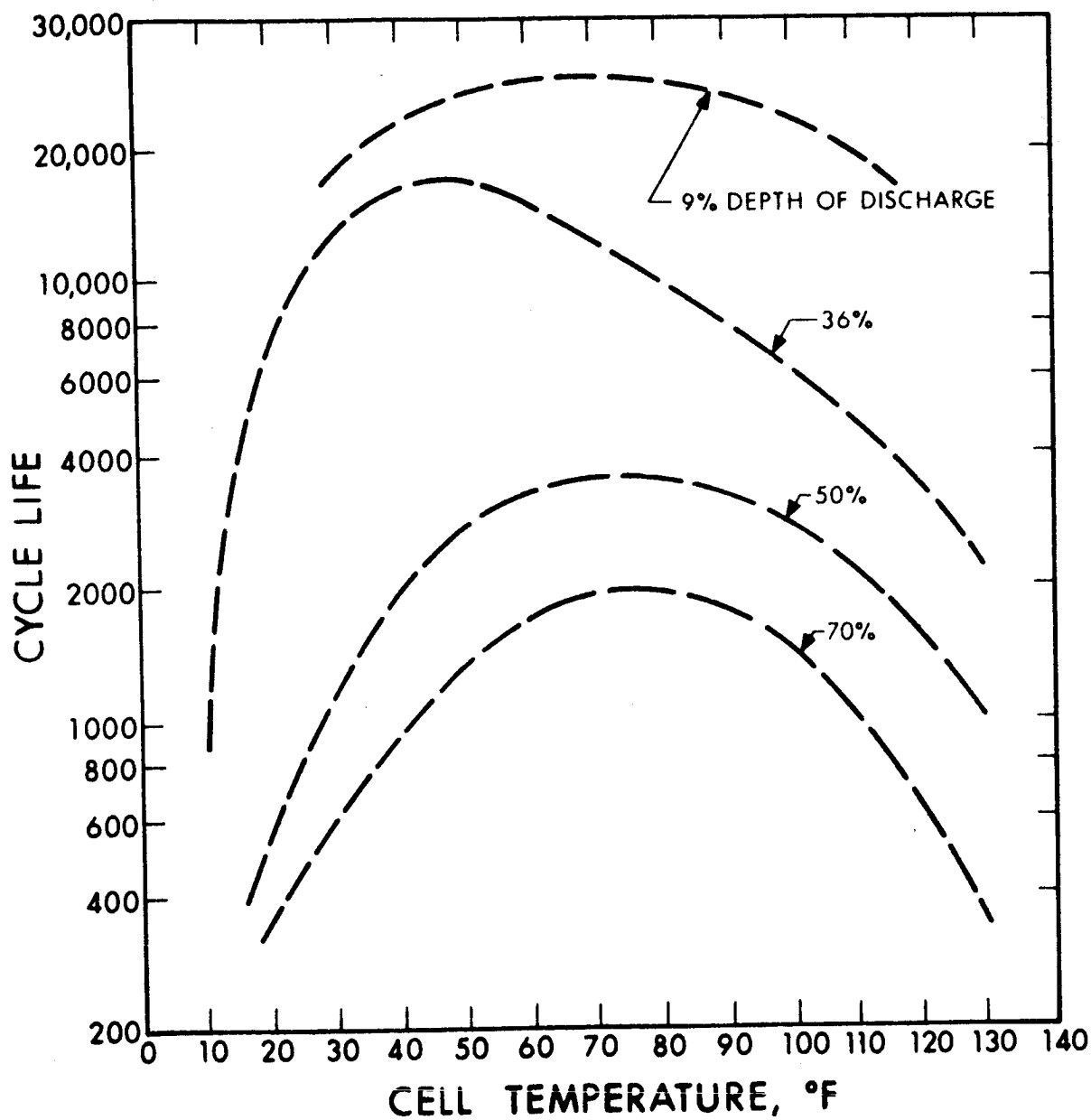


Fig. 5-29 Estimated Cycle Life of Ni-Cd Battery

They also have been subjected to loads of 60 g at 44–2,000 Hz, 40-g acceleration for 4.5 min perpendicular to the major face with no deleterious effects. Discontinuities, furthermore, were not detectable after random vibration of  $0.65 \text{ g}^2/\text{Hz}$  over a bandwidth of 20 to 2,000 Hz.

#### 5.4.8 Redundancy Considerations

The high reliability shown by solar-photovoltaic systems in space operation over periods greater than 1 yr can be attributed to the use of appropriate series-parallel circuits so that random component failures cause only a small degradation in the system performance. This technique would again be used in the present design.

The critical areas concerning power system operation are: deployment, boom rotation, battery failure, and the overall desire to operate usefully in the event of partial failure.

The deployment problem is partly alleviated by the use of a split array. This will permit useful experimentation in the event one-half of the array hangs up. However, the design using Vinson actuators offers inherently high reliability. There will be no need for prolonged storage in space, so that cold welding should not take place. In addition, there is sufficient impulse available in the hydrazine and ammonia systems to agitate or spin up the satellite as an emergency maneuver.

The boom rotation mechanism described earlier will carry a redundant drive motor, each driving through spring-loaded dogs so that, if one seizes, the other can drive the mechanism. Puncture of the harmonic drive seal by micrometeoroids is unlikely because it is shielded by two concentric walls, but it is planned to use a low-vapor-pressure grease so that the lubrication will remain effective for many months. Failure of the thin-wall harmonic drive casing due to fatigue can be avoided by designing an adequate fatigue life in a standard manner. By using high-starting-torque DC motors, deterioration of the bearings or binding of the sliprings will first appear as a high power demand to maintain rotational speed. It can be planned that the stalling failure



of one half-array is monitored so that the failure of the other half-array can be anticipated. It will then be possible to stop the latter in a chosen relation to the first, either to provide maximum power for a short time each day or to provide about one-third power for half of each day, depending on the status of the various experiments.

Battery failure will be guarded against by 50-percent redundancy so that two out of three battery modules can supply the entire load. These battery modules will be separated or thermally isolated to prevent one unit from affecting another if it overheats. Total battery failure will leave the satellite partially operational because the power regulation and all circuit protection systems will be designed to operate safely on emerging from an eclipse condition. Latching relays will be employed instead of solid-state switches to provide the correct restart sequences.

## 5.5 PROPULSION

This subsection describes the engineering effort and analyses conducted to define the total vehicle propulsion system. This work encompasses the orbit-injection motor system and the secondary propulsion systems for injection attitude control, orbit attitude control, and stationkeeping.

The selection of primary and secondary propulsion system is intimately connected with selection of the configuration of the orientation control system. The selected system will first be described and the matrix of alternatives explained. Then the rationale that led to selection of the primary and secondary propulsion systems will be established; finally, the choice of subsystems and components will be described.

The following areas are of particular interest and are covered in this subsection:

- The monopropellant hydrazine system chosen for injection control, station acquisition, and injection-error correction.
- The ammonia resistance jet system for attitude control
- The cesium-ion engines for attitude control and stationkeeping

### 5.5.1 Selected System

The primary propulsion system for the ATS-4 vehicle is the Delta spherical solid motor, TE-364-3. A description of this motor, as well as the considerations involved in its selection, is given in subsection 5.5.3.

The secondary propulsion systems consist of monopropellant hydrazine, ammonia resistance jets, and cesium-ion engines. As previously described, LMSC has chosen to provide three-axis control of the vehicle beginning with separation from the Centaur vehicle through all phases of orbit operations. Vehicle control during the transfer-ellipse coast phase is handled by the ammonia resistance jet system and is described in subsection 6.1. Three-axis control during engine burn will be accomplished by monopropellant hydrazine reaction motors employing Shell catalyst thrusters.

Pitch and yaw control is accomplished by four 60-lb thrust motors located on the rear face of the equipment section. Sizing of these motors involved the thrust misalignment errors of the TE-364-3 type engine, plus the moment arms permitted by the vehicle configuration and provides a control torque level 50 percent in excess of the maximum disturbance torque. Tankage was provided for a total of 2,260 lb-sec of impulse propellant. Four 1-lb hydrazine motors are mounted together in pairs, with the two 60-lb thrust motors on the Y-Y axis. Since this system becomes inoperative following injection, it is intended to permanently disable the thrusters by means of a squib-actuated valve.

In the matrix analysis that compared low-thrust hydrazine motors, resistance jets, and ion engines for station acquisition and injection error correction, the ion engines were eliminated because of the 120-day period needed to reduce the given 100-ft/sec injection errors. From the standpoint of  $I_{sp}$  and total system weight, both the hydrazine system and the resistance jet system were closely comparable. Because of the deployed vehicle system, Fig. 5-1, the following choice could be made in the location of tankage and thrusters for this purpose:

- Locate two additional 1-lb-thrust hydrazine motors on the equipment section, on the Y-Y axis, and utilize hydrazine tankage available for injection control. In addition, provide two 1-lb thrust hydrazine motors on the same axis in the sensor section, plus tankage.
- Provide two additional resistance jets plus tankage in the equipment section.

The comparison matrix for this choice is shown later in Table 5-8. Because of the higher thrust level of the hydrazine system and correspondingly shorter time to trim injection errors, it was decided to include the additional motors and tankage in the sensor section. Fifty-two lb of hydrazine propellant, corresponding to 230 ft/sec velocity change, have been included for the station-acquisition/injection error-correction  $\Delta V$  requirements. This impulse propellant is divided equally between the equipment section and sensor section tankage.

The total vehicle hydrazine system therefore consists of four 60-lb thrust motors for injection pitch and yaw control, four 1-lb motors for injection roll control, and four 1-lb motors for station acquisition and injection error correction. Ten motors are located in the equipment section and two in the sensor section.

The requirement for precision attitude control ( $\pm 0.1$  deg) is equally as important as the requirements imposed in design of the 30-ft reflector. As described previously, LMSC chose a sensor system composed of a body-mounted gyro package, horizon sensor, and star-field tracker, with backup supplied by the interferometer experiment. This system presumes use of mass-expulsion devices for attitude control.

The choice of mass-expulsion propulsion systems, including the selection-comparison matrices, has been published in various monthly reports submitted earlier. In general, the tradeoff analyses involved comparisons of system weight, thrust levels, total impulse requirements, and reliability. Two completely redundant systems were chosen.

For the basic attitude-control system, ammonia resistance jets of 2-mlb thrust were chosen on the basis of system weight, force level, compatibility with orbit lifetime, and state-of-the-art availability. These motors, six in total, are located on the sensor section in two clusters of three each. A tankage capacity for 3,500 lb-sec of ammonia (17.5 lb) has been provided in the recommended configuration. This quantity provides an approximate margin of 15 percent above the presently estimated impulse requirement for 2-yr operation.

The cesium-ion bombardment engine is ideally suited to performing attitude control functions, as well as stationkeeping operations, for the ATS-4 vehicle. The following characteristics are of interest:

- High Specific Impulse
- Extremely Low Thrust Levels
- Excellent Ratio of Expendables to Total Impulse
- Maximum Advancement of Technology

Cesium-ion engines are located on the periphery of the 30-ft parabolic antenna in four clusters of three engines each. The use of identical clusters was dictated by economic reasons, i.e., lower development costs. These clusters are on the X-X and Y-Y axes. Each cluster has two engines of 250- $\mu$ lb thrust and one engine of 500- $\mu$ lb thrust. A complete description of these engines is given in subsection 5.5.6. To perform the tasks of three-axis attitude control and stationkeeping, six of the 250- $\mu$ lb thrusters are used, with the four 500- $\mu$ lb thrusters reserved for east-west and north-south stationkeeping. Such a total of 12 engines is available, there are two redundant 250- $\mu$ lb engines that are placed on Y-Y axis.

The cluster containing this pair of engines and its opposite number are oriented to provide roll-control torques and north-south stationkeeping. By using the redundant 250- $\mu$ lb pair in this manner, only the cluster providing stationkeeping thrust need be powered in the standby mode. Because the time of north-south thrusting exceeds that for east-west, placement of the redundant thrusters along the Y-Y axis minimizes electrical power requirements.

A simplified diagram of the primary and secondary functions of the vehicle secondary propulsion system is shown in Fig. 5-30. The significant attributes of the selected system lie in the wide range of backup functions that become available. For example, during the ascent coast phase, the resistance jet system provides primary attitude control through the horizon sensors and gyro package. The secondary function of this system is to back up the ion engines for spacecraft orbital attitude control. The choice of a primary versus a secondary role for the resistance jet system as shown here is made purely on the basis of technology, since the ammonia resistance jet system is equally as competitive in weight as the ion-engine system.

The hydrazine system performs a triple function, being primary in injection control and station acquisition/change, and backup for stationkeeping, to the limit of the propellant available. In the latter case, the hydrazine system backs up the ion-engine system (which has relatively unlimited propellant storage).

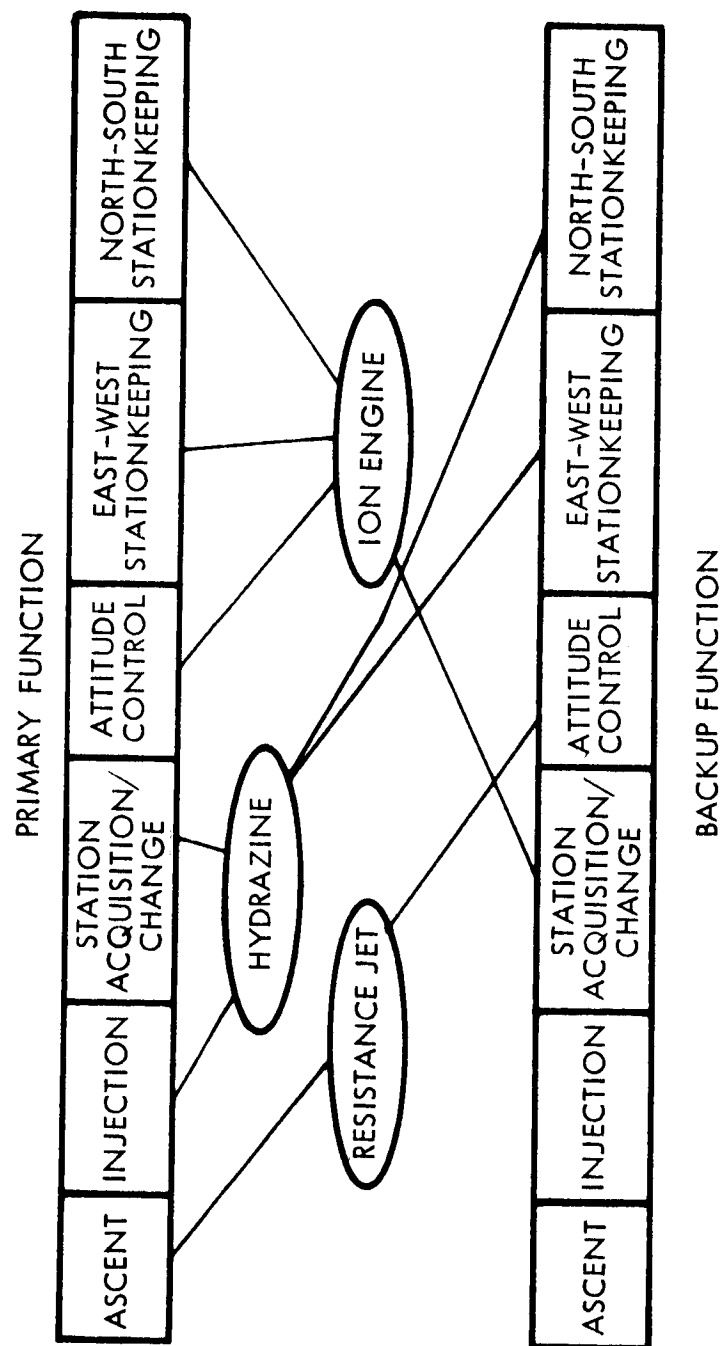


Fig. 5-30 Secondary-Propulsion Functions

The ion engines are shown as primary for attitude control and stationkeeping and are backed up by the resistance jets for attitude control and by the hydrazine system for stationkeeping. Each cluster contains 2.2 lb of cesium. This quantity is equivalent to 11,000 lb-sec of impulse; a division of impulse was used that allows 5,000 lb-sec for stationkeeping and 6,000 lb-sec for attitude control. The total impulse capacity for the spacecraft (44,000 lb-sec) provides for the required 2-yr life with a margin in excess of 50 percent. Thus, from the point of view of impulse quantity, in attitude control there is complete redundancy between the resistance-jet system and the ion-engine thrusters.

#### 5.5.2 Table of Alternatives

In Table 5-7, alternate sets of thruster configurations are compared. The recommended system has been described in subsection 5.5.1; this subsection will describe the matrix analysis that led to this selection.

As shown in the table, seven combinations of propulsion systems were compared for four operations, namely, station acquisition/change, stationkeeping, attitude control, and backup attitude control.

Alternative 1 utilizes ion engines for both station acquisition/change and stationkeeping, as well as backup attitude control. This system has much to recommend it; however, it was deleted on the basis of excessive time required to perform the station acquisition/change maneuver and because it provides no redundant attitude control backup. In addition, when several of the maneuvers are accomplished simultaneously, excessive power is required.

Alternatives 2 and 4 were all resistance jet and all ion engine. They were deleted since they take excessive time to perform the station acquisition/change maneuver, and while providing redundancy, the redundant equipment has common failure modes with the primary equipment.

Table 5-7

## THRUSTER ALTERNATIVE CONFIGURATIONS

Operation	Recommended	Alternative					
		1	2	3	4	5	6
Station Acquisition Change	Hydrazine (4)	Ion engines (4)	Resistance jets (12)	Ion engines (4)	Ion engines (4)	Resistance jets (4)	Resistance jets (4)
Station-keeping	Ion engines (4)	Ion engines (Same 4)	Resistance jet (Same 12)	Ion engines (Same 4)	Ion engines (Same 4)	Resistance jets (Same 4)	Ion engines (4)
Attitude Control	Resistance jets (6)	Resistance jets (6)	Resistance jets (Same 12)	Resistance jets (6)	Ion engines (12)	Resistance jets (4)	Resistance jets (4)
Attitude Control Backup	Ion engines (6) + (2)	Ion engines (6)	Resistance jets (Same 12)	Redundant valves, separate tanks	Ion engines (Same 12)	Redundant valves, separate tanks	Redundant valves, separate tanks

Thrust levels: Hydrazine: 1 lb; Resistance jet: 2 mlb; Ion engines: 0.5-mlb stationkeeping, 0.25-mlb attitude control.



Alternatives 3, 5, and 6 are split systems in which redundancy is provided by means of separate systems. Besides the basic problem of taking extensive time to perform station acquisition and change maneuvers, these systems are excessively complicated and, even though redundant, are not necessarily more reliable.

Table 5-8 compares the recommended and alternative systems in more detail. In this table several additional factors are considered, including total system weight, equivalent power weight (a requisite for comparisons of ion engines), number of thrusters, redundancy, and technology advance.

The recommended system weighs more than the six alternatives, requires equivalent power to alternative 1, and requires more equivalent power than all others. It has more thrusters. It does provide, however, all of the factors of effective redundancy (two dissimilar systems vs. two similar systems), performance, and technology advance that LMSC believes important to the ATS-4 mission. The technological advance was the primary selection criterion over alternative 2. It makes the most efficient use of each system (hydrazine, resistance jet, ion engine), yet permits the broadest possible backup capability.

The hydrazine system is utilized at thrust levels that are well within current state-of-the-art; at this thrust level (1 lb) injection errors are terminated in the shortest possible time.

The primary candidates for secondary propulsion (attitude control and stationkeeping) are the ion engine (cesium contact and mercury bombardment versions which have operated in space) and the resistively heated gas jet (a nitrogen propellant version which has also operated in space).

The cesium bombardment engine has the most extensive accumulated lifetime (in ground test) and the highest power efficiency in the useful range of specific impulse (3,000 to 5,000 sec) of the present generation of available flight-type ion engines, and was selected for design analysis. The cesium contact and mercury bombardment engines are quite close in capability and can be regarded as alternative candidates.

Table 5-8

## COMPARISON OF THRUSTER ALTERNATIVES FOR ATS-4

System	Recommended	Alternative					
		1	2	3	4	5	6
Total Weight, lb	335.7	253.7	317.5	200.4	179.4	207.9	267.9
Equivalent Power Weight, lb	150.5	150.5	57.4	107.8	129.6	57.4	89.8
Number of Thrusters	22	18	12	10	16	8	12
Attitude Control Redundancy	Ion engines/ resistance jets	Ion engines resistance jets	Redundant resistance jets	Redundant valves, separate tanks	Redundant ion engines	Redundant valves, separate tanks	Redundant valves, separate tanks
Translational Redundancy	Ion engine/ hydrazine	Yaw maneuver	Yaw maneuver	Yaw maneuver	Yaw maneuver	Yaw maneuver	Ion engines/ resistance jets
Technology Advance	Maximum	Near maximum	None	Minimum	Near maximum	None	Minimum
Time to Stop 100-fps Injection Errors	43 min.	120 days	15 days	120 days	120 days	15 days	15 days

The ammonia resistance jet has qualified for space operation and combines the simplicity of operation of the flight-operated device with improved specific impulse and propellant storage. The low thermal inertia type is somewhat lighter in weight and more efficient than the thermal storage type, but the latter can also be considered an excellent candidate.

The choice of specific impulse is not highly critical, although much analysis has been performed to optimize the specific impulse for electric propulsion missions. It can be shown readily that if power efficiency is independent of specific impulse, system weight is minimized (for a given thrust and force impulse) for that value of specific impulse that makes the propellant with its tankage weigh the same as the power supply. However, efficiency does vary with specific impulse, and with thruster lifetime to some extent, so optimization becomes more complex. In practice, with present designs, the ion engine should be operated at 4,000 to 5,000 sec to keep its power-to-thrust ratio low, and the ammonia resistojet at 200 to 250 sec to provide long life. If a thruster were available at 50 percent efficiency or better over the specific impulse range, the optimum  $I_{sp}$  would be about 1,000 to 1,500 sec. Such thrusters as the colloid thruster promise operation in this range. However, satellites that use the technology demonstrated on ATS-4 will include extended operating life and should employ much lower specific-weight power supplies, putting the optimum specific impulse in the range of 2,000 to 3,000 sec. In this range the competing technologies are the bombardment ion engine, colloid thruster, sublimation plasmajet, and Hall accelerator, all of which are under active development at present.

#### 5.5.3 Injection Motor

During the initial phase of the ATS-4 program, LMSC conducted a review of applicable injection motor systems. Results of this survey were recorded in Technical Notes 13, 16, 18, and 19. The survey investigated the applicability, availability, state-of-art, and costs of injection motor systems of various types. The net result was the decision to concentrate on spherical solid motors currently available.

For the spacecraft weight and total impulse required, four candidate motors were considered. These are shown in Table 5-9.

Table 5-9

CANDIDATE MOTORS

Motor	Thrust (lb)	Total Impulse (lb/sec)	Availability (Mo)	Unit Price (\$)	No. Tested
Surveyor	8,740	356,700	10	85,000	17
Burner II	9,250	402,500	10	88,000	7
Delta	9,983	415,000	10	90,000	2
Optimized	9,000	525,500	18	125,000(a)	0

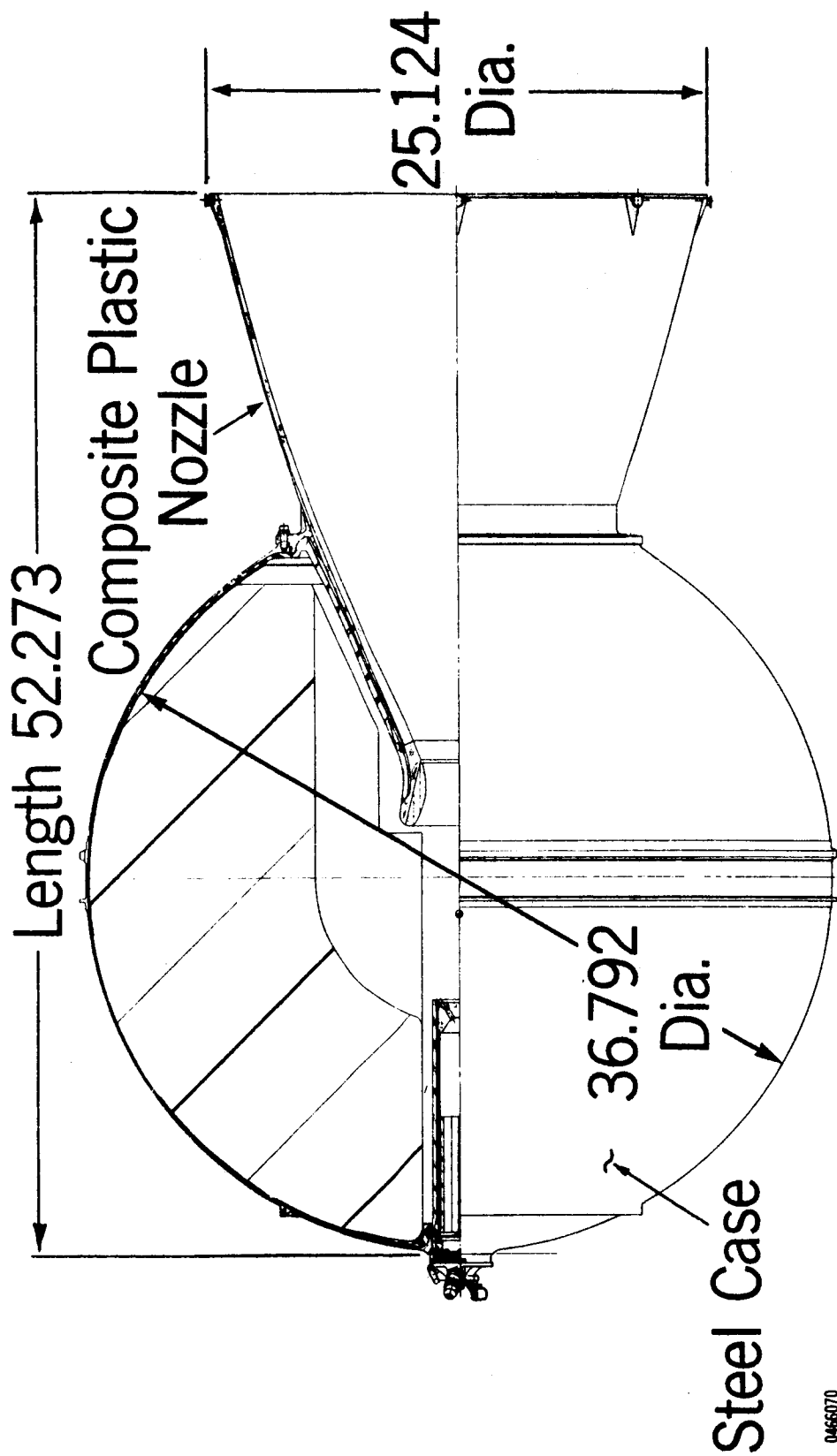
(a) Plus \$1.2 M development cost.

Of these candidate motors, the Delta motor, TE-364-3, most closely meets the total impulse requirements of ATS-4. A drawing of this motor is shown in Fig. 5-31. The characteristics of an optimized motor, outlined in Table 5-9, do not vary significantly from the Delta motor. The Delta motor provides an additional performance margin of 200 lb, but, on the basis of availability and performance versus the development costs of the optimized motor, the Delta motor was chosen.

#### 5.5.4 Hydrazine System

Thruster Sizing, Weight, and Impulse Requirements. The hydrazine system was sized to provide kick-stage attitude control and station-acquisition/change. The total  $\Delta V$  required for station acquisition plus injection-error correction was determined to be 230 fps. The propellant weight necessary (at  $I_{sp} = 230$  sec) to reduce these error is 51.3 lb, based on a 1,600-lb spacecraft.

Kick-stage attitude control propellant requirements were based on use of four 60-lb thrust motors for pitch and yaw, and four 1-lb motors for roll control. Based on



0465070

Fig. 5-31 Delta-Injection Motor, TE-364-3

the configuration shown in subsection 5.1, and assuming a 0.25-deg thrust misalignment in the kick motor, 175 ft-lb of control torque are required. Thruster locations, assuming a 4-ft lever arm, therefore require approximately a 44-lb minimum-thrust thruster. The 60-lb motors thus give adequate thrust margin and permit some latitude in thruster location, c.g. and thrust misalignment factors, and thrust level variation. The propellant weights for all hydrazine systems are as follows:

- Kick-stage attitude control: 9.8 lb
- Station acquisition/change: 51.3 lb

The total weight of the hydrazine system, including propellant, tankage, thrusters, etc., is shown in Table 5-10.

Table 5-10  
HYDRAZINE SYSTEM WEIGHT

Item	Weight (lb)
Initial Acquisition/Change	
Injection Attitude Control Propellant	9.8
60-lb Thrusters (4)	24.0
1-lb Thrusters (4)	6.0
Plumbing, Valves, etc.	7.0
Vernier Propulsion	
Impulse Propellant (230 fps)	51.3
N <sub>2</sub> H <sub>4</sub> Tankage	14.0
Plumbing, Transducers, Valves	15.2
1-lb Thrusters (4)	<u>6.0</u>
TOTAL	133.3

Selection Criteria. The hydrazine monopropellant system was selected after an investigation of bipropellants, monopropellants, and cold nitrogen mixtures. Thrust misalignment total impulse requirements for the kick-stage motor and the relatively short lever arms precluded nitrogen from the practicable candidate list. Bipropellants, while highly developed, were found to be inconsistent with the low thrust levels required for station acquisition/change, in terms of reliability and availability. Bipropellants for kick-stage attitude control were competitive, but complex, and required an additional propellant type for roll control.

Of the monopropellants, 90 percent hydrogen peroxide has been most successful up to the present time. This success is due to the effectiveness and stability of the highly developed silver-base catalysts that decompose the peroxide with satisfying regularity and offer specific impulses in the 180- to 170-sec range. Hydrazine, utilizing the Shell-type catalyst, has been equally reliable in numerous extended life tests and has the added advantage of higher specific impulse. In addition, hydrazine stores well and does not exhibit the long-term decomposition characteristics that can be found with peroxide.

Because of the simplicity of the catalyst motor system, monopropellant hydrazine has been successfully tested in motors with thrust as low as 0.1 lb. The maximum test effort has been in the 1.0- to 5.0-lb range. Thus, current test data, plus the advantages of simple injector design, no mixture ratio control, lack of residuals, and reduced operating temperatures, all tend to make the selection of monohydrazine optimum for the ATS-4 requirement.

#### 5.5.5 Ion-Engine System

Requirements for Attitude Control and Stationkeeping. The ATS-4 vehicle is basically an earth-oriented 30-ft dish with supporting electronics and feed horn mounted in front of the dish, and solar panels mounted behind the dish on a north-south oriented boom. Attitude control and stationkeeping thrusters will be placed on the periphery of the dish to allow a clear cone of operation.

Cesium bombardment ion thrusters and ammonia gas resistojets have been chosen as the most appropriate thruster candidates for both attitude control and stationkeeping. It is planned that the ATS-4 will have two complete and independent attitude control systems, one a resistojet and the other an ion engine. In addition, the ion-engine system will be used for stationkeeping.

Attitude Control Design. Solar pressure and translational thrust misalignments are the main cause of attitude control perturbation. Solar pressure on the dish has been investigated with several dish-sun orientations. Solar pressure on the solar panels will cause different torques in roll and yaw depending on whether the array is symmetrical or offset to one side. Translational thrust misalignments are assumed as acting at an angle of 3 deg at a distance of 16 ft, causing a torque of  $420\mu\text{lb-ft}$ . Of the 3 deg, 1 deg is due to thrust misalignment, 1 deg due to uncertainty of c.g. location, and 1 deg due to thermal distortions.

Table 5-11 summarizes the disturbing torques about each axis for the symmetric solar array and the offset array.

Table 5-11  
DISTURBING TORQUES

Cause	Torque ( $\mu\text{lb-ft}$ )		
	Yaw	Pitch	Roll
Translational Thrust Misalignment	420	420	420
Solar Pressure on Dish	0	70	70
Solar Pressure on Symmetric Array	15	75	15
Solar Pressure on Offset Array*	240	75	240

\*Assumed at  $1.6 \times 10^{-7}$  psf on a  $134\text{-ft}^2$ , 900-w panel.



The correcting torque, or control torque, about each axis is provided by a thruster of at least 250  $\mu\text{lb}$  with a moment arm of 15 ft. The control torque, therefore, is at least 3750  $\mu\text{lb-ft}$ , or about six times the worst expected torque shown in Table 5-12 for symmetric arrays.

Table 5-12  
MAXIMUM TOTAL TORQUES

Condition	Torque ( $\mu\text{lb-ft}$ )		
	Yaw	Pitch	Roll
Symmetric Array	435	565	505
Offset Array	660	565	730

The assumed moments of inertia of the ATS-4 satellite for attitude-control sizing were as follows:

- Pitch axis: 45,000 slug-ft<sup>2</sup>
- Roll axis: 45,000 slug-ft<sup>2</sup>
- Yaw axis: 15,000 slug-ft<sup>2</sup>

These values greatly exceed current estimates of the inertias. Low moments of inertia give higher angular velocities than high moments of inertia, but the duty cycles will be the same. The behavior of the control system has been evaluated using yaw axis moment of inertia so that the results can be extended to pitch and roll axes without fear of under design.

Limit cycling as a means of attitude control lends itself readily to modifications and becomes self-adapting to various situations. In this technique, position sensors are used to detect a zone of  $\pm 0.1$  deg about zero. It is assumed that it is possible to tell from which direction the  $+0.1$  deg or  $-0.1$  deg position is crossed. It is not possible to accurately predict the magnitudes or senses of the disturbing torques. The basic limit cycle concept is modified here as follows. All limit cycle thrusts are of equal

impulse, and if one of the thrusts fails to move the spacecraft back inside the  $\pm 0.1$  deg angular position zone, the thruster that has just fired will thrust again.

A workable limit cycle is shown in Fig. 5-32. This limit cycle was designed for the yaw axis with attitude control corrective torquers of  $375 \mu\text{lb}$  (an earlier design value) acting on a 15-ft moment arm. Under conditions of no disturbing torque, each attitude control torquer is on for about 3.5 percent of the time. Under conditions of  $440 \mu\text{lb-ft}$  of disturbing torque, one thruster is on nearly 10 percent of the time and the other is on about 2 percent of the time.

The thrust values of torquers now considered are  $250 \mu\text{lb}$  and  $500 \mu\text{lb}$  rather than  $375 \mu\text{lb}$ , as in Fig. 5-32. The figure does, however, demonstrate the principle of limit cycling and can be used to estimate the percent of time each torquer may be on.

It is interesting to note that even in the presence of disturbing torques one of the control thrusters occasionally aids the disturbance. This situation will arise due to lack of adequate rate information. As disturbing torque increases, however, the percent on-time of the disturbance-aiding thruster diminishes to zero and the limit cycle is supported entirely by one thruster counteracting the disturbance. The maximum disturbing torque that can be corrected is equal to the corrective torque. Under this condition, the corrective torquer is on 100 percent of the time.

From the foregoing discussion it is concluded that torquers whose thrusts are on the order of  $375 \mu\text{lb}$  will operate, on the average,  $3\frac{1}{2}$  to  $4\frac{1}{2}$  percent of the time. Torquers whose thrusts are on the order of  $250 \mu\text{lb}$  will operate an average of 5 percent of the time if symmetric array is used. This 5-percent per thruster average results in an attitude control required impulse of 5,000 lb-sec for six attitude control thrusters operating on a 2-yr mission. This figure is used as a design requirement.

Stationkeeping. The three major position perturbation forces result from luni-solar gravitation, Earth triaxiality, and solar pressure. Luni-solar gravitation, if uncorrected, will tilt the ATS-4 orbit  $0.8525 \text{ deg/yr}$  or  $0.00235 \text{ deg/deg}$  and cause an apparent north-south oscillation in the ATS-4 position. Solar pressure forces of about  $77 \mu\text{lb}$  will cause eccentricities to build up in the ATS-4 orbit and will become a

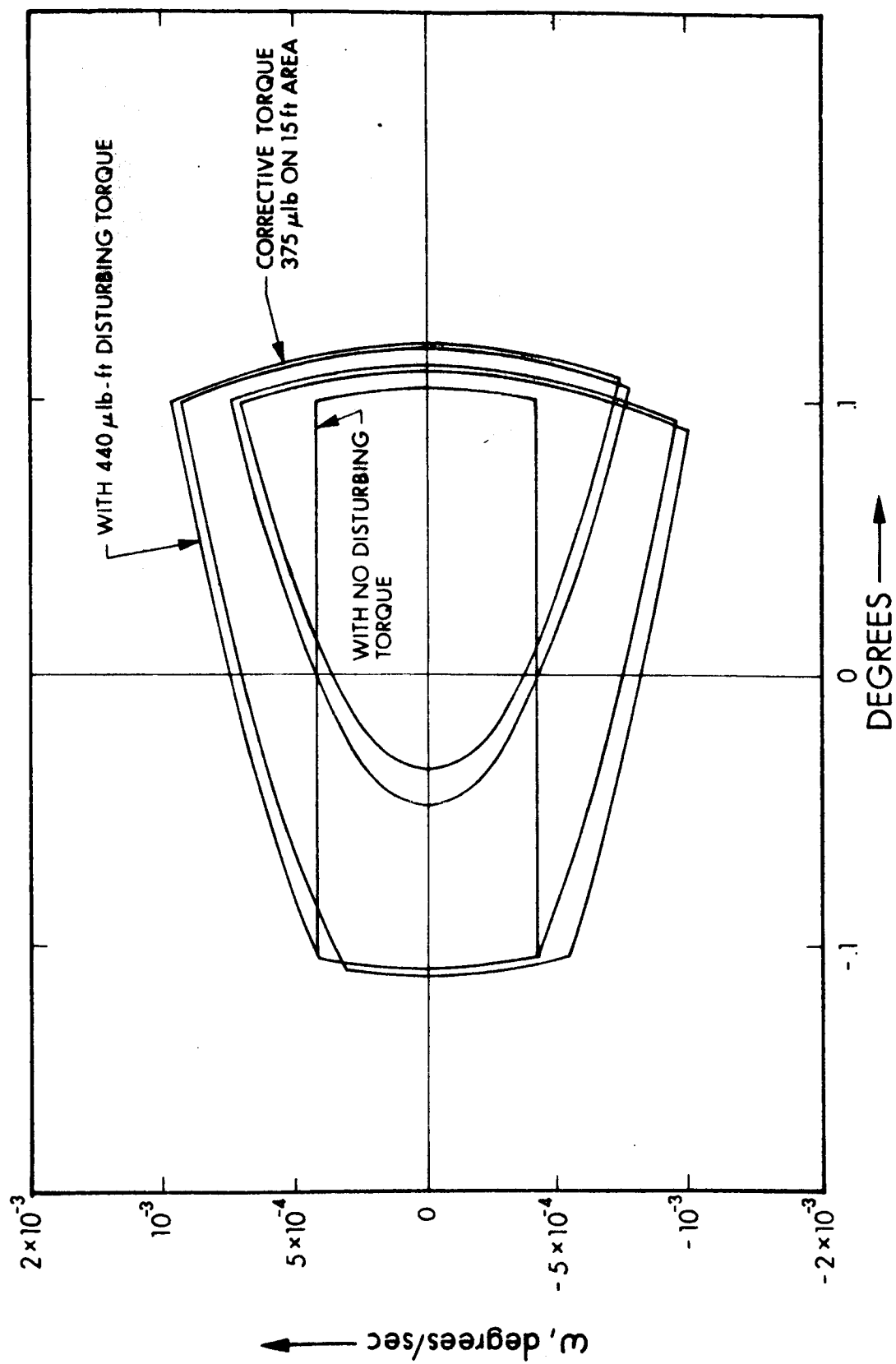


Fig. 5-32 Attitude Control Limit Cycle Behavior

maximum of  $1.46 \times 10^{-3} \mu\text{lb}$  in six months causing daily longitudinal oscillations of  $\pm 0.166$  deg. Earth triaxiality causes an additional east or west perturbation which, if uncorrected, results in a slow east-west oscillation that may be as large as 180 deg of arc.

For a nominal 1800-lb satellite, the north-south (or latitude) stationkeeping requirement can be met by using the thrust levels given in Table 5-13 twice each sidereal day, alternately to the north and south, midway between the times of crossing the ecliptic. Notice that as the amount of thrusting time per 12 hr increases, the  $\Delta V$  per year and the total impulse per year both increase as  $\alpha/\sin \alpha$ , where  $2\alpha$  is the anomaly through which thrusting occurs. The most efficient way to correct north-south disturbances in terms of required yearly impulse is thus to apply large thrusts of short duration twice each sidereal day. This condition is approached for thrust levels of 2,000  $\mu\text{lb}$  and thrusting times of only 1.62 hr out of 12.

Two candidate thruster sizes considered for latitude stationkeeping are 500  $\mu\text{lb}$  and 2,000  $\mu\text{lb}$ . Table 5-07 indicates that each 500  $\mu\text{lb}$  thruster will thrust about 7.8 hr out of 12, or 32 percent of the 24-hr sidereal day, if uninterrupted. The total yearly impulse is 10,000 lb-sec. Each 2,000  $\mu\text{lb}$  thruster will thrust 1.62 hours out of 12, or 6.2 percent of the time. The total yearly impulse for the 2,000- $\mu\text{lb}$  thruster is 8,500 lb-sec. The mission requires that regardless of which thrust level is used, north-south stationkeeping be in effect for 1 yr only, the satellite orbit being allowed to tilt during the second yr.

Assuming an average solar radiation pressure of 80  $\mu\text{lb}$ , an 1,800-lb satellite will experience an average acceleration of  $4.5 \times 10^{-8}$  g. To prevent orbit eccentricity from building up, east and west thrusters can be fired near sunrise and sunset with the following candidate thrust levels and corresponding uninterrupted thrusting times:

Thrust Level, $\mu\text{lb}$	250	500	2,000
Thrusting Time per 12 hr, hr	3.9	2.0	0.55
Time On per Thruster, percent	16	8.4	2.3
Yearly Impulse, Both Thrusters, lb-sec	5,000	5,300	5,800

Table 5-13

## NORTH-SOUTH THRUSTING REQUIREMENTS FOR THE 1800-LB ATS-4

Requirement	Thrusting Time Per 12 hr (hr)					
	12	10	8	6	4	1.62
$\Delta V/\text{yr}$ , ft/sec	235	204	180	167	158	151
Acceleration, $10^{-7}$ g	2.35	2.45	2.70	3.34	4.74	11.2
Thrust, $\mu\text{lb}$	423	440	481	600	850	2,000
Yearly impulse (both thrusters), lb-sec	13,350	11,600	10,100	9,450	8,910	8,520

These thrustings occur at discrete spacecraft-sun orientations and hence occur the same time each solar day. There is one less solar day per year than sidereal day so the east-west thrusting times will shift in phase with respect to north-south thrusting times.

An additional function of the east-west thrusters is to cancel out the effect of earth triaxiality by thrusting 1.0 lb-sec east or west per day. If this thrusting takes place at the same time each sidereal day, a very small eccentricity will build up, and if the impulse occurs once each solar day, much of the potential eccentricity buildup may be cancelled in the course of a year. A good time to cancel triaxiality, then, is right after the solar gravitation correction. East-west thrusting to negate triaxiality for the 2-yr mission will require a maximum of 700 lb-sec of impulse from either thruster.

Description of Ion-Thruster System. Since six thrusters are needed for attitude control and four for stationkeeping, a minimum arrangement would employ ten thrusters as shown in Fig. 5-33. Here the thrusters are mounted on the antenna rim. Since the center of gravity of the spacecraft may be several feet from the plane of the antenna rim, it may be necessary to perform translational thrust somewhat out of the horizontal plane. However, the added radial component of thrust will not seriously perturb the

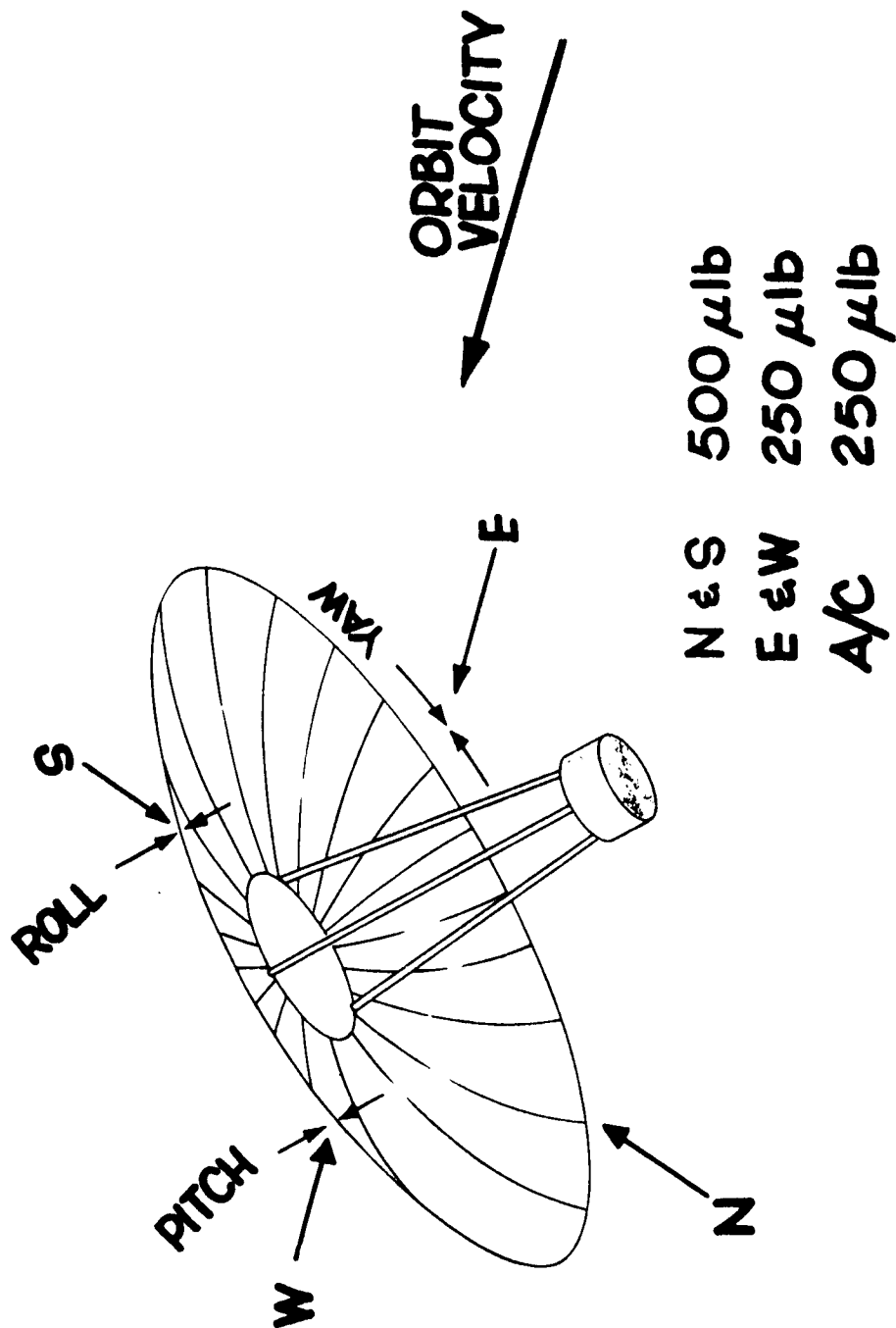


Fig. 5-33 ATS-4 Ion-Thruster Location

orbit since (1) the effects of north-south and east-west pairs of thrusters are mutually correcting, and (2) the orbit perturbation would be so small that it could be readily corrected by the thrusters themselves.

As shown in Fig. 5-33, three thruster modules would be needed, a single 500- $\mu$ lb, two clusters of three 250- $\mu$ lb, and one cluster of two 250- $\mu$ lb thrusters with one 500- $\mu$ lb unit. Because of the development costs and operational inconvenience of such cluster modules, it is preferred to make a single cluster design, (the two 250- $\mu$ lb cluster plus one 500- $\mu$ lb unit) serve at all four stations. Thus the selected configuration uses 500- $\mu$ lb thrusters for all four translational corrections, and there is a redundant pair of thrusters for pitch.

A cesium-bombardment ion engine designed for stationkeeping operation on a classified satellite is shown in Fig. 5-34. The unit shown comprises the propellant storage and feed system, ionization chamber, and accelerating and neutralizing system. Cesium propellant is contained in an annular chamber in which thin nickel vanes are arranged radially to provide passages tapering toward a porous nickel wick. Surface tension forces carry liquid cesium (cesium melts at about 28°C) into the wick and along to a vaporizer where it can be evaporated by applied heat. When the vaporizer heater is de-energized, the cesium cools rapidly and the mass flow falls essentially to zero (i.e., it is reduced by six or more orders of magnitude). There is no valve in the system; vaporizer sealing for launch is achieved by utilizing an acrylic cement or cadmium, which is removed readily by heating.

From the vaporizer, the cesium passes over a hot tungsten cathode into a discharge chamber whose wall is a cylindrical magnet. A cylindrical anode attracts electrons from the cathode. In spiralling through the applied magnetic field, the electrons collide with many cesium atoms, giving rise to many secondary electrons and cesium ions, thus producing a plasma. The potential between the cathode and the chamber walls is adjusted so that some cesium ions are attracted to the cathode with enough energy to keep it hot (after initial heating) but far below the energy level to cause sputtering damage.

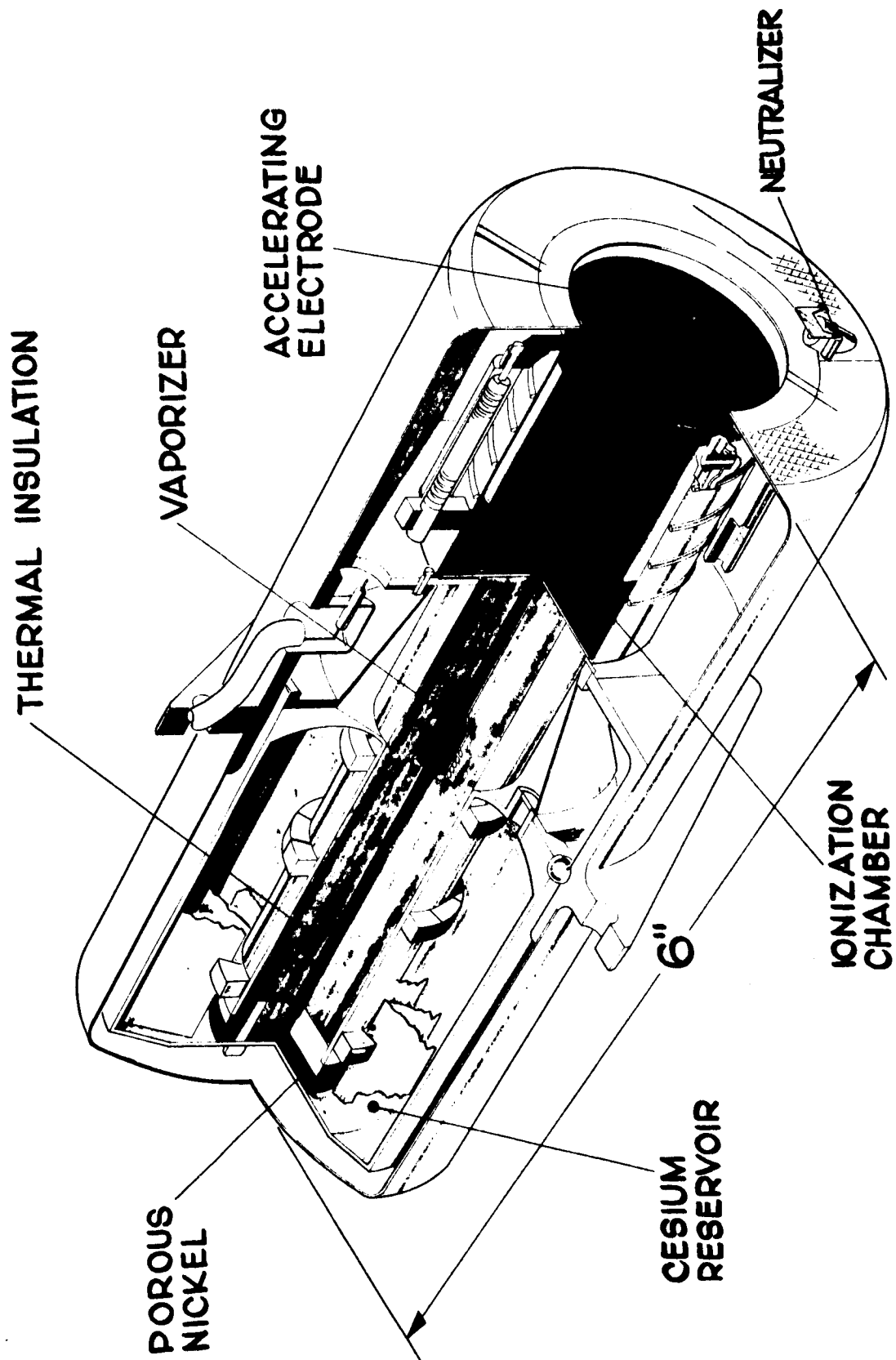


Fig. 5-34 Cesium-Bombardment Ion Engine (Cutaway View)



The ionization chamber is closed by a perforated plate, and a second plate, the accelerating electrode, is arranged as shown with matching perforations. The chamber is maintained at a high positive potential (about 2 kv) with respect to spacecraft ground, and the accelerating electrode at a negative potential (-600 v). The plasma in the chamber terminates in a meniscus which is concave outwards at each hole. Ions leave the surface of this meniscus attracted by the strong field, and are focused so that they are accelerated through the apertures in the negative electrode. Outside the engine they are joined by electrons supplied by a neutralizer mounted externally to the beam but coupling to it by a cesium plasma discharge.

Ion engines of this type have demonstrated lifetimes in excess of 8,000 hr, and examinations of thruster hardware after tests (terminated voluntarily) indicate operating lifetimes of at least several years.

A schematic of the typical cluster for ATS-4 is given in Fig. 5-35. A common reservoir feeds all three thrusters and its internal geometry will differ from the annulus shown in Fig. 5-34 by having a tee-shaped wick and a set of radial vanes arranged like orange slices, all meeting on the transverse of the tee. The reservoir is electrically connected to the ionization chambers, and hence a single high-voltage supply will be used and kept on at all times. The cathode heaters, chamber heaters (to prevent cesium condensation), and accelerating voltage will share common power supplies, and all will be kept in continuous operation.

Individual vaporizer heaters will supply cesium to the appropriate thruster on command and with a response time of a few seconds. Control logic will ensure that only one thruster in a cluster is commanded at once. Stationkeeping thrust will be interrupted to provide attitude control, the thrust decay taking 10 to 15 sec.

Over the past 5 yr, special purpose PC&C units for ion engines have been developed to a high level of performance and light weight. Units to operate single thrusters have been built and operated with the thrusters for over 1,000 hr in compatibility tests. Overall power efficiency of 90 percent has been achieved in units handling 100 w of output power.

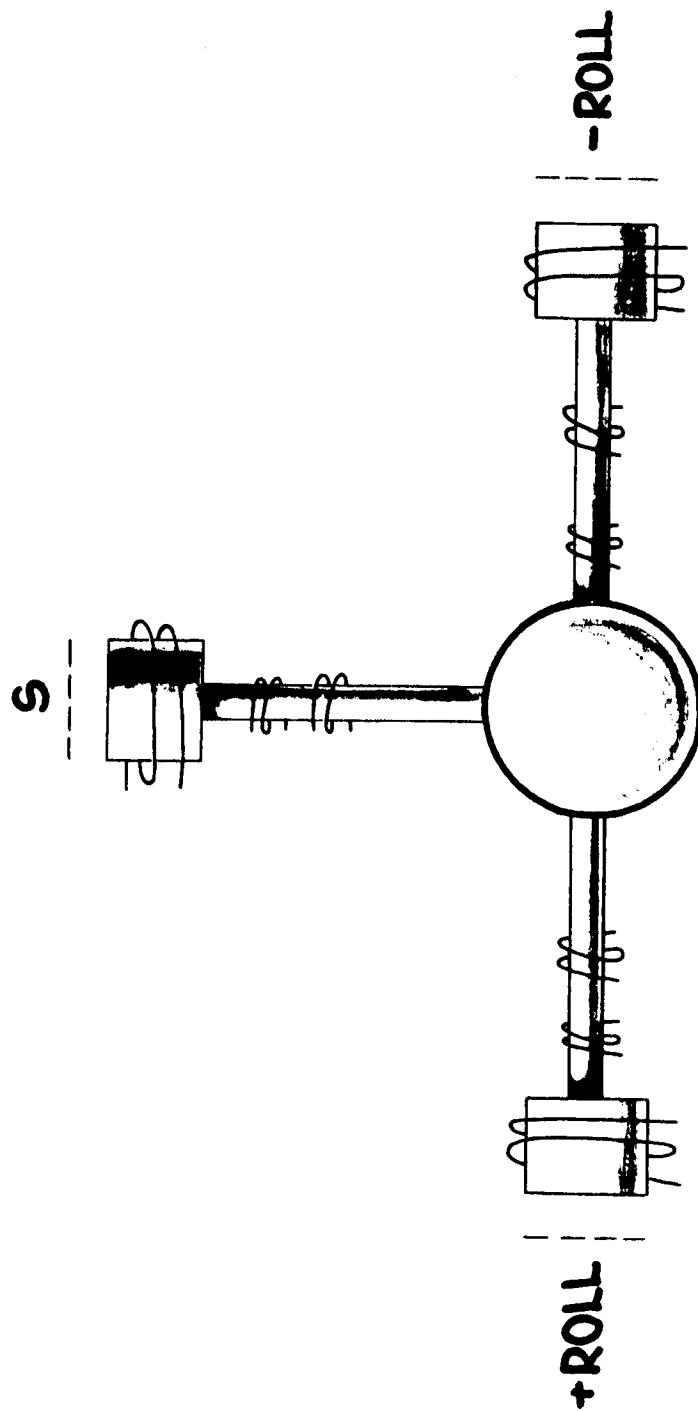


Fig. 5-35 Ion-Engine Cluster Concept

The PC&C unit provides all of the power required by the thruster elements. The control portion provides engine startup, shutdown, and steady-state control. It carries overload and short-circuit protection, and ensures that the vaporizer circuits are not energized whenever either of the high-voltage supplies are off.

Adaptation of this design to operate a cluster can be readily made by using individual vaporizer heater supplies and individual cathode-bias controls for cathode heating.

Thrusters have been built and operated over the range 10  $\mu$ lb to 10 mlb at specific impulses from 3,000 to 10,000 sec. It was determined early in the study that a specific impulse of 5,000 sec was suitable for the mission because (1) it gives near-minimum power per unit thrust (see Fig. 5-36), (2) most of the lifetime testing has been performed at this value, and (3) PC&C designs have selected components to operate at the voltages corresponding to this specific impulse. Optimization of specific impulse to minimize propulsion system weight for the ATS-4 application indicates that a value  $I_{sp} = 4,500$  sec would save about 10 lb of system weight. However, the growth to longer operation life and the use of lighter solar panels would put the optimum back in the range 5,000 to 6,000 sec.

Figures 5-37 through 5-40 are EOS empirically derived graphs that were used to size the ion-thruster system. Using these curves, the performance and weight of typical 500- and 250- $\mu$ lb thrusters used separately for stationkeeping and attitude control are as given in Table 5-14.

In designing clustered engines the following design assumptions were used:

- Twelve-thruster configuration, four clusters of three engines each. Each cluster has one 500- $\mu$ lb attitude control thruster.
- Cluster functions are south translation and roll, north roll (redundant roll), east pitch, west yaw.

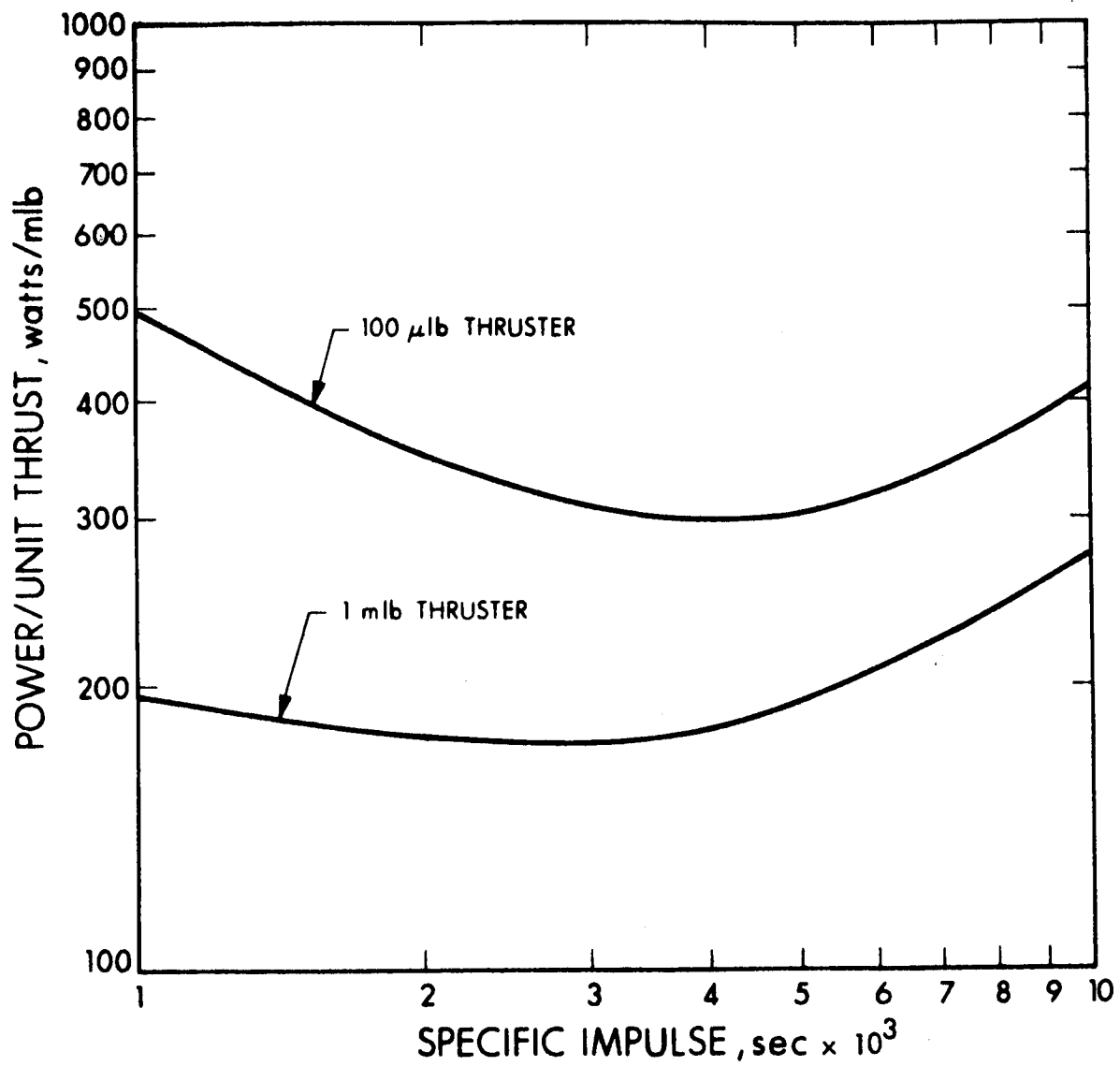


Fig. 5-36 Performance of Bombardment Ion Engines

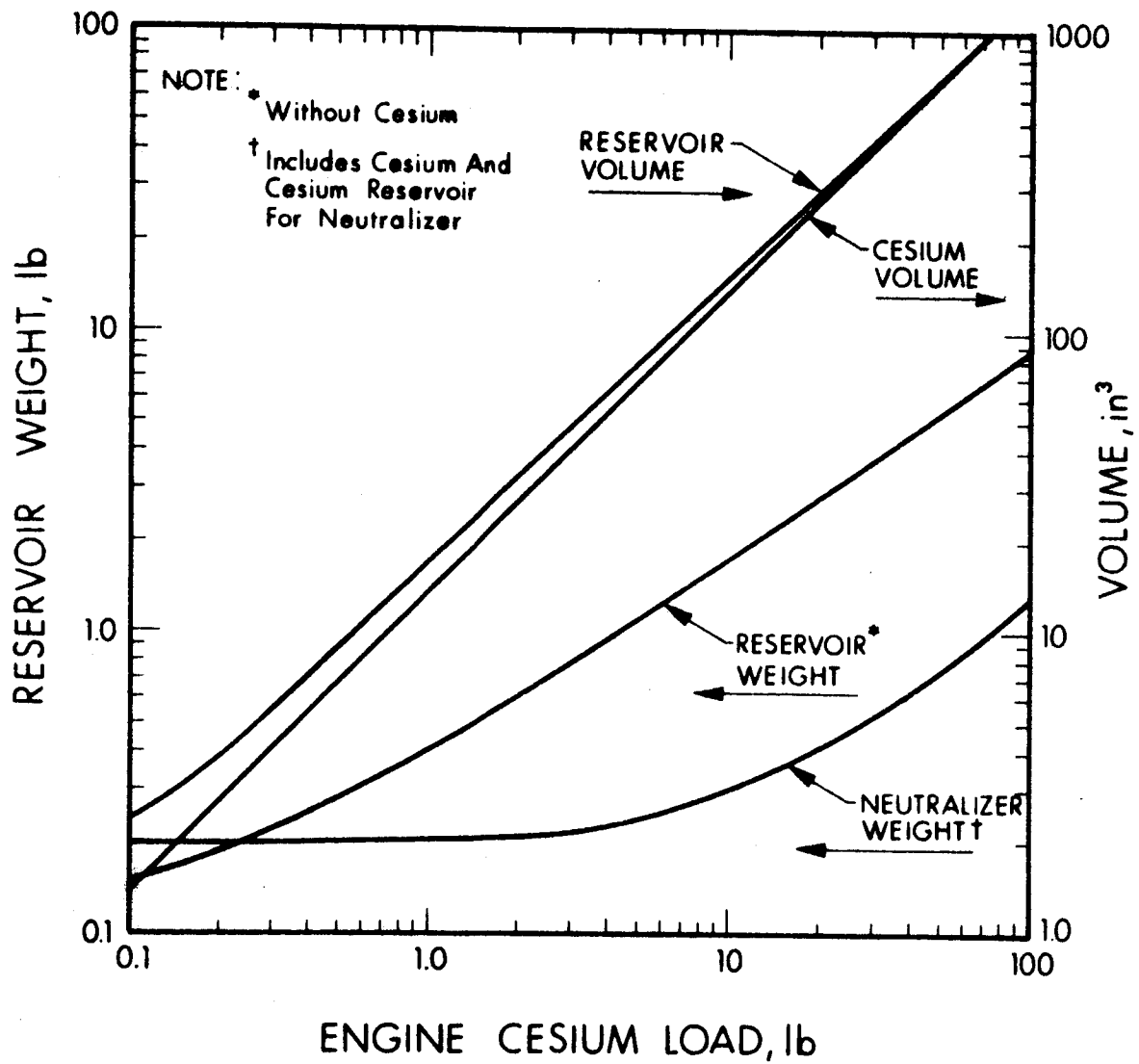


Fig. 5-37 Weight of Cesium Reservoir and Neutralizer

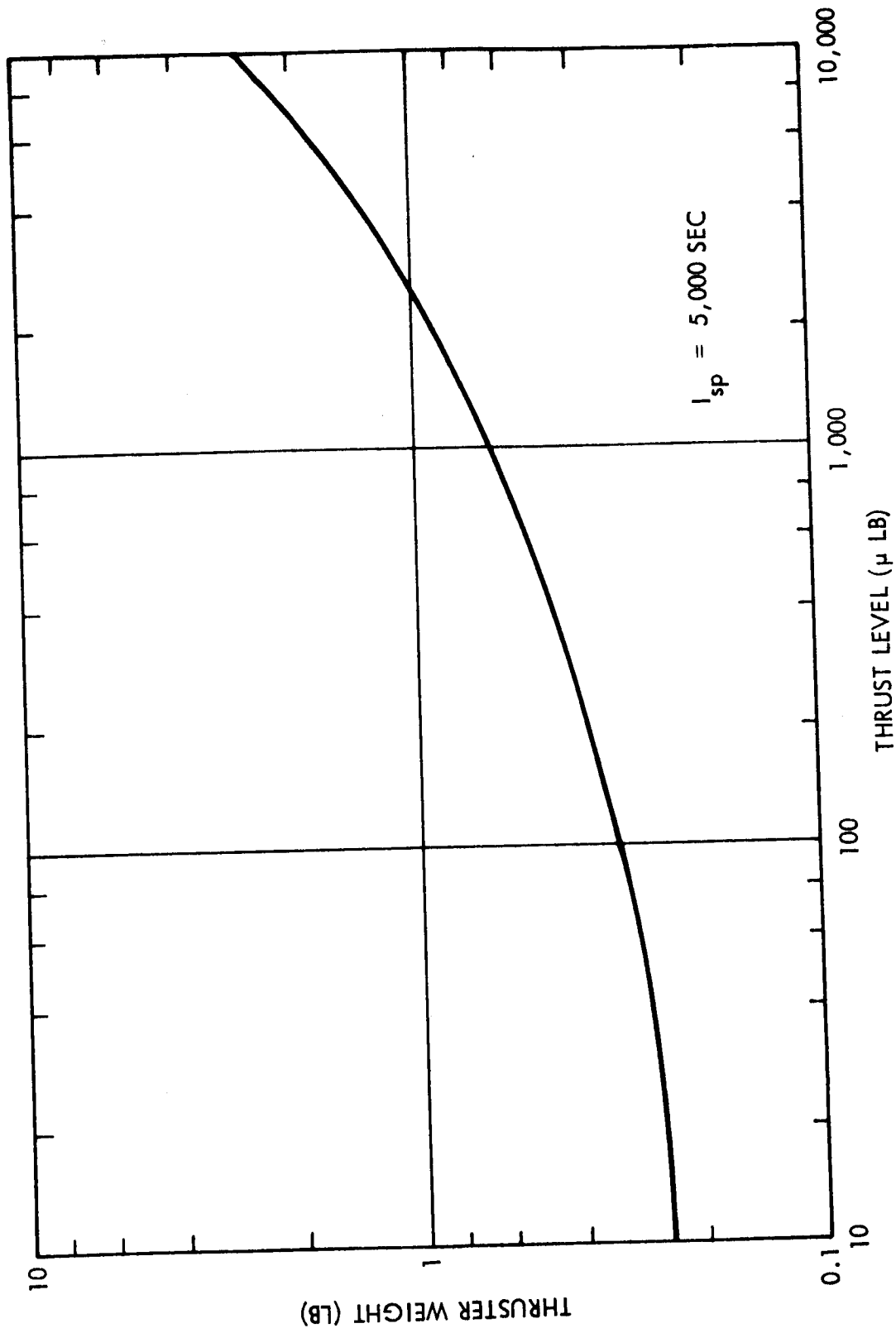


Fig. 5-38 Ion-Thruster Weight

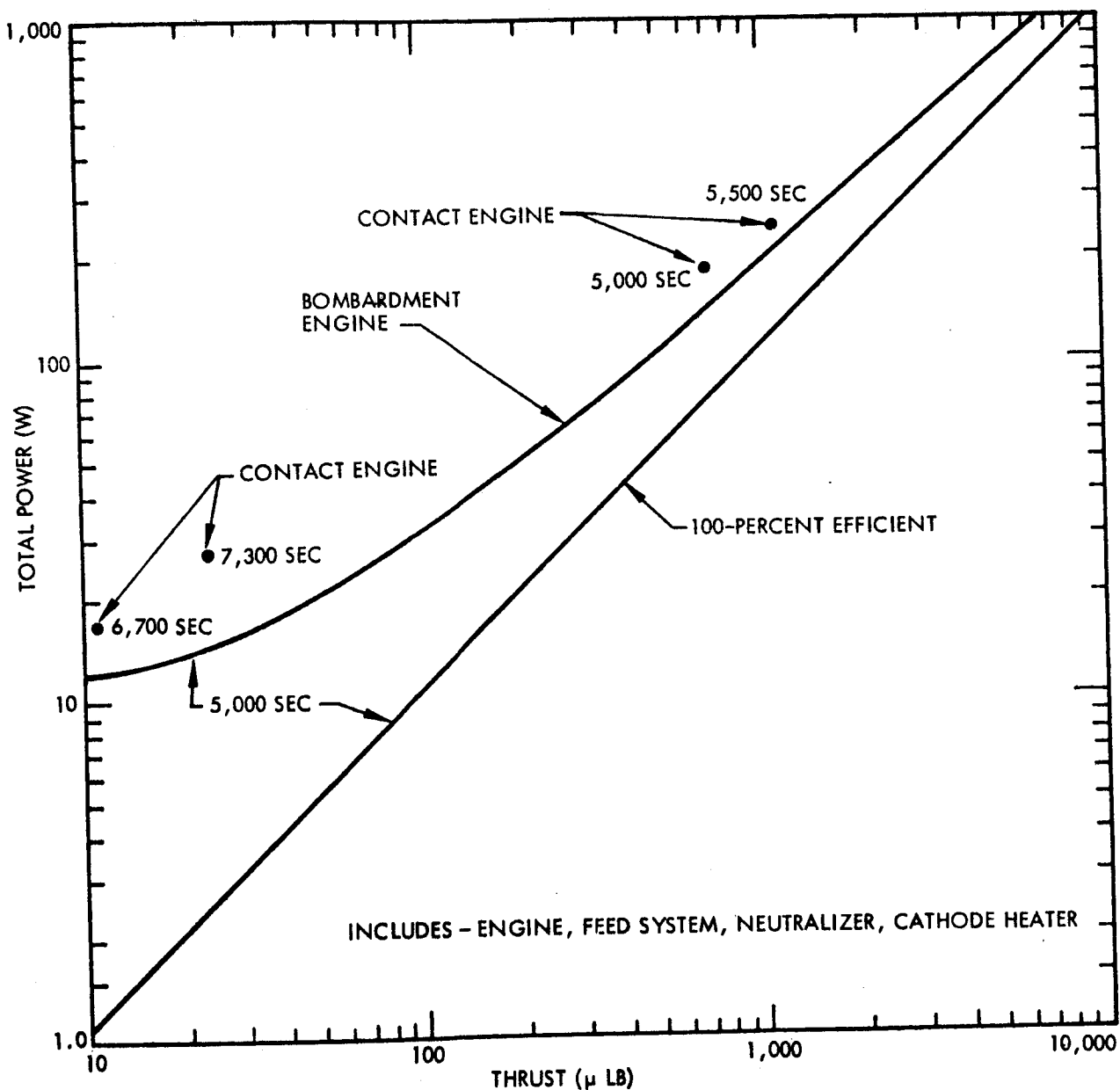


Fig. 5-39 Power Required for Ion Engine

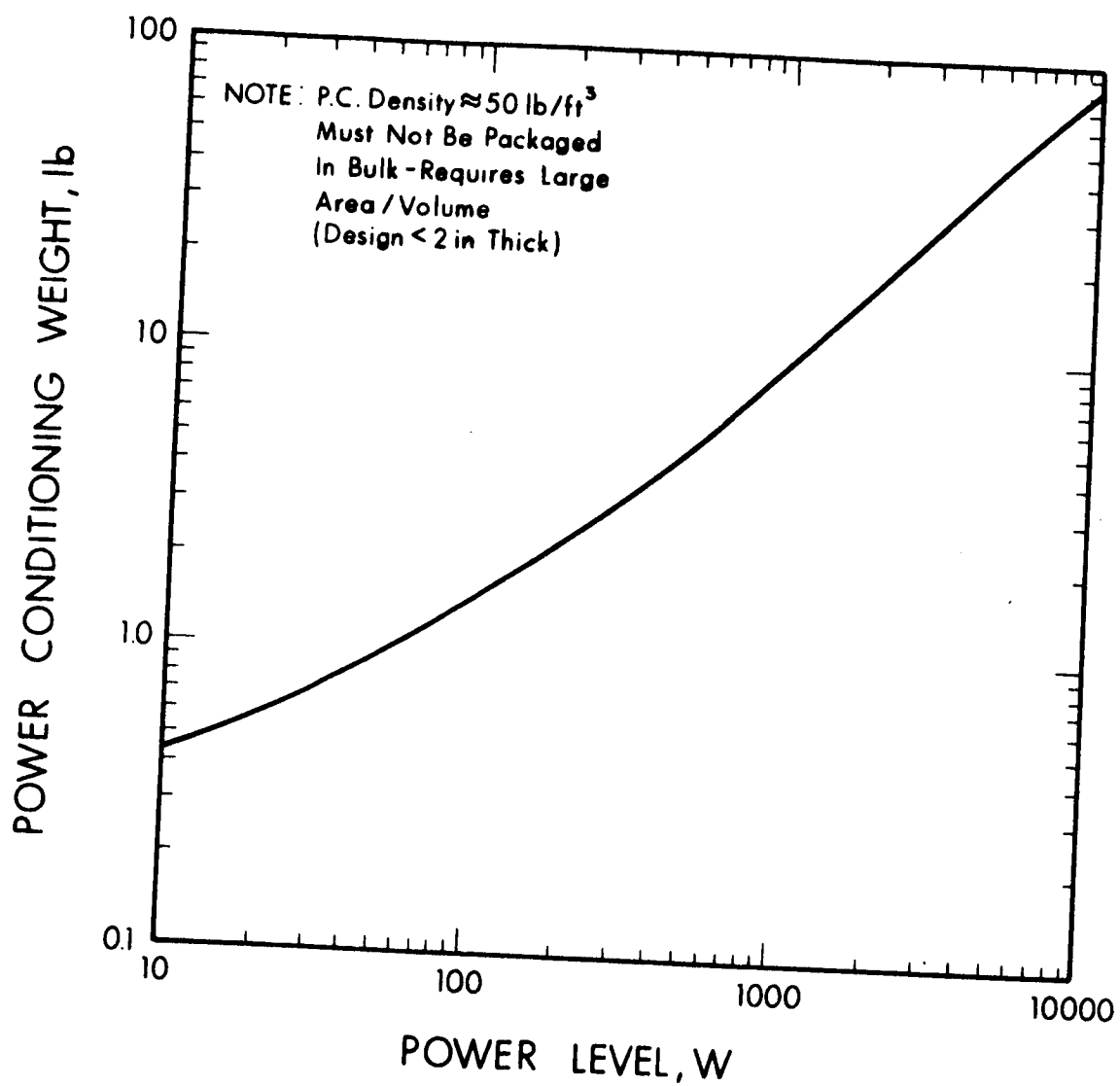


Fig. 5-40 Power Conditioner



Table 5-14

## PERFORMANCE AND WEIGHT OF SEPARATE ION THRUSTERS

Item	500- $\mu$ lb Thruster	250- $\mu$ lb Thruster
Specific Impulse, sec	5,000	5,000
Total Weight, lb	5.1	4.1
Thruster	0.5	0.4
Cesium	1.2	1.0
Reservoir and Feed	0.45	0.4
Neutralizer	0.2	0.2
Structure	1.15	1.1
PC&C	1.6	1.0
Power to Thruster, w	103	58
Power to PC&C, w	113	65

- Shared feeds for clusters.
- Each cluster shares high-voltage power conditioning and control and feed heater power, cutting PC&C weight to 0.7 of separate unshared units.
- Packaging weight factor of 1.5.
- Standby power is 5 w/thruster.
- Only one thruster per cluster can be on at one time, and only two in the spacecraft. Stationkeeping will be interrupted for attitude control impulses.
- No north-south stationkeeping during second year.
- Solar panel weight due to thrusters is 1/6 lb/w (see subsection 5.5.5).
- Battery weight is 0.1 lb/w-hr (see subsection 5.5.7).

The maximum demand would be for 1.2 hr of operation, during an eclipse.

- Each cluster carries cesium for stationkeeping (6,000 lb-sec), attitude control (3,000 lb-sec), and a contingency of 2,000 lb-sec. This total of 11,000 lb-sec requires 2.2 lb of cesium.

On this basis, the system weights and operating conditions are as given in Table 5-15.

Table 5-15  
PERFORMANCE AND WEIGHT OF ION THRUSTER SYSTEM

Item	Per Thruster	Total System
Thruster Weight, lb	9.8	39.2
Cesium	2.2	8.8
Reservoir and Feed	0.65	2.6
Neutralizer	0.6	2.4
Thrusters	1.3	5.2
Structure	2.4	9.6
PC&C	2.65	10.6
Maximum Power, w	123	266
Stationkeeping	113	226
Attitude Control	65	130
Standby	15	50
Power System Weight, lb	-	76.3
Solar Panels	-	44.4
Batteries	-	31.9
Total Weight, lb		115.5

#### 5.5.6 Resistance Jet System

General Description of Thruster. Gas expulsion systems in which thermal energy is added by  $I^2R$  heating of part of the thruster hardware are known as resistance jets or resistojets. Two classes of this thruster are available for use in spacecraft control. The first is the so-called thermal storage resistojet containing a refractory heating element with a high thermal heat capacity. Low-level power is continuously supplied to the heater element, and the propellant flow is pulsed when required. The thermal heat capacity of the thruster is sufficiently great that the heater element temperature remains essentially constant for short pulses, thereby producing constant specific

impulse. The second type, the fast heatup resistojet, contains a lightweight heater element with a low thermal heat capacity. This thruster consists of a thin-walled metallic tube with an integral contoured expansion nozzle. The propellant vapor is passed through the heated tube and expanded through the nozzle, which produces thrust. In this type of thruster, both power and propellant flow are pulsed (in contrast to the thermal storage where only propellant flow is pulsed). In contrast to the thermal storage device, the heat capacity of the fast-heatup unit is held to a minimum. The primary advantage of this type of thruster is that electric power does not have to be supplied continuously; consequently, average power is very low for typical attitude-control missions.

Thruster Status. The two laboratories actively engaged in resistance-jet micro-thruster development are General Electric, Evandale, and AVCO Space Systems Division. The thrust levels being investigated are from 1  $\mu$ lb to 0.05 lb (at AVCO) and from 10 to 50 mlb (at General Electric).

The General Electric thruster employs the thermal storage concept. The thruster operates at 15 mlb, simulating attitude-control functions, and at 50 mlb, simulating stationkeeping. Both ammonia and hydrogen as propellant have been successfully operated. Specific impulses of 560 sec at a pressure of 3 atmospheres and a temperature of 2,500°K have been measured using hydrogen as propellant; specific impulses of 260 sec at a chamber pressure of 3 atmospheres and a temperature of 2,500°K have been measured using ammonia. A continuous input power of 29 w is required to obtain this thruster performance. The above data are based on pulsed operation with an "on" time of between 0.050 and 2.0 sec, with duty cycles from 1.11 to 4.44 percent, with 45 sec between pulses. Taking the 2.0-sec pulses to be the worst possible case encountered in attitude-control operation, the temperature drop in the thruster heating element was found to be only 23° F, corresponding to a drop of specific impulse of only 1.3 sec. Thruster performance has not been reported for higher duty cycle operation. It can be postulated, however, that it would begin to drop very rapidly as duty cycle increases. Total accumulated thruster running-times are well over 100 hr.

At AVCO Space Systems Division, the primary emphasis has been at thrust levels of 10 to 600  $\mu$ lb. The thruster concept employed is that of low thermal inertia with fast heatup. Ammonia propellant has been employed with emphasis on low power requirements. At a thrust of 7.5  $\mu$ lb and a chamber pressure of 0.034 atmospheres, a specific impulse of 150 sec requires 4 w of power. For a thrust level of 310  $\mu$ lb and a chamber pressure of 0.367 atmospheres, a specific impulse of 265 sec requires 30 w of power.

Pulsing and steady-state data have been recorded, and total accumulated thruster operating times in excess of 300 hr have been reached. When employed as an attitude-control thruster operating on high duty cycles (i. e. , greater than 5 percent) or when operating as a stationkeeping thruster, the thruster performance (i. e. , specific impulse) remains constant after an initial slight decrease in the millisecond-of-time range. Power is required only when the thruster is operating.

A thruster of the AVCO type has been developed for operational use on ATS-3 (spacecrafts D and E) for the inversion maneuver, and it is currently being installed in the ATS-B spinning satellite for demonstration purposes. A schematic is shown in Fig. 5-41 in which the zero-g propellant handling scheme can be seen. The constant-pressure valve may admit liquid or gaseous ammonia into the pre-plenum chamber, and a heated splashplate provides the latent heat of evaporation, thus preventing evaporative cooling from providing a spurious low-pressure signal that would admit additional liquid before it is needed.

Design Data. Table 5-16 and Fig. 5-42 give the weights of ammonia storage and regulator systems at a specific impulse of 200 sec. This value of  $I_{sp}$  was chosen to be somewhat conservative with regard to performance and thus helps ensure long-life operation. Propellant and tankage weights are not noticeably affected by thrust level or cluster configuration. The propellant and tanks can be shared by all thrusters, and their weight depends on total required impulse only.

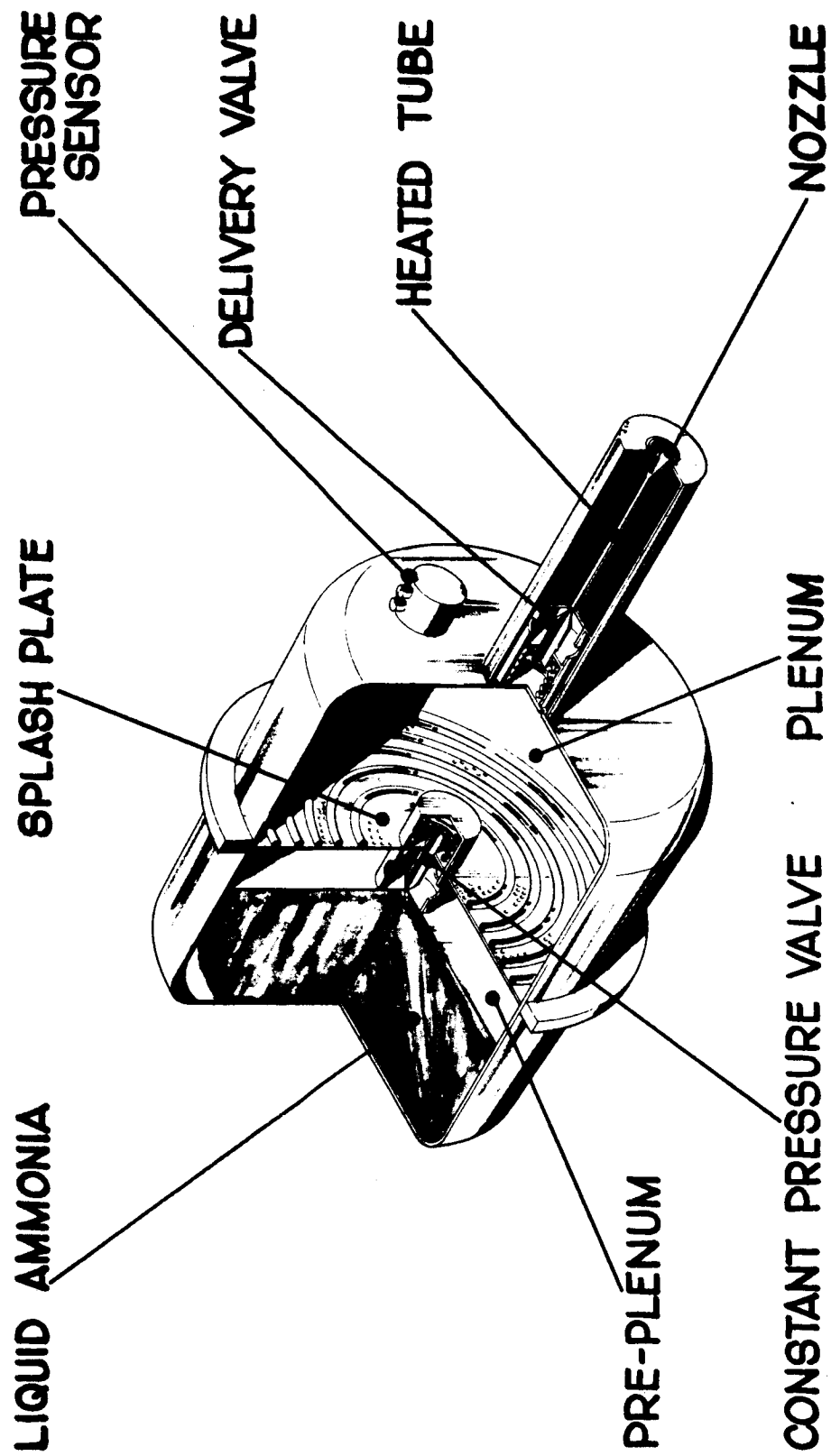


Fig. 5-41 Ammonia Resistojet

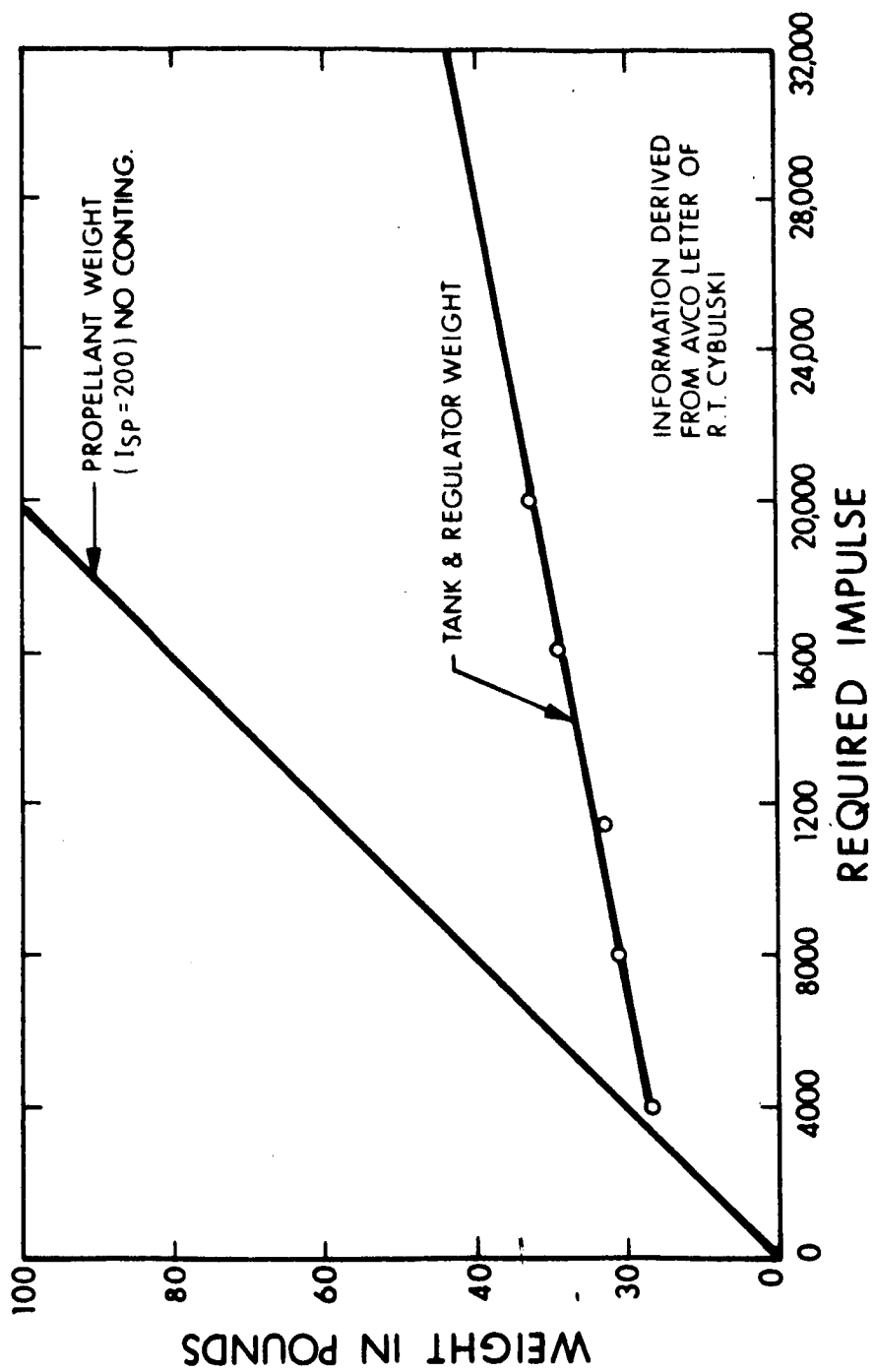


Fig. 5-42 Resistojet System Weight vs. Required Impulse

Table 5-16  
PROPELLANT STORAGE AND FEED SYSTEM WEIGHT BREAKDOWN

Item	1	2	3	4
Propellant Weight Stored, lb	20.0	40.0	57.0	80.0
Propellant Tank Inside Diam. , in.	12.7	16.0	17.7	20.1
Propellant Tank and Mounting, lb	9.9	13.8	15.9	21.4
Pressure Regulation, lb	6.4	6.4	6.4	6.4
Total System Weight, lb	36.8	60.7	79.8	108.3

The thruster units themselves can be mounted remote from the tank, with the propellant lines adding some convenient extra volume to the plenum chamber. Each thruster will use quad-redundant valves for reliability, and a typical thruster and valve assembly will weigh approximately 1 lb.

Resistojet system power depends upon nozzle efficiency and thermal efficiency. The type of resistojet considered here is able to run continuously for hours and hence does not require a thermal reservoir with all its associated radiant losses. The overall efficiency of the resistojets considered here is about 15 to 18 percent.

Figures 5-43 and 5-44 show the power required by the resistojet for various values of thrust. Each point is numerically labeled, and each number refers to a reference given on one of the figures. Both figures also show lines of constant efficiency. Several estimates regarding power for submillipound resistojets have been made, and these are shown in Fig. 5-43. From Fig. 5-43, it is seen that 15 w of power for a 500- $\mu$ lb thruster is a reasonable figure. There is no direct performance information regarding resistojet power for 2,000- $\mu$ lb thrusters, but if one extrapolates from the information given in Fig. 5-43, one finds that a 2,000- $\mu$ lb thruster should require between 45 and 55 w of power. This includes power loss in the power-conditioning (direct operation from 22 to 29 v), signal-conditioning and ammonia storage and feed systems. An additional fix is provided by the data of Fig. 5-44, which includes a

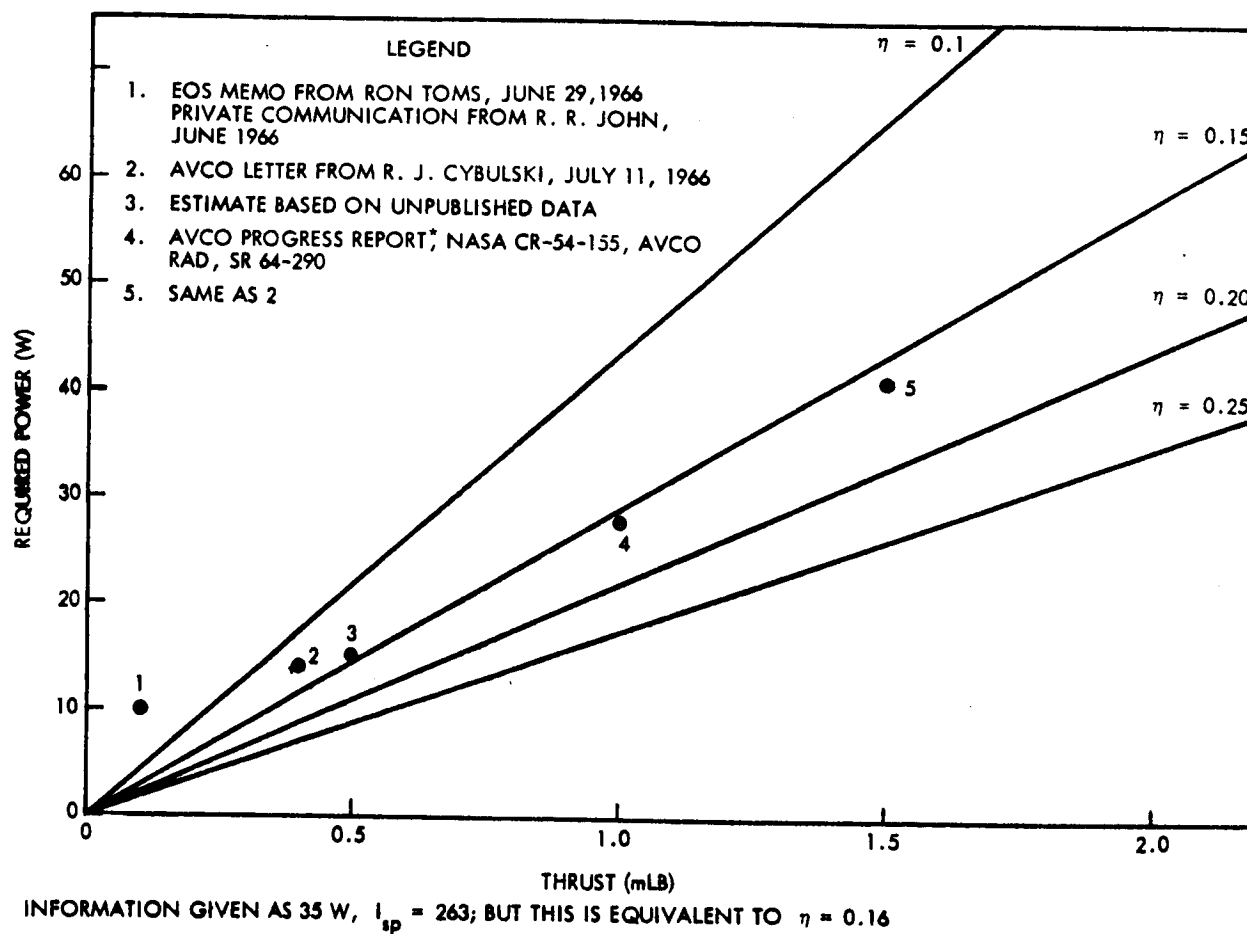


Fig. 5-43 Power vs. Thrust Level for Resistojets of  $I_{sp} = 200$  sec (First Estimates)



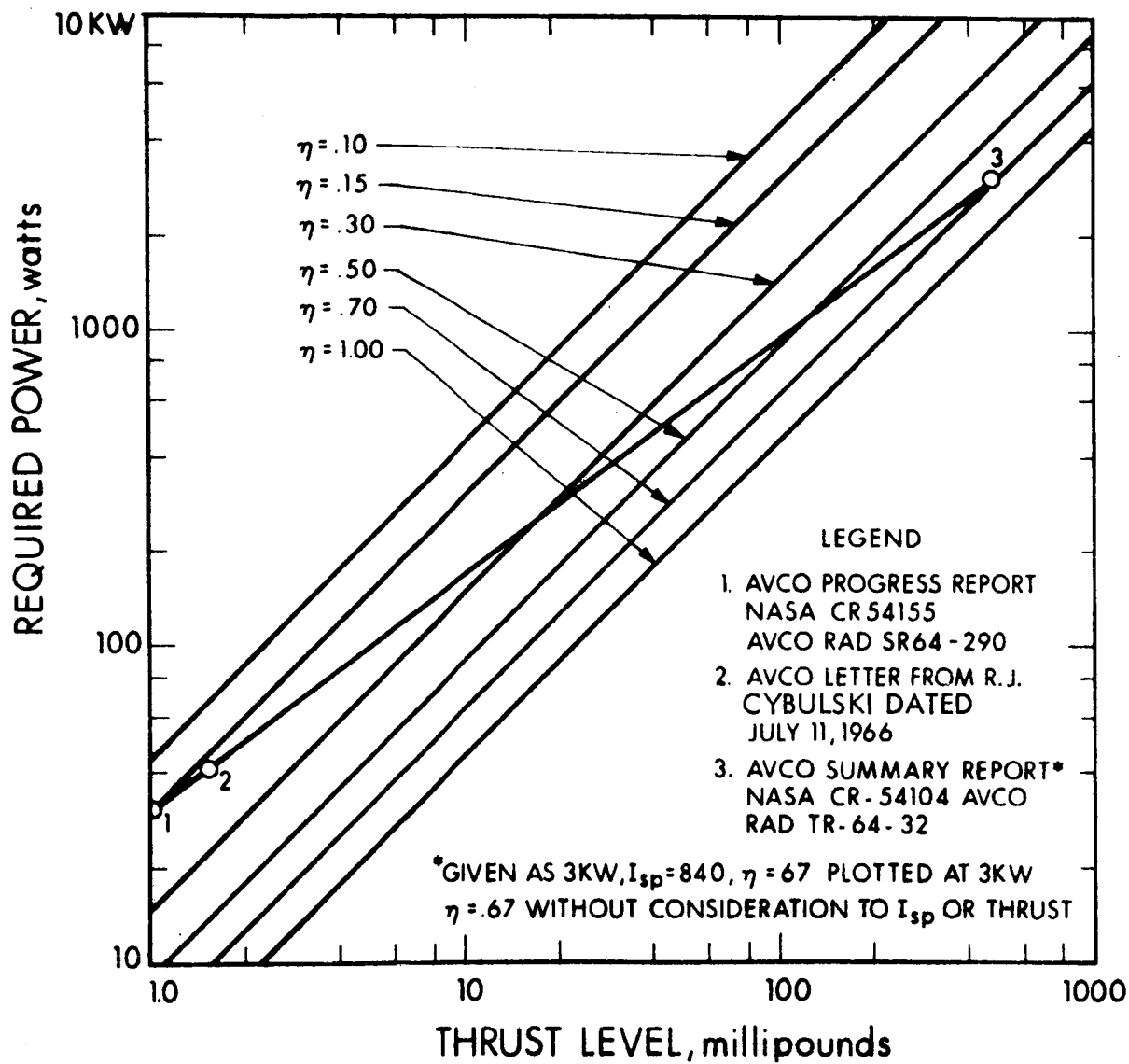


Fig. 5-44 Power vs. Thrust Level for Resistojets of  $I_{sp} = 200$  sec (Second Estimates)

3-kw resistojet with a 6 percent efficiency. A linear interpolation between the low-thrust and high-thrust information indicates that a 2,000- $\mu$ lb thruster requires about 50 w. The figure of 50 w for the 2,000- $\mu$ lb thruster is used in this report. This figure corresponds to an efficiency of 17.5 percent.

Specific Resistojet System. An arrangement of six thrusters for attitude-control only, based on the AVCO low-thermal inertia resistojet, was selected for the ATS-4 design. The pairs for roll and pitch would be mounted on the spacecraft lower equipment section and would share a common tank. The pair for yaw would be mounted on the antenna rim or on the phased-array boom.

During operation of the phased array, the resistojets will be used for attitude control. The following are additional design assumptions:

- Specific impulse is 200 sec.
- Standby power for the feed and control system is included in the 50-w peak power.
- Solar panel weight due to thrusters is 1/6 lb/w.
- Battery weight is 0.1 lb/w-hr.
- Total impulse provided is 3,500 lb-sec.

On the basis of these assumptions, resistojet system weight is as given in Table 5-17.

Table 5-17  
RESISTOJET WEIGHT AND PERFORMANCE  
(Total Impulse = 3,500 lb-sec)

Item	Weight (lb)
Propellant	17.5
Tanks and Regulators	19
Thrusters	6
Solar Array	9
Batteries	6
Total Weight	57.5

## 5.6 TRACKING, TELEMETRY, AND COMMAND

### 5.6.1 Command Summary

Command requirements for the ATS-4 are of two types: discrete on/off relay control and digital words of various lengths. The digital words correspond to various required frequency settings associated with the 30-ft parabolic antenna tests; specific phase readings that are processed by the interferometer attitude-control servo system, etc. These command types can be accommodated by the existing tone-command encoding equipment available at the ATS-4 ground stations. Digital command words are readily processed with conventional digital-command systems such as the unified S-band system but this handling is not required for the ATS-4 application since rapid commanding is not essential for synchronous satellite applications. Digital word loading can be accomplished by using three discrete commands for "reset," "one bit," and "zero bit." These commands are sent sequentially so as to fill a serial shift register or other storage device with any required bit length. This technique is being used successfully on the Gemini Agena Target Vehicle, where a 24-bit velocity-to-be-gained word is loaded for orbit-adjust control.

Command requirements associated with the 30-ft parabolic antenna include the following:

- Seven commands for power "on" for each of the seven frequency ranges
- A single power "off" for all seven receiver units, transmitter units, and associated electronics
- Three commands for loading a digital word corresponding to the desired frequency of operation (this word controls a frequency synthesizer that selects one of a number of CW frequencies spaced across each frequency band.)

A total of 22 commands is needed for control of the 30-ft parabolic antenna experiment.

The phased-array experiment requires a number of discrete commands for selecting each beam position. For the case of the 16 switchable feeds and lens arrangement, the following commands are required:

- Two commands for on/off control
- Sixteen commands for single-feed selection and one command for reset (The 16 commands must be duplicated for each of four beams, which results in a total of 65 commands including reset.)
- Two commands for mode selection (i.e., pilot tone or command select modes)

A total of 69 commands is allocated for the phased-array experiment.

The interferometer experiment requires the following command functions:

- Two commands for on/off control
- Three commands for mode select (i.e., single-station mode, two-station mode, and open-loop readout mode)
- Three commands for "one," "zero," and "reset" digital register loading (This register would contain the required stored-phase readings for attitude control. An 80-bit register would accommodate four "coarse" 10-bit words and four "fine" 10-bit words.)

Eight commands are required for interferometer control.

The various vehicle subsystems require on/off and mode-select control. The TT&C equipment is powered on by a "power tone" until a separate power-on relay is latched by either the primary or backup command receiver. The TT&C commands are the following:

- Three commands for primary command receiver "on," backup command receiver "on," and receiver power to "standby"
- Two commands for primary PCM telemeter mode select (i.e., high data rate via 4-GHz or low data rate via 136-MHz telemetry transmitters)

- Three commands for primary telemeter "on," backup telemeter "on," and telemeter "off"
- Two commands for tracking mode or command and telemetry mode select
- Seven commands for backup command and telemetry via the 30-ft dish

A total of 17 commands is required for TT&C functions.

The attitude-control subsystem utilizes a horizon-sensor system or the interferometer as an attitude reference. When the interferometer is commanded to the open-loop readout mode, this same command connects the horizon sensor to be the attitude reference.

The commands required by the attitude-control subsystem are the following:

- Three commands are required for "one," "zero," and "reset" loading of a digital register that controls bias setting applied to the horizon sensor. These bias settings are, in effect, pointing commands for the 30-ft parabolic antenna.
- Three commands are required to load a second register for pitch, roll, and yaw-rate and polarity commands. These commands provide programmed pointing control necessary for antenna pattern measurements.
- Three commands are required to load a third register for deadband control.
- Three commands are required to load a fourth register that will contain control constants for the adaptive autopilot.
- Six commands are required to select between primary and backup gyros.
- Two commands perform power "on" and "off."

A total of 26 discrete commands is needed for the attitude-control subsystem.

The power subsystem utilizes the following 17 discrete commands:

- A single command for solar-array deployment.

- Two commands provide speed control of the continuous-drive motor for each solar-array wing necessary for optimum sun angle.
- Six commands provide on/off isolation of three individual batteries in the event of a short, overheating, or other malfunction.
- Four commands provide on/off power isolation of each solar-array wing.
- Four commands are required for charge controller selection and on/off control.

The propulsion subsystem requires 23 discrete commands as follows:

- Eight commands are required for on/off control of the four (north, south, east, and west) stationkeeping ion motors.
- Two commands provide on/off control of the attitude-control ion motors.
- Two commands provide on/off control of the resistance jets.
- Two commands control the control channel commanding the resistance-jet thrusters.
- Two commands select the control channel commanding the ion engines.
- Two commands apply electrical on/off control of the ion thrusters.
- Four commands provide for on/off control of the station-acquisition hydrazine thrusters.
- A single command for kick motor "on" provides the command to circularize the orbit.

The total ATS-4 system-command requirements result in 182 commands, summarized in the following:

30-ft Parabolic	22
Phased Array	69
Interferometer	8
TT&C	17
Attitude Control	26
Power	17
Propulsion	<u>23</u>
Total	182 discrete commands

The proposed command capability is provided by redundant decoders with 216 commands each. This provides a growth capability of 34 additional commands. Any remaining spare capability can be used to provide redundant commands in the same decoder for certain mission-critical commands.

#### 5.6.2 Instrumentation Summary

The ATS-4 system can be expected to require an extensive instrumentation system, since the sole function of ATS-4 is to provide experimental data. The total telemetry bandwidth requirements and telemetry multiplexing allocations can be derived from a statement of the telemetry instrumentation schedule. A summary of the schedule is considered below. Each set of data points can be converted to an equivalent PCM bit rate and the complete list summed to give an estimate of the required telemetry bandwidth in order to size the telemetry transmitter. The total number of data points will serve to size the telemetry multiplexing. The estimated instrumentation requirements are summarized in Table 5-19.

The data in Table 5-19 result in the summary Table 5-18.

Table 5-18  
SUBSYSTEM INSTRUMENTATION SUMMARY

Subsystem	Number of Points	Equivalent (bps)
30-ft Parabolic Experiment	111	815.4
Phased-Array Experiment	90	742.8
Interferometer Experiment	62	2,291.1
TT&C	260	1,196.0
Attitude Control	204	9,857.4
Power	41	4,014.8
Propulsion	68	267.4
Structures	<u>44</u>	<u>9,613.6</u>
	880	28,798.5
20 percent Spares	<u>176</u>	<u>5,760.0</u>
Total	1,056	34,558.5

Table 5-19

## ATS-4 INSTRUMENTATION REQUIREMENTS

Data Type	Number Required	Accuracy (%)	Sample Rate (sps)	Equivalent (bps)
<b>30-ft Parabolic Antenna Experiment:</b>				
Temperature	30	1	0.01	2.4
Strain Gage	30	1	0.01	2.4
Flex. Monitor System	7	(10-bit)	0.01	0.7
Flex. Monitor System	10	1	0.01	0.8
Receiver Signal Power	3	1	10	240.0
Receiver AGC	3	1	10	240.0
Transmitter Output Power	4	1	10	320.0
RF Diagnostic	14	5	0.1	5.6
Miscellaneous Diagnostic	<u>10</u>	5	0.1	<u>4.0</u>
	111			815.4
<b>Phased Array:</b>				
Temperature	4	1	0.1	0.4
Receiver Signal Power	2	1	10	160.0
Receiver AGC	2	1	10	160.0
Transmitter Output Power	2	1	10	160.0
Miscellaneous Diagnostic	16	5	0.1	6.4
Switch Current	<u>64</u>	5	1.0	<u>256.0</u>
	90			742.8
<b>Interferometer:</b>				
Coarse Phase	4	(10-bit)	10	400.0
Fine Phase	4	(10-bit)	10	400.0
Reference Phase	1	(10-bit)	10	100.0
Analog Phase (b/u)	9	1	10	720.0
Receiver Signal Power	8	1	10	640.0
RF Diagnostic	12	5	0.1	4.8
Mechanical Diagnostic	8	1	0.01	0.7
Miscellaneous Diagnostic	<u>16</u>	1	0.01	<u>25.6</u>
	62			2,291.1
<b>TT&amp;C:</b>				
Command Status	216	(1-bit)	1	216.0
Message Acceptance	2	5	1	8.0
Miscellaneous Diagnostic	30	5	0.1	12.0
Calibrates and Sync	<u>12</u>	1	10	<u>960.0</u>
	260			1,196.0



Table 5-19 (Cont.)

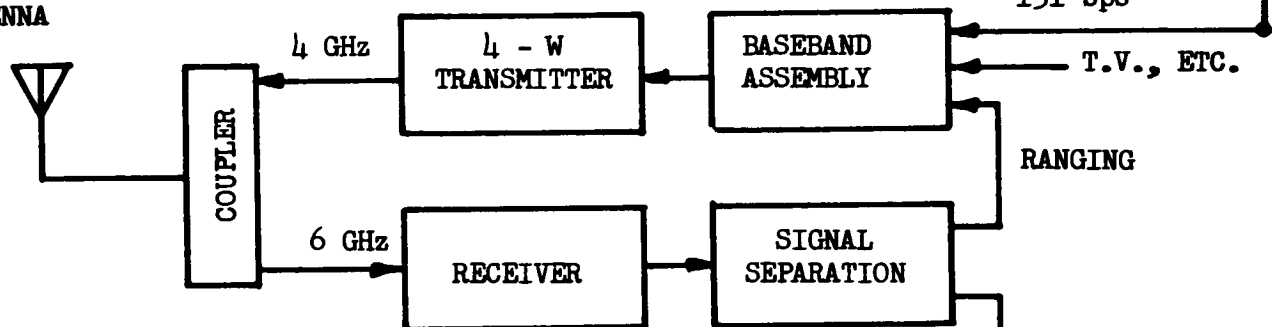
Data Type	Number Required	Accuracy (%)	Sample Rate (sps)	Equivalent (bps)
<b>Attitude Control:</b>				
Horizon Sensor	8	1	1	64.0
Pressure	10	5	0.1	4.0
Pulse Valve	16	5	50	3,200.0
Temperature	16	5	0.1	6.4
Attitude Integration	18	1	10	1,440.0
Error Signal	18	1	10	1,440.0
Gyro Signal	44	1	10	3,520.0
Logic State Monitor	30	(1-bit)	0.1	3.0
Command Storage Registers	4	(40-bit)	1	160.0
Equipment Voltages	10	1	0.1	8.0
Miscellaneous Diagnostic	<u>30</u>	5	0.1	<u>12.0</u>
	204			9,857.4
<b>Power:</b>				
Unregulated Voltage & Current	4	5	250	4,000.0
Battery & S/A Temperature	16	5	0.1	6.4
Charge Controller	6	5	0.1	2.4
Miscellaneous Diagnostic	<u>15</u>	5	0.1	<u>6.0</u>
	41			4,014.8
<b>Propulsion:</b>				
Ion-Motor Voltage	16	5	0.1	6.4
Kick-Motor Instrumentation	6	5	10	240.0
Valve & Thruster Status	20	5	0.1	10.0
Pressure	6	5	0.1	3.0
Temperature	10	5	0.1	4.0
Miscellaneous Diagnostic	<u>10</u>	5	0.1	<u>4.0</u>
	68			267.4
<b>Structures:</b>				
S/A Strain	8	1	50	3,200.0
Structure Temperature	14	5	0.1	5.6
Squib Vibration	2	5	800	6,400.0
Miscellaneous Diagnostic	<u>20</u>	5	0.1	<u>8.0</u>
	44			9,613.6

### 5.6.3 System Diagram

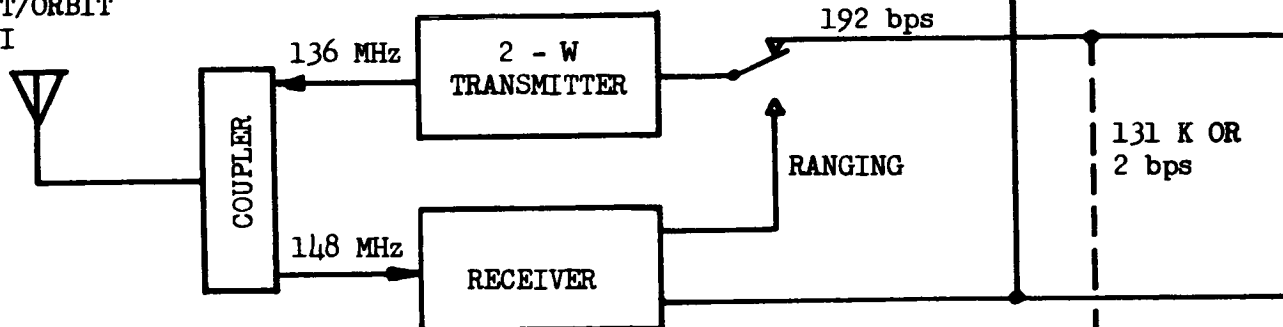
The vehicle TT&C system configuration is shown in Fig. 5-45. The TT&C ground/vehicle interface consists of two transponders. The primary unit consists of a 4-w transmitter operating at 4 GHz and a 6-GHz receiver, together with their associated baseband assembly and signal-separation circuitry. This unit is basically identical with earlier ATS equipment and therefore would be compatible with ground-station equipment, eliminating the need for new vehicle-equipment development. The unit would accommodate the turnaround PRN ranging signal, high-data-rate primary PCM telemetry data, TV, or other additional data having a composite bandwidth of 1 MHz. The 4-GHz down link may be used to relay data received from the 30-ft parabolic antenna receivers to demonstrate possible satellite applications. The second or backup transponder is also compatible with the proposed ATS ground stations. This equipment consists of existing VHF flight-proven hardware. The command receiver is a 148-MHz AVCO unit that accepts the tone-digital-command tones provided by the ground-command console. A 2-w telemetry transmitter operating at 136 MHz permits transfer of low-rate telemetry data. Low-rate data at 192 bps can be processed by existing ground-station telemetry-data-handling equipment. The VHF telemetry system operates during ascent and injection phases via an omni antenna and provides data transfer of a minimal PCM data train containing ascent performance and failure-diagnostic data. These data validate initial vehicle operational sequences and also permit a backup telemetry output in the event of malfunction in the primary PCM system. The minimal PCM telemeter is not required to service the high-data rate and the many data channels required by the ATS-4 experiments. Therefore, the minimal PCM telemeter can be satisfied by a flight-qualified unit used on previous ATS launches.

The primary PCM telemeter provides for all ATS experimental data, as well as complete failure-diagnostic data. The summarized telemetry schedule given in subsection 5.6.2 indicated approximately 1,056 data channels, with a composite bit rate of more than 34 kilobits per second (kbps) as a minimum requirement.

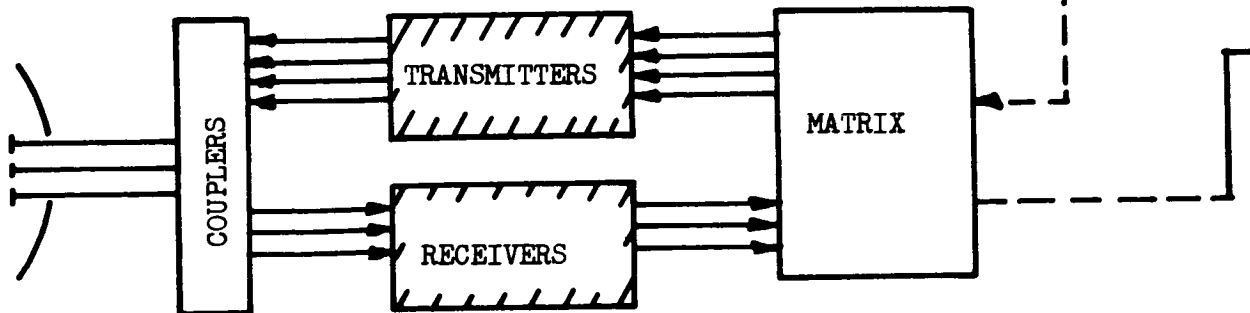
TT&C ORBIT ANTENNA



ASCENT/ORBIT OMNI



30 FOOT PARABOLIC



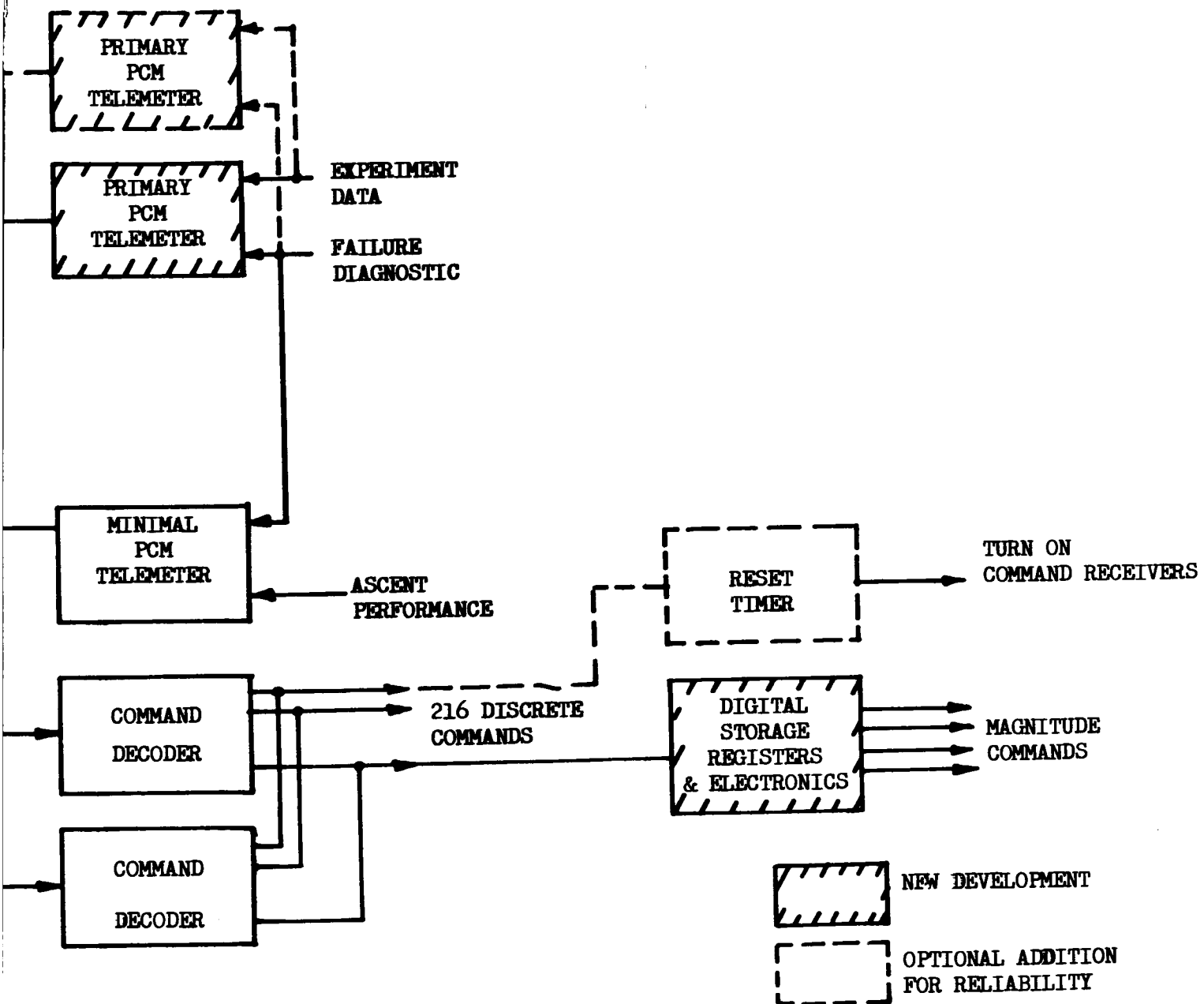


Fig. 5-45 Block Diagram of ATS-4 TT&C Subsystem

The actual number of channels and bit rate will be higher because of constraints imposed by powers-of-two requirements of timing. Also, since the bit rate is not excessive, it may be raised by providing all telemetry with 1-percent accuracy. Figure 5-46 shows the design of the primary telemeter multiplexer. The telemeter exceeds the channel requirements shown in Table 5-20, which were obtained from the telemetry instrumentation schedule of subsection 5.6.2.

Table 5-20

PRIMARY PCM TELEMETER REQUIREMENTS

Data Type	Number	Accuracy (Percent)	Required Sample Rate (sps)
Analog	98	1	0.01
Analog	10	1	0.1
Analog	8	1	1.0
Analog	125	1	10.0
Analog	8	1	50.0
Analog	275	5	0.1
Analog	66	5	1.0
Analog	6	5	10.0
Analog	16	5	50.0
Analog	4	5	250.0
Analog	2	5	800.0
Digital	30	1-bit	0.1
Digital	216	1-bit	1.0
Digital	7	10-bit	0.01
Digital	9	10-bit	10.0
Digital	<u>4</u>	40-bit	1.0
	880		

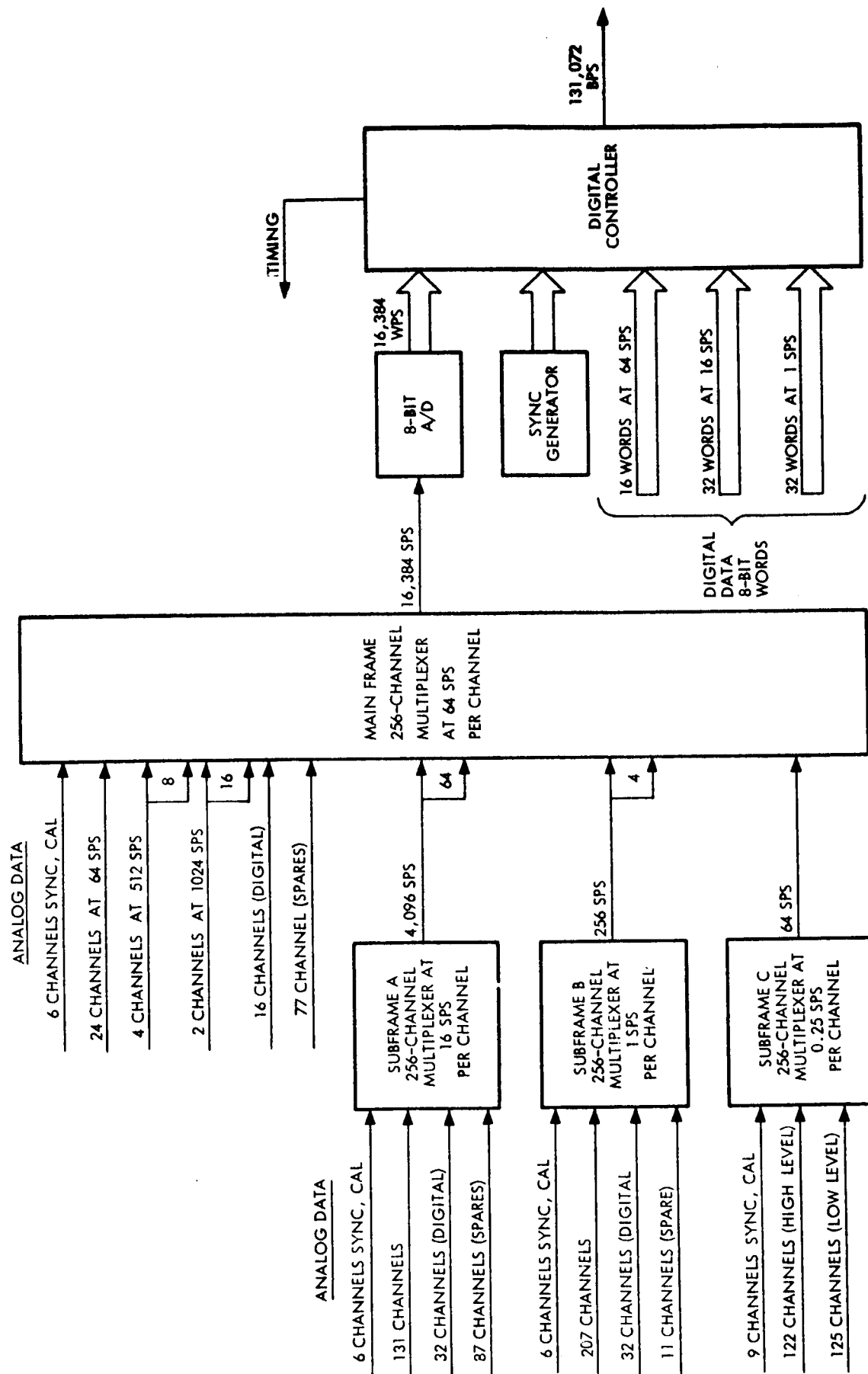


Fig. 5-46 Primary PCM Multiplexer Block Diagram

Table 5-21 shows the actual channel capabilities of the primary PCM telemeter.

Table 5-21

PRIMARY PCM TELEMETER CAPABILITIES

Data Type	Number	Accuracy (percent)	Available Sample rate (sps)
Analog	250	1	0.25
Analog	207	1	1.0
Analog	131	1	16.0
Analog	24	1	64.0
Analog	4	1	512.0
Analog	2	1	1,024.0
Analog (Spare)	11	1	1.0
Analog (Spare)	87	1	16.0
Analog (Spare)	77	1	64.0
Digital	32	8-bit	1.0
Digital	32	8-bit	16.0
Digital	16	8-bit	64.0

The sample rates shown in Table 5-21 are available with the normal PCM clock rate of 131,072 bps. The telemeter can operate at the 192-bps clock rate compatible with the VHF transponder. In the event of failure of the 4-GHz transmitter, the low-rate mode would provide static diagnostic data. The data sample rates are reduced by the ratio of clock rates so that the data frequency response is quite low. Main-frame data channels would be reported every 10 sec; subframe reporting would result in 0.7, 10, or 46 min between data samples. Operation in this failure mode would not be required where telemetry transmission is performed via the 30-ft parabolic antenna.

The telemetry multiplexing is standard IRIG format compatible with all IRIG PCM ground stations. Figure 5-46 shows that the primary PCM telemetry is composed of four 256-channel analog multiplexers. The main multiplexer operates at 64 samples per second (sps) per channel, which results in an output of 16,384 sps. These analog samples are digitized to 8 bits for 1-percent resolution. The analog-to-digital (A/D) converter outputs 8-bit parallel words at 16,384 words per second (wps). A digital controller accepts this digitized analog-data train and interleaves direct digital data and sync words at the appropriate times into channels reserved in the main and subframes. Finally, the controller converts the parallel 8-bit words at 16,384 wps into a serial wavetrain at 131,072 bps.

The main-frame multiplexer shows reserved channels for sync, calibrates, and digital data. High-rate data are achieved by supercommutating in groups of 8 and 16 channels. This supercommutation can be performed via external hardware for complete flexibility. However, a cost advantage is achieved if the telemetry is designed with a single gate that opens at each required supercommutation time. The primary disadvantage of the single-gate approach is that a final inflexible telemetry instrumentation schedule is required before the telemetry design can commence. Subframe A operates at 16 sps per channel and requires 64-channel supercommutation into the main frame. Subframe B requires four main-frame channels, and subframe C is directly multiplexed on a single channel. Table 5-22 shows the allocation by subsystem for various frequency-response capabilities.

The TT&C configuration is shown with a single primary PCM telemetry. A detailed reliability analysis is required before the proper redundancy can be applied. One approach (Fig. 5-45) is a completely separate parallel telemetry in standby redundancy. A second approach that has been utilized on the Telstar telemetry is redundant digitizers.

Command decoding is provided by the high alphabet (multitone) command decoder developed for the ISIS Program. This unit has been developed and qualified by AVCO Corporation and will be flight proved prior to the ATS-4 launchings. The unit uses



Table 5-22

## INSTRUMENTATION ALLOCATION

Subsystem	Analog (points)							Digital (bits)			
	1024 sps	512 sps	64 sps	16 sps	1 sps	0.25 sps	Total	64 sps	16 sps	1 sps	Total
30-ft Parabolic	—	—	—	10	—	94	104	—	30	40	70
Phased Array	—	—	—	6	30	54	90	—	—	—	—
Interferometer	—	—	—	17	37	—	54	90	—	—	90
TT&C	—	—	—	12	2	30	44	—	—	216	216
Orientation Control	—	—	16	80	68	6	170	—	190	—	190
Power	—	4	—	—	10	27	41	—	—	—	—
Propulsion	—	—	—	6	60	2	68	—	—	—	—
Structures	2	—	8	—	—	34	44	—	—	—	—
Total Required	2	4	24	131	207	247	615	90	220	256	566
Spares	0	0	77	87	11	0	175	38	36	0	74
Total Capability	2	4	101	218	218	247	790	128	256	256	640
Sync and Calibrate	—	—	6	6	6	9	—	—	—	—	—
Digital Reserved	—	—	16	32	32	—	—	—	—	—	—
Subframe A	—	—	64	—	—	—	—	—	—	—	—
Subframe B	—	—	4	—	—	—	—	—	—	—	—
Subframe C	—	—	1	—	—	—	—	—	—	—	—
Supercommutation	—	—	<u>64</u>	<u>—</u>	<u>—</u>	<u>—</u>	—	—	—	—	—
Total Channels			256	256	256	256					

a single-tone address followed by three sequential tones for command execution. A different address tone is used to select each decoder. The three sequential tones can be selected from six tones resulting in a total of 216 commands (i. e. ,  $6 \times 6 \times 6$ ). The command output is relay driver pulses at a maximum command rate of one command every 3.5 sec. Command validation is telemetered each second so that a practical command rate is 13 commands per minute. Magnitude commands require loading of serial digital registers where the command loading time is a function of register length. The digital storage registers and associated electronics shown in Fig. 5-45 are packaged with other digital electronics in the primary PCM telemeter unit.

A reset timer may be required for an additional command function. This device, used on some Agena flights, is a failure recovery device that switches the vehicle into a lost-bird mode. In this case all command receivers and the minimal PCM telemeter are turned on. This permits operational recovery when a single operating command receiver fails. The reset timer is reset by every valid command and prevents time accumulator overflow. In the absence of command reception, the timer is not reset; this causes timer overflow and causes the receiver to turn on. The results of a detailed reliability analysis may dictate inclusion of a reset timer. If system operation is controlled via a continuously powered 6-GHz receiver, standby backup is available from the VHF receiver, which includes a wakeup capability.

The normal VHF operation would be via an omnidirectional antenna that allows monitoring and commanding of the deployable devices. After the vehicle reaches the parking position and stability allows operation via the 4- to 6-GHz link, the primary telemeter is turned on and the VHF telemetry and command links are placed in standby.

#### 5.6.4 Link Calculation

The results of link gain calculations for the 4-GHz down link are shown in Table 5-23. These data are based on a 4-w transmitter radiating via a 42-deg beamwidth horn and being received via a 40-ft diameter antenna with a maser amplifier. The receiver

Table 5-23  
4-GHz DOWN LINK

Item	Gain	Loss
Vehicle		
Transmitter Power (4 w)	6 dbw	—
Line Loss (16 ft)	—	1.9 db
Antenna Gain (34-deg horn)	10	—
Pointing Loss	—	1.4
Propagation Path		
Free Space	—	196
Polarization	—	3
Ground		
Antenna Gain (40-ft diam.)	51	—
Tracking Loss	—	<u>1</u>
	+67 dbw	-203.3 db
Received Signal Power	-136.3 dbw	—
Receiving System		
Boltzmans Constant	-228.6 dbw/Hz/°K	—
$T_s = T_A + T_R = 30 + 55 = 85^\circ\text{K}$	19.3 db °K	—
Bandwidth (1 MHz)	60.0 db Hz	—
Noise Power	-149.3 dbw	—
C/N	13 db	—
Threshold	9 db	—
Margin	4 db	

bandwidth of 1 MHz is based on transmission of 131-kbps NRZ PCM data and a FM deviation ratio, D, of 1:6. The modulating frequency,  $f_m$ , is taken as the third harmonic of a 131-kbps NRZ square wave or 196 kHz. The resulting bandwidth is given by:

$$\begin{aligned} B_{IF} &= 2 f_m (D + 1) \\ &= 2 (196 \text{ kHz}) (1.6 + 1) \\ &= 1 \text{ MHz} \end{aligned}$$

The required FM improvement threshold is given by:

$$\begin{aligned} \text{improvement threshold} &= 5 + 5 \log 1/2 B_{IF} / \text{message BW} \\ &= 5 + 5 \log 1/2 10^6 / 196k \\ &= 9 \text{ db} \end{aligned}$$

A C/N of 13 db exceeds the required threshold, and the resulting FM improvement is calculated as follows:

$$\begin{aligned} I &= 3/2 D^2 \frac{B_{IF}}{f_m} \\ &= 3/2 (1.6)^2 \frac{10^6}{196k} \\ &= 19.6 = 12.9 \text{ db} \end{aligned}$$

Thus, the output S/N is obtained as follows:

$$\begin{aligned} S/N_{\text{out}} &= C/N + I \\ &= 13.0 + 12.9 = 25.9 \text{ db} \end{aligned}$$

To minimize errors, the C/N should be well above threshold. The IRIG recommended value for error probability of 1 in  $10^5$  bits is 13 db for a PCM/FM system. A 13-db C/N satisfies this requirement.

The results of 6-GHz up-link calculations are shown in Table 5-24. These data show an 18.8-db margin for a 1-MHz bandwidth when the ground transmitter is radiating 10 kw. This would permit a reduction in the available ground radiated power to 1 kw. However, since this ground power is available, it serves the additional capability of command entry via the directional vehicle horn antenna in the event of some temporary loss in vehicle stability. The 1-MHz bandwidth would accommodate the PRN range code placed on the baseband together with the command signal on a VCO located in frequency above the PRN range code.

The backup telemetry link, which provides ascent performance monitoring and on-orbit failure diagnostic monitoring, operates in the VHF region. The results of link-gain calculations in Table 5-25 are based on a vehicle omnidirectional antenna gain of -3 db. This gain can be achieved over a 90-percent spherical coverage and would permit failure telemetry reception from a tumbling bird. The actual gain experienced during an active stabilized ascent and in orbit would be about +6 db, which would provide a +9-db margin under normal operating conditions. VHF is not an optimum space-ground transmission frequency, so signal fades will be experienced. At VHF, a 3-db fade margin is frequently used as a compromise for acceptable performance. This would reduce the normal mode C/N to 19.1 db and the tumbling mode C/N to 10.1 db, which would result in no change in normal performance but would result in increased bit error probability for the tumbling mode. The increase would involve a worst case of  $10^{-4}$  bit error rate. The data bandwidth of 2 kHz is based on a bit rate of 192 bps and deviation ratio of 2.4. The bandwidth is calculated as follows:

$$B_{IF} = 2 f_m (D + 1) = 2 \text{ kHz}$$

where  $f_m = 1.5 \times \text{bit rate} = 288 \text{ Hz}$  and  $D = 2.4$ .

FM improvement is calculated as follows:

$$I = 3/2 D^2 \frac{B_{IF}}{f_m} = 59.8 = 17.7 \text{ db}$$

Therefore, the output signal-to-noise is  $13 + 17.7$  or  $30.7 \text{ db}$ .

The VHF up link for backup command operation is considered in the link gain calculations of Table 5-26. These data show a comfortable margin of 25 db, which should satisfy worst-case tumbling conditions including all probable signal fades.

Table 5-24  
6-GHz UP LINK

Item	Gain	Loss
Ground		
Transmitter Power (10 kw)	40 dbw	—
Line Loss		2 db
Antenna Gain (40-ft diam.)	54.5	—
Propagation Path		
Free Space	—	200.5
Polarization	—	3
Vehicle		
Antenna Gain	13.5	—
Routing Loss	—	3
Line Loss (16 ft)	—	<u>2.4</u>
	+108.0 dbw	-210.9 db
Received Signal Power	-102.9 dbw	—
Noise Power (B = 1 MHz, NF = 10 db)	-133.7 dbw	—
C/N	30.8 db	—
Threshold	<u>12 db</u>	—
Margin	18.8 db	—

Table 5-25

## 136.47-MHz DOWN LINK

Item	Gain	Loss
Vehicle		
Transmitter Power (2 w)	3 dbw	—
Line Loss (16 ft)	—	0.7 db
Antenna Gain (90 percent omni-directional)	—	3.0
Propagation Path		
Free Space	—	167.3
Polarization	—	3
Ground		
Antenna Gain	20	—
Line Loss	—	1
Tracking Loss	—	1
	23.0 dbw	-176 db
Received Signal Power	-153 dbw	—
Noise Power (B = 2 kHz, NF = 4.5 db)	-166.1 dbw	—
C/N	13.1 db	—

Table 5-26

## 148.26-MHz UP LINK

Item	Gain	Loss
Ground		
Transmitter Power (2.5 kw)	34 dbw	—
Line Loss	—	1 db
Antenna Gain	14	—
Tracking Loss	—	1
Propagation Path		
Free Space	—	168
Polarization	—	3
Vehicle		
Antenna Gain	—	3
Line Loss	—	0.7
	<hr/> +48 dbw	<hr/> -176.7 db
Received Signal Power	-128.7 dbw	—
Noise Power (B = 10 kHz, NF = 10 db)	-153.7 dbw	—
C/N	25 db	—



#### 5.6.5 TT&C Antennas

The primary TT&C orbit antenna is a 4- to 6-GHz horn antenna. The minimum beamwidth must provide complete earth coverage during stable on-orbit operation. At synchronous altitude, the earth subtends an angle of 17 deg. For the worst case, when the vehicle is pointed at one earth horizon and is communicating at the opposite, the minimum beamwidth must be twice 17 deg or a total of 34 deg. A 34-deg beamwidth corresponds to a 13.5-db peak antenna gain. The effective gain would be down 3 db for the worst case considered above. At the lower up-link frequency of 4 GHz, this same aperture results in a gain of 10 db and beamwidth of 51 deg. This wide beamwidth results in a pointing loss of only 1 db for off-axis pointing of 17 deg. The antenna is located on the forward equipment section and collimated with the 30-ft parabolic antenna.

The VHF omnidirectional antenna is a quarter-wave whip (25 in.) located on the sensor section and oriented parallel to the pitch axis. This configuration results in an optimum gain pattern for ascent and orbit operations since the antenna null is directed along this axis.

#### 5.6.6 Weight and Power Summary

The TT&C size, weight, and power are summarized in Table 5-27. Total TT&C equipment weight is 50.5 lb.

Table 5-27

## TT&amp;C SIZE, WEIGHT, AND POWER

Equipment	Number Required	Size L by W by H (in.)	Weight (lb)	Power (w)
Transponder, 4 to 6 GHz Receiver	1			3
Transmitter, 4 w	1	4 x 3 x 1.5	3	25
Baseband Assembly	1	4 x 3 x 3	6	1
Signal Separation	1	4 x 3 x 0.25	0.4	1
Coupler	1	4 x 3 x 0.25	0.3	1
	1	-----	0.5	—
Orbit Antenna, 4 to 6 GHz	1	-----	0.8	—
Transponder, VHF Receiver (AVCO 184003)	1	-----	---	—
Transmitter, 2 w	1	3.5 x 5 x 1	1.0	0.084 S/B, 0.170
Coupler	1	3 x 5 x 2.5	2.3	22
	1	-----	0.5	—
Ascent/Orbit Antenna, VHF	1	-----	0.5	—
PCM Telemeter, Primary(a)	1	-----	---	—
Main Multiplexer	1	3 x 5 x 4	3.5	14
Submultiplexer A	1	3 x 5 x 2.8	2.5	9.5
Submultiplexer B	1	3 x 5 x 2.8	2.5	9.5
Submultiplexer C	1	3 x 5 x 2.8	2.5	10
Power Supply & Calibrates	1	3 x 5 x 4	6	19
PCM Telemeter, Minimal	1	3 x 5 x 8	9	25
Command Decoder	2	6 x 6 x 2.5	2(4.75)	0.001 S/B, 1.5
Total			50.5	

(a) Includes digital storage registers for magnitude commands.

## 5.7 EXPERIMENT INTEGRATION

### 5.7.1 Integration Approach

By its nature, the ATS-4 orbit-vehicle system represents a study in systems and components integration. Each of the major experiments has its individual effect on the ultimate configuration. The parabolic antenna has by far the most profound effect; its design involves consideration of the structure, the shroud, dynamics, the feed, etc. Likewise, the requirement for precise attitude control, significant in itself, has influence on the entire spacecraft configuration as well as on the several subsystems. LMSC's approach to this systems integration problem, with particular emphasis on the experiments, is outlined in the following subsections. This section of the report is concerned with the problems of integrating the experiments. Section 8 defines the methodology and procedures that LMSC has developed to solve these problems.

As systems contractor for various Air Force space programs, and as associate contractor with NASA for a wide variety of booster vehicle programs, LMSC had identified and categorized the tasks of system and subsystem integration. During this period, beginning in 1954 for the Air Force, and in 1957 for NASA, LMSC has integrated hundreds of payloads into the basic Agena vehicle. These payloads have involved complete systems as well as "piggyback" payloads for many scientific and government agencies. Each has presented differing problems. Each experiment has had the following general integration characteristics:

- Volume, Weight, and Form or Configuration. The 30-ft parabolic antenna is an example of an experiment that presents an integration problem because of its physical characteristics, both stowed and deployed.
- Operational Characteristics. The experiment or payload may, when in operation, require isolation, demand a specific field of view, emit gasses or ionized clouds, emit a characteristic RF signal, operate at extreme temperatures, or demand excessive power. The interferometer experiment and the phased-array experiment are typical examples of payloads that, when operating, demand isolation and specific fields of view. The phased-array system has the characteristics of high power consumption when in operation.

- Environmental Requirements. The payload may require special environmental control, either in ascent or on orbit, or may exhibit degradation in operational characteristics when subjected to changes in environment. The solar-array system, while not technically an experiment, is an example of a system that degrades because of environment.

Problems associated with integration of the experiments will be examined in the following subsections, based on the general characteristics described above and on such special characteristics as may be pertinent.

#### 5.7.2 Orientation Control Experiment

The equipment necessary to meet the  $\pm 0.1$ -deg attitude-control requirement does not exhibit integration problems insofar as equipment weight, form, or configuration are concerned. Alignment-accuracy provisions between the horizon sensors, the gyro package, and the interferometer are stringent. Normally this equipment must be aligned to  $\pm 1$  min if the overall requirement of 0.1 deg is to be met. In the LMSC design, all three units, as well as the antenna feed, are located close to each other in the sensor section. The internal reference axes of the attitude-sensing equipment and the equipment mounting surfaces, therefore, present a somewhat easier alignment problem.

The horizon sensor, as well as the star-field sensor, requires specific fields of view. Since the interferometer also needs an unobstructed field of view, spatial layout problems exist in the sensor section for the location of this equipment. Should problems exist in the planar location of the interferometer, horizon sensor, and the star-field sensor, the diameter of the sensor segment could be increased, but this would increase weight and cause additional blockage of the parabolic antenna.

The star-field sensor and the horizon sensor are subject to electromagnetic interference. The sensor section also houses the X-band transponders for the parabolic antenna, since the shortest possible transmission line between the transponder and the antenna is desirable if line losses are to be held to a minimum. A potential EMI problem, therefore, exists between these components.

A similar problem may exist with respect to the horizon sensor. The sensor segment houses hydrazine nozzles (1-lb thrust) and ammonia resistance jet clusters. Emission of gasses from these motors may be hazardous to the horizon-sensor optics as well as to the star-field-sensor optics. Analyses must be made of molecular flow paths from these motors to determine whether shielding is required.

Intrasystem Integration. The LMSC system design for guidance and controls is based on utilization of gyro, horizon, and star-sensor references, with mass-expulsion devices to determine and maintain vehicle orientation through all phases of the mission, including ascent, injection, orbit operations, and orbit maneuvers. A series of tradeoff analyses was conducted to select the optimum mass-expulsion systems for each phase and to size them. The basic system sensors and electronics for guidance and controls must operate in several modes, the selected mode being dependent upon the operation required and the force levels necessary. An intrasystem integration problem thus exists between the basic sensors, the electronics, and the several modes of control, i.e., monopropellant hydrazine, ammonia resistance jet, and ion engines.

Mode selection for ascent through injection is sequential, with the main hydrazine system for injection control being commanded inoperative at the termination of the sequence. Mode selection for orbit operations is a commanded function, the experiment being enhanced by choice of systems and the reliability factor increased because of redundancy. Nevertheless, integration of all the mode choices within the guidance and controls system will require an extensive program of analysis and simulation, in addition to the review of problems outlined in subsection 5.7.2.

Acceptable Variations. From the standpoint of system integration, the LMSC-proposed guidance and controls system is relatively unaffected by changes in the general configuration. For example, the entire system retains the capability of assimilating either a rigid-panel type antenna or a flexrib antenna without change. It would be possible to utilize spin stabilization for the ascent and injection mode insofar as the attitude-control system is concerned; however, the LMSC analysis, which compares spin stabilization with three-axis control during all phases of ascent and injection, shows

that, once the orbit mode of operation has been selected (in this case, a sensor-mass expulsion system), little or no gain in either accuracy or simplicity is realized by using ascent and injection spin. In addition, spin stabilization complicates the moment of inertia problem, restricts the use of auxiliary experiments or payloads, and imposes stringent requirements on vehicle components (antennas, booms, etc.) to withstand the lateral g loads.

### 5.7.3 Parabolic Antenna

The parabolic antenna represents the most significant integration problem in the ATS-4 system. The entire vehicle design is dependent upon the requirements of the parabola; the configuration assembly, the location of equipment, and the location of the solar arrays are all affected by the antenna.

Weight and Power Allocations. A weight budget of 220 lb has been allocated to the reflector. This includes the center drum and the deployment mechanism. An additional 22 lb has been estimated for special instrumentation to monitor antenna surface flexure (this weight allocation includes instrumentation involving feed boom excursions). See subsection 6.2.1.

While the flexrib-type antenna has a metalized cloth reflector surface, the number of ribs and the opacity of the cloth require that the solar arrays be outboard of the antenna rim. An additional length of boom is required to compensate for the 22-deg equatorial offset.

Several means are available to deploy the antenna. Electrical drive is the most convenient; however, a blow-down hydraulic system has been investigated. The antenna will deploy in approximately 2 min and will require 1/4 hp working through a reduction drive.

The integration problem will require that the stringent weight goal be met; since there is sufficient volume available for stowage, the furled diameter may be permitted to increase.

Mounting Provisions. From the vehicle-design standpoint, the flexrib-type antenna provides little or no problem in mounting. The furled antenna is housed in a two-faced drum. The rear face of the drum, which includes the deployment motor, is attached to fittings on the forward face of the equipment section. The integration problem involves alignment of the drum with the extended feed, rather than alignment of the drum with the equipment section. Since the sensor section houses the antenna feed, as well as the tri-beam device, and the two support struts attach to the lower, or feed side of the antenna drum, alignment of the drum to the equipment section is not pertinent. Thermodynamic flow paths between the equipment section and the antenna drum will be a design consideration in that it will be important to maintain long time-constant temperature fluctuations in the drum so that thermal deflections are not transmitted to the rib butts.

Ascent loads will be carried through the antenna drum to the inner equipment section rings. The flexrib concept permits stacking of the antenna drum and the sensor section, permitting compact packaging and straight load paths.

Electrical Interface. The antenna is a passive unit. Electrical power is supplied only to the extension motor. If a blow-down hydraulic system is employed, only the deployment signal is required.

The antenna supports environmental instrumentation and wiring. There are 32 strain-gage points and 32 temperature pickups with associated wiring. EMI problems may exist with this installation. The antenna drum will also provide a junction-box location for the wiring harness runs between the equipment section and the sensor section. This junction box will be located within the drum as close as possible to the tri-beam mounting base.

Acceptable Variations. The basic LMSC design for ATS-4 can accommodate either a flexrib-type antenna or an unfolding petal type. Integration problems with the petal type are more stringent than with the flexrib, since the petal type requires a longer vehicle L/D ratio, a permanent stiffened feed boom, a considerably longer shroud, and a somewhat more complicated design for ascent stowage of the solar arrays. The compact stowage of the flexrib-type antenna eliminates these integration problems.

Space allocation permitted for stowage of the furled flexrib antenna is generous. Should further development of the flexrib indicate enlargement of the drum or changes in the type of ribs, skin, or type of deployment power, there will be little or no effect on the basic design or subsystems. The depth of the drum affects the length of the shroud on an inch-for-inch basis.

#### 5.7.4 Phased-Array Antenna

Weight and Power Allocations. In the equipment list and weight discussion (subsection 5.3.5), a weight of 112 lb has been allocated for the phased-array experiment. This weight allocation, if maintained, is not excessive. The unit must, however, be extended beyond the periphery of the antenna so that it can obtain an unobstructed field of view. It is located in the orbital operational position by means of a small tri-beam machine that extrudes a 4-in. beam to a total length of 18 ft. The weight allocation for the machine and boom is 19 lb. This weight is conservative since it is based on the current model of tri-beam machine, which extends a 6-in. beam for a distance of 20 ft at an elevation of 5 deg, in a 1-g field. This machine weighs 19 lb and is equipped with motors and clutches to retract the beam. Its reliability has been demonstrated in more than 200 extensions and retractions without failure. The extension motor provides 600 in.-oz torque, and the machine is geared to an extension speed of 74 in./min.

The integration problem most conspicuous with the phased array (Hughes design) is the 408-w input power required. This high input load necessitates programming of the device operationally. The phased array also generates considerable heat, but the location of the device in the operational mode negates this problem.



Mounting Provisions and Electrical Interface. The phased-array is mounted within a section of equipment rack on the -Z axis. On ascent, the tri-beam device is planned to be within the compartment, with the phased-array mounted externally. Ascent loads and dynamics will be taken through mounting bolts located on the equipment section rings and shear-web stringers. Separation of the device for extension will be by pyrotechnics. The compartment must also contain reels for storage of power and instrumentation cables.

Acceptable Variations. Some variance is permitted in the location or mounting provisions for the phased array. Should it become possible, upon further study, to mount the phased array on the sensor section, this location would be preferable to the present plan to mount the unit on an extension boom. The latter location, however, was chosen because of the sensitivity of the interferometer to multipath reflections.

The boom-mounted location of the device complicated the orbit dynamics problem, although the type of boom contemplated is estimated to have better than 10 percent damping. Subsequent test may prove this figure to be extremely conservative. The problem remains, however; and the phased array, its power consumption, and its effect on the vehicle guidance and controls system involves a significant integration problem.

#### 5.7.5 Interferometer

Weight and Power Allocations. A weight allocation of 36 lb has been assigned to the interferometer. This figure was obtained from Cubic Corporation, whose basic design parameters were followed in the integration of the unit into the ATS-4 vehicle. The weight of the unit is not necessarily an integration problem, nor is the power requirement of 12 w.

Mounting Provisions. Mounting of the interferometer presents an integration problem that has several secondary effects on the vehicle design. The unit must be mounted so that it has a clear and unobstructed field of view. This includes peripheral equipments mounted near the unit in the plane of the antenna horns. This requirement was one of

two significant requirements that prompted mounting the unit at the base of the sensor section and caused a transfer of the phased array from that location to a boom-mounted location above the parabolic antenna. Initial design studies had shown the phased-array experiment in the middle of the sensor section, symmetrically arranged about the vehicle Y-Y axis. The interferometer antenna was located outside, and on a plane with, the phased-array antenna. Subsequently, the twin factors of increase in frequency for the interferometer and the subsequent disclosure of the multipath reflection problem caused the aforementioned shift in location of these units.

In addition, since the interferometer experiment is an integral portion of the attitude-control experiment, there was a requirement to align the vehicle guidance and control sensors and the interferometer. Thus, the gyro-reference package, the horizon sensor, and the star-field sensor are located adjacent to, and in close alignment with, the interferometer antenna plane. An integration problem thus exists in mounting of the unit, and provisions must be made for precise intraunit alignment.

Electrical Interface. The interferometer is extremely sensitive to EMI. Its location in the sensor section permits isolation of the unit and the least possible generation of multipath waveforms that would bias the accuracy of the received signal. Other than this problem, the unit will require only normal shielding.

Acceptable Variations. There appears to be no acceptable variation permitted in the locations of the interferometer. The type of unit selected, however, can cause a problem in vehicle design. The higher the selected frequency of operation, the smaller the encompassed area of the receiving antennas; the operating frequency of 5 GHz permits the location of the antenna horns within the diameter of the sensor section. Center-to-center distance between horns is 16 wavelengths. Should a lower frequency be selected, the longer wavelength will require that the distance between antenna horns increase. This could have significant effect on the size of the sensor section or could cause the antenna horns to be mounted outboard of the section. The latter is not preferred because of alignment and thermodynamic problems, as well as the effect of energy reflected by the parabola.

## Section 6

### EXPERIMENT DEFINITION

#### 6.1 ORIENTATION CONTROL

The attitude control system configuration was selected principally through consideration of reliability and flexibility in meeting experiment requirements of the ATS-4 mission. It is required for experiments that vehicle attitude be mentioned in the rotating orbital reference frame, and it must be possible to point the parabolic reflector off-nadir for sustained periods of time. Furthermore, the control system must be able to maneuver and re-stabilize the spacecraft within a short period of time.

To meet these requirements, separate coarse- and fine-mode mechanizations have been chosen. Attitude references are derived from a horizon sensor, an interferometer, and an inertial reference gyro system. The flight control electronics can operate as a conventional position-plus-rate autopilot with gyrocompassing for attitude-hold control modes or purely as an inertial hold capable of accepting rate commands for attitude changes. The fine-control mode uses a adaptive digital electronic system for more precise attitude accuracy. The selected actuation system is mass expulsion which was chosen for its simplicity, quick response, and proven long-lift reliability. Additional factors that led to the decision to select two separate systems were the need for high confidence of operation, 2-year reliability, and the potential advancement of technology.

##### 6.1.1 Selected System

Attitude stabilization is accomplished by two systems that provide coarse and fine modes. The interferometer, adaptive autopilot, and ion engines constitute the fine-mode system, and the horizon sensor, rate gyro, and resistance jets constitute the coarse-mode system. The functions of the interferometer and horizon sensors, as

well as the functions of the actuation systems, can be interchanged. In either mode, operation by inertial means is possible using only the gyros for attitude reference. This feature results in an inherent flexibility of operation.

The coarse-mode system is used during ascent coast and in orbit in a gyrocompassing mode, and control torques are provided by 2.0 mlb resistance jets. Inertial stabilization is used during injection burn, station acquisition, and station change thrusting with hydrazine actuation systems. Other functions that can be performed with inertial stabilization are as follows:

- Initial acquisition by solar arrays
- Orientation of spacecraft for station acquisition or change by allowing the vehicle to be slewed in yaw (reduces number of thrusters required)
- Maneuvering of spacecraft to attitude offsets and holding them to within the drift-rate accuracy of gyros (results in complete flexibility for pointing in any direction of space – useful for tracking deep space probes)

Accuracy of the coarse system is approximately 0.2 deg in pitch and roll and 0.9 deg in yaw.

The fine-mode system provides the spacecraft long life, high accuracy, attitude control capabilities by using a hybrid digital-analog electronic system in conjunction with the interferometer sensors.

### 6.1.2 Alternative Attitude Control Techniques

Along with mass expulsion techniques, two types of momentum storage systems were considered — reaction wheels and gyro actuators. Control methods that furnished insufficient control torques, not otherwise applicable for the ATS-4 mission, were not reviewed in any detail. These approaches included gravity gradient, electromagnetic torquing, and solar reflectance systems.

Any gyroscopic reaction system is principally sized by the momentum storage requirement determined by the cyclic disturbance it must counteract. The cyclic solar disturbance torque requirement is discussed in subsection 6.1.7.

Maximum daily pitch torque is over  $0.5 \times 10^{-4}$  ft-lb with an average value above  $0.3 \times 10^{-4}$  ft-lb. Roll-torque amplitude is a function of season and is a maximum during winter and summer solstices when the sun is at its maximum angle of 23.5 deg from the equator at noon and midnight. The average torque in roll at those times is comparable to that in pitch.

The momentum requirement for one-half a day, or 43,200 sec, at an average torque of  $0.3 \times 10^{-4}$  ft-lb is roughly 1.3 ft-lb-sec. A reaction wheel to handle this much momentum would weigh on the order 8 to 10 lb per axis. It is estimated that a much smaller wheel would be required in the vertical yaw axis. The gyros of a set of three reaction wheels for meeting these requirements are estimated to weigh about 20 to 25 lb.

A configuration of a gyro actuation system using four single-degree-of-freedom control-moment gyros that can be torqued to generate momentum changes in any desired direction also requires about the same weight for control actuation elements.

The electronic torquers and momentum desaturation equipment can add 10 to 15 lb to the system weight. A continuous power load of the order of 12 w imposes a weight penalty of about 3 to 4 lb for additional solar panels and batteries. Total system weight for either form of momentum storage control systems is about 40 lb. Not included is the weight required for the dynamic decoupling control logic.

The principal criteria for selection of an ion-engine type of actuator for the fine-control system are based on its ability to supply the wide range of control torque, ability to maintain accurate attitude control, and adaptability to different payload configurations without equipment changes, while acceptably meeting weight and power requirements. Furthermore, the 5,000 lb-sec/lb specific impulse capability makes it possible to extend the spacecraft lifetime at a negligible cost in weight (less than 3 lb/yr).

Estimated gyro-system weight requirements are comparable to those expected for an ion-engine system. Three thruster pairs of ion engines (each with 3,000 lb-sec of attitude-control impulse storage) weigh 20 lb a pair. The proposed digital adaptive electronic system could require up to 10 lb for the three-axis system. Electrical peak power is large (about 140 w), but the power requirement is by demand to counteract the torque environment. A 20 percent duty cycle, which is conservative and above expected needs, would require about 8 lb of solar panels. The ion-engine actuation-system weight is estimated at a little less than 40 lb total. Mass expulsion systems neither involve dynamic coupling nor require desaturation. The primary disadvantages of a mass expulsion system are (1) restriction of mission duration by fuel efficiency and weight and (2) determination of reliability by cycling requirements. The first of these disadvantages is minimized by the extremely high  $I_{sp}$  (5,000 sec) of the ion engine. The second disadvantage has been minimized by the design of an adaptive autopilot that extends limit cycle periods to several hundred seconds. Also, the valveless operation of the ion engine eliminates the primary low reliability (for a large number of cycles) source in standard mass expulsion systems.

The ammonia resistance-jet system that is used with the coarse control channels was chosen on the basis of weight for a flight-proven (circa 1970) mass expulsion system. The resistance jets provide a significant improvement in specific impulse over the common nitrogen mass expulsion systems. Furthermore, the ammonia system provides a reliable system for use in the ascent-coast phase as well as a redundant system for the long-term orbital operation.

### 6.1.3 Coarse Attitude Control Equipment

General equipment areas for the coarse mode are horizon sensors, rate gyros, and actuation systems. A number of different horizon-sensing techniques were investigated. Of those analyzed, the earth-edge tracking schemes are most promising. Horizon-sensor candidates are shown in Table 6-2. Minuteman-type rate gyros that use a pulse rebalance technique offer the highest reliability (Table 6-1). The resistance jets and hydrazine thrusters that make up the actuation system are discussed in subsection 5.5.

Horizon Sensors. The following five major horizon-sensing techniques are in general use today:

- Conical Scanning
- Horizon-Sector Tracking
- Radiant Balance
- Horizon-Edge Tracking
- Horizon-to-Horizon Sweep

Table 6-1

ATTITUDE CONTROL SYSTEM GYRO CANDIDATES

Item	Autonetics	UAC	Sperry	Honeywell
Package				
Number of Gyros	3	3	3	4
Power, w	30	30	20	46
Weight, lb	19	16	16	16
MTBF, hr	$6.8 \times 10^6$	$25 \times 10^3$	$7.2 \times 10^3$	$50 \times 10^3$
Gyro Type	Auton. G10B (2 DF)	Norden (SDF)	Sperry (SDF)	Honeywell (SDF)
Bearing	Gas	Ball	Ball	Gas

Table 6-2

## ATTITUDE CONTROL SYSTEM HORIZON SENSOR CANDIDATES

Parameter	System				
	ATL A-OGO(a)	BEC Edge Track(b)	ATL LLESS(c)	BEC Model II-C	Passive Horizon Sensor
Physical Description	Two heads + mixer, flexure mounted	Four gimbaled heads + mixer	Two heads + integrator, flexure mounted	Two heads + mixer	Two heads
Functional Description	Dithered mirrors optically chopped IR bolometer sensor	Servoed head nulls output of thermopile sensors	Heads scan across earth in two orthogonal scan planes	Conical scan bolometer	Measures difference of radiant energy from two sensors 180 deg apart
Power, w	5 at 28 vdc	5 at 28 vdc	7.0 at 24 vdc	20 at 28 vdc, ~400 at 115 vac	1
Weight (lb)	20	17	7.7	15	3
Output	Attitude DC	Attitude DC	Attitude DC	Attitude AC	Attitude DC
Error (deg)	0.05	0.06	0.37	0.5	0.08
Redundant Operation	Four trackers, any three will suffice	Four trackers, any three will suffice	None	Pitch only	None
Reliability, 2 yr	0.91	0.91	0.835	—	0.99

(a) Advanced Technology Division

(b) Barnes Engineering Corp.

(c) Long-life earth sensor system — Advanced Technology Division.



Conical scanning and horizon-sector tracking both have reliability limitations because of their use of moving parts to attain the necessary scanning motion. Radiant-balance schemes are limited to small-angle attitude perturbations about the local vertical. Horizon-to-horizon sweep methods do not exhibit the high reliability of the horizon-edge trackers. Table 6-2 compares various types of horizon sensors.

The two primary candidates for the coarse system, both of which are edge trackers, are the A-OGO sensor, made by the Advanced Technology Division of American-Standard, and the Thermopile Edge-Tracking Horizon Sensor by Barnes Engineering Company. Both sensors can be operated from low to synchronous altitudes. Table 6-2 shows a slight advantage in the weight and reliability for the Barnes edge tracker. The A-OGO design has limitations when used for large-angle attitude maneuvers at synchronous altitudes. These arise from the fact that the dithered field of view is constrained to a scan in a vertical plane of 90 deg. Thus, at synchronous altitudes, vehicle excursions from the local vertical greater than approximately  $\pm 8.7$  deg will force the field of view to its mechanical stops. Allowable attitude excursion from the local vertical is further limited by one-half the angle of the optical field-of-view dither amplitude. This limitation does not arise in the thermopile edge-tracker design with its optics gimballed for rotation in two axes. The thermopile edge tracker is the best selection on the basis of considerations regarding limitations in attitude maneuvers; selection is made on the assumption that the Barnes model will be operational within the ATS-4 time schedule. A brief functional description of the two sensors follows.

The A-OGO horizon sensor employs a four-point horizon-edge tracking technique. The system operates in the altitude range from 100 to 80,000 nm. Four infrared search-and-track units track points on the earth horizon separated 90 deg in vehicle azimuth. Angular displacement of the vehicle from the nominal vertical is accomplished after detection of infrared energy in the form of a narrow beam that is caused to oscillate, or dither, sinusoidally about the horizon. The narrow beam is formed by a telescope and a movable mirror, which is driven to follow the horizon as the vehicle moves. Angular displacements of the vehicle in pitch and roll are computed from the signals generated by the trackers.

The thermopile edge tracker operates in the altitude range from 70 to 100,000 nm. The sensor uses two optical heads 90 deg apart in azimuth on the vehicle. Each head contains two fields-of-view that bracket the limb of the earth. The horizon tracking signal is obtained by comparing the infrared radiance seen in two fields of view separated by a fixed angle in the elevation plane of each tracking head. Horizon-edge tracking is accomplished by applying a fixed downward drive to the servoed assembly so that the lower field of view is driven into the horizon by an amount sufficient to generate a bias signal equivalent to the fixed downward drive. This results in the lower field of view riding on the horizon during tracking as shown in Fig. 6-1. Vehicle attitude is obtained by measuring the difference between horizon declination angles furnished by each optical head. The thermopile edge tracker can measure altitude to within an accuracy of 0.06 deg. The sources of error are presented in Table 6-3.

Table 6-3  
SOURCES OF ERROR

Source	Error (deg)
Errors due to Horizon Variations at Synchronous Altitude and Without Radiance Balance	0.02
Transducer Readout Error	0.05
Noise and Drift Error	0.011
Gain Change Error (5 percent change)	0.015
Alignment Error	0.014
Total RSS	0.058

Inertial Reference Package (IRP). A comparison of various IRP's is made in Table 6-1. From Table 6-1 the best candidate for a 2-yr mission is obtained with the Autonetics G10B gyro package.



The Autonetics G10B free-rotor gyro is a high-reliability two-axis displacement gyro capable of torquing rates above 5 deg/sec. Except for the electrical components and a Mu-metal shield, the G10B gyro is constructed of aluminum. The sensitive or gyroscopic element consists of a simple flywheel rotor. The rotor, spun by means of an induction drive motor, is supported by a self-lubricated gas bearing. The spherical gas bearing affords the rotor three degrees of angular freedom, which permits definition of a spin axis and two displacement axes. Relative displacement between the rotor and case structure is sensed by a two-axis capacitor pickoff. A four-pole electromagnetic torquer produces attractive forces on a ferrite sleeve attached to the rotor, which results in controlled gyroscopic precession. This method of torquing coupled with slow-speed rotor operation permits extremely high torquing capability at low input power and inertial grade instrument performance.

The Autonetics G10B free-rotor gyro is the result of extensive experience in the design, development, and production of precision gyros for inertial autonavigation. The G10B gyro design is based on the G6B4 free-rotor gyro used in the Minuteman Program, but with reduced size, weight, and power consistent with the requirements for space applications. Figure 6-2 shows a cutaway of the G10 gyro.

Since the Autonetics free-rotor gyro uses an induction drive motor, electronic speed control is required to achieve the necessary rate scale factor accuracy and stability. In orbit, the rotor speed motor is run at 60 rps to minimize drift torques from turbulence in the gas bearing and at approximately 240 rps during ascent and apogee motor burn to provide the necessary bearing stiffness to survive the high-acceleration environment. The apogee motor shutdown signal commands reduction of the motor drive voltage, and the motor coasts to the slower speed within 3 min.

There are two methods to facilitate achievement of two-speed gyro rotor operation. One method is to switch control of the series regulator driving the gyro motor three-phase bridge from the output of the speed-control shift register (that portion of the speed controller that has an output proportioned to the difference in gyro rotor speed and a reference frequency) to a constant-voltage reference that has a magnitude such

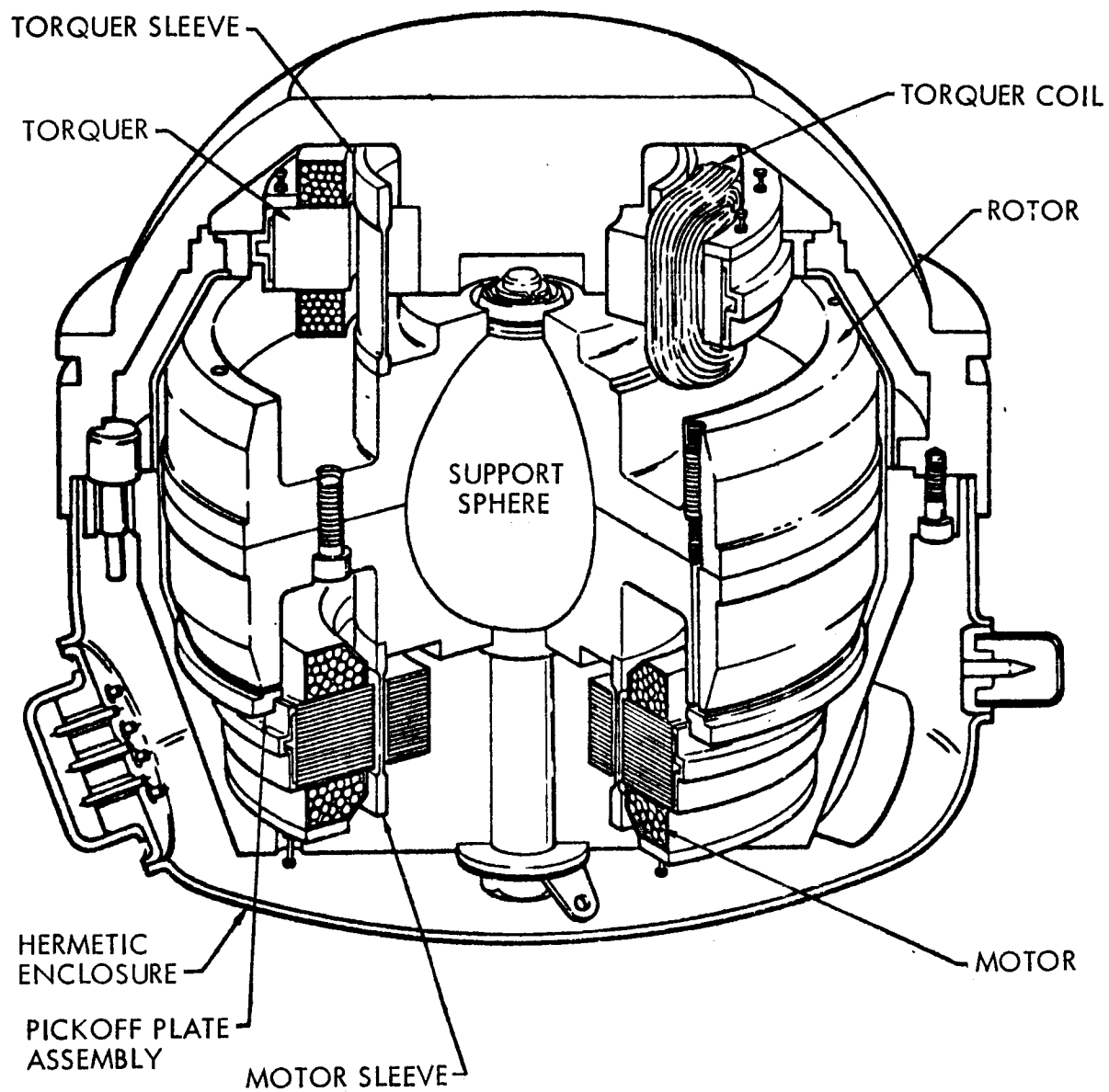


Fig. 6-2 Cutaway View of Autonetics G10B Gyro

as to cause a higher but constant voltage application at the driver bridge. The constant-voltage reference will be selected so that the increased bridge voltage will cause the rotor to rotate at the desired higher speed.

This method is relatively easy to incorporate, but does not furnish an accurate scale factor. The second method is to increase the frequency of the speed controller reference into the shift register. This method yields an accurate scale factor but presents some problems in mechanization. The basic difficulty is that the window of allowable voltage variation of the controller output and the input bandpass filter must be shifted up to the higher voltage and reference frequency.

Gyro updating is accomplished with the horizon sensors and gyrocompassing. Non-g-sensitive errors are shown in Table 6-4 and g-sensitive errors in Table 6-5.

The extremely high reliability and low drift qualifies this unit especially for long-life spacecraft applications. For a 2-yr mission, the two units required for complete three-axis attitude reference have an expected reliability of 0.997. No other gyro reference system considered in the survey comes close to this capability.

#### 6.1.4 Functional Analytic Description

Coarse System. The coarse-accuracy attitude control system maneuvers and maintains the vehicle orientation with respect to a rotating orbital reference frame. The system consists of three independent gyro reference control loops with horizon sensor for attitude trim control, gyro drift correction, and gyrocompassing.

Each of the pitch, roll, and yaw channels uses the integrated output of a precision rate gyro as the basic attitude reference. Functionally, the combined gyro and electronics have the same transfer function as a rate-integrating gyro system. The electronically derived attitude signal, in addition to being the integral of the inertial vehicle rate, can incorporate the integral of external driving signals, which is analogous to torquing a rate-integrating gyro. The control loop, as shown in Fig. 6-3,

Table 6-4

## G10B GYRO ERROR SOURCES

Error Source	Magnitude (rms)	Disturbance (rms)	Gyro Error (deg/hr-rms/maximum)					
			Pitch		Yaw		Roll	
			1 $\sigma$	3 $\sigma$	1 $\sigma$	3 $\sigma$	1 $\sigma$	3 $\sigma$
Random Drift	0.005 deg/hr	—	0.005	0.015	0.005	0.015	0.005	0.015
Bias								
Repeatability	0.30 deg/hr	—	0.3	0.9	0.3	0.9	0.3	0.9
Temperature Sensitivity	0.005 deg/hr/°F	13/ $\sqrt{3}$ = 7.5 deg	0.04	0.12	0.04	0.12	0.04	0.12
Torquer Axis Misalignment(b)								
Mounting and/or Calibration	1/3 mradian	—	0.006	0.018	0.08	0.24	0.08	0.24
Rotor Speed Variations	3 sec/rps	0.01 rps		neg		neg		neg
Temperature Variations	2.5 sec/°F	13/ $\sqrt{3}$ = 7.5 deg	0.001	0.002	0.024	0.072	0.024	0.072
Long-term Stability	30 sec	—	0.002	0.006	0.035	0.105	0.035	0.105
Spring-rate Cross Coupling	$5.42 \times 10^{-5} \frac{\text{deg/hr}}{\text{deg/hr}}$	—	0.008	0.0024	0.013	0.039	0.013	0.039
Torquer Scale Factor(b)								
Rotor Speed Variations	$\frac{1}{54.5} \text{ deg/hr-rps}$	0.01 rps	0.0002	0.0006	0.0002	0.0006	0.0002	0.0006
Temperature Variations	10 ppm/°F	13/ $\sqrt{3}$ = 7.5 deg	0.02	0.06	0.001	0.003	0.001	0.003
Long-term Stability	200 ppm	—	0.048	0.144	0.002	0.006	0.002	0.006
Spring-rate Direct Coupling	$1.25 \times 10^{-5} \frac{\text{deg/hr}}{\text{deg/hr}}$	—	0.003	0.009	0.0001	0.0003	0.0001	0.0003
RSS 3-sigma error			0.92		0.95		0.95	

(a) Rotor speed 54.5 rps; operating temperature range 61 to 87° F.

(b) Disturbance (rms): Pitch = 240 deg/hr, yaw = 10 deg/hr, roll = 10 deg/hr.

Table 6-5

G10B GYRO PERFORMANCE ERRORS (g-SENSITIVE)<sup>(a)</sup>

Parameter	Value
Mass Unbalance, deg/hr-g	0.5
Structural Compliance, deg/hr-g	0.5
Gas Bearing Incompressibility, deg/hr-g <sup>2</sup>	0.6
Gas Bearing Compressibility, deg/hr-g <sup>2</sup>	0.6
Axial g <sup>2</sup> sensitivity, deg/hr-g <sup>2</sup>	0.002

(a) Rotor speed = 240 rps

is inertially stable without the horizon sensor. In the pitch channel, a rate command input signal calls for a vehicle rate of 0.25 deg/min (corresponding to the orbital pitch rate) to keep the vehicle from diverging from the rotating orbit reference frame. Any deviation of the commanded rate from the true orbit rate or any gyro drift cause deviations in the attitude that would increase indefinitely unless an additional correction is incorporated into the system. Such correction is provided by integrating horizon-sensor signals along with the attitude rate. A gyro drift causes the spacecraft to offset to some equilibrium attitude at which the horizon-sensor signal would counter-balance the effective rate command of the drift. The output of the attitude integrator and the rate gyro signal are summed to form the control signal to the deadband and valve modulator that generates the control torques on the body. For small attitude errors slightly over the deadband, the valve driver system behaves as a pulse-width modulated system by using a minimum pulse width; as the error increases the pulse-width increases correspondingly, so the average torque over the pulse cycle is proportional to the error signal.

A low-gain feedback loop around the attitude integrator (called the decoupling loop) provides an improvement in system limit-cycle performance. The gain of this loop is matched to the horizon sensor gain on the order of 0.1 deg/sec rate per degree attitude; therefore, it is negligible in any attitude transient. At slow limit-cycle



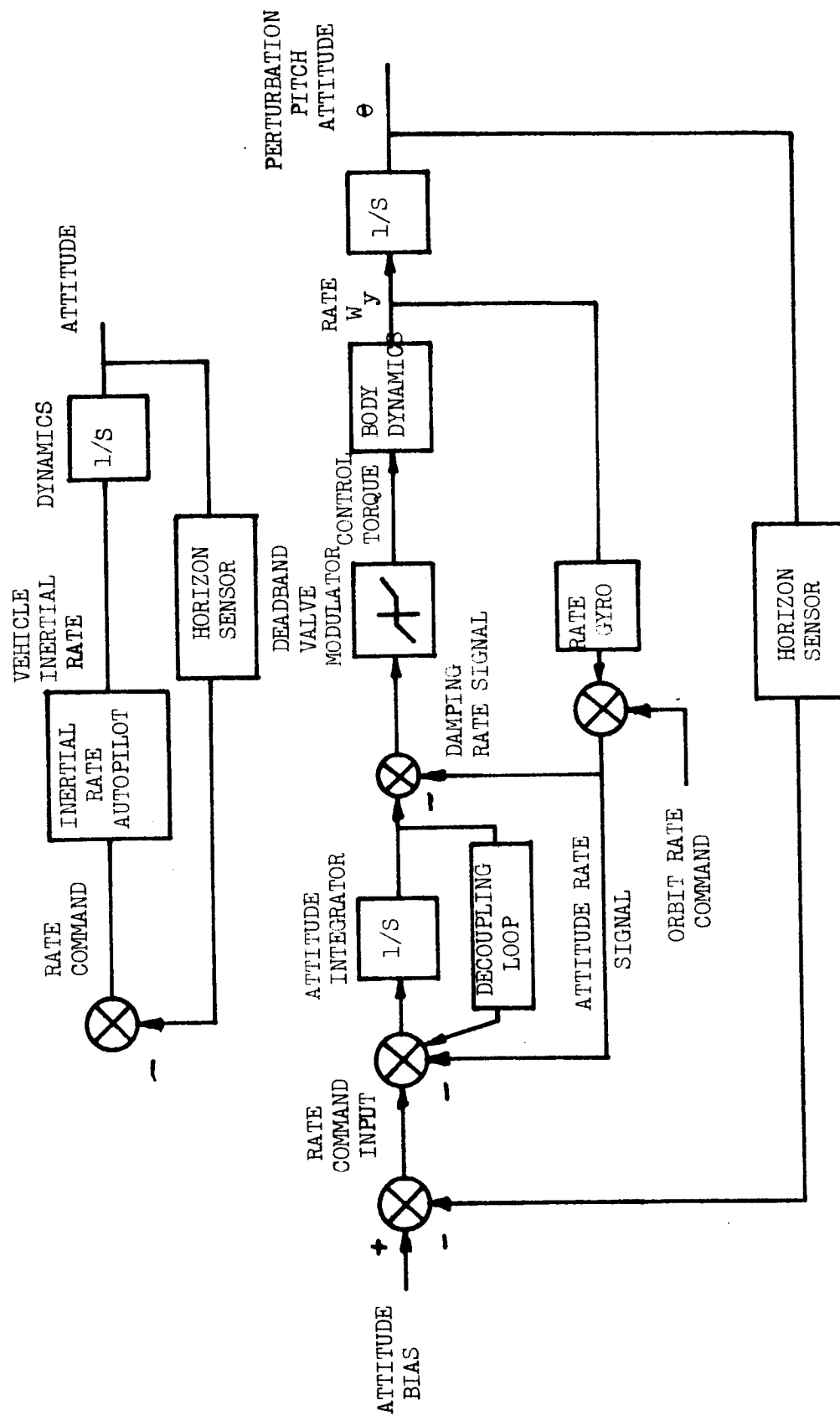


Fig. 6-3 Coarse-Mode Control Loop

rates where the nonlinearity of the deadband and minimum impulse bit operation dominate the system performance, the decoupling improves gas expenditure by reducing the effective integral feedback of the horizon-sensor input.

Gyrocompassing. The yaw attitude about the local vertical axis is controlled indirectly by a gyrocompassing technique. Except in the interferometer experiment, no direct measurement of yaw can be used for attitude control. Gyrocompassing is an exploitation of the dynamic coupling that exists between roll and yaw attitude in a body constrained to rotate uniformly in pitch. The ATS-4 coordinate frame, which defines the pitch, roll, and yaw axes, is shown in Fig. 6-4. Except for the second-order effects, roll-yaw dynamics are independent of pitch motion when the attitude deviations from the orbital reference frame are small.

The equations between vehicle inertial rates and the Euler angle rates indicate that oscillatory motion would exist between roll and yaw attitude if the inertial rates were constrained to zero. The frequency of this oscillation is the orbit rate. In such an oscillation, an offset in roll angle would interchange into the yaw axis during one-quarter of an orbit and then back again with reversed sign in another quarter orbit.

Figure 6-5 is a block diagram of the basic gyrocompassing system. The outputs of the integrators are the Euler angles of roll,  $\phi$ , and yaw,  $\psi$ , which are cross-coupled through the orbital rate,  $\omega_o$ . In this diagram the autopilot systems are shown as perfect inertial rate servo mechanisms with a transfer function of unity for rate command inputs. For the slow rates associated with gyrocompassing motion, neglecting the granularity effects of the deadband limit cycle, the vehicle average rate follows the input command rate on the average.

The roll axis is controlled directly through the roll horizon sensor, which commands the roll autopilot channel with sensor gain  $H_\phi$ . The yaw channel is also commanded by the same roll sensor. The effect of this additional cross coupling from roll to yaw

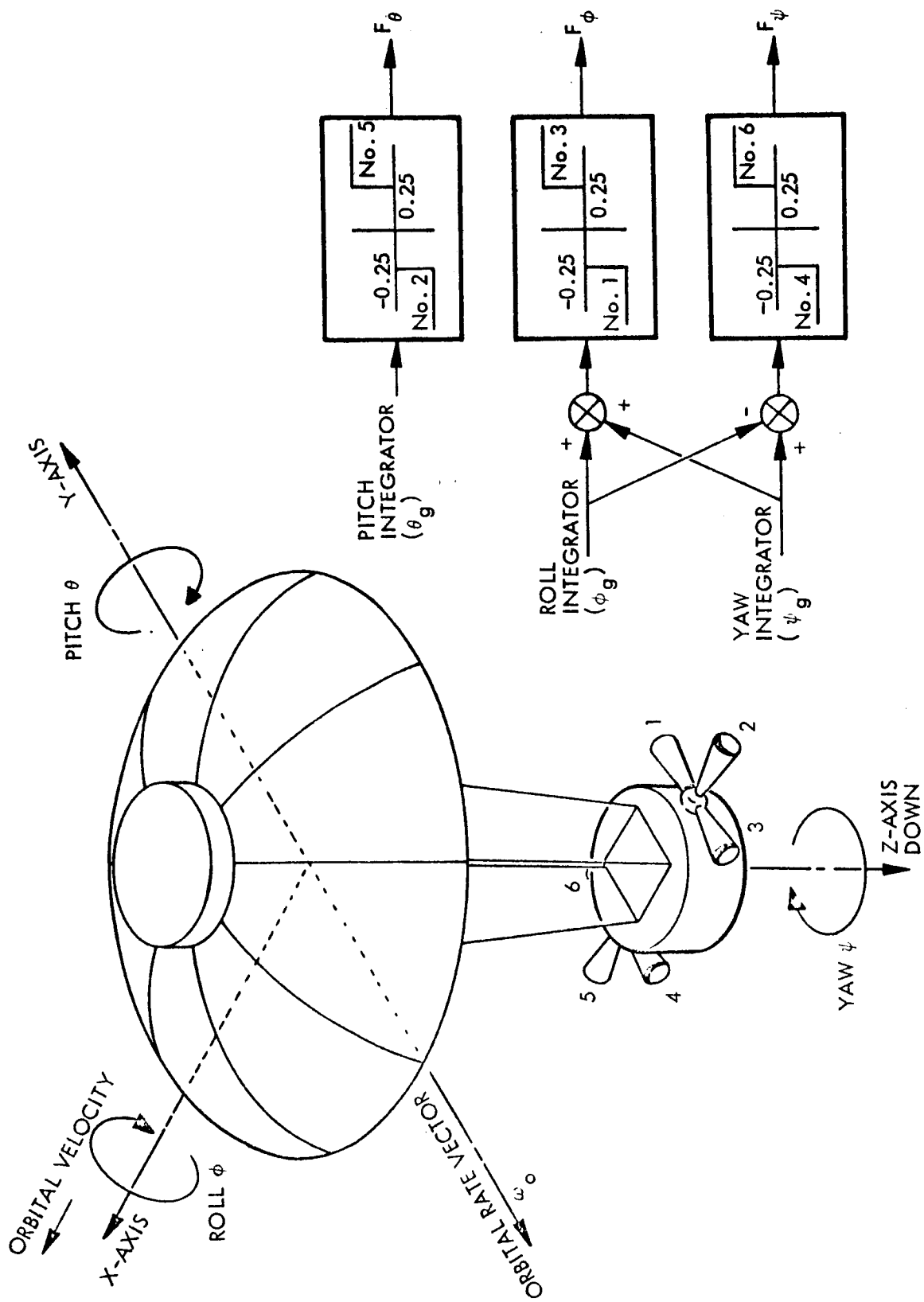
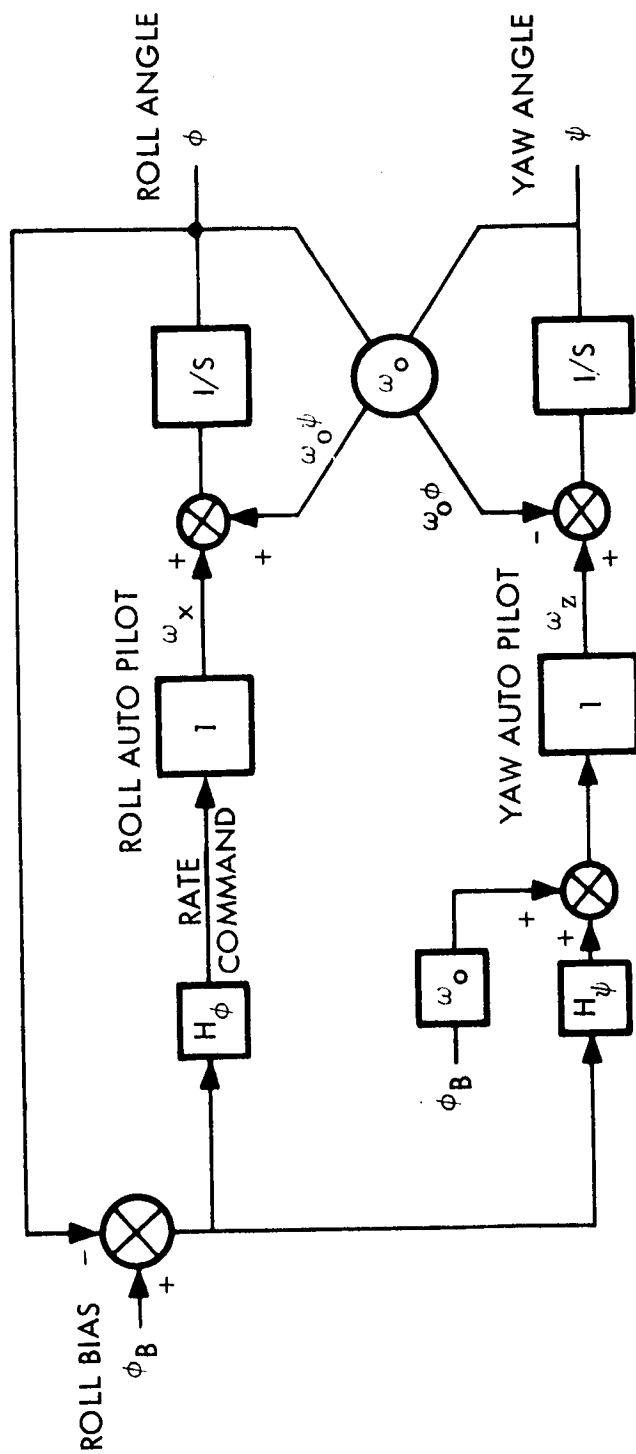


Fig. 6-4 Coarse-Mode Thruster Locations



BODY RATES:

$$\omega_x = \dot{\phi} - \omega_o \psi \text{ and } \omega_z = \dot{\psi} + \omega_o \phi$$

FOR "PERFECT" RATE COMMAND AUTOPILOT:

$$\begin{bmatrix} \dot{\phi} \\ \dot{\psi} \end{bmatrix} = \begin{bmatrix} -H_\phi & \omega_o \\ \omega_o & 0 \end{bmatrix} \begin{bmatrix} \phi \\ \psi \end{bmatrix} + \begin{bmatrix} H_\phi \\ H_\psi + \omega_o \end{bmatrix} \phi_B$$

$$\text{CHARACTERISTIC EQUATION} \\ s^2 + H_\phi s + \omega_o (H_\psi + \omega_o)$$

Fig. 6-5 Gyrocompassing Loop

is to increase the natural orbital cross-coupling term  $\omega_o$  by the sensor gain  $H_\psi$ . When the autopilot produces an inertial roll rate and an inertial yaw rate proportional to the roll angle with appropriate designs a stable closed loop results.

The characteristic equation that gives the roots of the closed-loop system is found by solution of the coupled differential equations. Gyrocompass mechanics have the characteristics of a damped second-order dynamic system:

$$S^2 + H_\phi S + \omega_o (H_\psi + \omega_o)$$

System damping depends on the roll-sensor gain, and system natural frequency is a function of both the orbital rate and the gyrocompassing gain  $H_\psi$ . For  $H_\phi = 1/4$  deg/min/deg and  $H_\psi = 5$  deg/min/deg, and with an orbital rate of  $\omega_o = 0.25$  deg/min, the characteristic equation is:

$$\begin{aligned} S^2 + 0.00425S + 2.46 \times 10^{-6} \\ = S^2 + 2 (0.85) (2.46 \times 10^{-3}) S + (2.46 \times 10^{-3})^2 \\ = S^2 + 2 \zeta \omega_n S + \omega_n^2 \end{aligned}$$

which has a natural frequency of  $2.46 \times 10^{-3}$  radians/sec and a damping ratio of  $\zeta = 0.85$ . That natural frequencies damp well within an orbit period is one of the principal advantages of this form of gyrocompassing. The roots of the closed-loop system are designed by the choice of sensor gains.

Off-Nadir Operation. The three-axis control system has the capability to maintain the vehicle at non-zero Euler-angle attitudes with respect to the rotating orbital reference frame. In pitch, an offset attitude command is used to bias the horizon-sensor signal to a new shifted equilibrium. The resulting attitude-error signal, which consists

of the difference between the input command and the measured pitch attitude, is algebraically summed to form the rate-command signal to the basic inertial autopilot system as shown in Fig. 6-3.

The offset command system for roll rotations is slightly more complicated than for the pitch case because of coupling between the roll and yaw axes in the gyrocompass system. If a bias were incorporated in the roll horizon sensor as in the pitch channel, the vehicle would come to the required offset roll equilibrium but would simultaneously result in a yaw error. Yaw error results since the inertial yaw rate to which the autopilot system responds fundamentally involves terms proportional to roll angle. If the vehicle were constrained to a roll angle,  $\phi$ , the linearized inertial yaw rate would be equal to the product of that angle in radians and the orbital rate ( $\omega_z = \omega_o \phi$ ). This cross coupling of roll angle into yaw rate can be eliminated by the addition of a small yaw-rate command to the yaw channel inertial autopilot to compensate for the effect.

If no yaw-compensating term is used, the resulting steady-state attitude with a roll horizon-sensor bias would be at the biased roll angle and a proportional offset in yaw. The amount of the uncompensated offset is a function of the sensor gains and orbit and is

$$\psi_{\text{uncompensated}} = \frac{H_{\phi}}{\omega_o + H_{\psi}} \phi_{\text{bias}}$$

For the sensor gain of  $H_{\phi} = 1/4$ ,  $H_{\psi} = 5 \text{ deg/min/deg}$ , and  $\phi_{\text{bias}} = 5 \text{ deg}$ , the resulting uncompensated yaw angle is  $1/4 \text{ deg}$ . This error is small enough to justify consideration of the elimination of the yaw-rate compensation.

Simulation Results. Digital simulation of a vehicle system in a gyrocompass mode was performed to verify the off-nadir operation for ATS-4. The simulation solved the complete system dynamics without any linearization of the Euler-angle transformations. The results shown in Figs. 6-6, 6-7, and 6-8 are traces of roll, pitch, and yaw histories

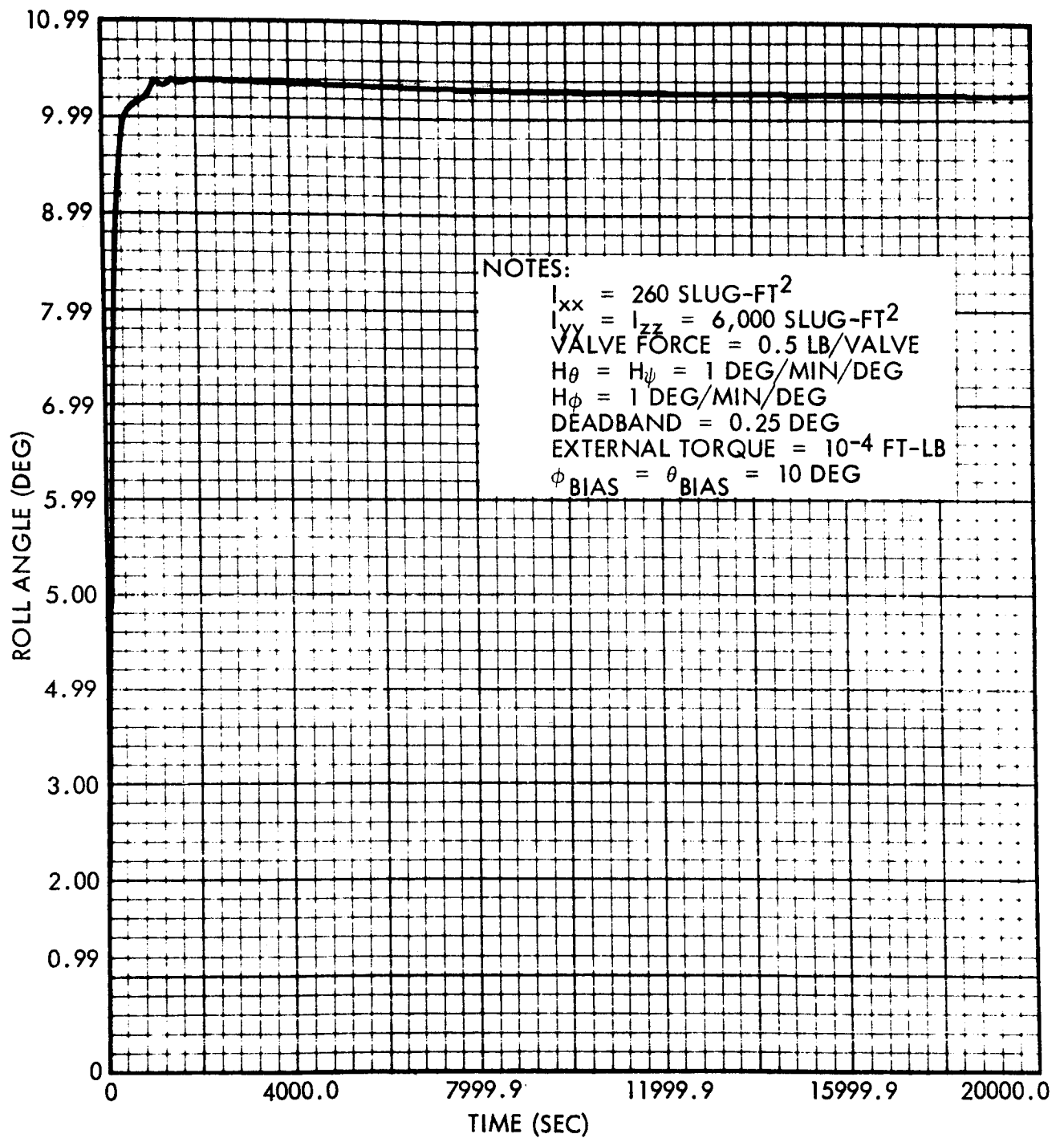


Fig. 6-6 Roll-Axis Response to Pointing Command

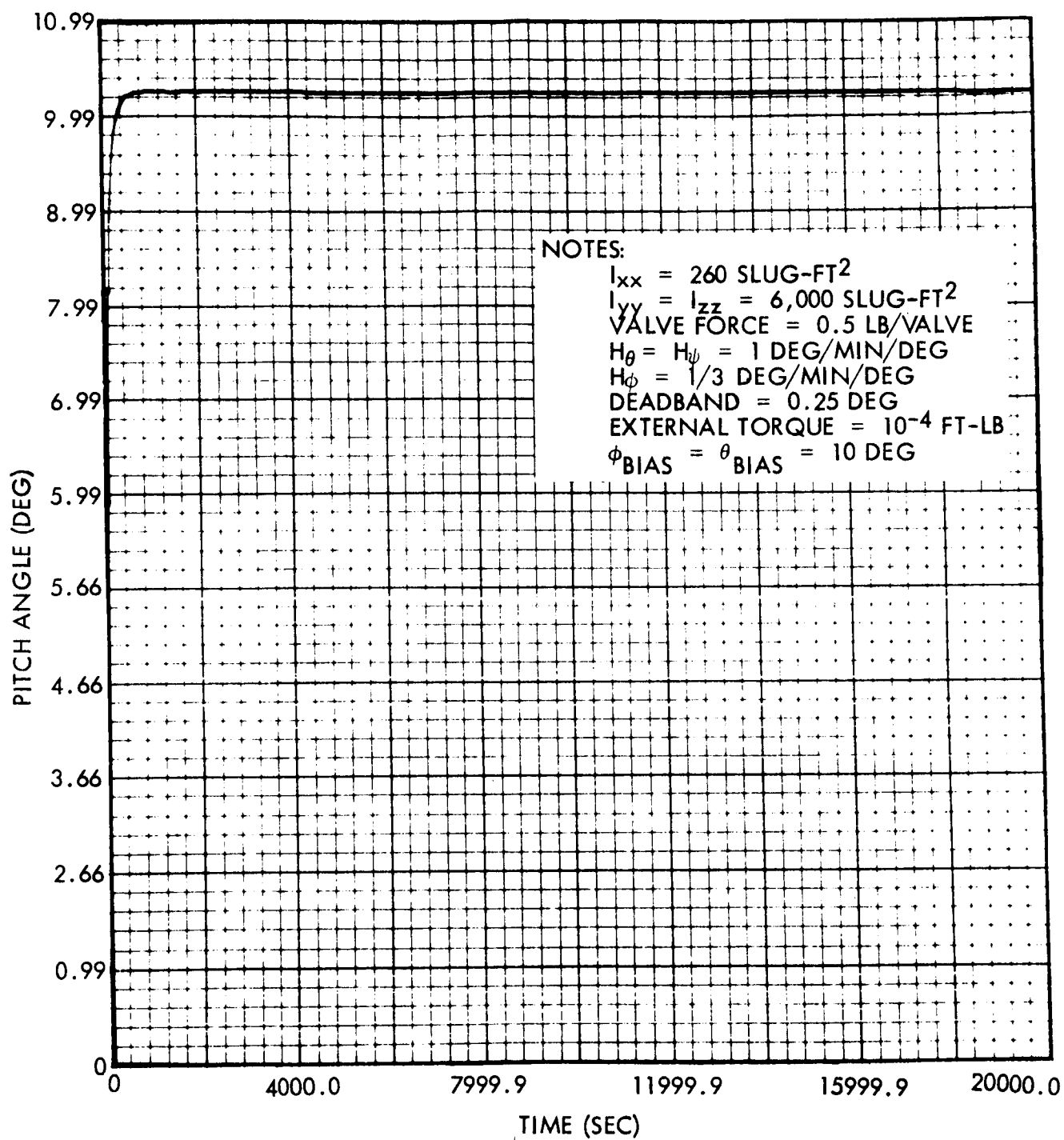


Fig. 6-7 Pitch-Axis Response to Pointing Command



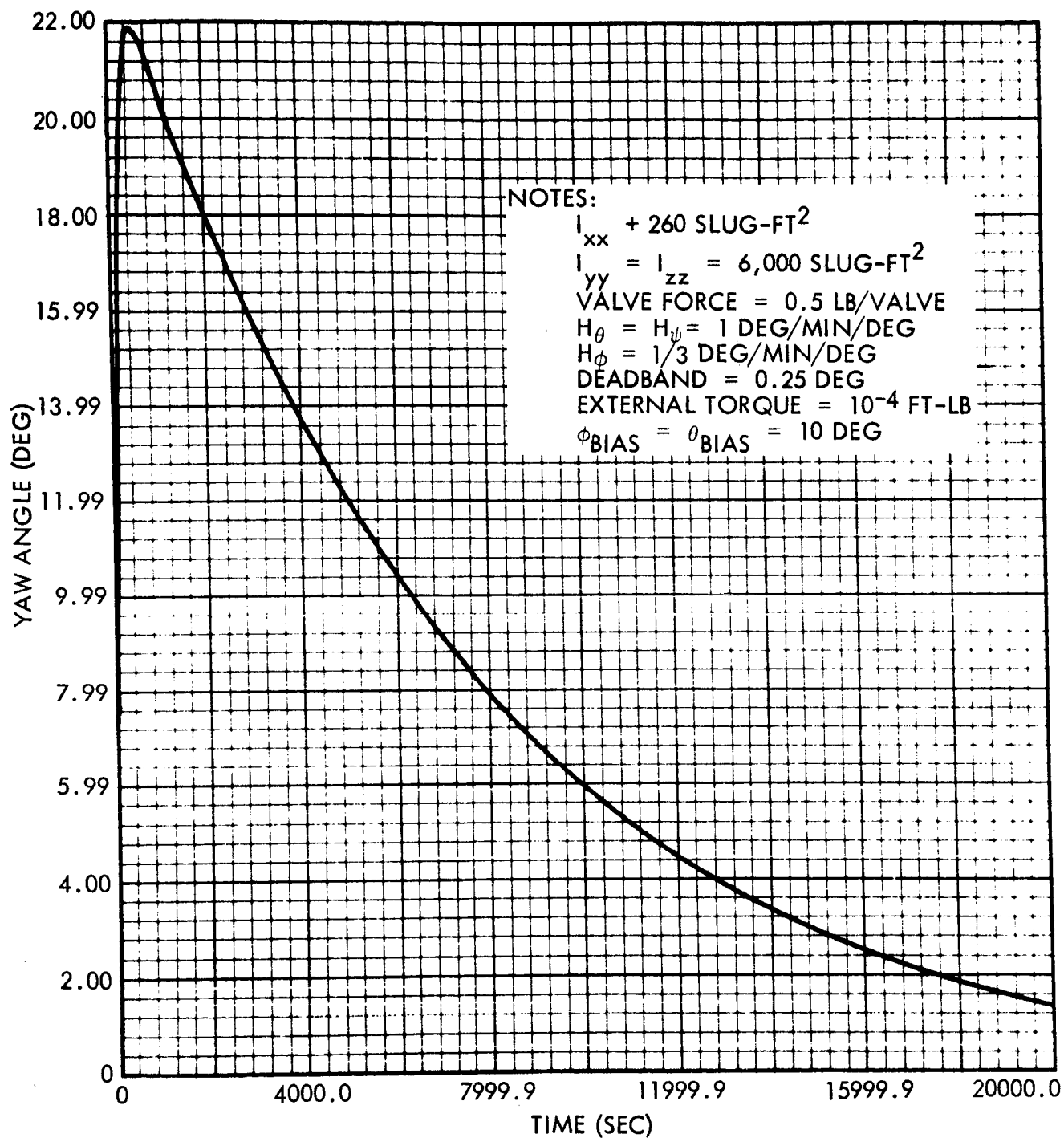


Fig. 6-8 Yaw-Axis Response to Pointing Command

for a synchronous vehicle initially stabilized for nadir pointing with step bias commands of 10.0 deg in both pitch and roll and a steady torque of  $10^{-4}$  ft-lb in all axes. The vehicle settles to steady-state pitch and roll values equal to the command plus the deadband within 1,000 sec. The yaw response shows a sharp offset that converges to zero yaw angle at a very slow rate. The sensor gains for this run in pitch, roll, and yaw were 1, 1/3, and 1 deg/min/deg, respectively, which were not optimized for response at the synchronous orbit rate. The yaw excursion is a result of the step roll sensor bias forcing the yaw rate through the gyrocompassing gain,  $H_{\psi}$ .

The yaw transient can be eliminated by modifying the procedure of commanding roll offsets by removing the gyrocompassing loop temporarily from the roll sensor to the yaw channel for the 1,000 sec required for roll response and then reconnecting the gyrocompassing loop. The yaw perturbation transient is negligible since net roll error is small at the time it is connected into the vertical axis system.

To demonstrate the stability of the off-nadir gyrocompassing after all transients have damped, a digital run was made with the vehicle initially set at the offset position of 10 deg in pitch and roll. The result of this run indicated completely stable operation in the presence of all the nonlinear influences in the dynamics existing at off-nadir attitudes. This result also confirmed the findings predicted from analysis of the linearized equations of motion.

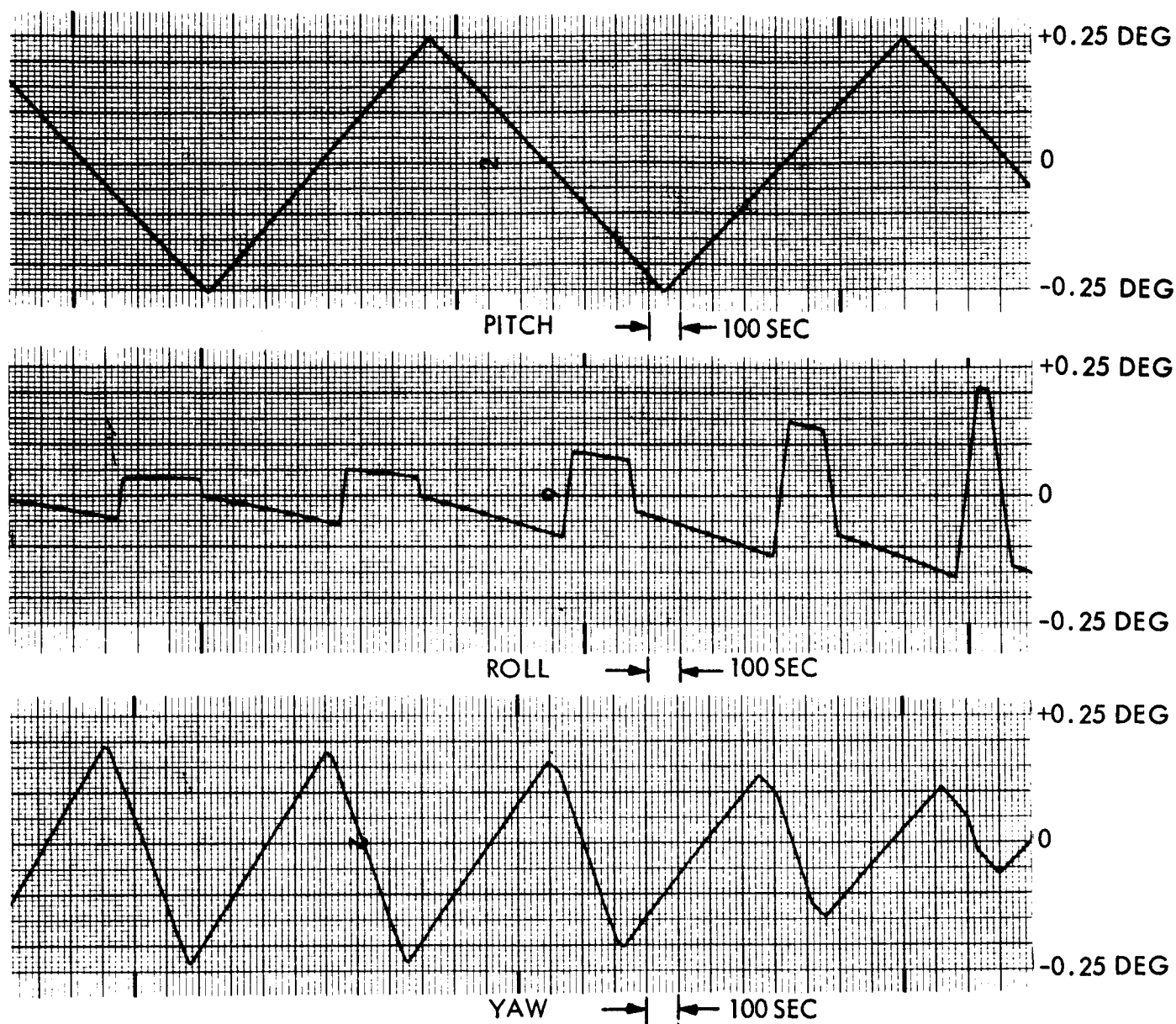
The effects of noise and limit-cycle operation with and without external torques were demonstrated on an analog simulation. The simulation available for the study used inertias ( $I_{xx} = 250 \text{ slug ft}^2$ ;  $I_{yy} = I_{zz} = 6,000 \text{ slug ft}^2$ ) that did not exactly duplicate ATS-4 inertias; however, the control laws were identical with the presently proposed coarse system. Thus the results are completely applicable. The analog simulation is a linearized model of the vehicle dynamics. The linearization involves small-angle approximations of the trigonometric functions. Comparison of results with the digital simulation (which contains no linearization) shows that the linearizing approximations do not mask any instabilities that may exist in the control system.

Steady-state operation of the attitude-control system is a limit cycle. Limit cycles exist because of the on-off or discontinuous operation of the actuation system and the deadband. Figure 6-9 shows limit-cycle operation in an environment free of external torques. The triangular waveshape seen in pitch is typical of uncoupled limit-cycle motion. The roll and yaw steady-state operation is not always a triangular limit cycle because the gas valves for the axes are coupled. This coupling consists of using the roll and yaw attitude signals to actuate one set of valves when the signal sum exceeds the deadband and using the difference to actuate the other pair of roll-yaw valves. The valves are arranged as shown in Fig. 6-4 so that an impulse from a roll-yaw valve gives a torque into both the roll and the yaw axes. Experience has shown that this form of cross coupling improves mass usage in low-torque environments since fewer gas firings are required for control. On occasion, one pulse can simultaneously reverse errors in both roll and yaw. The degree of performance improvement over a set of completely decoupled valves depends on the respective lever-arm-to-inertia ratio in each axis.

This torque free run was made with 0.5-lb valves and 0.020-sec minimum impulse. The ATS-4 system has 1/250 this thrust of 0.002 lb. The smaller thrust gives limit-cycle periods roughly 250 times those shown in Fig. 6-9.

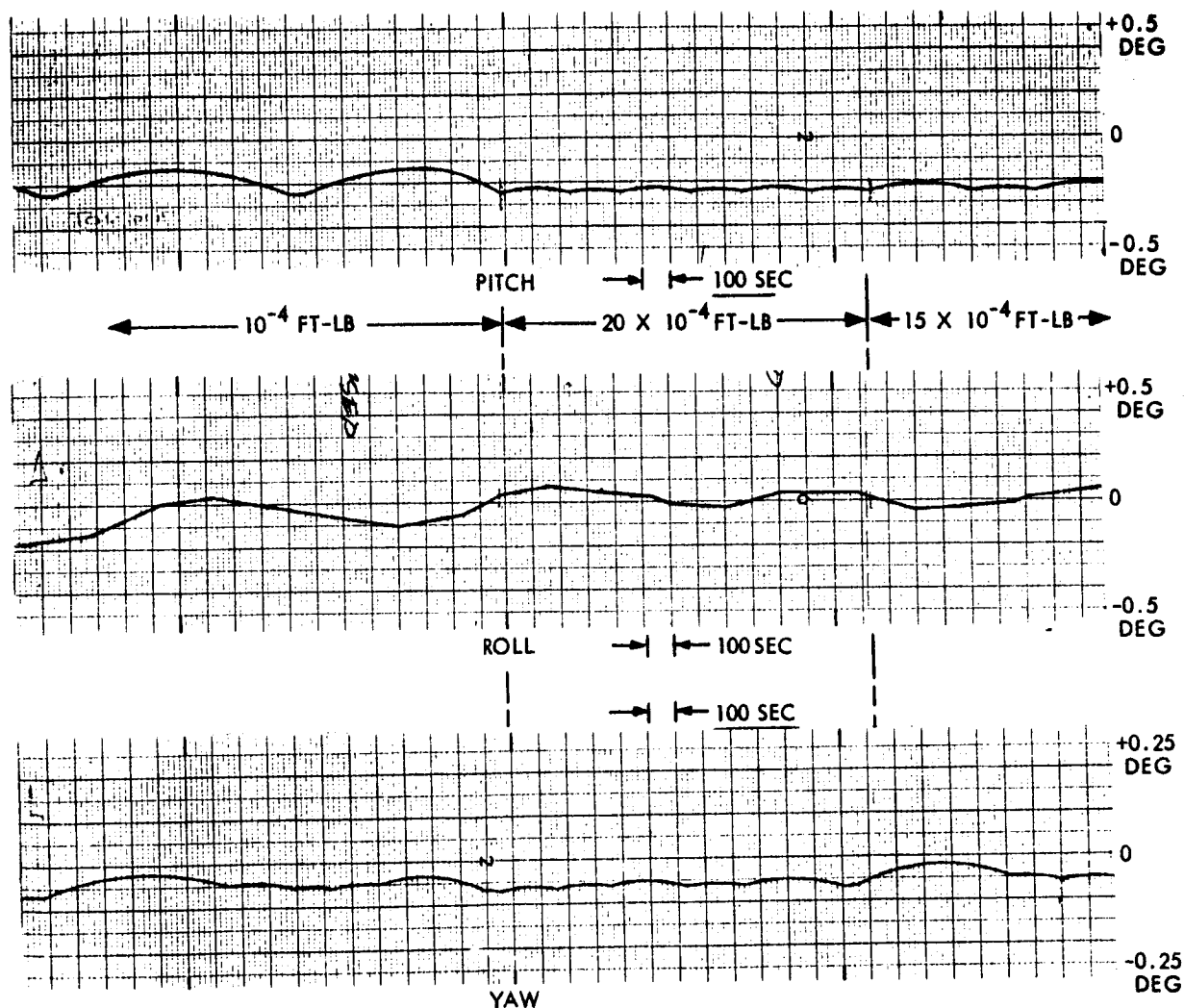
Figure 6-10 shows limit-cycle operation under the influence of external torques. For this condition, the limit cycle exhibits a scalloping characteristic against the deadband. It can be seen from Fig. 6-11 that as the external torque increases, the scallop amplitude decreases. The effect is to decrease the uncertainty in vehicle attitude below that associated with the  $\pm 0.25$ -deg deadband. Thus, for even large deadbands, the uncertainty in vehicle attitude is a function of the sign and magnitude of the external torque and control-system minimum impulse.

Figure 6-11 shows the effect of introducing horizon-sensor noise of 0.1 deg rms. The frequency range of the noise spectrum is from 0.001 to 0.1 Hz. This noise model represents a case 100 times greater than is expected with either an A-OGO or thermopile edge-tracker horizon sensor. The results show that the noise is heavily filtered by the



PARAMETERS:  $I_{xx} = 250 \text{ SLUG-FT}^2$  THRUST LEVEL = 0.5 LB/VALVE  
 $I_{yy} = I_{zz} = 6,000 \text{ SLUG-FT}^2$  DEADBAND = 0.25 DEG  
 $H_{\psi} = H_{\theta} = \frac{1 \text{ DEG/MIN}}{\text{DEG}}$   
 $H_{\phi} = \frac{1}{3} \frac{\text{DEG/MIN}}{\text{DEG}}$

Fig. 6-9 Coarse-Mode Limit Cycle Operation



PARAMETERS:  $I_{xx} = 250 \text{ SLUG-FT}^2$   
 $I_{yy} = I_{zz} = 6,000 \text{ SLUG-FT}^2$   
 $H_{\psi} = H_{\theta} = \frac{1 \text{ DEG/MIN}}{\text{DEG}}$   
 $H_{\phi} = \frac{1}{3} \frac{\text{DEG/MIN}}{\text{DEG}}$

THRUST LEVEL = 0.02 LB/VALVE

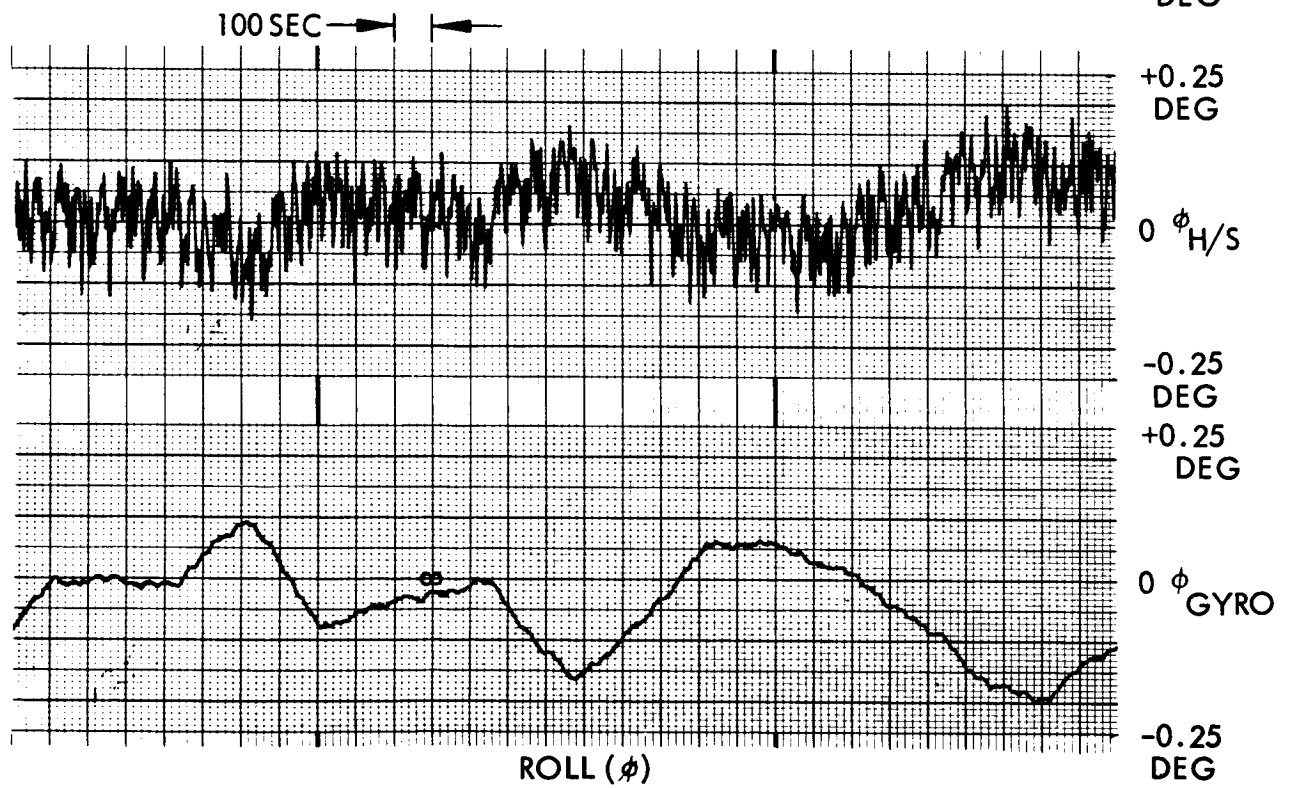
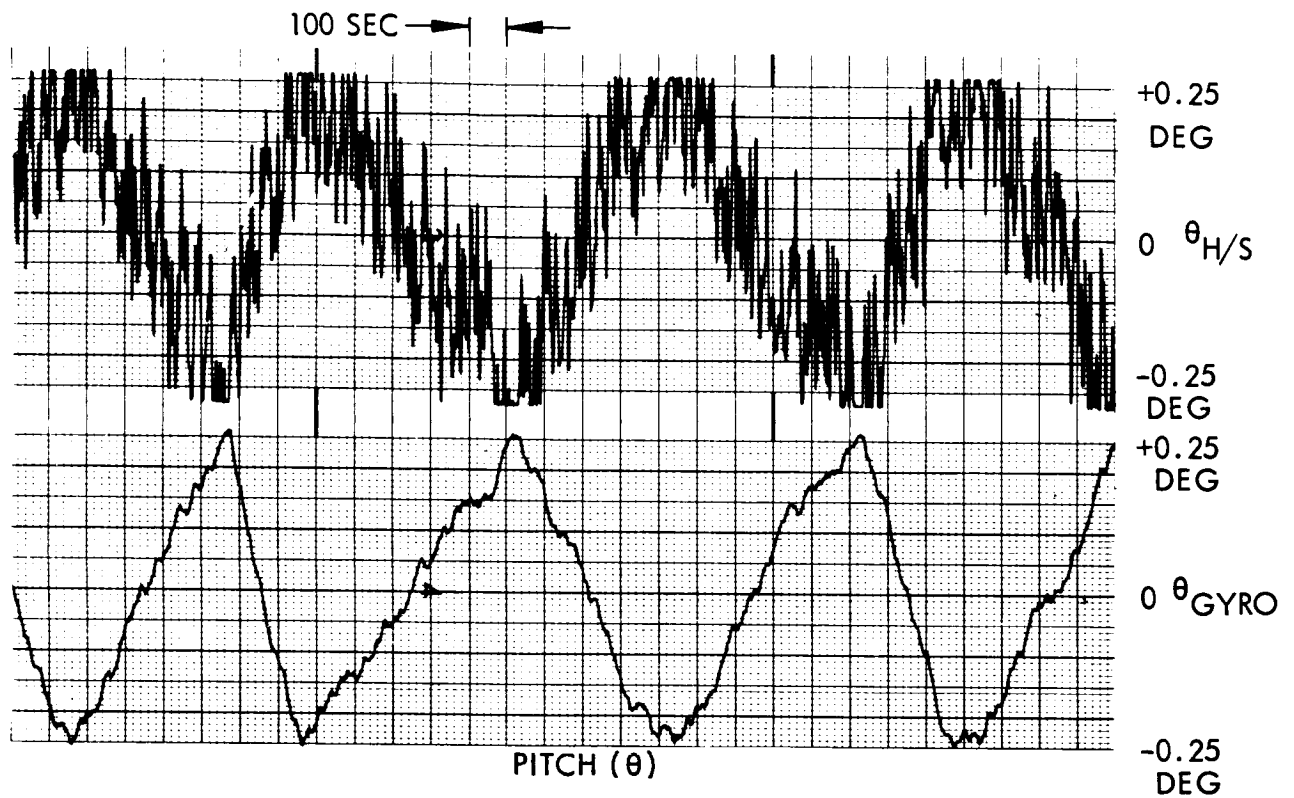
DEADBANDS = 0.25 DEG

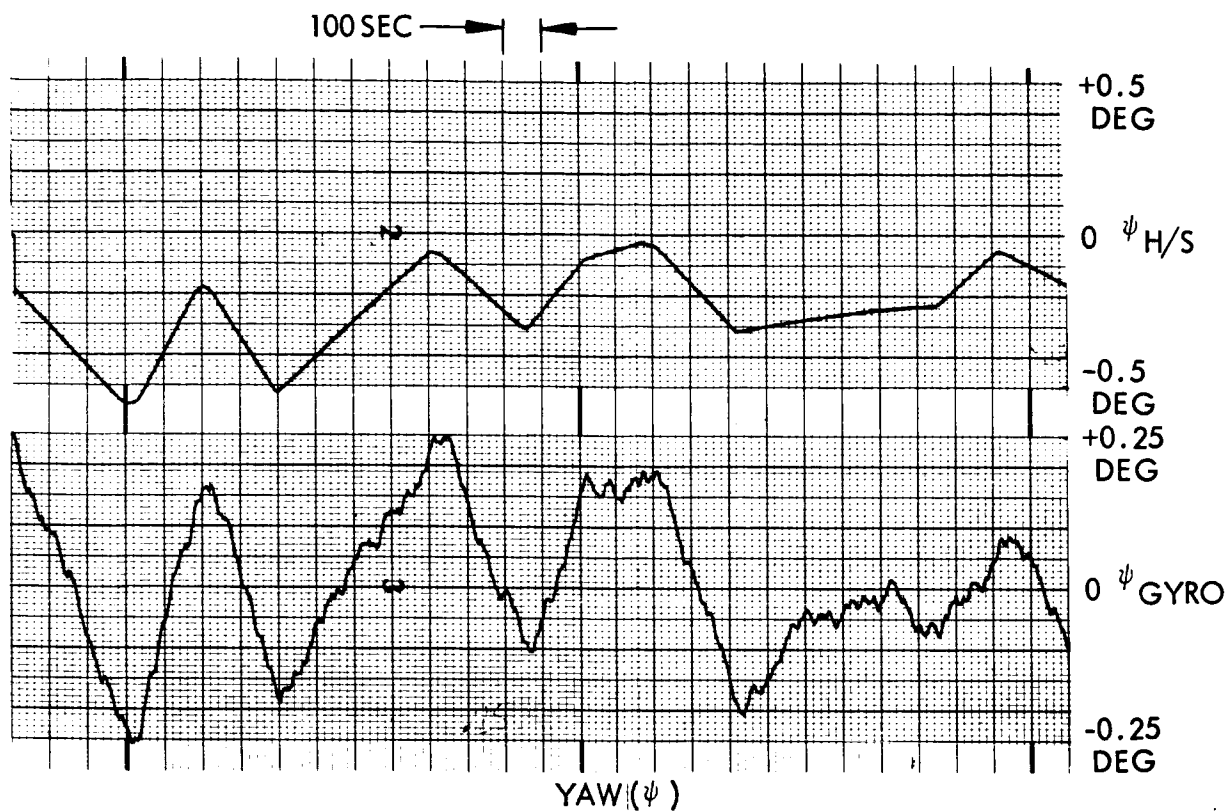
Fig. 6-10 Coarse-Mode Operation With Disturbing Torques

integrator and results in small attitude perturbations. In Fig. 6-11 the small yaw-attitude bias is the result of a transient introduced earlier in the run.

Ascent and On-Orbit Attitude Control. The spacecraft attitude during ascent coast (period between booster separation and injection motor burn) and on orbit is stabilized to a rotating orbital reference frame by the coarse system. This control system operates in the gyrocompassing mode as described earlier. A block diagram of the main components in the coarse system is shown in Fig. 6-12. From the figure it can be seen that the system may be grouped in three subdivisions (1) attitude sensing, (2) signal processing, (3) actuation. The attitude-sensing components were discussed in subsection 6.1.3. The actuation systems, consisting of the hydrazine and ammonia resistance-jet thrusters, were discussed in subsection 5.5. Signal processing includes the hybrid integrator, pulse-width modulator, and inverse modulator.

The hybrid integrator (Fig. 6-13) sums the triangular wave output of the buffer amplifier (a point available within the gyro package) with the DC signal from the horizon sensor and the feedback from the decoupling loop. This sum is fed to a relay whose output, a pulse train of constant frequency, is integrated digitally by the backward-forward counter. At this point, the attitude signal is in digital form and passes through a digital-to-analog converter for summation with the analog output of the G10B gyro. An understanding of how the hybrid integrator works can be gained by considering two cases: (1) no attitude error and (2) attitude error. In the first case, the horizon sensor output is zero and the buffer amplifier output waveform is symmetric about zero with period  $T$ . The output of the relay is a pulse train, with period  $T$ , symmetric about zero, and the counter output is zero at intervals of  $\Delta T$ . In the second case, the output of the horizon sensor biases the triangular wave of the gyro so that the output of the relay is nonsymmetric about zero. Thus, the counter at the end of the  $\Delta T$  has a digital value proportional to the attitude error. The use of the hybrid integrator eliminates the need for an analog integrator with its attendant drift problems. It also has the advantage over an integrator that is totally digital in that no analog-to-digital conversion is required.





PARAMETERS:

$$I_{xx} = 250 \text{ SLUG-FT}^2$$

$$I_{yy} = I_{zz} = 6,000 \text{ SLUG-FT}^2$$

$$H_{\psi} = H_{\theta} = \frac{1 \text{ DEG/MIN}}{\text{DEG}}$$

$$H_{\phi} = \frac{1}{3} \frac{\text{DEG/MIN}}{\text{DEG}}$$

THRUST LEVEL: 0.02 LB/VALVE

NOISE LEVEL = 0.1 DEG RMS

0.001 TO 0.1 HZ

DEADBAND = 0.25 DEG

Fig. 6-11 Coarse-Mode Operation With Horizon-Sensor Noise



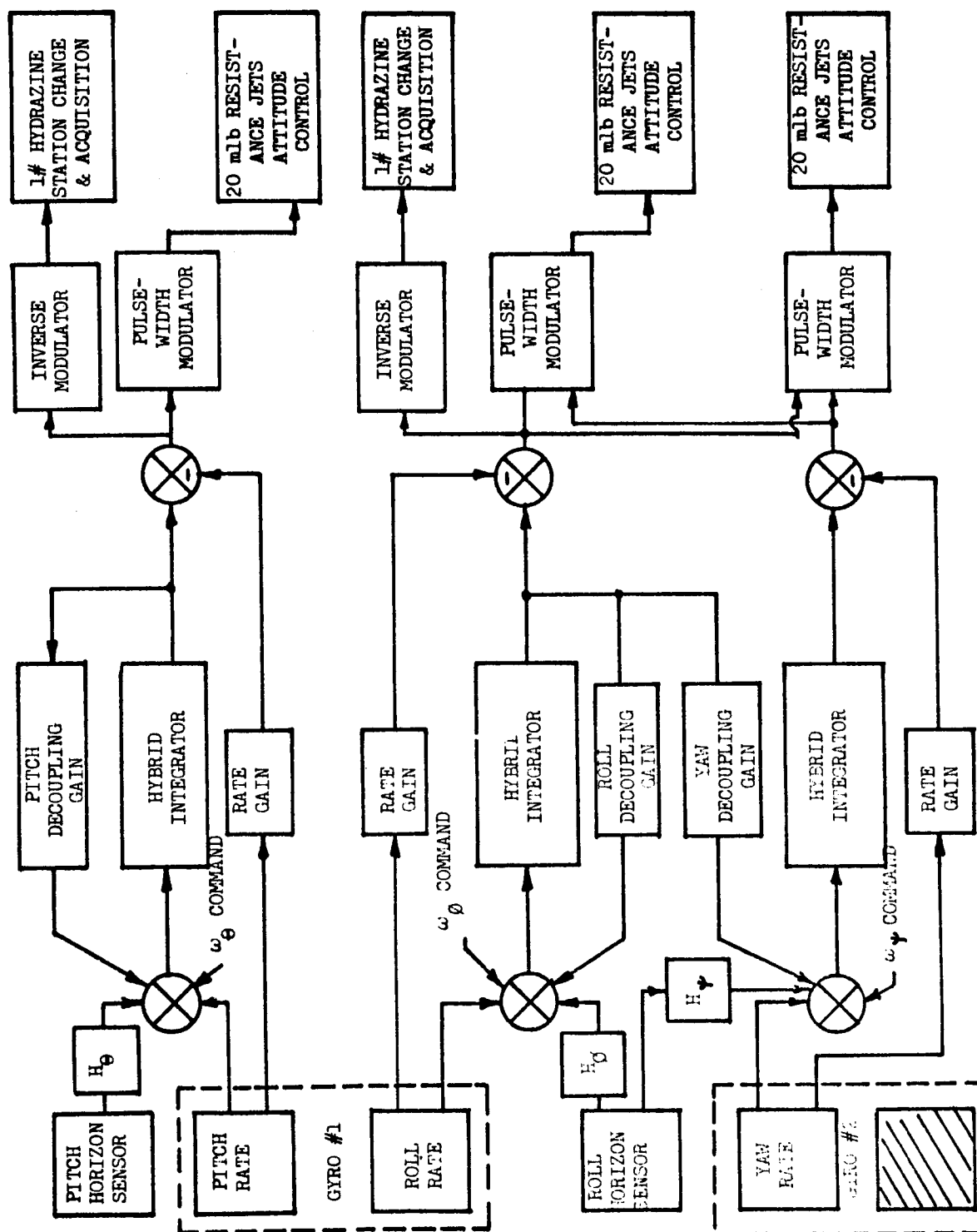
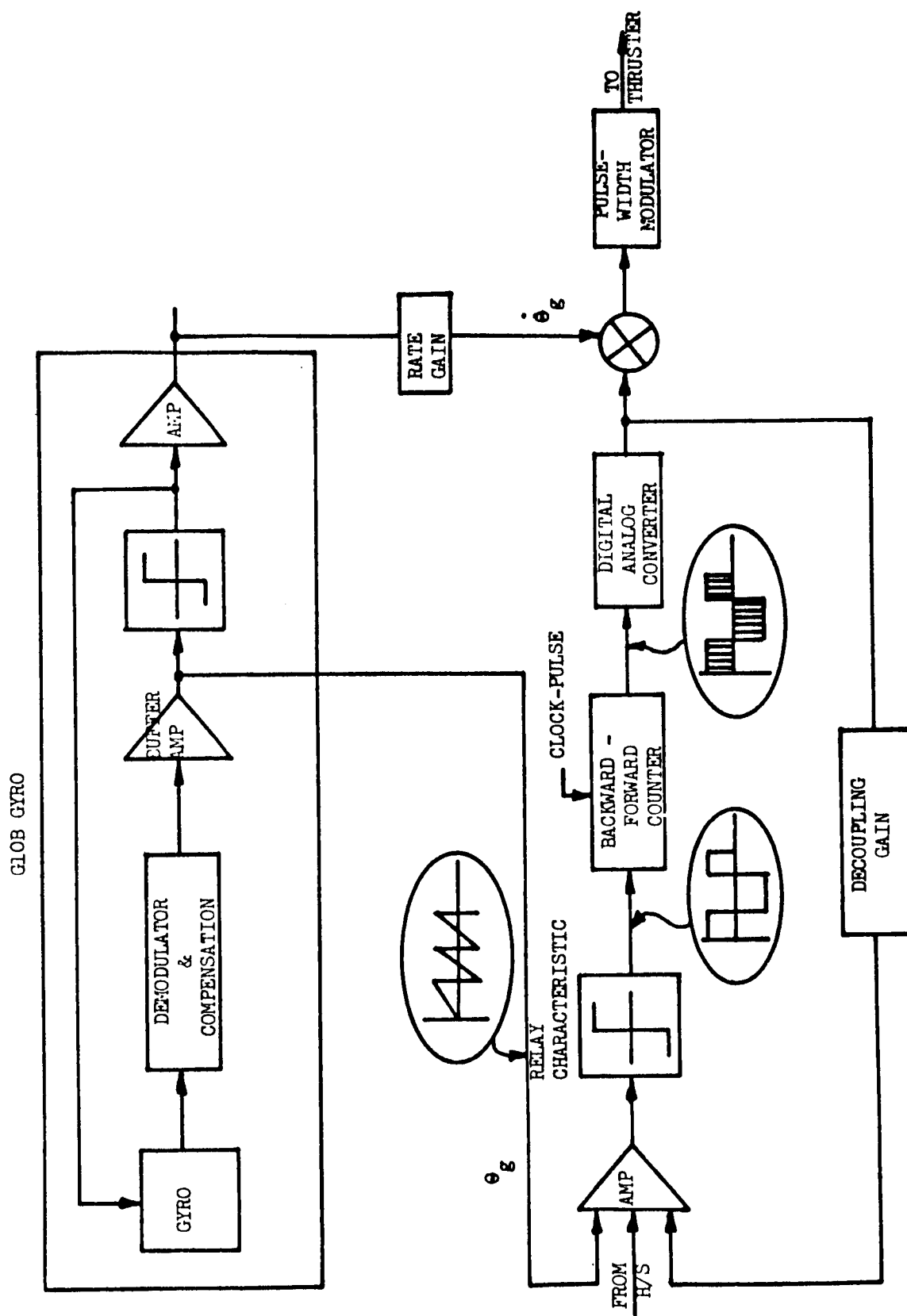


Fig. 6-12 Coarse-Mode Control System



**Fig. 6-13 Hybrid Integrator**

Pulse-width modulation is the method in which the modulator output, in response to a constant input, consists of a train of pulses whose frequency is fixed and independent of the input amplitude. The width of the pulse is varied in proportion to the input and varies from some preset minimum width up to the full pulse period. Because of the constant pulse frequency, the modulation factor is directly proportional to the pulse width. The pulse-width, pulse-frequency characteristics are shown in Fig. 6-14.

The inverse modulator is used during initial station acquisition and station change thrusting with 1-lb hydrazine thrusters. By the use of inverse modulation, the hydrazine thrusters can control torques resulting from thrust misalignment or differences in thrust levels. Thus, with inverse modulation, attitude control impulse is derived from the translational thrusters, and it is not necessary to increase the thrust level of the resistance jets to accommodate hardware uncertainties in the hydrazine system. Implementation of the inverse modulator requires two additions to the ascent on-orbit control system:

- Biasing of the hysteresis circuits (i.e., bias the pitch channel for east-west stationkeeping and the roll channel for north-south stationkeeping)
- Switching of the pulse-width modulator control from the resistance jets to the appropriate hydrazine thrusters

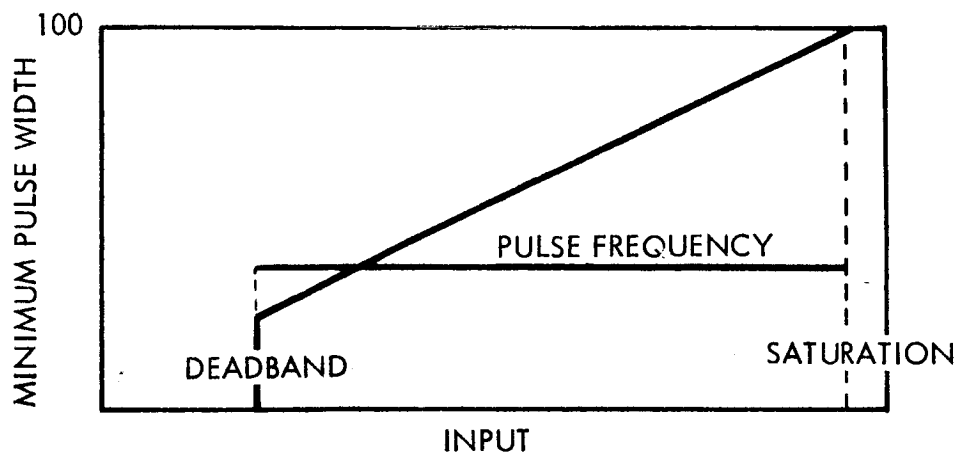


Fig. 6-14 Pulse-Width Modulator Characteristics

It should be noted that yaw attitude remains under resistance jet control. Figure 6-15 is a simplified block diagram of the inverse modulator. In this figure, the biases are just sufficient to trigger the hysteresis circuits. If there is a positive attitude error ( $+\theta$ ), gas valve 1 would be left on but the  $+\theta$  signal would trigger the negative hysteresis off and shut down gas valve 2, and the attitude will be driven back to null. When  $\theta$  is zero, gas valve 2 will again turn on. At the conclusion of station acquisition or change maneuver, control will be switched back to the resistance jet system.

Resistance Jet Coupling. Roll and yaw are dynamically coupled through the resistance jet thrusters. An impulse from one roll-yaw valve gives a torque in both the roll and yaw axes. No attempt is made to couple the pitch valves since they are dynamically uncoupled. An impulse in a pitch valve gives torque only about the pitch axis. Roll and yaw are dynamically coupled through the orbital rate.

Figure 6-4 shows that the output of pitch resistance jets Nos. 2 and 5 whose valves are activated only when the error signal is greater than the deadband. Thus, for a positive-pitch error, valve 5 is activated, and a negative error activates valve 2.

Figure 6-4 shows the coupling of the roll and yaw gas valves. There are no pure roll or pure yaw thrusters. The roll-yaw thrusters are actuated on the sum and difference of the attitude error. For an understanding of how the roll-yaw coupled-gas valves function, consider Fig. 6-4 and the following three cases:

- Case 1: A positive yaw error ( $\psi$ ) alone fires valves 3 and 6, while a negative yaw error would fire 2 and 4.
- Case 2: A positive roll ( $\phi$ ) alone fires valves 3 and 4, while a negative roll error fires 1 and 6.
- Case 3: If a positive yaw error (3 and 6) and a negative roll error (1 and 6) occur simultaneously, valve 6 and either 1, 3, or neither fire, depending on relative size of the roll and yaw errors  
(i. e., 1 valve if  $(\phi + \psi) < -0.25$  deg; 3 valve if  $(\phi + \psi) > -0.25$  deg; neither if  $-0.25 \text{ deg} < (\phi + \psi) < 0.25 \text{ deg}$ ).

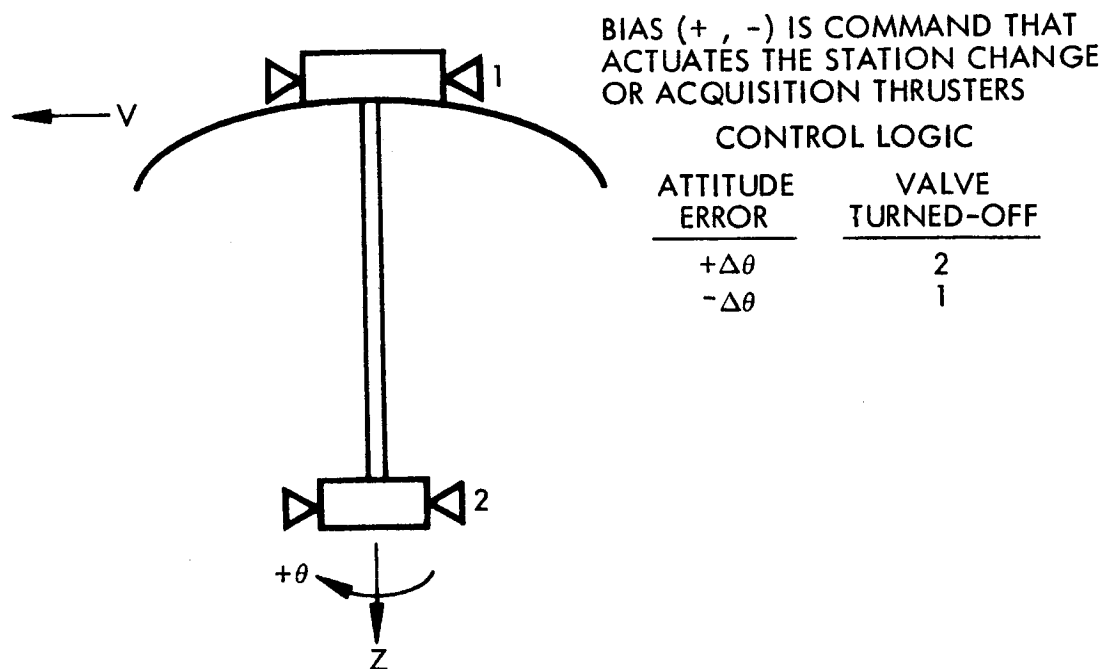
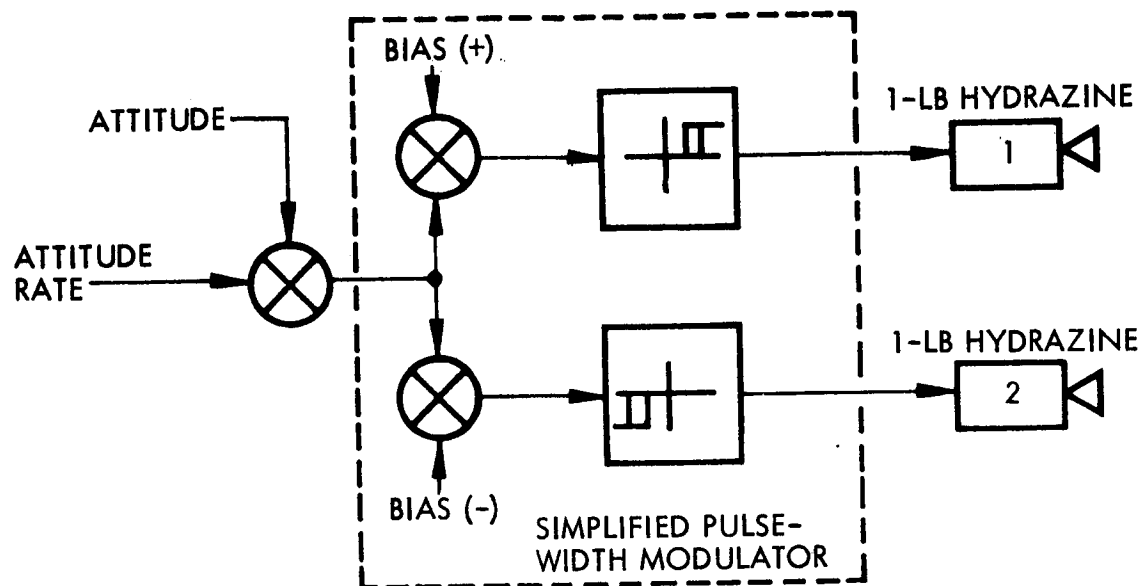


Fig. 6-15 Inverse Modulation Block Diagram

Cross-coupling performance is a function of vehicle inertia and thruster lever-arm ratios. This technique has been found to give improved attitude and gas-expenditure performance.

An analysis has been performed to determine attitude errors that can be expected from the coarse attitude control system during ascent-coast and on-orbit operations. The analysis considered the steady-state attitude errors that result from gyro drift, horizon sensor errors, deadband uncertainty, payload misalignment, power-supply variations, and null shift due to aging. The steady-state attitude-error contributions are tabulated in Table 6-6.

Substitution of numerical values (Table 6-7) results in pitch and roll errors of 0.2 deg and yaw errors of 0.880 deg. Gyro drift rates represent bias trimmed values. Uncorrected drift rates for the recommended gyro are 1.0 deg/hr. With this higher drift rate, the yaw attitude error would be approximately 4.46 deg; pitch and roll errors would be increased a negligible amount.

The effects of noise on the control system have been considered both analytically and with an analog simulation. Roll and yaw response to noise introduced at the horizon sensor has been studied; the integrator output does not indicate that  $\theta_c$ ,  $\phi_c$ ,  $\psi_c$  (commanded attitude) can be realized instantaneously but rather that  $\phi_c$  can be obtained without error. The attitude response due to noise is

$$\frac{\theta(S)}{\theta_N(S)} = \frac{K_\theta}{S + K_\theta}$$

$$\frac{\psi(S)}{\phi_N(S)} = \pm \frac{\frac{K_\phi}{K_\psi} \left( \frac{K_\psi}{K_\phi \omega_o} S - 1 \right)}{\frac{S^2}{\omega_o K_\psi} + \frac{K_\phi S}{\omega_o K_\psi} + 1}$$

Table 6-6  
ATTITUDE-ERROR SOURCES

Parameter	Contribution <sup>(a)</sup>	Parameter	Contribution <sup>(a)</sup>
<b>Pitch</b>		<b>Yaw (Continued)</b>	
Pitch Gyro Drift	$\frac{\dot{\theta}_d}{K_{HS\theta}}$	Limit-Cycle Amplitude	$\frac{\psi_{DB}}{\sqrt{3}}$
Pitch Torque Accuracy	$\frac{k\omega_o}{K_{HS\theta}}$	Horizon-Sensor Misalignment	$\frac{K_{HS\phi}}{\omega_o + K_{HS\psi}} \phi_{HS}$
Pitch Eccentricity Error	$\frac{\omega_o - \dot{\theta}_p}{K_{HS\theta}}$	Roll Gyro Misalignment	$\phi_\epsilon$
Limit-Cycle Amplitude	$\frac{\theta_{DB}}{\sqrt{3}}$	Yaw Gyro Misalignment	$\frac{K_{HS\phi}}{\omega_o + K_{HS\psi}} \psi_\epsilon$
Horizon-Sensor Error	$\epsilon_{HS}$	Payload Misalignment	$\psi_{PL}$
Horizon Uncertainty	$\frac{\epsilon_H}{2}$		
Horizon-Sensor Misalignment	$\theta_{HS}$	<b>Roll</b>	
Payload Misalignment	$\theta_{PL}$	Yaw Gyro Drift	$\frac{\dot{\psi}_d}{\omega_o + K_{HS\psi}}$
		Yaw Gyro Misalignment	$\frac{\omega_o \psi_\epsilon}{\omega_o + K_{HS\psi}}$
<b>Yaw</b>		Limit-Cycle Amplitude	$\frac{\phi_{DB}}{\sqrt{3}}$
Roll Gyro Drift	$\frac{\dot{\phi}_d}{\omega_o}$	Horizon-Sensor Error	$\epsilon_{HS}$
Yaw Gyro Drift	$\frac{K_{HS\phi}}{\omega_o (\omega_o + K_{HS\psi})} \dot{\psi}_d$	Horizon Uncertainty	$\frac{\epsilon_H}{2}$
Horizon-Sensor Error	$\frac{K_{HS\phi}}{\omega_o + K_{HS\psi}} \epsilon_{HS}$	Horizon-Sensor Misalignment	$\phi_{HS}$
Horizon Uncertainty	$\frac{K_{HS\phi}}{\omega_o + K_{HS\psi}} \epsilon_H$	Payload Misalignment	$\phi_{PL}$

(a) Symbols are as follows:

$K_{HS\phi}$ , $K_{HS\dot{\theta}}$ , $K_{HS\psi}$	gyro torquing gain (1/3, 1, 2/3 deg/min/deg)	$\theta_p$	pitch-program rate ( $0.735 \times 10^{-4}$ radian/sec)
$\phi_{DB}$ , $\theta_{DB}$ , $\psi_{DB}$	deadband (0.25 deg)	$\phi_{HS}$ , $\theta_{HS}$	horizon-sensor misalignment (0.02 deg)
$\phi_d$ , $\theta_d$ , $\psi_d$	gyro drift rate (0.2 deg/hr)	$\phi_{PL}$ , $\theta_{PL}$ , $\psi_{PL}$	payload misalignment (0.0005 deg)
$\omega_o$	orbit rate ( $0.735 \times 10^{-4}$ radian/sec)	k	pitch torquing accuracy (0.1 percent)
$\phi_\epsilon$ , $\psi_\epsilon$	gyro misalignment (0.228 deg)	$\epsilon_{HS}$	horizon-sensor error (0.08 deg)
		$\epsilon_H$	horizon uncertainty (0.166 deg)

Table 6-7

## ASCENT COAST AND ON-ORBIT ATTITUDE ERRORS, COARSE SYSTEM

Parameter	Three-Sigma Error (Deg)	Parameter	Three-Sigma Error (Deg)
Pitch		Yaw (Continued)	
Pitch Gyro Drift	0.00333	Power-Supply Variations	0.0500
Pitch Torquing Accuracy	0.000254	Horizon-Sensor Misalignment	0.0099
Pitch Eccentricity Error	—	Roll Gyro Misalignment(a)	0.2280
Horizon Sensor Error	0.0800	Yaw Gyro Misalignment(a)	0.1140
Horizon Uncertainty	0.0083	Payload Misalignment(a)	0.0005
Deadband Uncertainty	0.1445	Null Shift Due to Aging(a)	<u>0.1000</u>
Power-Supply Variations	0.0500	Total	0.8800
Payload Misalignment(a)	0.0005		
Null Shift Due to Aging(a)	0.1000	Roll	
Horizon-Sensor Misalignment(a)	<u>0.0200</u>	Yaw Gyro Drift	0.0050
Total	0.2002	Horizon-Sensor Error	0.0800
		Horizon Uncertainty	0.0166
Yaw		Deadband Uncertainty	0.1446
Roll Gyro Drift	0.7480	Power-Supply Variations	0.0500
Yaw Gyro Drift	0.3570	Horizon-Sensor Misalignment	0.0200
Horizon-Sensor Error (Roll)	0.0400	Yaw Gyro Misalignment	0.0015
Horizon Uncertainty	0.0084	Payload Misalignment	0.0005
Deadband Uncertainty	0.1445	Null Shift Due to Aging	<u>0.1000</u>
		Total	0.2002

(a) Alignment type errors.



$$\frac{\phi(S)}{\phi_N(S)} = - \frac{\frac{K_\phi}{K_\psi \omega_o} S + 1}{\frac{S^2}{\omega_o K_\psi} + \frac{K_\phi S}{\omega_o K_\psi} + 1}$$

where  $S$  = Laplace operator.

From the foregoing three transfer functions, it can be seen that the high-frequency noise gains ( $G_{HF}$ ) are dependent on the horizon-sensor torquing gains  $K_\theta$ ,  $K_\psi$  and  $K_\phi$  (i. e.,  $G_{HF\theta} = K_\theta/\omega$ ;  $G_{HF\psi} = K_\psi/\omega$ ;  $G_{HF\phi} = K_\phi/\omega$ ). The static gains ( $G$ ) are  $G_\phi = G_\theta = 1$  and  $G_\psi = K_\phi/K_\psi$ . The pitch channel appears as a typical first-order lag to noise inputs. From the roll and yaw gain vs. frequency plots in Fig. 6-16, the noise gain peaks for a frequency band defined by  $\omega_o$  and  $K_\psi$ . Thus, any selection of gyrocompassing gains will be based on consideration of expected noise frequencies.

The effects of noise on the attitude control system were also studied on an analog computer. The results of this study were discussed earlier in this subsection and in Fig. 6-11. This figure shows the effects of introducing horizon sensor noise of 0.1 deg rms (0.001 to 1.0 Hz). The figure shows that the noise is filtered heavily by the gyros and results in small attitude perturbations. This noise model represents a case worse than would ever be expected with either an A-OGO or thermopile edge-tracker horizon sensor.

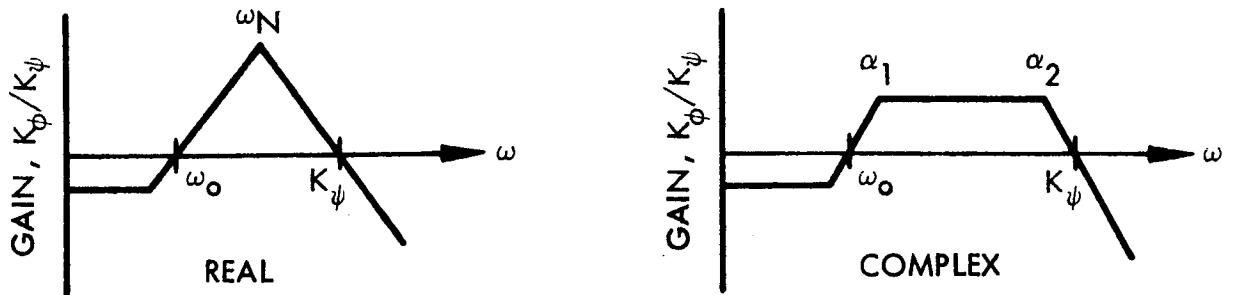


Fig. 6-16 Bode Plot With Real and Complex Second-Order Roots

Injection Motor Burn, Inertial Stabilization. The coarse attitude control system has the capability of stabilizing the spacecraft to an inertial reference frame. This ability is used during the injection-motor burn and can be employed to perform maneuvers and to hold off-nadir attitudes. Inertial stabilization employs rate gyros, hybrid integrators, pulse-width modulators, and hydrazine and resistance-jet actuation systems. These components, except the hydrazine thrusters, are the same ones used for the ascent-coast/on-orbit attitude control systems.

Attitude information is obtained by integrating the output of the rate gyro. The integrator output is summed with the rate signal from the gyro. This sum is pulse-width modulated to generate the driving functions for the actuation systems. In the inertially stabilized system, the hydrazine system is used during injection-motor burn. The resistance-jet system is used for attitude control during ascent coast and on orbit. Although the ion engines have been considered primarily as part of the fine control system, they also could be used in the inertially stabilized mode.

It should be noted that the inertial stabilization system does not employ gyrocompassing for updating of gyro drift. Thus, the rate at which attitude errors increase is proportional to the drift rate of the gyros. In a nonacceleration environment, this drift rate is 0.2 deg/hr if a drift trim bias is applied.

Injection errors due to the inertial attitude control system result from the errors from the orientation maneuver for injection-motor burn, g-sensitive gyro-drift errors during the burning time, and errors at beginning of the orientation maneuver.

Attitude errors generated during the orientation maneuver for apogee motor burn are listed in Table 6-8.

Table 6-8

## ORIENTATION FOR APOGEE MOTOR-BURN ATTITUDE ERRORS

Maneuver	Three-Sigma Gyro Torquing Error					
	Pitch		Roll		Yaw	
	(deg/hr)	(deg)	(deg/hr)	(deg)	(deg/hr)	(deg)
Pitch, 90 deg @ 3 deg/sec	9.75	0.081	14.9	0.124	14.9	0.124
Yaw, 53 deg @ 0.5 deg/sec	2.75	0.083	2.75	0.083	1.83	0.054
Total of RSS Error		0.1145		0.290		0.135

Single axis maneuvers were used for the computations in Table 6-8. More complicated maneuvers would have attendant cross-coupling reduction along certain axes. As an example, since torquer-axis misalignment produces cross-coupling errors, a pitch maneuver followed by (or occurring simultaneously with) a yaw maneuver will produce a smaller total yaw error than that which would have resulted from the pitch maneuver alone.

Injection errors associated with the apogee motor-burn result from g-sensitive gyro drifts. An acceleration-dependent error model can be written as follows:

$$\begin{aligned}\dot{\theta} &= -CA_{\theta} - DA_{\psi} - BA_{\phi}A_{\theta} + EA_{\phi}A_{\psi} + FA_{\phi}^2 \\ \dot{\phi} &= -CA_{\phi} - DA_{\psi} + BA_{\theta}A_{\phi} - EA_{\psi}A_{\theta} + FA_{\theta}^2 \\ \dot{\psi} &= CA_{\psi} - DA_{\phi} - BA_{\theta}A_{\psi} - EA_{\phi}A_{\phi} + FA_{\theta}^2\end{aligned}$$

where

$\theta, \phi, \psi$  = pitch, roll, and yaw body rates, respectively

$A_\theta, A_\phi, A_\psi$  = accelerations along vehicle axis

C = mass unbalance coefficient, 0.5 deg/hr-g

D = structural compliance coefficient, 0.5 deg/hr-g

B = gas bearing incompressibility coefficient, 0.6 deg/hr-g<sup>2</sup>

E = gas bearing compressibility coefficient 0.6 deg/hr-g<sup>2</sup>

F = axial g<sup>2</sup> sensitivity coefficient 0.002 deg/hr-g<sup>2</sup>

The error associated with each of the foregoing coefficients represents the standard deviation. The errors found in Table 6-8 are the 3 $\sigma$  values of g-sensitive gyro errors. The assumptions made in calculating the g-sensitive gyro errors are as follows:

- $A_{\phi_{ave}} = 3.715 \text{ g}$
- Thrust misalignment =  $\pm 0.25 \text{ deg}$
- Burn time = 64 sec for optimized kick motor\*
- Gyro rotor speed = 240 rps
- Thrust level = 9,000 lb
- Weight at ignition = 3,700 lb
- Weight at burnout = 1,800 lb

Since the g-sensitive drift coefficients are well behaved in the G10B gyro, they could be reduced further by torquing the gyro during the apogee motor burn as a function of the vehicle acceleration. It should be noted that this analysis was performed for the optimized kick motor. The actual errors will be less than those stated because the recommended kick motor has a shorter (42 sec) burn time.

---

\* This analysis was based on the use of an injection motor optimized for the ATS-4 mission and launch vehicle. The use of the Delta motor, with its 42-sec burn time, would result in reduced values of the acceleration-sensitive drift errors.

The attitude errors at the start of the orientation maneuver are those due to the ascent coast control system. These errors are calculated earlier in this subsection. Table 6-9 is a tabulation of attitude control system injection errors.

Table 6-9

INJECTION ATTITUDE ERRORS

Phase	Pitch (deg)	Roll (deg)	Yaw (deg)
Coast Phase	0.200	0.200	0.880
Orientation for Apogee Motor Burn	0.115	0.146	0.135
Apogee Motor Burn	0.0029	0.098	0.098
Total of 3 sigma error	0.230	0.266	0.866

Injection errors are affected only slightly by the g-sensitive gyro drifts. The larger attitude uncertainty in yaw results from the initial yaw error at the start of the orientation maneuvers.

Flexibility Effects. The dynamic flexibility effects are the oscillation of the structure caused by external forces on the system. The principal excitations are due to force impulses from the control system and the orbit adjust engine. Along with oscillation in the antenna line of sight, the structural elasticity can under certain circumstances also cause interaction with the control system to produce self-sustaining oscillations. The preliminary analysis has indicated that even though the minimum weight structure has a very low natural frequency, there are no significant flexibility effects related to the control system. This result is primarily due to the low level of forces that will be used in the system, the deadband nonlinearity, and the magnitude of limit-cycle periods.

The bending displacement at any vehicle station is the sum of all elastic modes. Each term in the sum is a product of the mode shape, which is a function of vehicle station location, times a time-varying dynamic term. System deflections are measured with respect to the elastic axis, which is defined along with the mode shapes in such a way that the lateral and angular momentum contributions due to bending oscillations of the distributed structure are identically zero. The line of the elastic axis will shift and rotate as a rigid axis. The general displacement,  $u$  and rotation  $u'$  from the elastic axis are:

$$u = \sum_{i=1}^{\infty} \phi_i(Z) q(t)$$

and

$$u' = \sum_{i=1}^{\infty} \phi_i'(Z) q(t)$$

where  $\phi_i(Z)$  is the  $i$ th mode shape,  $\phi_i'(Z)$  is the slope of that shape, and  $q(t)$  is a dimensionless time-varying oscillating factor.

The attitude measured by the control system is

$$\bar{\theta} = |\theta| - \phi'(Z) q(t)$$

where  $|\theta|$  is the rotation of the elastic axis and  $\phi'$  is the mode slope at the end of the feed.

From structural analysis of the modal dynamics, the generalized mass of this system is found to be  $M_B = 0.577 \text{ lb-in-sec}^2$ , and the natural frequency,  $\omega_B$ , is 1.2 radian/sec. This mode shape was derived as explained in subsection 5.3.2.

The system differential equations consist of the rigid-body equation describing the rotation of the elastic axis and a bending excitation equation for each mode considered. At the present time, only the lowest bending frequency has been included in the control-system analysis. Higher modes generally have smaller amplitudes and are further attenuated by the electronic filters in the system. The rigid-body equation is:

$$I |\ddot{\theta}| = \tau_{\text{ext}}$$

and the bending equation is:

$$M_B (\ddot{q} + \omega_B^2 q) = \phi_1 F_1 + \phi_2 F_2$$

where  $I$  is the total vehicle inertia about the center of mass and  $\tau_{\text{ext}}$  is the external torque on the system including gas valve forces and solar disturbances. The coefficients of the forcing function in the bending equation are the modal deflections at the point of application of the control and orbit adjust jets. In general, the righthand side of the bending equation represents the virtual work of the forcing function on the mode shape per unit of the bending coordinate  $q$ .

Figure 6-17 is a block diagram of the control system with one bending mode.

The transfer function of the bending coordinate to the forcing functions is in the form of a simple harmonic oscillator. Since the control and adjust forces are known to be in the form of impulses and steps, the peaks of the bending transients can be calculated in closed form. The modal characteristics giving deflections and slopes are based on system structural analysis.

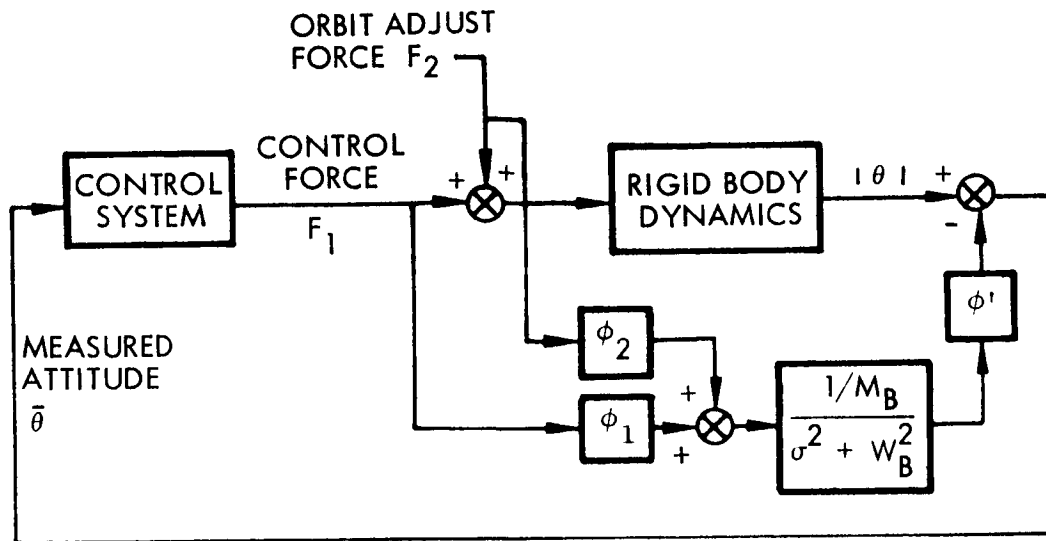


Fig. 6-17 Control System Block Diagram With Single Bending Mode

For an impulse in the control force  $F_1$  at the feed, lasting for  $\Delta t$  sec, the bending response at that location is:

$$\bar{\theta} = \frac{F_1 \Delta t}{M_B W_B} \phi_1 \phi_1' \sin W_B t \text{ (radians)}$$

For  $F_1 = 0.002$  lb and the minimum impulse bit corresponding to 0.02 sec, and the assumed modal characteristics given earlier, the angular amplitude is  $11.4 \times 10^{-10}$  deg, which is negligible. This oscillation is reduced in time by structural damping. A step-forcing function from the orbit adjust jet of 1.0 lb hydrazine thrust gives a transient response of

$$\theta = \frac{F_2 \phi_2 \phi_1'}{M_B \omega_B^2} (1 - \cos \omega_B t) \text{ (radians)}$$



which also will be damped in time. The force  $F_2$  is applied at the equipment section in the parabola. The maximum amplitude of this bending motion is  $2 \times 10^{-3}$  deg. This transient eventually damps to a steady state value of  $1 \times 10^{-3}$ . From the two foregoing equations it can be seen that the transients are amplified with any reduction in the structural stiffness that cuts the natural frequency of the bending dynamics. The impulsive response of the basic control system varies inversely with  $\omega_B$  but the orbit adjust transients go inversely with the square of the bending frequency.

The small size of the transient peaks indicates that there is little possibility of noticeable interaction between the flexibility dynamics and the operation of the control system. However, any final flexural stability analysis must be reviewed with an analog computer simulation of the complete closed-loop control system and a detailed dynamic flexibility model. This analysis will determine the control system stability in the presence of translational, lateral, and torsional disturbances on the antenna structures. Also, the study will show what structural damping is required. Studies are underway with nonhomogeneous boom materials and energy-absorbing joints that can supply the necessary damping.

#### 6.1.5 Functional Analytic Description – Fine Attitude Control System

The fine attitude control system consists of an interferometer for attitude determination, an adaptive autopilot to optimize limit cycle operation, and ion engines for actuation. A block diagram of the system is shown in Fig. 6-18. The interferometer and adaptive autopilot are discussed below; the ion engines are discussed in subsection 5.5.5.

Attitude Sensing. The three-axis attitude sensing by the interferometer requires two ground stations. If only one ground station is available, pitch and roll information can be obtained and yaw would come from either the yaw gyro of the coarse attitude control system or through polarization of the ground station signal. The fine attitude control system can stabilize the vehicle without using the interferometer if the inertial

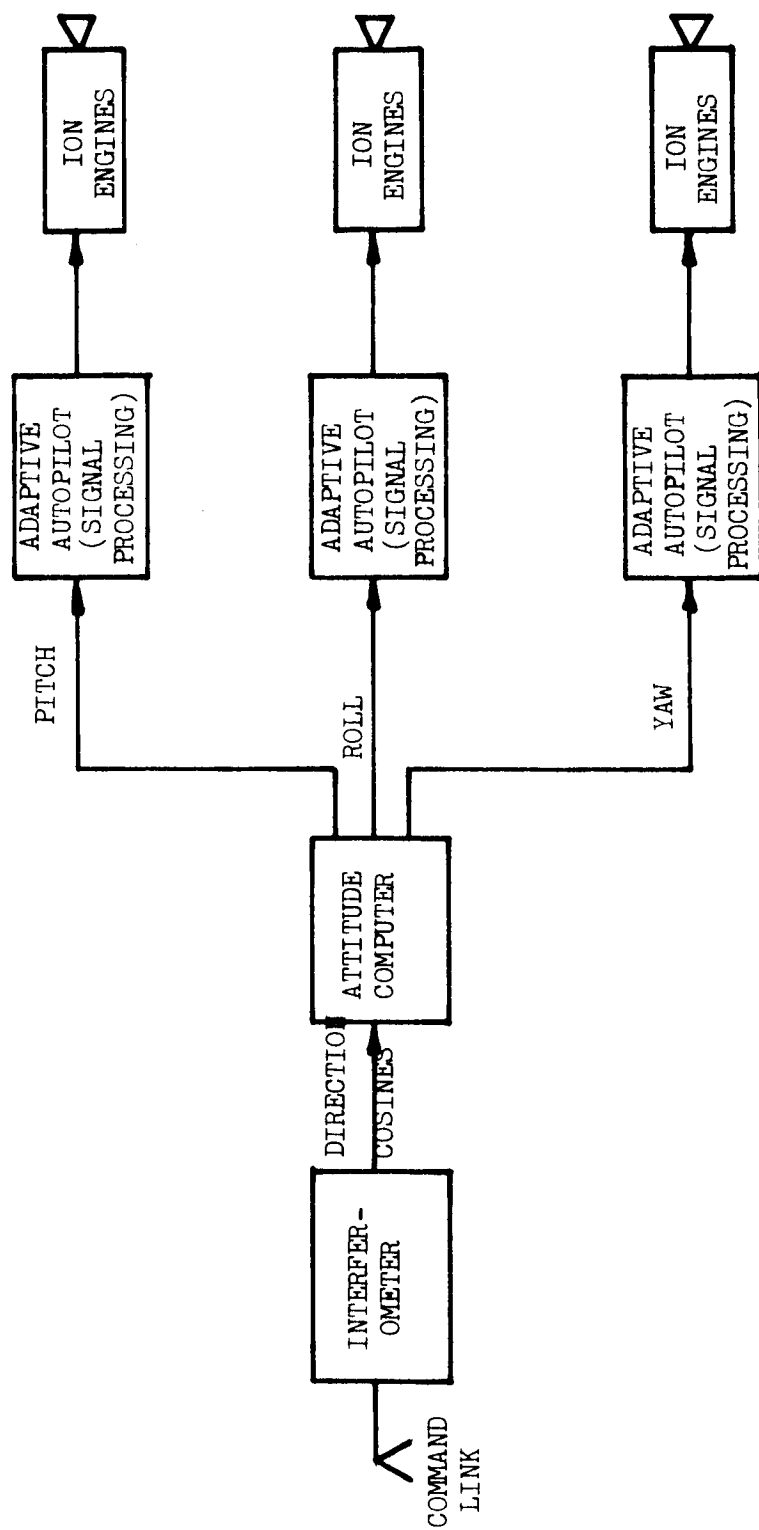


Fig. 6-18 Block Diagram of Fine Attitude-Control System

reference package and hybrid integrator are used to drive the adaptive autopilot. Gyro updating can then be done on a periodic basis with the interferometer. This technique frees the ground station for other functions during those periods when the ATS-4 is not being used.

The interferometer furnishes extremely accurate attitude information ( $\pm 76$  sec). The outputs of the interferometer are direction cosines of the line-of-sight (LOS) vectors to the ground stations. See Fig. 6-19. By using two ground stations, three-axis attitude information can be obtained.

A block diagram of the proposed interferometer attitude sensing system is shown in Fig. 6-20. The reference coordinate transformation, performed on the ground, changes the direction cosines of the LOS vectors from the satellite to stations 1 and 2 into a new coordinate system defined by the commanded vehicle attitude,  $\phi_c$ ,  $\theta_c$ , and  $\psi_c$ . The attitude control system then aligns the vehicle to this new coordinate set.

In Fig. 6-20 the block labeled Interferometer Transformation combines the direction cosines of the LOS vectors in the  $\phi_c$ ,  $\theta_c$ ,  $\psi_c$  (commanded) coordinate system and the vehicle coordinates to form the error signals for the attitude control system. These error signals, representing the Euler angles between the commanded vehicle attitude and the actual attitude, can be generated on-board the satellite by receiving orbital coordinate information via a ground radio link.

To use the direction cosine outputs of the interferometer, it is necessary to develop a transformation that relates them to the vehicle position relative to some reference coordinate system.

This transformation will be

$$\begin{bmatrix} X_2 \\ Y_2 \\ Z_2 \end{bmatrix} = [A] \begin{bmatrix} X_1 \\ Y_1 \\ Z_1 \end{bmatrix} \quad (6.1)$$

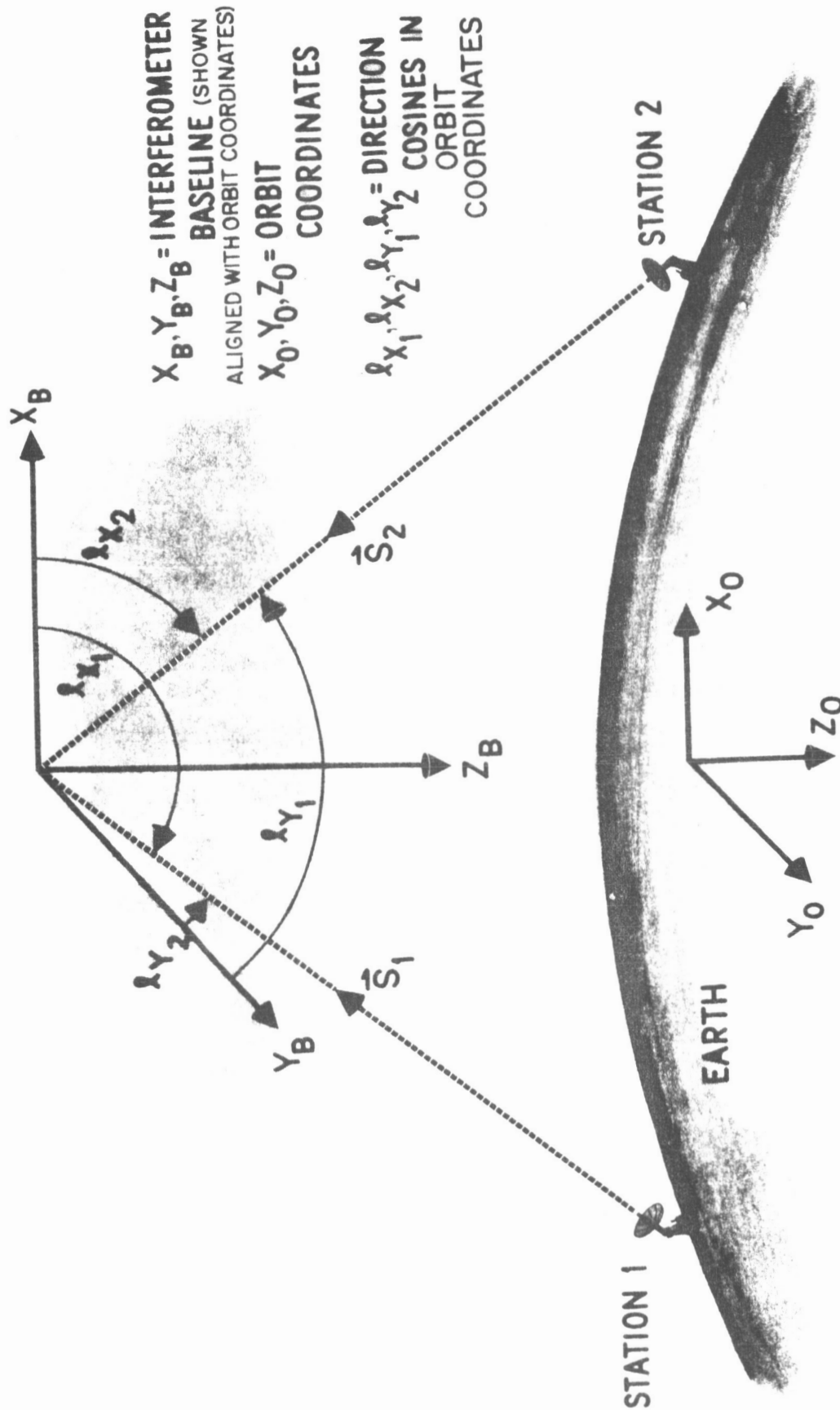


Fig. 6-19 Interferometer Geometry

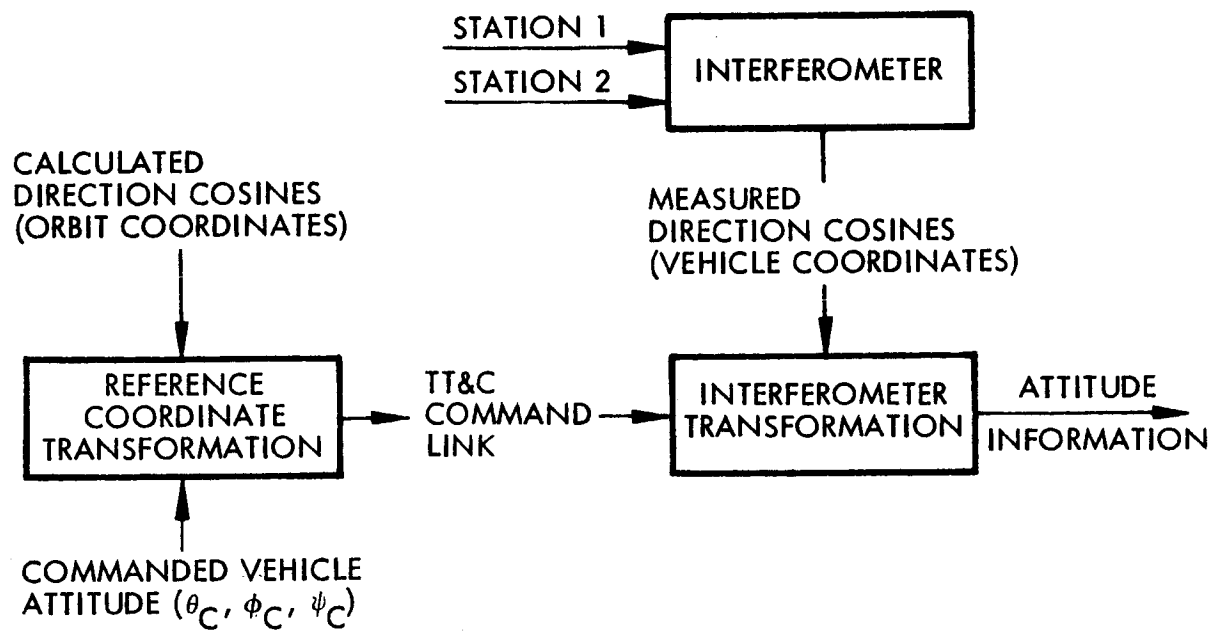


Fig. 6-20 Interferometer Attitude Measurement

where

[A] = required transformation  
 $X_1, Y_1, Z_1$  = reference (orbital) coordinate frame  
 $X_2, Y_2, Z_2$  = vehicle coordinate frame

An intermediate coordinate frame  $X_3, Y_3, Z_3$  can be formed so that

$$\begin{bmatrix} X_1 \\ Y_1 \\ Z_1 \end{bmatrix} = [B] \begin{bmatrix} X_3 \\ Y_3 \\ Z_3 \end{bmatrix} \quad (6.2)$$

and

$$\begin{bmatrix} X_2 \\ Y_2 \\ Z_2 \end{bmatrix} = [C] \begin{bmatrix} X_3 \\ Y_3 \\ Z_3 \end{bmatrix} \quad (6.3)$$

Solving for  $X_3, Y_3, Z_3$  in Eq. (6.2) and substituting in Eq. (6.3) yields

$$\begin{bmatrix} X_2 \\ Y_2 \\ Z_2 \end{bmatrix} = [C][B]^T \begin{bmatrix} X_1 \\ Y_1 \\ Z_1 \end{bmatrix}$$

The intermediate coordinate frame is formed by taking vector products of the LOS vectors  $\bar{S}_1$  and  $\bar{S}_2$  to obtain three orthogonal vectors:

$$\begin{aligned} \bar{P} &= \bar{S}_2 \\ \bar{U} &= \bar{S}_1 \times \bar{S}_2 \\ \bar{V} &= \bar{S}_2 \times [\bar{S}_1 \times \bar{S}_2] \end{aligned}$$

The three orthogonal vectors forming the intermediate coordinate frame are

$$\begin{aligned}
 X_3 &= \frac{\bar{S}_2}{|\bar{S}_2|} = \hat{P}^{(3)} \\
 Y_3 &= \frac{\bar{S}_1 \times \bar{S}_2}{|\bar{S}_1 \times \bar{S}_2|} = \hat{U}^{(3)} \\
 Z_3 &= \frac{\bar{S}_2 \times [\bar{S}_1 \times \bar{S}_2]}{|\bar{S}_2 \times [\bar{S}_1 \times \bar{S}_2]|} = \hat{V}^{(3)}
 \end{aligned} \tag{6.4}$$

When the same set of cross-products are performed in reference frame (1), then

$$\begin{aligned}
 \bar{P}^{(1)} &= \bar{S}_1^{(1)} \\
 \bar{U}^{(1)} &= \bar{S}_1^{(1)} \times \bar{S}_2^{(1)} \\
 \bar{V}^{(1)} &= \bar{S}_2^{(1)} \times \bar{S}_1^{(1)} \times \bar{S}_2^{(1)}
 \end{aligned}$$

where

$$\bar{S}_1^{(1)} = \bar{S}_1 \text{ coordinatized in the reference frame}$$

$$\bar{S}_2^{(1)} = \bar{S}_2 \text{ coordinatized in the vehicle frame}$$

form

$$\begin{aligned}
 x_1 &= \frac{\bar{s}_2^{(1)}}{|\bar{s}_2|} = \hat{p}^{(1)} \\
 y_1 &= \frac{\bar{u}^{(1)}}{|\bar{u}^{(1)}|} = \hat{u}^{(1)} \\
 z_1 &= \frac{\bar{v}^{(1)}}{|\bar{v}^{(1)}|} = \hat{v}^{(1)}
 \end{aligned}
 \tag{6.5}$$

Again taking the cross-products coordinatized in vehicle frame (2) yields

$$\begin{aligned}
 \bar{p}^{(2)} &= \bar{s}_2^{(2)} \\
 \bar{u}^{(2)} &= \bar{s}_1^{(2)} \times \bar{s}_2^{(2)} \\
 \bar{v}^{(2)} &= \bar{s}_2^{(2)} \times [\bar{s}_1^{(2)} \times \bar{s}_2^{(2)}]
 \end{aligned}$$

where  $\bar{s}_1^{(2)}$  and  $\bar{s}_2^{(2)}$  represent the vectors  $\bar{s}_1$  and  $\bar{s}_2$  coordinated in the vehicle frame

$$\begin{aligned}
 x_2 &= \frac{\bar{s}_2^{(2)}}{|\bar{s}_2|} = \hat{p}^{(2)} \\
 y_2 &= \frac{\bar{u}^{(2)}}{|\bar{u}^{(2)}|} = \hat{u}^{(2)} \\
 z_2 &= \frac{\bar{v}^{(2)}}{|\bar{v}^{(2)}|} = \hat{v}^{(2)}
 \end{aligned}
 \tag{6.6}$$



Using the information in Eqs. (6.2 ) through (6.6 ),

$$\hat{P}^{(1)} = [B] \hat{P}^{(3)} = [B] \begin{bmatrix} 1 \\ 0 \\ 0 \end{bmatrix}$$

$$\hat{U}^{(1)} = [B] \hat{U}^{(3)} = [B] \begin{bmatrix} 0 \\ 1 \\ 0 \end{bmatrix}$$

$$\hat{V}^{(1)} = [B] \hat{V}^{(3)} = [B] \begin{bmatrix} 0 \\ 0 \\ 1 \end{bmatrix}$$

Noting that the intermediate coordinate frame is a set of unit vectors

$$[B] = [\hat{P}^{(1)}, \hat{U}^{(1)}, \hat{V}^{(1)}] \quad (6.7)$$

Also, the same process can be made with the vehicle coordinates.

$$\hat{P}^{(2)} = [C] \hat{P}^{(3)} = [C] \begin{bmatrix} 1 \\ 0 \\ 0 \end{bmatrix}$$

$$\hat{U}^{(2)} = [C] \hat{P}^{(3)} = [C] \begin{bmatrix} 0 \\ 1 \\ 0 \end{bmatrix}$$

$$\hat{V}^{(2)} = [C] \hat{P}^{(3)} = [C] \begin{bmatrix} 0 \\ 0 \\ 1 \end{bmatrix}$$

which yields

$$[C] = [\hat{P}^{(2)}, \hat{U}^{(2)}, \hat{V}^{(2)}] \quad (6.8)$$

By using Eqs. (6.1) and (6.7), the transformation  $[A]$  can be obtained relating the vehicle position to the reference (orbital) coordinate frame. It is also observed that the Euler angle relationship is

$$\begin{bmatrix} X_2 \\ Y_2 \\ Z_2 \end{bmatrix} = \begin{bmatrix} \cos \psi \cos \theta & \sin \psi \cos \theta & -\sin \theta \\ & \sin \phi \cos \theta & \\ & \cos \phi \cos \theta & \end{bmatrix} \begin{bmatrix} X_1 \\ Y_1 \\ Z_1 \end{bmatrix}$$

Combining elements of the two representations of  $[A]$  and solving for the Euler angles  $\theta, \phi, \psi$  gives, for small angle approximations

$$\theta = -(b_{31} c_{11} + c_{32} c_{12} + b_{33} c_{13})$$

$$\phi = b_{31} c_{21} + b_{32} c_{22} + b_{33} c_{23}$$

$$\psi = b_{21} c_{11} + b_{22} c_{12} + b_{23} c_{13}$$

Calculation of the Euler angles  $(\theta, \phi, \psi)$  requires only the determination of certain elements of the  $[B]$  and  $[C]$  matrix. Defining the direction cosines of the two LOS vectors in the reference and the vehicle coordinates as

$\ell_{X_i}, \ell_{Y_i}, \ell_{Z_i}$  = direction cosines of LOS in reference coordinates;  $i = 1, 2$   
ground stations

$m_{X_i}, m_{Y_i}, m_{Z_i}$  = direction cosines of LOS in vehicle defining  $[B] = [\hat{P}^{(1)}, \hat{U}^{(1)}, \hat{V}^{(1)}]$  coordinates;  $i = 1, 2$  ground stations

The cross-product vectors for the [B] matrix are

$$\overline{P}^{(1)} = \begin{bmatrix} \ell_{X_1} \\ \ell_{Y_1} \\ \ell_{Z_1} \end{bmatrix}$$

$$\overline{U}^{(1)} = \begin{bmatrix} \ell_{X_1} \\ \ell_{Y_1} \\ \ell_{Z_1} \end{bmatrix} \times \begin{bmatrix} \ell_{X_2} \\ \ell_{Y_2} \\ \ell_{Z_2} \end{bmatrix} = \begin{bmatrix} \ell_{Y_1} \ell_{Z_2} - \ell_{Y_2} \ell_{Z_1} \\ \ell_{X_2} \ell_{Z_1} - \ell_{X_1} \ell_{Z_2} \\ \ell_{X_1} \ell_{Y_2} - \ell_{X_2} \ell_{Y_1} \end{bmatrix} = \begin{bmatrix} U_X^{(1)} \\ U_Y^{(1)} \\ U_Z^{(1)} \end{bmatrix}$$

$$\overline{V}^{(1)} = \begin{bmatrix} \ell_{X_2} \\ \ell_{Y_2} \\ \ell_{Z_2} \end{bmatrix} \times \begin{bmatrix} U_X^{(1)} \\ U_Y^{(1)} \\ U_Z^{(1)} \end{bmatrix} = \begin{bmatrix} \ell_{Y_2} U_Z^{(1)} - \ell_{Z_2} U_Y^{(1)} \\ \ell_{Z_2} U_X^{(1)} - \ell_{X_2} U_Z^{(1)} \\ \ell_{Z_2} U_Y^{(1)} - \ell_{Y_2} U_X^{(1)} \end{bmatrix} = \begin{bmatrix} \overline{V}_X^{(1)} \\ \overline{V}_Y^{(1)} \\ \overline{V}_Z^{(1)} \end{bmatrix}$$

Then

$$\hat{P}^{(1)} = \begin{bmatrix} \ell_{X_1} \\ \ell_{Y_1} \\ \ell_{Z_1} \end{bmatrix}$$

$$\hat{U}^{(1)} = \frac{\begin{bmatrix} \ell_{Y_1} & \ell_{Z_2} & -\ell_{Y_2} & \ell_{Z_1} \\ \ell_{X_2} & \ell_{Z_1} & -\ell_{X_1} & \ell_{Z_2} \\ \ell_{X_1} & \ell_{Y_2} & -\ell_{X_2} & \ell_{Y_1} \end{bmatrix}}{\sqrt{\left[\bar{U}_X^{(1)}\right]^2 + \left[\bar{U}_Y^{(1)}\right]^2 + \left[U_Z^{(1)}\right]^2}}$$

$$\hat{V}^{(1)} = \frac{\begin{bmatrix} \ell_{Y_2} & U_Z^{(1)} - \ell_{Z_2} & U_Y^{(1)} \\ \ell_{Z_2} & U_X^{(1)} - \ell_{X_1} & U_Z^{(1)} \\ \ell_{X_2} & U_Y^{(1)} - \ell_{Y_2} & U_X^{(1)} \end{bmatrix}}{\sqrt{\left[V_X^{(1)}\right]^2 + \left[V_Y^{(1)}\right]^2 + \left[V_Z^{(1)}\right]^2}}$$

and for the [C] matrix

$$\hat{P}^{(2)} = \begin{bmatrix} m_{X_1} \\ m_{Y_1} \\ m_{Z_1} \end{bmatrix}$$

$$\hat{U}^{(2)} = \frac{\begin{bmatrix} m_{Y_1} & m_{Z_2} & -m_{Z_1} & m_{Y_2} \\ m_{X_2} & m_{Z_1} & -m_{X_1} & m_{Z_2} \\ m_{X_1} & m_{Y_1} & -m_{X_2} & m_{Y_1} \end{bmatrix}}{\sqrt{\left[U_X^{(2)}\right]^2 + \left[U_Y^{(2)}\right]^2 + \left[U_Z^{(2)}\right]^2}}$$

$$\hat{V}^{(2)} = \frac{\begin{bmatrix} m_{Y_2} U_Z^{(2)} - m_{Z_2} U_Y^{(2)} \\ m_{Z_2} U_X^{(2)} - m_{X_2} U_Z^{(2)} \\ m_{X_2} U_Y^{(2)} - m_{Y_2} U_X^{(2)} \end{bmatrix}}{\sqrt{[V_X^{(2)}]^2 + [V_Y^{(2)}]^2 + [V_Z^{(2)}]^2}}$$

Now evaluating the necessary elements of the B and C matrix

$$b_{21} = \ell_{Y_2}$$

$$b_{31} = \ell_{Z_2}$$

$$b_{22} = \frac{\ell_{X_2} \ell_{Z_1} - \ell_{X_1} \ell_{Z_2}}{\sqrt{[U_X^{(1)}]^2 + [U_Y^{(1)}]^2 + [U_Z^{(1)}]^2}}$$

$$b_{32} = \frac{\ell_{X_1} \ell_{Y_2} - \ell_{X_2} \ell_{Y_1}}{\sqrt{[U_X^{(1)}]^2 + [U_Y^{(1)}]^2 + [U_Z^{(1)}]^2}}$$

$$b_{23} = \frac{\ell_{X_2}^2 \ell_{Y_1} + \ell_{Y_1} \ell_{Z_2}^2 - \ell_{X_1} \ell_{X_2} \ell_{Y_2} - \ell_{Y_2} \ell_{Z_1} \ell_{Z_2}}{\sqrt{[V_X^{(1)}]^2 + [V_Y^{(1)}]^2 + [V_Z^{(1)}]^2}}$$

$$b_{33} = \frac{\ell_{X_2}^2 \ell_{Z_1} + \ell_{Y_2}^2 \ell_{Z_1} - \ell_{Y_1} \ell_{Y_2} \ell_{Z_2} - \ell_{X_1} \ell_{X_2} \ell_{Z_2}}{\sqrt{[V_X^{(1)}]^2 + [V_Y^{(1)}]^2 + [V_Z^{(1)}]^2}}$$

$$c_{11} = m_{X_1}$$

$$c_{12} = \frac{m_{Y_1} m_{Z_2} - m_{Z_1} m_{Y_2}}{\sqrt{[U_X^{(2)}]^2 + [U_Y^{(2)}]^2 + [U_Z^{(2)}]^2}}$$

$$c_{13} = \frac{m_{X_1} m_{Y_2}^2 - m_{X_2} m_{Y_1} m_{Y_2} + m_{X_2} m_{Z_1} m_{Z_2} - m_{X_1} m_{Z_2}^2}{\sqrt{[V_X^{(2)}]^2 + [V_Y^{(2)}]^2 + [V_Z^{(2)}]^2}}$$

$$c_{21} = m_{Y_2}$$

$$c_{22} = \frac{m_{X_2} m_{Z_1} - m_{X_1} m_{Z_2}}{\sqrt{[U_X^{(2)}]^2 + [U_Y^{(2)}]^2 + [U_Z^{(2)}]^2}}$$

$$c_{23} = \frac{+ m_{X_2}^2 m_{Y_1} - m_{X_1} m_{X_2} m_{Y_2} - m_{Y_2} m_{Z_1} m_{Z_2} + m_{Y_1} m_{Z_2}^2}{\sqrt{[V_X^{(2)}]^2 + [V_Y^{(2)}]^2 + [V_Z^{(2)}]^2}}$$

Evaluation of the  $b_i$  elements is obtained from the knowledge of the longitude and latitude of the two tracking stations and the satellite and its altitude. The geometry of the problem is shown in Fig. 6-21. The direction cosines of the two LOS vectors in the orbit frame are

$$\ell_{X_i} = \sqrt{1 - \ell_{Y_i}^2 - \ell_{Z_i}^2}$$

$$\ell_{Y_i} = \frac{R \sin L_i}{|\bar{S}_i|}$$

$$\ell_{Z_i} = \cos \left( 2 \tan^{-1} \frac{r}{s - R} \right)$$

where

$i = 1$  or  $2$  denotes LOS vector being used

$$|\bar{S}_i| = \sqrt{R^2 \sin^2 L_i + [(R+h) \cos \Delta\lambda_i - R \cos L_i]^2 + [(R+h) \cos \Delta\lambda_i]^2}$$

$$\Delta\lambda_i = \lambda_i - \lambda_{\text{satellite}}$$

$$s = \frac{1}{2} (2R+h + |\bar{S}_i|)$$

$$r = \sqrt{\frac{(s - R)(s - R+h)(s - |\bar{S}_i|)}{s}}$$

$R$  = radius of earth

$h$  = altitude of satellite

$\lambda_i$  = longitude of tracking station

$L_i$  = latitude of tracking station

The small angle approximation is valid in application of the Euler transformations because the control system's task is to drive the Euler angle to zero. Thus, even for attitude maneuvers, the reference coordinates in which the Euler angles are measured have been biased by the commanded attitude so that when the vehicle is at the commanded attitude the Euler angles are zero.

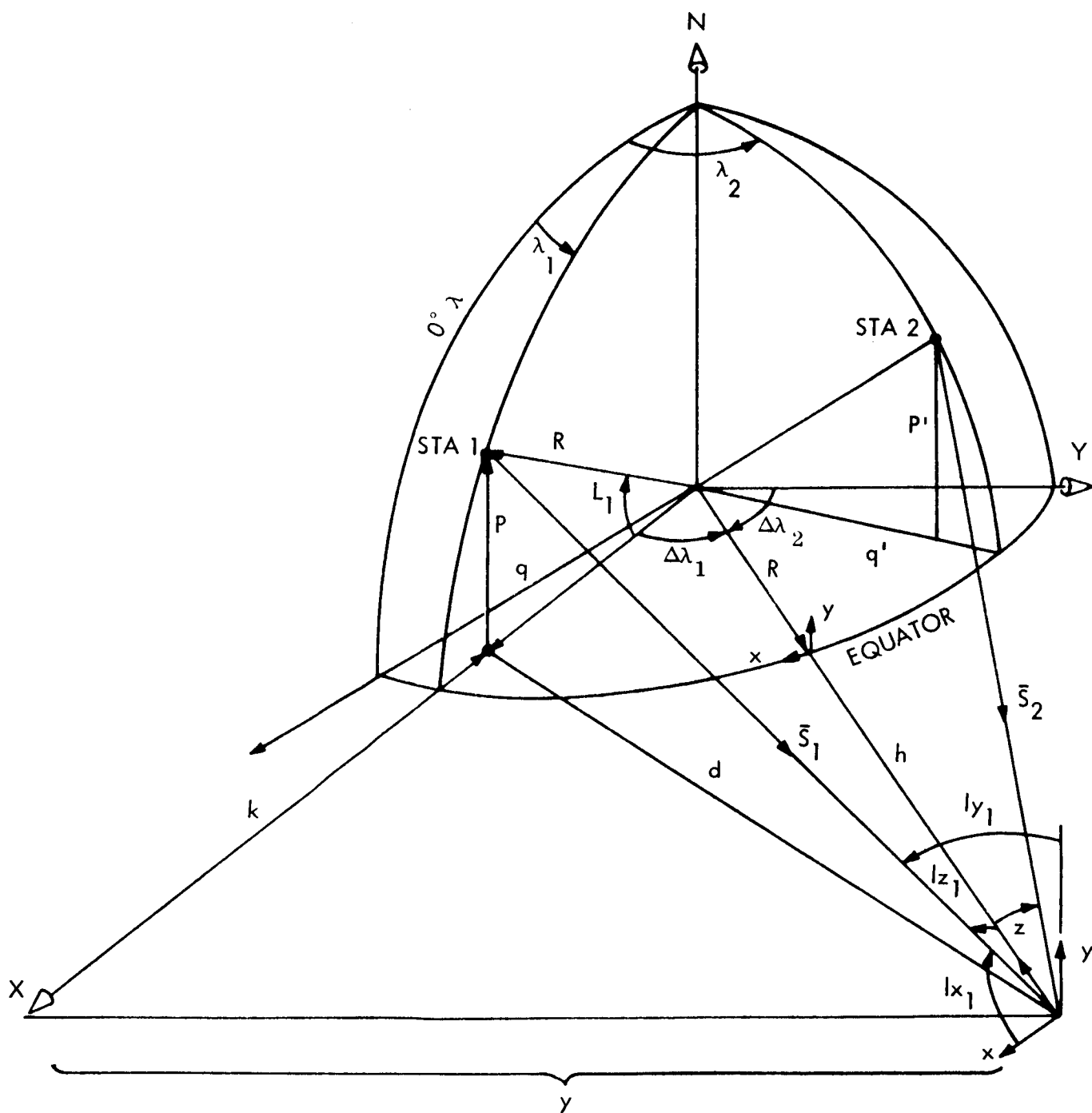


Fig. 6-21 Interferometer Direction Cosine Geometry



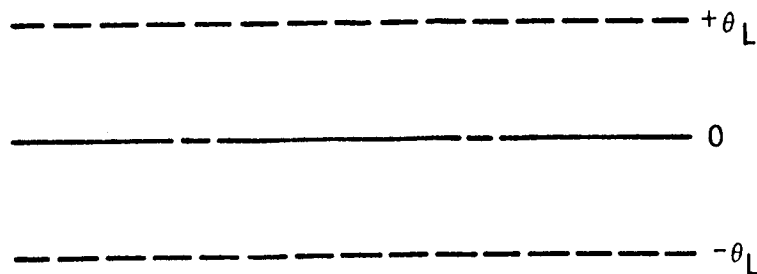
Adaptive Autopilot. An analysis was made of the ATS-4 requirements to determine the optimum configuration for the attitude-control autopilot. The control system for the ATS-4 orientation-control experiment must satisfy the following criteria:

- Minimize impulse propellants
- Maintain control accuracy of 0.1 deg
- Minimize firings (thrust cycles)
- Minimize sensor noise effects

The justification for these criteria is as follows:

- Weight of impulse propellant is determined by (a) the spacecraft torque profile and (b) control-system efficiency. Optimizing a control system for minimum-impulse propellant will result in a 10 to 25 percent variation in control-system weight. Since ion engines with specific impulse of 5,000 lb-sec/lb have been selected, the cost of impulse propellant has been minimized and the other criteria assume primary importance.
- Control accuracy is the primary criterion for selection of the preferred configuration of the orientation-control experiment.
- The requirement for 2-yr life dictates that the number of thrust cycles be minimized. By limiting the maximum frequency of the control forces, the interactions with structural dynamics are reduced.
- The effects of sensor noise must be minimized so that (a) attitude accuracy is not impaired and (b) false valve firings are reduced.

A modified bang-bang controller will be used in preference to a proportional controller, because of the loss of efficiency when ion engines are throttled. With a bang-bang system, deadband limits must be established; normally, these limits are set symmetrically about the desired value of the controlled variable as shown at the top of the next page. The required accuracy of the ATS-4 orientation-control experiment is  $\pm 0.1$  deg. Because other error sources are present and nonzero time is required to impart angular momentum to the spacecraft, the deadband limits ( $+\theta_L$ ,  $-\theta_L$ ) must be set



at values less than 0.1 deg, e.g.,  $\pm 0.03$  deg. The expected three-sigma random error for the projected horizon sensor is of this order of magnitude. Use of this form of deadband limits could result in false thruster firings, resulting in attitude errors, excessive thrust cycles, and wasted control impulse.

A more optimum (but more complex) set of deadband limits can be devised if it is recognized that for the majority of time, the spacecraft is under the influence of disturbing torques. These torques will force the spacecraft to operate along one of the deadbands as shown in Fig. 6-22. This operation results in an attitude error distribution which is highly skewed toward the deadband limit; the form of error probability distribution is shown in Fig. 6-23 for symmetric deadbands.

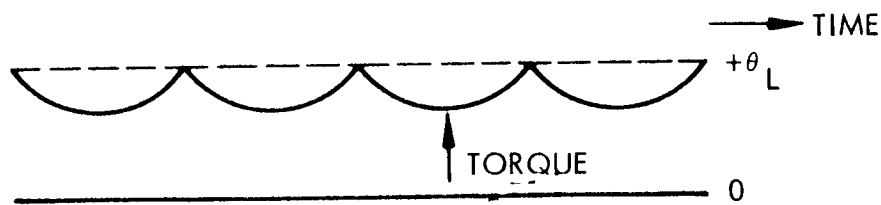


Fig. 6-22 Deadband Operation Under Constant Torque

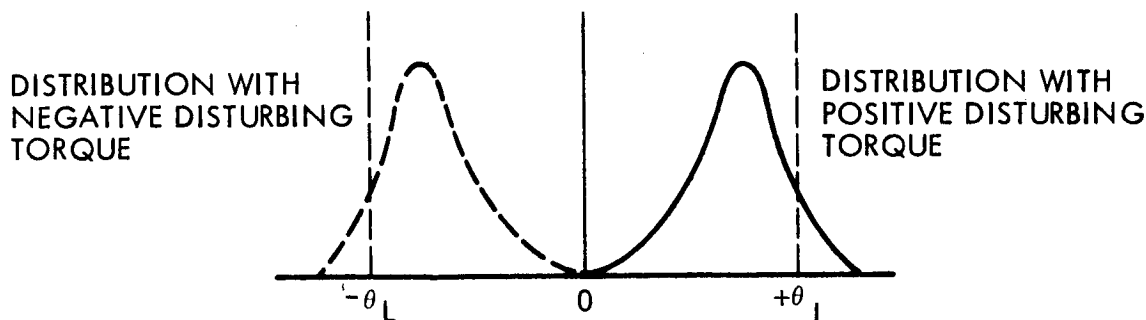


Fig. 6-23 Attitude-Error Probability Distribution

With the requirement of 0.1-deg error, it would be desirable to have an error distribution centered about the zero-attitude error and having a narrow spread about zero. If a system were devised to set the upper deadband limit at zero when the spacecraft is under the influence of positive torques and to set zero as the lower limit for negative torques, this form of distribution could be achieved. The result of this switching is to slide the plus and minus limits and their corresponding distributions inward until the limits are coincident with the zero error line. A block diagram for this system is given in Fig. 6-24.

The selective deadband controller operates in the following manner. (See Fig. 6-25 for attitude versus time plot.) If the system is operating initially in the presence of a negative disturbing torque, the deadband select relay will be set in the upward position feeding error signals to the negative torque channel. The spacecraft will continue to operate in the upper half deadband with a "scallop" limit cycle until the sign of the disturbing torque reverses. When torque reversal occurs (A), the spacecraft will be accelerated out to the upper limit of the upper half-deadband ( $+\theta_L$ ) and will begin a scallop cycle operation. The control pulses from this upper limit are counted, and, after a preset number of torque pulses have occurred, it is assumed

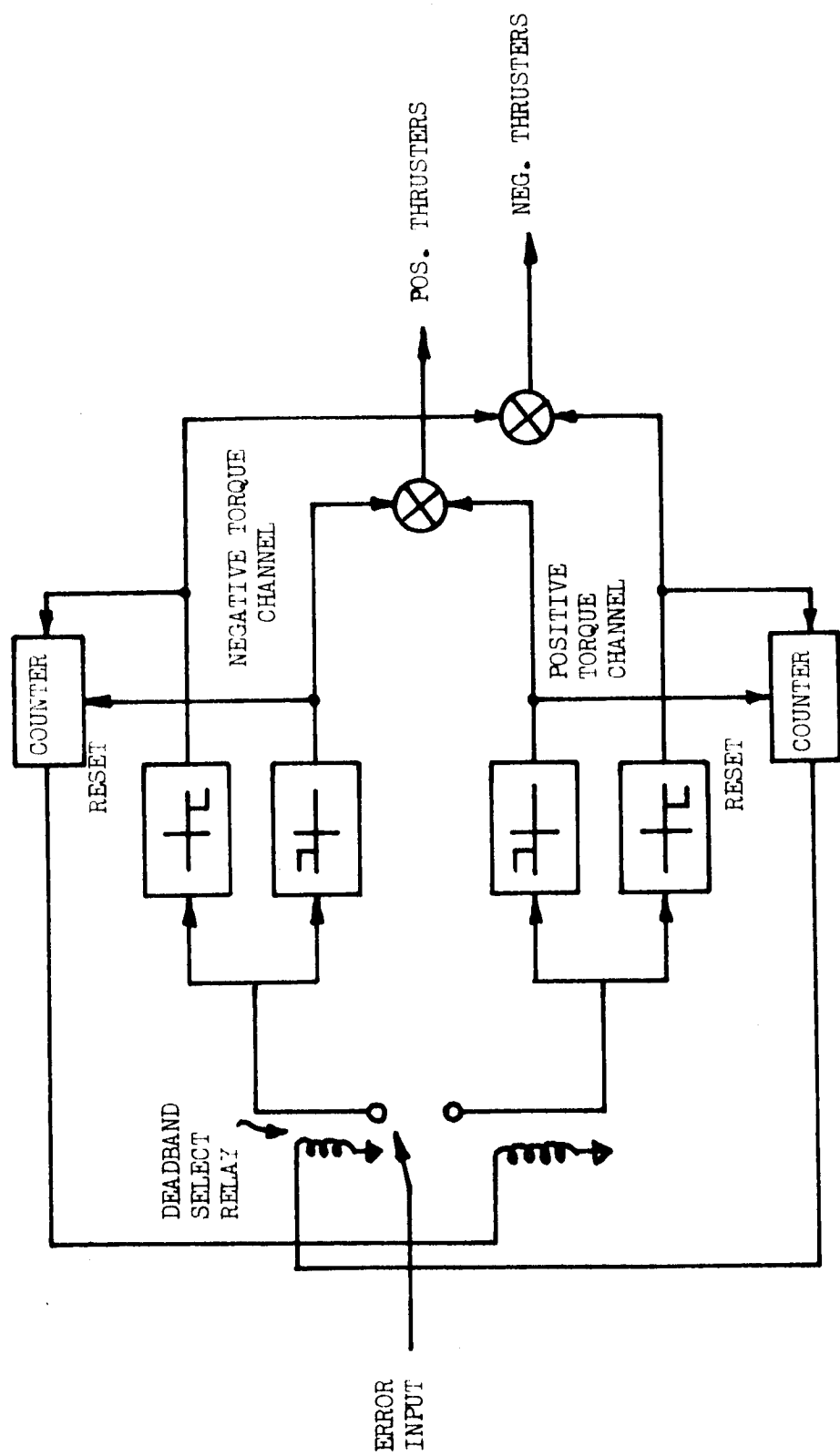


Fig. 6-24 Block Diagram of Deadband Selection Logic

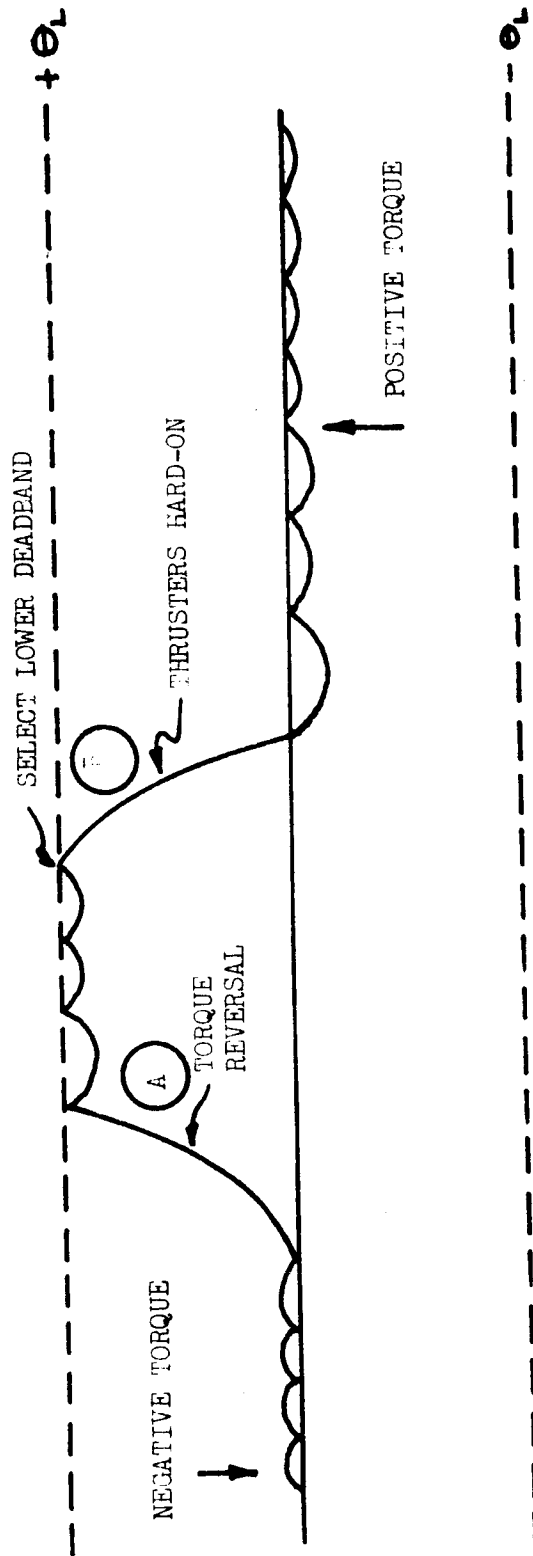


Fig. 6-25 Attitude vs. Time Plot

that a torque reversal has occurred. The deadband select relay is then set to the lower position (B) and the positive torque channel is activated. The spacecraft will then continue to scallop cycle against the upper (zero degree) limit of the lower half-deadband until another torque reversal occurs. The negative torque channel counter will be reset by the first pulse from the lower half-deadband upper limit output.

As mentioned above, the effects of sensor noise must be minimized to reduce false thruster firings. With a deadband controller, noise which, when combined with the signal, does not exceed the deadband limits has no effect upon system operation. For this reason, it would be desirable to widen the deadband; however, opening the deadband conflicts with the requirement for high accuracy. With the selective deadband controller, the upper and lower deadband limits ( $+\theta_L$  and  $-\theta_L$  in Fig. 6-25) can be set at large attitude errors (e. g.  $-0.15$  deg) with little effect upon attitude accuracy since these limits are used only during period of torque reversal transients. The maximum excursion into the deadband can be controlled simply as will be shown in a following section.

The effect of deadband selection on noise suppression is shown in Fig. 6-26 in comparison with a symmetric deadband having limits of  $\pm 0.03$  deg. The sensor noise is assumed to be Gaussian with an RMS value of  $0.06$  deg. The effect of noise for  $\theta = 0$  deg and  $+0.03$  deg is shown. Values of suppressed noise are given as percentages of the total area under the Gaussian curve. In the figures, the shaded areas represent the noise signals that can cause incorrect thruster firings. Note that the shaded area for the selective deadband case is greatly reduced from the symmetric case.

Because the use of wide deadbands will permit large attitude excursions away from the zero attitude error position, a method of controlling the maximum amplitude of the scallop cycles must be devised. Also, a method of controlling the frequency of thrust cycles is needed to limit the number of cycles to prolong thruster life. The following

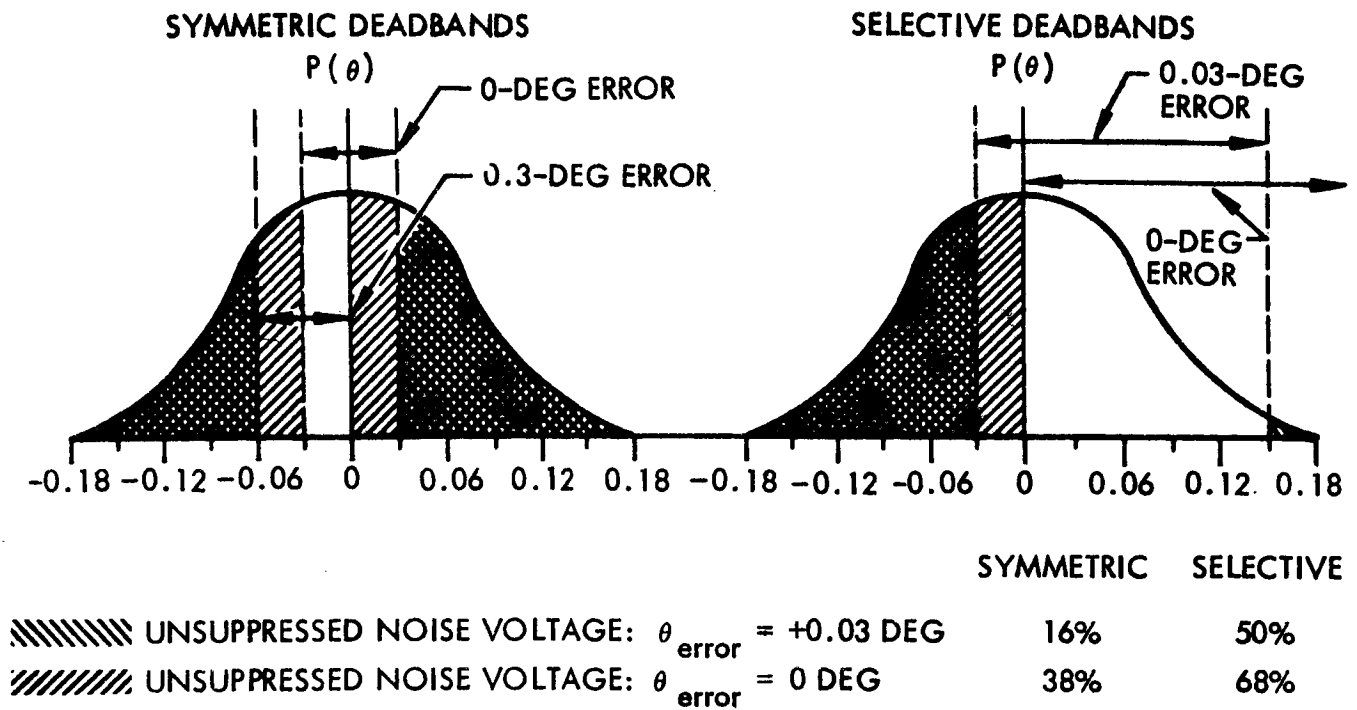
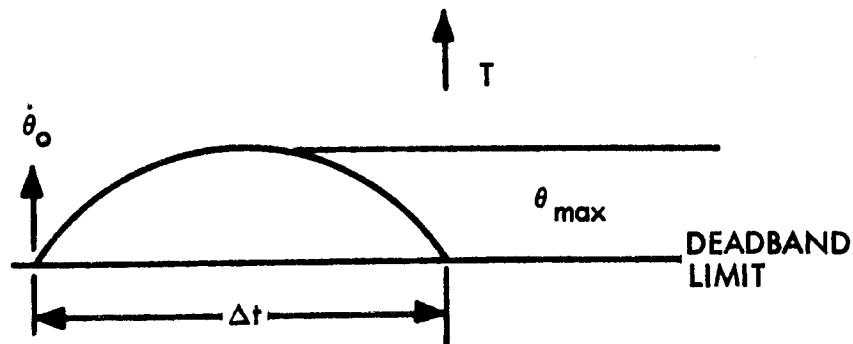


Fig. 6-26 Deadband Noise Suppression

relation for the amplitude and period of the scallop cycle are derived. The derivation assumes slowly varying disturbing torques, an assumption that is valid for the ATS-4 mission. Using the sketch below, it can be seen that the equations for scallop dynamics are:



$$\theta(t) = \dot{\theta}_0 t + \ddot{\theta} \frac{t^2}{2} = \frac{h}{2I_\theta} t + \frac{T}{2I_\theta} t^2$$

$$0 = \frac{h}{2I_\theta} \Delta t + \frac{T}{2I_\theta} (\Delta t)^2$$

$$\Delta t = - \frac{h}{T}$$

$$\theta_{\max} = \theta \left( \frac{\Delta t}{2} \right) = \frac{h}{4I_\theta} \Delta t + \frac{T}{8I_\theta} (\Delta t)^2 = \frac{h\Delta t}{4I_\theta} - \frac{h\Delta t}{8I_\theta} = \frac{h\Delta t}{8I_\theta}$$

or

$$h\Delta t = 8I_\theta \theta_{\max}$$

where

- $h$  = impulse bit angular momentum
- $T$  = disturbing torque (quasi-constant)
- $I_\theta$  = moment of inertia
- $\Delta t$  = scallop cycle period
- $\dot{\theta}_0$  = angular velocity when entering the deadband
- $\theta_{\max}$  = amplitude of cycle

Thus, there exists a relation between the magnitude of the control impulse bit and the scallop cycle period which, when satisfied, will control the amplitude of scallop cycle excursion into the deadband. The relation is shown graphically in Fig. 6-27.



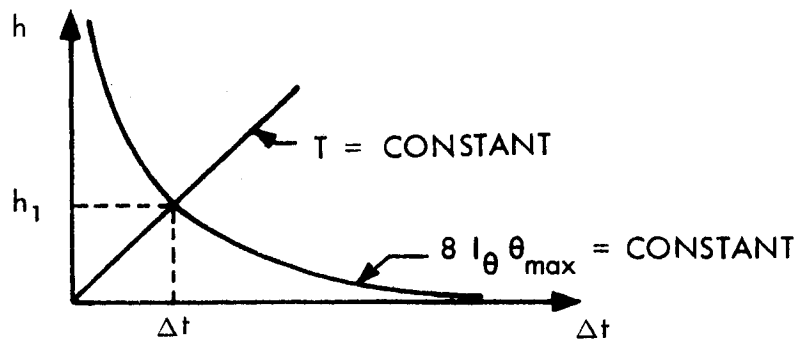


Fig. 6-27 Impulse-Bit Control Equation

The hyperbolic function ( $h\Delta t = 8I_{\theta} \theta_{\max}$ ) may be approximated with a digital mechanization a "staircase" function, the lowest step of which has the impulse limited by the minimum impulse bit desired. This approximation results in a two-to-one variation in  $\theta_{\max}$  for variations in the magnitude of the disturbing torque. A form of digital controller has been developed conceptually. A description of the controller is given in the following paragraphs.

The most important consideration in the controller is the method of maintaining a constant product for  $h\Delta t$ . This product is selected on the ground and loaded into two storage registers in the spacecraft via the TT&C command link. The two registers are shown in Fig. 6-28. The H register contains a binary number proportional to the allowable magnitudes of the control impulse bits. The E register contains another binary number which is proportional to the expected values of  $\Delta t$  corresponding to given values of  $h$ .

The contents of the H register are transferred into a counting register (CH register) and are counted down at a constant rate determined by the last scallop cycle period,  $\Delta t$ . Normally, the control thrusters remain as long as the contents of the CH register are greater than zero. The frequency used to countdown the register are derived from a crystal-controlled clock/binary frequency divider chain. If, for example, the value of  $\Delta t$  for the last scallop cycle was less than the expected value, the counting

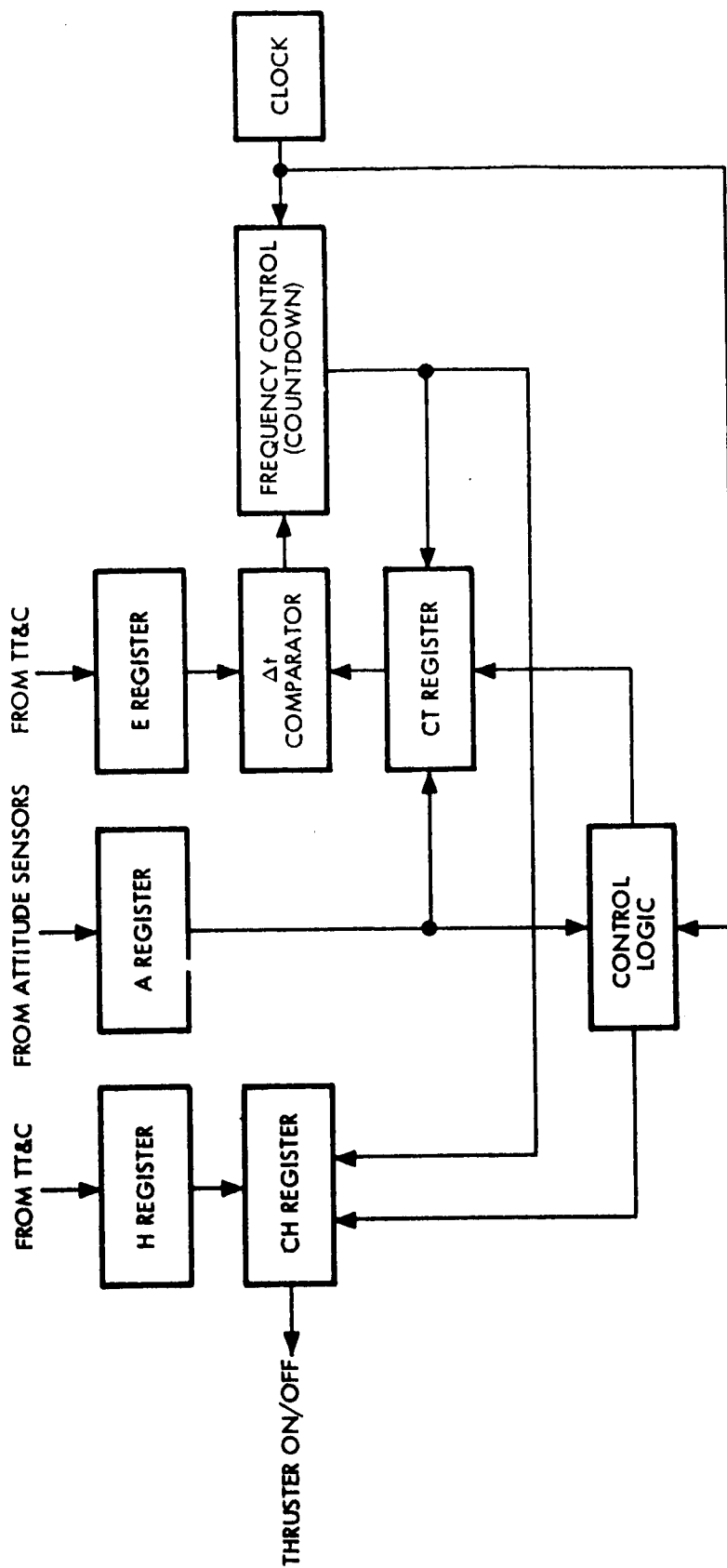


Fig. 6-28 Impulse-Bit Controller Block Diagram

frequency input to the CH register would be reduced by a factor of two. This reduction would be accomplished by selecting the next lower stage in the frequency divider and results in doubling the magnitude of the impulse bit.

The relation of the actual value of  $\Delta t$  to its expected value contained in the F register is determined in the comparison gates shown in Fig. 6-28. The actual value of  $\Delta t$  is determined by counting up the CT register at a constant frequency from the time of entry into the deadband until the subsequent exit from the deadband. The frequency is selected from the appropriate output of the frequency divider. In the case mentioned previously where the counting frequency input to the CH register was divided by two, the input frequency to the CT register would be doubled by selecting the next higher output of the frequency divider. This change effectively doubles the expected value of  $\Delta t$  and maintains the product of  $h$  and  $\Delta t$  equal to a constant.

A detailed sequence of events upon which the control logic would be based is given in Table 6-10. It should be noted that the A register (see Fig. 6-28) contains the attitude error data and is used to determine when the deadband is entered and exited. In addition, it is important to recognize that the size of the impulse bit will be changed only if the actual scallop cycle period is less than the expected value of  $\Delta t$  or greater than twice the expected value. The digital approximation to the control equation ( $h\Delta t = 8I_{\theta \max}$ ) that results is shown in Fig. 6-29.

In reviewing the control logic sequence (Table 6-10), it can be seen that at least one impulse bit of the commanded size will be fired at each deadband crossing and, if the deadband has not been entered, additional impulse will be fired until deadband entry occurs. In addition, steps 9 through 15 of Table 6-10 are included to permit the control system to stabilize the vehicle after a transient resulting in a high body rate. The procedure represented by the logic sequence causes the control system to continue to increase the size of the impulse bit applied until the deadband is entered.

The increase in the bit size is recognized by the control logic of the frequency divider which adjusts the size of the impulse bit and the magnitude of the expected  $\Delta t$  as

Table 6-10

## IMPULSE-BIT CONTROLLER SEQUENCE OF EVENTS

Step Number	Operation
1	Exit deadband, stop countup of CT register.
2	Compare contents of E register (expected $\Delta t$ ) with contents of the CT register (actual $\Delta t$ ). If $CT < E$ , increase impulse bit by $2x$ , reduce $\Delta t_{exp}$ by $1/2x$ ; if $E \leq CT < 2E$ , keep same impulse bit and $\Delta t_{exp}$ ; or if $CT \geq 2E$ , decrease impulse bit by $1/2x$ , increase $\Delta t_{exp}$ by $2x$ .
3	Transfer contents of H register into CH register; initiate thrust and countdown of CH register; clear CT register.
4	Initiate countup of CT register when deadband is entered.
5	When contents of CH register equal zero, terminate thrust.
6	If deadband has been entered, stop.
7	If deadband has not been entered, retransfer contents of H register into the CH register and reinitiate thrust.
8	Continue thrust until (1) the deadband is entered (then stop) or (2) the contents of the CH register is zero.
9	If deadband has not been entered when CH reaches zero, retransfer contents of H register into CH register; countdown CH register without thrust.
10	Repeat step 9 if deadband has not been entered by the time the contents of CH register reach zero (repeat once only).
11	If deadband has not been entered, increase impulse bit by $2x$ and decrease $\Delta t_{exp}$ by $1/2x$ .
12	Transfer contents of H register into CH register; initiate thrust and countdown of CH register.
13	Terminate thrust if (1) deadband is entered (then stop) or (2) contents of CH register is zero.
14	If deadband has not been entered, repeat steps 12 and 13 (once).
15	If deadband has not been entered after repeat of steps 12 and 13, repeat steps 9 through 14 until deadband is entered. Note that step 11 cannot occur if the maximum impulse bit has already been selected.

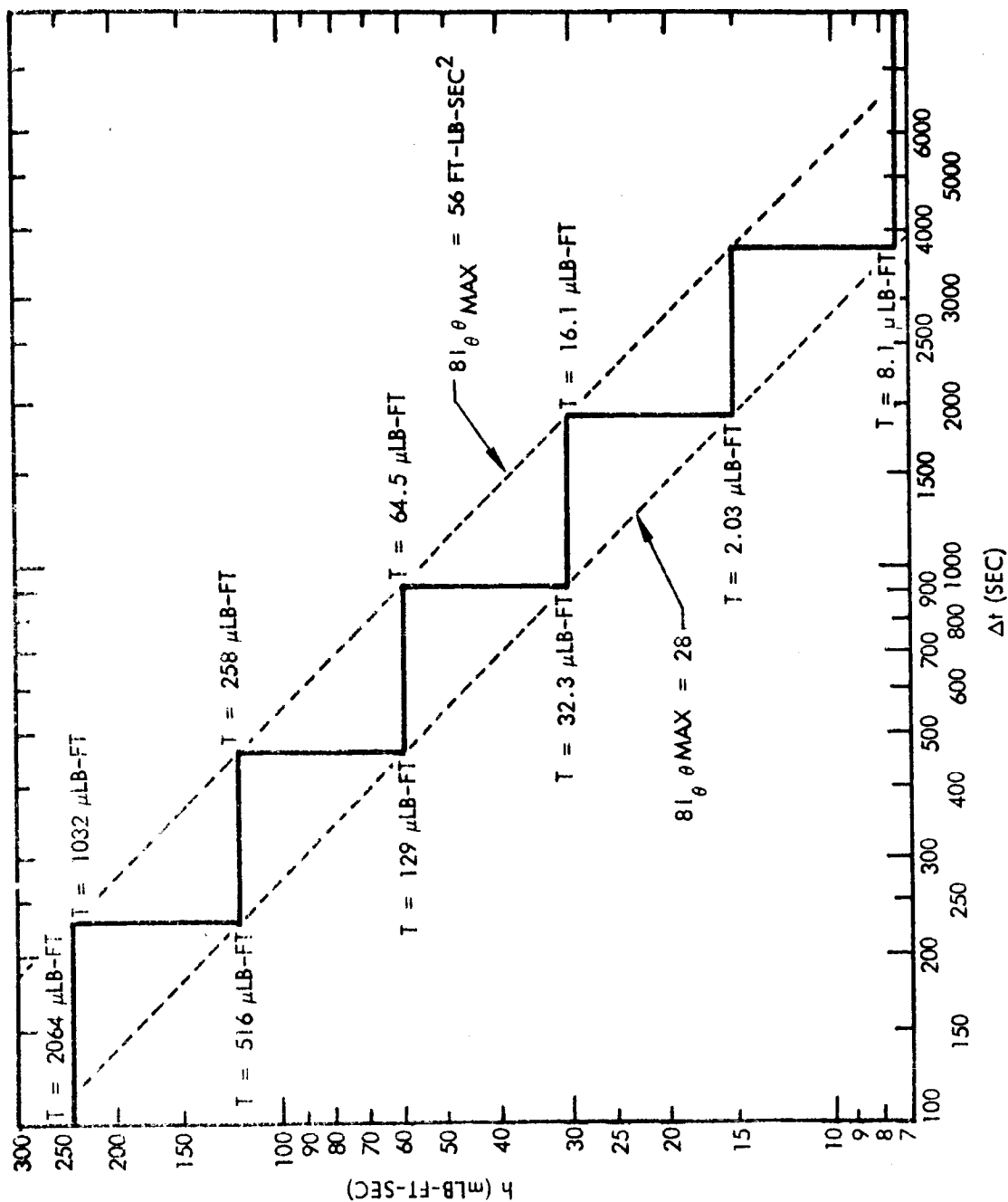


Fig. 6-29 Digital Approximation to Control Equation

described above. The maximum size of bit applied is limited by the allowable input frequencies to the CH register; however, the maximum impulse bits can be applied repetitively. The bits are fired with intervening quiescent periods (see Fig. 6-30); the technique tends to minimize the body rate when entering the deadband. It should be noted, however, that other logical sequences are possible for controlling the application of impulse during transient conditions. These alternatives will be evaluated in order to optimize the controller.

Some sizing has been done on the elements of the impulse bit controller. The system parameters used in this sizing are as follows:

$$I_{\theta} = 4,000 \text{ slug-ft}^2$$

$$\theta_{\max} = 0.05 \text{ deg}$$

$$\text{control torque } (T_c) = 3.75 \text{ mlb-ft}$$

$$h\Delta t = 8I_{\theta} \theta_{\max} = 28 \text{ ft-lb-sec}$$

$$\text{For } T_{\max} = 0.7 \text{ mlb-ft}$$

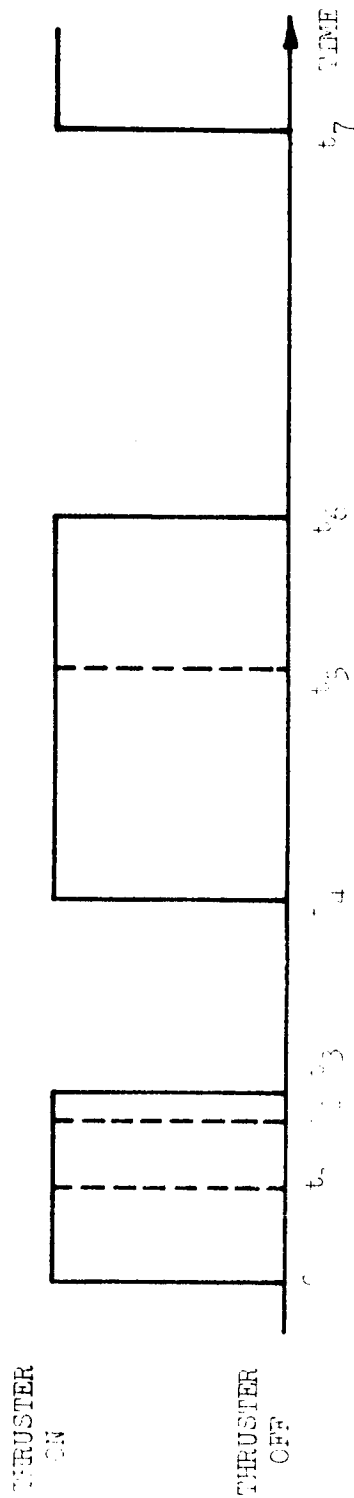
$$\Delta t_{\min} = 200 \text{ sec}$$

$$h_{\max} = 0.14 \text{ ft-lb-sec}$$

$$\text{For } T = 0.007 \text{ mlb-ft}$$

$$\Delta t = 2,000 \text{ sec}$$

$$h = 0.014 \text{ ft-lb-sec}$$



$$t_3 - t_4 - t_5 = \frac{1}{2} (t_6 - t_4) + \frac{1}{2} (t_7 - t_6)$$

# SEQUENCE:

- 0 -  $t_1$  - THRUSTER ON
- $t_1 < t_2 < t_3$  - THRUSTER OFF IF DEADBAND ENTERED
- $t_3$  - THRUSTER OFF EVEN IF DEADBAND HAS NOT BEEN ENTERED
- $t_4$  - THRUSTER ON IF DEADBAND HAS NOT BEEN ENTERED
- $t_4 < t_5 < t_6$  - THRUSTER OFF IF DEADBAND ENTERED
- $t_6$  - THRUSTER OFF EVEN IF DEADBAND HAS NOT BEEN ENTERED
- $t_7$  - THRUSTER ON IF DEADBAND HAS NOT BEEN ENTERED

Fig. 6-30 Transient-State Bit Control

Eight-bit resolution is recommended for the H, CH, E, and CT registers to provide 0.4-percent resolution of the  $h\Delta t$  product. Six allowable pairs of values for  $h$  and  $\Delta t$  permit control over a 1024:1 range of disturbing torques.

Each pair of  $h$  and  $\Delta t$  values is represented by a step on the staircase function plotted in Fig. 6-29. The corresponding values for the impulse bits and the scallop cycle period are given in Table 6-11.

Table 6-11

IMPULSE-BIT MAGNITUDE AND EXPECTED SCALLOP PERIOD

Impulse Bit Magnitude (mlb-ft-sec)	Thruster On Time (sec)	Expected Scallop Period (sec)
7.5	2.0	> 3,712
15.0	4.0	1,856 - 3,712
30.0	8.0	928 - 1,856
60.0	16.0	464 - 928
120.0	32.0	232 - 464
240.0	64.0	< 232

The method of periodic impulse application described above results in reducing the effective control torque by one-half. In order to provide the ability to use the full value of control torques, pseudo-rate (derived-rate) circuits are used for thruster control against the outer deadbands. This form of control will provide stability in the presence of disturbances that result in torques in the range of one-half to one times the available control torque. In addition, pseudo-rate control will provide for low body rates during the transient occurring when the opposite deadband is selected after a torque reversal (Fig. 6-25).



The pseudo-rate circuit is mechanized digitally using a storage register, a counting register, and a pair of logical comparison And/Or gates. The block diagram for the gates and registers is shown in Fig. 6-31. A binary number representing the attitude error is stored in the A register. The V register is a counting register programmed to provide linear approximation to a long-lag integrator. The contents of the V register are counted towards a maximum magnitude when a thruster is on and allowed to count down towards zero when both thrusters are off. The rate of counting is determined by the contents of the register to approximate an exponential rise or decay (see Fig. 6-32). The variable countdown (and countup) frequencies are derived from the binary frequency divider discussed above, and the appropriate divider output is determined by the contents of the V register.

For example, if the contents of the V register,  $C(V)$ , lie between  $V_{\max}$  and  $1/2 V_{\max}$ , the most significant bit of the V register must contain a one. Thus, if bit  $V_8$  (Fig. 6-31) contains a one, the maximum frequency,  $f$ , would be used to countdown until  $V_8$  changes to zero. At this time, the counting frequency would be reduced by one-half. The countup frequencies are similarly selected based upon the complemented contents of the V register.

This technique provides an approximation to a lag network since the time to halve (or double) the register contents is approximately constant. The approximate time constant of the circuit is:

$$T = \frac{V_{\max}}{0.695f}$$

The contents of the A and V registers are compared in a pair of deadband gates that provide an output when the difference between the contents of the two registers exceeds a value  $\Delta$ , a binary number representing the outer deadband attitude limit. The logic equations DPOS and DNEG are given in Table 6-12. When DPOS or DNEG gives an output, the appropriate thruster is fired, the V Register is counted up, and the torque

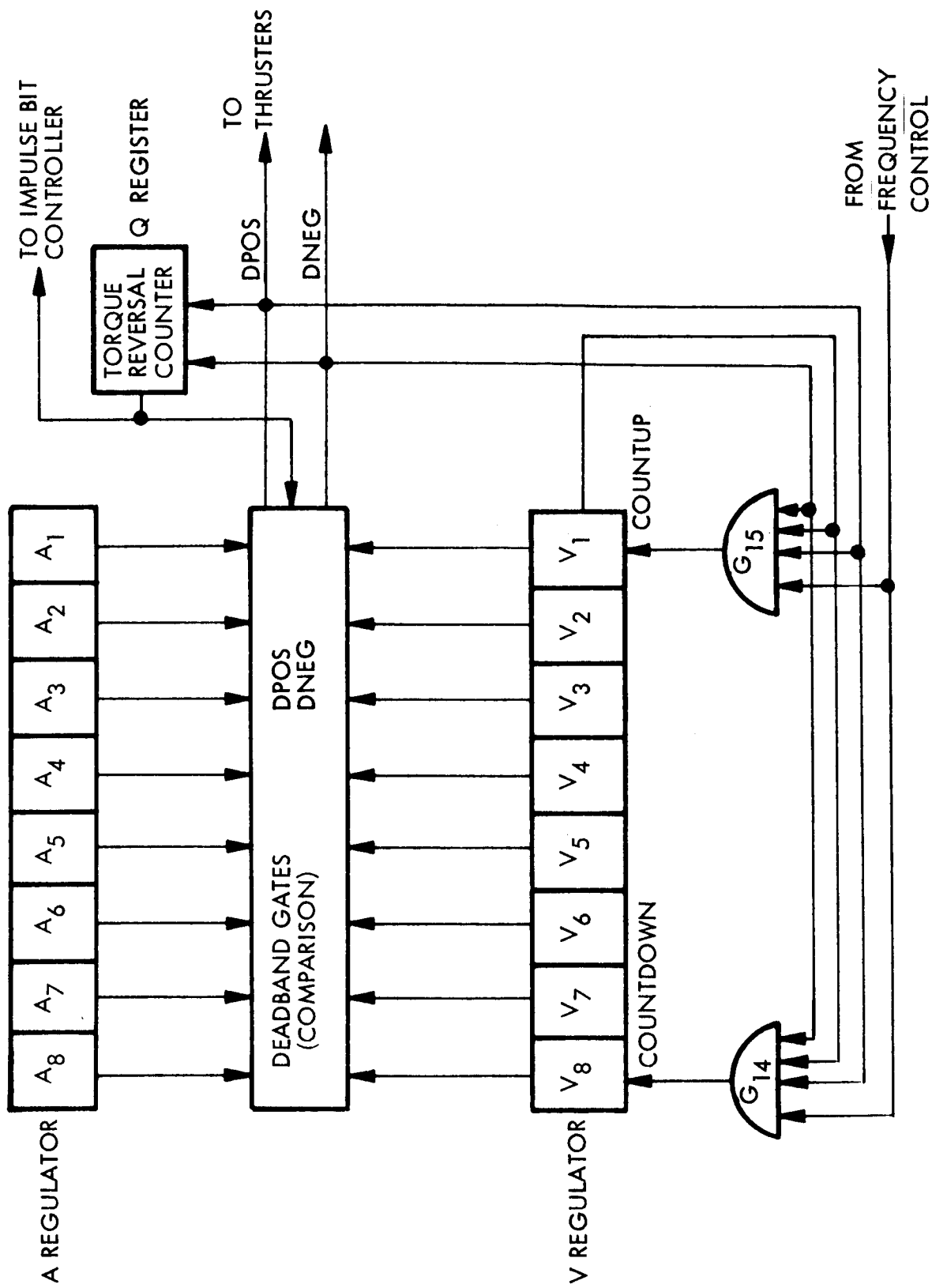
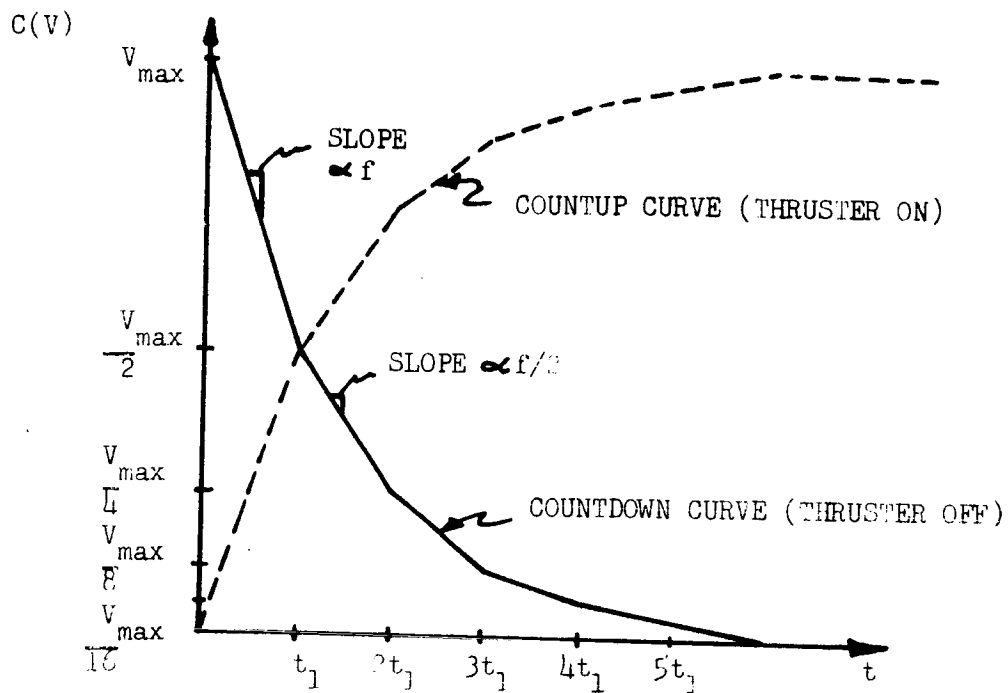


Fig. 6-31 Digital Pseudo-Rate Circuit Block Diagram



CONTENTS OF  
V REGISTER  
 $C(V)$

COUNTDOWN  
FREQUENCY

$$\frac{V}{2} < C(V) \leq V$$

$f$

$$\frac{V}{4} < C(V) \leq \frac{V}{2}$$

$f/2$

$$\frac{V}{8} < C(V) \leq \frac{V}{4}$$

$f/4$

.

.

.

.

.

.

Fig. 6-32 V-Register Counting Control

Table 6-12

## LOGIC EQUATIONS FOR DEADBAND GATES

LOGIC EQUATIONS:

$$\begin{aligned}
 \text{DPOS} = & \left\{ A_m \bar{V}_m \left[ \left[ \frac{\bar{A}_{m-1} V_{m-1} \cdot \bar{A}_{m-2} V_{m-2} \cdot \dots \cdot \bar{A}_{n+1} V_{n+1}}{\bar{A}_{n-1} \bar{V}_{n-1} + A_{n-2} \bar{V}_{n-2} + \dots + A_2 \bar{V}_2} \right] + \left[ \left( A_n V_n + \bar{A}_n \bar{V}_n \right) \cdot \left( A_{n-1} \bar{V}_{n-1} + \left( \bar{A}_{n-1} \bar{V}_{n-1} \right) \right) \right. \right. \right. \\
 & \cdot A_{n-2} \bar{V}_{n-2} \left. \left. + \dots + \left( A_{n-1} \bar{V}_{n-1} + A_{n-2} \bar{V}_{n-2} + \dots + A_2 \bar{V}_2 \right) \cdot A_1 \bar{V}_1 + A_n \bar{V}_n \right] \cdot \left[ \bar{A}_{m-1} V_{m-1} \cdot \bar{A}_{m-2} V_{m-2} \right. \right. \\
 & \cdot \dots \cdot \bar{A}_{n+1} V_{n+1} \left. \left. \right] + A_{m-1} \bar{V}_{m-1} \cdot \left[ A_m V_m + \bar{A}_m \bar{V}_m \right] \cdot \left[ \frac{\bar{A}_{m-2} V_{m-2} \cdot \dots \cdot \bar{A}_{n+1} V_{n+1}}{\bar{A}_{m-2} V_{m-2} \cdot \dots \cdot \bar{A}_{n+1} V_{n+1}} \right] \right\} \\
 & + \left( \left[ \frac{\bar{A}_{m-2} V_{m-2} \cdot \dots \cdot \bar{A}_{n+1} V_{n+1}}{\bar{A}_{n-1} \bar{V}_{n-1} + A_{n-2} \bar{V}_{n-2} + \dots + A_2 \bar{V}_2} \right] \cdot \left[ \left( A_n V_n + \bar{A}_n \bar{V}_n \right) \cdot \left[ A_{n-1} \bar{V}_{n-1} + \left( \bar{A}_{n-1} \bar{V}_{n-1} \right) \cdot A_{n-2} \bar{V}_{n-2} \right. \right. \right. \right. \\
 & + \dots + \left. \left. \left( \frac{\bar{A}_{n-1} \bar{V}_{n-1} + \dots + A_2 \bar{V}_2}{\bar{A}_{n-1} \bar{V}_{n-1} + \dots + A_2 \bar{V}_2} \right) \cdot A_1 \bar{V}_1 \right] + A_n \bar{V}_n \right] + \dots + A_{n+1} \bar{V}_{n+1} \cdot \left[ \left( A_m V_m + \bar{A}_m \bar{V}_m \right) \right. \right. \\
 & \cdot \dots \cdot \left. \left. \left( A_{n+2} V_{n+2} + \bar{A}_{n+2} \bar{V}_{n+2} \right) \right] \cdot \left[ \left( A_n V_n + \bar{A}_n \bar{V}_n \right) \cdot \left[ A_{n-1} \bar{V}_{n-1} + \left( \bar{A}_{n-1} \bar{V}_{n-1} \right) \cdot A_{n-2} \bar{V}_{n-2} \right. \right. \right. \\
 & + \dots + \left. \left. \left( \frac{\bar{A}_{n-1} \bar{V}_{n-1} + \dots + A_2 \bar{V}_2}{\bar{A}_{n-1} \bar{V}_{n-1} + \dots + A_2 \bar{V}_2} \right) A_1 \bar{V}_1 \right] + A_n \bar{V}_n \right] \cdot \bar{Q} + \left\{ A_m \bar{V}_m + \dots + A_1 \bar{V}_1 \cdot \left[ A_m V_m + \bar{A}_m \bar{V}_m \right] \right\} \\
 & \cdot \dots \cdot \left[ A_2 V_2 + \bar{A}_2 \bar{V}_2 \right] \cdot Q
 \end{aligned}$$

DNEG is equivalent to DPOS with A's and V's transposed.

m = number of bits in the A and V registers

DNEG = 1 implies (A - V) > Δ where Δ = 2<sup>n</sup>

Q = Q register contains all 1's

reversal counter contents are increased by one. When the Q register contains all ones, the opposite deadband is selected and the last major term DPOS (representing  $\Delta = 0$ ) is used to force the attitude error to zero. When the new deadband is entered, the Q register is reset to zero and the impulse bit controller output is switched to the opposing thruster.

An integrated block diagram for the adaptive autopilot composed of the impulse bit controller, digital pseudorate circuits, and deadband selection and control logic is shown in Fig. 6-33.

#### 6.1.6 Experiment Operations

The orientation control experiment described in the preceding section provides a flexible arrangement with which several configurations of control systems can be evaluated in the orbital environment. As mentioned previously, there are two basic orbital control systems included in the basic spacecraft design. One system, identified as the coarse system, provides approximately 0.2-deg attitude accuracy in pitch and roll and 0.9-deg accuracy in yaw. This system is used in the ascent phase prior to the injection-motor burn phase and during synchronous orbit operation when control to 0.1-deg accuracy is not required. The coarse system uses a horizon sensor and three two-degree-of-freedom gas bearing gyros for attitude references and a form of gyrocompassing to maintain a yaw reference. The sensor and gyro output signals are processed by digital electronics to provide commands to a set of six 2-mlb ammonia resistance jet thrusters that generate the required control torques.

The second (or fine) system which provides accurate ( $\pm 0.1$  deg) control for orienting the parabolic reflector uses the RF interferometer as the primary attitude reference. Two modes of operation are possible with the interferometer. If two ground stations radiate reference signals to the interferometer, the resulting direction cosine outputs can be processed by a minimal on-board digital computer to provide pitch, roll, and yaw error signals. The interferometer can also be used with a single ground radiator

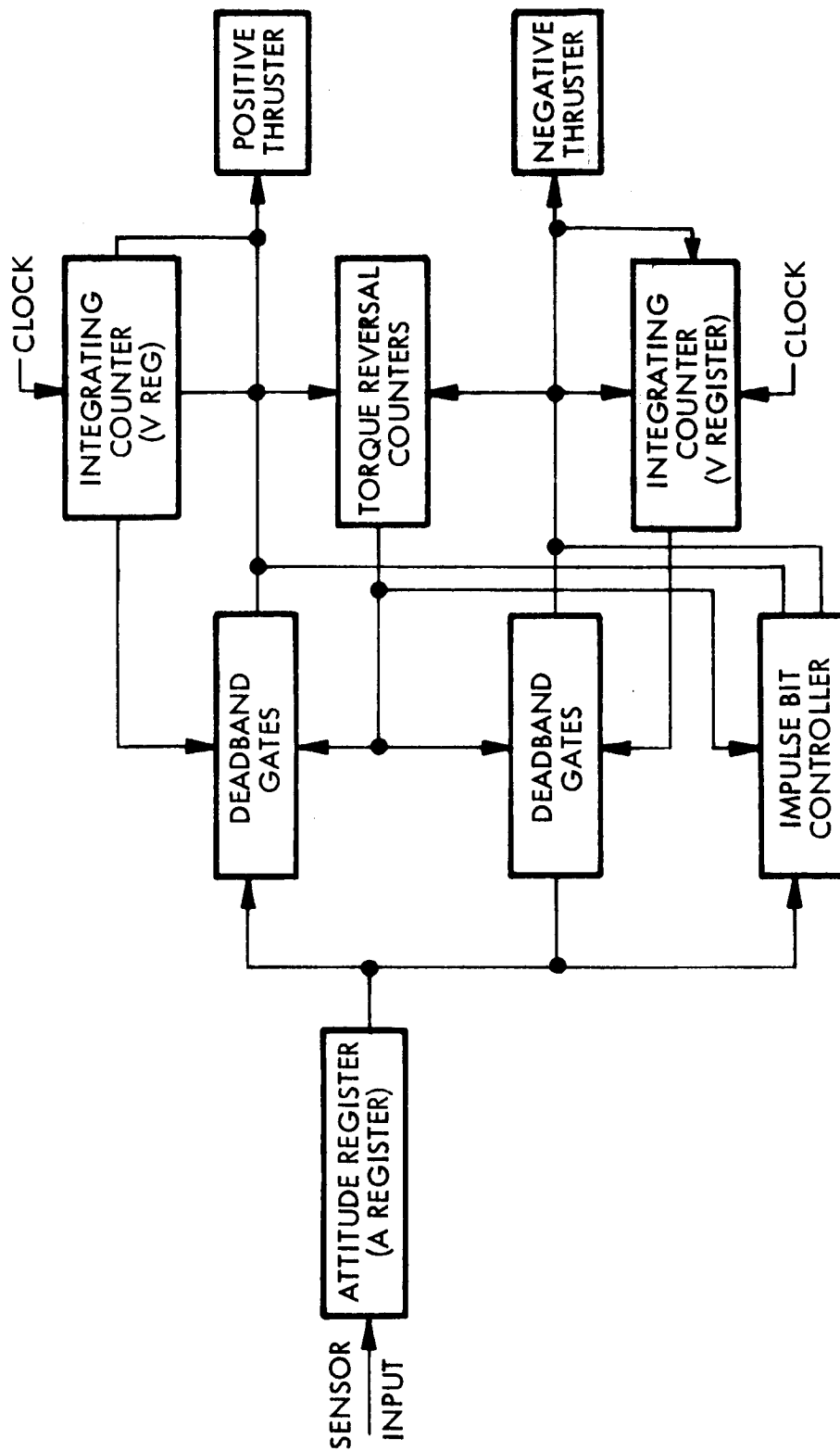


Fig. 6-33 Adaptive Autopilot Block Diagram

to provide pitch and roll error signals; this mode requires the use of an independent yaw reference. Two yaw references have been recommended for evaluation: use of the yaw gyro output and use of polarization sensing to derive yaw error signals.

The interferometer outputs are processed by an adaptive digital autopilot that controls the size of the control impulse bits to optimize the amplitude of the attitude excursions as a function of the frequency of control thrust cycles. The control torques for the fine control system are provided by a set of six cesium bombardment ion engines.

Alternate Configurations. To provide a comparative evaluation of system performance, it is desirable to obtain data on both the coarse and fine system over extended periods. In addition, provisions for modifying the system configuration should be provided to evaluate other operational modes.

The first alternate mode that must be incorporated provides attitude stabilization in an inertially fixed reference frame. This mode uses the basic coarse system with the horizon sensors removed from the control loop and uses the three-axis rate gyro package as an inertial reference. This mode of control is required for orientation of the spacecraft to the proper attitude for kick-motor burn and for stabilizing the vehicle during the burn period using hydrazine control thrusters. In addition, the mode can be used to control the vehicle during the initial synchronization of the solar arrays, to point the spacecraft in some arbitrary direction (at a planetary probe, radio star, etc.), and to permit rapid reorientation of the spacecraft from one ground station to another.

Another mode of operation would replace the horizon sensor with the interferometer in the coarse-mode channel to make a comparative evaluation of the two autopilot configurations. Since the coarse system accuracy is governed primarily by the horizon sensor accuracy, use of the interferometer as an attitude reference with a corresponding reduction in the coarse autopilot deadband width by ground command will provide an alternate fine-mode backup to the adaptive autopilot channel.

In similar fashion, capability would be provided to feed the horizon sensor and/or gyro output signals into the adaptive autopilot in lieu of the interferometer outputs. This configuration provides an alternate coarse mode of operation. The alternate mode would be evaluated in comparison to the basic coarse mode system on the basis of control accuracy, impulse expenditure, and response time.

It would also be possible to interchange the resistance jets between the coarse and fine mode outputs to provide another comparative evaluation between the two basic systems. The use of the ion engines with the pulse width modulator output of the coarse mode autopilot must be evaluated further to determine the ability of the ion engines to respond to short-duration pulses.

It should be noted that the capability to vary the control system configuration provides, in addition to a broad spectrum of experimental modes, a very flexible, redundant system to assure that the 2-yr lifetime requirement of ATS-4 is met.

Parameter Variations. Both the coarse and fine mode control systems would be provided with the capability of varying various system parameters. This variation technique would be used to verify the results of analyses and simulations made in developing the control system design. Data taken of system performance under varying parameters would be related to analytic results and would provide a basis for optimizing the design of control systems for spacecraft which will follow ATS-4. Table 6-13 lists the parameters which will be variable.

In addition to varying the parameters of the control system, it would also be of interest to vary the appropriate parameters of the spacecraft. For example, the deployment of a solar sail would cause a change in the profile of solar torques as a function of time. The results of this profile change could be used to validate the design analysis of the spacecraft center-of-solar-pressure/center-of-mass relationship. Also, a known constant torque could be applied to the spacecraft to confirm the estimates of natural disturbing torques derived from other control system telemetry data. Finally, the spacecraft moments of inertia could be varied by extending booms with tip weights to evaluate the effects upon the control system.



Table 6-13

**CONTROL-SYSTEM VARIABLE PARAMETERS**

Coarse Mode	Fine Mode
Horizon Sensor Gains  Gyro Drift Trim Biases Rate Gyro Output Scale Factors Deadband Limits Pulse Width Modulator	Interferometer Output Scale Factors Control Equation Constants Deadband Limits  Pseudo-Rate Circuit Time Constant; Upper or Lower Deadband Selection

Experiment Sequence of Events. The sequence of events covering the ascent, injection, and deployment of the spacecraft was discussed in Section 4. Once the spacecraft deployment sequence has been completed, the operation of the various elements of the orientation control experiment can be initiated.

The recommended operational sequence of the experiment is given in Table 6-14. The operational philosophy represented by the sequence is characterized by evaluation of system elements on an open-loop basis prior to giving control of the spacecraft to those elements. This approach reduces the possibility of experiment failure affecting the spacecraft by validating the performance of spacecraft equipment prior to committing them to use.

Table 6-14

## ORIENTATION-CONTROL EXPERIMENT SEQUENCE

Event Number	Operation	Purpose
1	Simultaneous operation of interferometer, horizon sensor, and star-field scanner	Calibrate attitude references; equipment status validation
2	Nadir-oriented operation of coarse system	Confirm spacecraft torque profile, structural stability, impulse usage, and control-system response
3	Off-nadir operation of coarse system in conjunction with low-frequency operation of parabola	Verify coarse-mode pointing capability; confirm moving-target tracking capability
4	Inertially fixed operation of coarse system with star-field scanner readout	Determine gyro drift rates; insert proper drift trim biases
5	Activation of fine system using single-station interferometer mode	Evaluate performance of adaptive autopilot and ion engines, refine disturbing torque profile, demonstrate high-accuracy pointing
6	Two-station operation of interferometer open-loop (coarse system control)	Validate interferometer and attitude computer operation
7	Operation of fine system using two-station interferometer mode in conjunction with high-frequency operation of parabola	Confirm results of design analyses; evaluate impulse usage and control system accuracy; confirm horizon-to-horizon reorientation capability
8	Variation of control-system parameter (Table 6-22)	Confirm design analyses
9	Evaluation of alternate configurations	Make comparative evaluation of alternate modes
10	Variation of spacecraft parameter	Confirm design analyses

As shown by Table 6-14, the sequence moves from the less complex modes of operation into the more sophisticated in logical sequence. Calibration of the attitude references is performed prior to the time they are made an active part of the system. Operation of the coarse mode and the fine mode is performed prior to exercising the modes that involve interchanging of sensors and control actuators. A performance evaluation of the basic modes is performed prior to varying the parameters of the control system and of the spacecraft to confirm the primary design analysis.

It is felt that this sequence permits maximum experimental flexibility while maintaining the required high reliability to minimize jeopardy to the other experiments.

#### 6.1.7 Attitude Control Impulse Calculations

Control system impulse must be expended to overcome external disturbances, perform the required attitude maneuvers, and to balance stationkeeping thruster misalignment. These primary control gas users will be discussed separately. The vehicle parameters used for the analysis are inertias  $I_{xx} = 3,170 \text{ slug-ft}^2$ ; and  $I_{yy} = 5,589 \text{ slug-ft}^2$ ;  $I_{zz} = 5,230 \text{ slug-ft}^2$ ; and lever arms  $l_{xx} = 12.5$ ,  $l_{yy} = 12.5$ ,  $l_{zz} = 3 \text{ ft}$ .

The primary disturbance torque on the vehicle is the solar disturbance. The secondary disturbance torques are quite insignificant in comparison. The secondary disturbance torques include those torques due to earth albedo (misaligned 15 deg from local vertical),  $3.0 \times 10^{-6} \text{ ft-lb}$ ; torques due to solar winds,  $10^{-9} \text{ ft-lb}$ ; and an equivalent torque due to micrometeoroid impact,  $10^{-12} \text{ ft-lb}$ .

Solar disturbances for the 30-ft flexrib antenna are calculated by scaling down results from a solar disturbance study made on an 80-ft flexrib antenna. The scaling factor used was the cube of the ratio of antenna diameters. The solar disturbing torque was calculated for the 80-ft reflector based on a maximum solar pressure of  $2 \times 10^{-7} \text{ psf}$  and a pure area moment disturbance with no consideration given to reflection and re-radiation effects. Shadowing and shine-through were evaluated in the resultant area moment calculation. Figure 6-34 shows a plot of the solar disturbance pitch, roll, and yaw torque vs. sun aspect angle.

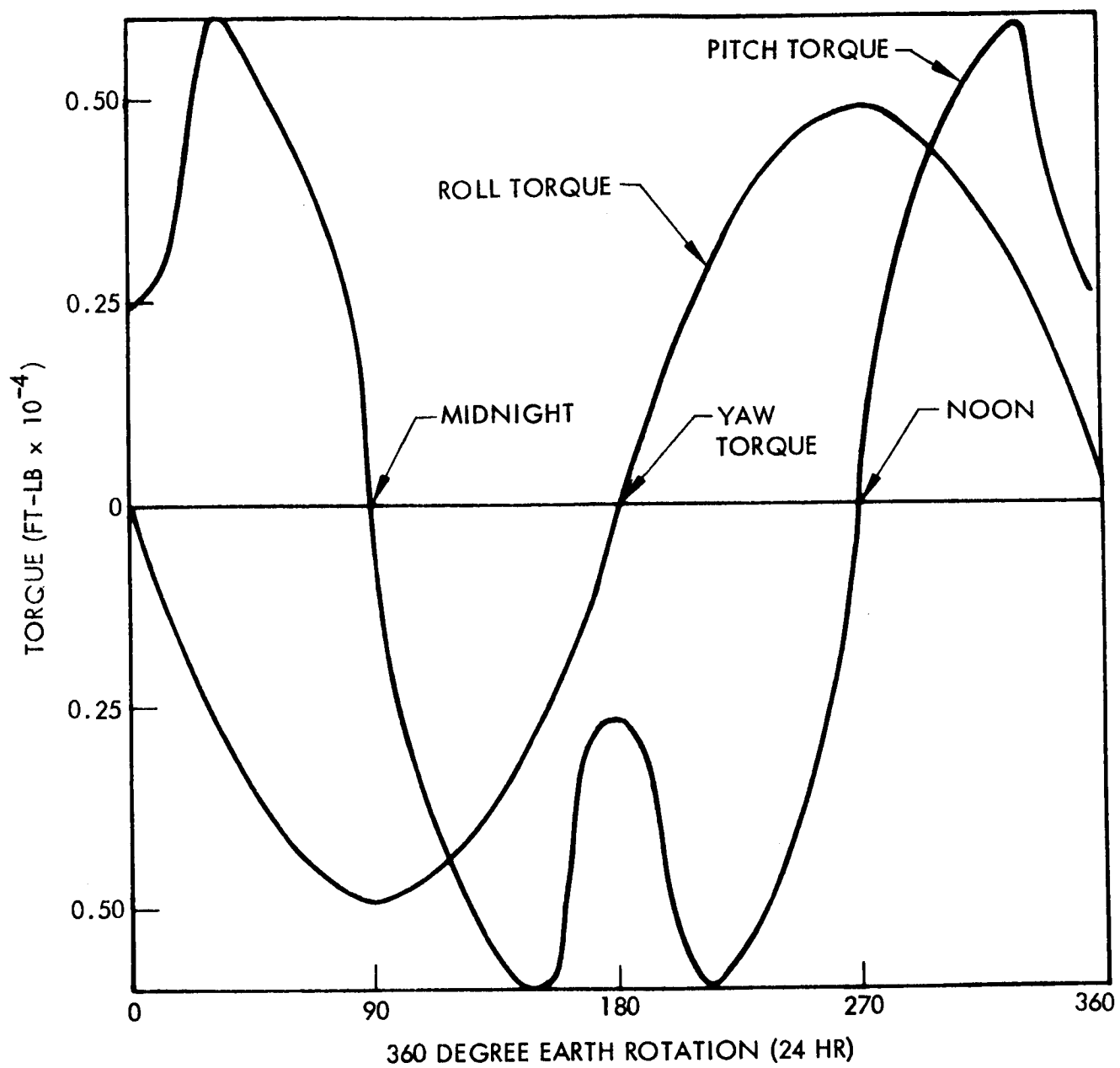


Fig. 6-34 Solar-Torque Profiles

The actual shape of the solar disturbance torque curve changes with changes in the system center of gravity. The average torque value decreases by approximately  $0.1 \times 10^{-3}$  ft-lb for every 1 ft increase in center-of-pressure/center-of-gravity separation.

The roll torque was not computed directly since its effect can be approximated by the pitch case. The maximum roll torque occurs during the summer solstice; the peak roll torque is approximately  $0.51 \times 10^{-4}$  ft-lb for a sun position 30 deg off the vehicle symmetric axis. The 30-deg angle off high noon will contribute  $0.46 \times 10^{-4}$  ft-lb of torque. The peak roll torque at the winter solstice is approximately  $0.3 \times 10^{-4}$  ft-lb, reducing to approximately  $0.51 \times 10^{-5}$  ft-lb near the equinox. The average roll torque that the control system must overcome is  $0.16 \times 10^{-4}$  ft-lb.

The vehicle is nearly symmetric in yaw, resulting in small solar disturbances. Assuming 0.1-ft center-of-gravity/center-of-pressure offset and a cross-sectional area of  $80 \text{ ft}^2$ , the solar torque is  $1.6 \times 10^{-6}$  ft-lb.

The effects of attitude maneuvers requiring the expenditure of control impulse are:

- Reorientation from horizon to horizon
- Tracking a low altitude satellite
- Antenna pattern scanning
- Gravity gradient when off nadir
- Magnetic torques

To reorient the vehicle attitude from horizon to horizon in 30 min requires an average rate

$$\Delta\omega = \frac{17.4 \text{ deg}}{57.3 \text{ deg/radian}} \times \frac{1}{1,800 \text{ sec}} = 0.169 \times 10^{-3} \text{ radian/sec}$$

The impulse (J) required for 180 such maneuvers is

$$J = 180 I \Delta \omega$$

where  $I$  is the inertia. The results are given in Table 6-15.

To determine gas consumption for tracking a low-altitude target, the assumption was made that the target was in a 90-min polar orbit whose orbital plane is normal to the local vertical of the ATS-4 satellite. A polar orbit represents the case where maximum gas consumption occurs. If tracking is accomplished through pitch and roll maneuvers then

$$= \frac{|\bar{M}|_{\text{ave}} \times T}{R}$$

where

$$\begin{aligned} |\bar{M}|_{\text{ave}} &= 0.638 (M_{x \text{ max}} + M_{y \text{ max}}) \\ |\bar{M}_x|_{\text{max}} &= \text{maximum roll torque} \\ |M_y|_{\text{max}} &= \text{maximum pitch torque} \\ T &= \text{orbital period of low-altitude satellite} \\ R &= \text{thruster lever arm} \end{aligned}$$

The result for 180 such maneuvers is shown in Table 6-15.

The parabolic antenna radiation pattern characteristic can be mapped by scanning the pattern back and forth across a ground station. The optimum method of doing this on a gas consumption basis is to use a square spiral scan. If this technique is used, the control gas impulse ( $J$ ) required is (using pitch and roll maneuver)

$$J = \frac{4RI}{lT} \sum_{k=0}^{n-1} (12 + 16K) r$$

where

- R = one-half the total pitch and roll angle scanned
- r = main antenna lobe radius
- l = gas valve lever arm
- n = number of spirals necessary to sweep out R
- T = time in which scan is to be completed
- I = inertia

The angular diameter of the scan pattern and, consequently, the control impulse required are a function of the frequency at which the pattern is being mapped. Gas consumption was calculated for scanning maneuvers at 800, 1,700, 2,100, and 2,300 MHz (each frequency scanned twice for  $T = 60$  min) and 7,300 and 8,000 MHz (each frequency scanned four times for  $T = 30$  min). The gas consumption results are shown in Table 6-15.

Table 6-15  
ATTITUDE-CONTROL SYSTEM GAS CONSUMPTION

Item	Maximum Impulse Required for 30-ft Flex Rib (lb-sec)
Solar Disturbances (for 2 yr)	800
Gravity Gradient Torques (7 deg Offset for 10 mo)	28
Antenna Scanning	1,000
Limit Cycle	200
Magnetic Torques	30
Attitude Maneuvers	75
Stationkeeping Unbalance	900
Solar Winds and Micrometeoroids	—
Total	3,033

When the parabolic antenna is pointing off nadir, gravity gradient torques are acting to align it to the local vertical. The gravity gradient torques are

$$M_{\theta} = -\frac{3}{2} \omega_o^2 (I_{xx} - I_{zz}) \sin 2\theta$$

$$M_{\phi} = -\frac{3}{2} \omega_o^2 (I_{xx} - I_{yy}) \sin 2\phi$$

where

$\omega_o$  = orbit rate

$\theta, \phi$  = pitch and roll euler angles

The torques are generally on the order of  $1.5 \times 10^{-5}$  ft-lb/deg. If the attitude is assumed offset 7 deg in pitch and roll and held for 10 mo, the impulse required is 56 lb-sec. This value is shown in Table 6-15

Magnetic torques due to electric currents in the vehicle also contribute to control gas consumption. The total solar array electrical output is 900 w at 28 vdc; the maximum current is 33 amp, which was assumed to circulate in a loop with an area of  $1 \text{ m}^2$ . The magnetic torque on the vehicle is:

$$T = \overline{M} \times \overline{B}$$

where

$T$  = torque in N/m

$\overline{M}$  = magnetic moment in amp-turns/m<sup>2</sup>

$\overline{B}$  = flux density in Wb/m<sup>2</sup> ( $1.265 \times 10^{-7}$  Wb/m<sup>2</sup> at 19,000 nm)

Evaluating the magnetic torque gives  $T = 40.2 \times 10^{-7}$  ft-lb. For 2 yr, this represents an impulse of 17 lb-sec. The impulse could be reduced further by careful design in the vehicle wiring layouts.



Attitude disturbance torques will be present on the vehicle during stationkeeping due to thruster misalignment of the stationkeeping ion thrusters. These torques must be compensated for by the attitude control system. The control gas impulse required during stationkeeping was approximated by assuming an 0.8-ft thruster misalignment, a vehicle mass of 51.3 slugs, and a stationkeeping velocity of 279 ft/sec. Thus, assuming a 12.5-ft lever arm for the control thrusters, the required impulse is 900 lb-sec.

#### 6.1.8 Attitude Verification

An extremely accurate and independent attitude sensor is required to verify the accuracy of the spacecraft attitude-control system. This requirement can be met with a star-field reader (SFR), which will independently monitor vehicle attitude and rates by measuring stellar positions relative to the satellite. Computation of vehicle attitude and rates is derived by applying stellar map-matching techniques with computers on the ground. Star-mapping techniques make use of the angular difference between star sightings. These angles are then compared with differences in the stored computer star catalog. When a match is achieved, a coordinate transformation is performed to obtain the vehicle attitude in inertial space. Star detection and readout of the SFR will be transmitted to the ground by a telemetry link.

Possible SFR candidates were compared on the basis of their ability to meet the following requirements: (1) three-axis attitude measurement with an accuracy of 6.0 min of arc and (2) lifetime of 90 days accumulated over a 2-yr period. The accuracy requirement is consistent with that of the spacecraft fine attitude-control system. The lifetime requirement assumes that attitude verification measurements would be made during various periods of the mission, but not continuously. The possible candidates are listed in Table 6-39. Basically, the sensor candidates can be considered as falling into two groups: those with a narrow field of view (FOV) (3 deg to 30 deg) and those with an FOV in excess of 30 deg. Table 6-16 shows that the desired star-position measurement process is handled differently by these two groups. The large FOV group utilizes a rapid-scan technique and relies upon detecting brighter stars, separated at large angles. The narrow FOV group uses a conventional rotating slit pattern or an electronic scan technique to detect the more abundant dimmer stars because of the

Table 6-16

## ATTITUDE VERIFICATION CANDIDATES

Company	Star-Field Reader Model	Accuracy	Detector Type	Telescope Design Aperture Size IFOV(a)	Star-Magnitude Probability	Scan Technique	Readout	Sun Protection	Size, Weight, Power
Control Data Corporation	Wide-angle celestial-attitude sensor	1.2 arc-min.	Photomultiplier with a rotating fiber-optic assembly, EMI tube 9514S	46 deg IFOV, 3.3-in.-diam. optics	+3.4 mv 0.999 prob. (read star relative brightness)	Rotating fiber-optic assembly with double slit	Dynamic Research 16 Optisyn 2 5-12/bit word per star	-	4.5-in. diam. x 12 in. 10 lb 12 w
General Precision (Aerospace)	Star-field Scanner	1.0 arc-min	Photomultiplier	15 x 30 min 2.75-in. optics	+3 mv	-	Digital	-	2.75-in. diam. x 12 in. 24.5 lb 35 w
United Aircraft Corp. System Center	Star-field scanner	2 arc-min	Photomultiplier ITT	15-deg IFOV	+55 mv 0.99 prob.	Electronic scan	Electronic scan matrix	Sun sensor and mechanical shutter	5.5-in. diam. x 3.6 in. 12.3 lb 6.0 w
ITT Federal Laboratories	Stellar-pattern mapper	1.0 arc-min	Photomultiplier	Two each telescopes 22-deg IFOV	+3 mv	Electronic scan	Digital	Mechanical shutter	3-in.-diam. x 11-in. telescope 3 in. x 5 in. x 6 in. electronics 11 lb 7.0 w

scarcity of the bright stars for the smaller selected FOV telescope design. The three preferred candidates are discussed separately, in order of their preference, in the following:

- The Control Data Corporation celestial-attitude sensor uses a 50-deg field-of-view telescope design. The instantaneous field of view (IFOV), which is  $15 \text{ deg} \times 4 \text{ min}$ , is scanned over the FOV by a rotating fiber-optic assembly (Fig. 6-35). The fiber assembly focuses the stellar field scanned onto a photomultiplier face plate. Stellar detection is based on threshold crossings. The star sensor sends three types of information to the computer: (1) the angle encoder reading at the time each star appeared in the slit, (2) the number of encoder counts that occurred while the star was visible in the slit, and (3) a digital indication of the relative height of the star pulse; this is obtained from a peak detector and an analog-to-digital converter. The encoder provides 13-bit resolution.
- The United Aircraft Corp. Systems Center star-field reader consists of an optical system that detects stars to fifth-order magnitude in a 15-deg FOV. A photomultiplier detects and amplifies the detected star image. The scanning electronics locates the star image in a calibrated X-Y coordinate system and stores position information in a register until initiation of the readout command. The system weighs 12.3 lb, measures 13.6 in. long by 5.5 in. in diameter, and consumes 6.0 w of power.
- The International Telephone and Telegraph Federal Laboratories stellar-pattern mapper comprises an optical system, multiplier phototube, deflection circuitry, high-voltage power supply, and digital logic circuitry. The unit will detect stars of +2 magnitude to +3 magnitude. Information readout is in real time. The stellar-pattern mapper employs a 10-deg square FOV optical system with 4,096-element resolution. The unit weighs 7 lb and uses 5.5 w of power.

The Control Data unit is recommended for ATS-4. This preference is based on the fact that the unit uses a large field of view, which gives a higher assurance of detecting a sufficient number of bright stars. This system also has the advantage that a smaller star catalog is required in the data-reduction system.

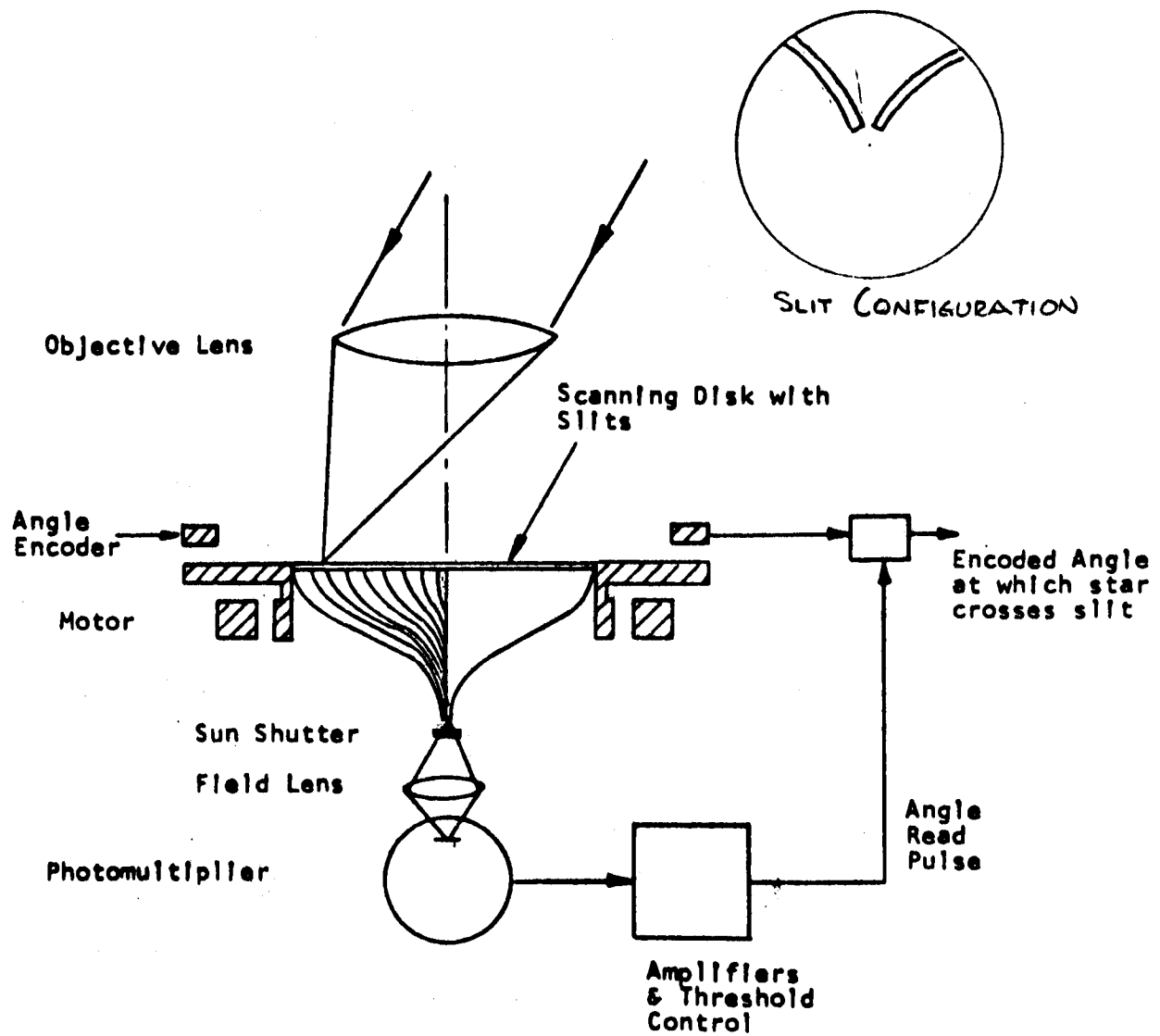


Fig. 6-35 Star-Field Reader Block Diagram.

## 6.2 EVALUATION OF PETALINE AND FLEXRIB ANTENNA CONCEPTS

Early in the ATS-4 study, a selection was made of two antenna types that would be investigated in some depth during the study. These particular antennas were selected on the basis of work that had been done earlier by Electro-Optical Systems and by Lockheed Missiles & Space Company. Both have remained as candidates throughout the study because they are both feasible designs and offer somewhat complementary advantages; in particular, the petaline appears to be inherently more capable of operation at higher frequencies than the flexrib (assuming thermal distortion problems can be solved) and the flexrib offers the possibility of larger diameters without excessive penalty to the spacecraft.

In the evaluations of subsections 6.2.1 and 6.2.2, the growth factors are neglected and a comparison is based on the following weighted criteria as applied to the ATS-4 work statement:

- Ground Test Capability. Both antennas can be ground deployed and tested with a minimum of aids; however, three problems are encountered with the petaline:
  - (1) Gravity must either assist or oppose the action of the springs that erect the petals, so it will not be possible to get a natural space deployment.
  - (2) Air damping may affect the operation unless the tests are conducted in a vacuum chamber.
  - (3) The large furled size (7 by 16 ft) makes the petaline more difficult to handle in ground testing.
- Tolerances. Tolerances include built-in approximations, manufacturing allowances, thermal distortion, and dynamic distortion. The tolerances stated by the designers are based on approximate analyses (included in the report) and estimates based on earlier designs:

<u>Error Source</u>	<u>Petaline (in.)</u>	<u>Flexrib (in.)</u>
Approximation error	0	0.019
Manufacturing	0.075	0.030-0.060
Thermal	0.012-0.070	0.020
Dynamic	Negligible*	Negligible*

- Simplicity. The mechanisms associated with each antenna are simple, direct-acting devices. One basis of comparison might be a parts count as follows:

<u>Petaline</u>	<u>Number</u>	<u>Flexrib</u>	<u>Number</u>
Petals	36	Ribs	20
Springs	36	6-element rib guides (20)	120
Dashpots	36	Gear-box assembly	10
72-element scissors (2)	144	Motor	1
Petal locks	<u>252</u>	Ring Gear	<u>1</u>
Total parts	504		152

- Producibility. On the basis of previous work, it has been concluded that the antennas are equally difficult to produce.
- Weight

<u>Petaline</u>	<u>Weight (lb)</u>	<u>Flexrib</u>	<u>Weight (lb)</u>
Petals	132	Ribs	118
Feed support (charged at half for petal support)	31	Cloth	12
Base plate	42	Hub assembly	70
Latching mechanism	12	Shroud penalty	<u>8</u>
Unfurling mechanism	36		208
Shroud penalty	<u>50</u>		
	303		

\*With thrust levels of 300  $\mu$ lb.

- **Installation Problems.** The principal installation problem is a result of the long dimension of the furled petaline. A significant shroud extension and a structure to anchor the petals are necessary during the ascent phase. The lengthy package complicates spin-control mechanisms if a spinning ascent to orbit is utilized; since the LMSC configuration does not spin, no penalty was assigned for this constraint. The furled volumes are as follows:
  - (1) Petaline: 7-ft diam. by 16.5 ft long =  $640 \text{ ft}^3$
  - (2) Flexrib: 4.5-ft diam. by 1.5 ft long =  $24 \text{ ft}^3$
- **Requirement for New Technology.** It is judged that no new materials, processes, or inventions are required to produce either design.
- **Rigidity.** Deployed rigidity is considered because of its possible effect on control-system stability. Both antennas should be adequate in this regard since they are sufficiently rigid for ground testing. The flexrib is inferior to the petaline because it is more flexible in yaw.
- **Flight Proven Techniques.** The folding petal antenna has not flown on any space vehicles; the flexrib configuration has been flown repeatedly and successfully, but the rib design was different from that which is currently proposed and the diameter was about one-third of the ATS-4 antenna.
- **Deployment Reliability.** A complete failure-mode analysis has not been performed on either antenna. The petaline deployment is simple and the scissors arrangement should prevent a petal from sticking; the locking mechanism could be a problem, particularly if the petals were distorted by ascent heat loads. However, the failure of a few locks would not seriously affect performance. The flexrib is deployed under positive mechanical drive and depends on the motor and associated gearing to operate through its complete erection sequence, since partial deployment would not provide a parabolic surface. At this stage of the design, the two concepts are considered to have equal reliability.
- **Deployment Torques.** The spacecraft must remain oriented during deployment, so if torques are developed they must be opposed by the control system. The petaline antenna should produce no net torque during the erection cycle. The flexrib will produce a yaw torque as the drum unwinds and, although the net angular momentum remains constant, the control system must expend propellant to hold the yaw attitude during the erection cycle.

- **Costs.** The rough order of magnitude (ROM) costs for developing the antennas beyond the engineering model currently in procurement (two ground test and two flight models) are \$4.2 million for the petaline antenna and \$1.7 million for the flexrib. A list of values assigned to the weighted criteria is as follows:

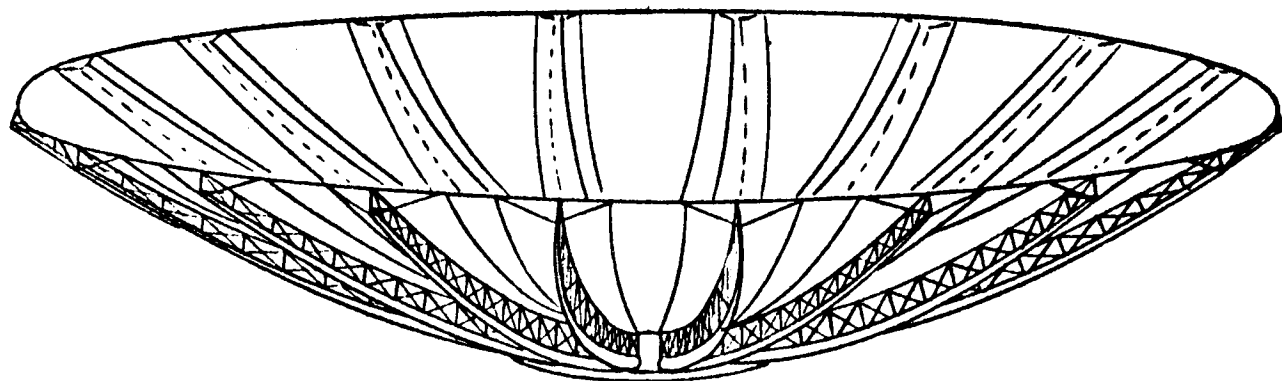
<u>Criteria</u>	<u>Weight</u>	<u>Petaline</u>	<u>Flexrib</u>
Ground Test Capability	10	8	10
Tolerances	10	9	10
Simplicity	5	9	10
Producibility	3	10	10
Weight	5	7	10
Installation Problems	5	3	10
Requirement for New Technology	4	10	10
Rigidity	1	10	6
Flight Proven Techniques	6	—	—
Reliability of Deployment	5	10	8
Deployment Torques	1	10	7
Total	550	405	473
Normalized		74	86

On the basis of the foregoing evaluation and ROM cost estimates, the flexrib design is recommended for the ATS-4 program.

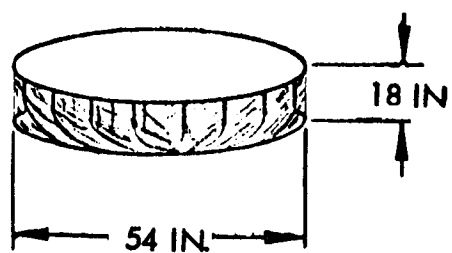
#### 6.2.1 Flexrib Antenna

The flexrib reflector consists of radial ribs to which is attached a flexible, reflective fabric. The surface of the paraboloid is formed, therefore, by a series of flat panels. The reflector has approximately 60 panels, formed by either 20 or 30 ribs. Two or three panels are formed between each rib by an attachment to the back edge of the rib. For stowage the ribs and skin are spirally wrapped about a center hub. The flattened cylinder formed by the stowed antenna has a diameter one-sixth to one-tenth of the deployed parabola. As shown in Fig. 6-36, the furled package is 4.5 ft in diameter, and 1.5 ft deep, not including feed cone, supports, and mounting brackets.





OPEN



FURLED

Fig. 6-36 30-ft-Diam. Flexrib Antenna

The flexrib design combines excellent furled-to-unfurled dimensional ratio, can be relatively lightweight, and presents few dynamic or environmental problems in the stowed position during ascent, since the wrapped ribs and skin are very densely packed.

Surface Tolerance Analysis. The flexrib antenna concept exhibits an inherent error because the paraboloidal surface, a figure of revolution, is approximated by a number of cylindrical surfaces. This technique is analogous to the approximation of a circle by a regular polygon of many sides. The approximation error must be held to a small portion of the total error budget. Increasing the number of panels in the flexrib design reduces the approximation error, but it also increases the weight of the structure. The number of panels must be chosen in such a way as to provide the optimum compromise between weight and performance.

The design approach used by LMSC in flexrib antenna development is to limit contour inaccuracies to a value that produces 0.5 db or less degradation in gain. This specification is compatible with communications application; for other uses, where beamwidth, null position, and sidelobe level are critical, the specification would be appropriately modified. According to the classic work of Ruze, this design yields a surface inaccuracy of  $\lambda/37$  rms, if the errors are random and are uniformly distributed over the aperture. Since some errors are systematic and are weighted favorably by the aperture illumination (thereby reducing their effect), some relaxation of this tolerance is permissible.

The three major errors are (1) approximation error ("the flat panel effect"), (2) thermal and dynamic errors, and (3) manufacturing error. The first two are systematic errors (they occur for every reflector made from the same prints), whereas the last one is a random error (peculiar to the particular reflector). The following comments apply to a 30-ft flexrib reflector at 8 GHz.

Approximation error can be reduced by increasing the number of panels used. The 60 panels contemplated for this reflector result in an rms deviation of approximately 0.0184 in. Treated as a random error, this deviation would produce a gain degradation of 0.1 db. Radiation pattern analysis shows, however, that with a feed pattern

having the shape of the fourth power of the cosine (zero at  $\pm 90$  deg), the gain degradation would be 0.08 db and would be even less for more tapered aperture distributions. This error can be reduced by adding more panels to increase the weight. For example, 100 panels would reduce the gain degradation to 0.0145 db and the rms deviation to 0.0066 in.

Determining the deviations due to the operating environment is a different process. This problem is being analyzed for a 50-ft reflector at 4 GHz with 54 panels; the results will be applicable to the case at hand since (1) the reflector is a 2/1 scale of a 25-ft 8-GHz reflector, or (2) the innermost 30 ft of aperture would be accurate enough for 8-GHz operation. The dominant error in this category is the deflection due to the thermal gradients. The procedure is to determine the temperature distribution (three-dimensionally) from the position in orbit and from the orientation; to determine the resulting structural deflections by analyzing the interaction of the ribs, the hub, the reflecting mesh, and the rib stiffeners; and then to compute the effect on electrical performance. This error is a function of time, and the design can therefore be optimized for average conditions or for the more important conditions. Since the thermal error is a systematic error and often has a radial distribution similar to that of the approximation error, its effect is somewhat less severe than would be predicted for a random error of the same rms magnitude. Thermal deflections normally are biased in the direction of the axis of the reflector, allowing the designer to build in a compensating pre-bias for average conditions.

In view of the foregoing, one can be optimistic about the thermal problem. The present status of the analysis on the 50-ft reflector is that thermal gradients have been defined but have not been completely converted into the resulting deflections. In a worst-case condition, the maximum deflection due to thermal effects is 0.200 in. at the rib tip. Converting this to an rms value and scaling to a 30-foot diameter, one finds an approximate rms deviation under worst conditions of 0.040 in. This value,

however, is preliminary; various optimization options have not been utilized. Under average conditions when the design is further refined, the thermal error can be realistically estimated to be about the same as the approximation error, i.e., about 0.020 in.

Manufacturing tolerances are the most difficult to estimate in advance of construction. Fortunately, a certain figure can be set as a target and, if the measurement accuracy is compatible with this figure, the reflector can be worked into tolerance during construction. The chief contributors to the manufacturing errors are rib contour inaccuracies and skin ripples. The former are the usual inaccuracies of cutting a contour to a specific curve. Skin ripples are more complicated, depending on cutting the skin to a specific pattern, fastening the panels together accurately, and then attaching the skin to the ribs with the correct amount of appropriately distributed prestress.

The first large-aperture X-band reflector flexrib techniques was a 15-ft parabolic cylinder constructed in 1964. The rms deviation estimated from gain measurements was about 0.100 in. including both manufacturing and approximation errors. This error would now be considered unacceptable, in view of the techniques developed since then, but it gives a starting point. The relatively large rms error was due to the following reasons:

- The surface was a rectangular segment of a parabolic cylinder, rather than a paraboloid; a balanced circumferential stress distribution was therefore not attainable.
- No fixtures were used for fastening the skin panels together or for fastening the skin to the ribs; such fixtures are necessary for large apertures.
- An adequate gravity compensating fixture was not available for the testing.
- Since the antenna was not protected from the wind during the test phase, surface contour degraded seriously between the time of construction and the time of final test (because of skin stretch).

Changes in concept since the construction of this reflector include vastly improved rib designs, better skin materials, and better manufacturing and handling methods. Taking these considerations into account and extrapolating to the 30-ft diameter, a pessimistic estimate of the manufacturing error would be 0.060 in. rms, and an optimistic estimate would be 0.030 in. rms.

An overall tolerance can then be predicted for a 30-ft 8-GHz reflector of the flexrib type. If the approximation error is 0.0185 in. rms, the thermal and dynamic errors 0.020 in. , rms, and the manufacturing error between 0.030 and 0.060 in. rms, then the overall error ranges from 0.0405 to 0.0657 in. , rms. The optimization procedures described in connection with thermal errors can also be applied to the sum of all systematic errors (approximation, thermal, and dynamic). If the manufacturing error is near the pessimistic end of its range, further reduction of the systematic errors over the figures given above would not have a significant effect on the overall error. The gain degradation due to the total error, treated as random, would be between 0.5 and 1.3 db.

Achievable tolerance as a function of diameter was obtained by extrapolating from the 50-ft reflector. It was assumed that each reflector would be designed to have the same approximation error. The variation of thermal and dynamic error was taken as square law, and the variation of manufacturing error was taken as linear.

Energy of 0.25 hp will be sufficient to deploy the antenna. This figure is based on estimates made in connection with the 50-ft antenna (0.25 hp for 5 min) and on the fact that a motor-driven 20-ft flexrib was deployed on the ground with a 0.25 hp motor.

Thermal deflection is a systematic error and usually it is radially dependent in a manner similar to that of the approximation error; it is therefore less serious than the equivalent random error unweighted with regard to location. A complete analysis of the thermal properties of the 50-ft reflector (now being developed at LMSC) has been made. Structural deflections due to thermal gradients were computed for a large-aperture flexrib antenna in a previous LMSC study.

Estimates for weight versus diameter were obtained by extrapolation from the 50-ft antenna, which has been carefully studied from a weight standpoint. The proper number of ribs have been added to ensure operation at 8 GHz. Since the weight figure obtained in this way for the 30-ft diameter was within a dozen pounds of a previous weight estimate given on a more detailed basis for the 50-ft reflector, the method of extrapolation appears to be reasonably good.

A preliminary structural analysis has been completed for the 50-ft parabolic antenna reflector that LMSC is now fabricating. This demonstration model is, in many respects, similar in design to the 30-ft-diameter antenna proposed for the ATS-4 vehicle. The analysis is concerned with the strength of the antenna for 1-g deployment, as well as with the suitability of the design and the materials for stowage and deployment.

Deployment Technique. The technique for deployment of the antenna is illustrated in Figs. 6-37 through 6-39. The antenna shown in the illustrations is a 20-ft model constructed by LMSC to test and demonstrate the flexrib concept. Its main purpose was to evaluate hub design and to verify the structural capacity and durability of the ellipsoidal shaped ribs. The unit is mounted in a wooden transportation crate. For photographic purposes, the antenna skin has been removed, and strings have been attached between the rib tips; with the cloth skin in place, much of the deployment cycle is obscured.

Figure 6-37 shows the beginning of the deployment cycle. The antenna drum is rotated clockwise (in this case by a 0.25-hp electric motor), driving the tips of the ribs outward tangentially; the fulcrum against which support is derived is the candle, or "shoe," affixed to the nonrotating base of the antenna drum. Each rib is positioned by the spring-loaded shoe and is supported, for ground-test purposes, by the V-shaped fingers. A closeup of this shoe is shown in Fig. 6-38.

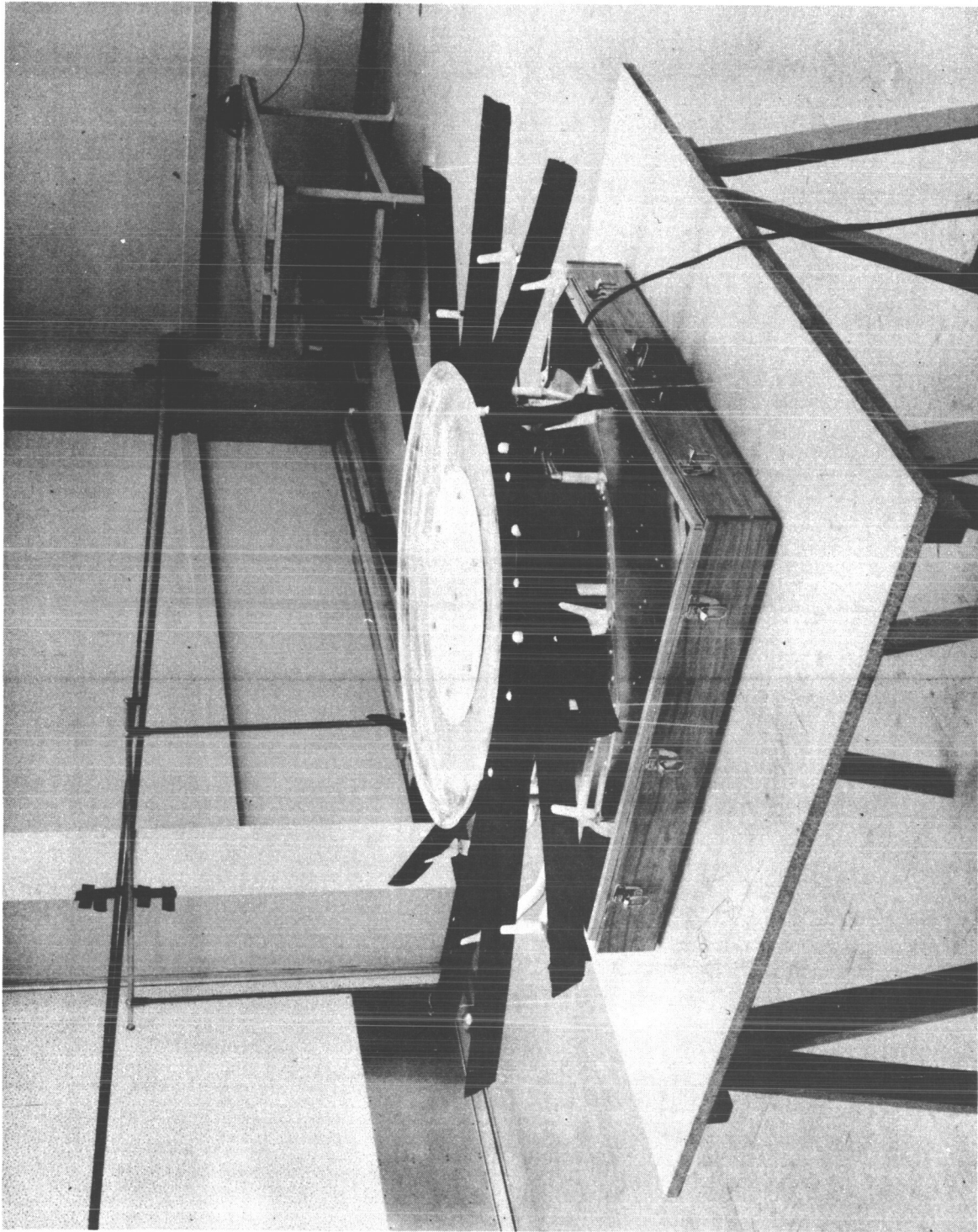


Fig. 6-37 Beginning of Antenna Deployment Cycle

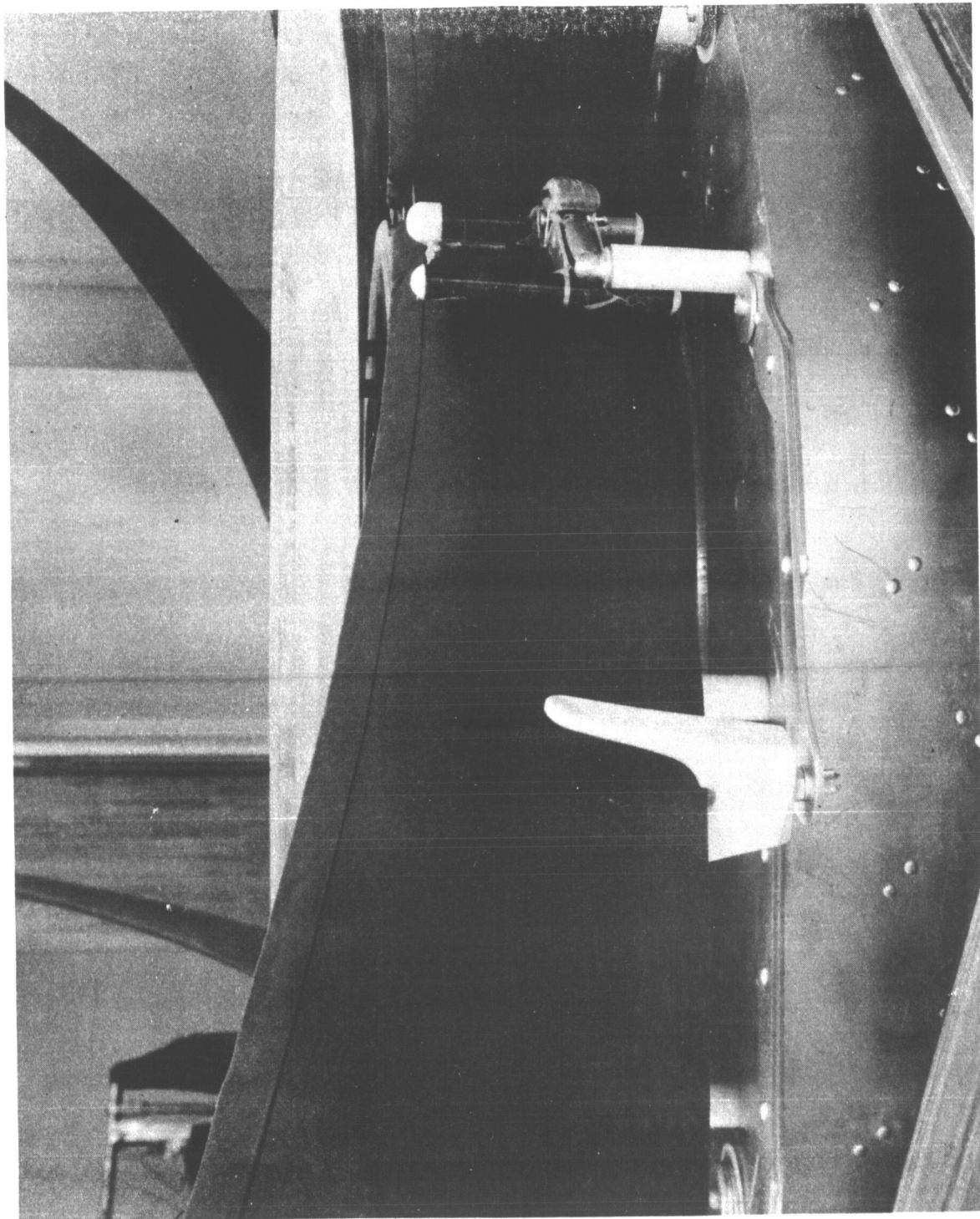


Fig. 6-38 Closeup of Guide Shoe and Support



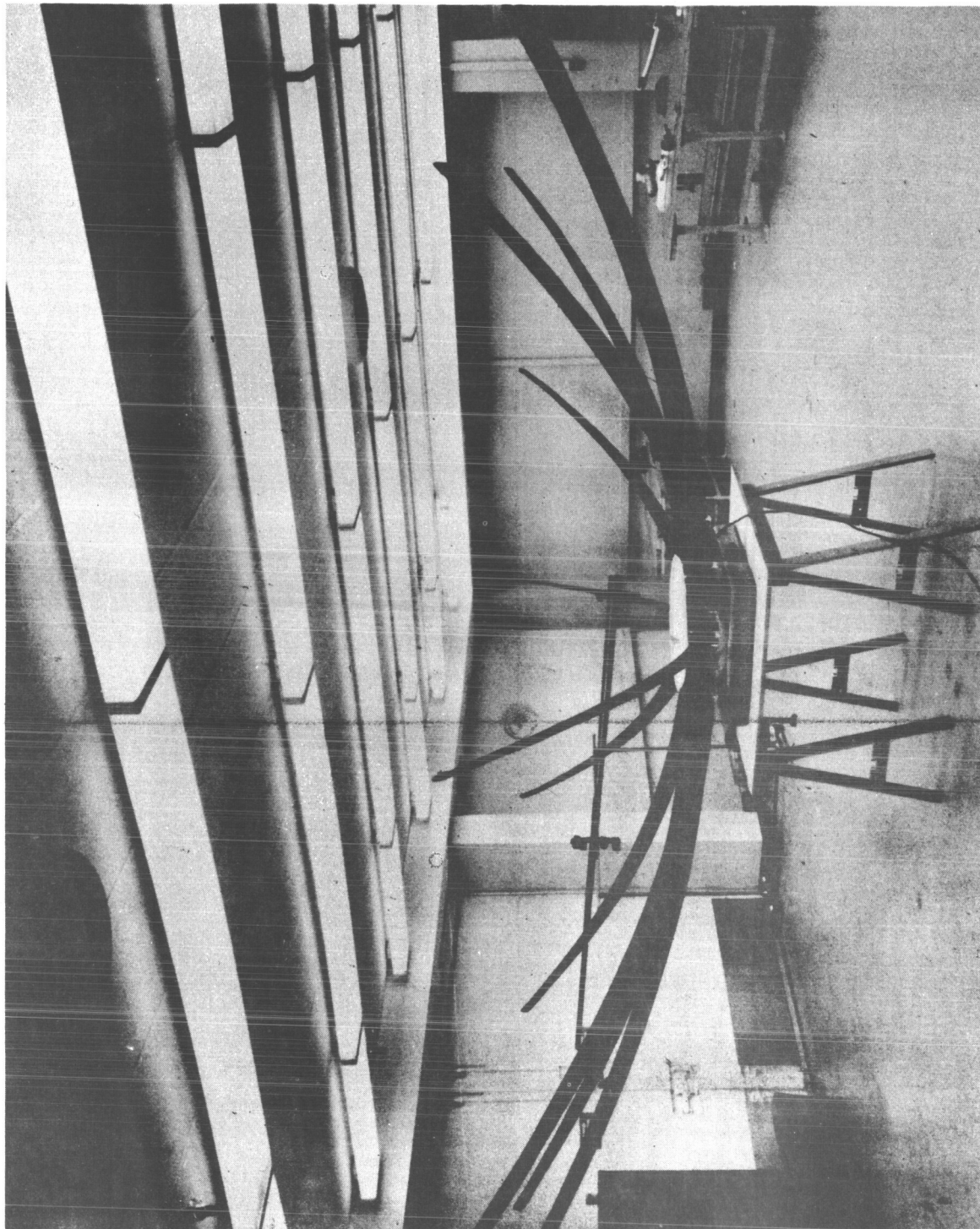


Fig. 6-39 Fully Deployed Flexrib Antenna (20-ft-diam. Model)

Continued rotation of the drum forces the wrapped ribs to extend. Each rib is mounted to the drum with a hinge. As the antenna is nearing its full extension, the hinge point of each rib swings past the shoe, still using the latter as a fulcrum, and the rib tips describe a short arc, the ribs now being radial to the hub rather than tangential. At this point the motor is stopped, and the antenna is fully deployed, as shown in Fig. 6-39. The strings representing the cloth are taut.

This demonstration antenna has been deployed over 30 times. Several of the ribs have been subjected to 600 retractions and extensions to determine durability. The ribs, approximately 10-ft in length, can be supported without aid from the tip end horizontally, and can be wrapped around a drum with a diameter of less than 1 ft. Each rib is aluminum, formed by hammer swaging.

For this model, the two halves of the ribs are simply butted together and joined by small sections of plastic tape. The tape permits the sections to be completely flattened when wound on the drum, and also permits the slight lateral movement between the sections that occurs because of differential radius. When the ribs are wound into the drum, each rib is rotated or torqued about its longitudinal axis to account for the difference in height between the butt of the rib and the tips. Since the two halves of the rib were joined with tape, no buckling or deformation of the rib occurred.

In general, this deployment sequence is typical of the power-driven flexrib type of antenna and would be used on any rib type proposed for the ATS-4 vehicle.

Fabrication and Materials. The following techniques, developed by LMSC in the production of flexrib-type antennas, will be utilized for fabrication of the 30-ft parabola. Each rib will be formed in a fabrication jig that ensures proper location of each component in the open-truss rib.

The upper and lower beams of the open truss will be contoured by local impact swaging. This work will be performed on a large-surface table, using templates to indicate the contour. As the beam is worked in the free state, i.e., without clamps or other devices to inhibit the natural state of the material, the process allows for precise contour

control. Ribs can be fabricated to 0.010 in. of the theoretical contour. The nature of this process is such that more exacting tolerances can be readily achieved where required. Residual stresses created by forming are minimized because bending and spring-back are not a part of the process, and the swaging is essentially uniform along the entire length of the rib beam. After completion of the 30-ft-diameter antenna, each rib will be temperature cycled and checked against the theoretical contour during the cycling to assure that fabrication quality is uniform and within allowable tolerances. Fabrication of the rib on a flat table in a relaxed or unrestrained position is a good simulation of the zero-g condition. Design of this antenna with an f/D ratio of 0.5 will make fabrication of the ribs easier because the curvature of the ribs is less than for the more common 0.4 f/D antenna.

The two half-shell stiffeners for each rib can be formed by techniques developed and used on many other flexrib antennas built by LMSC. The process is a straightforward die-forming method that embodies use of a power brake and rubber pad. The forming stress inherent in this process is essentially normal to the rib contour and has minor influence upon the rib during temperature cycling. This member is also free to expand or contract without disturbing the rib contour.

The reflective skin of the antenna is a light-weight marquisette. Techniques have been developed for sewing such materials. The panels are plated by an electroless copper plating process developed explicitly for antenna use. After plating, a silicon coating is applied to each reflective panel by an electrostatic spray process that coats the fabric uniformly without closing the open cells. Each panel is then placed on a forming jig for fitting and bonding. The panels are bonded together with a silicon adhesive material similar in composition to that of the protective spray.

The deployment mechanism components will be fabricated in the LMSC shop. The inner and outer rings of the hub will be formed from sheet metal and rolled extrusions and then machined to final dimensions. All of the gears for the deployment mechanism will be enclosed except the main ring gear and the pinion.

Special lubricants have been developed and evaluated for the enclosed nonhermetically sealed gear boxes.

Boom-Machine Description. The boom mechanism is designed to assemble, extend, retract, and disassemble a lightweight, thin-web beam with a triangular, box, or other type cross section. In the development model, the beam is made of three preformed webs that are flanged at 30 deg along both edges. The mating portions of strips of Velcro tape, as well as a series of mating fasteners at appropriate intervals, are bonded to each flange.

Each web is loaded onto a reel situated on the underside of a base plate. On the upper side of the base plate are three pairs of power-driven pressure rollers through which the beam flanges pass. Above these pressure rollers are three roller fair leads, one for each corner of the beam.

The power-driven forming rolls pull the webs from the reels and then press the flange edges together. Extension is by means of friction between the rubber roller surfaces and the web. Extension may also be accomplished by means of sprocket wheels and appropriate sprocket holes in the web flange. Power can be derived from electrical, hydraulic, or compressed-gas motors.

The three sets of forming wheels are linked by jointed shafts, thus making all three wheel sets drive at a constant rate. The three web reels are also linked by shafts. The rate at which the web is pulled from the reel is determined by clutches on these wheels, so the tendency of the web to unwind because of spring tension is controlled. The webs pass from the reel over a rotating disc. This disc keeps the Velcro tapes from touching until they are mated by the drive wheels. A machined finger is between the disc and the drive wheels, positioned at a point just before the entrance of the flanges to the rollers. Adjustment of the position of this finger assists in aligning the beam.

The length of beam that can be produced is dependent entirely upon reel size and strength of the beam. In space, beams in excess of 100 ft can be formed as well as retracted. The beam length for ATS-4, if the device is used for forming the feed boom, would be approximately 18 ft. This length is well within the capability of the machine since a boom of similar dimensions has been extended and retracted over 200 times horizontally in a 1-g field. The forming machine in this case is housed in the lower equipment section away from the main equipment section and parabola. Boom extension can be controlled to within 0.010 in.

### 6.2.2 Petaline Antenna

System Description. The petaline antenna system consists of a parabolic reflector, an electronic feed subsystem, and a feed support structure. The reflector is made from 36 petals, each constructed from an electroformed "hollow core" structure; the feed support is a tripod tubular structure. The arrangements of the Cassegrainian and non-Cassegrainian systems are shown in Figs. 6-40 and 6-41. The antenna arrangements (as packaged into the launch vehicle) are as shown in Fig. 6-42.

Results of an analytical study by EOS indicate that the proposed design will meet the system requirements with regard to both electrical performance and weight allocation. A weight summary is presented in Table 6-17, and system characteristics are summarized in Table 6-18.

Fabrication and Materials. The petal structure will be fabricated by the electroforming process.\* A typical electroformed structure is shown in Fig. 6-43.

The antenna petal is fabricated by preparing an aluminum mandrel of flat aluminum sheet stock that is set up and drilled (or punched) to the required hole pattern. The drilled aluminum sheet (Fig. 6-44) is then formed between two masters until the paraboloidal surface is formed. At this point of the operation, the surface error will be approximately  $\pm 0.100$  in. Further treatment is performed by local hammering. After this process the sheet is cut along the indicated contour. The finished mandrel accuracy is better than  $\pm 0.050$  in. a finished mandrel is as shown in Fig. 6-45.

After the mandrel has been cleaned and prepared, it is mounted in a reciprocator and electroformed in an electroplating bath. After the required thickness of nickel (2.5 mils in this case) has been deposited on the mandrel, the aluminum is removed by etching with dilute hydrochloric acid.

---

\*Electroforming is defined as a production, or reproduction, of articles by electro-deposition upon a mandrel (or mold) that is subsequently separated from the deposit. The electroforming process has the advantage that an extremely lightweight and relatively stiff structure can be produced with high surface accuracy. The process permits fabrication of the structure as an integral unit without welded or bonded joints.

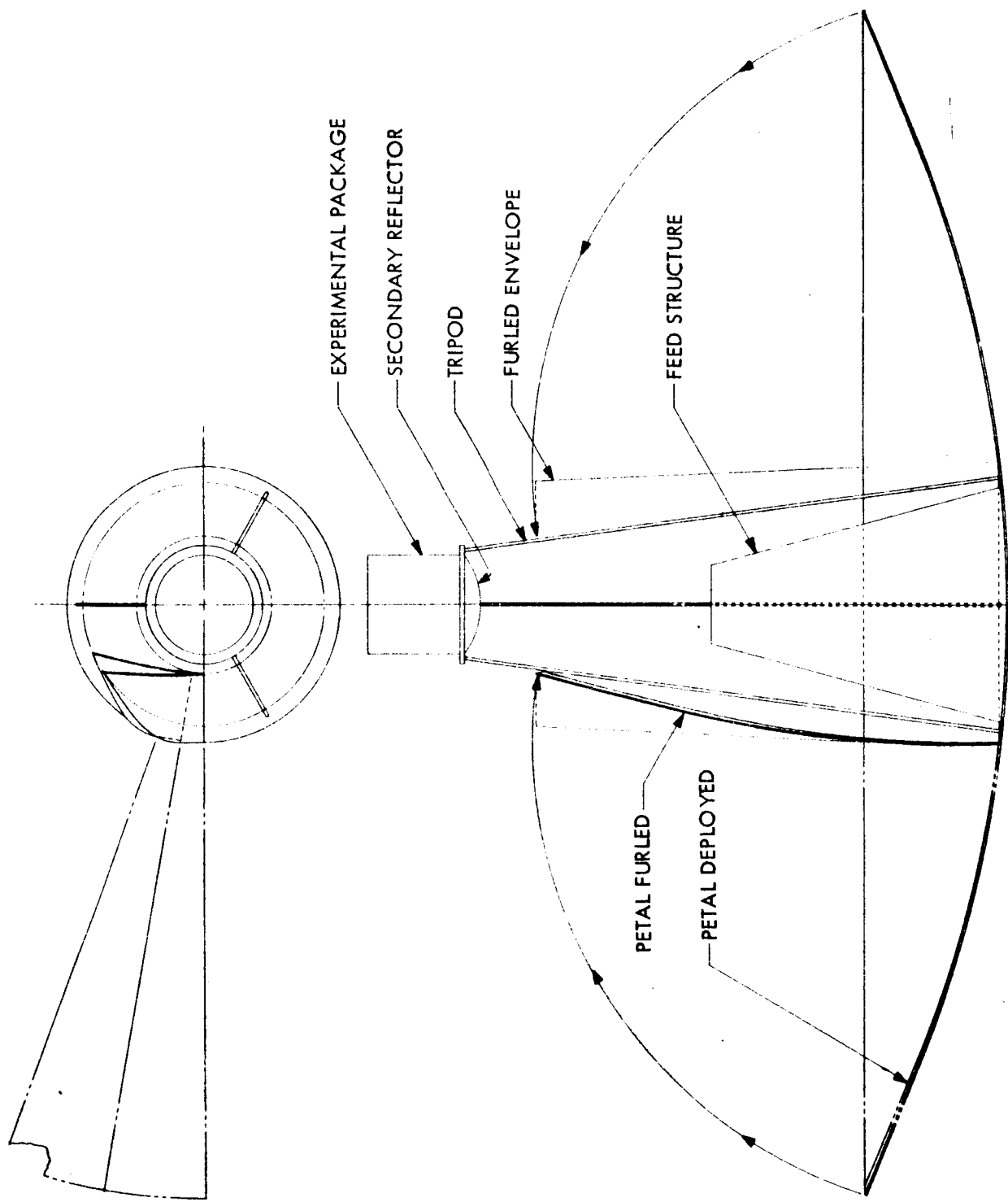


Fig. 6-40 Conceptual Design of Cassegrainian Antenna System With  $F/D = 0.5$

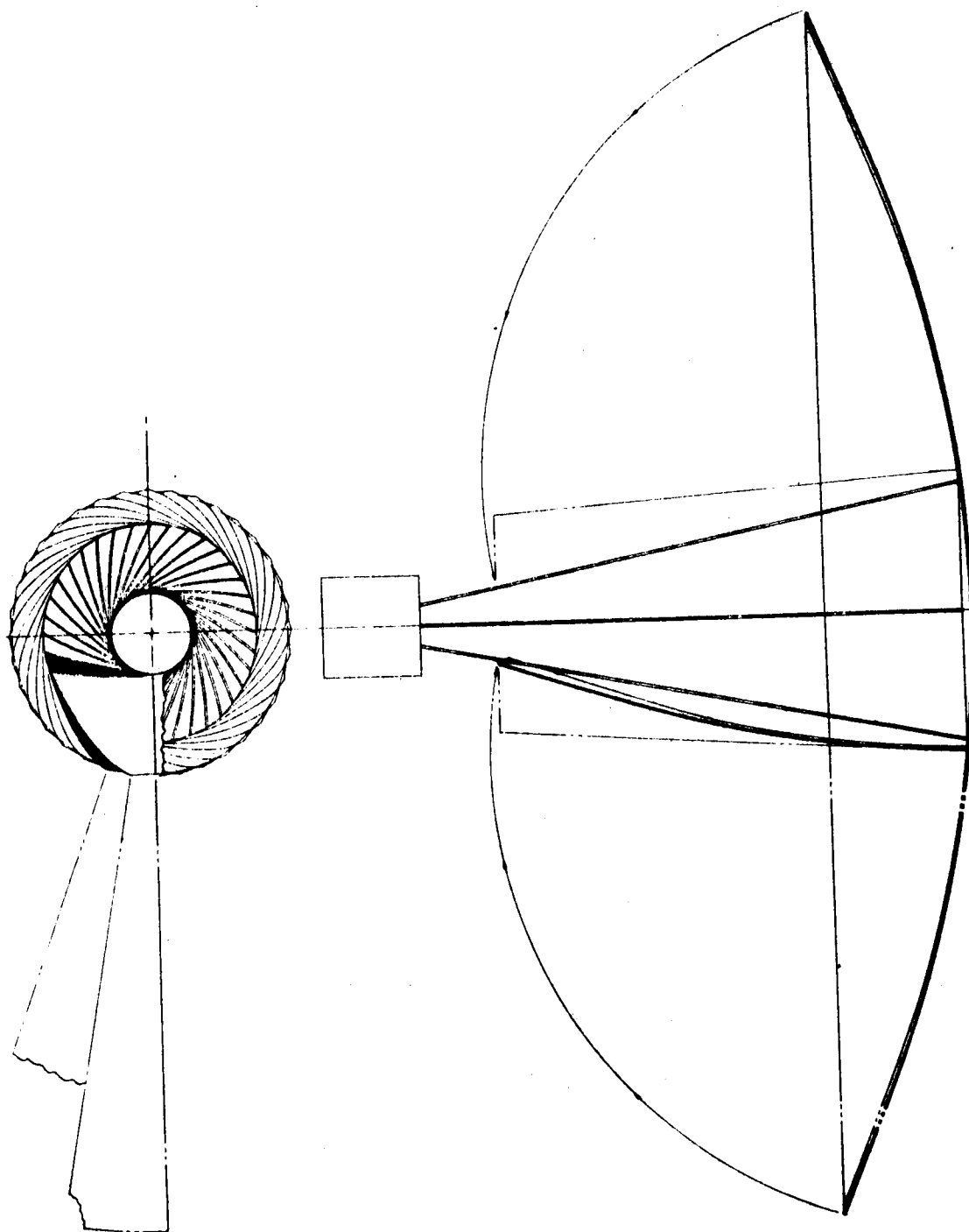


Fig. 6-41 Conceptual Design of non-Cassegrainian Antenna System With  $F/D = 0.5$



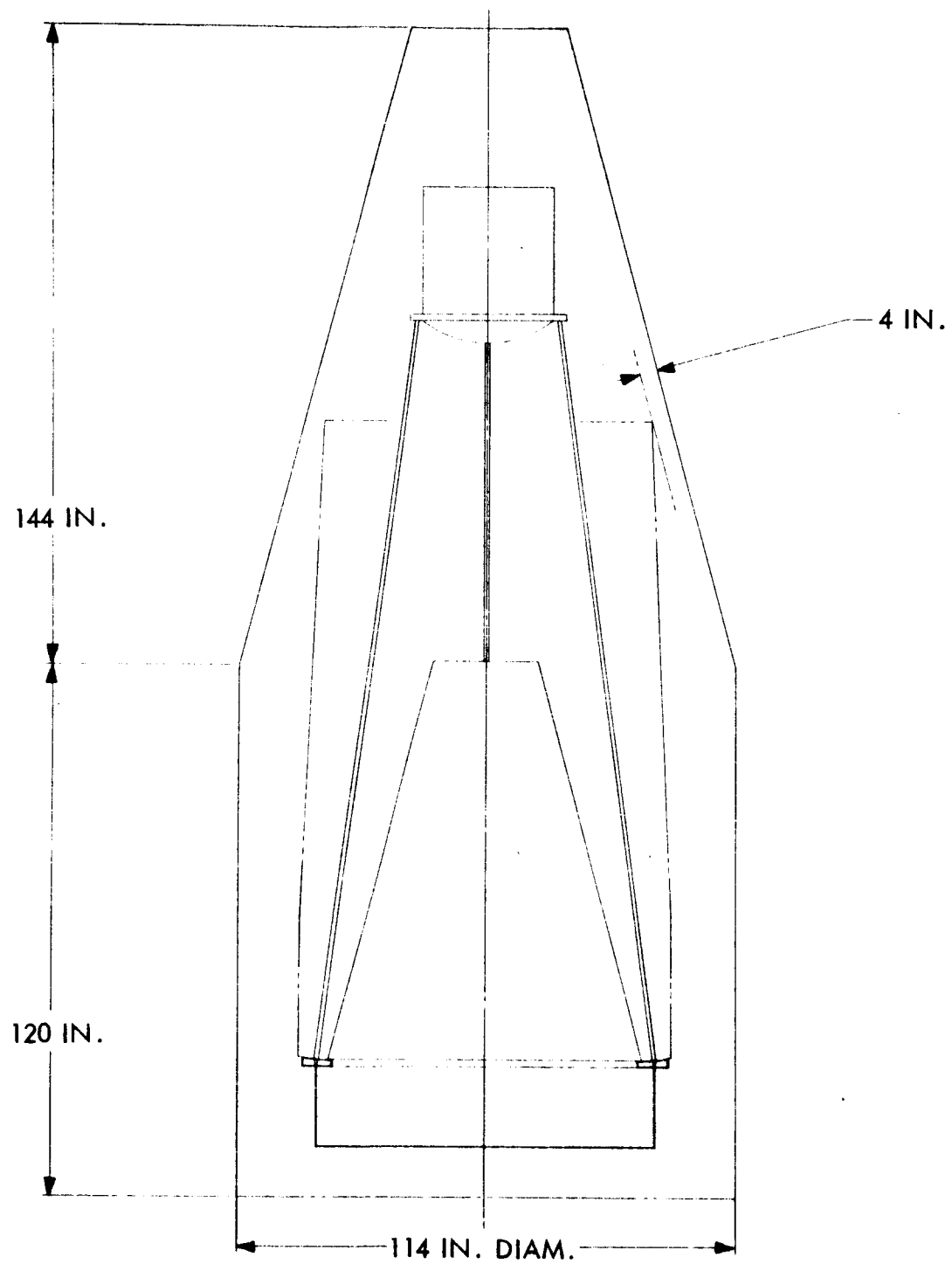


Fig. 6-42 Furled Antenna Packaged in Launch Shroud

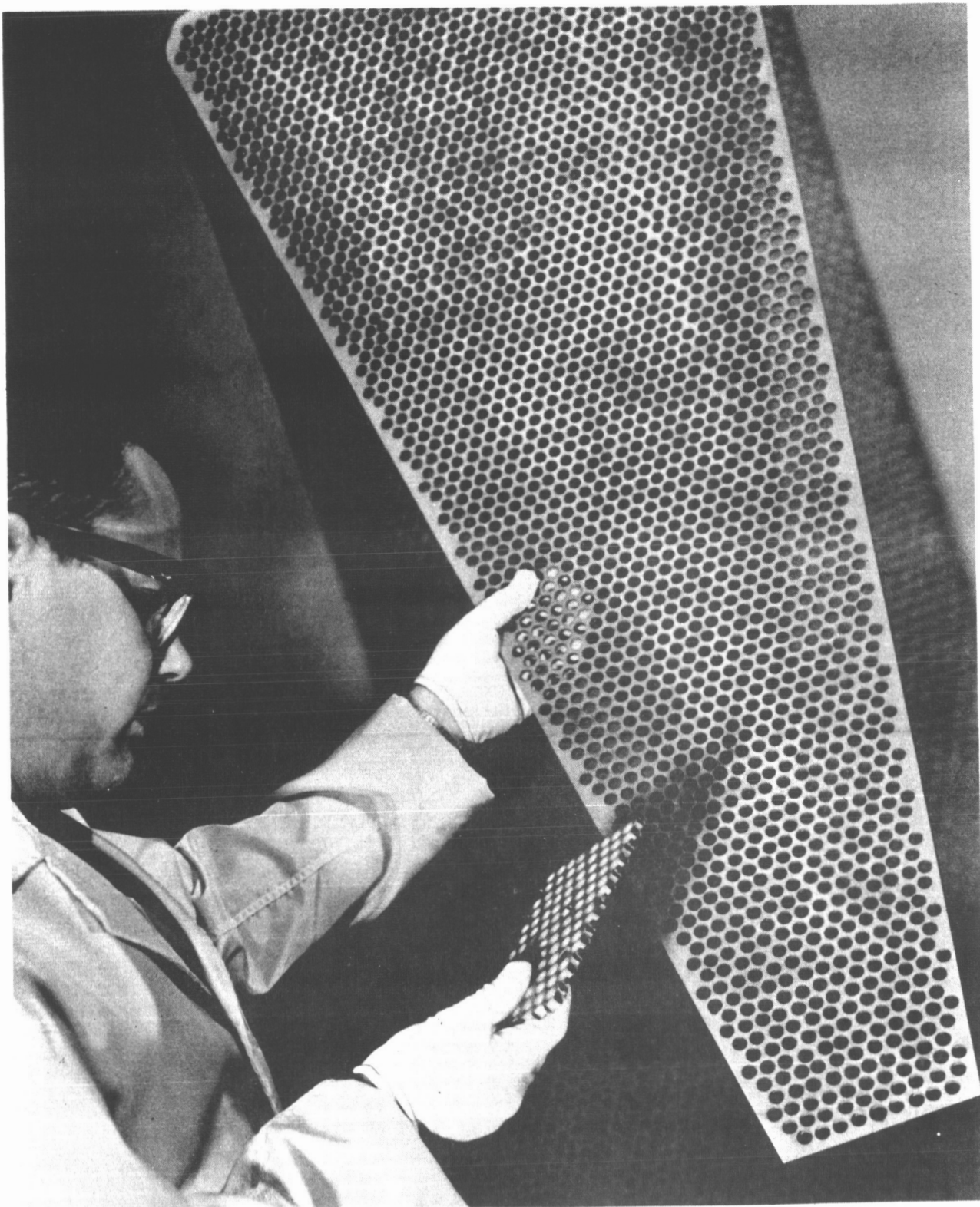


Fig. 6-43 Typical Electroformed Structure

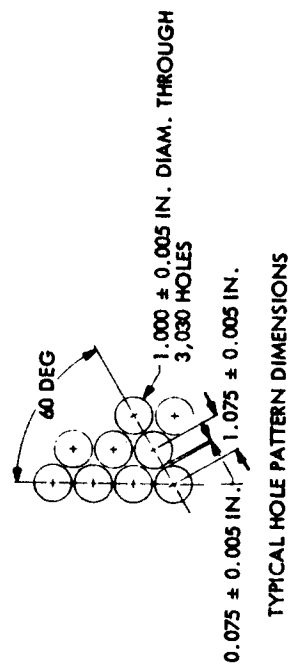
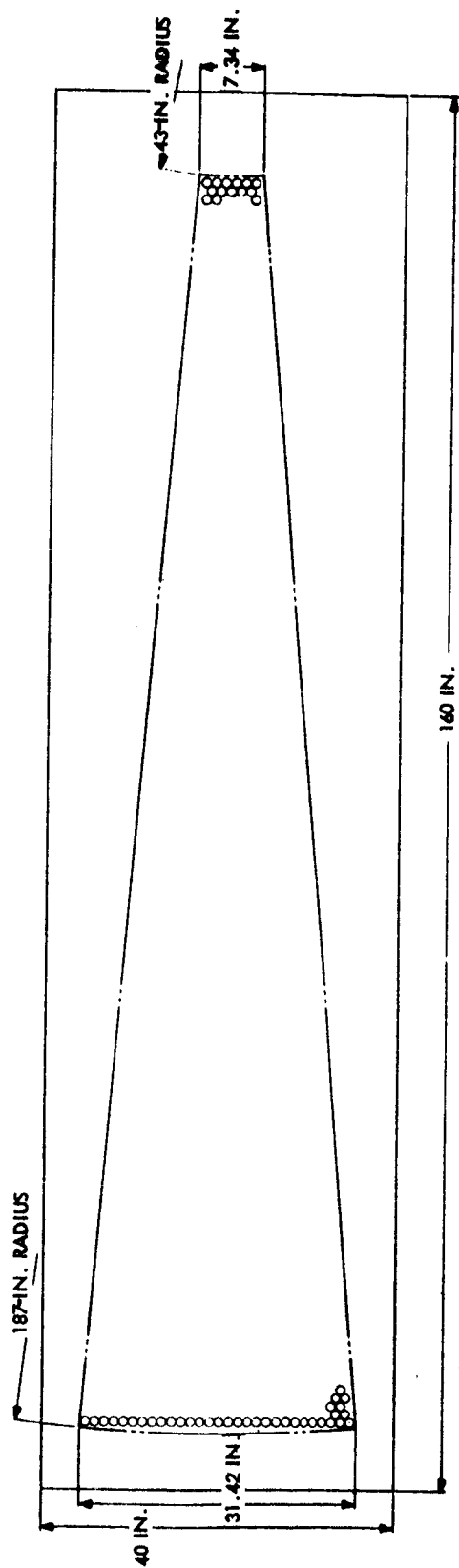


Fig. 6-44 Flat Layout - Electroforming Mandrel

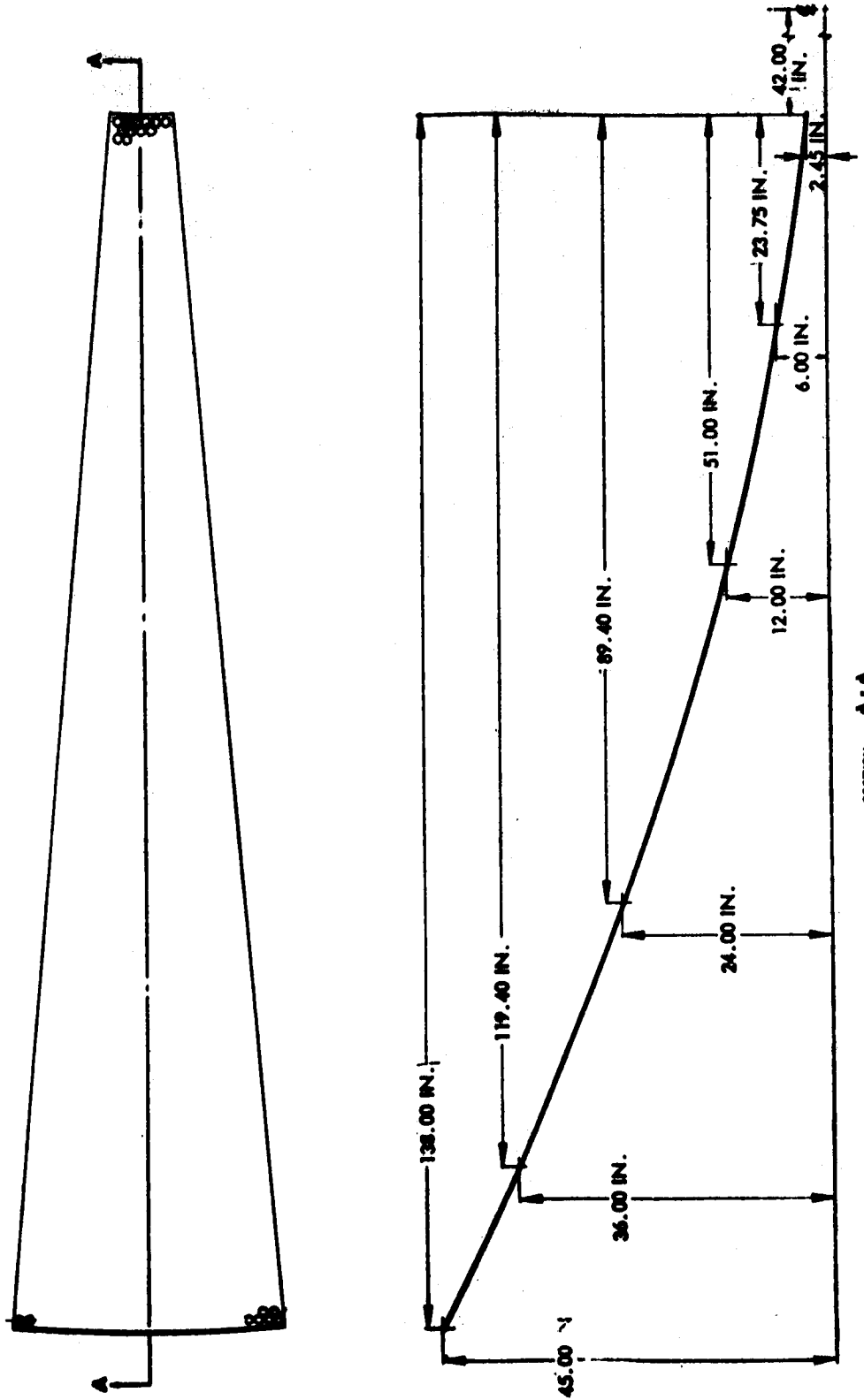


Fig. 6-45 Formed-Petal Electroforming Mandrel

Table 6-17

## WEIGHT SUMMARY

Item	Weight (lb)	Specific Weight (lb/ft <sup>2</sup> )(a)
Petal	132	0.187
Feed Support	62	0.088
Base Plate	42	0.060
Latching Mechanism	12	0.017
Unfurling Mechanism	36	0.051
Total	284	0.403

(a) Specific weight is based on aperture area

Table 6-18

## ANTENNA SYSTEM CHARACTERISTICS

Parameter	Value
Aperture Diameter, ft	30
f/d ratio	0.5
Number of Petals	36
Package Diameter, ft	7
Package Height (including experimental package), ft	16.5
Open Area, percent	78.5
Operating Frequency, GHz	up to 8
Opening of RF Screen, in.	0.125
Structural Accuracy, in.	±0.075
Thermal Distortion at Maximum Heat Flux, in.	<0.1

The use of nickel, which is a ferromagnetic material, presents no difficulty. A conservative estimate indicates that the resulting magnetic moment will be approximately 20 amp-m. Interaction with the earth magnetic field gives rise to a disturbing torque of  $10^{-6}$  lb-ft. This is at least two orders of magnitude less than the torques resulting from solar radiation pressure and thruster misalignment. However, if a magnetic measurement is to be performed, the magnetometer should be mounted at 10 m in order to reduce the field to about 1 gamma.

Design of the antenna petal structure is based minimum weight considerations that are commensurate with maximum open area. The resulting design has a hole spacing that exceeds the dimensional limits for X-band frequencies. To achieve the  $<0.125$ -in. spacing required for X-band, a preformed metallic screen is attached to the structural petals.

Several different methods for manufacturing this mesh have been investigated. Many of these methods have been eliminated since they do not provide good electrical contact at the wire crossings. The best fabrication method for overcoming this problem involves copper-flashing the desired screen structure. This can be done on fine wire meshes. The resulting mesh will have a copper surface thickness that exceeds the minimum required to overcome skin effects. This mesh is attached to the nickel structure.

The critical consideration in attaching this mesh is maintaining the geometric accuracy across the open faces of the petal. This can be done by preshaping the screen over the petal surface prior to attachment. The inherent strength of this screen can be modified by changes in copper plating thickness and by undercoating with nickel substrate. The physical properties of the mesh can, therefore, be made to suit design requirements, including bridging the holes while maintaining the parabolic geometry.

Surface Tolerance Analysis. Minute manufacturing defects can degrade phase distribution, boost side-lobe levels, and raise antenna-noise temperatures. An antenna cannot

be built without phase error. The magnitude of these errors places an upper limit on gain, independent of antenna size. Robieux has analyzed the effect of finite errors for large, rigid-reflector antennas. He characterizes the manufacturing precision of an antenna by

$$\frac{E}{d} = 10^{-m}$$

where

- E = manufacturing tolerance
- d = largest aperture dimension
- m = manufacturing precision

A value for  $m$  that approaches 4 is a reasonable present-day limit. The best 30-ft ground antenna error achieved to date is 0.01 in. rms for which  $3 < m < 4$ . Figure 6-46 is a plot of realizable gain (assuming 100 percent antenna efficiency) versus  $m$  and  $d/\lambda$ . This curve shows how the tighter tolerances needed at higher frequencies increase the difficulty of attaining higher gain.

Ruze defined the reflector degradation mathematically as

$$P(\phi, \theta) = P_o + S \frac{4C^2 \pi^2 \delta^2}{\lambda^2 G_o} \exp \frac{-\pi^2 \mu^2 C^2}{\lambda^2}$$

where

- $\theta, \phi$  = angles in polar coordinates
- $\mu$  =  $\sin \theta$
- C = correlation interval (that distance, on the average, where errors become essentially independent)

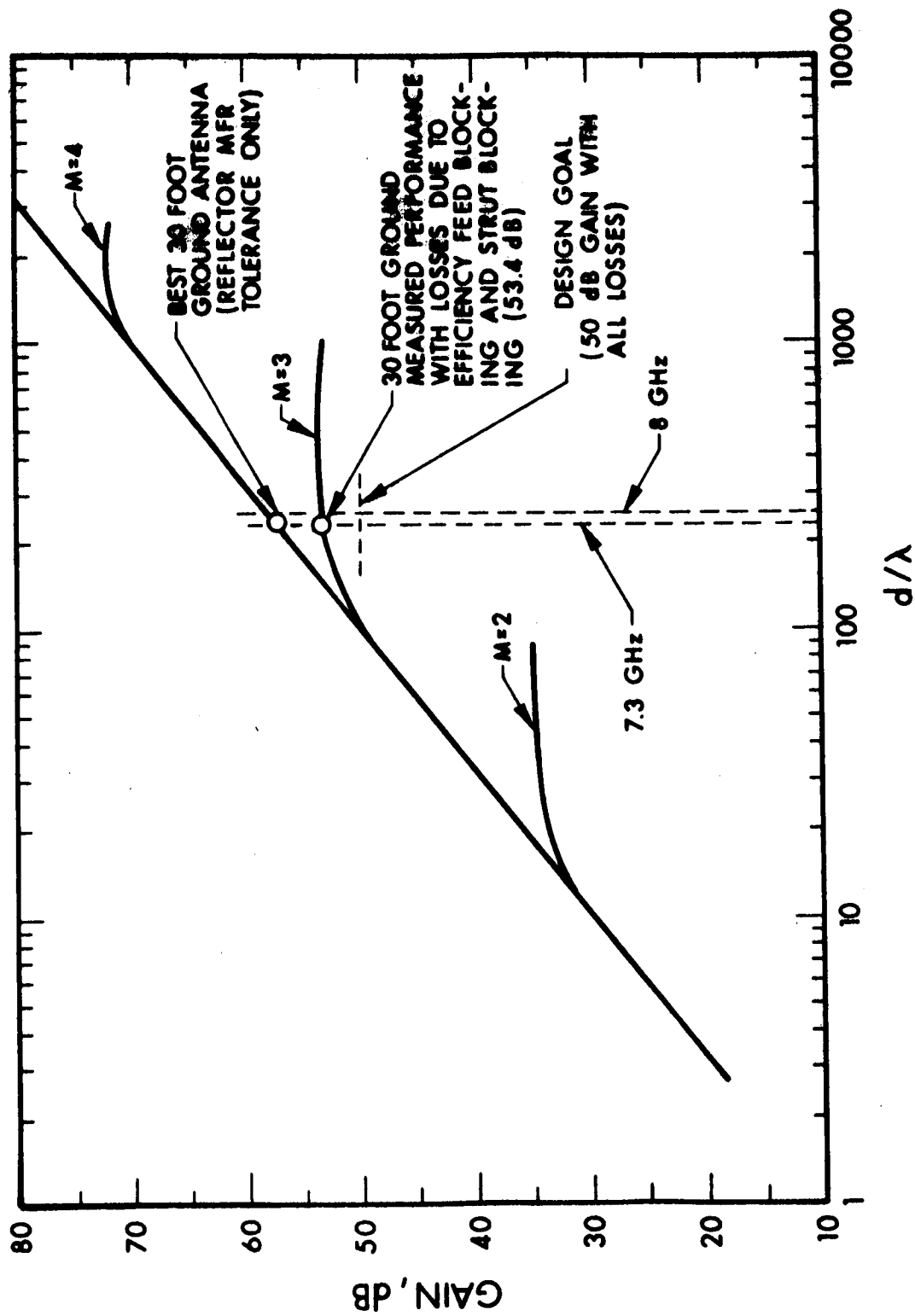


Fig. 6-46 Realizable Gain



$P_o$  = desired radiation pattern (no error)

$S$  = obliquity factor =  $\cos \theta (\cos^2 \theta + \sin^2 \phi)$

$\bar{\delta}^2$  = mean-square phase error in radians

$G_o$  = gain of no-error antenna

The first term represents the pattern in the absence of errors, and the second term describes the disturbing pattern introduced because of the presence of errors. The spurious side-lobe radiation is proportional to the mean-square error and is also proportional to the square at the correlation interval expressed in wavelengths.

The reduction in gain, assuming the errors are small, may be established by the approximation:

$$\frac{G}{G_o} \approx 1 - \frac{3}{4} \frac{\bar{\delta}^2 C^2 \pi^2}{\lambda^2} \quad \frac{C}{\lambda} \ll 1$$

and is approximately

$$\frac{G}{G_o} \approx 1 - \bar{\delta}^2 \quad \frac{C}{\lambda} \gg 1$$

and  $\bar{\delta}^2 = 4 (2\pi/\lambda)^2 W^2$  where  $W$  is the rms mechanical distortion. Expressed exponentially, this equation for  $C \gg \lambda$  becomes

$$G = G_o \exp \left[ - \left( \frac{4\pi W}{\lambda} \right)^2 \right]$$

where

$G_o$  = gain of perfect reflector =  $\eta (\pi D/\lambda)^2$

$\eta$  = aperture efficiency (assume 100 percent)

$D$  = reflector diameter

$\lambda$  = wavelength of frequency of interest (8 GHz = 0.122 ft = 1.476 in.)

$G$  = gain of the antenna in the presence of surface irregularities

The foregoing formulas consider only random errors covering areas several wavelengths square on the reflector surface and are simplifications of Ruze's equations. The gain degradation  $\Delta G$  in db is given by

$$\begin{aligned}\Delta G &= 10 \log \frac{G}{G_o} \\ &= -683 \left( \frac{W}{\lambda} \right)^2 \text{ db}\end{aligned}$$

This is plotted in Fig. 6-47.

Differentiating shows that maximum gain occurs at a wavelength  $\lambda_m = 4\pi W$ . At higher frequencies ( $\lambda < \lambda_m$ ), the gain degradation because of surface irregularities overcompensates the normal increase in gain  $G_o$  as the wavelength decreases.

Since the maximum gain with  $W \neq 0$  is 4.3 db lower than the gain of a perfect reflector ( $W = 0$ ) at the same frequency, it is customary to design a reflector so that the frequency of maximum gain is somewhat higher than the frequency that will be used.

Figure 6-48 plots gain loss as a function of random phase error for several intervals of  $C/\lambda$  after Ruze's work and shows the importance of keeping the correlation interval small. This figure also indicates the dynamic interrelationship of the error effects

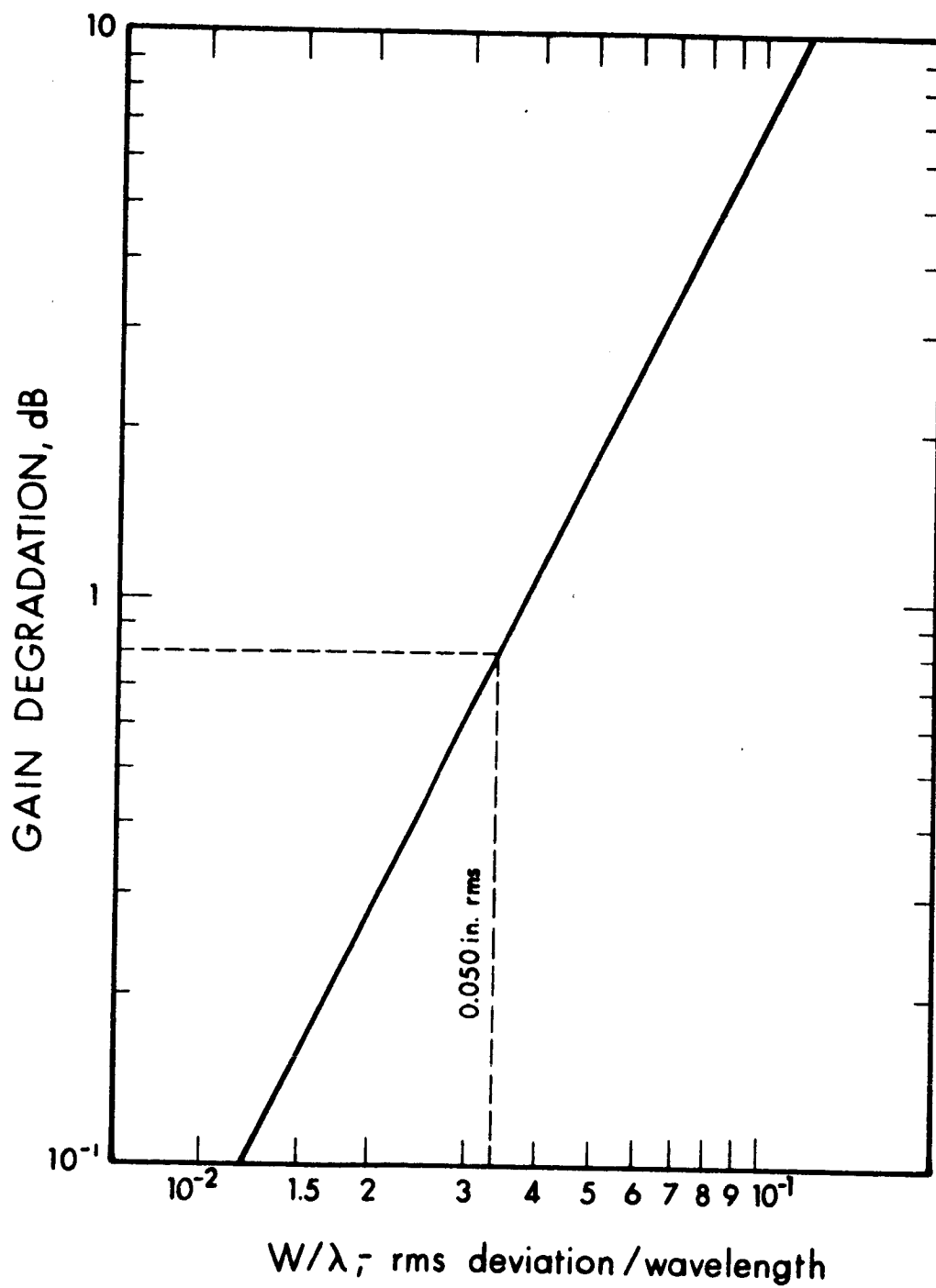


Fig. 6-47 Gain Degradation

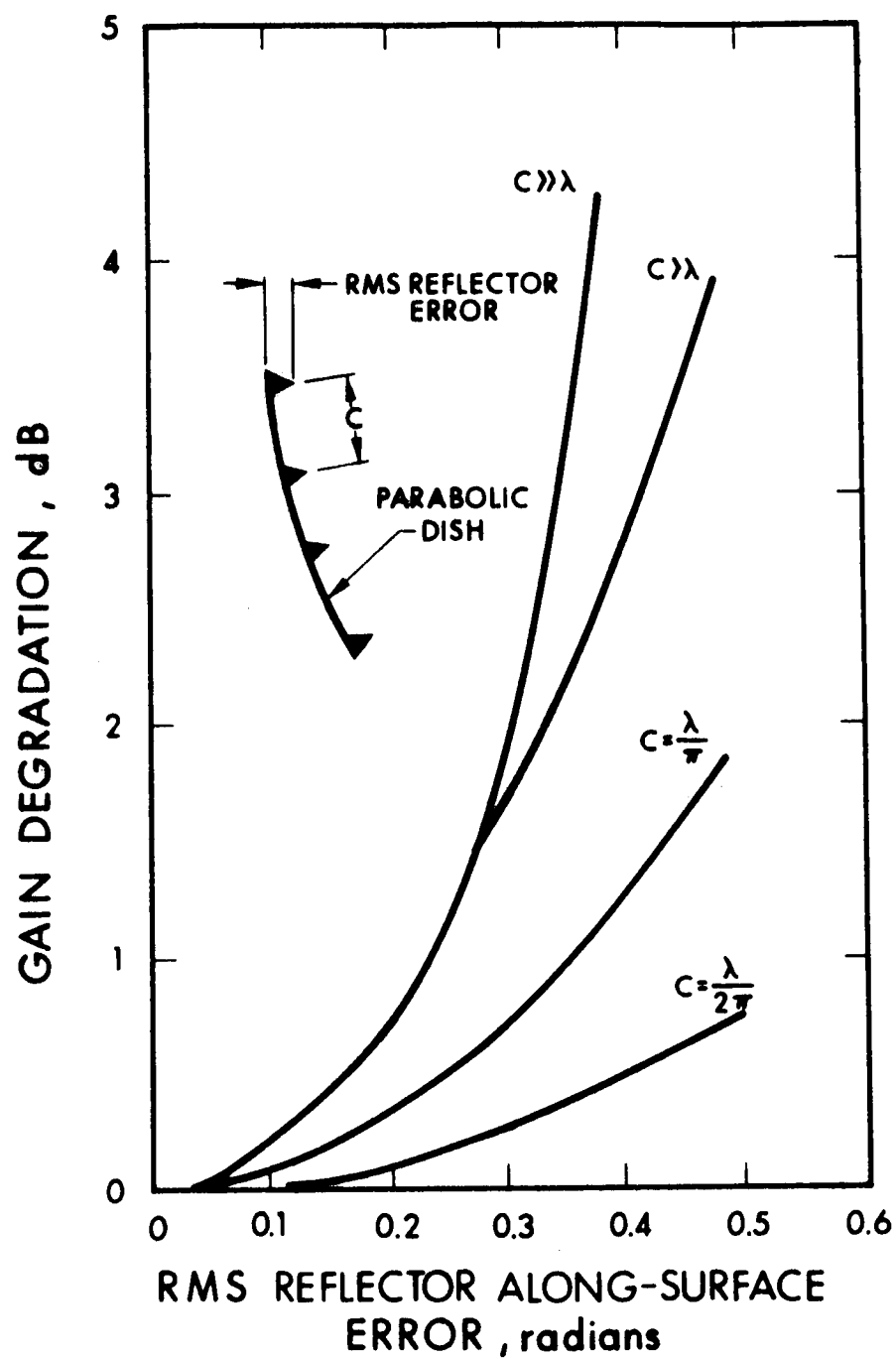


Fig. 6-48 Gain Degradation With Random Phase Errors

C and  $\lambda$  . Since errors are unavoidable in a reflecting surface (rivet heads, etc.), they should be small ,i.e., small compared to a wavelength.

**Petal Design Considerations.** Petal design factors include open area, weight, moment of inertia, and local crippling stress requirement. Parametric variations of these factors can be determined rapidly from the data presented in this subsection. This information will be used extensively in the petal structural analysis that follows.

- **Hole pattern.** The pattern selected is triangular as shown in Fig. 6-49. The opaque and open areas can be calculated by considering the parallelopiped unit cell and the circular area of the holes within the cell.
- **Opaque and open areas.** The following parameters apply:

$$\text{Area of unit cell} = 2a \sqrt{3}a$$

$$\text{Opaque area} = 2 \sqrt{3}a^2 - \pi d^2/4$$

$$\text{Open area} = \pi d^2/4$$

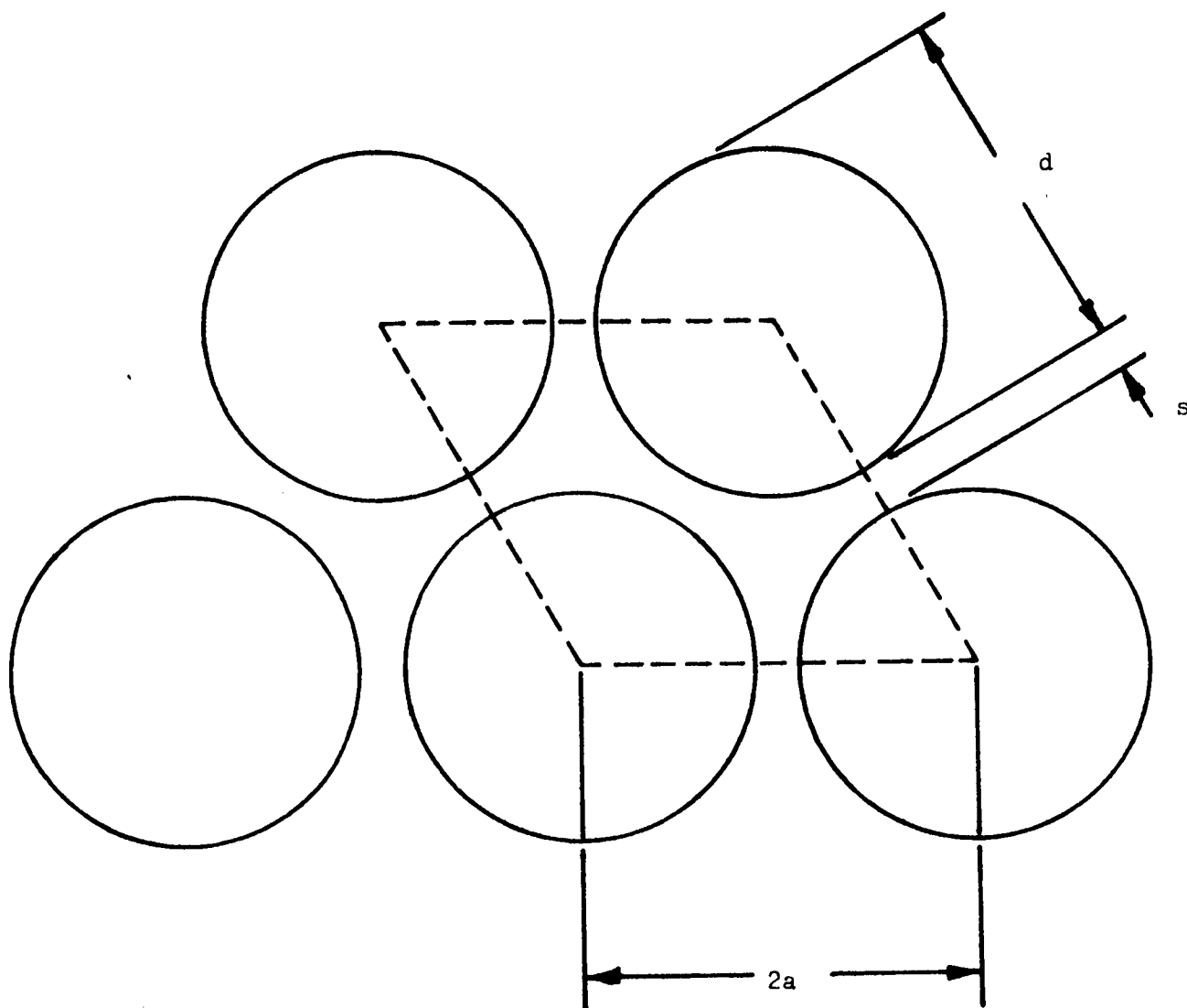
$$\text{Percent open area} = 22.7 (d/a)^2$$

Table 6-19 lists open area as a function of  $d/a$  and the clearance between holes for a 1-inch-diameter hole.

Table 6-19  
OPEN AREA

(d/a)	Open Area (%)	Hole Diameter (in.)	Clearance (in.)
1.78	71.5	1	0.125
1.86	78.5	1	0.075
1.91	82.0	1	0.050

Past fabrication experience indicates that a clearance of 0.050 in. is an absolute minimum below which the mandrel material begins to tear during drilling. For the ATS-4 antenna, a clearance of 0.075 in. is selected to ease the fabrication problems.



$2a$  = HOLE SPACING

$d$  = HOLE DIAMETER

$s = 2a - d$  = CLEARANCE BETWEEN HOLES

Fig. 6-49 Hole Pattern

- Weight per unit area. Weight per unit area can be calculated by considering the amount of material required for the front and back surfaces and the cylindrical spacers between the surfaces. The relation for the weight per unit area is given by

$$W = \left[ 2 - 0.454 \left( \frac{d}{a} \right)^2 + 0.907 \left( \frac{d}{a} \right) \left( \frac{h}{a} \right) \right] t \rho$$

where

$h$  = petal thickness

$t$  = skin thickness = 0.002 in.

$\rho$  = material density = 0.321 lb/in.

Figure 6-50 shows the specific weight of the petal as a function of petal thickness for three different  $d/a$  ratios. The curves are for the hole diameter of 1 in. and skin thickness of 2.0 mils. It should be noted that the specific weight is strictly a function of the  $d/a$  and  $h/a$  ratios if the skin thickness is held constant. Figure 6-50 is, therefore, applicable to other hole diameters as long as the petal thickness is determined on an "equivalent" basis.

- Moment of inertia. The moment of inertia of the petal determined at the minimum cross section is shown in Fig. 6-51. Figure 6-52 shows the moment of inertia of the petal at the radius (from focal axis) of 3.5 ft, which is the hinged point. This moment of inertia will be used to determine the bending stress induced during deployment.
- Crippling stress. With flat plates under loaded conditions, the plate surface tends to cripple locally in a small area. Although the crippled petal may be structurally sound, local crippling introduces surface error that cannot be tolerated. With the triangular pattern, the area from which crippling occurs is the tri-cusp area formed by three adjacent circles. The critical crippling stress is given by

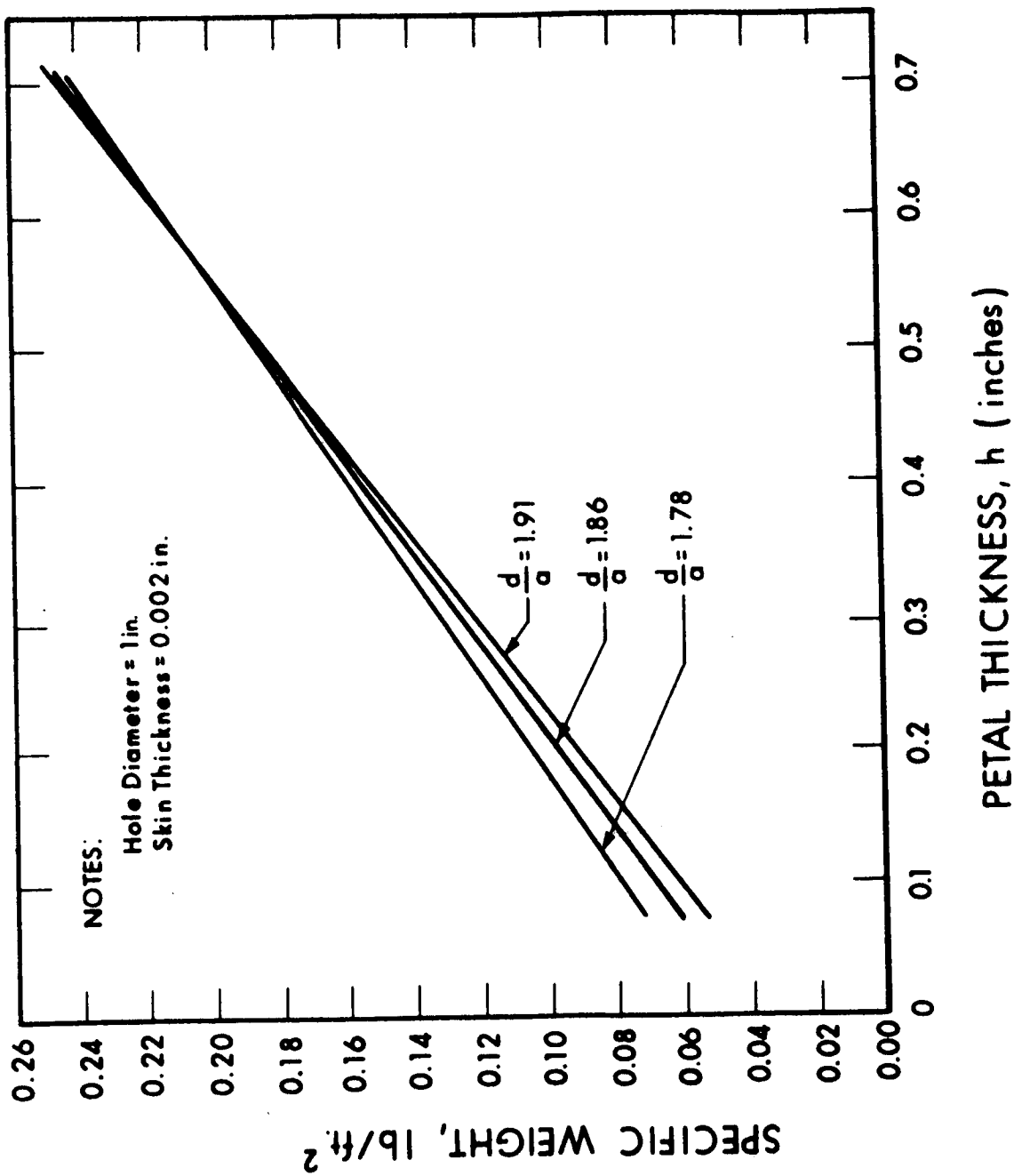
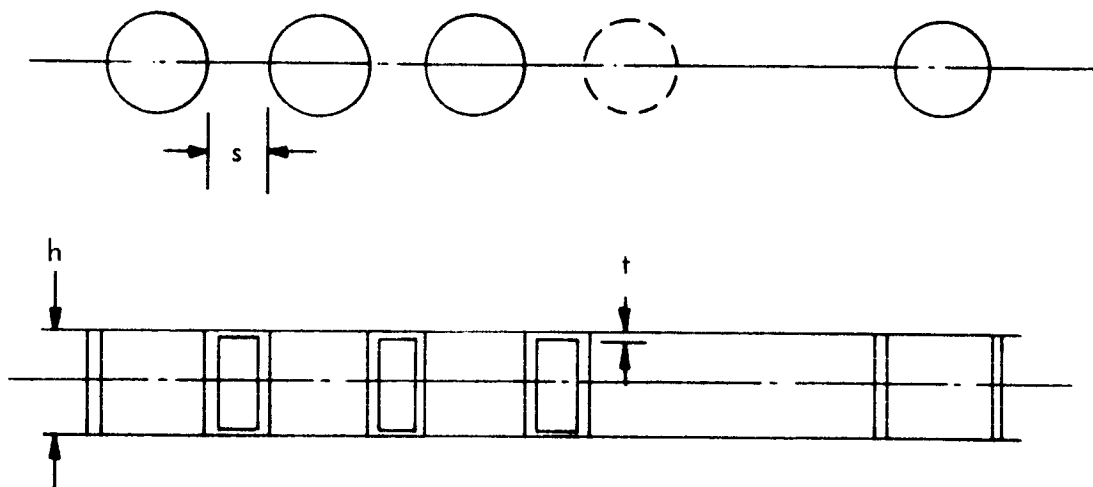


Fig. 6-50 Petal Specific Weight vs. Thickness





$$I = 2N \frac{sth^2}{4} \frac{th^3}{12}$$

WHERE

I = MOMENT OF INERTIA

N = NUMBER OF HOLES AT THE CROSS SECTION

Fig. 6-51 Petal Cross Section

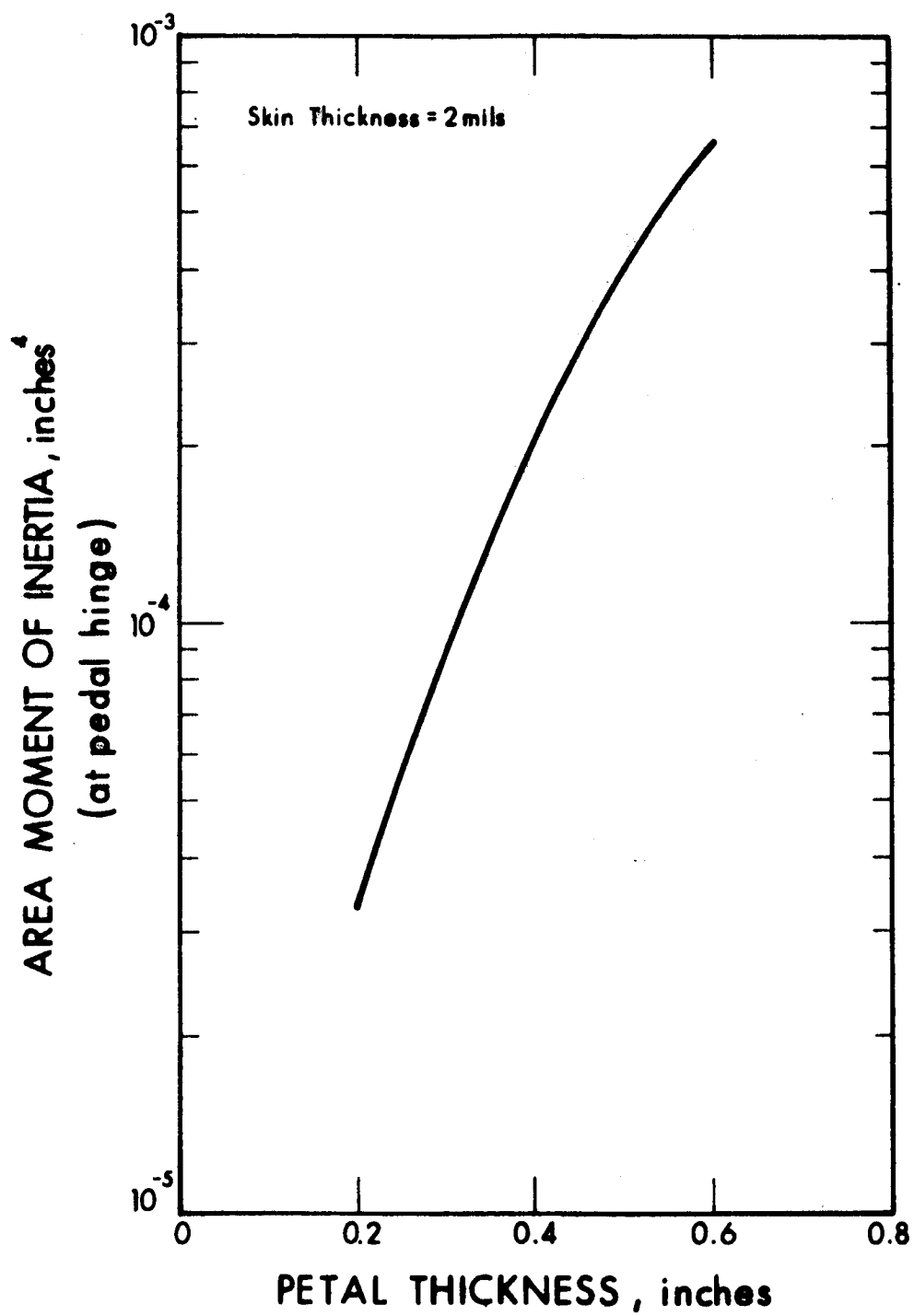


Fig. 6-52 Area Moment of Inertia

$$\sigma_{cr} = \frac{K \pi^2 E}{12 (1 - \nu^2)} \left( \frac{t}{4a - 1.732d} \right)^2$$

where

K = constant = 12 (confirmed by test at EOS)

E = modulus of elasticity =  $25 \times 10^6$  psi

$\nu$  = Poisson's ratio  $\approx 0.3$

For  $a = 1.075/2 = 0.5375$ ,  $t = 0.002$ , and  $d = 1.0$ , critical crippling stress  $\sigma_{cr} = 6,250$  psi.

For the petal weighing approximately 2.5 lb under quasistatic launch load of 11.5 g, the load stress at the petal root will be approximately 3,500 psi. The margin of safety in this case will be about 0.78.

- Stress vs. hole diameter. Since the petal weight is strictly a function of the  $d/a$  and  $h/a$  ratios, it appears that by increasing the hole diameter the petal thickness may be increased (to obtain greater moment of inertia) without weight penalty. However, the allowable crippling stress will be reduced significantly. Table 6-20 illustrates the effect of increasing hole diameter with the  $d/a$  and  $h/a$  ratios held constant.

The pattern design selected for further evaluation will be the petal with 1-in.-hole diameter and 0.075-in. clearance. It should be noted that this design has a hole pattern similar to the hollow-core substrate of the lightweight solar panel being fabricated by EOS. The hollow-core structure has a hole diameter of 1 in. and clearance of 0.050 in.

Table 6-20

## CHANGE IN STRESS FOR TWO HOLE DIAMETERS

Parameter	1-in. Hole Diameter (design)	2.5-in. Hole Diameter
Clearance Between Holes, in.	0.075	0.17
d/a	1.86	1.86
Open Area, percent	78.5	78.5
Design Specific Weight, lb/ft <sup>2</sup>	0.112	0.112
h/a	0.465	0.465
Petal Thickness, in.	0.25	0.56
Moment of Inertia (root), in. <sup>4</sup>	$5.6 \times 10^{-5}$	$5.3 \times 10^{-4}$
Crippling Stress, psi	6250	1240

Petal Structural Analysis. The complex geometry of the petal makes stress analysis a difficult task without the use of a computer. The analysis, therefore, was performed with a computer routine developed for this purpose. This routine, called LESAR (Linear Elastic Structural Analysis Routine) has proved satisfactory for the analysis of structures such as the ASTEC solar collector and solar panels for various spacecraft. This routine can handle a three-dimensional system if it is suitably modeled. Modeling a three-dimensional biconvex panel, however, is quite difficult. Since the transverse curvature of the petal is fairly small, the petal was modeled by considering only the parabolic shape along the longitudinal axis. This model does not introduce significant errors and permits the petal to be analyzed as a two-dimensional structure with varying properties.

The mathematical model upon which this analysis is based was obtained by dividing the petal into 14 approximately equal segments. Each segment was approximated by the uniform width, average section modulus, and average shear area calculated for each segment. The inertia of the segments was approximated by lumped masses at the joints between the segments. One-half of the calculated mass of a segment was placed

at each joint adjacent to that segment. The mass moments of inertia of equivalently uniform beams about their ends were used to approximate the rotary inertia of the segments.

The division of the petal into segments and the location of each joint is shown in Fig. 6-53. Each joint was considered to have three degrees of freedom as follows:

- Displacement in the axial ( $X_1$ ) direction
- Displacement in the lateral ( $X_2$ ) direction
- Rotation about the axis perpendicular to the plane of  $X_1$  and  $X_2$

The computer program used in this analysis allows for restraint in any degree of freedom in the structure.

In the launch configuration, joint 1 was constrained in the  $X_1$  and  $X_2$  directions. This corresponds to the hinge point at the petal base. The tip of the petal, joint 15, was allowed neither to rotate nor to move in the  $X_2$  direction. This corresponds to a semiclamped condition of the petal tip. Two or three intermediate joints were constrained in the  $X_2$  direction, but were allowed to rotate and to deflect in the  $X_1$  direction. These constraints are simulations of the use of restraining bands.

Two computer runs were made. Petal characteristics, restraining conditions, and loading conditions for each run are summarized in Table 6-21. Results of the computer analysis indicate that the 1/4-in. petal, as exemplified by Run 1, is adequate only for launch static loads but fails to survive the dynamic environments. The 3/8-in. petal, however, meets both static and dynamic requirements. Maximum deflection was found to be 0.47 in. The first six natural frequencies were 17.7802, 25.4411, 30.3138, 43.3077, 58.8649, and 72.0932 cps.

Deployment Technique. The operation of mechanisms employed to unfurl and to latch the petals are somewhat interdependent. However, both are vital to the achievement of a true parabolic reflector in space.

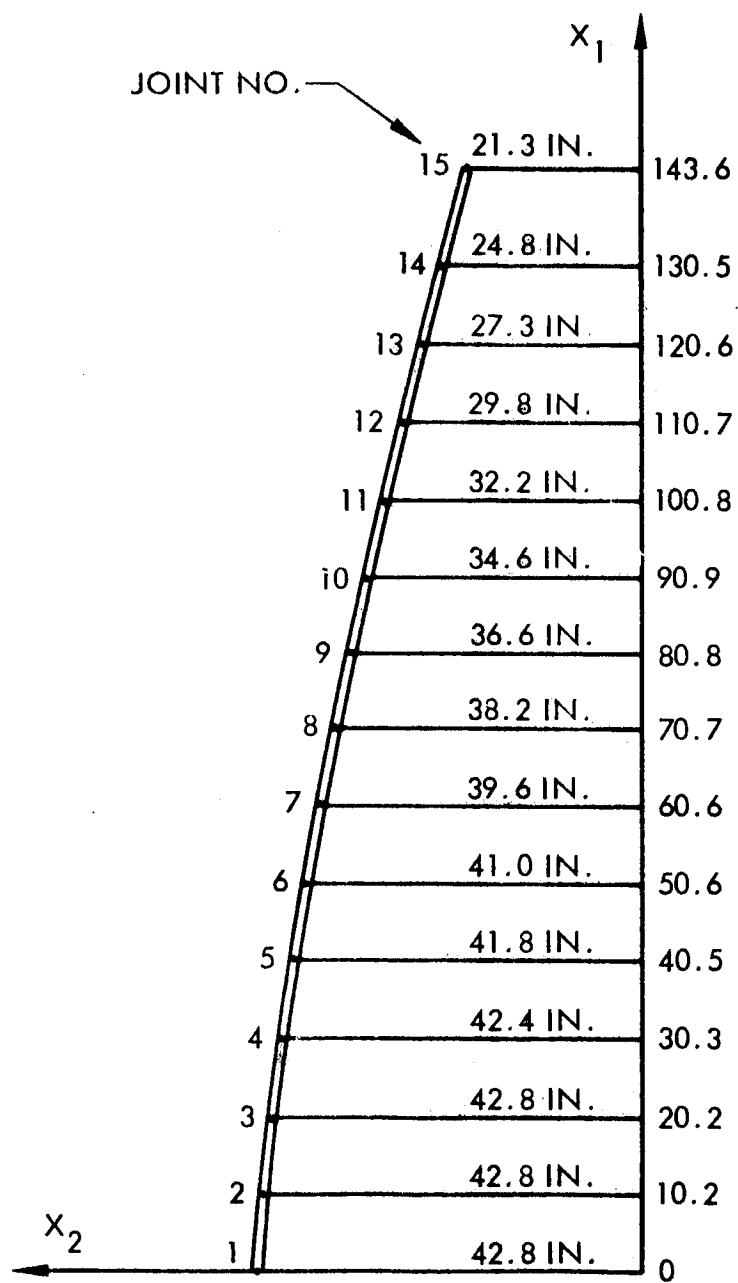


Fig. 6-53 Coordinates of ATS-4 Antenna Petals

Table 6-21

**CHARACTERISTICS, CONSTRAINTS, AND LOADING FOR PETAL  
STRUCTURAL ANALYSIS**

Item	Run 1	Run 2
<b>Characteristics</b>		
Petal Thickness, in.	0.25	0.375
Skin Thickness, mils	2	2.5
Crippling Stress (Failure Criterion), psi	6250	9750
Weight per Petal, lb	2.216	3.660
<b>Constraints</b>		
Joint 1	$X_1$ and $X_2$	$X_1$ and $X_2$
Joint 15	$X_2$ and no rotation	$X_2$ and no rotation
Joints 6 and 10	$X_2$	—
Joints 4, 7 and 11	—	$X_2$
<b>Static Loading</b>		
Longitudinal, g	7.4	7.4
Lateral, g	2.0	2.0
<b>Dynamic Loading</b>		
Longitudinal, g	3.0	3.0
Lateral, g	1.5	1.5

The mechanism to deploy the petals on-orbit requires the same careful design as the petals. It must be very light in weight and extremely reliable. Design requirements for the antenna deployment mechanism are based upon the following:

- The furled petals must be held immobile during launch and ascent. The petals must also be supported so that permanent deformations from the acceleration forces will be avoided.

- The petals must hinge and unfold so that they remain clear of each other as they move to the open position.
- The petals must move smoothly and uniformly in a desired path (within close tolerances) toward their final position.
- The petals must be locked so that the final position of each petal is correct and so that the antenna forms a true paraboloid.

On the basis of a preliminary evaluation, the following method is selected as the one that will satisfy the foregoing requirements.

The petals are restrained during the period when they are subjected to the greatest forces. Four squib-actuated bands will be used to hold the petals at the tip and three other intermediate places. Placement of the intermediate bands will be determined from a launch analysis to minimize petal deflections. In operation, the squibs will fracture the individual bands after ascent and jettison the shroud so that the petals will be forced to operate. The type of hinge mechanism EOS proposes to use for this antenna is shown in Fig. 6-54. It is set at an angle to the centerline of the petals so that they can deploy properly. A torsion spring is furnished to open the petals. A torsion spring is more desirable than a torsion bar since its spring rate can be designed to have a shallower slope than the bar will have and, consequently, less drop in available force at the end of the stroke.

A dashpot is provided to smooth the motion of the petal so that it will not acquire excessive momentum which might exceed the potential energy of buckling at the end of petal travel. A shot pin that will interlock the petals at the end of their travel will be used so that the antenna becomes an integral unit.

The need to have all the antenna petals rigidly tied together cannot be over-emphasized. The primary reason for this is to minimize the reflector surface errors caused by thermal distortion or transitory perturbing force during spacecraft maneuvers.



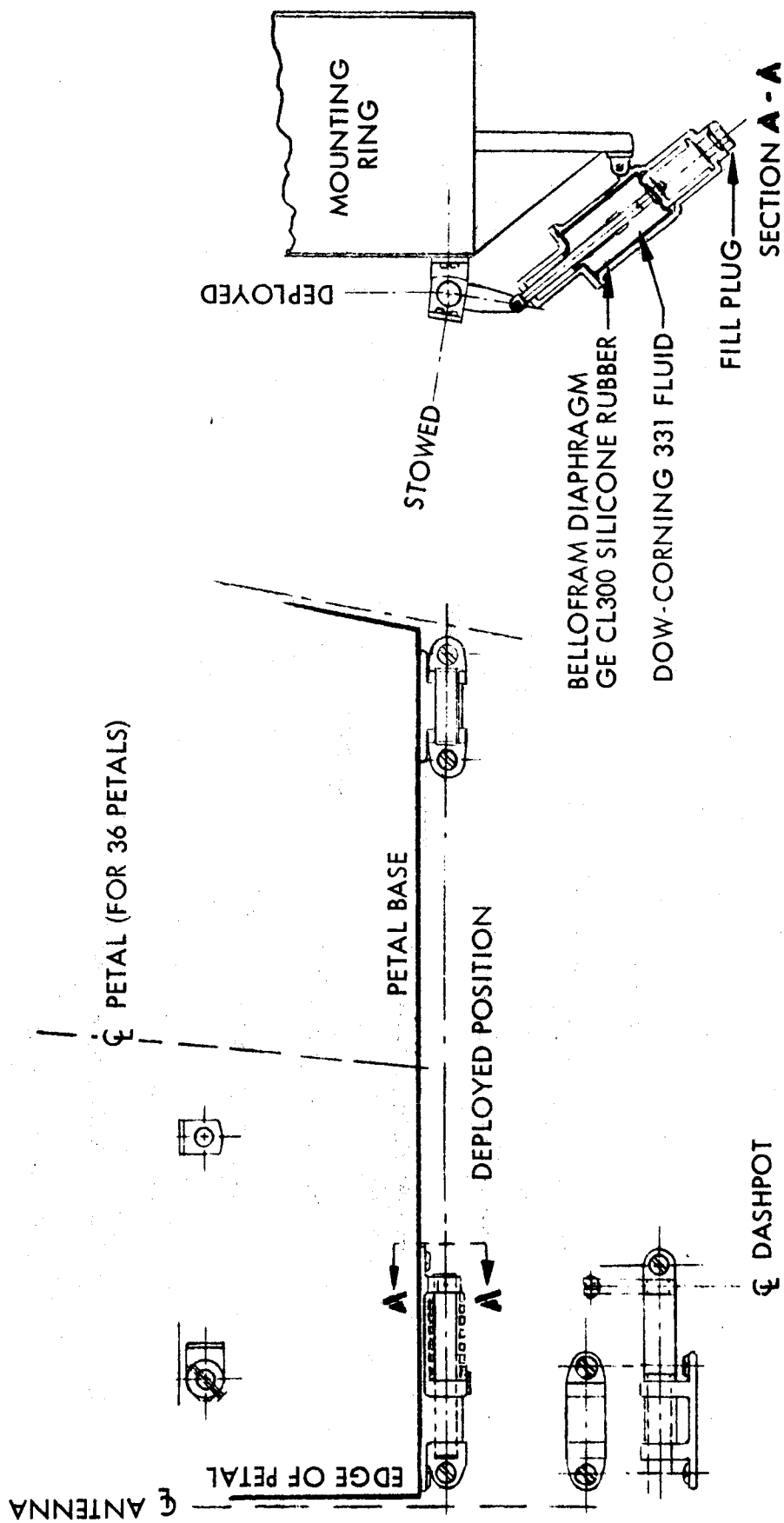


Fig. 6-54 Unfurling Mechanism

The magnitude of thermal deflection decreases as the number of ties between petals increases. Table 6-22 illustrates the order of magnitude of deflection determined from thermal analysis and experiment. The case corresponds to the instant the antenna aperture is normal to the sun with the absorptivity/emissivity ratio of unity.

Table 6-22

ORDER OF MAGNITUDE OF DEFLECTION

Number of Ties	Deflection (in.)
Zero (root fixed)	3
End pinned	1
Three ties	0.2
Five ties	0.05
Seven ties	0.012

Several types of latching mechanisms have been considered. The recommended type consists of lazy tongs and spring-loaded pins. Two lazy tongs will be employed – one at the petal tips and the other at the midpoint. Their movement is as shown in Fig. 6-55. In the fully deployed position, the lazy tongs are locked firmly by the latching pins. Thus, the petals are tied together at the tip and the midpoint.

Two other intermediate places will be latched together by spring-loaded pins. Operation of a pin depends on movement of two adjacent petals as are shown in Fig. 6-56. As the two petals come closer together, the tapered petal initiates latching by pushing the spring-loaded (torsional) cover backward. This will allow the spring-loaded (translational) pin to move forward and latch the two petals together.

Tripod Feed Support Analyses, Structural and RF. The height of the feed support and the point of termination on the reflector will be determined since the dimensions affect overall integration of the spacecraft.

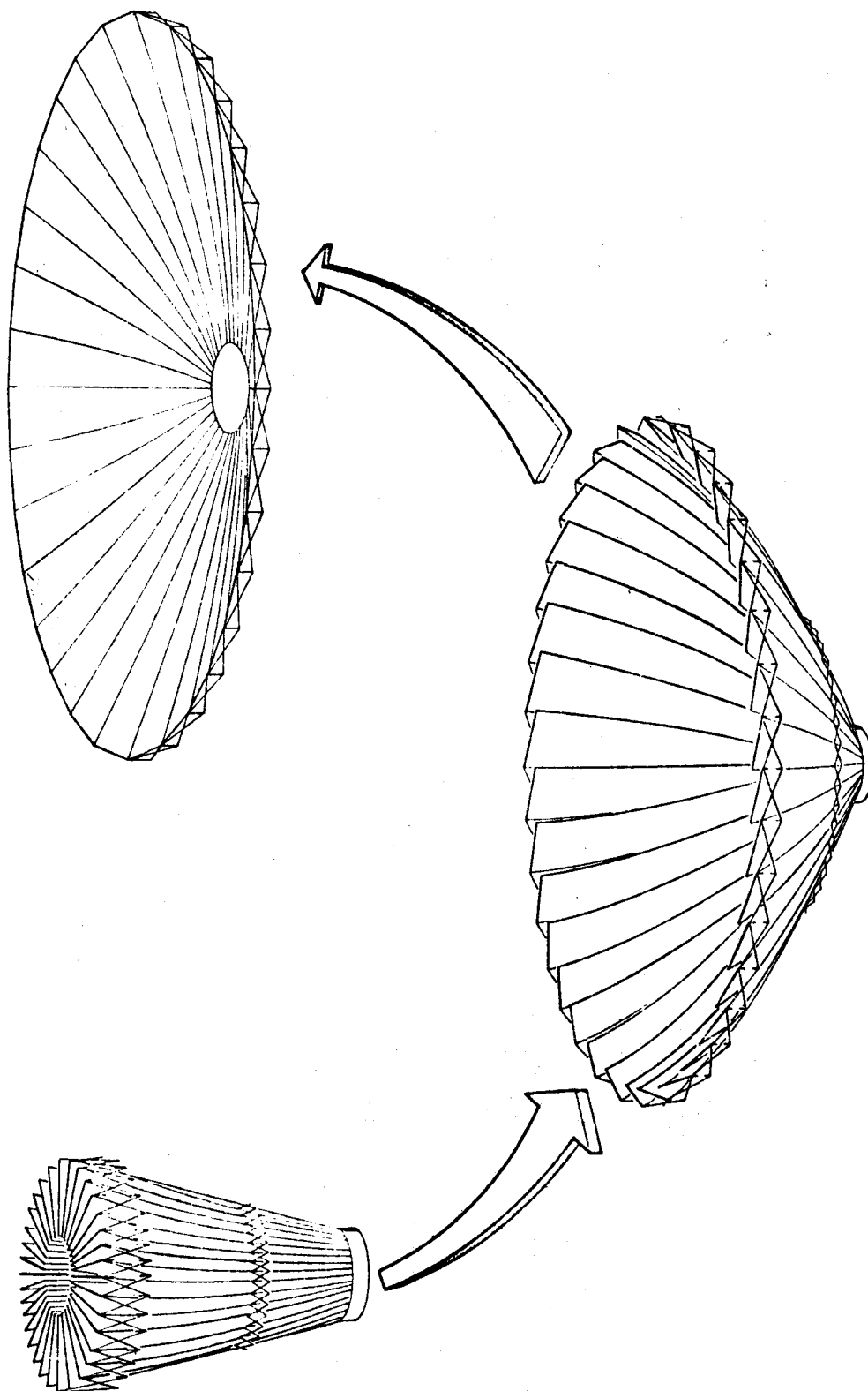


Fig. 6-55 Lazy-Tong Linkage

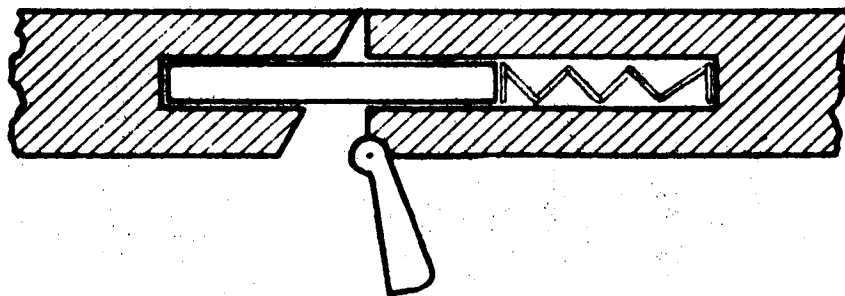
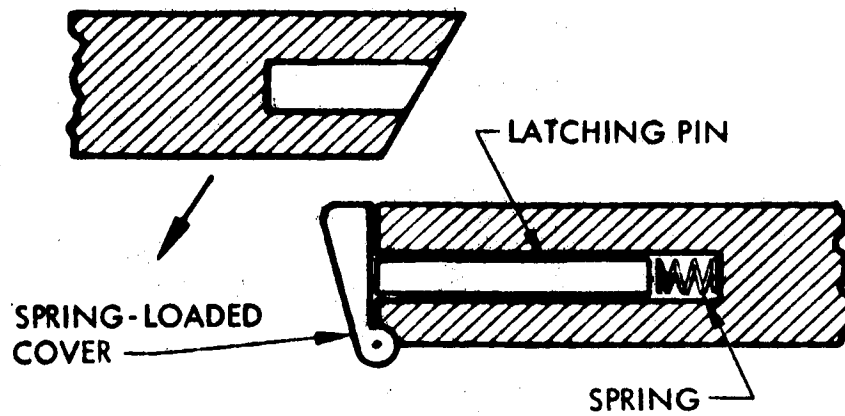


Fig 6-56 Petal Latching Mechanism

For an  $f/D$  ratio of 0.5, the focal length is 15 ft. This is also the height of the feed support, for a non-Cassegrainian systems. For the Cassegrainian system, the height is a function of the secondary reflector focal length and the desired magnification factor that varies usually from 2 to 6.

The feed support for the Cassegrainian system shown in Fig. 6-57 is 14 ft high. This is determined by a simplified analysis as follows. The effective focal length is given by

$$f_e = \frac{f_1}{f_2} \times f$$

where

$f$  = primary reflector focal length

$f_1$  = distance from the feed to the secondary reflector

$f_2$  = secondary reflector focal length

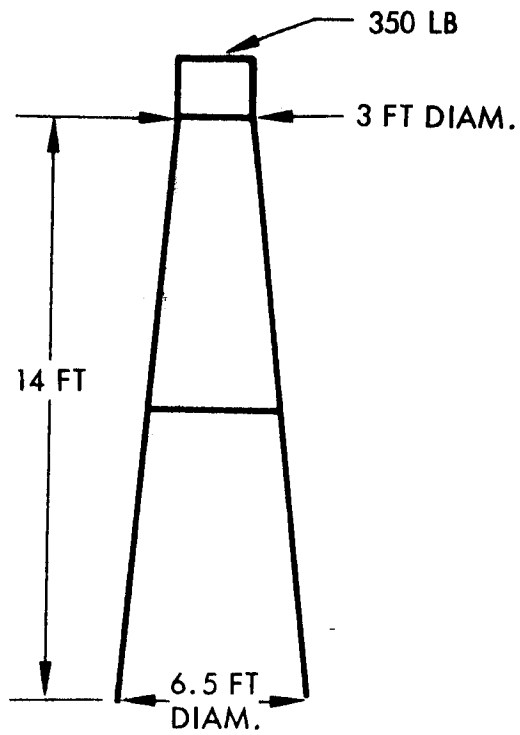
$f_1/f_2$  = magnification factor

If  $f_2/D_2 = 0.5$  and  $D_2 = 3$  ft are assumed, then  $f_2$  is 1.5 ft. The feed cone height ( $x$ ) and the magnification factor will be as shown in Table 6-23.

Table 6-23  
MAGNIFICATION VS. FEED HEIGHT

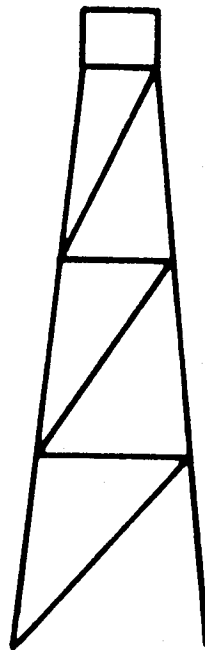
$x$ (ft)	$f_1$ (ft)	$f_1/f_2$
4	9.5	6.35
6	7.5	5
7.5	6.0	4
10	3.5	2.34

The feed support and feed cone arrangement shown in Fig. 6-57 corresponds to the case of a magnification factor of 4.



(a) CONFIGURATION 1

WEIGHT = 28 LB



(b) CONFIGURATION 2

WEIGHT = 62 LB

Fig. 6-57 Feed Support Configurations

The size of the tripod structure was first determined from the static-load requirements. The launch-dynamic loads were found to be the determining factor as in the case of the petal analysis. The structure was therefore analyzed by the use of the LESAR code.

Two configurations were considered. In the Configuration 1, 2.25-in.-diameter aluminum tube with 1/16-in.-thick wall was used. The tripod structure was terminated at a base diameter of 6.5 ft. The experimental package, which weighs 350 lb, was taken as a cylinder with a diameter of 3 ft. The three legs were tied together at midpoint. Configuration 2 is similar except the three legs were tied at two intermediate points and diagonal members were included as shown in Fig. 6-57. The loading conditions were the same as those used in the petal structural analysis.

To reduce RF degradation, all the tie members will be made of fiberglass, which is essentially transparent to the RF beam.

Results of the computer analysis, summarized in Table 6-24, indicate that Configuration 1 is unstable. This is primarily because of the long beam section with a large weight attached to its end. By increasing the number of cross-tie members, the tripod structure is made stiffer, which results in an increase of natural frequencies. Although its deflection is 3.7 in., Configuration 2 is considered acceptable, considering the structure length of 14 ft.

A technique for predicting the effects of various feed support members (which is analogous to the approach discussed above) has been derived\* and verified experimentally. This projected blockage area of reflector of diameter  $d_r$  caused by a pair of feed support struts is exact only if the strut extends from the feed to the perimeter of the reflector. If, for example, the struts are attached effectively to the reflector at a point one-fifth of the radius, then the outer four-fifths of the reflector will have a pie-shaped shadow area. Some diffraction will occur, of course, around the strut and the illumination intensity will vary, but a first-order approximation can be made by examining strut geometry.

---

\*S. Schuer, Microwave Antenna Theory and Design, New York, McGraw-Hill Book Company, Inc., 1949, p. 190-192

Table 6-24

## SUMMARY OF COMPUTER RUN RESULTS

Parameter	Configuration 1	Configuration 2
Feed Support Weight, lb	28	62
Natural Frequencies, cps		
First	2.1515	9.8632
Second	2.1405	9.8673
Third	2.7882	14.7057
Fourth	10.9476	39.7881
Fifth	11.9322	39.7883
Sixth	12.4297	44.3567
Maximum Deflection, in.	31.88	3.73

The maximum field intensity of the strut pattern relative to the maximum field intensity of the pattern from the unperturbed aperture is, for a pair of struts with the effective width  $W$

$$\frac{E_s}{E_r} = 1.55 \frac{W}{d_r}$$

This normalized field intensity is added to the theoretical first side-lobe level and subtracted from the peak of the unperturbed aperture to give a new relative first-side lobe level with strut blocking. The reduction in gain because of strut blocks is given by:

$$\frac{G_s}{G_o} = 20 \log \left( 1 - 1.55 \frac{W}{d_r} \right)$$



For the first strut diameter of 2.25 in., the effective width because of proximity to the feed is approximately 5 to 7 in. In the worst case:

$$\begin{aligned}\frac{E_s}{E_r} &= 1.55 \times \frac{7 \text{ in.}}{360 \text{ in.}} \\ &= 0.0302\end{aligned}$$

For a tripod structure, the above ratio will be 1.5 times the value shown. The effects of the cross-tie members are somewhat difficult to assess. To be conservative, it will be assumed that the degradation of cross-tie members is equal to that of three-legged members. (This should be quite conservative since all the tie members are actually transparent to RF.) Thus:

$$\begin{aligned}\frac{E_s}{E_r} &= 0.0315 \times 1.5 \times 2 \\ &= 0.0945\end{aligned}$$

The gain loss can be calculated as:

$$\begin{aligned}\frac{G}{G_o} &= 20 \log (1 - 0.0945) \\ &= -0.858 \text{ db}\end{aligned}$$

### 6.2.3 Instrumentation

The ATS-4 vehicle provides an ideal means for investigating and developing the technology of onboard verification and monitoring of deployed devices and their subsequent alignment deviations. The monitor system should have the following characteristics:

- Provide verification of deployment
- Provide an initial measurement of the error in deployed alignment versus prelaunch ground-test alignment

- Measure all subsequent motion or misalignment of the deployed device or object
- Data output should be sufficiently accurate to relate deployment or subsequent alignment errors of a device to performance variations of the device

Verification of Deployment. The ATS-4 vehicle will deploy all or most of the following devices:

- Parabolic antenna reflector
- Parabolic antenna feed and/or feed boom
- Solar arrays
- Phased-array experiment (possible two deployments)

It is assumed that the vehicle has sufficient telemetry capacity to verify initiation of all deployments. It is important to note that the monitoring system should be separate from the conventional status telemetry system. To examine this further, let us assume the following example. The primary antenna is deployed following orbit injection and vehicle stabilization by an onboard timer. The status telemetry system can verify the timer command initiation. Status telemetry can also verify the firing of squibs or pin-pullers to release the array, initiate motors, etc. This is the extent to which verification of an event is established by normal telemetry. The monitoring system could establish (1) that the antenna completed the deployment cycle, (2) that all ribs or skins were aligned and locked, (3) that orbit deployment was within tolerances established by ground test, (4) additional measurement of surface anomalies because of thermal gradients, etc.

Items (1) and (2) fall within the scope of this section of the discussion. It must be ascertained that the deployment signal was not only generated and received, but that deployment was accomplished. Once deployment is complete, it is necessary to establish the accuracy to which it was accomplished and to relate this accuracy to prior ground test data. This must be done as soon as possible, since the vehicle is subject immediately to orbit operational conditions that will affect the accuracy of the antenna (i.e., thermal reflection of individual ribs of panels).

Several methods are available for verification that both booms and antennas were deployed. Double switching telltales, either with switch opening or closure, can signal completion of an event. Normally, only event initiation is monitored, i.e., squib or pin-puller firing is monitored, with the assumption that the device completes its operational cycle. Each joint in an unfolding structure should be instrumented to determine complete joint lock until completion of the deployment sequence. In the case of ATS-4, for each solar-array arm, complete verification would include (1) timer signal initiation, (2) squib or pin-puller initiation, (3) arm extension and lock, and (4) panel deployment and lock.

Although the ultimate objective is to assess antenna performance in terms of the radiation pattern and gain of the system, such measurements will only reflect the gross effect of the interaction of several critical components. Such interactions may involve the feed radiation pattern, feed-support interference, boresight inaccuracies, and reflector surface error. It is, therefore, desirable to separate these effects so that the area of difficulty may be pin-pointed and future improvements realized. The design of devices and the measuring techniques should be guided by the following:

- The technique for measurement in space should be equally applicable to ground testing. Ground measurements will not only provide the opportunity to calibrate the instrument but will also increase the confidence level of the measurements in space.
- The measurement system should not interfere with the antenna primary experiment.
- The measurement system should not introduce any appreciable RF degradation in the system.

Three types of measurement systems are discussed in the following subsections — an autocollimator system, a strain-gage system, and an optical scanning system. Each presents a feasible scheme for accomplishing deflection measurement.

Autocollimator Devices. The primary function of the proposed alignment monitor system is to measure structural alignment deflections continuously and to telemeter the data to the ground data-processing center. One type of alignment monitor system consists of miniature electronic autocollimators, their associated reference mirrors, and other processing electronics.

The autocollimator employs a fused-quartz body for minimum temperature-change offset. It has extremely low-noise amplifiers, and weighs less than 3 oz. In commercial applications, this type of instrument has a demonstrated resolution of 0.02 arc-sec and null stability on the order of 0.25 arc-sec.

The autocollimator provides a method for continuous, automatic, noncontact operation by generating electrical error signals as precise functions of the magnitude and direction of angular displacement between two points (i.e., the monitor and its reference mirror). With the monitor placed on a given object with a specific alignment, and the reference mirror placed on a second object, the deviation of relative alignment between the two points can be measured. The electronic autocollimators use a modulated light source, such as a gallium-arsenide laser diode source. The light is collimated by the autocollimator optical system, transmitted to the reference mirror, and returned to the monitor. The initial light output is focused through a single aperture to the reference mirror and is returned to a detector reticle comprising two square apertures. Balanced and oppositely polarized detector elements are located behind the dual aperture. When the system is aligned properly, light spill-over as a result of edge diffraction results in equal out-of-phase detector-element output signals that null each other. If the position of the object deviates, however, an error signal is generated. A two-axis system uses two orthogonal pairs of detectors.

Measurement of Orbital Antenna Deflection. Measurement of changes in antenna configuration and boresighting can be achieved with miniature electronic autocollimators. Changes in shape of the antenna are likely to consist of deflections normal to its

surface, which results in a change of focal length of the antenna as a whole or of localized areas. In addition to changes of the antenna surface, it is probable that there will be deflections of the feed-horn support. Lateral deflection of this element causes a change in the effective pointing direction of the antenna, which may be in any direction normal to the axis.

These deflections may be measured precisely from a reference base plate mounted at the vertex of the dish. The deflections of the feed mast may be measured with a dual-axis autocollimator at the center of this plate with its light beam directed outward to the feed horn, on which a reflector is mounted. The reflector returns the light to the autocollimator, and the detector system generates electrical analog signals proportional to deflections in two orthogonal directions, both normal to the line of sight. These may be converted to digital form for transmission if desired.

The term autocollimator is normally applied to instruments designed to measure angular deflection of the reflector. In this case, more meaningful information is derived from the translation of the feed horn normal to the axis, since this results in a change in effective pointing direction of the antenna. (It will be realized that pure rotation of the feed horn about its own center would not change the pointing direction.)

For the foregoing reason, the unit would be modified slightly so that its beam is focused not at infinity, but at the reflector itself. The reflector, instead of being a plane mirror, is a trihedral prism or mirror cluster (set of corner reflectors). The result is that the autocollimator becomes completely responsive to translational movements of the feed horn and insensitive to angular changes. This is, of course, exactly the converse of a standard autocollimator, looking at a plane mirror, sensing only rotation and not translation. Tentative dimensions of this system would include the following:

- Aperture: 1.20 in.
- Focal length: 3.0 in.
- Reticle size: 0.010 in.

- Reflector aperture: 1.25 in.
- Measuring axes: Two, orthogonal to each other and to line of sight
- Working distance: 15 ft
- Linear measuring range:  $\pm 0.256$  in. in each axis
- Digital resolution: 0.002 in., using eight-digit code
- Accuracy: 0.010 in. over full linear range

For measuring deviations of the edge of the dish, a cluster of autocollimators may be mounted on the same base plate. From four to six instruments will be pointed at a like number of reflectors secured to the edge of the interior of the dish, and equally spaced around the periphery. For this system, the following options exist:

- These projectors may be adjusted to give outputs proportional to either angular or translational motion.
- They may measure deviations in either one or two directions.

Since the effect of distortion of the dish is to change direction of the electromagnetic energy emanating from the antenna, there is some value in making this system a true autocollimating system. That is, angular deflections characterizing a certain part of the antenna would give a direct indication of the change in direction of energy from that portion.

If it is predicted that the entire dish may change shape symmetrically (i.e., deepen or flatten), a single-axis system arranged to measure the downturn or upturn of the antenna rim should tell the whole story. If, as seems more likely, the deflections are expected to be asymmetrical, there would be considerable value in making this a two-axis system. Both bending and twisting of a given section of the dish could then be measured, so deviations in antenna emission direction would be known in both meridional and skew planes.

Such a measuring system would include four or six autocollimators operating from a common "mixer box" and an equal number of plane mirrors. Appropriate dimensions and specifications would then be approximately as follows:

- Aperture: 1.20 in.
- Focal length: 3.0 in.
- Reticle size: 0.012 in.
- Reflector aperture: 1.25 in.
- Measuring axes: Two, orthogonal to each other and to line of sight
- Working distance: up to 15 ft
- Linear measuring range:  $\pm 256$  arc-sec in each axis
- Digital resolution: 2 arc-sec with eight-digit code
- Accuracy: 10 arc-sec over full measuring range

Assuming that the error curve is itself parabolic, the foregoing linear measuring range corresponds to a deflection of  $\pm 0.125$  in. at 13.5 ft distance from the vertex.

Alternatively, this system may be made to measure translation, and could measure the  $\pm 0.125$  in. directly. It should be noted, however, that any twist could not be measured using this approach. Only motion normal to the skin could be sensed, and this would yield less useful information. (In other words, the second axis along which a dual-axis translation-measuring system could measure would be, in this application, in a tangential direction to the skin. Such motion is hardly to be expected, although it could be made to indicate whether the petals had snapped to their fully deployed position.)

The selected unit should incorporate all techniques, materials, and components appropriate for high reliability and a 3-yr mission.

Gallium arsenide light-emitting diodes would replace standard tungsten lamps for greater resistance to shock, vibration, and decay as a function of time. Hybrid micro-circuitry with high-rel parts would be exploited to the maximum extent.

Automatic gain control and provisions for in-flight calibration would provide continued assurance of calibration.

The mixer box would include all necessary power supplies operating from the vehicle 28-v supply, as well as processing circuitry to convert the output to digital form for transmission.

A tentative power budget is 1-w for the foregoing system, assuming that cycling is employed from one channel to the next. Each unit would require a package with a 4-in. length and 2-in. diameter, while the mixer box might be 3 by 4 by 6 in. Total weight for five units and mixer box should be approximately 2 lb.

Strain-Gage Technique. Use of a strain gage to measure the mechanical deflection is not new. The relationship between resistance change and strain in the wire used in strain-gage construction can be expressed as:

$$\frac{\Delta R}{R} = K \frac{\Delta L}{L}$$

where K is the so-called gage factor. For Constantan, the gage factor is approximately 2 and a high-gain amplifier is normally required. For semiconductor strain gages similar to those marketed by Micro-System Instrument Div. of EOS, the gage factor is approximately 150. Therefore, the amplifier requirement for the solid-state device will not be as stringent.

It is planned that 18 (out of 36) petals will be instrumented. For each petal, the strain gages will be located near the pin joints, in this case for a total of five locations per petal. Two types of instrumentation will be required at each location. The first will be that which measures simple beam deflection. This will correspond to the case when the antenna is normal to the sun. When the antenna is illuminated edgewise, there will be both simple beam and torsional deflections. The torsional component will be measured by the second type of strain-gage arrangement.



Figure 6-58 shows the mounting location of the instrument and the detailed arrangement of the two types of strain gages. Figure 6-59 shows the Wheatstone circuits for the two types. Signal augmentation factors are as follows:

- Type 1: factor =  $2(1 + \mu) \approx 2.6$
- Type 2: factor = 4

where  $\mu$  is the Poisson's ratio of nickel (approximately 0.3).

The following simplified calculation illustrates the order of magnitude of the strain and the resulting output signal. For a flat plate of thickness  $t$ , existence of a temperature difference of  $\Delta T$  will cause the plate to assume a spherical curvature with a radius  $t/\Delta T\alpha$ . If the edges are fixed, the maximum bending stress will be  $(1/2) \Delta T\alpha E / (1 - \mu)$  — compression on the hot surface and tension on the cold surface. The strain is then

$$\begin{aligned}\epsilon &= \frac{1}{2} \Delta T\alpha / (1 - \mu) \\ &= \frac{1}{2} (2^\circ\text{C}) \times \frac{13.4 \times 10^{-6}}{^\circ\text{C}} / (1 - 0.3) \\ &= 1.9 \times 10^{-5}\end{aligned}$$

The output signal is related to the input voltage, strain, and gage factor by

$$\begin{aligned}e_o &= \frac{2(1 + \mu) \epsilon K e_i}{4} \\ &= \frac{2.6 \times 1.9 \times 10^{-5} \times 150 \times 10}{4} \\ &= 18.5 \text{ mv}\end{aligned}$$

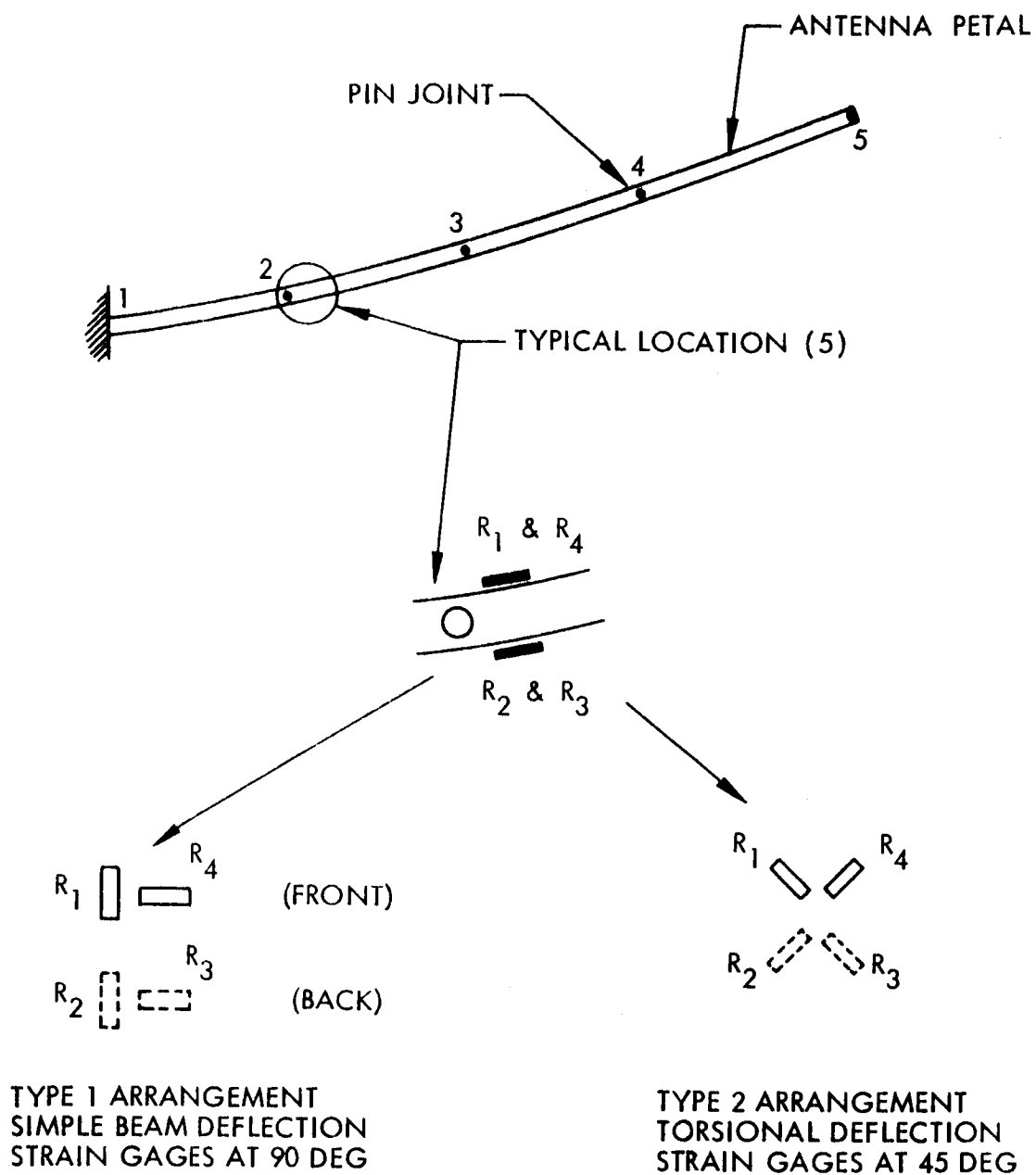


Fig. 6-58 Strain-Gage Instrumentation

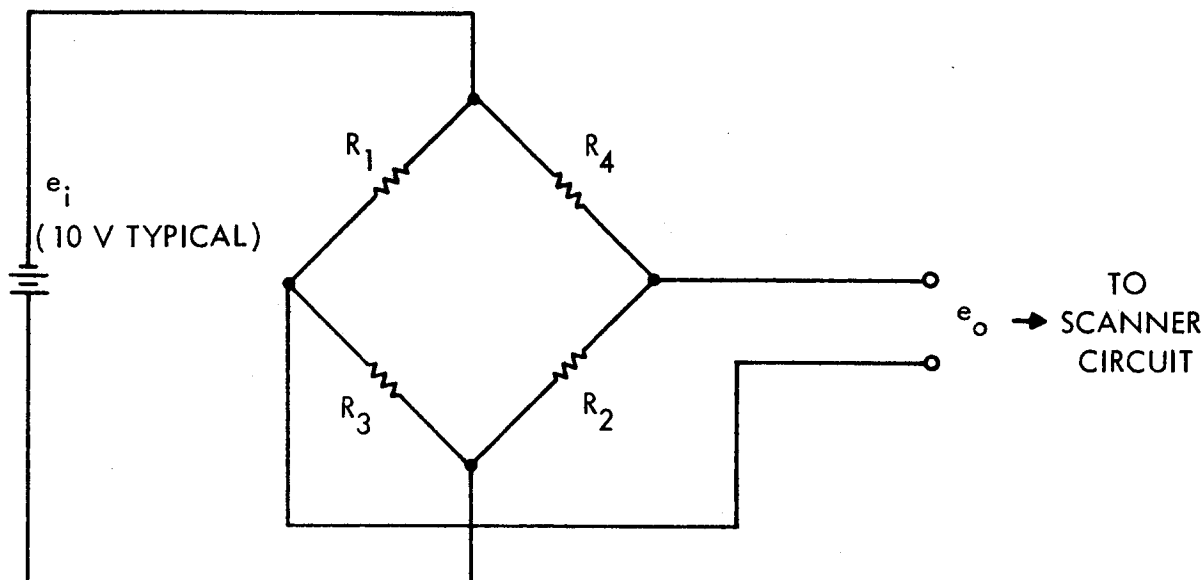


Fig. 6-59 Strain-Gage Circuit Diagram

Table 6-25 lists some of the significant features of the strain-gage technique.

Table 6-25

SUMMARY OF STRAIN-GAGE SPECIFICATIONS

Parameter	Value
Number of Petals Instrumented	18
Number Strain-Gage Units per Petal	10
Number of Strain-Gages per Unit	4
Signal Output Voltage, mv	20
Compensated Temperature Range, °C	25 to 125
Accuracy, Percent	1
Precision Range, in.	0.005

Optical Technique. An alternative optical technique has also been studied. As shown in Fig. 6-60, this optical measuring system consists of a light source, reflecting mirrors, a scanning window, and a light detector. The light source is a 100-w tungsten bulb whose power is pulsed to conserve the drain from the spacecraft power system. The mirror, which has a diameter of 1-in. is placed behind the RF screen and in the hole of the electroformed petal so that there will be no surface error introduced to the antenna dish. Four mirrors are required for each petal. It is planned that 18 petals will be monitored. Each mirror is located between two pin joints where maximum deflection occurs. The mirror can be fabricated separately and mounted on the petal later. However, the better solution will be to electroform the mirror directly when the petal is electroformed.

The scanning window consists of two rotating discs. The first one has a rectangular slit to select the mirror peripherally; the second has a helical slit that rotates to select the mirror radially. The combination of the two discs makes it possible to scan the 72 mirrors individually.

A radiation tracking transducer (RTT)\* will be used as the light detector. The RTT is a semiconductor device that converts the X-Y coordinates of a light spot projected on its surface into voltages  $V_x$  and  $V_y$  proportional to the displacements X and Y. A typical output of the RTT is shown in Fig. 6-61.

The following calculation illustrates the concept feasibility; the information serves also as a basis of optical system specifications:

- Scanning Window Sizing. For a 12-ft petal with ends fixed and three intermediate pins, the effective beam length is 3 ft. Assume the expected maximum deflection is 0.050 in. This represents a change in angle of

$$\frac{0.05}{3 \times 12} = 1.39 \times 10^{-3} \text{ radians}$$

---

\*See for example, Electro-Optical Systems, Inc., Radiation Tracking Transducer, by John S. Winslow, et al., EOS Report 100-Final-Part B, ABMA Contract DA-04-ORD-1093, 15 Nov 1960.

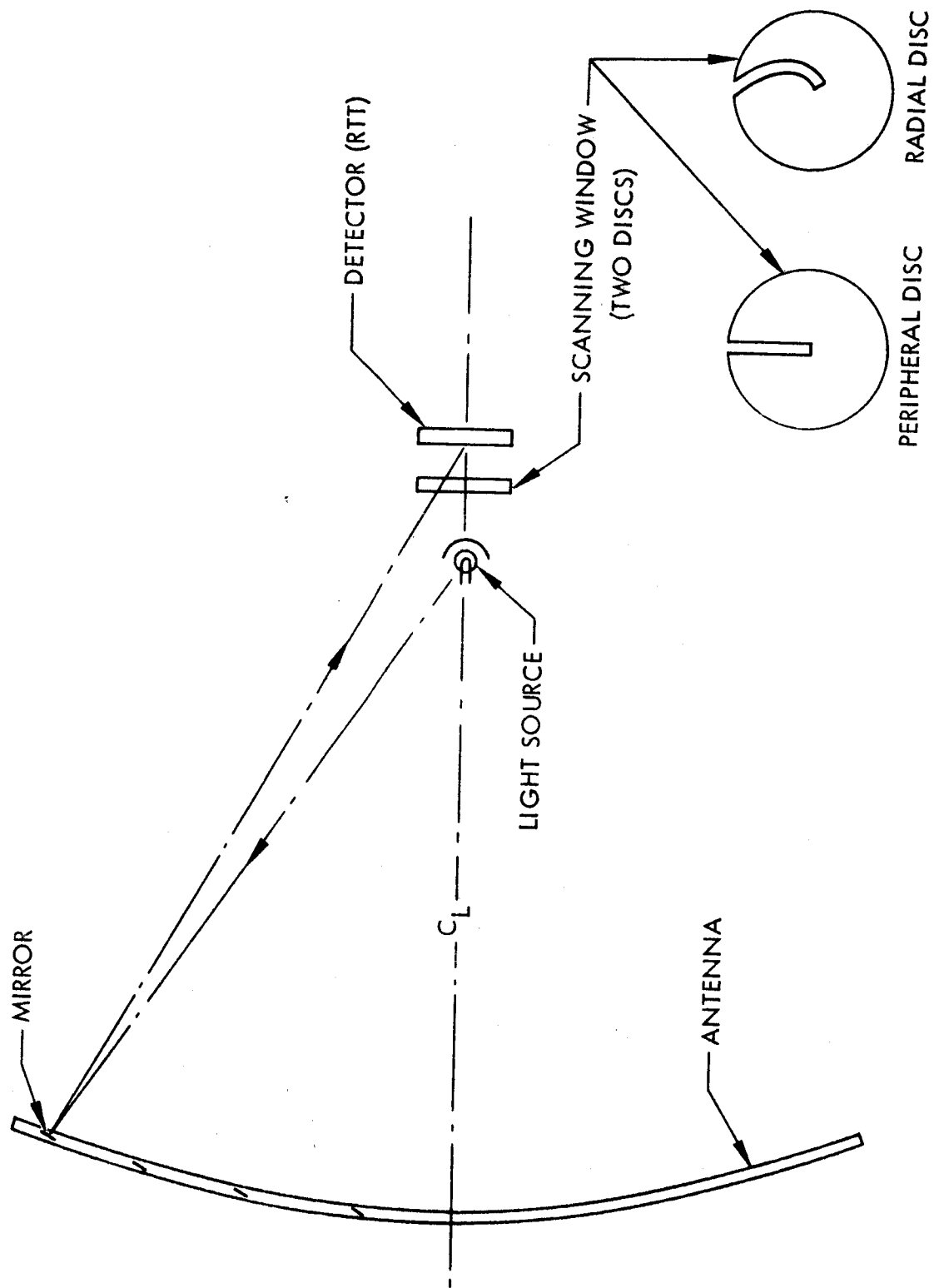


Fig. 6-60 Schematic of Optical System

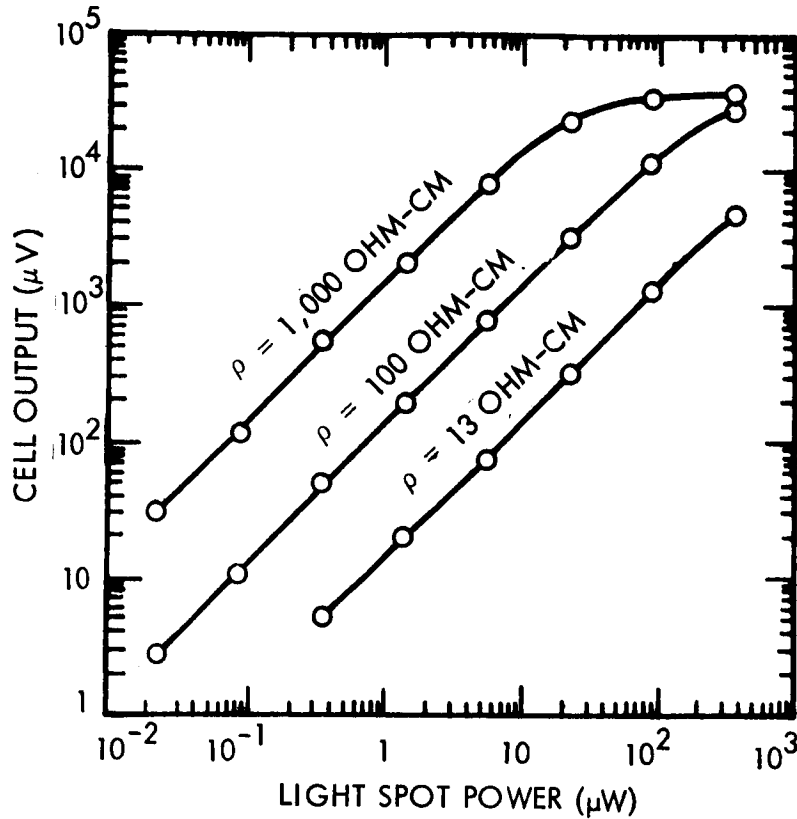


Fig. 6-61 Detector Output Characteristics

A change of  $1.39 \times 10^{-3}$  radians at the mirror will cause a change in angle at the detector of  $2 \times 1.39 \times 10^{-3}$  radians. The required window opening is (assuming that the scanning window is 15 ft away from the mirror) then

$$2 \times 1.39 \times 10^{-3} \times 15 \times 12 = 0.5 \text{ in.}$$

- **Light Source.** The light-spot power received at the detector (assuming a mirror efficiency of 85 percent and mirror diameter of 1 in.) is

$$\frac{100}{2\pi} \times \frac{(\pi/4)(1)^2}{(15 \times 12)^2} \times 0.85 = 328 \mu\text{w}$$

Since the light spot on the detector will be essentially the image of the filament of the light bulb, the intensity, for a filament area of  $0.05 \text{ cm}^2$ , is

$$\frac{328}{0.05} = 6.560 \text{ mw/cm}^2$$

- Detector Output. For the light-spot power of  $328 \mu\text{w}$ , the RTT output will be approximately 30 mv (see Fig. 6-64).
- Background Radiation Level. If nickel petal reflectivity is 0.5, the reflection from the sun radiation will be approximately  $70 \text{ mw/cm}^2$ . To ensure that this background radiation is kept to a minimum, the detector will be placed 5 in. away from the scanning windows. For a 0.5-in. opening, this will appear like an f/10 discriminator. The radiation intensity at the detector is then

$$70 \frac{\text{mW}}{\text{cm}^2} \times \frac{(\pi/4)(0.1)^2}{2\pi} = 87.5 \mu\text{w/cm}^2$$

Thus, background radiation can be kept to approximately 1 percent of the light source.

- Summary. On the basis of the foregoing analysis, the feasibility of the optical system for the antenna geometrical measurement is clearly established. Typical specifications of the optical system are listed in Table 6-26.

The cost of developing a strain-gage or optical system has been established to be approximately \$75,000.

Table 6-26  
OPTICAL SYSTEM SPECIFICATIONS

Parameter	Value
Mirror Diameter, in.	1
Number of Mirrors per Petal	4
Total Number of Mirrors	72
Maximum Mirror Movement, arc-min	5
Light Source Power (pulse type), w	100
Scanning Window Opening, in.	0.5
Light Spot Power, $\mu$ w	330
RTT Output, mv	30
Background Radiation, percent	1



#### 6.2.4 Antenna Feed Description

In order to cover the large frequency band and satisfy the different polarization requirements at X-band, multiple feeds must be used. Circular polarization is required from 100 to 2,300 MHz. A conical spiral antenna could cover this range, but is not practical due to the large dimensions required. A feasible approach would be to use a separate antenna for the 100 MHz requirement and limit the conical spiral to a low frequency of 800 MHz. The size of the conical spiral is determined by making the base diameter equal to a half wavelength at the lowest operating frequency (a diameter of 8 in. at 800 MHz, as shown in Fig. 6-62). This half-wavelength base minimizes end effects caused by currents, resulting from construction imperfections, flowing past the active region. The upper truncation diameter is generally made less than a quarter wavelength at the highest operating frequency so that the feed point, basically a linear dipole, will not be energized. Since the upper frequency is 2,300 MHz, the diameter must be 1.5 in. or less. An apex angle of 30 deg was chosen to properly illuminate the reflector and results in a total length of 8.6 in. The spiral apex, the high frequency region, is placed at the focal point to minimize quadratic phase error. This is accomplished at the expense of the lower frequencies.

The separate 100 MHz antenna could be either a crossed dipole with reflectors or a planar equiangular spiral, mounted over a ground plane. The planar spiral is recommended since it simplifies problems associated with the unfurling operation and the furled volume requirement. Also, the planar spiral does not require phase shifters and has better off-axis circularity. The 800- to 2,300-MHz conical spiral is mounted in front of the 100-MHz planar spiral. This location will have virtually no effect on the operation of the 100 MHz antenna since the blockage diameter is small compared to a wavelength.

At X-band, a 1.2-in. diameter circular waveguide is necessary to support the  $TE_{11}$  mode and to avoid the higher order modes that cause cross polarization, etc. By dielectrically loading the waveguide with teflon or an equivalent material, the diameter can be reduced to approximately 0.8 in. The waveguide can be mounted inside the 800- to 2,300-MHz antenna so that it protrudes at the apex. The waveguide run will

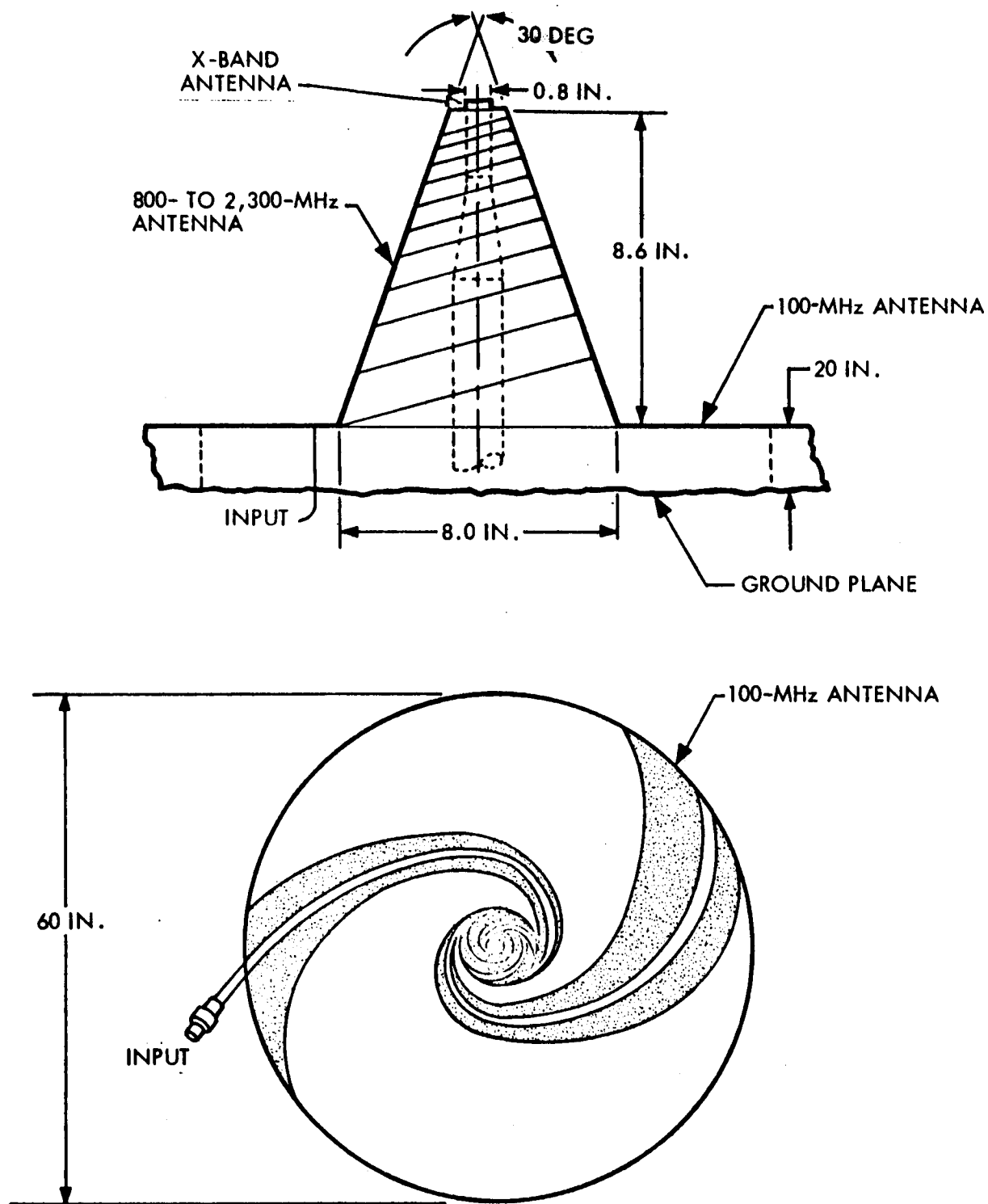


Fig. 6-62 30-ft Parabola Spiral Feed Antennas

have very little effect on the conical spiral, particularly at frequencies below 2,300 MHz. Circular polarization of either sense can be provided, if desired later by the addition of a quarter-wave plate in the waveguide. This configuration is shown in Fig. 6-62.

There is probably no unique solution to the requirements — the proposed antennas were chosen on the basis of efficiency. Since some blockage is inevitable when using a number of feeds at different frequencies to illuminate a parabola, the proposed configuration minimizes the blockage effects by confining them to the low frequency antenna. The proposed antenna yields more bandwidth than required and therefore should have more operational flexibility.

#### 6.2.5 Link Calculations, Equipment Descriptions, and Antenna and Feed Weights

The link gain calculations for the seven links associated with the 30-ft parabolic antenna experiment are shown in Table 6-27. In each case where down-link antenna pattern measurements are performed, the 85-ft diameter ground antenna is used to minimize the required vehicle transmitter power. The calculations show the following required output power:

- 24 w at 100 MHz
- 2 w at 800 MHz
- 0.77 w at 2,300 MHz
- 0.33 at 7,300 MHz

These output levels permit a link closure with a full 10-percent bandwidth when the vehicle 30-ft parabolic is oriented to give peak gain. To achieve antenna-gain pattern variations down to 30 db below peak gain, a 30-db margin is required. Since gain can be traded for bandwidth, a 30-db or one-thousandth reduction in bandwidth will allow link closures with the same vehicle transmitter powers. This configuration permits two modes of operation — a 10-percent bandwidth and a 0.01-percent bandwidth. The wide-band mode permits wide-band operation for uses such as tracking and telemetry data readout from a second satellite. The narrow-band mode is limited antenna-pattern measurements. If operation is considered with the 40-ft diameter ground

Table 6-27

## PARABOLA EXPERIMENTS LINK CALCULATIONS

Item	Up Links						Down Links					
	1,700 MHz		2,100 MHz		8,000 MHz		100 MHz		800 MHz		2,300 MHz	
	Gain	Loss	Gain	Loss	Gain	Loss	Gain	Loss	Gain	Loss	Gain	Loss
Transmitter Power, dbw	30		30		30		0		0		0	
Line Loss, db		2		2		2		3		3		3
Antenna Gain, db	27.6		29.5		37.5		17.0		35.1		44.2	
Pointing Loss, db		1		1		3		0		0		0.5
Propagation Path												
Free Space, db		190.0		191.7		203.4		165.0		183.2		192.4
Fade Margin, db		1		1		0		4		2		1
Polarization, db		3		3		3		3		3		3
Receiver												
Antenna Gain, db	41.5		43.3		55.0		26.1		44.1		53.2	
Line Loss, db		3		3		3		2		2		2
Pointing Loss, db		0.5		0.5		1		0		0		1
Total	99.1	-200.5	102.8	-202.2	122.5	-215.4	43.1	177.0	79.2	193.2	97.4	202.9
Received Signal Power, db	-101.4		-99.4		-92.9		-133.9		-114.0		-105.5	
Noise Power, dbw	-111.3		-110.4		-104.6		-129.1		-120.0		-115.6	
Threshold, db	9		9		9		9		9		9	
Sensitivity, dbw	-102.3		-101.4		-96.6		-120.1		-111.0		-106.6	
Required Transmitter Power, dbw							13.6		3		-1.1	
Required Transmitter Power, w							24		2		0.77	
Margin, db	0.9		2.0		3.7							
											117.3	214.0
											-96.7	
											-110.5	
											9	
											-101.5	
											-4.8	
											0.33	

(a) Vehicle Antenna 30 ft; Ground Antenna 85-ft Receiver; 6-ft Transmitter at S-Band, 4-ft at X-Band; Range 22,000 nm; Bandwidth 10 percent of  $f_0$ ;  
Vehicle Receiver NF 10 db; Ground Receiver NF 4.5 db.

antenna, a 6.5-db loss in gain from the 85-ft diameter antenna will result, reducing the available 10-percent bandwidth 6.5 db down to about 2.2-percent bandwidth. The resulting available bandwidths are given in Table 6-28.

Table 6-28  
AVAILABLE BANDWIDTHS

$f_o$	85-ft Antenna		40-ft Antenna
	10% Bandwidth (MHz)	0.01% Bandwidth (kHz)	2.2% Bandwidth (MHz)
100 MHz	10	10	2
800 MHz	80	80	18
2,300 MHz	230	230	51
7,300 MHz	730	730	164

These bandwidths indicate that primary telemetry transmission or other useful communication can be demonstrated.

A 10-percent antenna bandwidth must be demonstrated for the 30-ft parabolic at each frequency. A practical approach that will demonstrate the antenna bandwidth involves compiling antenna gain patterns at selected frequencies throughout each band. This will permit any performance degradation to be determined across the frequency band. Ten frequencies, or 1-percent separation, were selected for measurements across each 10-percent band. This results in 70 different frequencies required for the 30-ft parabola experiment. A frequency synthesizer was considered as a generator for the 70 exciter and local oscillator frequencies. However, the seven required bands do not lend themselves to this technique because they are not convenient multiples of a basic reference oscillator. Therefore, the approach selected was to use completely separate transmitters and receivers. (Some economy could be realized by considering frequency multiples and resulting reassignments of operating frequencies.) Gain pattern measurements can be made by having the receiving systems use logarithmic response instead of linear to provide a 30 db dynamic response. Logarithmic response can be obtained by detecting the outputs of the final two stages of the IF receiver and adding them linearly.

The operation of each transmitter and receiver is considered below. Figure 6-63 illustrates the 100-MHz transmitter. The output of a basic 1-MHz crystal oscillator is multiplied in a step recovery diode multiplier to provide the required ten frequency steps from 95 to 104 MHz. These frequencies are separated in a filter bank followed by diode switches that select the desired frequency. The selected output is amplified to the required 24 w.

The 800-MHz transmitter, shown in Fig. 6-64, uses the same basic technique as the 100-MHz device except that a 8-MHz reference is used to generate ten steps from 80 to 160 MHz. A 680-MHz local oscillator is used to up convert to provide steps from 760 to 840 MHz. The selected frequency is amplified to the required 2 w.

Figure 6-65 shows the 2,300-MHz transmitter configuration. The 800-MHz system technique is used with a 23-MHz reference. A 2,150-MHz local oscillator up converts the ten steps to between 2,219 and 2,449 MHz. A solid-state amplifier provides a 0.77-w output.

The 7,300-MHz transmitter, shown in Fig. 6-66, uses a different approach than those considered above. The step-recovery-diode technique cannot be used for this frequency band. Frequency selection is performed by choosing a crystal local oscillator to serve as a reference frequency for a phase-locked VCO. The VCO is tuned and locked to the desired frequency. The 2-w VCO output is multiplied to the desired frequency and provides the required 0.33-w output. The wide frequency range requires three VCO's since a single VCO cannot cover the complete range. The device can be phase or amplitude modulated — a more complicated phase-lock system would be required for frequency modulation.

The receivers for 1.7 and 2.1 GHz are configured as shown in Fig. 6-67. A transistor preamplifier is followed by a tunable YIG filter that limits the wideband noise. A selectable LO fixes one of the 10 required frequencies and is amplified in a 60-MHz IF amplifier. The 8-GHz receiver (Fig. 6-68) is similar except that a tunnel-diode preamplifier is used to provide a low noise figure for X-band operation.

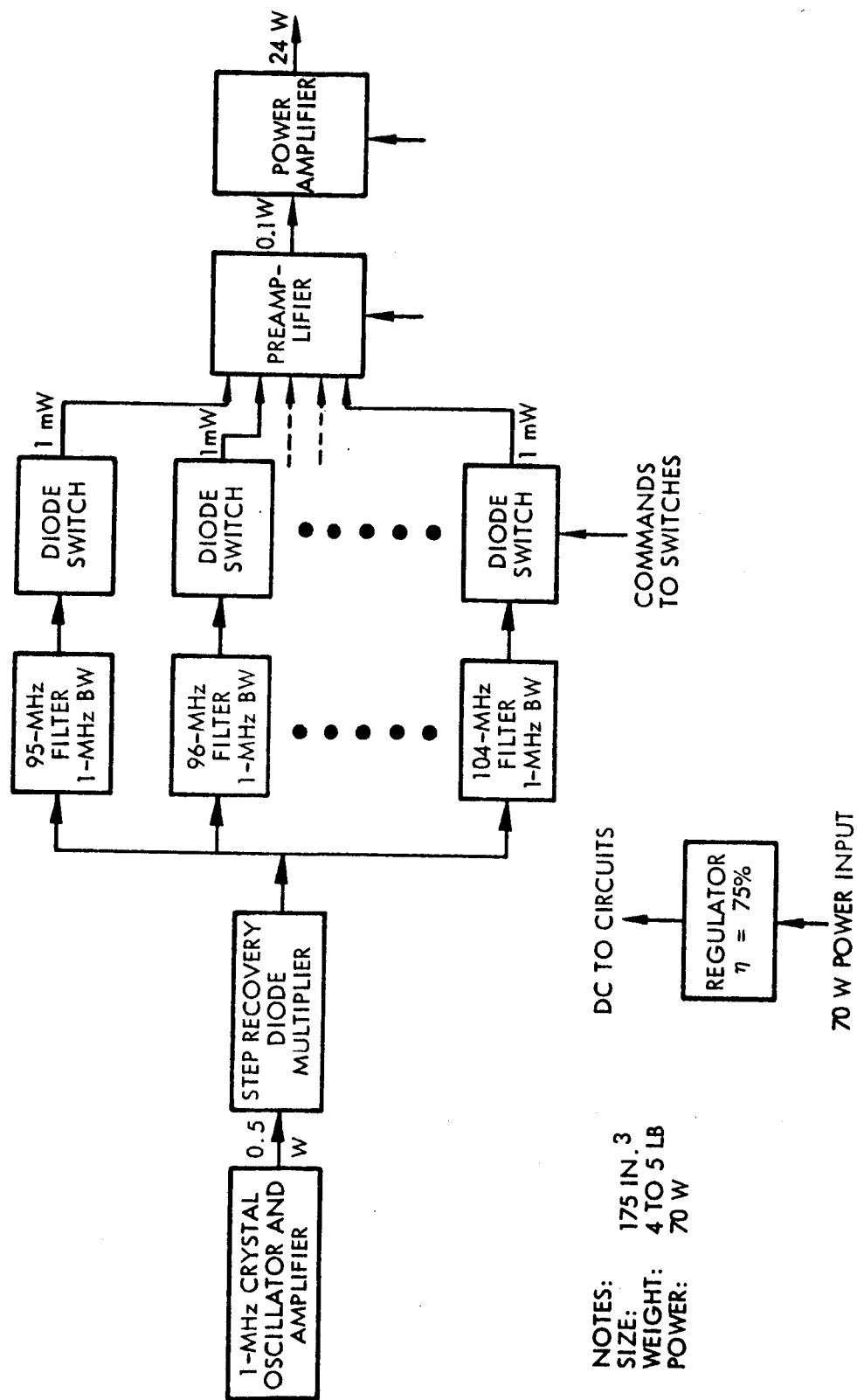
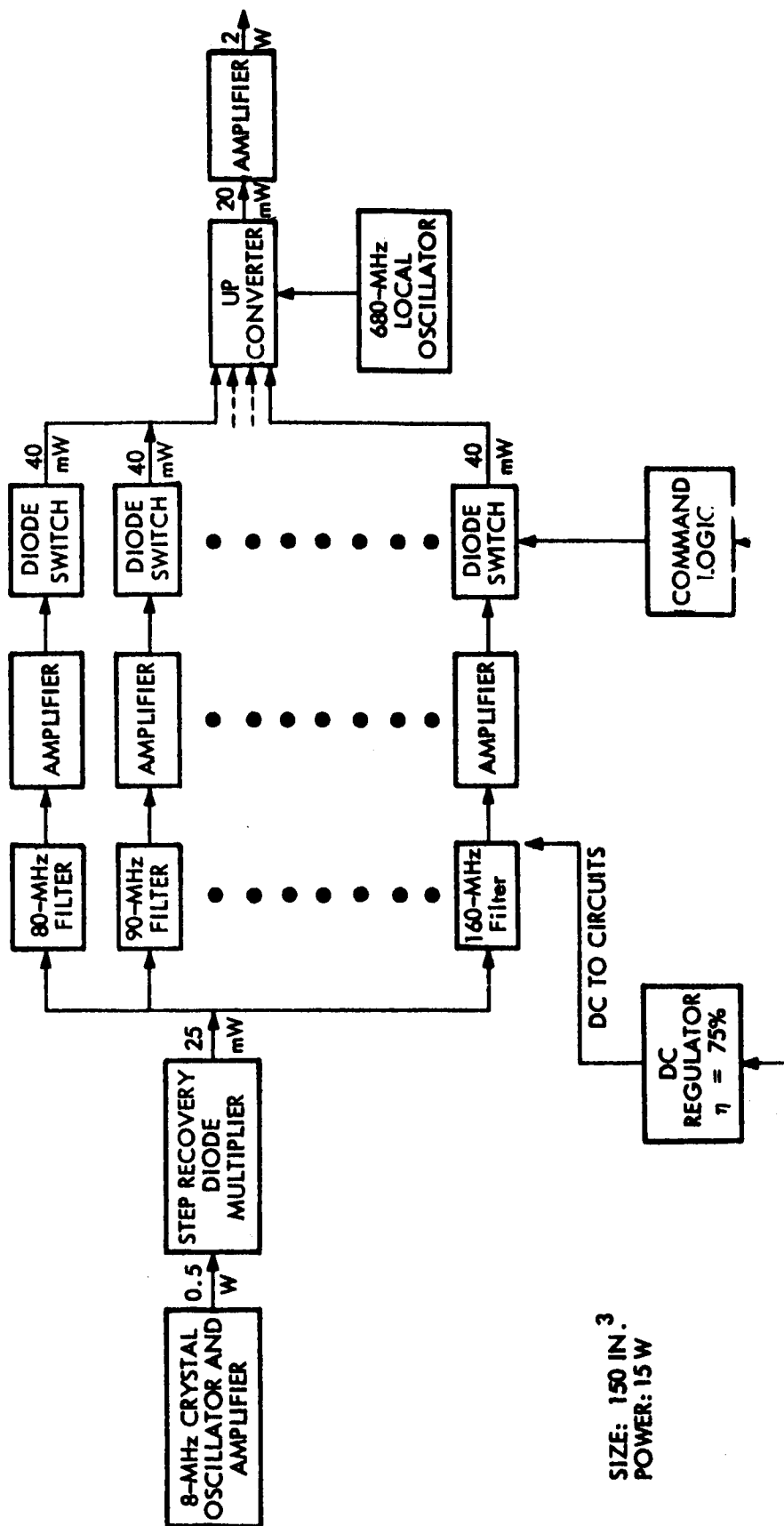


Fig. 6-63 100-MHz Transmitter



SIZE: 150 IN.<sup>3</sup>  
POWER: 15 W



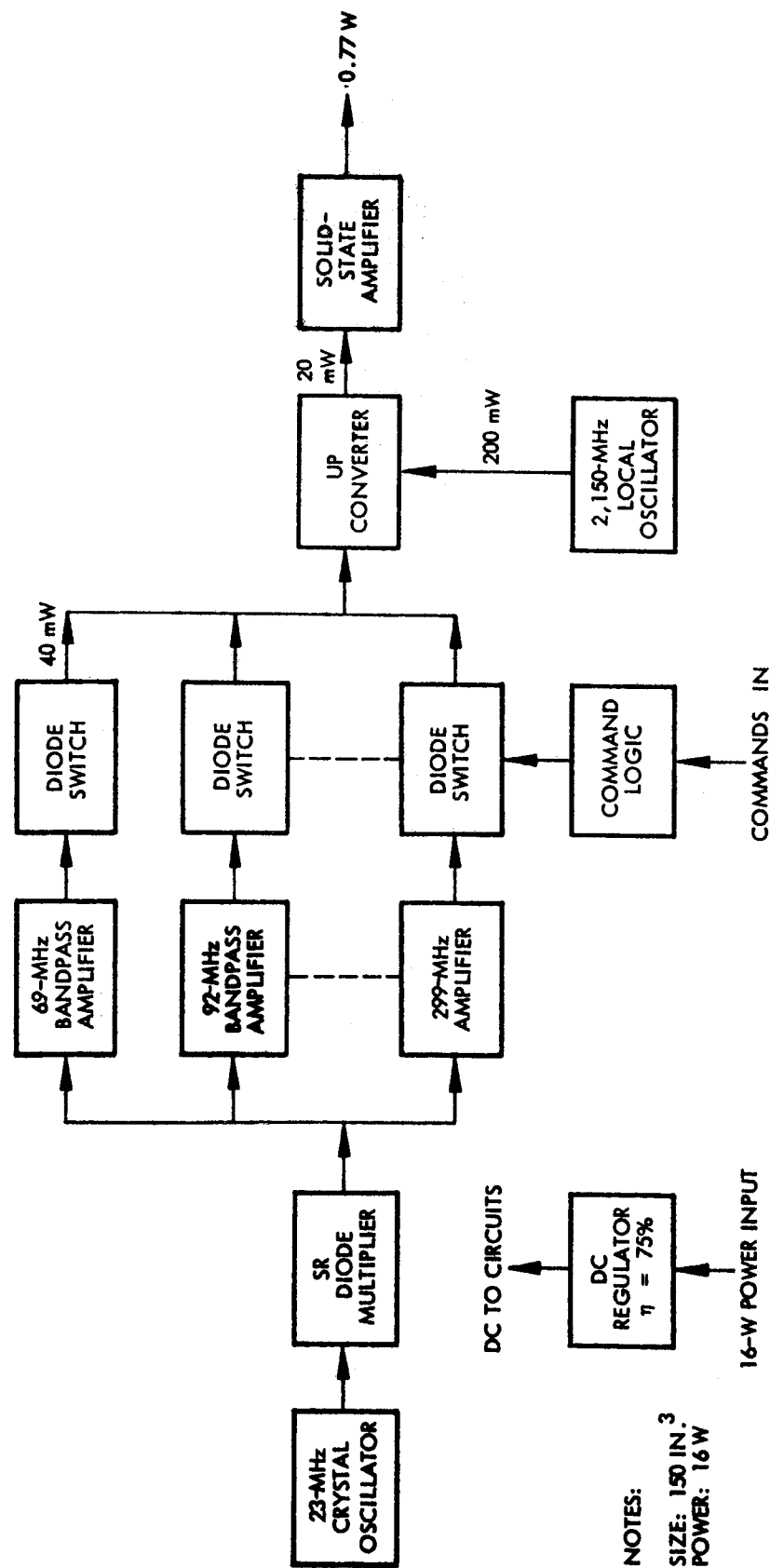


Fig. 6-65 2,300-MHz Transmitter

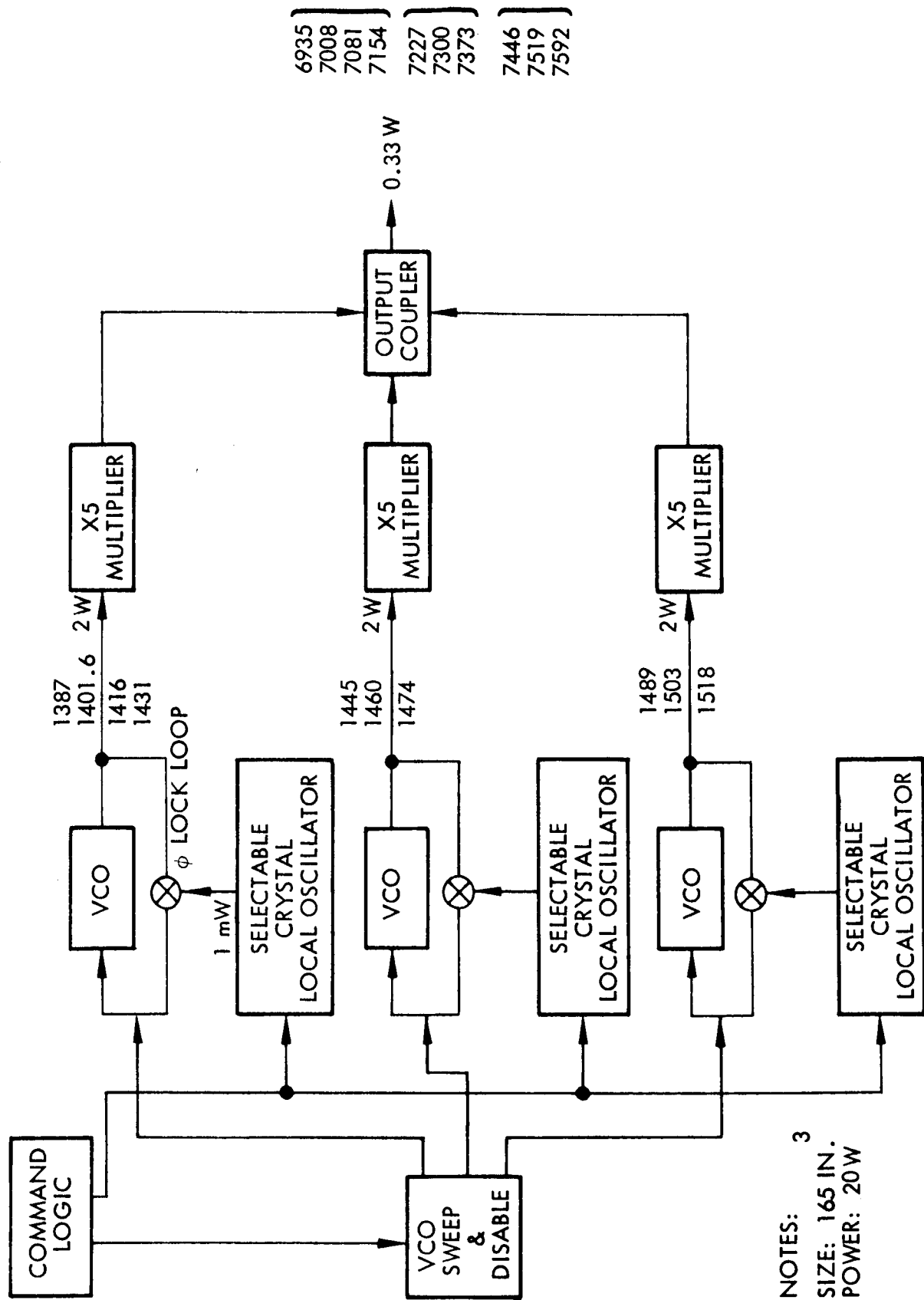


Fig. 6-66 7,300-MHz Transmitter

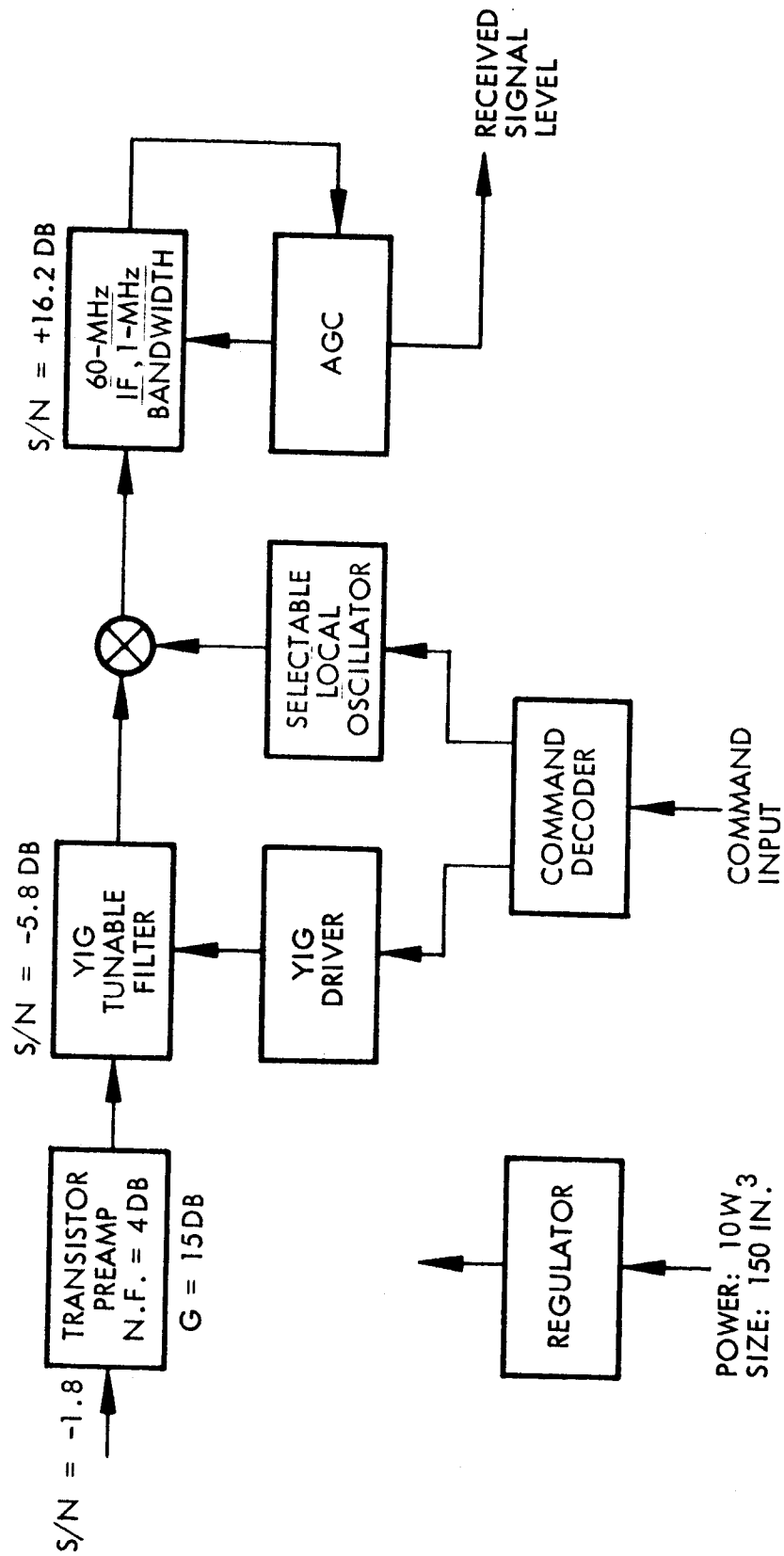


Fig. 6-67 1.7- and 2.1-GHz Receivers

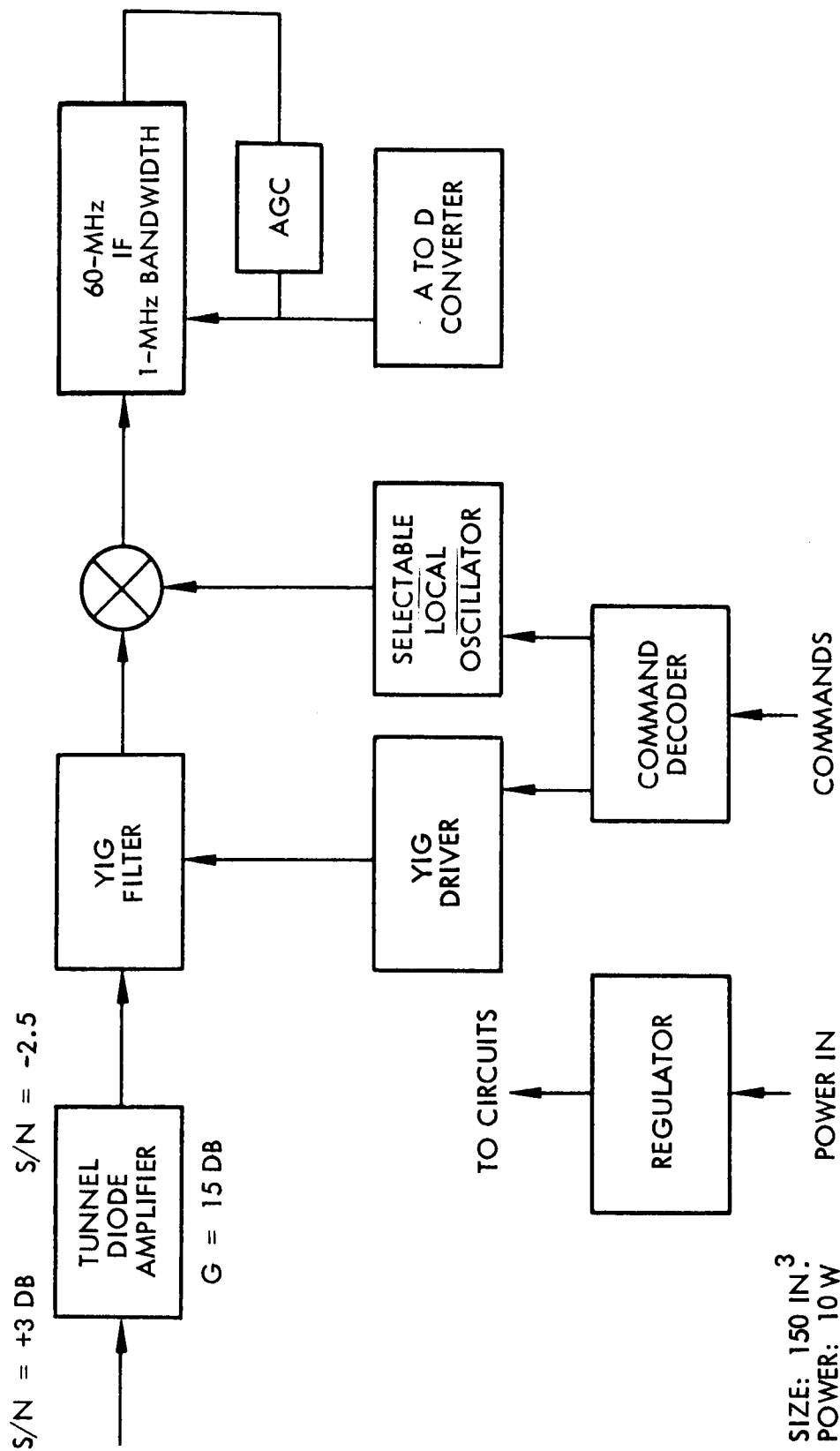


Fig. 6-68 8-GHz Receiver

A duplexing system is required to utilize the three feeds associated with the 30-ft parabola. The required duplexing scheme is shown in Fig. 6-69.

Total equipment weight is 46 lb. A unit breakdown for size, weight, and power is shown in Table 6-29.

Table 6-29

30-FT PARABOLA RF-SYSTEM CHARACTERISTICS

Equipment	Size (in. <sup>3</sup> )	Weight (lb)	Input Power (w)
100-MHz Transmitter	175	8	70
800-MHz Transmitter	150	7	15
2,300-MHz Transmitter	160	7	16
7,300-MHz Transmitter	165	7	20
1,700-MHz Receiver	150	5	10
2,100-MHz Receiver	150	5	10
8,000-MHz Receiver	150	5	10
Duplexers and TR Switches	50	2	—
Total		46	—

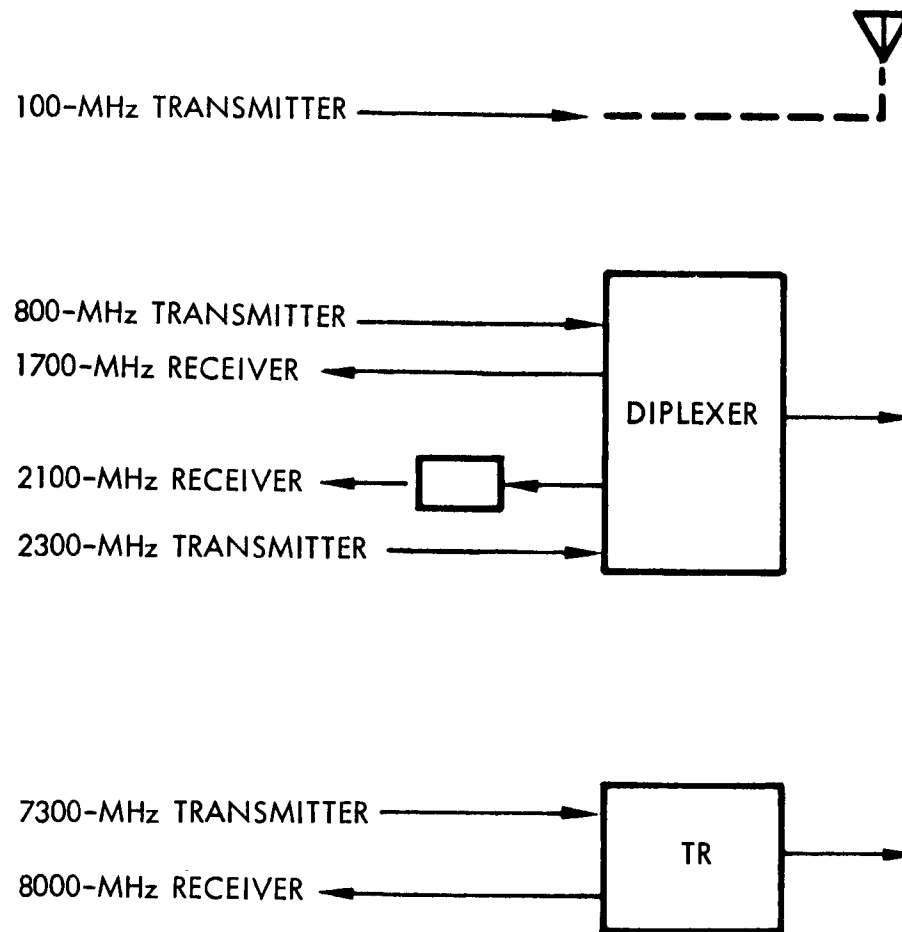


Fig. 6-69 Diplexing System

## 6.3 PHASED ARRAY

### 6.3.1 Requirements and Objectives

The purpose of the ATS-4 phased array experiment is to demonstrate the feasibility of a synchronous satellite communications system using a high-gain, electronically steerable array with multibeam capability. To achieve this purpose the experiment must demonstrate the following:

- Deployment of the phased array system
- Alignment of the array to the reference axes
- Steering of the array beams to within 0.1 deg of the direction of desired fixed or mobile ground stations by purely electrical means (without physical motion)
- Tracking of the ground stations (either by self-tracking or by command) at rates and accuracies compatible with the satellite stabilization system
- Acquisition of the desired signals
- Multibeam capability

Specific technical requirements include: operation between 7 and 8 GHz, at least four beams (two for transmission and two for reception), a beam gain between 30 and 45 db and command signals or pilot signals for control. The multibeam capability can be demonstrated by an experiment in which two independent channels of communication are handled simultaneously using four different ground stations (for example, station A to station B and C to D). Operation would not be limited to that particular mode, however. It is assumed that the frequency may be used to identify and separate signals for the ATS-4 experiment.

### 6.3.2 Study Objectives

The general objective of the study, to select a phased array system which meets the purpose, requirements, and objectives outlined above, may be narrowed down to

one more specific: to select an array system that can provide a 45-db gain with a weight compatible with present day synchronous altitude payloads.

The ATS-4 experiment requires gains ranging from 30 to 45 db. Certain sophisticated array systems are in advanced stages of development and would be logical candidates if the 30-db gain would meet future needs. LMSC studies of applications likely to follow the ATS-4 experiment indicate that the 45-db gain is more realistic. The higher gain figure obviously provides enhanced performance over a given link, but in the synchronous satellite application the extra margin allows access to the system by more ground stations of lesser capability. In some cases, 45-db gain is actually needed to close the link with the bandwidth required for the intended application. Unfortunately, LMSC studies have shown that available 30-db systems cannot be extrapolated to 45 db — a multiplication by 32 in aperture area — without incurring a weight which would be prohibitive for synchronous satellite applications. Therefore, to improve upon what is now available, LMSC has explored only those concepts which are feasible at 45 db. Once the ground rules for extrapolation have been determined, a 30-db version of the system could be flown on the ATS-4 program to demonstrate the feasibility of the concept.

### 6.3.3 System Comparisons and Tradeoffs

A number of high-gain antenna systems employing electronic beam steering techniques have been considered for the ATS-4 phased-array experiment. Candidate systems included:

- Conventional phased arrays
- Switched multiple-beam systems
  - Reflectors with multiple feeds
  - Lenses with multiple feeds
  - Butler matrix arrays
- Self-phasing arrays



Conventional Phased Arrays. The conventional phased array (wherein the phase of each individual radiating element is controlled through transmission line phase shifters) can be ruled out almost immediately because of its weight and complexity in the 45-db size and because of the difficulty of obtaining multibeam operation. Beam pointing information can be derived by command signals, by sensing relative phases on pairs of elements (with a pilot signal), or by signals from a preprogrammed control unit with the proper input data from vehicle attitude sensors. As an example of the complexity involved, a 45-db gain array with 0.5 wavelength element spacing would require 13,000 elements for a 75-percent efficient aperture. Increasing the spacing to 0.7 wavelength and pairing elements (one control device per pair of radiators) would reduce the number of control devices to about 3,000. With solid-state devices weighing, for example, one ounce each, the control devices alone would weigh 200 lb. This is for a single beam. To get three additional beams the signals must be separated at each radiator, or separate arrays must be used. In either case the weight of control devices would come to 800 lb and to this must be added the weight of the radiators and the interconnecting circuitry. Obviously, this is not a promising configuration.

Switched Multiple Beam Systems. In a switched multiple-beam array a number of individual beams are formed covering the desired angle of scan. The first-order approximation of steering is simply a matter of selecting the correct beam. The economy of the switched multiple-beam array arises from the fact that for a single beam one control device is required for every beamwidth in a limited scanning sector, rather than for every element in the array. If the scanning sector is unlimited, it can be shown that the switched-beam array is just as complex as the conventional phased array. Reflectors and lenses that have wide-angle scan capability can be used in a switched multiple-beam system by replacing the moving feed with multiple feeds arranged along the feed path.

Parabolic reflectors have poor wide-angle scan characteristics due to the appearance of coma as the feed is moved laterally off axis to steer the beam. Gain and sidelobe degradations occur when the reflector is scanned only a few beamwidths. The scan possibilities can be improved by increasing the focal length or by adding a second

surface of reflection to correct for coma. The Cassegrainian feed accomplishes this by effectively magnifying the focal length. Parabolic reflectors can be electronically scanned by using an array of feeds in the vicinity of the focal region to synthesize the proper phase front for an offset beam, but this technique has not been fully developed.

Spherical reflectors have the geometry necessary for wide-angle scanning but are less efficient than a paraboloid because the reflector must be made oversized to accommodate the scan angle.

Dielectric lenses were ruled out because of weight and unfurling problems, but the use of a metallic plate lens appears feasible. One type, namely a constrained binormal or two-point-corrected lens, can provide the angular coverage required for the ATS-4 application. This lens, which forms the basis for the LMSC system, will be described in detail in a later section.

The more familiar form of the switched multiple-beam array employs a Butler beam forming matrix. The Butler matrix is a linear, passive, bilateral network that forms N beams from N array elements, each beam appearing at a separate output port. This network consists of hybrids and fixed-phase shifters, the number of these components increasing rapidly as N increases. While feasible at the 30-db gain size, the Butler system appears to be too complex and heavy at 45 db. This point will be discussed in detail later.

Self-Phased Arrays. Self-phasing antennas are comprised of an array of elements, each of which has its own electronic circuitry that automatically phases the elements to produce a beam in the direction specified by the pilot signal. The array focuses itself to receive an incoming signal, processes the signal, and then refocuses for

transmission. As will be seen, this type of array is difficult to extrapolate to the 45-db-gain case because of the weight penalty.

Comparisons of Specific Systems. Both switched-beam and self-phasing arrays have been studied by other organizations. The self-phasing array has been studied by Hughes and by the Bell Laboratories\* and the switched-beam antenna has been investigated by Hughes, Sperry, and LMSC\*\*. On NASA programs Hughes has bread-boarded both kinds of array and is currently constructing a 64-element self-phased array. The design objectives of the Hughes self-phased array are a minimum gain of 30 db with an effective radiated power (ERP) of 25 dbw. The weight objective, exclusive of power supplies and r-f local oscillators, is 110 lb. The 64-element array design is a planar configuration of concentric circular rings with nonuniform inter-element spacings.

Extrapolating the 30-db gain array to the 45-db case requires a multiplication of the number of elements by  $2^5$ , or 32. Using the Hughes 30-db gain self-phased array as a basis for extrapolation, a 45-db gain array would require 2,048 elements. It is, of course, not fair to multiply the weight by the same factor since this would increase the radiated power as well as the gain by 15 db for a total increase in ERP of 30 db. Reduction in transmitter power in each elemental system would save considerable weight over the figure of  $32 \times 110 = 3,520$  lb. It is difficult to arrive at a weight estimate based on the Hughes system because no weight breakdown is available for a system meeting the 110-lb design objective at 30 db. LMSC estimates would place the weight

---

\*Hughes Aircraft Company, Design Review Report for High-Gain, Self-Steering Antenna System - Engineering Model, by R. A. Birgenheimer and C. Lew, Contract NAS 5-10101, Culver City, Calif., Mar 1966.

Bell Telephone Laboratories, A Self-Steering Array Repeater, by C. C. Cutler, R. Kompfner and L. C. Tillotson, Technical Journal 42, pp 2013-2032, 1963.

\*\*Hughes Aircraft Company, Spacecraft Antenna Systems - Interim Engineering Report Phase 1 - Final Report, by W. H. Kummer and A. T. Villeneuve, Contract NASA 5-3545, Culver City, Calif., Jan 1965.

C. A. Belfi, C. Rothenberg, L. Schwartzmen, R. E. Tilley, and A. Wills, "A Satellite Data Transmission System," IEEE Trans. AP-12, pp 200-206, 1964  
Lockheed Missiles & Space Company, ATS-4 Study Program Technical Report, LMSC-A772825, 1965.

for a 45-db system at a minimum of 2,000 lb. This weight plus the complexity of handling 2,048 channels make the self-phased system unattractive. It should be pointed out that a net increase of 15 db in ERP could be effected by raising the gain of the array by 7.5 db and the transmitted power by 7.5 db. This would require 365 elements, multiplying the weight by 5.7 (for a total of 627 lb), and multiplying the power consumption by the same factor.

A switched multiple-beam antenna using a Butler matrix and designed for 45-db gain would require an extremely large number of radiating elements, hybrids, and phase shifters. The radiating elements of this kind of array are usually spaced between a half-wavelength and a wavelength. This would require 10,000 elements and an even greater number of hybrids and phase shifters. Using the Hughes 64-element 30-db gain configuration as a basis for extrapolation, the projected system would have 2,048 radiating elements, 11,264 hybrids, and 7,884 phase shifters. The weight estimate for the Hughes switched-beam array is listed as 175 lb with separate arrays used for transmission and reception. Extrapolation in this case leads one to the same conclusion as before. Note, however, that in this instance the weight penalty arises from the increased complexity of the beam-forming system. It is this problem that the LMSC system is designed to solve.

#### 6.3.4 The LMSC Switched Multiple-Feed System

The LMSC system exploits the fact that only a narrow cone of coverage is required from synchronous altitude by using a metallic lens. The lens provides system gain and uses electronic switching of feeds to supply beam steering. The combination of a lens with multiple feeds (hereafter referred to as the "beam forming lens") is designed to provide a function similar to that of a Butler matrix. The properties of the beam-forming lens will be discussed in this section; the switching and electronic system will be described in the next.

Metallic lenses are of two basic types, as shown in Fig. 6-54. In both the normal and the constrained lens, the polarization is parallel to the plates and the index of refraction is determined by the plate separation "a" from

$$\eta = \sqrt{1 - \left(\frac{\lambda}{2a}\right)^2}$$

A normal lens provides focusing in the E-plane and, since the lens is a region having an index of refraction different from that of free space, Snell's law applies. In the constrained lens, focusing occurs in the H-plane (the plane perpendicular to the plates), but Snell's law does not apply, even though an interface exists between two regions of differing indices of refraction. This is because in the H-plane the lens plates constrain the wave to pass through the lens in a certain direction regardless of the angle of incidence. This action gives rise to the name "constrained lens."

The lenses shown in Fig. 6-70 are cylindrical with focusing provided by the lens in one plane only. Focusing in the other plane is provided by the line source feed. In the constrained lens shown the plate spacing is held constant, making the index of refraction constant over the lens aperture, and the thickness of the lens is varied. It is also possible to hold the thickness constant and vary the plate spacing. To make the constrained lens shown in the figure into one that provides focusing in both planes for a point source feed (rather than a line source), the constraining action must be provided in the E-plane as well as the H-plane. This can be done very simply by providing orthogonal plates in the lens (like an "egg crate") and if the E-plane plate spacing is the same as the H-plane spacing, the lens will accept all polarizations. The plates perpendicular to the E-plane of a wave do not affect the index of refraction for that wave polarization. Since the index of refraction is the same for all cells of the lens, the lens surface contours can be surfaces of revolution about the axis of the lens.

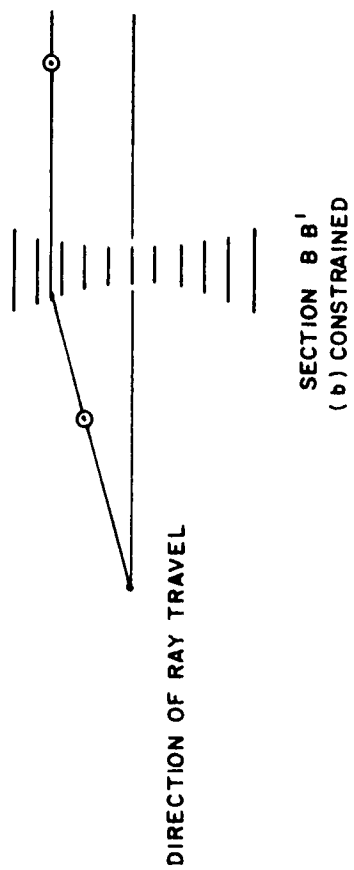
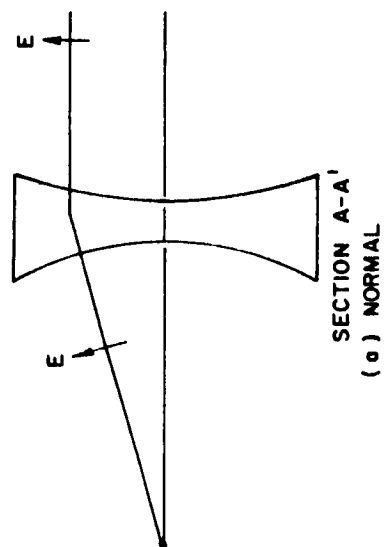
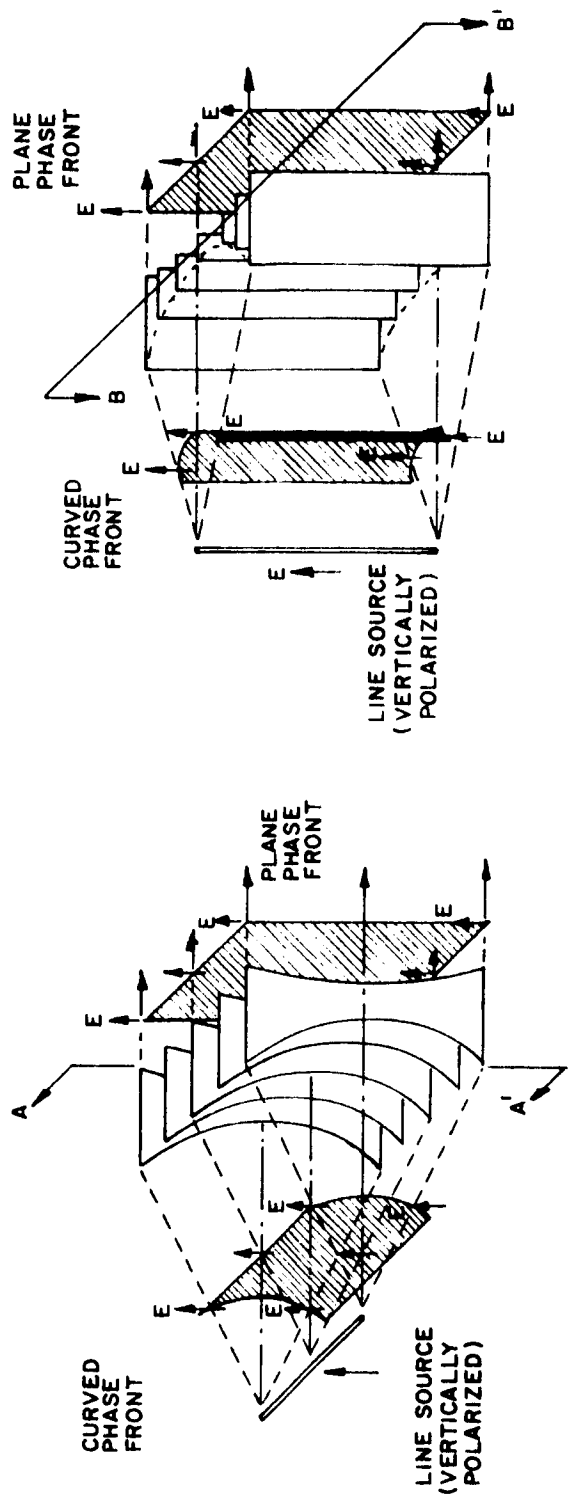


Fig. 6-70 Normal and Constrained Lenses

The principal advantage of a constrained metallic plate lens is the wide-angle scan obtainable. Several designs of wide-angle two-point-corrected metallic plate lenses in cylindrical form have been analyzed by Ruze\*. Ruze's work for two-dimensional lenses with line source feed elements has been extended to three-dimensional lenses with point source feed elements by Ellis et al.\*\* and Fine and Reynolds\*\*\*. The more important lens surface design formulas for constrained lenses with index of refraction less than unity apply to both the rotational and the cylindrical surfaces.

Astigmatism is the aberration that first limits the scan angle in rotationally symmetric versions of the two-point-corrected lens. Typical experimental results indicate a scan angle (without serious degradation) of about  $\pm 10$  to  $\pm 15$  beamwidths, sufficient for this application. The lens surface would be rotationally symmetric and would have a diameter of 10 ft if an overall aperture efficiency of 55 percent could be achieved; however, to allow margin for losses due to switching and to over-illumination of the lens by the small feeds, a lens diameter of 12 ft is better. The beams are spaced to overlap at just below the -3-dB level. The lens is fed by an arrangement of multiple feeds, each feed illuminating the entire lens aperture to provide a separately available beam. The half-power width of the beams will be about 0.9 deg, but the crossover beamwidth is about 1.05 deg. To cover the angle subtended by the earth, approximately 256 beams will be required.

Consider the beam arrangement shown in Fig. 6-71. If, to form a single beam of the multibeam system, the output of a single feed is selected, then the system link must accommodate a gain reduction of about 3 to 4 dB at angles where two beams intersect (point  $P_1$ ) and 6 to 8 dB at points where four beams intersect in a common point (point  $P_2$ ). This gain reduction or fluctuation as a function of scan angle can be minimized by combining two, three, or four adjacent beams in a power divider to form the

---

\*J. Ruze, "Wide Angle Metal Plate Optics," Proceedings of the IRE, Vol. 38, p. 53, Jan 1953.

\*\*Ellis, W., Fine, E., and Reynolds, G., A Point Source Binormal Lens, US Air Force Cambridge Research Center, Bedford, Mass., Rept. No. E-5067 Mar 1951.

\*\*\*Fine, E., and Reynolds, G., A Point Source Binormal Lens With Wide Angle Focal Points, US Air Force Cambridge Research Center, Bedford, Mass., Rept. No. E5095, May 1953.

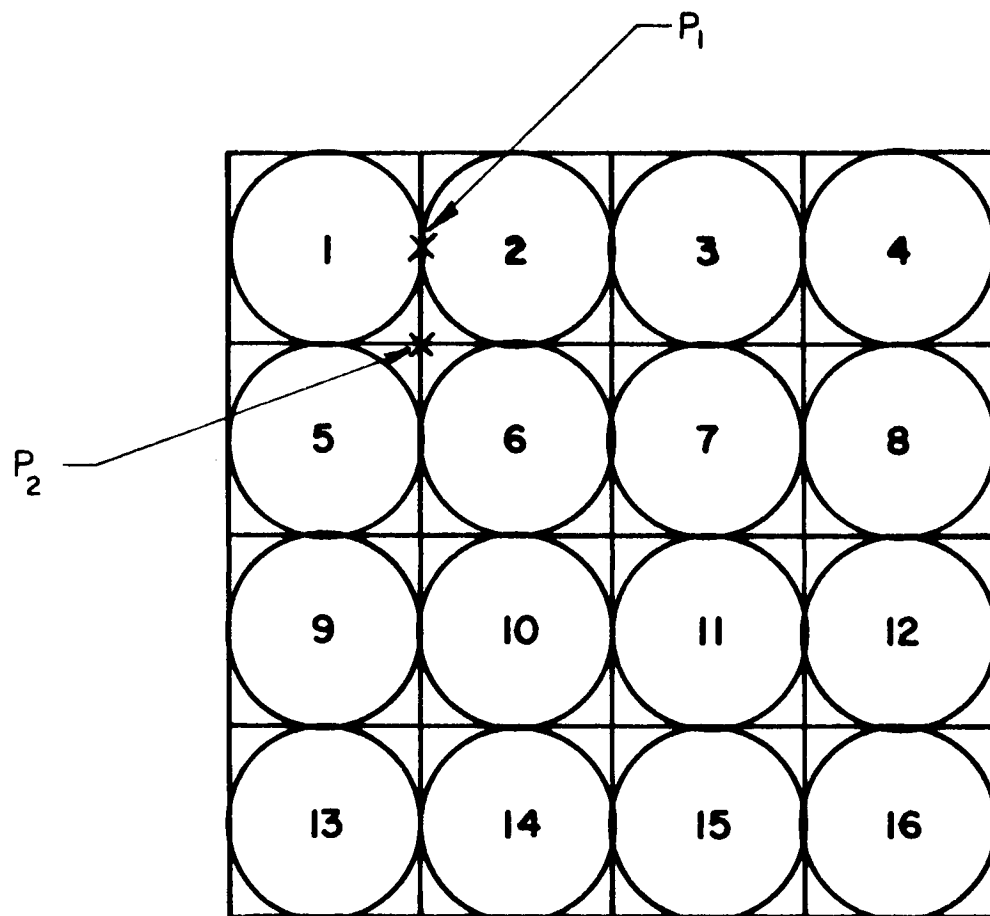


Fig. 6-71 16 of 256 Positions (Circles Represent 3-db Contours)



composite single beam required. The amount of fluctuation will depend on the cross-over level that can be achieved; this will be determined by the feed design.

One significant design consideration is the bandwidth of the lens system. Since the signals are separated by means of the frequencies of the pilot signals, the system must handle four times the r-f bandwidth plus an allowance for guard bands. The equation shows the index of refraction to be a function of wavelength. Therefore, phase distortion of the aperture field must be determined as a function of frequency. Fradin\* shows that the bandwidth capabilities of an E-plane metallic plate lens can be improved by zoning or stepping the lens. For a maximum phase shift of  $\pi/2$  radians and for an index of refraction of 0.5, curves depicting the bandwidth capability of a smooth lens (as a function of thickness) and of a stepped lens (as a function of the number of steps M) are shown in Fig. 6-72. This figure shows that an 11-percent bandwidth is obtainable with a stepped lens of three steps. For ATS-4 experiment, this would mean an 800-MHz bandwidth for a center frequency of 7,400 MHz.

Physically, the constrained lens would be the unfurlable type and, when furled, would form a package approximately 12 ft long by 8 in. square which would fold against the feed elements. The lens would be extended to its operating position by booms that would be mechanically erected. After extension, the lens would unfold to form the operational configuration shown in Fig. 6-73. The lens would have nine subdivisions, each about 4 ft square. These subdivisions would be hinged so that they would fold flat on one another when furled. Each section of this "egg crate" design would be individually spring loaded and fitted with stops to assure erection in the final operational shape. Each of the nine square cavities formed by the array extension would be fitted with aluminum foil cross strips which would form individual cells. The lens and feed elements, not including electronic circuitry and r-f system components such as r-f switches, filters, electronic power dividers, and so forth, would weight approximately 100 lb. A table of weights for the complete system will be given in the next section. For a 30-db minimum gain system, such as might be flown as an ATS-4 experiment to demonstrate feasibility, the lens would be 2.5 ft in diameter and would weight between 8 and 9 lb. It would have 16 feeds arranged in a circular pattern 8 in. in diameter.

---

\*A. Z. Fradin, Microwave Antennas, Pergamon Press, 1961

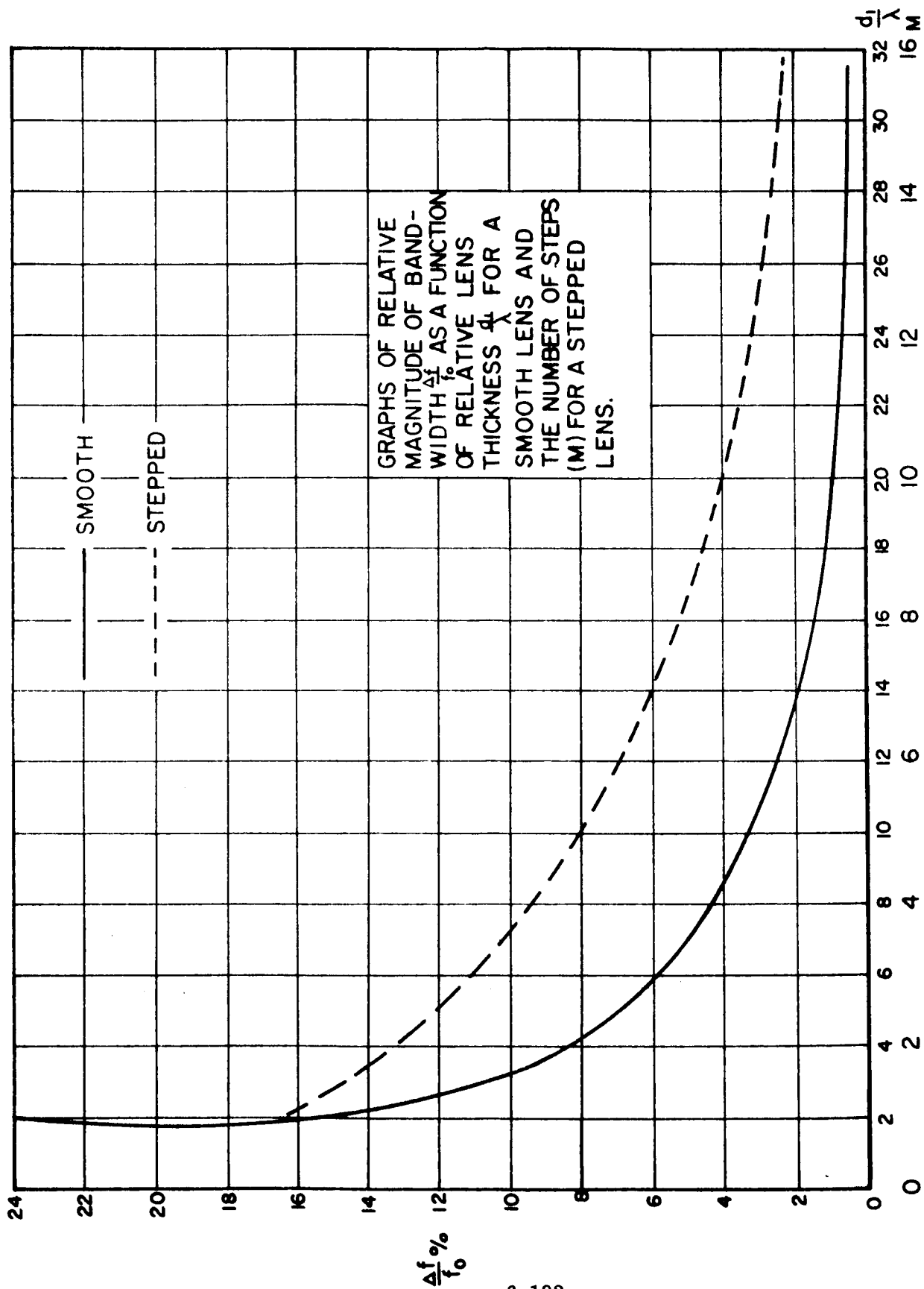


Fig. 6-72 Lens Bandwidth

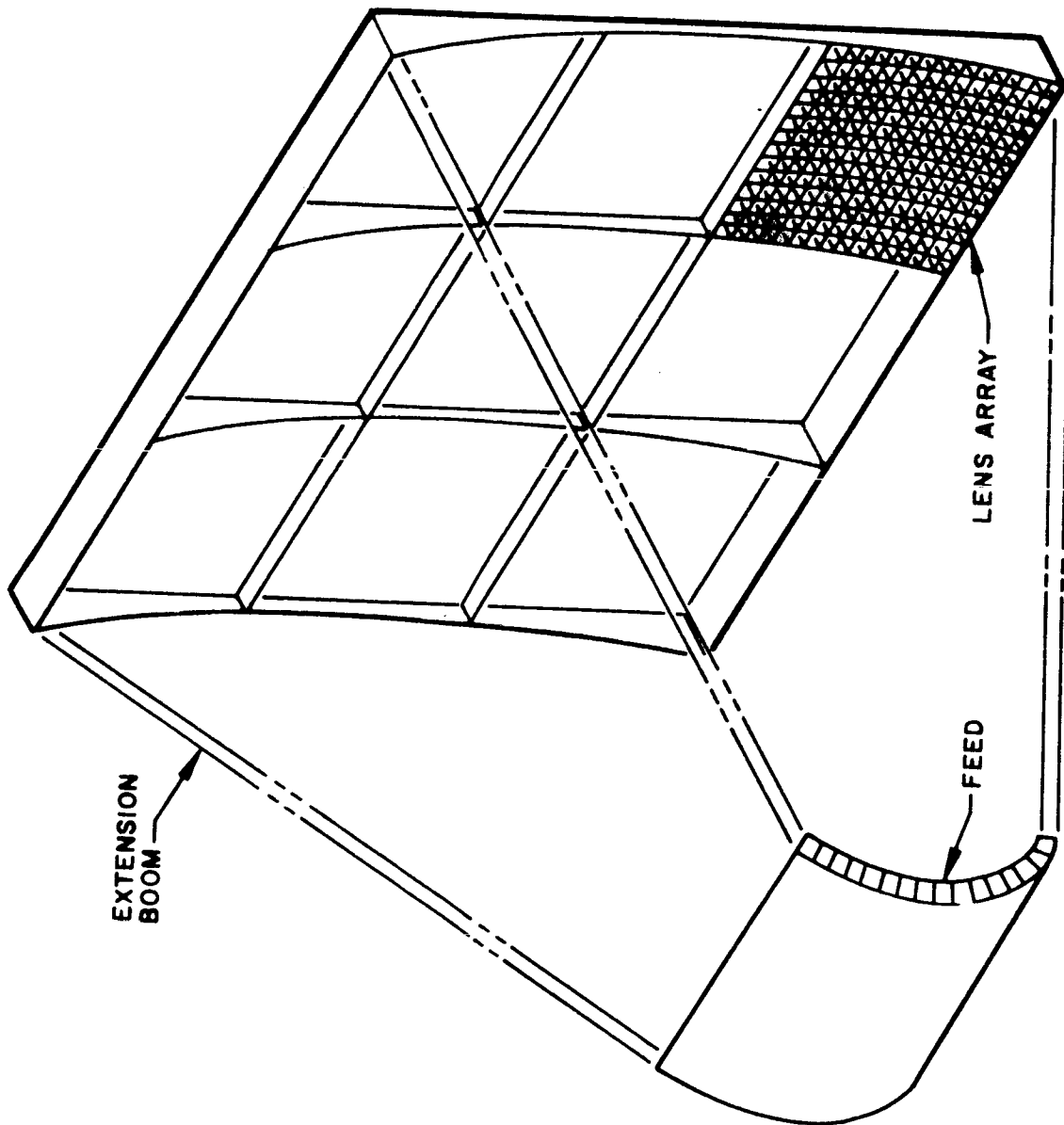


Fig. 6-73 45-db Lens Array

### 6.3.5 The Switching and Electronic System

The switched multiple beam system consists of four major building blocks:

- A beam-forming lens (including multiple feeds)
- Signal collection networks
- Electronic subsystems
- Transponders

Figures 6-74 and 6-75 show the relationship of these blocks to each other in a system that provides two system beams (a single channel). Extrapolation to a complete four-system-beam configuration is easily made\*.

The beam-forming lens is described in subsection 6.3.4. One such system is required per complete array, regardless of the number of system beams provided. The size and weight of this lens are a function of the gain desired.

Each system beam has its own signal collection network – four such networks will be required for the ATS-4 system. A signal collection network consists of solid state switches (one for each lens beam), four collecting lines, four bandpass filters (to block out the other three system beams and pass the desired one) and the switch control circuitry. The size and weight of the collection system are therefore dependent on the gain desired. The RF inputs to this network (in the receiving case) are the 256 output ports of the beam-forming lens and the outputs are the highest amplitude signals on each of the four collecting lines.

Figure 6-71 shows the lens beam arrangement for a 16-beam system; the 256-beam system would simply be a 4 by 4 repetition of the arrangement shown in the figure. (The beams could also be staggered in the manner of racked billiard balls to raise the cross-over level at the point where three [instead of four] beams cross over, but this complicates the tracking and the power division problems.) A system beam can be steered

---

\*It is important to distinguish between the four beams provided by the complete system and the 256 static beams formed by the beam-forming lens. The former will be called system beams and the latter lens beams.

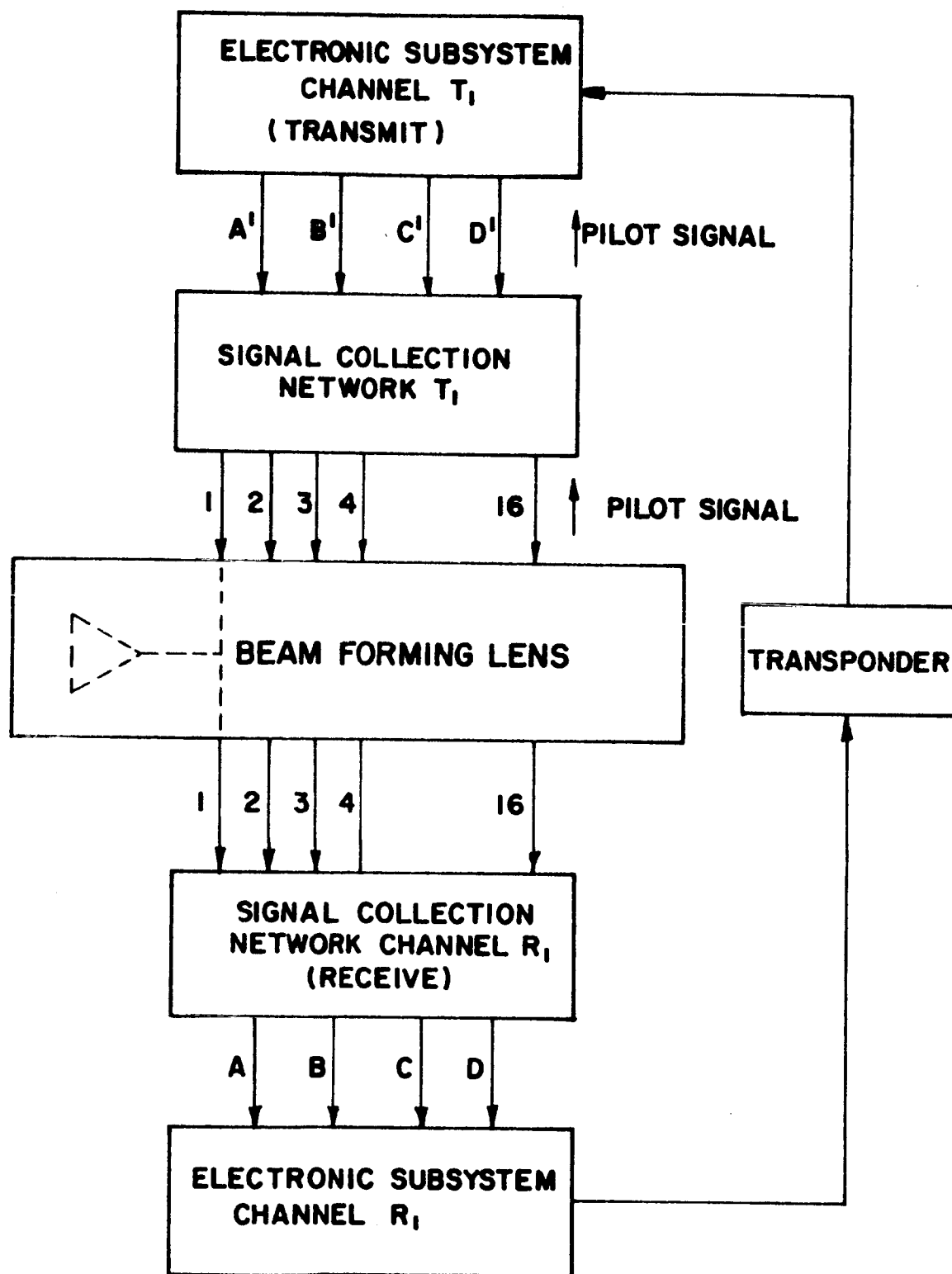


Fig. 6-74 Single-Channel (Two-Beam) Configuration

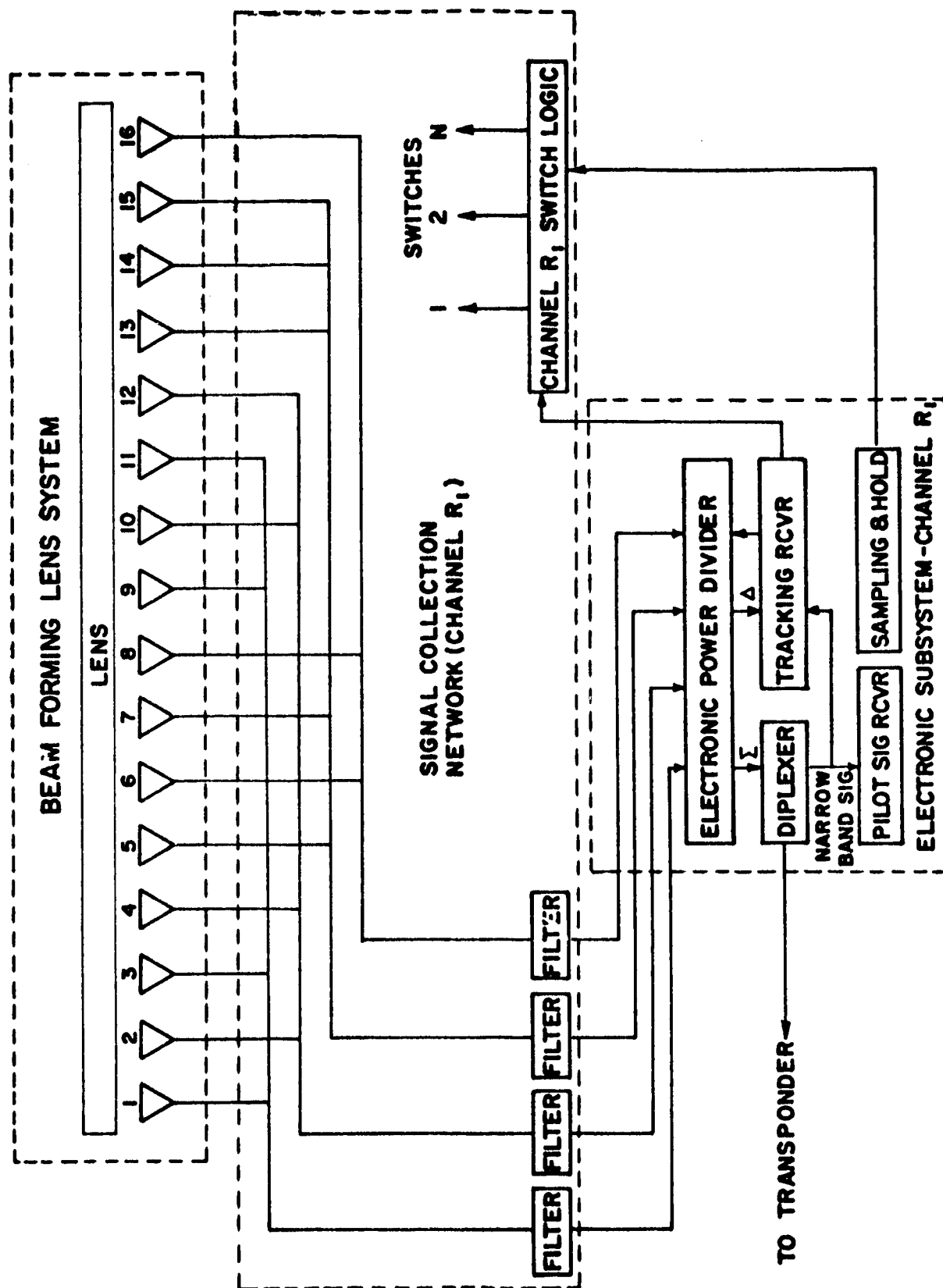


Fig. 6-75 Block Diagram of Switch Multiple-Beam System

between any two adjacent lens beams by the proper power division between the corresponding ports of the beam-forming lens. For example, if the power division between ports corresponding to lens beams 1 and 2 is  $(1, 0)$ , then the system beam is coincident with lens beam 1; if  $(1/2, 1/2)$ , the system beam is halfway between; and if  $(0, 1)$ , the system beam is coincident with lens beam 2. Intermediate positions follow for intermediate ratios of power division. When the system beam must be steered within the area defined by four lens beams in a square arrangement, it is necessary to obtain the proper power division among four lens beams. This means that all four lens beams must appear at different lines before being combined in the variable power divider. This is the familiar four-color map problem. From Fig. 6-71 it can be seen that lens beams 1, 3, 9, and 11 form one set and that the other sets are  $(2, 4, 10, 12)$ ,  $(5, 7, 13, 15)$ , and  $(6, 8, 14, 16)$ . Thus four collecting lines are needed.

In acquiring a signal, the switching control circuit samples the lens beams in sequence. It can be shown that if the pilot signal is within the area defined by a square of four lens beams, and if the side lobes of the lens beams are suppressed to the proper levels, each of the four highest pilot signals of the entire system will appear on different collecting lines and the four associated lens beams will form a square.

The next step is to combine the outputs of the collecting lines in the proper ratios to form the desired system beam in the direction of the incoming pilot signal, to provide tracking signals, and to split off the information channel. This is done by the electronic subsystem. The electronic subsystem is independent of the gain of the array and one electronic subsystem is needed per system beam formed. The electronic subsystem furnishes the inputs that control the switching circuitry for the associated signal collection system.

The four output signals from the signal collection system, which have been filtered to remove all but the signals associated with the desired pilot frequency, are combined together in the electronic power divider in proportion to their amplitudes to form a sum signal. The electronic power divider is a variable two-level hybrid network that also forms difference signals for tracking the pilot signal in two angular coordinates. The action is similar to a four-horn amplitude-amplitude monopulse system with a steerable electrical boresight axis. The sum signal goes to a diplexer where a narrow-band portion is split off at the pilot frequency to be used as a reference in the tracking

system. In a receiving electronic subsystem, the diplexer also splits off the wide-band data signal that goes to the transponder. A transmitted signal is applied to the electronic power divider through the diplexer.

The final building block is the transponder. The transponder is independent of the array gain desired (but, of course, is dependent on the ERP needed). One transponder is needed for each pair of system beams formed, i.e., for each channel; thus two would be required for the ATS-4 system. The wide-band information signal coming from a receive electronic subsystem is down converted through an i-f amplifier that gives a large gain and establishes the information bandwidth of the system. The information signal is then up-converted by mixing the information signal with a local oscillator signal of r-f frequency. The upper sideband at the output of the up-converter would then be passed by a transmit filter to the input of a traveling wave tube amplifier, raising the signal to the level required for transmission. The filters in the collection system admit the transmitted signal and the pilot signal. The filter in the transponder blocks out the pilot signal frequency associated with the direction in which the beam will be transmitted. If this did not happen, the transmitted signal would lock the transmitted beam in the direction of the pilot signal when first acquired.

The characteristics of these building blocks are summarized in Table 6-30.

Table 6-30

# SYSTEM BUILDING BLOCKS

Building Block	Depends on Array Gain	Number Required For 4 Beams
Beam-Forming Lens	Yes	1
Collection System	Yes	4
Electronic Subsystem	No	4
Transponder	No	2



The signals are separated by the different frequencies associated with each system beam pilot signal. The beam-forming lens must have a bandwidth that is four times the r-f bandwidth of a signal plus allowance for guard bands; this was discussed in the previous section. Each of the 256 outputs of the beam-forming lens is connected to four collection systems through four switches. The junction bandwidth requires some care in design but is not a real problem. When any switch is open (breaking the circuit) it must reflect the proper impedance (such as an open circuit in shunt) to the other three beam circuits; since lines are short, this is not a problem. The difficulty occurs when a switch is closed; then the filter in that circuit must reflect the proper impedance to the other three circuits. Admittedly, the proper location for the filter is right next to the switch, but this would require 256 filters per collection system instead of four, increasing the weight. Instead, it will be necessary to carefully design the stop impedance of the filters and perhaps to design the collection systems for the total array bandwidth so that the filter impedance will be properly reflected to the junction. The key principle is short, equal transmission lines and parallel branches.

The system described performs the automatic steering required by the ATS-4 experiment. There are some interesting special features that could be incorporated if desired. For example, the automatic tracking could be disabled on command and the beam may be pointed by a command signal. This would be useful in the ATS-4 experiment to compare pilot signal operation with command signal operation. It might also be advantageous to have the transmitting ground station direct the retransmission from the satellite; the ground receiving station would then only monitor the satellite without having to transmit a pilot signal. Another feature that might be incorporated is a beam synthesis mode. For this, more collecting lines would be required in each collecting system, but the total number of switches would not be increased. The electronic power divider and the logic circuitry would be more complex. Uses for the synthesis mode would be to

- Form a variable width beam on both transmitting and receiving to investigate the relationship of antenna beamwidth to stabilization accuracy (beamwidths broader than the minimum beamwidth from the aperture may be obtained by synthesis)

- Form a broad beam for acquisition
- Form two or more beams of reduced gain for transmission from one ground station to several widely separated receiving stations (two such receiving stations could be handled in the conventional ATS-4 configuration by parallelizing down links)
- Introduce a selective interference rejection feature into the system by producing nulls in the receiving patterns at proper angles in the sidelobe regions.

#### 6.3.6 Power Link Calculations, Weight Considerations

The communication link from a relay satellite in synchronous orbit with a high-gain, electronically self-steerable antenna system to a relatively small ground terminal will be examined in this section. To enhance the reliability of the transmission of wide-band information signals in such a link, it is desirable to obtain the maximum effective radiated power from any selected self-steerable antenna system. The effective radiated power is defined as the gain of the antenna system times the total r-f power into the antenna. Therefore, to assure efficient use of the proposed 45-db gain, lens-multiple feed, self-steerable antenna systems, the losses incurred from the output of the r-f amplifier to the output of the lens antenna become critical. Although the design objectives specify the antenna system in terms of a 45-db gain figure, the effective radiated power concept allows for tradeoffs in terms of weight, power input, and cost effectiveness of any 45-db gain self-steerable antenna system when compared with the previously considered 30-db gain antenna system.

A ground terminal having a 15-ft parabolic antenna and a transmitter power of 10 kw results in a received signal power of -115.5 dbw. This ground-station configuration was selected for comparison purposes because it has been used in evaluation of other phased-array designs. The actual proposed ground-station configuration would receive via the 40-ft-diam. antenna and transmit via a 15-ft-diam. antenna, using a 1-kw transmitter. The details of the ground station are outlined in subsection 7.1. Using a satellite antenna gain of 45 db, the signal levels throughout the electronics

Table 6-31

## LINK GAIN

Parameter	Signal Levels (dbw)	Component Gain (db)	Signal-to-Noise Ratio (db)
<u>Information Signal</u>			
Received Signal Level (Isotropic)	-115.5		
Receive Antenna Gain		45.0	
RF Losses		-1.0	
RF Switch (Insertion Loss)		-1.5	
Bandpass Filter		-2.5	
Electronic Power Divider		-2.0	
Diplexer		-2.0	
Signal Level at Mixer Input	-79.5		
Mixer Loss		-8.0	
Wide-Band IF Amplifier (Input)		+70.0	+39.5
Signal Level at Output	-17.5		
Up Converter		-10.0	
Bandpass Filter		-2.0	
Signal Level to TWT Amplifier	-29.5		
TWT Amplifier		40.0	
Signal Level at Output of TWT Amplifier	+10.5		
Diplexer		-2.0	
Electronic Power Divider		-2.0	
Bandpass Filter		-2.5	
RF Switch (Insertion Loss)		-1.5	
RF Losses		-1.0	
Signal Level at Input to Transmit Antenna	+1.5		
Effective Radiated Power	+46.5		
Transmit Antenna Gain		45.0	+18.5

Table 6-32

## WEIGHT ESTIMATES

Subsystem	Weight (lb)	
	30 db	45 db
Lens and feeds	10	100
Collecting (4)		
64 switches @ 3 oz/switch	12	
4 Collecting lines	4	
1,024 switches @ 3 oz/switch		192
4 collecting lines		16
Electronics (4)	48	
Transponder (2)	<u>16</u>	<u>16</u>
	100	394

configuration previously discussed were calculated to determine the effective radiated power of the proposed LMSC switched multiple-beam antenna system. Table 6-31 lists the signal levels and component gains for the information signal channel.

Table 6-32 presents a breakdown of the weight of the multiple-feed lens system both for 30-db and 45-db antenna gains. The weight estimate is listed in terms of four subsystems, namely, the multiple-feed lens antenna, the collection subsystem, the electronics subsystem, and the information signal transponder.

### 6.3.7 Conclusion

This section has proposed a constrained lens-switched multiple-feed antenna system that can meet the design objective of 45-db gain. For the ATS-4 experiment, a 30-db version of the LMSC switched-beam system could be flown to demonstrate the feasibility of the higher gain version. The prime consideration in the selection of the LMSC switched-beam system has been the weight penalty incurred when extrapolating other antenna systems studied from a gain of 30 db to 45 db.

## 6.4 INTERFEROMETER EXPERIMENT

The incorporation of a radio interferometer in the ATS-4 system is a stated requirement of the spacecraft work statement. As discussed in subsection 6.1, the interferometer is used in the recommended configuration to provide attitude-error signals to the fine-mode system of the orientation experiment. An analysis of the method of an interferometer/computer combination providing three-axis attitude errors using two ground stations is included in that discussion.

Other studies have been performed to determine the optimum interferometer configuration to permit meaningful experimentation to be performed with the ATS-4 spacecraft. In addition, certain problems have been defined that concern integration of the interferometer experiment into the spacecraft system.

The results of these studies are described in the following subsections.

### 6.4.1 Recommended Interferometer Configuration

The initial consideration in determining the recommended configuration was that of accuracy and ambiguity resolution. The measurement accuracy of the interferometer is a function of the antenna spacing in wavelengths. A spacing of two wavelengths will provide nonambiguous readout of attitude angle for a range of approximately 15.5 deg. This is of the order-of-magnitude of the angle subtended by the earth when viewed from synchronous altitude.

To provide 0.1-deg (attitude) accuracy with a phase measurement accuracy of  $\pm 1.0$  electrical deg, a baseline of 1.6 wavelengths is required. Since the phase-resolution error is only one component of the total error, a 16-wavelength baseline should be incorporated in addition to the two-wavelength baseline to limit the total output error to approximately 0.02 deg (three-sigma). The results of a detailed error analysis are given in Table 6-33.

Table 6-33

INTERFEROMETER ERROR SOURCES FOR A 16-WAVELENGTH BASELINE  
AND 20-DEG OFF-AXIS SOURCE

Error Source	Definition	Space Angle Errors (sec)
Finite resolution	Phase angle measurement	36
Phase jitter	For S/N = 7 db at phase detector input	46
Phase instability	IF drift	1
Multipath	Reflection from objects near antennas	0
Antenna phase pattern	Pattern asymmetry	18
Baseline misalignment	Mechanical calibration	36
Baseline instabilities	Temperature effects	1.3
Propagation effects	Corrected refraction at 2.5-deg elevation angle	1
Frequency stability	For one part/million stability	0.001
Calibration error	Residual after calibration	20

RMS = 76 arcsec = 0.021 deg

The use of a single 16-wavelength baseline in each axis with ambiguity resolution provided by the use of multiple frequencies was reviewed and discarded because of the additional ground-station complexity required.

In subsection 6.1.5, the use of the interferometer in a two-station mode was discussed. This mode requires that the interferometer be capable of processing two reference signals in either a time-shared or simultaneous manner. The high-accuracy (fine) control system will have the capability of processing the interferometer direction cosine outputs to provide pitch, roll, and yaw error signals. It is estimated that the fine-control system will require an attitude-error sampling rate of 5 samples per sec. Because of the need for this sampling rate and the requirement for interferometer data smoothing, it would appear more feasible to provide for operation of the two ground stations on separate frequencies with continuous analog processing of the two signals with periodic (5 samples per sec) analog-to-digital output conversion.

The interferometer-control system interface must also provide for interferometer operation in a single-station mode. This mode could be used either in a null-pointing (orientation of the spacecraft yaw axis at the radiating ground station) manner or in an offset-pointing mode (where the spacecraft is pointed at a passive ground location that is remote from the radiating station). It should be noted that this mode of operation can provide only pitch and roll error signals; as mentioned in subsection 6.1.5, the integrated yaw-gyro rate output would be used as a yaw reference.

To determine the effects on performance of the interferometer and the control system, provisions should be included for varying the interferometer output smoothing times. By varying these time constants, the optimum smoothing time can be determined for use of the interferometer as an attitude sensor for a synchronous satellite.

Interferometer reference signals are generated by a beacon transmitter provided for this purpose at each ATS-4 ground station. The selected frequency of operation is 5 GHz, which is separated in frequency from other vehicle radiations. A 1-kw transmitter and a 10-ft-diam. parabolic antenna provide the required beacon signal. This radiated power provides a 6.5-db carrier-to-noise ratio with a 1-MHz IF bandwidth

and 8-db noise figure. Details of the ground equipment and link-gain calculations are given in Section 7. The ground system utilizes a fixed antenna that must be positioned in angle to within  $\pm 0.4$  deg. Vehicle antenna operation is possible with an orientation of  $\pm 30$  deg.

Provisions for encoding of the reference signals and corresponding decoding by the interferometer should be included to permit discrimination against interfering radiations.

The critical design parameters for the ATS-4 interferometer are given in Table 6-34.

Table 6-34

ATS-4 INTERFEROMETER CRITICAL DESIGN PARAMETERS

Item	Description
Operating Frequency	5 GHz, Two Channels Separated by $> 10$ MHz
Baseline Lengths	$2\lambda$ , $16\lambda$ for Each Axis
Output Characteristics	Two Direction Cosines per Channel 8-bit Digital Format, 5 Samples per Sec Output Capability with Single-Channel Input
Accuracy	$\pm 0.02$ deg Equivalent Direction Cosine Error
Antenna Beamwidth	35 deg
Weight	40 lb, maximum
Input Power	15 w, maximum

#### 6.4.2 Interferometer Experiment Interfaces

The interferometer has been chosen as the attitude-control system reference for use when high pointing accuracy ( $\pm 0.1$  deg) is required. For this reason, the mechanical alignment of the interferometer to the spacecraft reference axes must be accomplished to a high degree of precision (20 sec of arc). The relative alignment of the interferometer can be calibrated during the orbital phase by the spacecraft primary attitude



reference, i.e., the star-field sensor (see subsection 6.1.8). By use of this method of inflight calibration, deviations from the prelaunch alignment calibration introduced by booster environment, thermal deflections, and structural aging effects can be detected and evaluated.

Because interferometer accuracy is dependent on precise matching of the phase patterns of the antennas located on a common baseline, care must be taken in antenna installation design to prevent asymmetric pattern distortion. Techniques for providing this protection include isolation of the interferometer antennas from other antennas to the maximum extent possible, elimination of structural RF resonances near the interferometer operating frequency, elimination of structural reflections, and provision of a symmetrical and similar ground-plane configuration for each antenna.

Because of potential deterioration in accuracy by electromagnetic interference, rigid EMI control procedures must be imposed upon the design, installation, and testing of the interferometer and spacecraft. Isolation of the interferometer by means of filtering, harness shielding, and proper bonding and grounding of the equipment must be incorporated to eliminate the interference effects of the various experiment and spacecraft equipments.

## 6.5 EXPERIMENT PLAN

A preliminary orbital test plan was developed to provide ground rules for the spacecraft studies, and particularly for the ground facility plan. Further definition of the experiments as they are developed will be necessary for the next iteration. The plan specifies the spacecraft operating modes, a possible test sequence, and a specific set of measurements for each experiment.

### 6.5.1 Operating Modes

Test. During the test mode, the spacecraft will be in continuous, two-way communication with Rosman and, through Rosman, with the Mission Control Center at GSFC. The spacecraft-Rosman links will be maintained through the spacecraft TT&C subsystem, employing antennas and electronic equipment separate from the experiments. Command test signals and range/range-rate signals (periodically) will be transmitted to the spacecraft; telemetry, test signals, and range/range-rate signals will be received.

Rosman will compute orbital elements, stationkeeping or station-changing requirements, will reduce test data and telemetry, and will transmit essential data to GSFC.

Interrupted. There will be instances when ground-station operation will be interrupted, either because of equipment failure or because of other satellite-support tasks. During these intervals, it should be possible to keep the spacecraft stabilized and all equipment operating without ground assistance so that testing can be resumed without elaborate reacquisition.

Quiescent. When ground equipment is shut down for longer periods (several days or more), either as a part of the planned schedule or to accommodate major changes in equipment, it would be desirable to deactivate the spacecraft to reduce radio interference and to conserve expendables. During these periods, the satellite should revert to a coarse attitude-control system, operating independently of the ground. With proper preparation, orbital position drift would be small and predictable.

Emergency telemetry and command receivers would remain active to permit reacquisition to provide warning of out-of-tolerance conditions.

Transfer. It may be desirable to transfer control to a ground station other than Rosman for certain experiments. The design should permit this with minimum disturbance to the spacecraft.

Failure. The equipment arrangement and test planning must allow useful data to be obtained even if some equipment fails. Table 6-35 shows the effect of the major experiments of one-at-a-time failures of spacecraft equipment items. A cross-hatched block indicates that a failure of a component affects the conduct of an experiment. Except for one-time events, almost complete independence has been achieved.

#### 6.5.2 Orbit Injection

Injection should be well within view of an appropriate ground station so that events can be telemetered, emergency commands sent in the event of sequencer failure, and the initial drift rate determined.

#### 6.5.3 Deployment

Deployment of solar arrays and antennas should take place immediately after injection and should be telemetered and perhaps monitored with a TV camera. For highest reliability, the deployment sequence should not involve serial events.

#### 6.5.4 Operating Checks

A series of functional operating checks should be made on sensors, thrusters, receivers, transmitters, and experimental antennas (plus secondary experiments).

Table 6-35

## EFFECTS OF EQUIPMENT FAILURE ON MAJOR EXPERIMENTS

Major Components	Experiments			
	Orientation	Parabola	Phased-Array	Interferometer
Parabola Deployment <sup>(a)</sup>				
Phased-Array Deployment <sup>(a)</sup>				
Solar-Array <sub>1</sub> Deployment <sup>(a)</sup>				
Solar-Array <sub>2</sub> Deployment <sup>(a)</sup>				
Phased-Array Electronics				
Interferometer Electronics				
Horizon Sensor				
Gyro Package				
Autopilot Electronics				
Adaptive Autopilot				
Resistance Jets				
Ion Jets				
Solar-Array Drive <sub>1</sub>				
Solar-Array Drive <sub>2</sub>				
Regulator <sub>1</sub>				
Regulator <sub>2</sub>				
Battery				
Wideband Receivers				
Wideband Transmitters				
UHF Transponder				
VHF Transponder				
Hi-rate Telemeter				
Lo-rate Telemeter				
Command Decoder <sub>1</sub>				
Command Decoder <sub>2</sub>				

(a) One-time events.

#### 6.5.5 Parabola Contour Measurements

Optical measurements of the parabola and feed system should be conducted as follows:

- Measure contour at approximately 3-hr intervals for 24 hr to evaluate thermal effects.
- Measure critical points while attitude thrusters are operating.
- Measure critical points while stationkeeping thrusters are operating.

#### 6.5.6 Interferometer Tests

For this plan, it is assumed that three kinds of attitude sensors are available, namely, calibration sensor (starfield reader), primary sensor (interferometer), and secondary sensor (horizon sensors). Interferometer tests should be conducted as follows:

- Calibrate secondary sensors.
- Calibration should be repeated over a 24-hr period to evaluate thermal distortions and effect of sun aspect.
- Calibrate primary sensors.
- Measure transfer characteristic of primary sensor.
- Verify accuracy of command biases in sensor signal.
- Demonstrate ability of interferometer to provide position fixes on selected ground transmitters.

#### 6.5.7 Orientation-Control-System Tests

The following procedures should be followed in testing the orientation-control system:

- Using the primary attitude sensor as a reference, verify the ability of the orientation-control system to maintain an accurate orientation.
- Measure thruster fuel/power consumption, duty cycle, and attitude error as a function of deadband settings.
- For optimum deadband setting, monitor thruster performance and attitude error over a 24-hr period.

- Determine effect of stationkeeping propulsion on attitude error.
- Determine time to reduce errors to tolerance after change in attitude of up to 17 deg.
- Measure attitude error when responding to a commanded rate of up to  $10^{-2}$  rad/min.
- Repeat for the secondary (baseline) orientation-control system.
- Analyze attitude and stationkeeping thruster operation to validate assumptions regarding perturbing forces.

#### 6.5.8 Parabolic Antenna Tests

The following tests should be accomplished:

- Evaluate the electrical performance of the antenna system and verify by RF power measurements the ability of the orientation-control system to direct the antenna beam.
- Measure antenna gain, boresight direction, and beamwidth for each specified frequency by angular displacement of satellite platform.
- At highest frequency, determine stability of gain and pointing direction with respect to thermal effects, attitude-thruster torques, and station-keeping forces.
- Verify ability of the system to point at fixed targets and to "command-track" moving targets by direct measurement of signal strength in the communication links.

#### 6.5.9 Phased-Array Antenna Tests

The test plan for this antenna will depend on whether pilot tone control, commands, or both are used for beam pointing. For the command system, the following tests should be performed:

- Measure gain, boresight direction, and beamwidth of each transmit and receive beam by angular displacement of satellite platform.

- Measure interaction and cross-talk among beams.
- When commanded, demonstrate simultaneous capability on four beams to four ground stations.
- Show ability to maintain required gain when "command-tracking" a moving target.
- Demonstrate ability to maintain operation by means of a ground-command loop during attitude oscillations such as might occur with a gravity-gradient system.
- Determine limitation on a fast-scan operational mode for possible application to readout of ground or airborne sensors.

For the pilot-tone system, the following tests apply:

- Verify antenna gain, boresight direction, and beamwidth of each transmit and receive beam by off-setting the pilot-tone direction, using a number of separated ground transmitters, or using a pilot-tone transmitter in an aircraft.
- Demonstrate simultaneous transmission and reception on four beams under control of pilot tones.
- Evaluate susceptibility of pilot tones to capture by unintentional interfacing sources.
- Demonstrate ability to maintain communications during angular oscillations of satellite platform.

#### 6.5.10 Secondary Experiments

No secondary experiments are assigned.

#### 6.5.11 Operating Demonstrations

After all the basic engineering data have been obtained, it would be useful to run communication experiments between land stations, ships, aircraft, and satellites to evaluate

the reliability, flexibility, and limitations of the ATS-4 techniques. These experiments might continue intermittently during the life of the vehicle.

In general, three test methods might be used to verify lifetime: extrapolation of short-term testing, full-term continuous operation, and full-term intermittent operation. These are not uniformly effective in evaluating the four factors that may limit life: depletion of expendables, wearout, environmental degradation, and random failure. Table 6-36 indicates which factors may be evaluated by the various test methods.

Table 6-36  
RESULTS OF TEST METHODS

Test Method	Depletion	Wearout	Environmental Degradation	Random Failure
Extrapolation of Short-Term Tests	Yes	No	Not reliable	Not Reliable
Full-Term, Continuous Operation	Yes	Yes	Yes	Yes
Full-Term, Intermittent Operation	Yes	Possible	Yes	Possible

#### 6.5.12 Preliminary Test Schedule

Figure 6-76 shows the preliminary schedule for the orbital test plan.



Item	1 Mo	1 Mo	1 Mo	3 Mo	18 Mo
Injection -----▼					
Deployment -----▼					
Drift to Station-----▶					
Operating Checks-----■					
Contour Measurements--■					
Interferometer-----■					
Orientation -----■					
Parabola -----■					
Phased Array-----■					
Secondary Experiments-					
Operating Demonstration					
Life Tests-----■					

Fig. 6-76 Preliminary Test Schedule

## Section 7

### GROUND SYSTEM DEFINITION

#### 7.1 HARDWARE REQUIREMENTS

Ground support requirements for the ATS-4 program can be satisfied by existing STADAN stations. Some ground station augmentation is required to support the various RF experiments. All ground augmentation can be accomplished using existing equipment designs with the exception of VHF and low UHF antenna feed designs for the 85-ft ground antenna. The ground stations utilized include Tananarive for initial tracking support, Rosman for primary support, and secondary support from Mojave and a mobile station located at Toowoomba, Australia. Primary TT&C is via a 4 to 6 GHz system and backup TT&C via a VHF system. S-band, C-band, and X-band transmitters are required for experiment signal sources. New frequency down converters enable the use of existing receiving systems.

The RF interface with the ATS-4 vehicle requires ten RF links. These are shown in Fig. 7-1. The vehicle TT&C equipment design has been configured to utilize the existing capabilities of the ATS ground stations as much as possible. The primary TT&C link operates at 4 GHz on the down link and 6 GHz on the up link. Existing ATS ground station transmitting and receiving equipment operating at VHF (148-MHz up link and 136-MHz down link) are compatible with existing ATS and other ground stations. Tracking using the range and range rate system may be performed via the primary or backup links using existing equipment. Command encoding is performed by the tone system contained in the command console. Backup telemetry at the low data rate can be processed by the existing data handling equipment. The primary high rate telemetry system will require the addition of a complete standard PCM ground station.

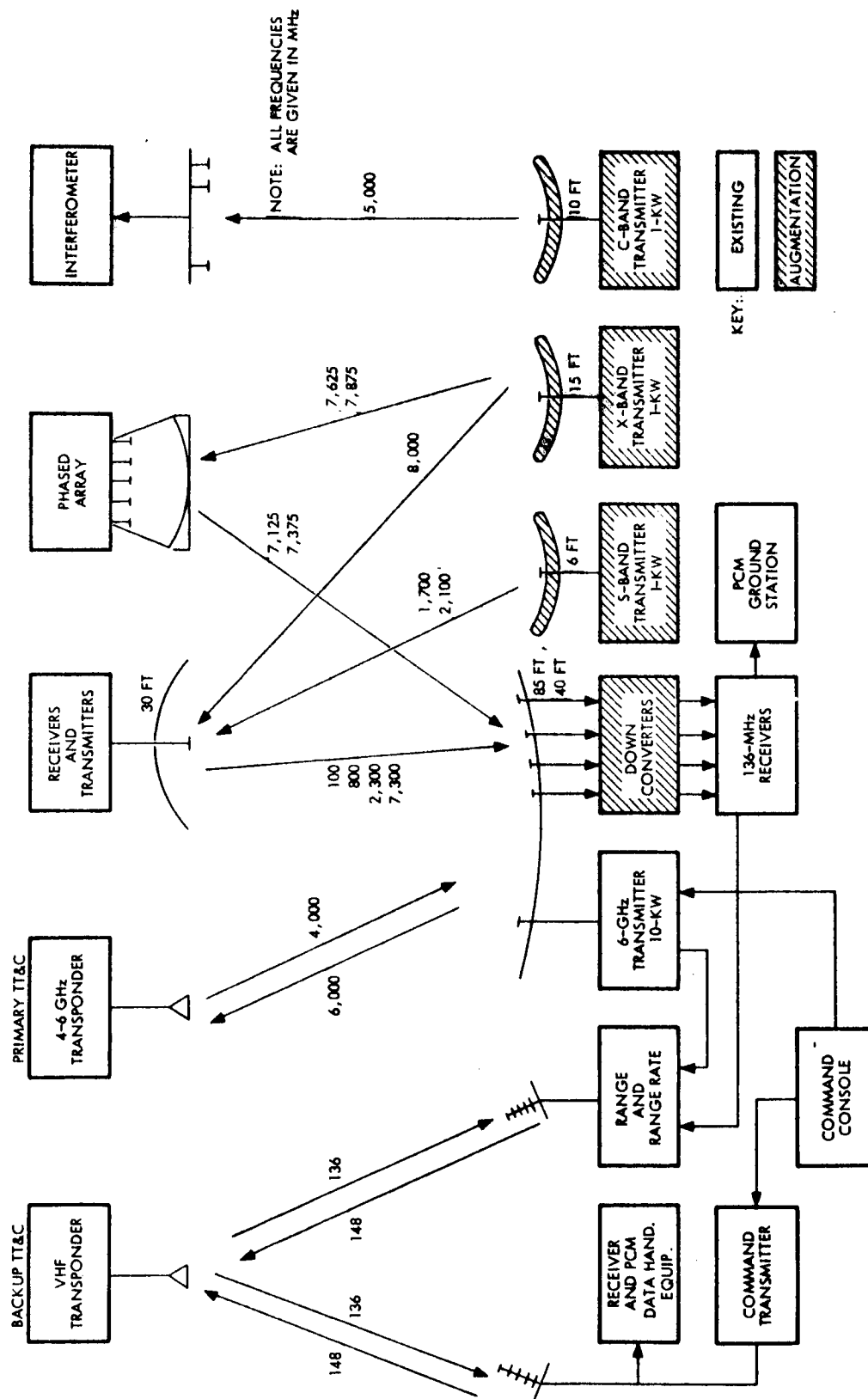


Fig. 7-1 Ground-Vehicle Interface

Four down-link frequencies are involved in the 30-ft parabolic antenna experiment that are not compatible with the existing Rosman 85-ft diameter antenna receiving system. The present system operates multiband with multiple feeds and parametric amplifier down converters. Each frequency is down converted to 136 MHz and presented to a bank of 136-MHz receivers. The limited tuning range of the paramp down converters will not permit their use on the required ATS-4 frequencies. Additional paramp converters will permit operation at 100 MHz, 800 MHz, 2,300 MHz, and 7,300 MHz for the 30-ft parabolic antenna experiment. Two additional units are required for reception of phased array channels at 7,125 MHz and 7,375 MHz.

Three ground transmitter systems are required for up links associated with the vehicle experiments. An S-band transmitter of 1-kw output power together with a 6-ft parabolic fixed antenna provides for transmission at 1,700 MHz and 2,100 MHz to the vehicle 30-ft parabolic antenna experiment. The 8,000-MHz transmission is provided by an X-band transmitter with a 15-ft parabolic antenna. This unit must also radiate data signals for the phased-array experiments at 7,625 MHz and 7,875 MHz. The third transmitter is the 1-kw beacon signal with a 10-ft parabolic antenna used with the interferometer experiment. The link calculations for the 30-ft parabola antenna experiment are given in Table 6-27. The interferometer experiment link calculation is shown in Table 7-1. Tables 7-2 and 7-3 show the up- and down-link calculation for the phased array. Figure 7-2 shows the equipment configuration required for the three additional transmitters.

## 7.2 SOFTWARE REQUIREMENTS

The major software requirements are as follows:

- (1) Ephemeris generation
- (2) Command generation for housekeeping, stationkeeping, etc.
- (3) Diagnostic telemetry processing (power, propulsion, etc.)
- (4) Experiment performance telemetry processing
- (5) Orientation control command generation for 30-ft antenna pattern measurements

- (6) Antenna pattern data processing using vehicle orientation, signal levels, antenna deformation, etc.
- (7) Phased array pointing command generation using ephemeris, orientation, ground target location, etc.
- (8) Interferometer command generation for null and off null pointing control
- (9) Processing star field scanner data for orientation calibration
- (10) Processing data from 30-ft antenna contour measurements as a function of solar illumination angle, thrust, time, etc.

Table 7-1  
INTERFEROMETER LINK CALCULATION

Link Segment	Gain	Loss
Ground		
Power (1 kw)	30 dbw	2 db
Line Loss		
Antenna Gain (10-ft diam)	41.5	
Pointing Loss ( $\pm 0.4$ deg)		1
Propagation Path		
Free Space		199
Polarization		3
Vehicle		
Antenna Gain (60 deg beamwidth)	8.5	
Line loss		1
Pointing Loss ( $\pm 30$ deg)		3
Total	80 dbw	-209 db
Receiver Signal Power	-129 dbw	
Noise Power (BW = 1 MHz, NF = 8 db)	-135.5 dbw	
C/N	6.5 db	

Table 7-2  
PHASED-ARRAY UP LINK

Link Segment	Gain	Loss
Ground		
Transmitter Power (1 kw)	30 dbw	
Line Loss		2 db
Antenna Gain (15-ft diam.)	48.5	
Pointing Loss ( $\pm 0.3$ deg)		3
Propagation Path		
Free Space		202
Polarization		3
Vehicle		
Antenna Gain	30	
Fine Loss		9
Total	<u>108.5 dbw</u>	<u>-219 db</u>
Receiver Signal Power	-110.5 dbw	
KTBN (B = 10Mc, NF = 10 db)	-123.7 dbw	
Threshold	<u>12 db</u>	
Sensitivity	-111.7 dbw	
Margin	+1.2 db	

Table 7-3  
PHASED-ARRAY DOWN LINK

Link Segment	Gain	Loss
Vehicle		
Transmitter Power (10 w)	10 dbw	
Line Loss		9 db
Antenna Gain	30	
Propagation Path		
Free Space		202
Polarization		3
Ground		
Antenna Gain (40-ft diam.)	57	
Line Loss		2
Pointing Loss ( $\pm 0.11$ deg)		3
Total	<u>97 dbw</u>	<u>219 db</u>
Received Signal Power	-122 dbw	
KTBN ( $B = 10$ Mc, $NF = 4.5$ db)	-129.2 dbw	
Threshold	<u>6 db</u>	
Sensitivity	-123.2 dbw	
Margin	+1.2 db	

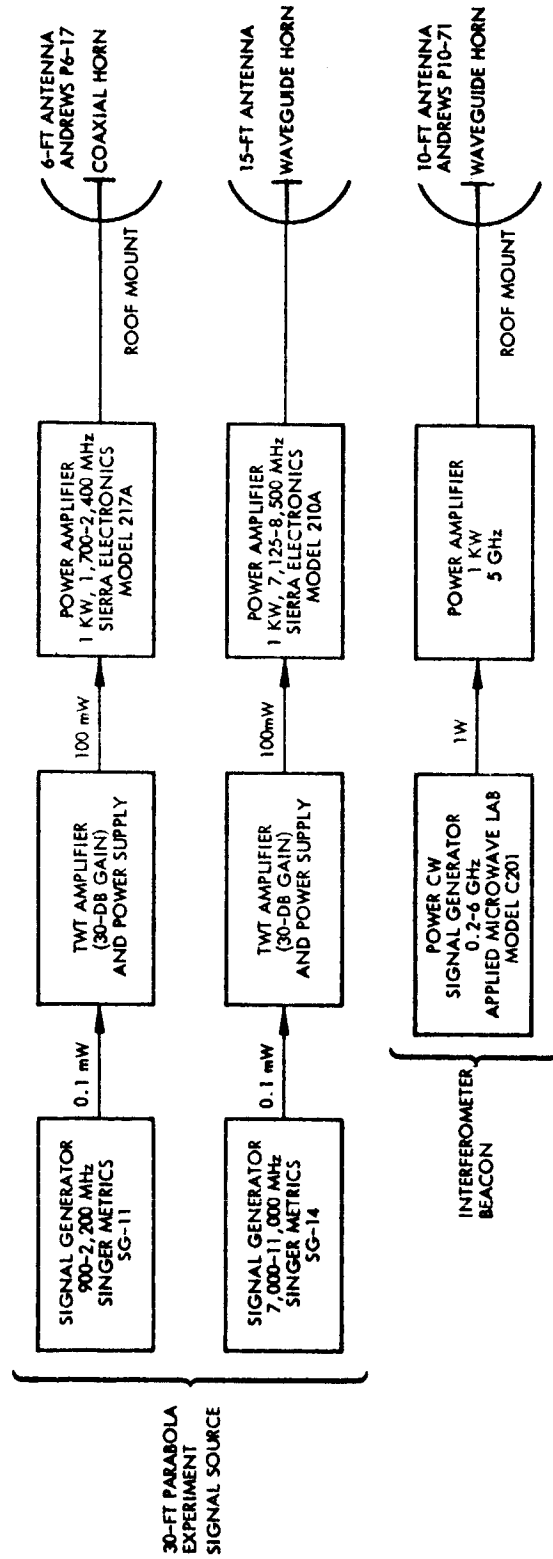


Fig. 7-2 Ground Transmitter Configuration



Ephemeris generation, item (1), is derived from range and range rate measurements and provides inputs for injection error corrections, stationkeeping corrections, and geometry data for antenna pointing command generation.

Command generation, item (2), involves formatting and time sequencing those commands required to maintain all vehicle subsystems. These commands include telemetry and tracking readout control, mode selection and redundant equipment selection, power regulation control, and propulsion control.

Diagnostic telemetry processing, item (3), will develop power profiles, propulsion life capabilities, performance vs. time for various subsystems, and failure diagnostic analysis.

Experiment performance telemetry processing, item (4), will involve performance parametric analysis of each experiment, equipment characteristics vs. time, and performance degradation vs. time.

Item (5) will provide the programmed commands required to drive the vehicle in a controlled scan pattern for link gain measurements and antenna pattern development.

Item (6) will reduce the collected antenna pattern measurement data using the measured vehicle orientation, normalized signal levels, effects of antenna deformations due to thermal and orientation control effects.

Item (7) will derive the required commands for phased array pointing control. This involves geometry considerations including ephemeris, orientation, ground target location, etc.

Interferometer command generation, item (8), involves similar geometry considerations covered by item (7) and will include generation of required phase angle commands for precise pointing control for off-null pointing. Null pointing will be provided by mode change commands.

Item (9) involves processing collected data from the star field scanner for calibrating the various orientation control devices. These computations involve star table inputs for geometry calculations and development of bias errors for the horizon sensor and interferometer.

Item (10) involves processing the 30-ft parabolic antenna pattern measurements developed under item (6). These data will generate a profile of antenna variations of gain, polarization, beam bending, etc., that will result from variations in solar illumination angle, thrust levels, and other system parameter as a function of vehicle life.

### 7.3 SYSTEM OPERATION

Ground station support begins during the ascent phase. Initial vehicle acquisition is accomplished by a spatial and frequency search and lock-on of the VHF telemetry transmission. This acquisition is aided by predetermined acquisition angle messages and expected dispersions. A wide beamwidth ground antenna of 9 deg at the 1-db point facilitates early acquisition. Ascent telemetry will monitor vehicle system status and command executions performed by a preprogrammed timer. An electronic DI/AN timer is used for the preprogrammed ascent functions. In the event of timer failure, the same command functions can be issued via the VHF command system. The normal operating mode will involve monitoring the timed sequence and issuing a real-time command a short time after the expected timed event. Kick-motor burn is not time critical so this event may be backed up by a real-time command.

After synchronous altitude is reached and the vehicle has been pitched over and placed in the normal operating orientation, the directive 4- to 6-GHz horn antenna permits transfer of TT&G operation from the VHF backup system. A final timer command applies power to the primary 4- to 6-GHz TT&G system. A real-time command is sent which turns off the backup VHF telemeter and places the VHF command system in standby or minimal power mode. The wide-band telemeter is synchronized at this time and deployment and initial operation of the various extendable devices can be monitored.

Normal system operation will be conducted with the 6-GHz command receiver energized at all times. The 4-GHz primary telemetry will be commanded on and off at the required experiment times.

PCM telemetry decommutation will be performed at the ground station and critical vehicle health points will be monitored. The PCM ground station provides storage of expected parameter values and indicates selected out-of-tolerance points. Final telemetry data processing is performed off-line where critical system monitor points are determined. These points are monitored and appropriate corrective command action taken to optimize vehicle life.

Tracking operations will not start until after injection into synchronous orbit. This injection will not be completely synchronous but will contain a planned drift rate where tracking will occur until the final orbit correction. Initial tracking will continue for 5 hr until it is established that an acceptable drift rate has been achieved. Subsequent tracking will refine the ephemeris and velocity vector so that final parking can occur. After orbit correction and each following stationkeeping correction, tracking data will be collected to verify that a proper parking orbit was obtained.

#### 7.4 EXISTING STATIONS/EQUIPMENTS EMPLOYED

Initial tracking support is provided by existing range and range rate equipment at Tananarive, Madagascar. Normal on-orbit support is provided by three STANDAN stations: Rosman Station at Rosman, North Carolina, which serves as the primary control and data collection station; Mojave Station at Barstow, California; and a mobile station at Toowoomba, Australia.

On-orbit tracking is performed by the Rosman station using a primary system consisting of an 85-ft dish with range and range rate via 6 GHz on the up link and 4 GHz on the down link. Backup tracking is via a range and range rate antenna operating at 148 MHz on the up link and 136 MHz on the down link. Tracking recording uses a Sanborn 350 and TE-404 X-Y data punch.

Primary telemetry reception is via the 85-ft dish and 4-GHz link using the Rosman station. Backup telemetry via the 136-MHz link is received at Rosman on the 136-MHz SATAN antenna and via an eight-element yagi at Mojave. GD/E telemetry receivers are used with Electrac 215 tracking filters and demodulators followed by a Electrac 215C diversity combiner. Post detection recording is performed using an Ampex FR-600. Backup/ascent telemetry is processed by existing PCM data handling equipment. Graphic outputs are provided using the Sanborn 850 and Honeywell Visicorder Model 906-C. Figure 7-3 illustrates the backup/ascent telemetry configuration. Augmentation is required for the primary telemetry decommutation.

Command encoding is performed with the Consolidated Systems Corporation tone command system contained in existing command consoles. Command transmission at Mojave uses the 242G, 2.5-kw VHF transmitter and 148-MHz yagi. At Rosman, GE 5kw or 1TA 120H transmitters are used with disk-on-rod antennas mounted on the 85-ft dish and with the SATAN antenna. Primary command transmission is via the 6-GHz link and 85-ft dish.

Existing power generating equipment and the NASCOM communications network will satisfy ATS-4 requirements.

## 7.5 NEW STATIONS/EQUIPMENTS REQUIRED

No new stations are required for ATS-4 vehicle support. However, one ground support requirement involves the demonstrated 0.5-deg tracking accuracy of the vehicle 30-ft parabolic antenna when under ground pointing control. The required 0.1-deg orientation accuracy can be demonstrated by pointing at a fixed ground station, allowing an orientation control system settling time, and calibrating the system using the star-field scanner. A dynamic problem is involved in active tracking by ground control. Possible operating modes include tracking moving targets such as ships, aircraft, ballistic missiles, and orbiting satellites. One possibility that serves as an excellent demonstration is tracking a low orbiting satellite and relaying telemetry transmissions. This demonstration is desirable for a number of reasons.

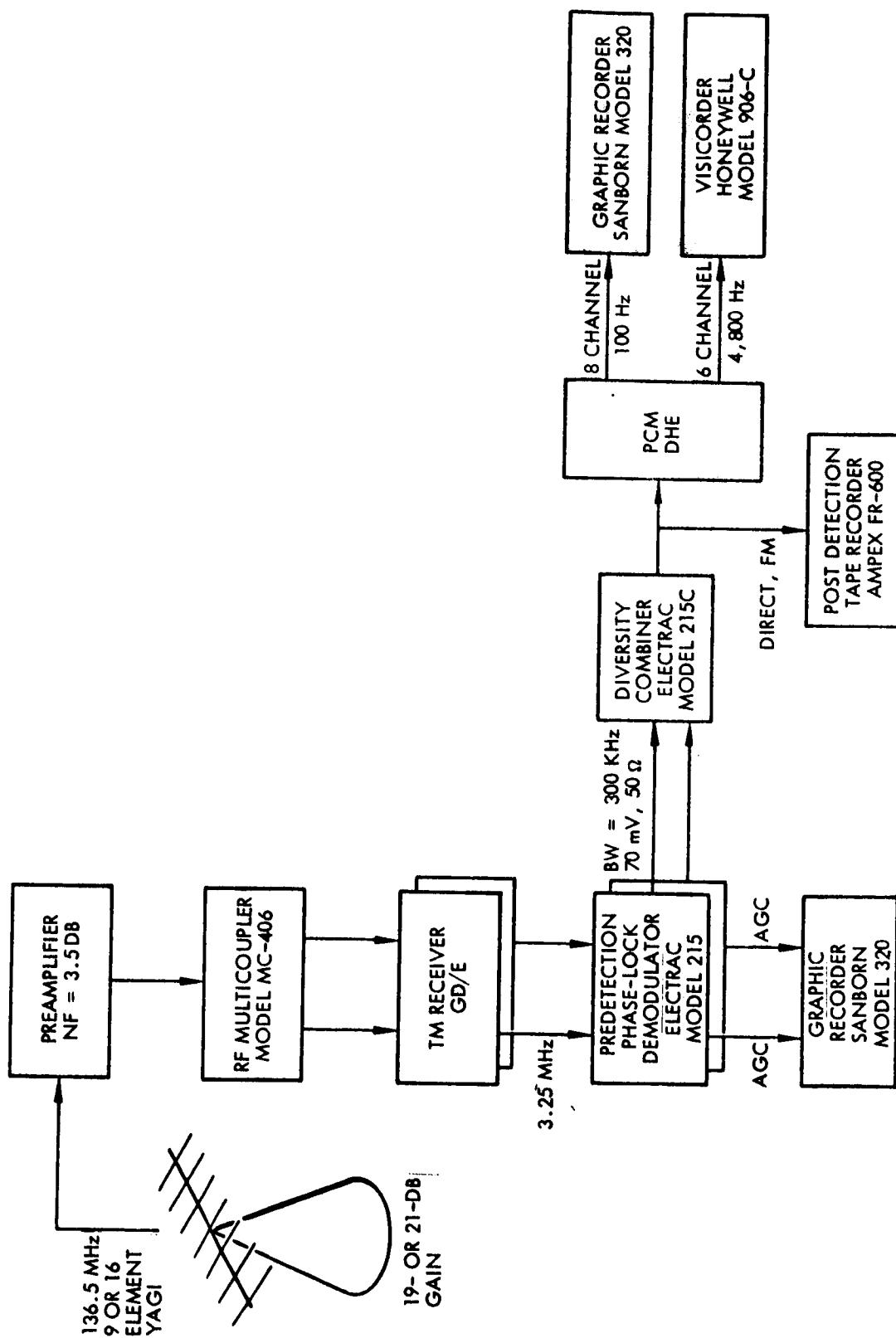


Fig. 7-3 Backup-Ascent Telemetry Configuration

It provides a moving target with a high enough angular rate so that the target would move out of the vehicle antenna beamwidth fast enough to demonstrate a signal level change for convenient ground operator command response. Satellite telemetry transmissions are in the 1,700-MHz range and can be compatible with the ATS-4 receivers. The 30-ft antenna beamwidth at 1,700 MHz is 1.35 deg and a nadir-pass satellite would traverse this beamwidth in 1.8 min. At this rate, ground commands can be issued to bias the vehicle orientation for antenna steering. For this application, one of the ten frequencies included in the 1,700 MHz receiver range would be selected to accept signals from the selected target satellite.

Some new equipment is required at the three ATS-4 stations. This equipment includes S-band, C-band, and X-band transmitters; frequency down converters for the receiving system; and a standard PCM ground station. New equipment augmentation was indicated in Fig. 7-2. These equipments include:

- S-Band Signal Source

- Signal Generator, Singer Metrics SG-11

- TWT Amplifier and Power Supplies

- Power Amplifier, Sierra Electronics, Model 217A

- 6-ft Parabolic Antenna, Andrews P6-17

- Coaxial Horn Feed

- Fixed Roof Mount

- X-Band Signal Source

- Signal Generator, Singer Metrics SG-14

- TWT Amplifier and Power Supplies

- Power Amplifier, Sierra Electronics, Model 210A

- 15-ft Parabolic Antenna

- Waveguide Horn Feed

- Fixed Roof Mount

- Data Modulator (phased-array experiment)